Diss. ETH No. 23648

Terahertz Spectroscopy of Two-Dimensional Nanostructures

A thesis submitted to attain the degree of

DOCTOR OF SCIENCES of ETH ZURICH

(Dr. sc. ETH Zürich)

presented by

FEDERICO VALMORRA

Dottore magistrale in Fisica, Alma Mater Studiorum
Università di Bologna (Bologna, Italy)

born on December 16, 1986
citizen of Italy

accepted on the recommendation of

Prof. Dr. Jérôme Faist, examiner
Prof. Dr. Thomas Ihn, co-examiner
Dr. Giacomo Scalari, co-examiner
Prof. Dr. Jérôme Tignon, co-examiner
Prof. Dr. Alessandro Tredicucci, co-examiner

2016

Summary

The terahertz energy range is delimited, on the low energy side, by high-frequency electronics and, on the high energy side, by long-wavelength optics and photonics. The THz-range then inherits specific features form both sides, making it very appealing for optoelectronics, science and technology.

This thesis deals with the spectroscopical investigation of several opto-electronical systems in the THz-frequency range. In particular, light-matter interaction is their common denominator. The different systems encompass electronic transitions, like inter-(sub-)band or Landau-level transitions in two-dimensional electron systems, and/or THz-cavities, like plasmonic waveguides or THz-split-ring resonators. The present work can be thus read following different paths.

From the point of view of basic physics, ultra-strong light-matter coupling is the main one. This relatively new regime of interaction has already been demonstrated in several different systems. In this thesis, building onto previous work on the ultra-strong coupling of the cyclotron transition in a GaAs-based 2DEG with THz-resonators, we enlarge such platform first towards a transport-based detection. To this aim, we make use of the phenomenon of microwave-induced resistance oscillations, allowing also the discussion of specific points of the proposed theories about its still unclear origin. Second, we study the interaction of graphene with the same THz-metasurface, both with and without magnetic field. When the latter system is in ultra-strong light-matter coupling, a Dicke phase transition had been predicted connected to its linear electronic dispersion.

Another important path deals with the spectroscopic investigation of the mentioned systems. The magneto spectroscopy of electronic transitions in THz-QCLs gives information on the different types of scattering present in the structure. The spectroscopy of dual metasurfaces coupled in the highly sub-wavelength near-field requires instead the discussion of optical complementarity and Babinet's principle from different angles. The spectroscopy of THz-resonators onto graphene provides more insights onto the modelling of the resonator itself.

Finally, from the point of view of optoelectronic devices, the magneto-spectroscopy of

THz-QCLs aims at providing additional information on the long-time issue of their maximum operating temperature, while graphene-based samples performed well as amplitude modulators of THz-radiation.

Sommario

L'intervallo di energie denominato "terahertz" è racchiuso, a basse energie, dall'elettronica ad alta frequenza, e, ad alte energie, dall'ottica e dalla fotonica a grande lunghezza d'onda. Per tal motivo, diverse caratteristiche dei due estremi precedenti confluiscono nella fisica del terahertz, rendendola molto interessante per l'opto-elettronica, e per la scienza e la tecnologia in generale.

Questo lavoro di tesi tratta dello studio spettroscopico di diversi sistemi opto-elettronici a frequenza terahertz. In particolare, l'interazione luce-materia è il loro comun denominatore. I diversi sistemi comprendono transizioni elettroniche, ad esempio transizioni inter-(sotto-)banda o tra livelli di Landau in gas di elettroni bidimensionali, e/o cavitá terahertz, come guide d'onda plasmoniche o risonatori a base di metamateriali. Il presente manoscritto si appresta perció ad essere letto seguendo diversi percorsi.

Dal punto di vista della fisica di base, il percorso di lettura principale segue l'accoppiamento ultra-forte tra radiazione e materia. Questo regime di interazione é relativamente nuovo ed é stato dimostrato in un certo numero di sistemi differenti. Questa tesi si fonda su lavori precedenti sull'accoppiamento ultra-forte tra la transizione di ciclotrone in gas di elettroni bidimensionali in GaAs con resonatori terahertz per ampliare il campo, prima di tutto in direzione della spettroscopia basata sul trasporto elettronico. A tal fine, verrá usato il fenomeno denominato "oscillazioni di resistenza indotte da microonde": le misure effettuate permetteranno anche la discussione di specifici problemi riguardo alla sua origine, ancora non chiara. Successivamente, la stessa metasuperficie di risonatori terahertz verrá studiata in interazione col grafene, sia in assenza sia in presenza di campo magnetico. Quando tale sistema entra nel regime di accoppiamento ultra-forte, ci si aspetta una transizione di fase di Dicke dovuta alla dispersione elettronica lineare del grafene.

Un altro percorso significativo segue lo studio spettroscopico dei sistemi menzionati. La spettroscopia in campo magnetico delle transizioni elettroniche nei laser terahertz a cascata quantica da informazioni sui diversi tipi di diffusione elettronica presenti nelle strutture. La spettroscopia di metasuperfici duali, interagenti nel campo prossimo a dis-

tanze molto più piccole della lunghezza d'onda, necessita e permette invece la discussione della complementarietà ottica e del principio di Babinet da diverse prospettive. La spettroscopia dei risonatori terahertz realizzati sul grafene fornisce informazioni sul miglior modo per modellizzare i risonatori stessi.

Infine, dal punto di vista dei dispositivi opto-elettronici, la spettroscopia in campo magnetico dei laser terahertz a cascata quantica punta a fornire informazioni per affrontare il problema persistente della massima temperatura di lavoro dei dispositivi. Invece, i dispositivi a base di grafene danno ottimi risultati in termini di modulatori d'ampiezza di radiazione terahertz.

List of publications

Parts of the present manuscript are published in the following articles:

Peer-reviewed articles - First authorships:

1. F Valmorra, G Scalari, K Ohtani, M Beck, J Faist, *InGaAs/AlInGaAs THz quantum cascade lasers operating up to 195 K in strong magnetic field*, New Journal of Physics **17** (2), 023050 (2015)

2. F Valmorra, G Scalari, C Maissen, W Fu, C Schönenberger, JW Choi, HG Park, M Beck, J Faist, *Low-bias active control of terahertz waves by coupling large-area CVD graphene to a terahertz metamaterial*, Nano Letters **13** (7), 3193-3198 (2013)

3. F Valmorra, G Scalari, C Maissen, W Fu, C Schönenberger, JW Choi, HG Park, M Beck, J Faist, *Interaction of single-layer CVD graphene with a metasurface of terahertz split-ring resonators*, SPIE OPTO, 86230S-86230S-6 (2013)

4. F Valmorra, M Bröll, S Schwaiger, N Welzel, D Heitmann, S Mendach, *Strong coupling between surface plasmon polariton and laser dye rhodamine 800*, Applied Physics Letters **99** (5), 051110 (2011)

Peer-reviewed articles - Co-authorships:

1. J Keller, GL Paravicini Bagliani, J Haase, C Maissen, F Valmorra, J Palomo, J Mangeney, J Tignon, SS Dhillon, G Scalari, J Faist *Coupling surface plasmon polariton modes to complementary THz metasurfaces tuned by inter meta-atom distance*, submitted

2. PQ Liu, IJ Luxmoore, SA Mikhailov, NA Savostianova, F Valmorra, J Faist, GR Nash, *Highly tunable hybrid metamaterials employing split-ring resonators strongly coupled to graphene surface plasmons*, Nature Communications **6**, 8969 (2015)

3. PQ Liu, F Valmorra, C Maissen, J Keller, G Scalari, J Faist, *Large-area gate-tunable terahertz plasmonic metasurfaces employing graphene based structures*, SPIE OPTO, 935707-935707-8 (2015)

4. PQ Liu, F Valmorra, C Maissen, J Faist, *Electrically tunable graphene anti-dot array terahertz plasmonic crystals exhibiting multi-band resonances*, Optica **2** (2), 135-140 (2015)

5. C Maissen, G Scalari, F Valmorra, M Beck, J Faist, S Cibella, R Leoni, C Reichl, C Charpentier, W Wegscheider, *Ultrastrong coupling in the near field of complementary split-ring resonators*, Physical Review B **90** (20), 205309 (2014)

6. G Scalari, C Maissen, S Cibella, R Leoni, P Carelli, F Valmorra, M Beck, J Faist, *Superconducting complementary metasurfaces for THz ultrastrong light-matter coupling*, New Journal of Physics **16** (3), 033005 (2014)

7. GL Paravicini-Bagliani, V Liverini, F Valmorra, G Scalari, F Gramm, J Faist, *Enhanced current injection from a quantum well to a quantum dash in magnetic field*, New Journal of Physics **16** (8), 083029 (2014)

8. IJ Luxmoore, CH Gan, PQ Liu, F Valmorra, P Li, J Faist, GR Nash, *Strong coupling in the far-infrared between graphene plasmons and the surface optical phonons of silicon dioxide*, ACS Photonics **1** (11), 1151-1155 (2014)

9. C Maissen, G Scalari, F Valmorra, C Reichl, D Schuh, W Wegscheider, M Beck, S de Liberato, D Hagenmüller, C Ciuti, J Faist, *Influence of resonator design on ultrastrong coupling between a two-dimensional electron gas and a THz metamaterial*, SPIE OPTO, 86231M-86231M-6 (2013)

International Conferences - First authorships:

1. F Valmorra, M J Süess, G Scalari, J Faist, *Extra-ordinary transmission and near-field interaction of paired dual THz-metasurfaces*, Terahertz Science, Nanotechnology and Applicaitons, Erice, Italy, 2016 Poster

2. F Valmorra, G Scalari, K Ohtani, M Beck, J Faist, *Magneto-spectroscopy of InGaAs/AlInGaAs THz Quantum Cascade Lasers*, MSS-17, Sendai, Japan, 2015 - Oral

3. F Valmorra, G Scalari, C Roessler, GL Paravicini Bagliani, T Hasler, T Ihn, K Ensslin, M Beck, J Faist, *Microwave-Induced Resistance Oscillations in split-ring-resonators-covered Hall-bars*, EP2DS-21, Sendai, Japan, 2015 - Poster

4. F Valmorra, G Scalari, K Ohtani, M Beck, J Faist, *Study in perpendicular magnetic field of the characteristics of InGaAs/AlInGaAs THz Quantum Cascade Lasers*, IQCLSW 2014, Policoro, Italy, 2014 Poster

5. F Valmorra, G Scalari, K Ohtani, M Beck, J Faist, *Study in perpendicular magnetic field of the characteristics of InGaAs/AlInGaAs THz Quantum Cascade Lasers*, ICPS 2014, Austin, Texas-USA, 2014 Oral

6. F Valmorra, G Scalari, C Maissen, W Fu, C Schönenberger, JW Choi, HG Park, M Beck, J Faist, *Interaction of single-layer CVD graphene with a metasurface of terahertz split-ring resonators*, Joint Annual Meeting of the Austrian Physical Society and the Swiss Physical Society, Linz, Austria, 2013 Oral

7. F Valmorra, G Scalari, C Maissen, W Fu, C Schönenberger, JW Choi, HG Park, M Beck, J Faist, *Interaction of single-layer CVD graphene with a metasurface of terahertz split-ring resonators*, SPIE Photonics West, OPTO Conference, San Francisco, California-USA, 2013 Oral

8. F Valmorra, G Scalari, C Maissen, W Fu, C Schönenberger, JW Choi, HG Park, M Beck, J Faist, *Interaction of graphene monolayer with the photonic modes of a TeraHertz metamaterial*, Quantum Science and Technology Conference, Ascona, Switzerland, 2012 - Poster

Acknowledgements

I am very indebted to my two PhD advisors, Prof. Jérôme Faist and Dr. Giacomo Scalari, who together guided my past five years of efforts towards this point. I am grateful that they gave me the opportunity to be part of the Quantum OptoElectronics group at ETH Zurich. In these years I could learn a lot from their experience and take advantage of their advices. In particular, I want to thank Prof. Faist for his farsight and his availability for a critical discussion on any topic, scientific and not, not to mention his openess towards student involvement in any sort of research-related activity. Second, but not less important, Dr. Scalari taught me how to deal with the labs and with experimental research and was always available to sort out and discuss any doubt that might have come up.

Dr. Beck and Dr. Ohtani were also ready to help sorting out any doubt about materials, samples and physics at any time; Mrs. Hug about administrative and financial matters.

I am also happy to have been involved into the National Centre of Competence in Research "Quantum Science and Technology" and into the European project "Graphene-On-Silicon Free Electron Laser", through which I could get to know, meet and discuss with interesting scientists from the same and neighbouring disciplines.

The group environment was also extremely important, supportive and motivating. When I joined I found a wonderful group that evolved and grew in time. I started more or less together with Curdin, Giancarlo, Christopher, Sabine and Gustavo, with whom I also shared the schedule (and related discussions) of the last months, preceded by countless moments together in the lab and outside of it.

The existing group, at the time I joned, was already powered socially and scientifically by a series of colleagues and friends I want to thank for the welcoming atmosphere and the introductions into each and every aspect of the PhD life: Alfredo, Andreas, Dana, Laurent, Fabrizio, Markus G. and Boris.

Early or later along the way many more colleagues joined, with whom I could always enjoy moments in the office or in the lab: Hanna, Cristina, Markus R., Selam, Peter, Janine, Gian Lorenzo, Lorenzo, Camille, Romain, Martin, Filippos, Matthew, Dima, Yves, Yong. There were nice moments with each of them, but It would be too long and out of topic to specifically address them here.

Finally, a thank you to Patrick and to the friends outside of the group: from other labs or outside of ETH, in Zurich and abroad, to keep me with a foot in the real world.

Last but not least, un ringraziamento alla mia famiglia che mi ha supportato anche in questa scelta.

Contents

List of Figures

List of Tables

Symbols and Abbreviations

$\hbar$	reduced Planck's constant
e	elementary charge
k_B	Boltzmann's constant
m^*	electron effective mass
m_e	free electron mass
2DEG	2-Dimensional Electron Gas
2DES	2-Dimensional Electron System
2DHG	2 Dimensional Hole Gas
CNP	Charge Neutrality Point
cSRR	complementary SRR
CVD	Chemical Vapour Deposition
DM-	Double-Metal-, referring to waveguides
dSRR	direct SRR, equivalent to SRR when not specified
EOT	Extra-ordinary Optical Transmission
FET	Field Effect Transistor
FIB	Focussed Ion Beam
FIR	Far InfraRed, synonym of THz, when meant as adjective
FTIR	Fourier-Transform InfraRed spectrometer
FWHM	Full Width at Half Maximum
LO-phonon	Longitudinal Optical-phonon
MBE	Molecular Beam Epitaxy
MIR	Mid InfraRed

MIRO	Microwave-Induced Resistance Oscillation
MPR	Magneto-Plasmon Resonance
QC-	Quantum Cascade-
QCL	Quantum Cascade Laser
QD	Quantum Dot
SdH	Shubnikov-de Haas
SEM	Scanning Electron Microscope
SP-	Single-Plasmon-, referring to waveguides
SRR	Split-Ring Resonator
TE	Transverse-Electric
TM	Transverse-Magnetic
USC	Ultra-Strong Coupling

The terahertz frequency range: general introduction and basic physical concepts

The TeraHertz (THz) region of the electro-magnetic spectrum lies indicatively between 100 GHz and 10 THz. This corresponds to wavelengths in the range 3 mm – 30 µm, energies of 0.4 meV – 41 meV and temperatures of 5 K – 480 K (cf. Fig. 0.1). This range has attracted in the last decades increasing attention for its technological potential.[1] In fact, on the one hand, THz-radiation is highly penetrating in non-metallic materials but non-ionising, while, on the other hand, several solid-state systems have characteristics and processes belonging to this energy region. Thus, THz-technology is important for spectroscopy of semiconductors, chemical compounds and biomedical samples, as well as for the investigation of carriers dynamics and for homeland security purposes.[2, 3]

On the other hand, the THz-region is of fundamental scientific importance, this being the bridge between optics and electronics as well as the energy landscape where a pletora of physical phenomena take place. While the latter point will be discussed in the next section, the first feature emerges by considering Maxwell's formulation of Ampere's circuital law

$$\nabla \times \mathbf{B} = \mu_0 \mathbf{J_{tot}},$$

the total current density $\mathbf{J_{tot}}$ being composed by charge and displacement current $\mathbf{J_c} + \mathbf{J_d}$. The first term is due to charge conduction $\mathbf{J_c} = \sigma \mathbf{E}$ and can be associated to electronics, whereas the second one is due to the oscillating dielectric polarisation as $\mathbf{J_d} = \partial \mathbf{D}/\partial t = -i\omega\epsilon\mathbf{E}$ and is related to optics. The THz frequency region is placed at the meeting point of optics and electronics, where the two current terms have comparable magnitudes. Such situation is challenging from the technological point of view because the concepts stemming from one of these fields are pushed to their limits towards the opposite one, resulting in poorer devices performances. Because of such situation, this frequency region

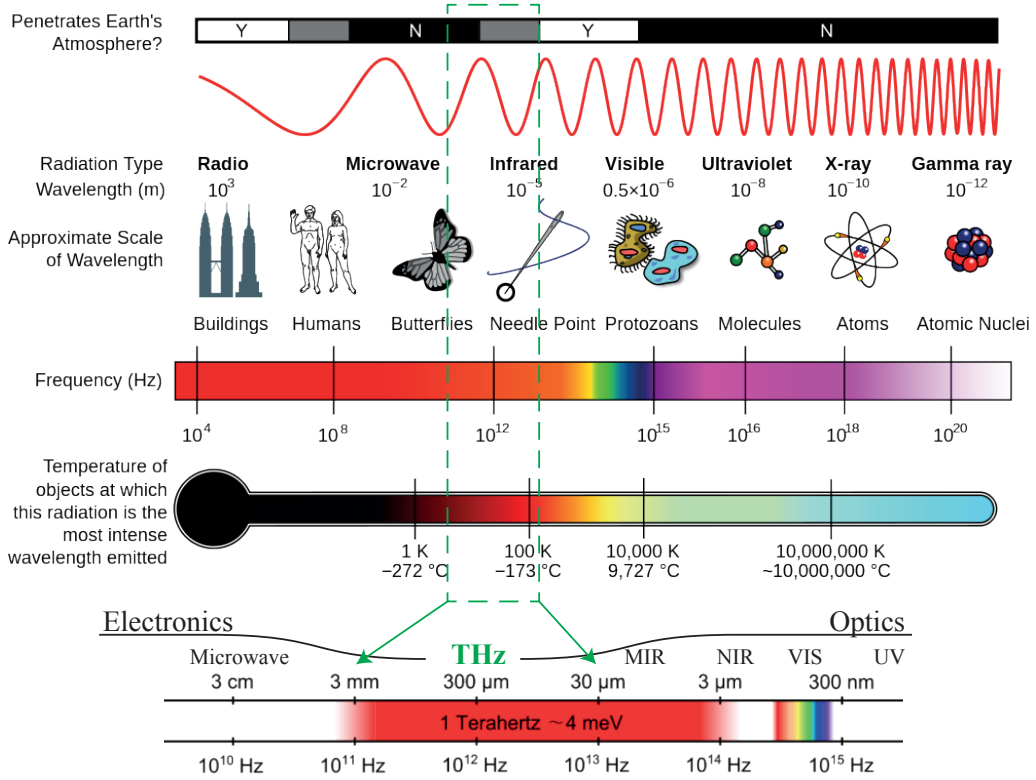

Figure 0.1 – The THz range, between optics and electronics. Adapted from [4, 5].

was often referred to as the *THz gap*.

More specifically, THz-electronic devices suffer mainly from long *RC*-time-constant and from the fact that room temperature is usually much hotter than the equivalent temperature of their energy scale. This results also in optical sources having to fight the phonon bath, as discussed later for THz-quantum cascade lasers. On the optics side, instead, the main issue is diffraction, especially when trying to conciliate device miniaturisation with micrometre- or millimetre-size radiation. As it is briefly introduced in the next section and discussed more clearly along the manuscript, these issues can be addressed in more or less depth, singly or together, e.g. with cryogenic temperatures, plasmonic structures and engineered materials.

0.1 Terahertz physics and materials

The THz-spectral region is very rich of interesting phenomena in several material systems, from semiconductors to oxides to more exotic topological insulators (cf. Fig. 0.2). In order to investigate and exploit such physics, spectroscopy setups and optical components are already available and used, but they do not present the variety and tunability

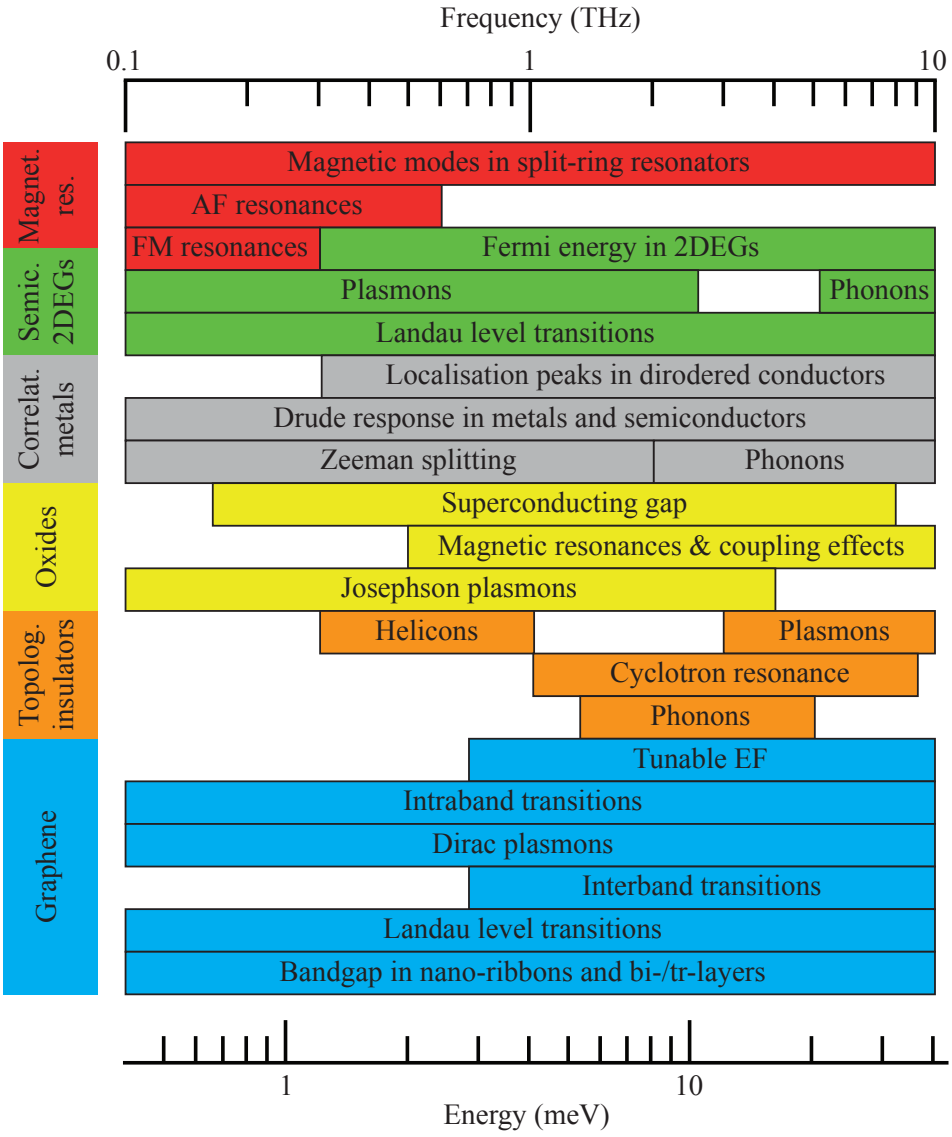

Figure 0.2 – Compilation of the main THz-phenomena in different solid-state systems. Adapted from [6, 7].

of the visible and near-infrared frequency range.[2] For example spectroscopy setups often rely on photoconductive generation of THz-radiation (cf. chapter 3), a mechanism that produces low-amplitude THz-pulses. Coherent, broadband, room-temperature sources are being researched, particularly in the form of THz-quantum cascade lasers (THz-QCLs), but they do not meet yet all requirements (a more in-depth discussion will take place later in the chapter).[8] From the point of view of optical manipulation, the most common semiconductors and several other materials are to some degree transparent and are used for windows and lenses. Instead, concerning phase and polarisation control, intense research activity is being undertaken, especially in the direction of plasmonics and metamaterials.[9, 10, 11]

In the presented work, metamaterials were mainly used as THz-cavities to focus radiation onto semiconductors such as III-V composites or graphene, where different electronic transitions were exploited. All these topics will be briefly introduced in the following sections. Later, the phenomena and devices that can be produced and studied by the combination of these elements will also be discussed.

0.1.1 Creating the desired long-wavelength optical properties: split-ring resonators and metamaterials

In the quest for light control, the holy grail is a fully tunable material whose permittivity and permeability can be chosen at will. The materials available in nature do not cover the full range of possible combinations and, for quite some time, optics had to restrain itself to the macroscopic domain. This is even more true for the THz-frequency range. In the visible range, this meant working with dielectrics as lenses and metals as mirrors, in the frame of geometrical optics where light beams propagate as straight lines in homogeneous media.[12] This is the case when the characteristic dimension of the entities interacting with the light are much larger than its wavelength, for instance centimetre-size optical elements for light with wavelength of some hundreds of nanometres.

Aiming at the microscopic control of the properties of light, one needs to decrease the ratio between the characteristic dimension of the interacting object and the wavelength of the radiation, as sketched in Fig. 0.3. To achieve this effect, technological improvements were fundamental, allowing the nanostructuring of materials at length scales unimaginable few decades before. Quite soon the field of artificial control of radiation split into two: on one side photonic crystals, on the other metamaterials.[13, 14]

Photonic crystals are dielectric-based structures where the refractive index is periodically modulated at the wavelength scale, creating optical bands and optical gaps, mapping

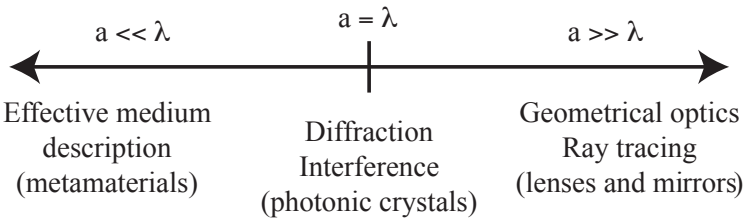

Figure 0.3 – Optics and photonics are governed by the ration between the dimensions of the object and the wavelength of the radiation.

what happens for electrons in (semi-)conducting materials.[13] Furthermore, extended functionalities can be obtained creating cavities and waveguides by suitably engineering structural defects.

Metamaterials, literally "beyond (natural) materials" from the Greek prefix "meta" meaning "beyond", are artificial materials whose constituent structures have an electromagnetic response at wavelengths much larger than their dimensions. Their effect on the light can therefore be modelled with an effective medium description, *de facto* closing the circle towards geometrical optics. In fact, the unit cells of such metamaterials behave as atoms and molecules in an ordinary material, the polarisation of the latter being substituted by the resonances of the first. The resonance condition is achieved by engineering the path of the ohmic or displacement currents in the object, thus determining the value of the effective permittivity and permeability.[15]

To understand the reason for so much interest, one should note that natural materials can display both negative and positive permittivity depending on whether they are dielectrics or conductors at the considered wavelength, while they all generally show only positive permeability above few THz. A schematic summarising such properties is presented in Fig. 0.4. This was thus a limitation for the full exploitation of the photonics capabilities and overcoming it allowed the demonstration of negative-index (left-handed) materials[16, 17], optical cloaking[18, 19] and hyperlensing[20, 21].

The initial, and still standard, way to control the refractive index is with the use of metallic rods and metallic split-ring resonators, whose combination gave the first left-handed material.[22] In the cited work, the array of suitably designed rods provides the wanted, negative effective permittivity ϵ_{eff} while the array of split-ring resonators provides the negative effective permeability μ_{eff}, resulting in a negative refractive index.[23]

Since the beginning, most attention was set onto the split-ring resonators, literally metallic rings with a slit that makes them C-shaped. The reason is that, along with the negative permeability, upon irradiation they also display a significant electric field concentration up to some orders of magnitude, within the slit.[23, 24]

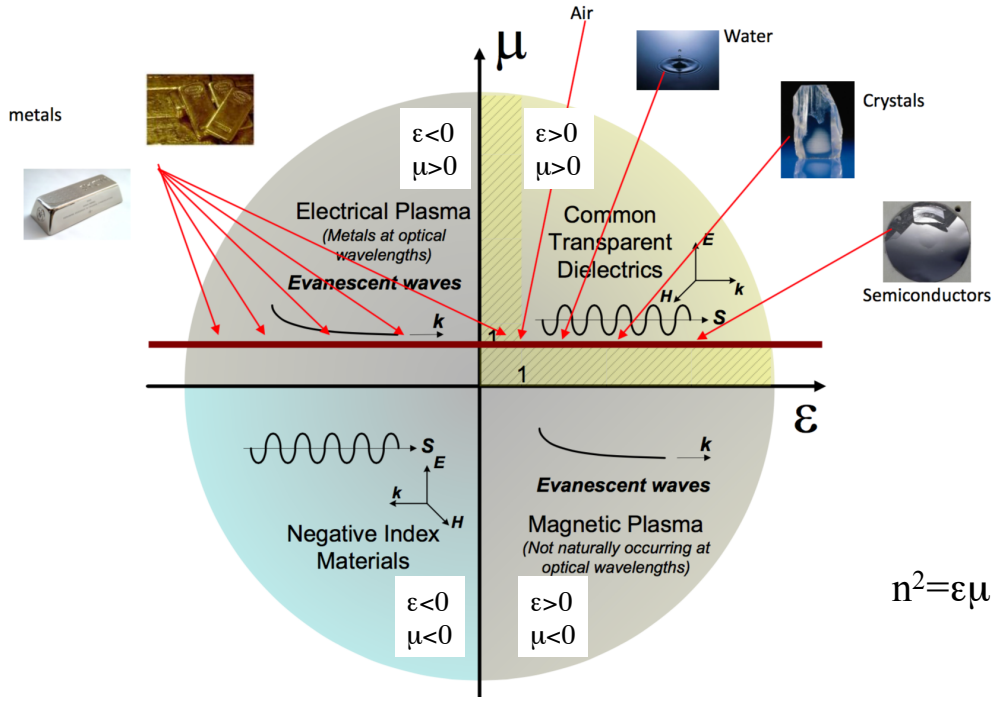

Figure 0.4 – The (ϵ, μ) plane for natural and artificial materials. Adapted from Shalaev

Considering again the ratio between the characteristic dimension and the wavelength, as a matter of fact often split-ring resonators have sides approximately one order of magnitude smaller than the wavelength they resonate at. Therefore it comes as no surprise that the first report was for the MHz-frequency range, corresponding to wavelengths of metres[25], while most subsequent realisations were in the GHz-frequency range where the wavelength is several centimetres long and the structure could be realised with standard millimeter-size printed-board techniques. With time and the improvements in micro- and nano-lithography techniques, split-ring resonators and metamaterials were realised up to the visible.[14]

Throughout the presented work, split-ring resonators (SRRs) were used mainly as highly focussing THz-cavities to increase the light-matter interaction. They were used by Scalari and coworkers to demonstrate ultra-strong light-matter coupling with Landau-level transitions. This phenomenon will be discussed later and is the basis on which Part III of this thesis relies on. The effective-medium description of the SRRs will become instead relevant concerning their dispersive interaction with the radiation. This will be particularly useful in chapter 4, when discussing the transmission properties of a particular variation of the used SRRs. The effective-medium concept will also be used for discussing the graphene/THz-SRRs modulator in chapter 8. A detailed discussion of the properties of the used THz-SRRs are discussed in chapter 3, along with the analytical modelling

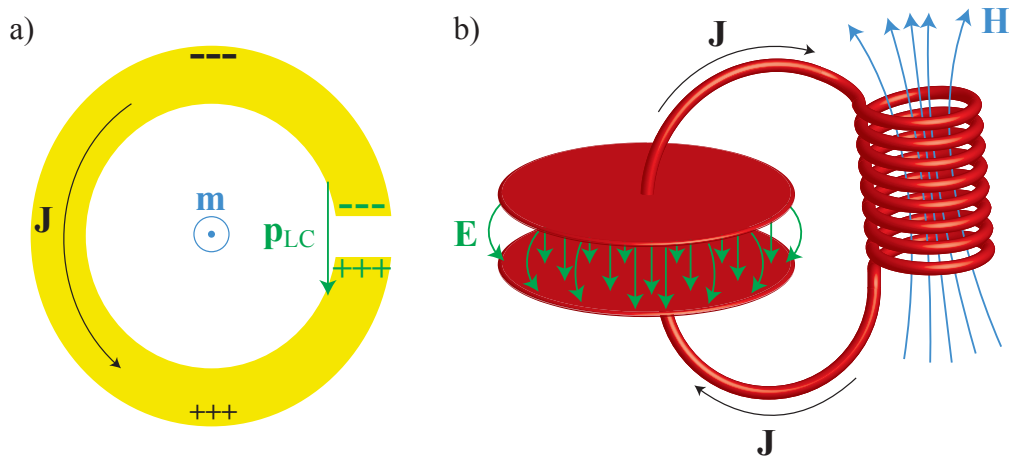

Figure 0.5 – a) Basic SRR-design with electric-LC-dipole p_{LC}, magnetic dipole m and induced current J. The accumulated charges are indicated by plus/minus signs, for the LC-mode (green) and the $\lambda/2$ mode (black). b) 3D rendering of the circuit and of the resonating E/H fields.

tools. The working principles are instead introduced in the next section.

Basic principles of THz-SRRs

Split-ring resonators were first introduced as (multiple) C-shaped metallic stripes. Such a structure can be schematised by both a magnetic (m) and an electric (p) dipole, the first being oriented out-of-plane and being connected to the current flowing into the metallic ring, the second being oriented across the slit and being connected to the charge accumulation/depletion at its sides, as sketched in panel a) of Fig. 0.5. In fact when an electro-magnetic wave impinges onto the structure with the electric (magnetic) field oriented along the electric (magnetic) dipole, the SRR couples to it and resonates, provided the radiation frequency matches the one proper of the SRR.[26]

Having this picture in mind, it is easy to associate the SRR to an RLC-circuit with series elements as sketched in panel b) of Fig. 0.5. In fact, the slit is naturally a capacitor that gets periodically charged by the current flowing in the circuit through the inductor, while the losses are accounted for by the resistance of the circuit. Such a comparison is therefore physically meaningful, not just a trick to perform analytical calculation when dealing with Lorentzian resonances.[23, 27]

Applying Kirchhoff's law to the skecthed RLC-series circuit, and substituting the $V(I)$ relation for the different elements, one gets the following loop equation

$$L\frac{dI(t)}{dt} + RI(t) + \frac{1}{C}\int_{-\infty}^{\tau=t} I(\tau)d\tau = 0 \tag{0.1}$$

that, by derivating once more and dividing by L, can be recast into the form of a second-order differential equation

$$\frac{d^2I(t)}{dt^2} + \frac{R}{L}\frac{dI(t)}{dt} + \frac{1}{LC}I(t) = 0. \tag{0.2}$$

It is straightforward then to determine the resonant angular frequency of the circuit to be

$$\omega_{SRR} = \frac{1}{\sqrt{LC}}, \tag{0.3}$$

while the dissipating term, with its first derivative, is connected to the quality factor

$$Q = \frac{1}{R}\sqrt{\frac{L}{C}}. \tag{0.4}$$

It is then clear that one can tune the resonant frequency by modifying the geometry of the SRR, hence the values of L and C.[27] Superconductors, with lower R and a sizeable kinetic inductance L_k, can provide higher Q-factors when these are limited by ohmic losses, while shifting the resonant frequency to lower frequencies for the same geometry.[28]

This same system is also the starting line for the treatment of superconducting circuits and qubits in circuit quantum electro-dynamics.[29] Considering for a moment the energy balance in the circuit, what happens during one oscillation is a transfer of energy from the capacitance to the inductance. In fact, when the capacitor charges, it stores the energy of the circuit by building up an electric field. Such energy will then be released in the circuit as a time-varying current that will load the inductor, that stores it as a magnetic field. The resistor, it being the dissipative element, gradually removes energy from the system.

The total energy of the circuit, for a moment ignoring the dissipation, can be written as a sum of the two potential energies

$$U = U_C + U_L = \frac{1}{2}CV^2 + \frac{1}{2}LI^2 = \frac{q^2}{2C} + \frac{\phi^2}{2L}, \tag{0.5}$$

where q indicates the charge on the capacitor's plates and ϕ the flux of the magnetic field at the inductor. Equation (0.5) represents under all aspects a harmonic oscillator and as such it is straightforward to introduce the canonical variables $\hat{q}$ and $\hat{\phi}$. It was also shown that they satisfy the bosonic commutation relation and one can then write the Hamiltonian[29]

$$\hat{H}_{LC} = \frac{\hat{q}^2}{2C} + \frac{\hat{\phi}^2}{2L}. \tag{0.6}$$

This can be directly re-written as

$$\hat{H}_{LC} = \hbar\omega_{SRR}\left(\hat{n} + \frac{1}{2}\right) \tag{0.7}$$

with $\hat{n}$ being the number operator for the photons in the circuit.

The work presented in this thesis instead takes place within the classical limit of the system, the Q-factors being too low and the excitation number too high to see effects of the quantisation. These stay nonetheless as an outlook for future investigations.

The most important task of THz-SRRs will be to adapt the wavelength of the THz-radiation to the dimensions of the systems interacting with it. In fact, a dimension mismatch is usually present, with a huge factor in the range $10^{-3} - 10^{-5}$. This mismatch is lifted within the capacitor of the SRR, where the E-field is tightly concentrated, and that can be seen as a plasmonic-like cavity, in all respects equivalent to a photonic cavity.

0.1.2 Inducing the desired low-energy electronic transitions: (quantum) confinement in semiconductors

Looking for defined electronic transitions in the THz-frequency range, one would first check for materials with very narrow bandgaps, having in mind inter-band laser diodes. Among the most common semiconductor compounds, the ones with the smallest gaps are InSb and InAs, with $E_g = 170$ meV and $E_g = 360$ meV, respectively.[30] These values correspond to frequencies of 41 THz and 87 THz, above the targeted range.

One way to obtain enegy levels spaced by the desired THz-energy is then to confine the electronic wavefunctions. In this thesis two different, complementary ways will be discussed: quantum confinement achieved with the growth of thin layers of semiconductors, resulting in quantum wells, and magnetic confinement induced with strong applied magnetic fields. The latter, in particular, is used for many investigations in the present thesis, perfoming magnetic studies of the system properties.

Intersubband transitions and two-dimensional electron gases in quantum wells

Quantum confinement in semiconductor is achieved by growing heterostructures, i.e. sequences of thin epitaxial layers with alternating compositions. The different bandgaps possessed by the materials provide the electronic confinement along the growth direction (conduction band offset), confining the electron wavefunctions into the material with lower conduction band edge energy.[31, 32]

The prototype of the quantum well is the infinite-potential square well defined by the potential

$$V(x) = \begin{cases} 0 & -\frac{L}{2} < x < \frac{L}{2} \\ \infty & \text{otherwise} \end{cases} \tag{0.8}$$

for a quantum well's width L.

The derived energy levels, calculated with Schrödinger's equation, are given by

$$E_n = \frac{\hbar^2 k_n^2}{2m^*} = \frac{n^2 \hbar^2 \pi^2}{2m^* L^2} \tag{0.9}$$

for quantised wavevectors $k_n = n\frac{\pi}{L}$ and effective electron mass m^*. The index n runs over the natural numbers.

The fact that the quantum well will be in a heterostructure, thus with a finite potential barrier and interacting with neighbouring ones, will change the energetic level spectrum and the shape of the wavefunctions. Nonetheless some insight can be gained already by the simplified formula.

First of all, for GaAs ($m^* = 0.067 m_e$), the first two levels have energy separation $E_{1,2} = 1$ THz for a quantum well's thickness of 64 nm. This gives an idea of the precision needed during the sample's growth. A broader introduction can be found in chapter 1 while a more extensive discussion is carried on in Ref. [32].

Second, this confinement takes place for wavevectors k_n along the growth direction, but the electrons are still free, with parabolic dispersion in the plane of the quantum wells. When most of the conduction electrons in the material are populating the lowest level, one speaks of a two-dimensional electron gas (2DEG). The most studied 2DEG type is the one created at the GaAs/AlGaAs interface. The two materials can be grown by MBE lattice-matched on top of each other (cf. also Fig. 1.6 in section 1.3 on page 45) and the electrons accumulate in the triangular well at the interface.

2DEGs in the GaAs/AlGaAs material system are one of the cleanest and most studied solid-state system for experimental physics: this is due to a continuous technological improvement in the growth strategies and conditions.[33] The main parameter that reflects such improvements is the electron mobility: since the first growths, it has been steadily increasing improving by three orders of magnitude till the current records exceeding 35 million $\mathrm{cm^2\,V^{-1}\,s}$[34, 35] for temperatures below 1 K and carrier densities of few 10^{11} $\mathrm{cm^{-2}}$. For ideally suppressed background doping and a suitable structure design, a mobility maximum of 100 million $\mathrm{cm^2\,V^{-1}\,s}$ was predicted.[36]

All single-2DEGs used in this thesis were grown in-house in the GaAs/$Al_{0.3}Ga_{0.7}As$

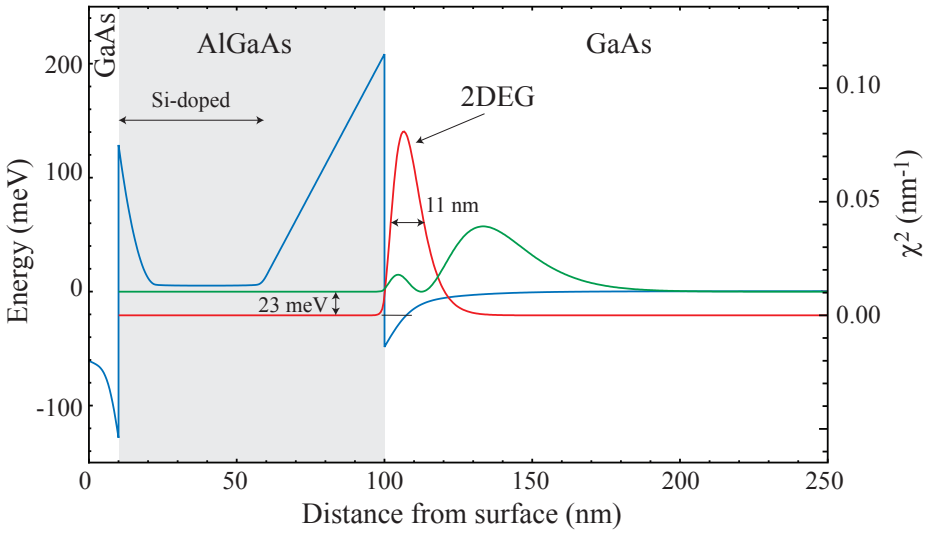

Figure 0.6 – Conduction band scheme (left axis) and electronic wavefunctions (right axis) of the 2DEG *EV*1452. The 2DEG forms in the triangular well at the GaAs/AlGaAs interface, 100 nm belowe the surface, with typical carrier densities of $n_s = 3.1 \times 10^{11}$ cm^{-2} with a mobility $\mu = 8 \times 10^5$ cm^2/Vs, measured at $T = 1.5$ K. About half of the AlGaAs layer is heavily volume-doped with Si atoms which provides the free electrons and it is capped by a thin doped GaAs layer. The electrons are confined approx. within 11 nm in the first state, 23 meV below the second one, which is already almost unconfined.

material system and their growth designs can be found in appendix A on page 233. The first 2DEG forms in the triangular well at the interface between the two materials in the heterostructure *EV*1452 whose conduction-band scheme, calculated with NextNano[1], is plotted in Fig. 0.6.

Two other 2DEGs, *EV*2109 and *EV*2124 were grown with a different doping scheme, in an attempt to increase the electron mobility (and to decrease the cyclotron linewidth, introduced below). To this end the so-called modulation doping technique, that spatially separates supplying impurities from electronic channel and collects the electrons in a square quantum well, was employed.[37]

Landau levels in magnetic field

Another, more elegant, way to induce electronic confinement is with the application of a magnetic field. When combined with the previous level of confinement, with the magnetic field orthogonal to the quantum well plane $\boldsymbol{B} = (0, 0, B)$, the system can be brough to a quantum-dot-like 3D confinement.

In general, on each electron in motion with velocity $\boldsymbol{v}$, $\boldsymbol{B}$ is responsible for a Lorentz

[1]Courtesy of C. Maissen.

force

$$\boldsymbol{F_L} = -e\left(\boldsymbol{E} + \boldsymbol{v} \times \boldsymbol{B}\right), \tag{0.10}$$

where the presence of an electric field $\boldsymbol{E}$ (e.g. from electric biasing) is also assumed. The equation of motion can then be derived, following Ref.s [30, 38, 39], including a friction term given by the collisions with scatterers at a rate $1/\tau$, as

$$m^* \left(\frac{d}{dt} + \frac{1}{\tau}\right) \boldsymbol{v} = -e\left(\boldsymbol{E} + \boldsymbol{v} \times \boldsymbol{B}\right). \tag{0.11}$$

Considering for a moment the magnetic field only, the equation of motion has an oscillatory solution with angular frequency

$$\omega_{cyc} = \frac{eB}{m^*} \tag{0.12}$$

and the electrons can complete an orbit if the time needed is shorter than the collision time τ. This condition is usually stated as $\omega_{cyc}\tau > 1$. One can then make use of Eq. (0.12) and substitute the formula for the mobility, $\mu = e\tau/m^*$: the condition becomes the well-known $\mu B > 1$, that highlights the importance of high-mobility samples. The two magnetic field regimes are thus accordingly classified: in the low field regime, $B < \mu^{-1}$, the classical Drude conductivity can be derived and used, whereas in the high-field regime, $B > \mu^{-1}$, the in-plane quantisation leads to non-classical effects like the quantum Hall plateaux and the Shubnikov–de Haas oscillations.

The two cases will be briefly discussed, considering the Hall-bar geometry, this being, on the one hand, the benchmark system for measuring transport in 2-dimensional electron gases (2DEGs) and, on the other hand, the actual shape of the samples investigated in chapter 7 on page 157. A sketch of the sample's shape with the contacts arrangement and the measuring circuit is presented in Fig. 0.7: the sample is etched into a bar of width W. Ohmic contacts are realised at the opposite ends of the bar, constituting the channel, on its sides with interval L, enabling four-point measurements. The behaviour of the sample can be described via Ohm's law $\boldsymbol{E} = \rho\boldsymbol{j}$, where, for the considered case, ρ is the symmetric rank-2 resistivity tensor, whose inverse is the conductivity tensor σ. In order to determine the values of the elements of the tensor in the plane, a current I is passed in the channel while the longitudinal resistivity ρ_{xx} and the transverse resistivity ρ_{xy} are determined via the voltages measured along and across the channel at the side

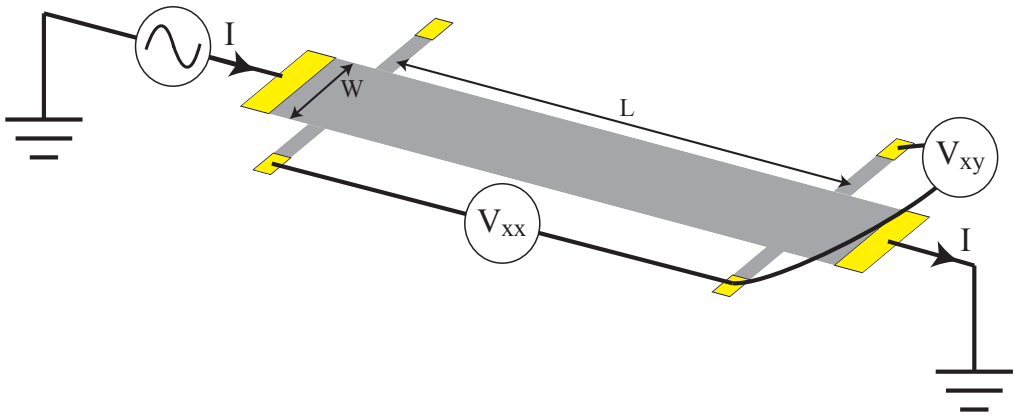

Figure 0.7 – Hall-bar sketch with measurement configuration

contacts as

$$\rho_{xx} = \frac{W}{L}\frac{V_{xx}}{I} \tag{0.13}$$

$$\rho_{xy} = \frac{V_{xy}}{I}. \tag{0.14}$$

These relations hold for a diffusive sample, whose dimensions are big compared to the electronic mean free path.

For low magnetic fields ($B < \mu^{-1}$) no additional quantisation is present and the Drude model can be used to describe the electronic motion. Solving Eq. (0.11) and writing the result in term of current density $\boldsymbol{j} = -en_s\boldsymbol{v}$, one obtains

$$\rho_{xx} = \frac{m^*}{n_s e^2 \tau} = \frac{1}{n_s e \mu} \tag{0.15}$$

$$\rho_{xy} = \frac{B}{en_s}, \tag{0.16}$$

the conductivity tensor elements being

$$\sigma_{xx} = \frac{n_s e^2 \tau}{m^*}\frac{1}{1+\omega_{cyc}^2\tau^2} \tag{0.17}$$

$$\sigma_{xy} = \frac{n_s e^2 \tau}{m^*}\frac{\omega_{cyc}\tau}{1+\omega_{cyc}^2\tau^2}. \tag{0.18}$$

From the measured resistivities of Eqs (0.14) one can therefore derive the sheet density

n_s and the mobility μ of the 2DEG as

$$n_s = \left(e \left. \frac{d\rho_{xy}}{dB} \right|_{B=0} \right)^{-1} \tag{0.19}$$

$$\mu = \frac{1}{\rho_{xx}(B=0)} \left. \frac{d\rho_{xy}}{dB} \right|_{B=0}. \tag{0.20}$$

These are the relations used to analyse the measurements in chapter 7 on page 157.

At high magnetic fields ($B > \mu^{-1}$) the in-plane confinement produces an additional quantisation that reshapes the electronic density of states and requires a quantum treatment: the connected investigation allows specific studies of single- and many-body quantum phenomena, like the integer and fractional quantum Hall effect or the 5/2 state.[33, 40, 41, 42]

The free-particle Hamiltonian

$$\hat{H}_{free} = \frac{\hat{\boldsymbol{p}}}{2m^*} + V(z) \tag{0.21}$$

is modified by the minimal coupling $\hat{\boldsymbol{p}} \to \hat{\boldsymbol{p}} + e\hat{\boldsymbol{A}}_B$. We can choose to work in the Landau gauge $\hat{\boldsymbol{A}}_{\boldsymbol{B}} = (-B\hat{y}, 0, 0)$ and, for the moment, consider the electrons as carriers of electric charge only (no spin). The new Hamiltonian is therefore separable into a B-independent part describing the confinement along z and producing the subband in the conduction and valence bands, and a into a B-dependent part for the in-plane coordinates:

$$\hat{H}_{plane} = \frac{1}{2m^*}((\hat{p}_x - eB\hat{y})^2 + \hat{p}_y^2). \tag{0.22}$$

The eigenvalues are determined as a product of the Bloch function with an envelope function. The latter is assumed to be constituted by a plane-wave along the x-direction while the y-dependent part is mapped to the Hamiltonian of a displaced harmonic oscillator. The eigenenergies constitute a ladder of levels named after Landau[43]:

$$E_{l,n} = E_l + \hbar\omega_{cyc,l}\left(n + \frac{1}{2}\right) \tag{0.23}$$

with quantum numbers $n \in \mathbb{N}_0$ labelling the Landau levels and l labelling the quantum well's levels. The cyclotron frequency is also labelled by the index l, for the case that different subbands have different effective mass values m_l^*.

When considering also the electron's spin σ, $\hat{H}_{plane}$ needs to be complemented by

$$\hat{H}_\sigma = -g^* \mu_B B \hat{\sigma} \tag{0.24}$$

that describes the Zeeman interaction of the electronic magnetic momentum with the magnetic field. Such term contributes $\pm\frac{1}{2} g^* \mu_B B$ to the energy balance, with $\mu_B = 5.79 \times 10^{-2}$ meV T^{-1} representing Bohr's magneton and g^* the effective Landé g-factor. Free electrons have $g = 2$ while (bulk) electrons in GaAs/AlGaAs have $g^* \simeq -0.44$, therefore reaching sizable Zeeman splitting only for relatively high B-values.

Sticking to the simplified picture of a perfectly quantised system, the Landau levels are delta-like functions in energy with a degeneracy given by the ratio B/ϕ_0, where $\phi_0 = h/e$ is the flux quantum. The degeneracy thus increases for increasing magnetic field by depleting higher-order Landau levels while the Fermi energy oscillates as a function of B.

When disorder and scattering processes are taken into account, the delta-like density-of-state functions get broadened into Lorenzians where conducting extended states lay at the centre while insulating localised states form the tails.[39, 44] When the magnetic field is now swept, the Fermi energy passes through the series of increasingly spaced Lorenzian-like state distributions, causing the resistivity of the Hall-bar to oscillate accordingly in the so-called *Shubnikov-deHaas oscillations*. An analytical solution for such system was derived, in the limit $\omega_{cyc}\tau \ll 1$, for weak long-range scattering by Ando and coworkers[45]: the formula for the longitudinal resistivity reads

$$\rho_{xx}(B,T) = \rho_{xx}(0,T)\left[1 - 2e^{-\pi/\omega_{cyc}\tau_q} \frac{2\pi^2 k_B T/\hbar\omega_{cyc}}{\sinh(2\pi^2 k_B T/\hbar\omega_{cyc})} \cos\left(2\pi \frac{h n_s}{2qB}\right)\right] \tag{0.25}$$

while for short-range scattering the prefactors of the oscillating term is different. The oscillations are, in both cases, periodic in $1/B$ with periodicity $2q/hn_s$ (in this formula, q denotes the electron charge to avoid confusion with the exponential function).

Finally, taking a closer look at the cyclotron transition in GaAs-based 2DEGs, two features make it interesting for the present work. First, for moderate B-fields, the cyclotron energy lies in the THz-range $E_{cyc} \simeq 3$ meV, as shown also by the measurments reported in Fig. 0.8, where the cyclotron absorption of the 2DEG $EV1452$ is displayed.

Second, the condition $\delta_{n,n+1}$ (cf. Eq. (0.34) later) identifies the pair formed by the last filled Landau level and by the next empty one as an effective two-level system. This fact will be important from the point of view of strong coupling, as discussed in the next sections.

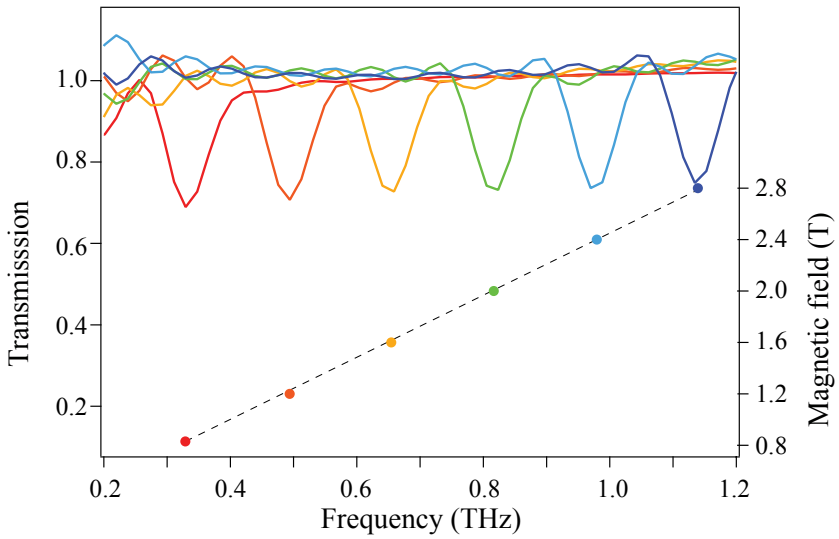

Figure 0.8 – Cyclotron absorption measured on $EV1452$ in transmission (left axis), showing also the linearity on B (right axis). Adapted from [28].

0.2 Light-matter interaction: from fundamentals to devices

In this section we will take advantage of the previously discussed systems to introduce THz-light-matter interaction. To this end we will first consider the interaction of freely propagating light with the previously derived Landau levels. Then we will consider the interaction of THz-light concentrated in a cavity with the available electronic transitions.

0.2.1 Optical transitions between Landau levels

We will discuss now the conditions, according to which electrons in the previously derived Landau levels can absorb THz-photons and undergo transitions. The transition rate can be computed using Fermi's golden rule[31, 46]

$$\Gamma^{tr}_{i\to f} = \frac{2\pi}{\hbar}\left|\langle\Psi_i|\hat{H}_{int}|\Psi_f\rangle\right|^2 \delta(E_f - E_i \pm \hbar\omega) \tag{0.26}$$

for which we need the interaction Hamiltonian $\hat{H}_{int}$. This can be determined by writing again a minimally coupled Hamiltonian in the Landau gauge, this time for the electromagnetic radiation:

$$\hat{H}_{mc} = \frac{1}{2m^*}\left(\hat{\boldsymbol{p}}^2 + e\hat{\boldsymbol{p}}\cdot\hat{\boldsymbol{A}}_{em} + e\hat{\boldsymbol{A}}_{em}\cdot\hat{\boldsymbol{p}} + e^2\hat{\boldsymbol{A}}^2_{em}\right) + V(z), \tag{0.27}$$

hence, neglecting higher order terms in $\hat{\boldsymbol{A}_{em}}$,

$$\hat{H}_{int} = \frac{e}{2m^*}\left(\hat{\boldsymbol{p}}\cdot\hat{\boldsymbol{A}}_{em} + \hat{\boldsymbol{A}}_{em}\cdot\hat{\boldsymbol{p}}\right) = \frac{e}{m^*}\hat{\boldsymbol{p}}\cdot\hat{\boldsymbol{A}}_{em}, \tag{0.28}$$

where the last equality assumes that the two operators commute.

Assuming to be working with a monochromatic wave whose electric field can be written as $\hat{\boldsymbol{F}}(\boldsymbol{r},t) = F\hat{\boldsymbol{\varepsilon}}\cos(\boldsymbol{q}\cdot\boldsymbol{r}-\omega t)$, the corresponding vector potential is given by

$$\hat{\boldsymbol{A}}_{em}(\boldsymbol{r},t) = \frac{iF}{2\omega}\left[e^{i(\boldsymbol{q}\cdot\boldsymbol{r}-\omega t)} + e^{-i(\boldsymbol{q}\cdot\boldsymbol{r}-\omega t)}\right]\hat{\boldsymbol{\varepsilon}} \tag{0.29}$$

where $\boldsymbol{q}$ and ω are wavevector and angular frequency of the electro-magnetic wave with polarisation along the unity vector $\boldsymbol{\varepsilon}$.

Working in the THz range, the wavevector of the photon is much smaller than any real-space coordinate within the considered system, therefore we can work in the dipole approximation and the exponential in (0.29) can be approximated by unity: the result is

$$\hat{H}_{int} = \frac{ieF}{2m^*\omega}\hat{\boldsymbol{\varepsilon}}\cdot\hat{\boldsymbol{p}}. \tag{0.30}$$

The temporal term gets removed by working in the rotating wave approximation. Then the matrix element that needs to be evaluated reads $\langle\Psi_i|\hat{\boldsymbol{\varepsilon}}\cdot\hat{\boldsymbol{p}}|\Psi_f\rangle$.

In general, the wavefunction $|\Psi\rangle$ can be written as the product of a Bloch's function $|u\rangle$, accounting for the lattice periodicity and not interacting with the field, and an envelope function $|f\rangle$. Because of the slowly spacially varying envelope function, one can write the matrix element as

$$\langle\Psi_i|\hat{\boldsymbol{\varepsilon}}\cdot\hat{\boldsymbol{p}}|\Psi_f\rangle = \langle u_i|\hat{\boldsymbol{\varepsilon}}\cdot\hat{\boldsymbol{p}}|u_f\rangle\langle f_i|\,f_f\rangle + \langle u_i|\,u_f\rangle\langle f_i|\hat{\boldsymbol{\varepsilon}}\cdot\hat{\boldsymbol{p}}|f_f\rangle. \tag{0.31}$$

For intersubband transitions the electrons stay within the conduction band, $u_i = u_f$, and consequently, because of the properties of the Bloch's function, $\langle u_i|\,u_f\rangle = 1$ and $\langle u_i|\hat{\boldsymbol{\varepsilon}}\cdot\hat{\boldsymbol{p}}|u_f\rangle = 0$. Finally, the selection rules are entirely determined by the envelope function.

In the presence of a magnetic field, in the Landau gauge ($\hat{\boldsymbol{A}}_B = (-B\hat{y},0,0)$), the envelope function can be written as a separable product

$$f_{l,n}(\boldsymbol{r}) = \frac{e^{ik_x x}}{\sqrt{L_x}}\varphi_n(y)\chi_l(z) \tag{0.32}$$

whose factors represent a plane wave along x, a function $\varphi_n(y)$ describing the n-th Landau

level and a function $\chi_l(z)$ for the l-th subband into the quantum well.

At this point the matrix element can be calculated taking advantage of the separation of variables

$$\begin{aligned}\langle\Psi_i|\hat{\boldsymbol{\varepsilon}}\cdot\hat{\boldsymbol{p}}|\Psi_f\rangle &\propto \int f_i^*(\boldsymbol{r})(\hat{\boldsymbol{\varepsilon}}\cdot\hat{\boldsymbol{p}})f_f(\boldsymbol{r})d\boldsymbol{r} \\ &\propto \frac{1}{L_x}\int e^{-ik_x x}\varphi_n^*(y)\chi_l^*(z)(\hat{\boldsymbol{\varepsilon}}\cdot\hat{\boldsymbol{p}})e^{ik_x' x}\varphi_{n'}(y)\chi_{l'}(z)dxdydz.\end{aligned} \tag{0.33}$$

Using the orthonormality relations of the wavefunctions and the properties of the harmonic oscillator, one can derive the following result for the allowed transitions:

$$\langle\Psi_i|\hat{\boldsymbol{\varepsilon}}\cdot\hat{\boldsymbol{p}}|\Psi_f\rangle \propto \varepsilon_x p_x \delta_{k_x,k_x'}\delta_{n,n'}\delta_{l,l'} + \varepsilon_y\delta_{k_x,k_x'}\delta_{n,n'\pm1}\delta_{l,l'} + \varepsilon_z\delta_{k_x,k_x'}\delta_{n,n'}\langle l|\hat{p}_z|l'\rangle \tag{0.34}$$

We can now discuss the meaning of Eq. (0.34). The first term of the calculated transition rate is identically zero unless the initial and final states are the same. This physically means that absorption/emission by free carriers (recall the plane wave along x) can occur only in the presence of a diffusion mechanism and can be disregarded in the present discussion. The second term allows a transition between neighbouring Landau levels $\Delta n = \pm 1$ of the same subband l. Such transition corresponds to emitting/absorbing a photon whose energy equals the cyclotron energy $\hbar\omega_{cyc}$. The photon is then y-polarised and propagates along the growth direction z (TE-transition). Finally, the third term allows the electrons to perform a transition between different subbands l, l' under the condition that the Landau index does not change, resulting in a magnetic-field-independent transition energy, instead determined by the subband energy difference. These photons are z-polarised and propagate into the plane of the quantum well (TM-transition).

0.2.2 Strong light-matter coupling

When the photons are concentrated by a cavity and are resonant with the electronic transition (two-level system) one might see strong light-matter coupling effects. Scalari and coworkers demonstrated few years ago that the interaction of the cyclotron transition in 2DEGs with the cavity created by the split-ring resonators can enter the regime of ultra-strong coupling.[47] Since this will be the starting point of the investigations in chapters 7 and 8, we will begin to introduce it here.

When the degree of coupling increases, the interaction cannot be treated as a perturbation any more and needs to be taken fully into account, diagonalising the system: we start thus again from the minimally coupled Hamiltonian of Eq. (0.27) and we write it in the second quantisation formalism, neglecting the additional external potential $V(z)$.

The complete Hamiltonian then reads[48, 49]:

$$\hat{H}_{tot} = \hat{H}_{mat} + \hat{H}_{cav} + \hat{H}_{int,1} + \hat{H}_{int,2} \tag{0.35}$$

$$\hat{H}_{mat} = \sum_{\boldsymbol{k}} \hbar\omega_{cyc} \left(b^{\dagger}_{\boldsymbol{k}} b_{\boldsymbol{k}} + \frac{1}{2} \right) \tag{0.36}$$

$$\hat{H}_{cav} = \sum_{\boldsymbol{k}} \hbar\omega^{cav}_{\boldsymbol{k}} \left(a^{\dagger}_{\boldsymbol{k}} a_{\boldsymbol{k}} + \frac{1}{2} \right) \tag{0.37}$$

$$\hat{H}_{int,1} = \sum_{\boldsymbol{k}} i\hbar\Omega_{\boldsymbol{k}} \left[a_{\boldsymbol{k}} \left(b^{\dagger}_{\boldsymbol{k}} - b_{-\boldsymbol{k}} \right) + a^{\dagger}_{\boldsymbol{k}} \left(b^{\dagger}_{-\boldsymbol{k}} - b_{\boldsymbol{k}} \right) \right] \tag{0.38}$$

$$\hat{H}_{int,2} = \sum_{\boldsymbol{k}} \hbar D_{\boldsymbol{k}} \left(a^{\dagger}_{\boldsymbol{k}} a_{\boldsymbol{k}} + a_{\boldsymbol{k}} a^{\dagger}_{\boldsymbol{k}} + a^{\dagger}_{\boldsymbol{k}} a^{\dagger}_{-\boldsymbol{k}} + a_{\boldsymbol{k}} a_{-\boldsymbol{k}} \right). \tag{0.39}$$

The hat on the creation and destruction operators was dropped to keep a lighter notation and the Hamiltonians are written neglecting the loss terms.

The total Hamiltonian $\hat{H}_{tot}$ has been split into the Hamiltonian of the matter part $\hat{H}_{mat}$ with ladder operators $b^{\dagger}_{\boldsymbol{k}}$, $b_{\boldsymbol{k}}$, the one of the cavity $\hat{H}_{cav}$ with ladder operators $a^{\dagger}_{\boldsymbol{k}}$, $a_{\boldsymbol{k}}$, and the interaction Hamiltonians containing the linear and quadratic terms in the photon operators, $\hat{H}_{int,1}$ and $\hat{H}_{int,2}$, respectively.

The linear interaction Hamiltonian $\hat{H}_{int,1}$ is the one derived from the $\hat{\boldsymbol{p}} \cdot \hat{\boldsymbol{A}}$-term and contains both resonant and anti-resonant terms, i.e. terms in both $\boldsymbol{k}$ and $-\boldsymbol{k}$, with coupling constant (Rabi splitting) $\Omega_{\boldsymbol{k}}$. Sometimes these terms are also termed *paramagnetic*.

The $\hat{\boldsymbol{A}}^2$-term is instead at the origin of $\hat{H}_{int,2}$. Strictly speaking, this term does not directly couple the matter and the photonic parts of the system but it is more a renormalisation due to the self-interaction of the polaritonic states: such Hamiltonian is in fact often named *diamagnetic*. The (self-)coupling constant, in the bosonic approximation of the system, can be written as

$$D_{\boldsymbol{k}} = \frac{\Omega^2_{\boldsymbol{k}}}{\omega_{cyc}} \tag{0.40}$$

and it is thus clear that this term is of higher order in the coupling constant $\Omega_{\boldsymbol{k}}$. Note that also this interaction Hamiltonian contains both resonant and anti-resonant terms.

A system is said to be in the *strong coupling* regime when the exchanged energy between the matter and light part is small but non-negligible with respect to the energy of the states themselves and higher than the loss rates. In this case the system is described by the so-called Jaynes-Cummings Hamiltonian[50]

$$\hat{H}_{JC} = \hat{H}_{mat} + \hat{H}_{cav} + \hat{H}^{RWA}_{int,1}, \tag{0.41}$$

where the quadratic interacting term has been dropped and the linear one in the rotating-

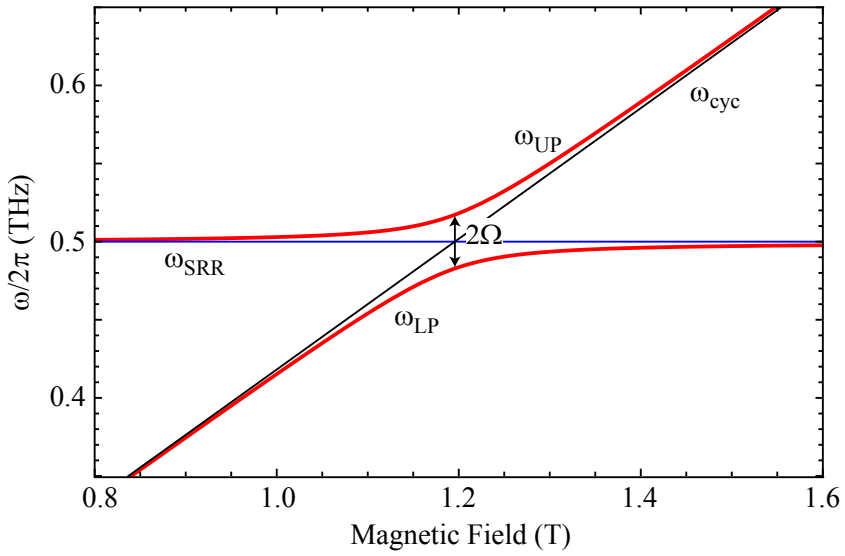

Figure 0.9 – Schematics of the strong light-matter coupling regime, showing the polaritonic branches.

wave approximation retains only the resonant terms in $\boldsymbol{k}$.

In this regime, when the two systems are brought into resonance, an anti-crossing pattern is formed as plotted in Fig. 0.9: the upper ω_{UP} and lower ω_{LP} polaritonic branches avoid each other with a reduced Rabi splitting given by Ω/ω_{res}, ω_{res} being the angular frequency at which the cavity ω_{SRR} and the cyclotron ω_{cyc} are resonant.

Such strong coupling regime was first investigated in the field of atomic physics[51, 52, 53] and it was later realised for the first time in a solid-state system[54] with a quantum well inserted into a Fabry-Perot cavity, displaying an anti-crossing when tuning the cavity resonance across the excitonic transition in the quantum well.

Nowadays such regime is widely present in solid-state physics and several optoelectronic devices were demonstrated displaying it, from quantum-well infrared photodetectors[55], to photovoltaic quantum cascade detectors[56], to electro-luminescent quantum cascade structures.[57, 58]

When the exchanged energy is comparable to the energy of the initial states, or even bigger, all terms of the Hamiltonian are needed to describe the system, that is said to be in the *ultra-strong coupling* regime. The details are discussed in chapter 6, but we will mention here that one of its main features is the presence of photons in the ground state of the system[48], a fact linked to different quantum optical features.

Finally, the ultra-strong coupling regime acts such that the polaritonic branches never vanish, as shown by the red curves in Fig. 0.10. This is, nonetheless, possible when the

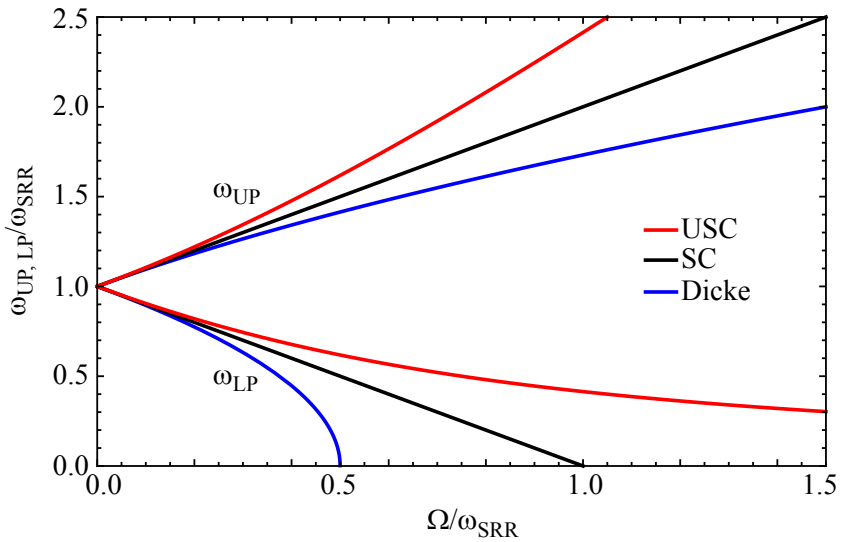

Figure 0.10 – Frequency behaviour of the polaritonic branches vs reduced Rabi frequency for a system in ultra-strong coupling (USC, red), for one in strong coupling (SC, black) and for one described by the Dicke Hamiltonian (Dicke, blue).

$\hat{\boldsymbol{A}}^2$-term can be neglected (blue lines):

$$\hat{H}_{Dicke} = \hat{H}_{mat} + \hat{H}_{cav} + \hat{H}_{int,1} \tag{0.42}$$

the lower polaritonic branch bends then towards negative energies and eventually dies out with infinite first derivative at $\omega = 0$. This fact results into the so-called superradiant Dicke phase transition [59] and it is debated whether graphene could allow to study such physics.[60, 61, 62]

Chapter 7 deals with the attempt of detecting the ultra-strong coupling status of the system in transport via the microwave-induced resistance oscillation phenomenon, while chapter 8 presents the results of the interaction of graphene with the THz-SRRs, in an attempt to realise the system able to give an answer on the Dicke phase transition.

0.2.3 Terahertz lasers and modulators

Light-matter interaction is also the essence of opto-electronics, one of the disciplines nowadays enabling most technological advancements and scientific reasearch. In fact, to be able to work with light and convert an optical signal into an electrical one, sources, detectors and modulators are needed.

This is particularly problematic in the THz-frequency range, for the characteristics of the available materials, some of which were discussed above. In this thesis, THz-QCL sources and THz-modulators will be discussed in part I and chapter 8, respectively.

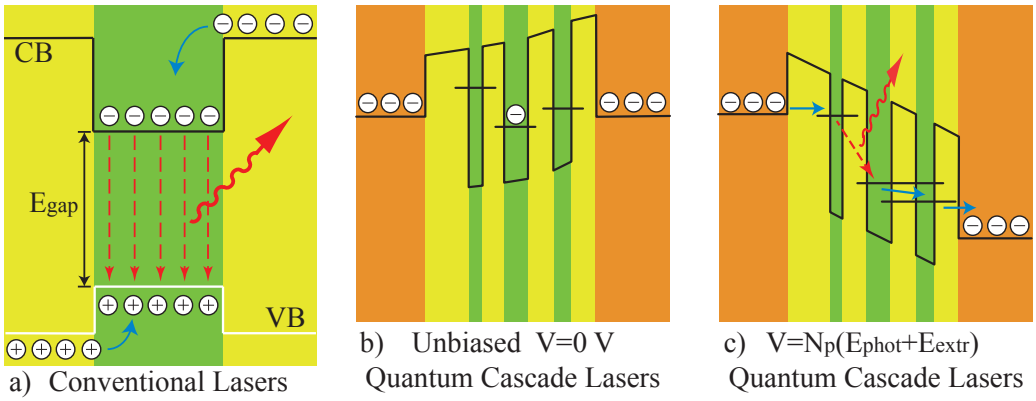

Figure 0.11 – a) Operation principle of a conventional semiconductor laser: the electrons accumulated at the bottom of the conduction band (CB) and the holes at the top of the valence band (VB) recombine across the gap emitting photons with $E_{phot} = E_{gap}$. b) Schematic band structure for an unbiased Quantum Cascade Laser: all involved states are in the CB and trap the electrons when unbiased. c) When a bias approximately equal to the number of periods (N_p) times the energy of the photon (E_{phot}) and of the extraction stage (E_{extr}) is applied, the electrons can flow through the structure and emit light. The comparison of b) and c) visualises the cascading principle for the carrier transport. Adapted from [64].

Quantum Cascade Lasers

Quantum cascade lasers (QCLs) are a source of coherent light for the mid- and far-infrared (MIR, FIR) frequency range, i.e. for wavelengths in the range 3-200 µm or frequencies in the range 1-100 THz, and were first demonstrated with emission at 4.26 µm in 1994 at Bell Labs by Jérôme Faist and coworkers in the group led by Federico Capasso[63].

This type of laser is conceptually different from the more standard semiconductor interband laser. The main difference is that QCLs rely on electrons undergoing transitions between quantised states within the conduction band while interband lasers rely on the recombination of electron and holes across the bandgap of the constituting material. Therefore one speaks of QCLs as unipolar intersubband devices in contrast to bipolar interband lasers. These properties, sketched in Fig. 0.11, have important implications both on the physics and on the realisability of the devices.

In order to better understand the novelty of QCLs, we focus for a moment on the interband lasers[65]. Their emission wavelength is rigidly connected to the bandgap of the used material and, therefore, changing its doping and/or the material itself is needed to enlarge the covered spectral range. This scheme results problematic when moving to increasingly longer wavelengths, i.e. smaller energies, where narrow bandgap materials are required, as mentioned in the previous sections. These are, on the one hand, relatively new and quite complex from the point of view of growth, doping and processing, while, on the other hand, such a narrow-bandgap-based interband laser operating at room temperature, as desirable for any device, will suffer enormously from non-radiative recombination of the

carriers. The principles of QCLs have also been used to re-think interband lasers and solve some of the previously mentioned issues: interband cascade lasers (ICLs) are nowadays available.[66, 67] The QCL, relying on transitions between states in the conduction band created by quantum confinement, can be designed for several different wavelengths within the same material system. Material parameters other than the bandgap are more important for the functioning of the QCL and are discussed in chapter 1.

As previously discussed, in order to obtain distinct levels into the conduction band, the key requirement is quantum confinement. Precondition for this is the possibility of reliably growing atomically precise layers of semiconductors that would constitute the heterostructure. Already at the end of the '60s, semiconductors' thin films could be grown[68], but the first doping processes and heterostructure's growths were made possible by key technological advancements at Bell Labs where J. R. Arthur and A. Y. Cho developed the first molecular beam epitaxy (MBE) machine[69, 70]. Widespread subsequent efforts improved the machine and the technique[71] and the growth of heterostructures became soon reliable. This, along with the parallel efforts in metal-organic chemical vapour deposition[72], opened the field of intersubband opto-electronics, where transitions between different confined states within a single (or multiple) quantum well were studied and engineered into devices.[73]

Soon after the growth of the first heterostructures, several proposals were published investigating the potential of superlattices (e.g. the work of Esaki and Tsu on superlattices[74]), among which were the first calculations by Kazarinov and Suris on light amplification using the intersubband transitions in a superlattice.[75] In particular, in such a system, light amplification is achieved by means of photon-assisted tunnelling from the lowest state of a quantum well to the excited state of the next quantum well. These states are brought to the suitable energy distance by biasing the superlattice, hence allowing a single electron to undergo as many of these transitions as the number of the quantum wells pairs, now stretched into a ladder by the applied electric field, as sketched in Fig. 0.11.

All these ingredients then justified the name of the class of devices, first realized 23 years later: Quantum Cascade Lasers.

The proposal of Kazarinov and Suris[75] foresaw light amplification at frequencies of the order of k_BT, i.e. some tens of milli-electronvolts, corresponding to THz-frequencies (recall room temperature is 25°C corresponding to 25.6 meV and to 6.19 THz). An important result in that direction was achieved by Helm and coworkers in 1989, which reported the first THz luminescence from a superlattice excited by sequential tunnelling.[76] However, the first QCL lased in the MIR range, also because of difficulties with the waveguides for the lower energy range. These difficulties would be overcome only eight years later by

a team led by Alessandro Tredicucci at the Scuola Normale Superiore in Pisa, resulting in the first THz-QCL lasing at 4.4 THz and up to 50 K.[77]

THz-QCLs represent nowadays a primary semiconductor-based, electrically pumped source in the THz-frequency range.[8] THz-QCLs realised in the GaAs/AlGaAs material system saw big improvements both in frequency coverage [78] and operating temperature [79] since their first demonstration[77], but room temperature operation is still missing. At the same time, difference-frequency generation in mid-infrared QCL shows now good performances at room temperature but the process is not very efficient while emitting single mode.[80, 81] Researchers are thus studying new materials and/or new schemes to increase the operating temperature of THz-QCLs.

Part I presents the magneto-spectroscopy study of THz-QCLs based on the new quaternary barrier material AlInGaAs. The results show relatively good perfomances of the new material system, despite perfoming worse than more established heterostructure types, and allowed us to compare the different reported material systems.

THz-modulators

Modulators are devices that allow one to manipulate the optical radiation, usually in amplitude and /or frequency, but control on the phase and other properties is also desirable and sometimes possible.

The limitations discussed in the previous sections for the available materials in the THz-frequency range, make THz-light modulation a challenging task and thus a topic of research. This is the case, especially because of the long wavelength of the radiation that results in a weak mode overlap with standard micrometric-sized systems.

One common way to face the size mismatch issue is to use metamaterials as radiation concentrators, such to increase the radiation/active layer overlap.[82] A good amplitude modulation still needs a comparatively long interaction path into the material, while requiring very limited doping to avoid strong absorption. On the other hand, this results in quite bulky and resistive devices that perform poorly as frequency modulators.

The combination of graphene with THz-SRRs is an interesting combination for this kind of study, allowing a big reduction of the interaction path, ideally at the monolayer level, while taking advantage of graphene's THz-properties: some devices had already been reported at the time of the investigations, but all with wide room for improvements.[83] The modulating capabilities of a graphene/THz-SRR sample, along its investigation within the frame of the Dicke phase transition, are the topic of chapter 8.

0.3 Outline of the manuscript

Part I describes the magneto-spectroscopy of quaternary barrier THz-quantum cascade lasers. Chapter 1 introduces the QCLs with particular emphasis on the important concepts for bringing them to the THz-frequency range. These are the starting point to discuss the measurements in chapter 2, after having explained how the technique works.

Part II is dedicated to the near-field interaction of dual THz-split-ring resonators. Chapter 3 presents the design of split-ring resonators used, both direct and complementary, along with the analytical transmission-line model and the time-domain spectroscopy setup used. Chapter 4 contains the measurements and analysis of the measured extraordinary transmission by the dual THz-split-ring resonators, where direct and complementary THz-SRRs are interacting in the deeply subwavelength near-field. Interestingly, despite the resonant nature of the THz-resonators, the transmitted signal is broadband and with approximately flat spectrum.

Part III wants to expand the ultra-strong light-matter coupling concepts towards, on the one hand, transport detection and, on the other hand, Dicke physics with graphene. Chapter 5 introduces graphene both from the theoretical and experimental point of view. First, its electro-optical properties, with and without magnetic field, are introduced. Second, particular attention is dedicated to the production and characterisation methods of the different kinds of graphene used in the thesis. Chapter 6 describes the features of the ultra-strong light-matter coupling regime, achieved when the THz-SRRs strongly interacts with the cyclotron transition in the 2DESs. This is both the basis and the outlook for the subsequent chapters. New measurements showing the absence of interaction between the polaritons connected to the different SRR-modes are also presented.

Chapter 7 discusses the hybrid transport-optical investigation performed on SRR-covered GaAs-based Hall-bars aiming at the detection in transport of the ultra-strong coupling. For this, the phenomenon of microwave-induced resistance oscillations was exploited, according to which, microwave irradiated Hall-bars display additional oscillations in the ρ_{xx} trace. The measured samples allowed us also to discuss the origin of this relatively new and not-yet-understood process.

Finally, chapter 8 presents the investigation of different kinds of graphene-based samples where the 2D-material interacts with the THz-SRRs. First, it is shown that the sample perfoms well as a THz-modulator. This is then followed by the magneto-optical investigation aiming at reaching and detecting the ultra-strong coupling between the resonators and the cyclotron transition in graphene.

Part I

Magneto-spectroscopy of quaternary-barrier Terahertz Quantum Cascade Lasers

Chapter 1

THz-Quantum Cascade Lasers

After the brief introduction in section 0.2.3 on page 21, this chapter presents the basic concepts needed to understand quantum cascade lasers, with special emphasis on those used in the next chapter for discussing the results of the performed investigation. In particular, the discussion will focus on the operating temperature of THz-QCLs, discussed from the point of view of the material systems and of the active-region schemes. To this aim, more attention will be put onto the different sources of losses. The last section will introduce the studied THz-QCLs: InGaAs/AlInGaAs THz-QCLs processed in gold and copper double-metal waveguides.

1.1 Basic Concepts of QCLs: active region scheme and waveguides

In order to introduce the THz-QCLs in the best possible way, both a historical and a logical path will be followed in the present section, starting with the analysis of the progenitor of the QCL family. For the complete treatment see Ref. [32].

1.1.1 Mid-Infrared QCLs

The first QCL was realised following the standard four-level system laser-architecture within the intersubband levels of the conduction band of an InGaAs/AlInAs superlattice, as shown in Fig. 1.1.[63] The *active region*, where the optical transition takes place, is constituted by a series of three quantum wells. These are arranged such that, at the alignment bias, the electrons populate the highest state $|3\rangle$, then radiate while decaying to state $|2\rangle$, from which they are extracted to state $|1\rangle$ that funnels them further into the cascade. An additional superlattice, termed *injector* acts as the ground state of

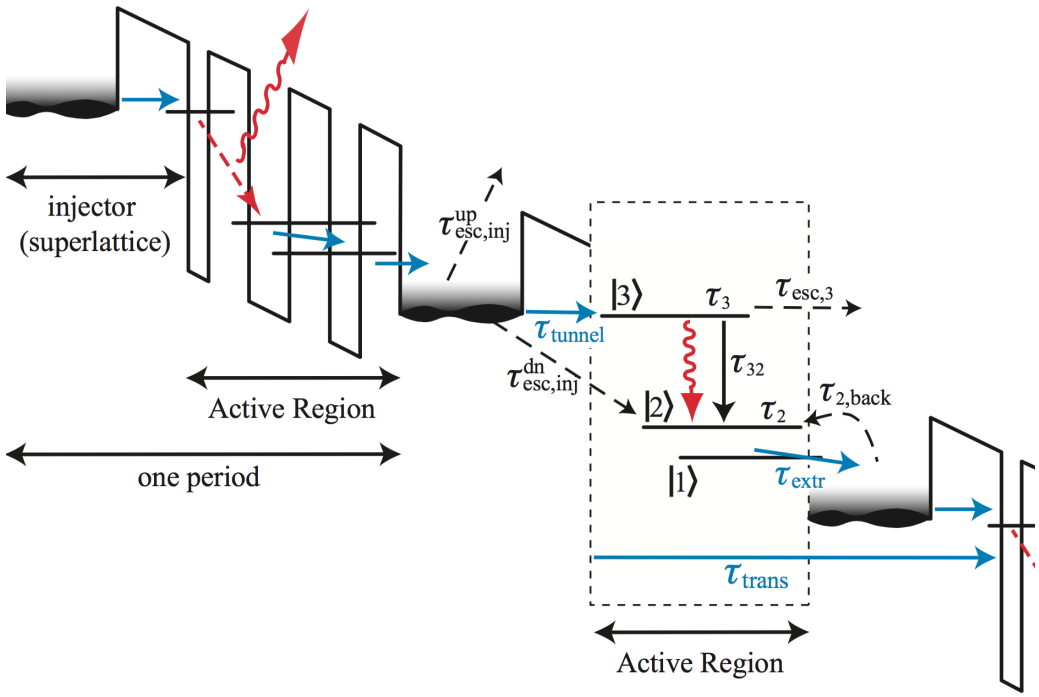

Figure 1.1 – Lasing scheme of the first QCL including the schematics of the lifetimes of the different non-radiative processes. The black arrows indicate the possible processes that decrease the efficiency of the lasing. The most important unavoidable direct competitor is the non-radiative transition τ_{32} (vertical solid black line). The electrons can by-pass the optical transition also via the escape paths (τ_{esc}) from the injector or the upper state $|3\rangle$ while the population inversion is reduced by back-filling processes (τ_{back}): these are all shown as black dashed lines. The blue arrows indicate instead the lifetimes associated with the electron transport, tunnelling to $|3\rangle$ or extraction from $|2\rangle$. Additional explanation in the text. Adapted from [32].

the laser, receiving the electrons from $|1\rangle$ and populating $|3\rangle$. Active region plus injector constitute the unit of the QCL, called *period*, that is repeated several times during growth to produce the cascade: the temporal cycle that electrons undergo in an optically pumped laser is substituted here by a spacial repetition of the four-level structure. Note that, in the following, *active region* will also be used to indicate the final structure consisting of several repetitions of the period; which one is meant will be clear by the context. For the discussed level arrangement to allow population inversion, the non-radiative lifetime of the transition $|3\rangle \rightarrow |2\rangle$, τ_{32}, has to be longer than the lifetime of the lower state $|2\rangle$, τ_2. For the present discussion, state $|1\rangle$ is assumed to have a short lifetime and the non-radiative transition $|3\rangle \rightarrow |1\rangle$ is assumed negligible, hence $\tau_{31}^{-1} \simeq 0$. These requirements are fulfilled by engineering the QCL design in the following ways, as sketched in Fig. 1.1:

- the different depopulation mechanisms for $|3\rangle$, mainly backfilling and escape to the continuum, are reduced so that the total lifetime is almost identical to τ_{32}, i.e. $\tau_3 = (1/\tau_{32} + 1/\tau_{esc,3})^{-1} \simeq \tau_{32}$. This is done by designing the injector as a

superlattice such that (i) the barrier that separates it from the next well is as high as possible; (ii) at alignment, an energy gap is placed in front of $|3\rangle$;

- non-radiative decay from $|3\rangle$ to other states is neglected, provided they are further away in energy than $|2\rangle$ and they are not resonant with (multiple) phonon transitions;

- $|2\rangle$ is rapidly depopulated to $|1\rangle$ by spacing the states by an energy approximately equal to the one of the Longitudinal Optical- (LO-) phonon of the material (e.g. 36 meV for GaAs);

- the extraction time from $|2\rangle$, $|1\rangle$ (τ_{extr}) and the filling time of $|3\rangle$ (τ_{tunnel}) are fast due to tunnel-coupling to the injector;

- additional loss paths from the injector, like population of higher levels ($\tau^{up}_{esc,inj}$) or tunnelling directly to the lower states ($\tau^{dn}_{esc,inj}$), are minimised by designing suitably spaced states.

In general the QCL architecture should be engineered to make the competing non-radiative lifetimes (black arrows in Fig. 1.1) as long as possible while decreasing the ones related to transport (blue arrows in Fig. 1.1). This optimisation process results in typical scattering times of the order of $\tau_{32} \simeq 1-10$ ps and $\tau_2 \simeq 0.1$ ps; the tunnelling rate from/to the injector for state $|3\rangle/|1\rangle$ is also of the order of 0.1 ps.[32]

The interplay of these different scattering times is summarised into the *effective scattering time* defined as

$$\tau_{eff} = \tau_3 \left(1 - \frac{\tau_2}{\tau_{32}}\right) \xrightarrow{\tau_2 \ll \tau_{32}} \tau_3. \tag{1.1}$$

This follows from the population inversion calculated at steady state from the rate equations of the system $\Delta n = \frac{J\tau_{eff}}{e}$, J being the current density flowing in the heterostructure and e the elementary charge value.

The lasing condition reads "gain=losses": the device starts lasing when the modal gain $g_c \Delta n$ is equal to α_{tot}, where g_c is the gain cross section defined as

$$g_c = \Gamma \frac{2\pi e^2 z^2}{\epsilon_0 n_{refr} L_p \lambda \gamma} \tag{1.2}$$

with Γ being the overlap factor of the optical mode with the active region, z the dipole strength of the transition, ϵ_0 the vacuum permittivity, n_{refr} the active-region refractive index, L_p the period length, and λ and γ the transition wavelength and broadening,

respectively. A more detailed explanation of these terms will be given by the end of the section.

This lasing condition defines the *threshold current density* J_{th} as

$$J_{th} = \frac{e\alpha_{tot}}{g_c \tau_{eff}}. \tag{1.3}$$

A similar equation can be written to characterise the transport through a single period: since the maximum current density J_{max} is directly proportional to the sheet carrier density n_s, a *transport time* τ_{trans} can be defined. The relation reads:

$$J_{max} = \frac{n_s e}{\tau_{trans}}. \tag{1.4}$$

It has to be noted that different relations can be found in the literature, depending on which approximations are made for the level system and which scattering times one wants to focus on. Often, for example, the resonant tunnelling time is parcelled out and $\tau_{trans} = \tau^*_{trans} + \tau_{tunnel}$, where τ^*_{trans} accounts then for the transport *after* the tunnelling took place.[84, 85]

In Eq.(1.4), the sheet carrier density n_s can be approximated by the doping of the heterostructure, often of the order of 10^{11} cm^{-2}. This doping is necessary to avoid the formation of space charge domains by ensuring electrical neutrality and providing free carriers for the transport. On the other hand, the intersubband (re-)absorption represents one of the biggest sources of losses for the device and exemplary values for 3 µm QCLs vary in the range $\alpha_{ISB} = 0 - 6$ cm^{-1}.[86, 87] Therefore the doping has to be minimised such that the losses are small, allowing a low J_{th}, but it must also allow a high enough J_{max}, since the power of the laser is proportional to the *dynamic range* $(J_{max} - J_{th})/J_{max}$.[78] Additionally, the ionised impurities that provide the doping electrons have an extremely detrimental impact on the emission wavelength, broadening and shifting the lasing transition.[88] For such reason the doping is placed as far as possible from the optical transition, i.e. in the injectors.

To bring the system into lasing another fundamental part is needed: the heterostructure needs to be inserted into a cavity. Because of a very high total dissipated power, the volume of the heterostructure in the final device needs to be small, and typically it is approx. 10 µm × 2 µm × 3 mm. Note that two out of three dimensions are comparable to the emission wavelength.

In the simplest solution, at the ends of the longest dimension, the mirrors of the cavity are directly determined by the cleaving of the heterostructure along one of its

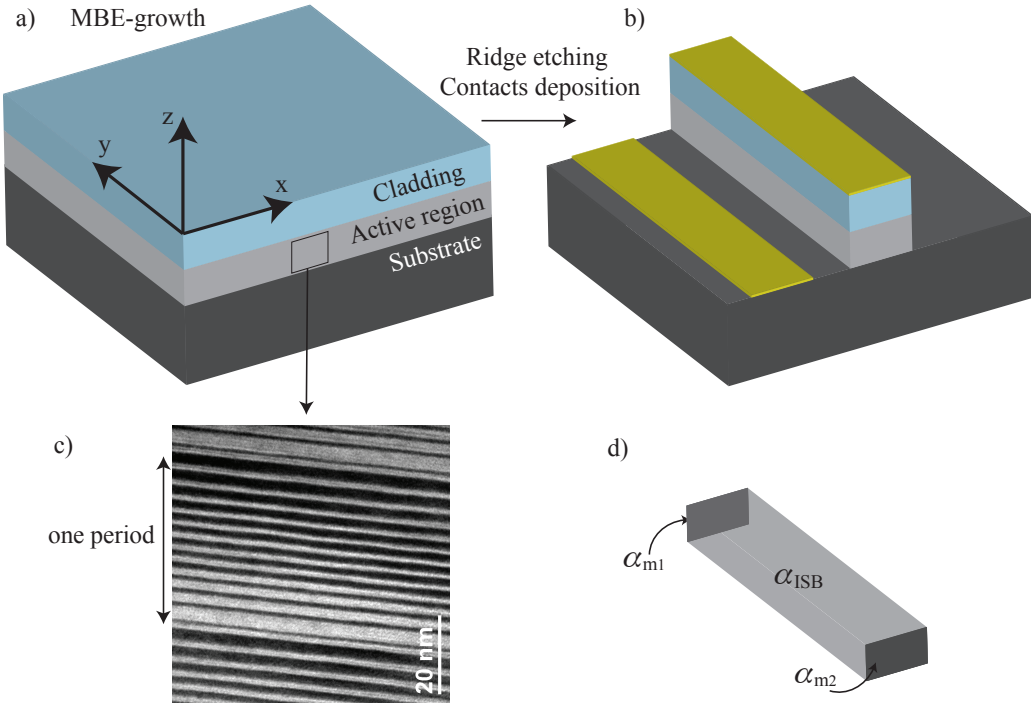

Figure 1.2 – a) Sketch showing the result of the MBE-growth: cladding and active region are grown onto the substrate. b) After several processing steps, the ridge is defined by etching and the contacts are deposited. For more details see [32]. c) Transmission Electron Microscope picture of one period of the active region: the colour contrast allows the identification of wells and barriers. (Courtesy of Dr. Süess) d) Identification of the ridge-related losses.

crystallographic planes (cf. panel d) of Fig. 1.2). The refractive index difference between the grown material and air, e.g. $n_{InGaAs} = 3.5$, is already enough for having a good mirror with reflectivity $R = \left(\frac{n_{InGaAs}-n_{air}}{n_{InGaAs}+n_{air}}\right)^2 \simeq 30\%$. This can be tailored with the use of high-/anti-reflection coatings of the laser facets.[89] From the reflectivities of the two facets $R_{1,2}$, one can then calculate the mirror losses as

$$\alpha_m = \alpha_{m1} + \alpha_{m2} = -\frac{1}{2L}\ln(R_1 R_2) \tag{1.5}$$

once the length of the device L is known: typical values are in the range 1-6 cm^{-1} for devices few millimetres long.

Then, in order to maintain enough gain, the light needs to be kept inside the active region while bouncing back and forth between the two facets. The most immediate way, at MIR-frequencies, would be to make use of the waveguiding properties of the heterostructure itself due to the refractive index contrast with air. This is nonetheless not a solution for the vertical direction, since the QCL needs to be (i) electrically pumped, i.e. it needs electrical contacts, and (ii) thermally cooled, to get rid of the heating due to the dissipated power. These two issues can be solved together with the waveguide realisation

by (re-)growing suitable semiconductor layers around it. In the (defined vertical) growth direction this is achieved by using doped substrates at the bottom and by growing a doped cladding on top, before placing the metallic contacts, as sketched in panels a) and b) of Fig. 1.2. For example, in a short wavelength MIR-QCLs grown with InGaAs/AlInAs, the active region can have an effective refractive index of about $n_{eff} = 3.3$ and be sandwiched between the InP substrate with $n_{InP} = 3.1$ plus a low-doped AlInAs layer and a top thick AlInAs cladding with $n_{AlInAs} = 3.2$. In the in-plane (horizontal) direction, instead, the active material is first etched to the wanted width and then surrounded by an insulating cladding with good thermal conductance and lower refractive index, e.g. InP or Si_3N_4. In general, dielectric waveguides have losses of $\alpha_w = 0.5 - 10$ cm^{-1} for $\lambda \leq 15$ µm and a cladding doping $n \simeq 10^{16}$cm^{-3} and they increase with frequency as $\alpha_w \propto \lambda^2$.[90, 86] Since these losses are due to free-carrier absorption, in some literature they are denoted as α_{fc}.

This immediately becomes problematic when moving with such a scheme to longer wavelengths. A longer wavelength requires a thicker cladding scaling proportionally to λ. This is, in the first place, not always possible and soon the mode will reach the top metallic contact (the bottom one is placed on the back of the substrates several hundreds of micrometres away), resulting on one side in a very strong absorption in the metal, on the other side into the excitation of a surface plasmon at the interface.[91] The solution resided in skilfully taking advantage of the metallic contacts and moving from a dielectric to a partly plasmonic waveguide, termed *single-plasmon (SP) waveguide*.[92] In fact, the excited plasmon has two advantages: (i) it concentrates much strongly the optical mode and (ii) the typical contact configuration is already arranged in the right polarisation for intersubband transition, i.e. Transverse-Magnetic (TM). Additionally the top cladding can be much thinner and less doped than for dielectric waveguides. From the imaginary part of the refractive index of the used metals, one would expect waveguide losses of about $\alpha_w = 14$ cm^{-1} (for Pd at 8 µm), instead the very first try showed quite higher losses of $\alpha_w + \alpha_{ISB} = 100 - 150$ cm^{-1} in the range $8 - 11.5$ µm, probably due to the phonons of the cladding.[92] Nonetheless, SP-waveguides are advantageous for wavelengths longer than 20 µm.[93]

At this point we can sum up all loss terms and get a formula for the total losses of the device, appearing in Eq. (1.3):

$$\alpha_{tot} = \alpha_m + \alpha_w + \alpha_{ISB} \tag{1.6}$$

recalling that α_m indicates the losses of both mirror facets, α_w the empty-waveguide losses, and α_{ISB} the re-absorption losses, both resonant and non-resonant. The last term

is proportional to the carrier density and can be written as

$$\alpha_{ISB} = g_{ISB} n_s, \tag{1.7}$$

where the total carriers can be approximated by the doping carrier density n_s and the proportionality constant g_{ISB} has the units of a cross-section and can be experimentally determined from the linearity of J_{th} with respect to n_s.[90] Note also that the loss values depend very strongly on the specific characteristics of the QCL, like design scheme, material system, emission wavelength: the ones reported are meant as examples, mainly to show the orders of magnitude.

Until this point only a single period of the QCL was discussed, assuming it is surrounded by a long series of other identical ones. Since the number of periods is directly related to the number of emitted photons per electron, the final power should benefit of a thick heterostructure. On the other hand, there are several concurring limiting factors: (i) the time stability of the MBE machine growing the heterostructure, (ii) the desired bias to be applied to the device at operation (and the resulting dissipated power), (iii) the overlap between the confined amplified optical field and the grown active region.

Concerning the MBE growth, extreme precision is required, both in thickness and composition of the quantum wells and barriers over hours of uninterrupted operation. Excellent heterostructures can be grown for more than twenty hours at a speed of approx. 1 µm/h, nonetheless shorter growths are advisable. The main factor determining the maximum number of periods of a QCL active region is given by the voltage that can be applied to the final device. Approximately, the alignment bias is given by the number of periods multiplied by the energy difference between the top-most and the lowest levels involved into the lasing process within one active region, as sketched in panel c) of Fig. 0.11 on page 22. The number of periods N_p is then chosen such that the required bias will be in the range 10-20 V and it scales inversely proportional to the emission energy for a constant N_p. Finally, the performance of the laser are closely related to the overlap factor Γ between the optical mode and the gain region. The most important influence comes via the gain cross-section of Eq. (1.2) that is proportional to Γ. A good compromise for dielectric waveguides is found for values in the range Γ=0.4-0.8 that allow good mode overlap with limited losses. At longer wavelengths, SP-waveguides perform better than dielectric ones, mainly because of the tighter confinement: it was calculated that, for similar active region dimensions, $\Gamma_{SP} = 0.7$ to be compared with $\Gamma_{diel} = 0.4$.[92] The mode profile of the first MIR-QCL with dielectric waveguide and the one with the first SP-waveguide are reported in panel a) and b) of Fig. 1.3, respectively.

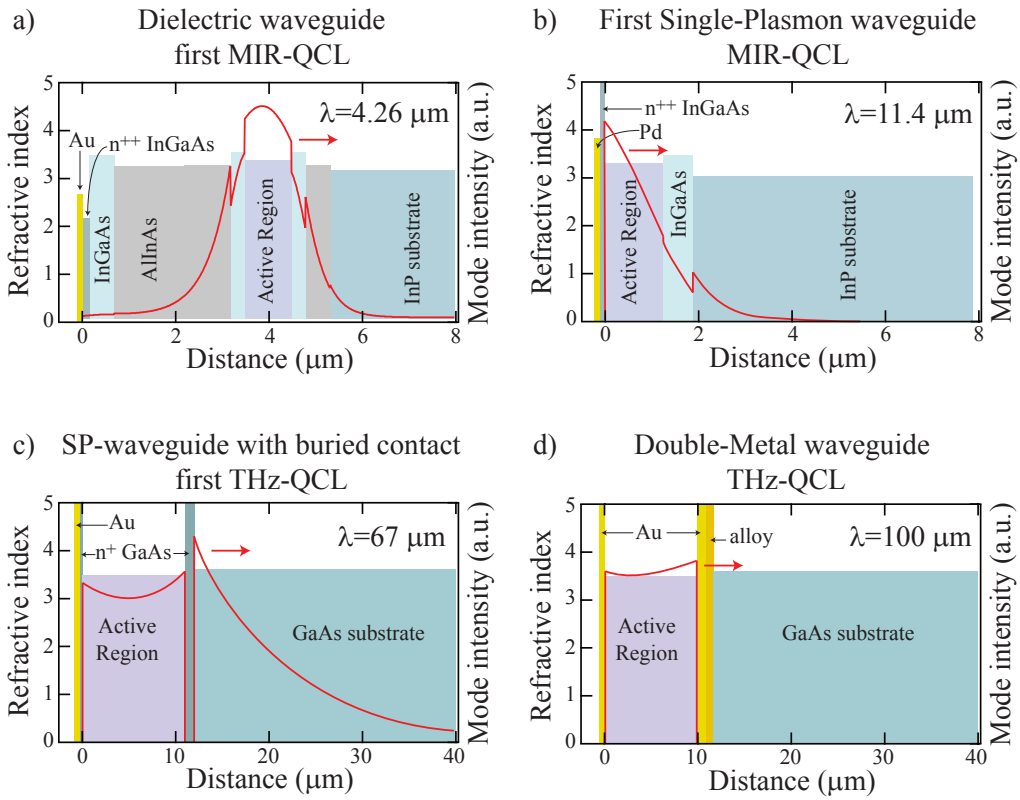

Figure 1.3 – Schematics of the different waveguiding principles for QCLs. The optical mode profile is plotted against the distance along the growth direction for the following structures and waveguides: a)dielectric waveguide for the first MIR-QCL (adapted from [32]); b)first realisation of the Single-Plasmon waveguide for a MIR-QCL (data from [92]); c)first realisation of a Single Plasmon waveguide with buried contact layer for the first THz-QCL (data from [77]); d)first realisation of a Double-Metal waveguide for a THZ-QCL (data from [94]). A sketch of the growth sequence is also reported and the refractive index of the different layers can be read on the left axes. Additional data concerning these QC-structures, and also for the first Double-Metal for a MIR-QCL[95], are collected in Table 1.1.

Since Γ is bound to 1, total overlap would seem the best option: this is not possible for dielectric and SP-waveguides. On the other hand, as it will be explained in the next pages, this is the case for double-metal waveguides. Given this interplay of mode overlap and losses for different waveguides at different wavelengths, what becomes then a good figure-of-merit for a waveguide is the ratio Γ/α_{tot}, that is proportional to the inverse of the threshold current density, according to Eqs (1.2)-(1.3). A general comparison will be discussed along Table 1.1.

The first QCL was realised with the InGaAs/InAlAs/InP material system and contained 25 periods, each 39.7 nm thick, that would align at a field of $\sim 10^5$ V/cm with $\Gamma_{diel} = 0.46$ and was lasing up to 90 K in pulsed operation mode.[63]

In the past decades the design of MIR-QCL has been continuously improved and different schemes have been implemented to solve specific issues. The best performing devices

under several points of view use either the "bound-to-continuum" design, where the lower laser level is merged to the injector state and it is constituted by a continuum of states[96], or the double phonon resonance extraction[97, 98]. These designs have been employed to demonstrate continuous-wave operation[99], high-temperature performance[100], high output power[101], operation in the comb regime[102] and THz generation by difference frequency generation[103].

Finally, different implementations have been realised concerning the type of cavity, the mode selection and the way of tuning: from distributed-feedback gratings of different orders[104, 105, 106], to photonic crystals[107], to ring cavities[108], to amplified systems[109], from external-cavity tuning[110], to thermal tuning within the pulse[111], to electrical tuning[112].

Nowadays MIR-QCLs span the range $\lambda = 2.63 - 28$ µm[113, 114], routinely show continuous-wave operation above room temperature and emit up to 5.1 W in continuous-wave operation[115]. Research is still needed and carried on, but this kind of lasers is technologically mature and already available on the market.

1.1.2 The necessary improvements for the THz-QCLs

As already mentioned, despite the fact that THz-emission was the first goal of the research that led to QCLs, the first THz-QCL was demonstrated in the GaAs/AlGaAs material system[77], eight years after the MIR-one. Moreover, to date no THz-QCL reached room-temperature operation. Soon after the first QCL, several groups reported THz-luminescence from Quantum Cascade (QC-) structures[116, 117, 118] but two main issues hindered lasing: the difficulty in achieving population inversion and the high losses due to the broad optical mode penetrating into the doped substrate.[119]

Concerning the wave-guiding problem, the first option was to use the SP-waveguide also in the THz frequency range. This unfortunately resulted in a very small overlap between the poorly confined optical mode and the active region. The solution implemented into the first THz-QCL was to grow a very thin, highly-doped layer (800 nm, 2×10^{18} cm^{-3}, Si) just below the active region on the substrate side, such that symmetric surface plasmons would be excited at its two interfaces, providing tight field-confinement and small penetration into the substrate. Another 200 nm-thick, 5×10^{18} cm^{-3} Si-doped layer was grown between the active region and the top metallisation as contact layer. This waveguide resulted in $\Gamma = 0.47$ and $\alpha_w + \alpha_{ISB} = 16$ cm^{-1}.

Single-plasmon waveguides performed very well also when applied to long wavelength MIR-QCLs.[95] In particular, Unterrainer and coworkers were the first to expand this concept and completely sandwich the active region between two metallic layers that would

let no field penetrate further, then called Double-Metal (DM-)waveguide. They compared SP- and DM-waveguides and showed that at $\lambda = 21$ µm the two solutions are almost equivalent: $\Gamma_{SP} = 0.92$ and $(\alpha_w + \alpha_{ISB})_{SP} = 40.2$ cm^{-1} while $\Gamma_{DM} = 0.98$ and $(\alpha_w + \alpha_{ISB})_{DM} = 37.8$ cm^{-1} using gold as contact metal.[95] When moving to longer wavelengths, the performances are not any more comparable: Γ_{SP} falls below 0.5 because of the increasing penetration into the substrate while $\Gamma_{DM} \simeq 1$. Williams and coworkers performed the same kind of comparison for a THz-QC-structure designed for $\lambda = 100$ µm (3 THz): $\Gamma_{SP} = 0.127$ and $(\alpha_w + \alpha_{ISB})_{SP} = 2.7$ cm^{-1} while $\Gamma_{DM} = 0.98$ and $(\alpha_w + \alpha_{ISB})_{DM} = 6 + 11.8 = 17.8$ cm^{-1} using gold as a contact metal.[94] In spite of the very low losses, the devices with SP-waveguides did not lase because of the very poor mode overlap. This shows the importance of the ratio Γ/α_{tot} that is more favourable for DM-waveguides. The mode profile of the first THz-QCL with SP-waveguide and the one with the first DM-waveguide are reported in panels c) and d) of Fig. 1.3, respectively. An overlap/losses comparison of all the different kinds of waveguides is then performed in Table 1.1 and shows how the figure-of-merit increases (almost chronologically) with increasing wavelength and with tighter plasmonic confinement.

Table 1.1 – Comparison of the different wave-guiding schemes, focussed on overlap factor Γ and losses α. The comparison includes the first realisation of each type of waveguide and of the first MIR- and THz-QCL. The waveguide and ISB losses are written separately when so identified in the corresponding literature. The figure-of-merit Γ/α_{tot} gives an idea of the achieved improvements and indicates an upper bound when the mirror losses were non-reported ('?'). The mode distribution and the structure composition of four of the five listed devices are shown in Fig. 1.3.

Waveguide type	QCL type	λ (µm)	Γ	$\alpha_w + \alpha_{ISB}$ (cm^{-1})	α_m (cm^{-1})	α_{tot} (cm^{-1})	Γ/α_{tot} ($\times 10^{-3}$ cm)	Ref.
Dielectric waveguide	first MIR	4.3	0.46	9	18.54	27.54	16.7	[63]
SP-waveguide	MIR	11.4	0.70	14+136	?	>150	<4.7	[92]
SP-waveguide with buried contact	first THz	67	0.47	16	4	20	23.5	[77]
DM-waveguide	MIR	21	0.98	38	?	>38	<25.8	[95]
DM-waveguide	THz	100	0.98	6+11.8	~6	~23.8	~41.2	[94]

Being the overlap factor already maximised, the only room for improvement comes from the reduction of the waveguide losses. In fact, soon after gold also copper was tested for the contact metallisation and it resulted in lower optical losses and higher operating temperature.[120] Belkin and coworkers compared the calculated waveguide losses for gold and copper DM-waveguides showing up to 50% reduction when employing copper.[121] They also mentioned that the same calculation performed for silver showed that it would perform better than gold, too, but not than copper. Copper was in fact the metal constituting the waveguide of the laser reaching the highest operating temperature.[79]

Concerning the mirror losses, DM-waveguides have the advantage that the sub-wavelength

modal confinement results into high reflectivity values $R \simeq 0.7 - 0.9$, for a facet vertical size (given by the active region thickness) of 10 µm and wavelengths in the range $\lambda = 50 - 300$ µm.[122] This, according to Eq. (1.5), justifies the low mirror losses of THz-QCLs.

On the other hand, DM-waveguides have the disadvantage of producing highly divergent far-field emission, whose correction saw several schemes being proposed. Some rely on various types of impedance-matching antennae or lenses added to or processed with the laser itself[123, 124, 125, 126], others more ingeniously make use of phase conditions to achieve, at the same time, also mode selection, for example in distributed-feedback gratings of different orders[127, 120, 128, 129], photonic-crystal[130, 131] or array/ring[132, 133] structures. For a more extensive discussion see [134].

We come now to the discussion of the active-region architecture. The first point to consider for THz-QCLs is that the emission energy lies below the LO-phonon energy of the used materials (recall, $E_{LO} \simeq$36 meV for GaAs, corresponding to 8.7 THz) that can be used to mark a boundary with MIR-QCLs, as sketched in panel a) of Fig. 1.4. This has important implications on the kind and strength of scattering processes that work against the lasing transition.[135, 136] LO-phonon emission plays the key role, being the scattering mechanism with the shortest lifetime ($\tau_{LO,e} \simeq$0.5 ps), and therefore the first one to be hindered to realise an efficient device. Alongside follows LO-phonon absorption ($\tau_{LO,a} \simeq$2-5 ps). For MIR-QCLs, also scattering by interface roughness plays an important role ($\tau_{IR} \lesssim$10 ps). On the other hand, THz-QCLs have wavelengths of several hundreds of micrometres that mitigate the effect of interface roughness and transitions energies below the LO-phonon energy that, in absence of a thermal population, forbid LO-phonon emission. The leading role as non-radiative scattering mechanism is then taken by electron-electron scattering ($\tau_{EE} \simeq$5-40 ps) and scattering by ionised impurities ($\tau_{II} \simeq$10-30 ps). If the system is particularly clean and the carrier densities very low, acoustic phonon scattering may be significant ($\tau_{AC} \simeq$300 ps).

With increasing temperature, the landscape changes: the electrons populate the higher energies of the subband while more phonons are present for the now-available scattering channel: both factors contribute to a stronger depopulation of the upper level. This will be discussed further in the next section.

The first THz-QCL relied on a scheme that is the scaled version of a MIR-chirped superlattice active region.[138] Therefore, like most of the other THz-designs at that time, the total active region energy is smaller than the LO-phonon energy. As previously said, this fact avoids reabsorption of the photons by the LO-phonon, but, at the same time,

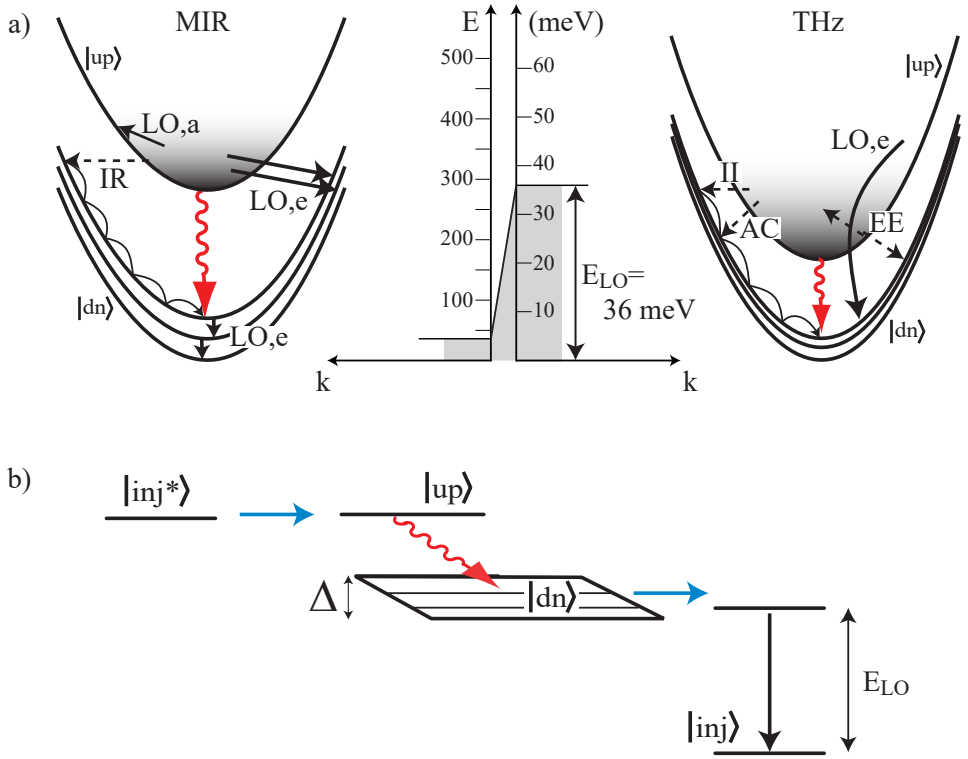

Figure 1.4 – a) Sketch of the parabolic dispersion of the electrons within the wells taking part into the lasing transition for a MIR-(left) and THz-QCL (right), highlighting the competing non-radiative scattering processes: *IR* interface roughness, *LO,e/a* emission/absorption of LO-phonons, *II* ionised impurities, *AC* acoustic phonons, *EE* electron-electron scattering. Note the different energy axes for the two. Adapted from [32]. b) THz-QCL active region scheme featuring a bound-to-continuum transition with resonant phonon extraction. Adapted from [137].

takes away from the researchers optical-phonon scattering as one of the most powerful tools to reduce the lifetime of the lower laser state.[139] This had to be compensated with skilful design of the active region where now elastic scattering is the catalyser for emptying the lower level, at the cost of a higher current density.

Several active region designs have been developed and tested over the years but here only one of the most successful will be discussed: the bound-to-continuum with resonant optical-phonon depopulation.[140, 141] For a broader and more detailed introduction on the different designs see the reviews by B. Williams[8] and M. Amanti et al.[137]. In bound-to-continuum or chirped-superlattice designs, the upper state lases onto a lower miniband. For this to take place, the miniband width (Δ in panel b) of Fig. 1.4) has to be, on the one hand, large compared to the broadening of the individual levels, $\gamma \simeq 1 - 4$ meV[142, 143, 144], and to the thermal energy $k_B T$ to keep a defined transition energy. On the other hand, Δ has to be small compared to the photon energy to avoid internal reabsorption. All these constrains can be, and are, met in the MIR-frequency range where the energies scales are much bigger, but impose strong limitations to THz-

QCLs. Additionally, in THz-devices, the total energy-distance of the upper level to the bottom of the lower miniband, $\Delta + h\nu$, should also be smaller than the LO-phonon energy to avoid fast non-radiative depopulation. This would bound THz-QCL operation to cryogenic temperatures.

The addition of the resonant extraction from the miniband, spatially far from the optical transition, somehow mitigates part of the above constraints, especially allowing a miniband narrower than the thermal energy.[139, 141] The initial design featured five quantum wells, but subsequent variations moved toward a reduction of their number presenting designs with four[137], three[145, 146], up to a double quantum well[147]. Such reduction of active region length was mainly done with the aim of reducing the total time an electron would spend per period, τ_{trans}: this reduction, in light of Eq. (1.4), would allow a higher J_{max} with consequent higher output power.

Let us summarise the active-region scheme based on bound-to-continuum transition with resonant phonon extraction presented in panel b) of Fig. 1.4: the electrons are injected via resonant tunnelling into the upper laser level $|up\rangle$, then they emit onto the spatially-separated lower mini-band (continuum-like) $|dn\rangle$ from which they are extracted to the injector $|inj\rangle$ via LO-phonon emission. Such design increases the upper state lifetime because of the diagonal transition and achieves a very short lifetime of state $|dn\rangle$ while cooling the carriers during the extraction, thanks to the resonant-phonon transition.

THz-QCLs nowadays can operate in all respects like their higher-frequency counterpart but in emitted power and operating temperature.[148] To date the best-performing devices reach T_{max}=199.5 K[79] and, at 10 K, emit 1 W peak power in pulsed-mode operation[149] and 160 mW in continuous-wave operation[150].

1.2 Maximum operating temperature and limiting factors

The biggest practical limitation of THz-QCLs is given by the maximum operating temperature. Its evolution in time is presented in panel b) of Fig. 1.5: as mentioned in the previous section, the still best-performing device reached T_{max}=199.5 K in 2012[79], starting from the first device operating up to 50 K. The devices are still not in the temperature range where electric coolers based on the Peltier effect can be used ($T_{min}^{Peltier} \simeq$230 K). For such reason, alternative sources of THz radiation have been investigated, the main one relying on difference frequency generation in MIR-QCL.[148] Nonetheless, they won't be discussed here because the present investigation aims at studying and understanding the physical properties of THz-QCLs to improve their temperature performance.

Panel a) of Fig. 1.5 collects the highest operating temperatures reached by THz-QCLs (in pulsed operation) as a function of the emission frequency, for the different lasing schemes and material systems. From the low-frequency side till about 3.5 THz the top-most points lie almost on a line, although steeper than $T = \hbar\omega/k_B$, once believed to be the fundamental limit.[151] At higher frequencies, instead, the T_{max} decreases rapidly because of increasing closeness to the LO-phonon energy, therefore requiring lower temperatures for thermally activated emission. Thus one can say that there is a *sweet spot* for THz-QCLs around 3 THz.

To better understand such a distribution of T_{max}, we consider further some aspects of the design of THz-QCLs. For long-wavelength QCLs, the photon energy starts to be comparable with the broadening of the states themselves. This, on the one hand, requires a higher precision in the design and growth to achieve the desired alignments while, on the other hand, reduces a lot the injection efficiency and the dynamic range of the laser.

Phenomenologically, the threshold current density monotonically increases in temperature. The higher-temperature part of the emission range can be modelled with an Arrhenius-like behaviour as

$$J_{th}(T) = J_0 \exp\left(\frac{T}{T_0}\right) \tag{1.8}$$

where J_0 is the initial value of J_{th} at the lower temperature side of the range and T_0 is a fitting parameter used to classify the devices according to their temperature behaviour. Therefore, the dynamic range of a QCL decreases for increasing temperature till closure, when $J_{th} = J_{max}$. Joining this to the previous consideration, it is understandable why THz-QCLs with longer wavelengths have lower T_{max}, resulting in an approximately linear relation.[8, 151] Kumar and coworkers showed that this limitation seems actually related to the QCL design, specifically to the resonant-tunnelling of carriers from the injector to the upper laser state, and suggested a new architecture based on an injector spread into the well of the upper state and populating it by scattering.[151] Their device reached $T_{max} = 163$ K, performing about 50 K better than competing ones at the same frequency ($f \simeq 1.8$ THz) but still far from the Peltier cooling region. Such design was termed "scattering assisted" and is reported in panel a) of Fig. 1.5 with violet dots.

This change alone was not sufficient to increase the general maximum operating temperature of THz-QCLs, therefore the optimisation of the specific processes is still needed. Going back to the non-radiative transitions exemplified as dashed black arrows in Fig. 1.1, all of them decrease the population inversion, either by decreasing the amount of electrons in the upper level or by increasing their amount in the lower level, and almost all of them are temperature-related. These transitions become relevant when the higher temperature of the electron distribution is such that the higher levels within the subbands get popu-

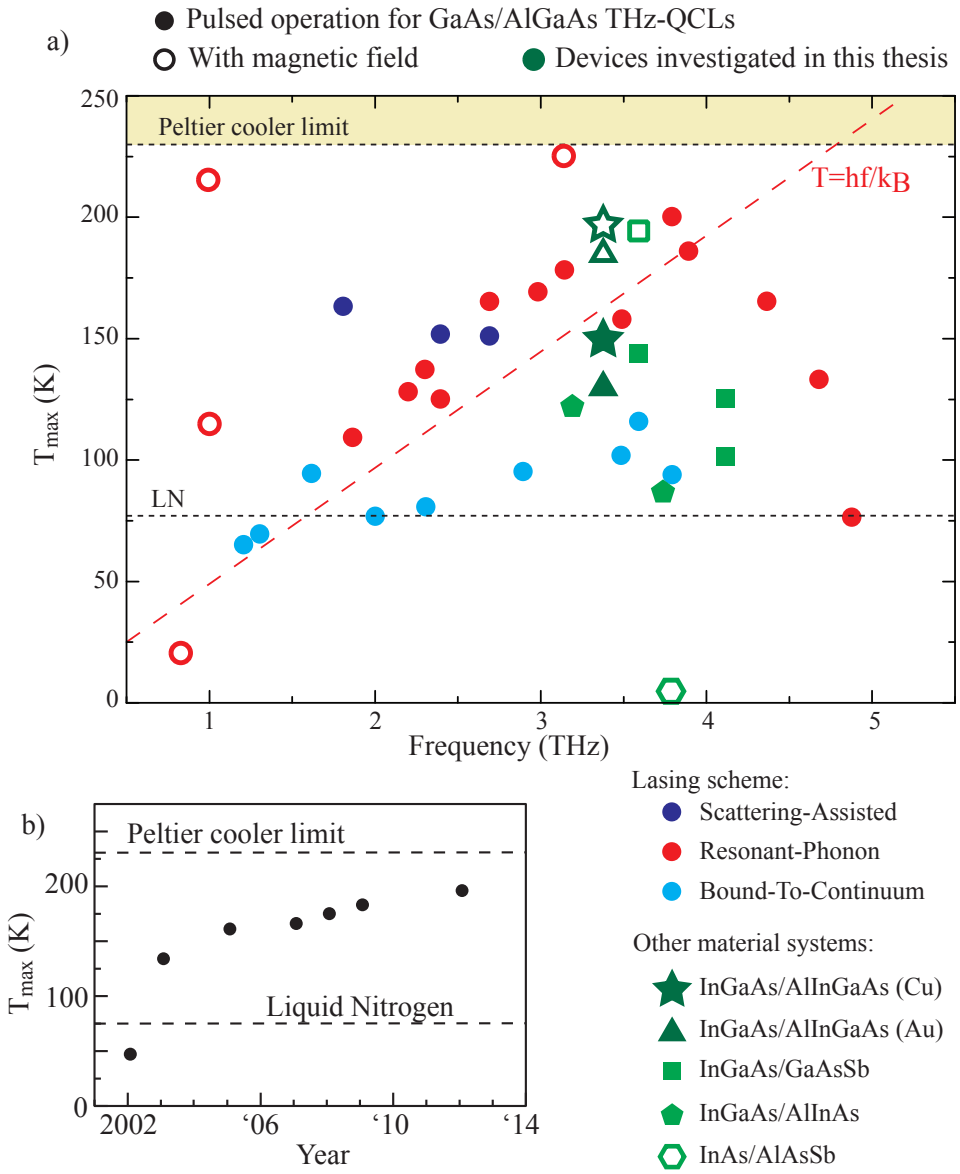

Figure 1.5 – a) Maximum operating temperature vs emission frequency for THz-QCLs. The best performing devices in the GaAs/AlGaAs material system for the different active region designs are reported (solid circles). Other material systems are marked in green symbols. All devices investigated in magnetic field are also reported as open symbols. The four devices discussed in this thesis are marked by dark green symbols. b) Maximum operating temperature of the best-performing THz-QCLs vs. year. Horizontal lines indicate the reference temperatures for two cooling methods. Adapted from [134, 148]

lated: this is the case particularly for the injector and for the upper lasing level. In fact the injector acts as an electron reservoir for the QCL containing permanently about 90% of the doping carriers. Usually only its lowest level is used in the QCL architecture, but with increasing temperature the population of the higher levels becomes non-negligible and carriers can either escape directly to the continuum and to the subsequent injector, or back-fill, through the extraction channel, the lower state of the lasing transition. Similarly, the population accumulating in the upper state of the lasing transition can either escape directly to the downstream injector or back-fill the one upstream.

In general, these two issues are both related to the barriers of the QCL design. A thicker and/or taller barrier would hinder both back-filling and escape of the electrons by an increased localisation of the wavefunctions. (A semi-quantitative treatment of the matter can be found in Ref. [32].) A thicker barrier is easy to achieve, since it would be sufficient to adapt the design. On the contrary, the height of the barrier cannot be adjusted by design. In fact, what the wavefunctions see as a barrier is the conduction-band offset between the two different materials constituting wells and barriers. This is a property of the material system and can be partially adjusted during growth by varying the composition of the alloy. Additionally, another important material parameter enters the game: the effective mass. These will be discussed in the next section.

Before moving on to discuss the material systems, let us briefly consider the last loss term left, not directly related to the QCL design: the waveguide losses. As mentioned in the previous section, several metals were investigated for DM-waveguides and copper resulted to be the preferred one. As we will also show, this improved the temperature performance of the lasers but not as much as hoped for. Hence they can in principle be reduced further, but this alone will not bring the THz-QCL in the peltier-cooling temperature range.

Therefore more drastic changes are required to deal with the thermally-activated phonons and two ways to face them were put forward: either get rid of them or take advantage of their presence. Following the first line, quite early it was realised that quantum dots (QDs) with their atomic-like levels could help via the "phonon bottleneck", i.e. by removing high-momentum density-of-states and therefore hindering phonon emission (cf. panel a) in Fig. 1.4).[152, 153, 154] Considerable effort was put in the study[155, 156, 157], design and realisation of QD-QC-structures where the transition takes place in the quantum dot plane embedded among the standard cascade of quantum wells.[158, 159, 160, 161, 162] A magnetic-field study we performed also showed a path to increase k-space overlap, beneficial for tunnelling injection.[163] Such devices would also provide some additional advantages, e.g. lower threshold and transverse-electric (TE-) emission due to the different

selection rules. The QDs' growth technique is still relatively young and the first attempts were not successful, despite a recently-reported, much-debated lasing structure.[164] Different solutions based on the same idea of lower-dimensionality were also tried, e.g. etching micro- and nano- pillars in the grown heterostructure[165, 166, 167], but the most elegant is the application of a magnetic field to a standard QCL, thus breaking the parabolic bands into sets of Landau levels.[168] This will be the topic of the next chapter.

From the other side, instead, to be able to take advantage of the phonon population, increased by the higher temperature, a THz-QCL was proposed that develops gain from the free-carrier absorption arising from transitions relying on LO-phonon-absorption. Such a scheme should ensure that the electronic population inversion is met also at high temperatures. Based on this scheme, a THz-QCL was designed and measured, but the actual phonon contribution remains unclear.[169]

1.3 Material systems

The first QCL was realised in the $In_{0.53}Ga_{0.47}As/In_{0.53}Al_{0.47}As/InP$ material system[63] but after a few years operation for the $GaAs/Al_{0.33}Ga_{0.67}As$ material system at 9.4 µm was also reported.[170] This was an important achievement because it formally proved the idea of QCLs being independent of the chosen material, relying on intersubband transitions. Afterwards, several material systems have been demonstrated for MIR-QCLs (cf. Ref.s [171, 86] and references therein).

The first THz-QCL was realised in the $GaAs/Al_{0.15}Ga_{0.85}As/GaAs$ material system and so, or with slightly different stoichiometry ($GaAs/Al_xGa_{1-x}As$ with x in the range $0.1-0.15$), are most devices till now produced and investigated. Despite the better maturity of this material system for growth and processing, several others were tested because of the specific improvements that they could bring to the challenge with the maximum operating temperature of THz-QCLs. The most important III-V semiconducting materials suitable for THz-QCLs are shown in Fig. 1.6, where their energy gap is plotted against lattice constant, along with the relevant ternary and quaternary compositions. L. Ajili and coworkers demonstrated the first THz-QCL in the InGaAs/AlInAs/InP material system[172], C. Deutsch and coworkers in the InGaAs/GaAsSb/InP material system[146] and, more recently, K. Ohtani and coworkers in the InGaAs/AlInGaAs/InP material system[173]. Last, M. Brandstetter et. al realised a THz-QCL in the InAs/AlAsSb/InAs material system but it lases only when reducing the losses with the help of a quantising magnetic field.[174] All devices were realised to emit close to the sweet spot, in the range 13-15 meV (approx. 3.0-3.5 THz), and their temperature performances can be compared

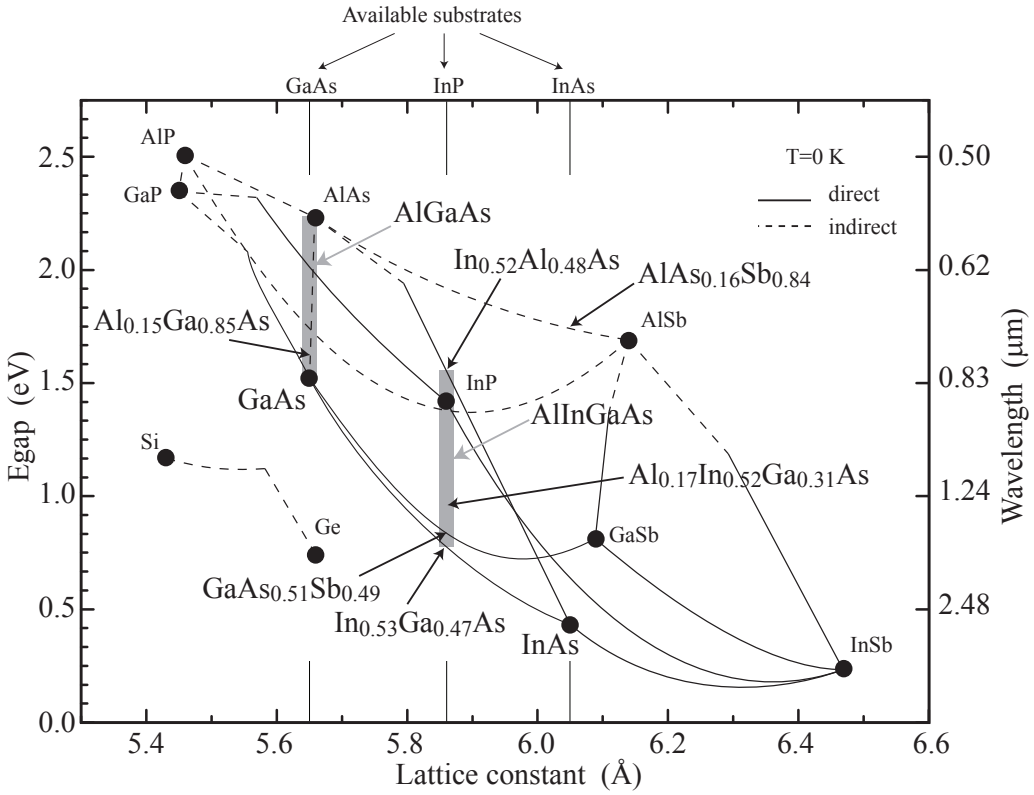

Figure 1.6 – Bandgap energy vs lattice constant of some semiconductor materials from group IV and III-V, along with the ternary and quaternary compositions used for THz-QCLs. All well/barrier materials discussed in Table 1.2 are positioned by arrows. The gray areas indicate the possibility of lattice-matched growth for a continuously varying composition of the material in the barriers, on GaAs or InP substrates. III-V nitrides are not included but would lie at a lattice constant of about 3.2 Å. Adapted from [175]

with the more standard ones in panel a) of Fig. 1.5 (green symbols).

As anticipated in the previous section, the important parameters, and reasons to change material system, are the conduction-band offset ΔE_{CB} and the effective mass m^*: these values for the different realised THz-QCLs are collected in Table 1.2. These parameters allow one to act on different points of the QCL scheme:

- the modal gain g_c depends on the effective mass as $g_c \propto 1/m^*$, via the dipole strength $z \propto 1/\sqrt{m^*}$ (cf. Eq. (1.2)). Therefore moving to materials with lower effective mass enhances the gain, hence the efforts in small-bandgap materials;

- the confinement of the electrons in the quantum well is approximately proportional to the square root of the height of the barrier[31], here ΔE_{CB}. Therefore, the larger ΔE_{CB}, the less electrons will escape from the state;

- the tunnelling rate of an electron from one quantum well to the coupled one with barrier height ΔE_{CB} and barrier width L_b is given by $\tau_{tunnel} \propto \exp(-\kappa L_b)$ with $\kappa =$

$\sqrt{2m^*(\Delta E_{CB} - E)}/\hbar$.[31] Therefore one can vary any two of the three parameters (τ_{tunnel}, ΔE_{CB}, L_b) to adjust the third one. One specific technological advantage comes by using materials with the proper ΔE_{CB} so that L_b is not too thin ($\gtrsim$ 1 nm): a very thin barrier needs a very fast moving shutter and it is more subject to growth imperfections;

- the refractive index of the active region and, especially, of the substrate have different values according to the used materials: fortunately this does not affect too much THz-QCLs when using DM-waveguides because the mode does not leak into the substrate. On the other hand one has to keep this in mind when designing devices with SP-waveguides.

An additional point to note is that not any material can be grown on any other one: the growth can take place when the lattice constants are not too different (at most few percent). Such a strong constraint for the choice of the material forces some compromises in the possible combinations: these are highlighted in Fig. 1.6 by the vertical lines in correspondence of the available substrates.

In order to increase the gain, and therefore the operating temperature of THz-QCLs, InGaAs based active regions, already used for MIR-QCLs, were the natural choice. The hope was to improve the performances by taking advantage of the 1/3 lower electron effective mass of InGaAs with respect to GaAs. This concerned the wells, but a suitable barrier material needed to be found. Again, inspired by MIR-QCLs, the first non-GaAs-based THz-QCL was realised in the InGaAs/AlInAs material system. Because such material system is lattice-matched only for a 3.5-times larger ΔE_{CB}, it was expected to be beneficial also in containing hot electrons. Unfortunately the first devices performed quite poorly[172] but subsequent improvements brought the operating temperature to 122 K[144] (green pentagons in panel a) of Fig. 1.5).

It became soon clear that such a higher ΔE_{CB} was more problematic than helpful: in fact the GaAs/AlGaAs ΔE_{CB} although much smaller was already quite good at confining the electrons, given the small energies in the THz-frequency range. Instead this big offset required then very narrow barriers down to the monolayer level, very difficult to grow reliably, as previously noted.

These issues were mitigated with the demonstration of the InGaAs/GaAsSb material system.[176] Also this combination is lattice-matched for a single stoichiometry with ΔE_{CB} 2.5-times larger than the one in GaAs/AlGaAs. Additionally, the barrier material has the advantage of a smaller electron effective mass very similar to the one in the wells. The devices realised with this material system reached T_{max} = 142 K, better than the

Table 1.2 – Comparison of material systems' relevant properties for THz-QCLs and obtained maximum operating temperature. In particular the well and barrier effective masses in units of fundamental electron mass m_e, the conduction band offset and the LO-phonon energy of the well material are reported. *For InAs-based THz-QCLs, lasing takes place only with an applied magnetic field.

Material system	$m^*_{well/barrier}$ (m_e)	ΔE_c (meV)	E_{LO} (meV)	T_{max} (K)	Ref.
$GaAs/Al_{0.15}Ga_{0.85}As$	0.067/0.080	150	36	199.5	[79]
$In_{0.53}Ga_{0.47}As/In_{0.52}Al_{0.48}As$	0.043/0.076	525	33	122	[144]
$In_{0.53}Ga_{0.47}As/GaAs_{0.51}Sb_{0.49}$	0.043/0.045	360	33	142	[146]
$In_{0.53}Ga_{0.47}As/Al_{0.17}In_{0.52}Ga_{0.31}As$	0.043/0.057	141	33	130	[173]
$InAs/AlAs_{0.16}Sb_{0.84}$	0.023/0.12	2210	29	4*	[174]

previous attempt but still far from the best performing one[146] (green squares in panel a) of Fig. 1.5). Further studies on symmetric structures revealed that the well/barrier interface of these materials is highly asymmetric and leads to strong interface roughness scattering, this being the main limitation for their performance.[177]

Continuing in the effort of using InGaAs wells, another option came from using AlInGaAs as a quaternary barrier material.[178, 179] Despite the stronger alloy scattering, the main advantage is the fact that this quaternary material is lattice matched to InGaAs for several stoichiometries, as shown in Fig. 1.6. In fact K. Ohtani and coworkers demonstrated the first THz-QCLs realised in the InGaAs/AlInGaAs material system, choosing the barrier composition such that it would give similar ΔE_{CB} as for the GaAs/AlGaAs material system: the QCL reached $T_{max} = 130$ K[173] (green full triangle in panel a) of Fig. 1.5). This material system and the devices realised with it are the subject of the presented investigation and will be introduced in the next section.

A further step into enhancing the gain with lower effective mass was suggested using the InAs/AlSb/AlAs material system, whose wells have 2/3 lower m^* than GaAs. To date, very thin barriers were investigated in this material system[180], to compensate for the extremely high ΔE_{CB}, but the only THz-QCL reported lases only with the help of an applied magnetic field[174] (green empty hexagon in panel a) of Fig. 1.5).

The solutions for THz-QCLs discussed above are very adequate for frequencies lower than the sweet spot (cf. discussion in the preceding section). When moving to higher frequencies, instead, the problem of phonon emission becomes worse. In fact all these material systems rely on InGaAs wells, whose LO-phonon is at even lower energies than the GaAs one, 33 meV vs 36 meV, respectively, and closer to the room temperature energy of 26 meV. For InAs the situation is even worse with an LO-phonon energy of about 29 meV. To face this issue, research in the GaN-based material system flourished since, because of its smaller lattice constant (3–4 Å), the LO-phonon lies at an energy of

92 meV. Additionally, the LO-phonon scattering rate is extremely fast, helping the lower state depopulation. Hence, this material system is expected to be robust also at room temperature.[181, 182, 183] However, the interface roughness is still a big issue while the 3-times larger effective mass reduces the available gain. Nonetheless the first absorption studies are encouraging.[184, 185, 186]

1.4 Object of the study: quaternary-barrier QCLs

The investigated QCLs were grown in $In_{0.53}Ga_{0.47}As/Al_{0.17}In_{0.52}Ga_{0.31}As$ lattice-matched to InP, using the same gain medium as the best device reported in Ref. [173].[1] The designed structure features four quantum wells realising a bound-to-continuum scheme with resonant-phonon depopulation. The properties of the states were calculated with a self-consistent Schrödinger-Poisson solver and the moduli of their wavefunctions at the calculated alignment field of $F = 7.2$ kV/cm are shown in Fig. 1.7. The MBE-grown heterostructure consists of 150 repetitions of the period. Starting from the injector well (underlined), with the barriers indicated in bold face, the following thicknesses were grown (wafer *EV*1894): <u>217</u>/**43**/111/**35**/132/**20**/128/**51**, all in Å. The doping is placed in the injector and is realised with Si with sheet density $n_s = 4.86 \times 10^{10}$ cm^{-2}. The detailed growth scheme can be found in Appendix A.1 on page 233. As anticipated in the previous section and collected in Table 1.2, the conduction band offset is $\Delta E_{CB} = 141$ meV while the electron effective masses are $m^*_{InGaAs} = 0.043m_e$ and $m^*_{AlInGaAs} = 0.057m_e$ for wells and barriers, respectively.

The structure relies on an optical transition between state $|5\rangle$ and the states of the lower miniband $|4\rangle - |3\rangle - |2\rangle$ which gets resonantly depopulated via LO-phonon scattering to state $|1\rangle$. The energy separations, dipole elements and oscillator strengths of the different possible transitions among the states of the active region, at the alignment field, are collected in Table 1.3. Additionally the energy separation between state $|2\rangle$ and $|1\rangle$ is 28.8 meV and the depopulation time from $|4\rangle$ to $|1\rangle$ is estimated to be $\tau_{41-LO} = 2.15$ ps at 50 K.

Considering the reported values, some are noteworthy: the very high oscillator strength for the lasing transition $|5\rangle \rightarrow |4\rangle$ and the optimised overlap of the wavefunctions within the miniband between state $|4\rangle$ and $|3\rangle$ and $|3\rangle$ and $|2\rangle$, testified by the strong dipoles, to facilitate electron transport away from the lasing transition. The oscillator strengths are

[1] Most of the content of this section appeared, in some parts *verbatim*, in F. Valmorra et al., *InGaAs/AlInGaAs THz quantum cascade lasers operating up to 195 K in strong magnetic field*, New Journal of Physics **17**, 023050 (2015)

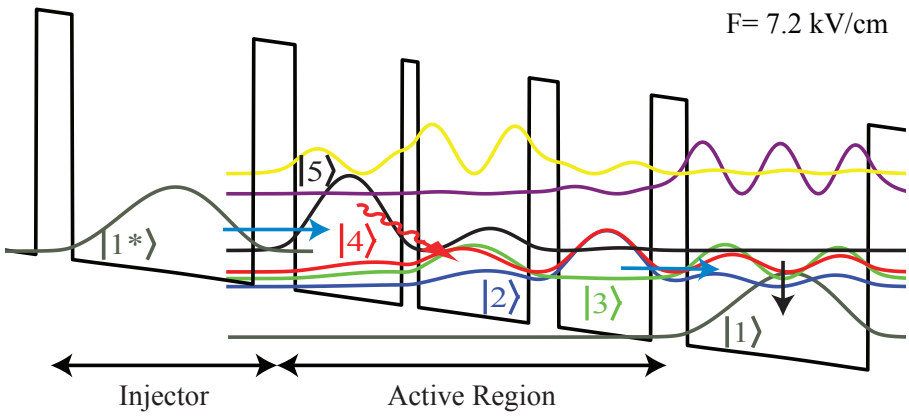

Figure 1.7 – Conduction band scheme and modulus of the relevant wavefunctions of the investigated QCLs at the calculated alignment field of $F = 7.2$ kV/cm. The upper state $|5\rangle$ lases onto the miniband $|4, 3, 2\rangle$. This is resonantly depopulated into the injector $|1\rangle$, that funnels the electrons into the next period ($|1*\rangle$). Cf. with panel a) of Fig. 1.4.

calculated with the formula

$$f_{ij} = \frac{2m_e}{\hbar^2 e} z_{ij} E_{ij}, \tag{1.9}$$

where z_{ij} and E_{ij} are the dipole element and the energy of the transition from state i to state j.

The grown wafer was then etched in ridges 150 µm wide and about 1.5 mm long and processed in DM-waveguide configuration with Au-Au waveguides (Ti/Au 5/500nm). For more details about the processing consult Ref. [32]. These QCLs with gold-based DM-waveguide were already reported to emit a maximum power in pulsed-mode $P_{max} = 35$ mW at 3.8 THz at 10 K and to operate up to a maximum temperature $T_{max} = 130$ K.[173] In order to improve the performance of these devices, the same process was repeated but the DM-waveguide was realised in copper (Ti/Cu 5/500nm) to benefit of the lower optical losses, as discussed in the previous sections. Two devices of each type were available for measurements. From now on, the two different device types will be denoted "Au-device" and "Cu-device".

In the following chapter, the measurements performed on all these devices with and

Table 1.3 – Energy, dipole element and oscillator strength of the possible transitions in the investigated QCLs, from the upper state $|5\rangle$ to the states of the lower miniband $|4, 3, 2\rangle$ and among the states of the miniband themselves.

	upper state to miniband			within miniband		
transition	$\|5\rangle \to \|4\rangle$	$\|5\rangle \to \|3\rangle$	$\|5\rangle \to \|2\rangle$	$\|4\rangle \to \|3\rangle$	$\|3\rangle \to \|2\rangle$	$\|4\rangle \to \|2\rangle$
energy (meV)	12.2	16.0	20.6	3.8	4.6	8.4
dipole (nm)	6.31	2.49	0.63	15.1	11.9	0.12
oscillator strength (abs.)	12.8	2.6	0.21	22.7	17.1	0.003

without magnetic field are presented, explained and used to tackle the issue of the maximum operating temperature of THz-QCLs.

Chapter 2

Magneto-spectroscopy of THz-QCLs

In this chapter, the issue of the maximum operating temperature of THz-QCLs realised in the new material system, presented in the previous chapter, will be investigated via magneto-spectroscopy.

As briefly introduced in section 0.1.2 on page 9, a quantum well containing a 2-dimensional electron gas (2DEG) confines the motion of the electrons in the plane creating discrete levels in the k-space associated with the direction of confinement.[1] These electrons still follow a parabolic dispersion regarding the in-plane wavevectors. When such system is placed in a region with a strong static magnetic field perpendicular to the quantum well's plane, also this paraboloid breaks up into discrete levels, named after L. Landau, with energy spectrum[43]

$$E_{l,n} = E_l + \left(n + \frac{1}{2}\right) E_{cyc,l}, \quad \text{with} \quad E_{cyc,l} = \hbar\omega_{cyc,l} = \frac{\hbar e B}{m_l^*} \tag{2.1}$$

where l and n are the subband and sublevel index, respectively, E_l is the energy at the bottom of subband l, B the magnetic field, e the elementary charge and m_l^* the effective electron mass for the given subband.

For standard III-V semiconductors, at typical experimentally accessible magnetic fields (usually in the range 0–10 T), the associated frequency lays in the THz range: for example the cyclotron energy separating the Landau levels in a GaAs-based 2DEG ($m^* = 0.067 m_e$) at $B = 1$ T is 1.73 meV (0.418 THz). Therefore, the advantage of using InGaAs is evident: its 1/3 lower effective mass with respect to GaAs allows one to reach a correspondingly higher confinement at a given magnetic field.

[1] Most of the content of this chapter appeared, in some parts *verbatim*, in F. Valmorra et al., *InGaAs/AlInGaAs THz quantum cascade lasers operating up to 195 K in strong magnetic field.*, New Journal of Physics **17**, 023050 (2015)

This change in the energy dispersion, from parabolic to discrete, had been already investigated as a help towards lasing in general[187] and was suggested also specifically for THz-QCLs[168] soon after the first observation of THz-luminescence from a cascade structure[76], even before the first QCL lased[63]. This idea has its roots in the same concepts mentioned in the previous chapter: substituting the quantum wells with fully confined objects (e.g. quantum dots) would strengthen the population inversion with respect to a temperature increase thanks to the phonon-bottleneck[188]. The application of a magnetic field along the growth direction results then in a very elegant way to test this idea by reversibly changing the dimensionality of the system with the possibility to tune its energies.[189] In fact two ladders of states are involved and move in energy with respect to each other in magnetic field: for certain magnetic field strengths the states will be at the right energetic distance to allow a single type of transition, let it be the photon emission, the LO-phonon scattering or electron-electron scattering. This will be directly reflected into the light emission of the QCL, allowing the so-called *magneto-spectroscopy* of the system. Its basics, the setup and the obtained results are discussed in the following sections.

2.1 Principles of magneto-spectroscopy

The general theory for electrons in strong magnetic field was introduced in section 0.1.2 on page 9. There it was highlighted that the Landau level picture can be used to describe the system for magnetic fields $B > 1/\mu$.

For the current technology, heterostructures with low-temperature mobility in the range 5×10^4–10^7 $\mathrm{cm^2\,V^{-1}\,s^{-1}}$ are possible, requiring magnetic fields higher than 0.001–0.2 T to be in the magnetic quantisation region. The electron mobility of the investigated samples can be as high as 10^5 $\mathrm{cm^2\,V^{-1}\,s^{-1}}$[190], allowing us to discuss the measurements in terms of Landau levels for fields higher than 0.1 T.

A first important detail to notice is that the derivation of the energy ladder of Eq. (0.23) relies on parabolic potentials, while this is not the form of the subband dispersion in a quantum well. To account for the non-parabolicity, the formula for the state energy, at a given magnetic field B and for a sublevel n, needs to be corrected (in first

approximation, ignoring the dependence of m^* on B) as follows:

$$E_n(B) = \frac{1}{2}(E_n(0) - E_G) + \frac{1}{2}\sqrt{(E_n(0) - E_G)^2 + 4E_G\left(E_n(0) + \left(n + \frac{1}{2}\right)\frac{\hbar e B}{m^*(0)}\right)} \tag{2.2}$$

where $E_n(0)$ and $m^*(0)$ are the energy of the state and the electron effective mass at $B = 0$ T, respectively, and E_G is the band gap of the material.[191, 192] For the present investigation, $E_n(0)$ are calculated by a self-consistent Schrödinger-Poisson solver and were given in section 1.4 on page 49, $E_G = 816$ meV for the used material system and $m^*(0) = 0.043 m_e$[2].[173] At least for the present design, although the wavefunctions are delocalised across the active region, weighting the effective mass on wells and barriers with the modulus of the wavefunction does not change significantly its value. Instead it would require the solution of the quantum-mechanical/electrical system for every considered biasing of the structure in a long and cumbersome way, therefore it was neglected and the sole m^*_{well} used.

Another point to discuss concerns the contribution of the Zeeman energy to the levels' energy. In the introduction it was calculated that, for GaAs at moderate fields, the correction can be neglected. For the present heterostructure, bulk $In_{0.53}Ga_{0.47}As$ has a g-factor of about $g^*_{bulk} = -4.0$ that slowly decreases when confining the wavefunctions into thin quantum wells.[193, 194] $In_{0.53}Ga_{0.47}As$/InP quantum wells of about 15 nm in thickness have $g^*_{QW} = -3.6$, corresponding to a correction of the Landau levels of about $\Delta E_\sigma = 0.21$ meV/T. Such heterostructure is very close to the one investigated here, both for composition and confinement, therefore we will use the related values for the present discussion. This energy splitting is significant, especially at high magnetic fields, but the larger level broadening allows us to neglect it.

In fact, so far we discussed the intersubband levels as if they were δ-like energy functions, despite generically mentioning their level broadening γ. Non-idealised levels at finite temperature are broadened in a Lorentzian fashion by mainly two factors: scattering processes and growth variations along the cascade sequence. The homogeneous broadening induced by the different kinds of scattering events (cf. Fig. 1.4 on page 40) is often dominated by impurity scattering, either due to the dopants or to the alloy mixture.

[2] When possible, the several parameters for this new material system needed in the following discussion were measured or found in the literature. Otherwise they were extrapolated from similar studies in similar materials.

This was studied in GaAs-based QCLs and it was found to behave as

$$\gamma(B) = \gamma(0)\sqrt{B} \tag{2.3}$$

with $\gamma(0) \simeq 1$ meV/T$^{1/2}$ at low temperatures.[142, 143, 195] The growth instabilities result instead in a structure-dependent inhomogeneous broadening. The two broadening types have comparable strengths, but at high magnetic fields, the homogeneous one is expected to dominate.[196] On the other hand, linewidth narrowing with magnetic field was also reported for QCLs based on vertical transitions.[197] All these considerations have to be nonetheless taken cautiously, since to date no complete theory is available to calculate the lifetimes for the states of THz-QCLs, and the values should be considered as an indication.

At a given magnetic field, Eq. (2.2) allows then the calculation of the relative position of the two (or more) sets of Landau levels corresponding to the upper and lower states of the lasing transition, and of the other states as well. An example is sketched in Fig. 2.1. At this point, a discussion of the possible transitions between the two ladders is needed. First, notice that the relative distance between the bottom of the subband dispersion and of the Landau levels with the same index remains unchanged in the parabolic approximation, while the non-parabolicity makes the levels approach each other for increasing index and magnetic field amplitude. Nonetheless, for the first few indices, the transition energy with and without magnetic field is almost unchanged, such that in principle the QC-structure is still capable of lasing. This takes place among states sharing the same Landau-level index. The main difference involves instead hot electrons, which can now emit a phonon only if a Landau level matches exactly the required energy. Changing the magnetic field amplitude allows one to tune this knob and to modify the relative distance of the Landau levels. Finally, when the energy distance of two levels is resonant with any of the scattering processes, there will be a transfer of electrons, usually resulting in lower photonic emission, while when no resonance is possible, the lasing will result enhanced: in these terms one can speak of magneto-spectroscopy.

In general, three kinds of depopulating transitions are possible in a QCL in strong magnetic field and were reported for both MIR- and THz-devices:

magneto-phonon resonance the electrons leave the upper state when a higher-index Landau level of the lower state is one LO-phonon away[198, 199, 200, 201]: $E_{up,m} - E_{dn,l} = nE_{cyc} + E_{LO}$ with $m, l, n \in \mathbb{N}_0$;

intersubband elastic scattering if the upper state is aligned with one of the Landau levels of the lower state, the population transfer is mediated by interface roughness

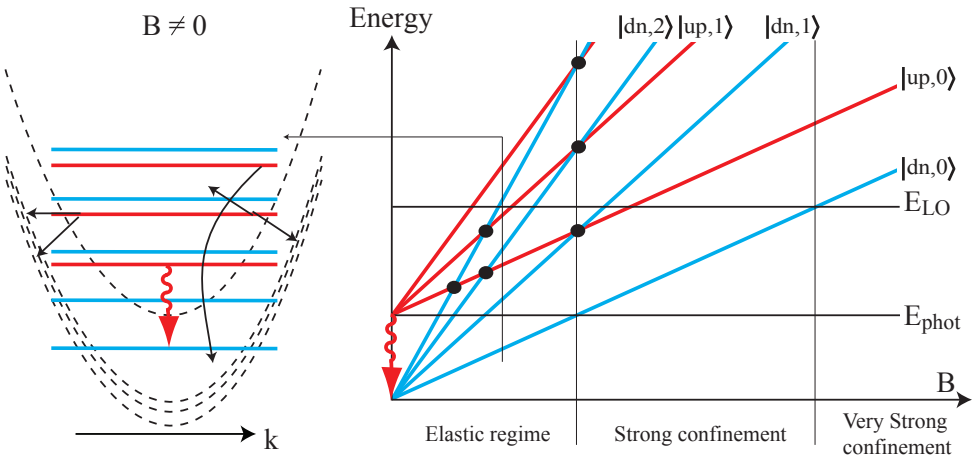

Figure 2.1 – Landau levels development in magnetic field for the subbands of the lasing transition of a THz-QCL. The different confinement regimes are also indicated relative to the resonance of the cyclotron transition with the photon and the LO-phonon. The quantisation, apart from specific resonant cases, removes final states to the non-radiative transitions (black arrows).

and impurity scattering[202, 118, 144, 203]: $E_{up,m} - E_{dn,l} = nE_{cyc}$ with $n = m - l \in \mathbb{N}$;

many-body elastic scattering electrons can change level also via electron-electron scattering when the alignment between two ladders is an integer multiple of half of the cyclotron energy[204, 205]: $E_{up,m} - E_{dn,l} = \frac{n}{2}E_{cyc}$ with $n = m - l \in \mathbb{N}$.

Finally, considering the optical transitions, it was derived that, as a consequence of Fermi's golden rule and of the fact that QCLs' intracavity field is TM-polarised, they are allowed only for index-conserving processes.[206] Therefore, apart from the small aforementioned energy change due to non-parabolicity, no further large tuning of the laser emission is possible in magnetic field. For transverse electric (TE-) modes, instead, transitions among Landau levels with $\Delta n = \pm 1$ are allowed, resulting in the so-called cyclotron emission[197] (cf. also section 0.2.1 on page 16).

In a THz-QCL, where the photon energy is smaller than the one of the LO-phonons, magneto-phonon resonance is hindered at low temperatures and elastic scattering is the main depopulation process among Landau levels.[78] This takes place when two levels cross, e.g. at the black dots positions in the $E(B)$ plot in Fig. 2.1. The number of low-energy crossings decreases for increasing magnetic field till the end of the *elastic regime* zone, marked by the resonance between the photon and the cyclotron transitions. At this point the laser does not emit any longer since the electrons in the upper level are elastically transferred to the Landau level at the same energy, but belonging to the Landau fan of the lower state. Tuning out of this resonance by increasing further the magnetic field amplitude, the laser is in the *strong confinement* regime: here the laser should lase

again not hindered any more by elastic depopulation channels. By further increasing the magnetic field, a second fundamental resonance is met when the cyclotron energy is equal to the LO-phonon energy. This marks the entrance into the *very strong confinement* regime where magneto-phonon resonance is possible.[207] Interestingly, no systematic investigation of the laser behaviour for magnetic fields beyond this point is present in the literature, apart from Ref. [196] where lasing is observed for different transitions than the designed ones till $E_c/E_{LO} = 1.5$.

The increasing magnetic field confines also the wavefunctions of the states, making the carriers more prone to be trapped around defects and impurities but at the same time making quite unlikely that they interact. This fact is helpful for the very low energy (long wavelength) emission. In fact emission at $f \lesssim 1$ THz was achieved only in presence of magnetic field[196, 205, 208], as marked by the red empty circles in panel a) of Fig. 1.5 on page 43.

To summarise, upon application of a perpendicular magnetic field the parabolic dispersion of the continuous states breaks into ladders of discrete Landau levels. The density-of-states function gets reshaped: most states become unavailable because of quantisation, but they are more numerous, when available. Non-radiative depopulation channels are blocked unless they are on resonance and this is directly reflected onto the light output of the laser.[209]

The application of magnetic field along the growth axis is therefore a very useful tool to investigate the QCL operation, in order to identify the different scattering mechanisms. This selective closing of non-radiative channels prolongs the upper state lifetime, resulting in a lower threshold current density (cf. Eq. (1.3)) and in a higher maximum operating temperature. Such kind of studies can therefore guide the future QCL designs to avoid specific non-radiative processes towards THz-QCLs operating at room temperature without magnetic field.

Magnetic field studies were performed for the different material systems where THz QCLs have been realised presented in section 1.3. The GaAs/AlGaAs QCL reached 225 K at 19.3 T[196], while the InGaAs/GaAsSb QCL showed laser action up to 190 K at 11 T[203]. All relevant magnetic-field results are collected as empty symbols in panel a) of Fig. 1.5 on page 43. Contrary to the high-field facilities required for GaAs-based devices, the low effective mass of InGaAs allows and fosters these studies that can be performed with lab-size superconducting magnets, like the one described in the next section.

2.2 Experimental methods and setup

For the present investigation, two devices of each type, with Au- and Cu-DM-waveguide, were measured. The features that will be discussed were found in both devices of each type, unless differently stated. Since they were processed in pairs, they are not only nominally identical but perform as well in a very similar way. Therefore, the measurements best exemplifying the discussed concepts will be shown in the following, these being always reproducible.

The QCL ridges of each pair are neighbours on the same substrate and are In/Au soldered onto a copper submount that can then be fixed to the different sample holders. The submounts have contact pads bonded to the QCLs terminals allowing the connection to the electrical instrumentation, as sketched in the inset b) of Fig. 2.2.

The QCLs were driven in current in pulsed mode at frequencies of about 30 kHz, i.e. the applied current is a square wave with an adjustable ratio between the on and off time, termed *duty cycle*. The reason for the pulsed mode is that a very short on-time is desirable to keep the active region temperature as low as possible and close to the one of the submount where the thermometer is placed (the QCLs cannot operate in continuous wave). Duty cycles in the range 0.3–2% were used: the source signal is constituted by a burst of 500 to 1000 micro-pulses with widths between 95 and 345 ns. The specific value is determined as a balance between pulse length and large-enough signal on the optical detector. Since we will not discuss the amplitude of the emitted light, the different duty-cycle values still allow a meaningful comparison of the measurements. A justification of this assertion, along with a discussion of the influence of the duty cycle on the QCL performance, can be found in appendix B on page 237. Additionally, the driving pulse is then square-wave-modulated at 30 Hz to match the liquid-Helium-cooled bolometer response-speed. This pulsing scheme is called macro-micro configuration.

The scheme of the electrical measurements can be seen in panel a) of Fig. 2.2. The bias was applied to the top contact of the QCL ridge from the high-impedance output of an *Agilent 8114A 100V/2A* pulser. The current was detected with a *Integrated Sensor Technologies* current probe (model 711S, conversion factor 1 mV/mA) inserted in the biasing line, whose voltage is visualised on a *Tektronic TDS 3034B 4-ch* digital oscilloscope through the 50 Ω port. The voltage at the QCL terminals is measured in a 4-point configuration connecting the top contact to the high-impedance input of the oscilloscope via a 50 Ω resistor. The oscilloscope was triggered by the pulser and measured both current and voltage lines, then read by a computer-based Labview program. In such a way the $J - V$ characteristics of the lasers can be recorded.

The submount with the QCLs was fixed onto a proper holder to place it in the centre

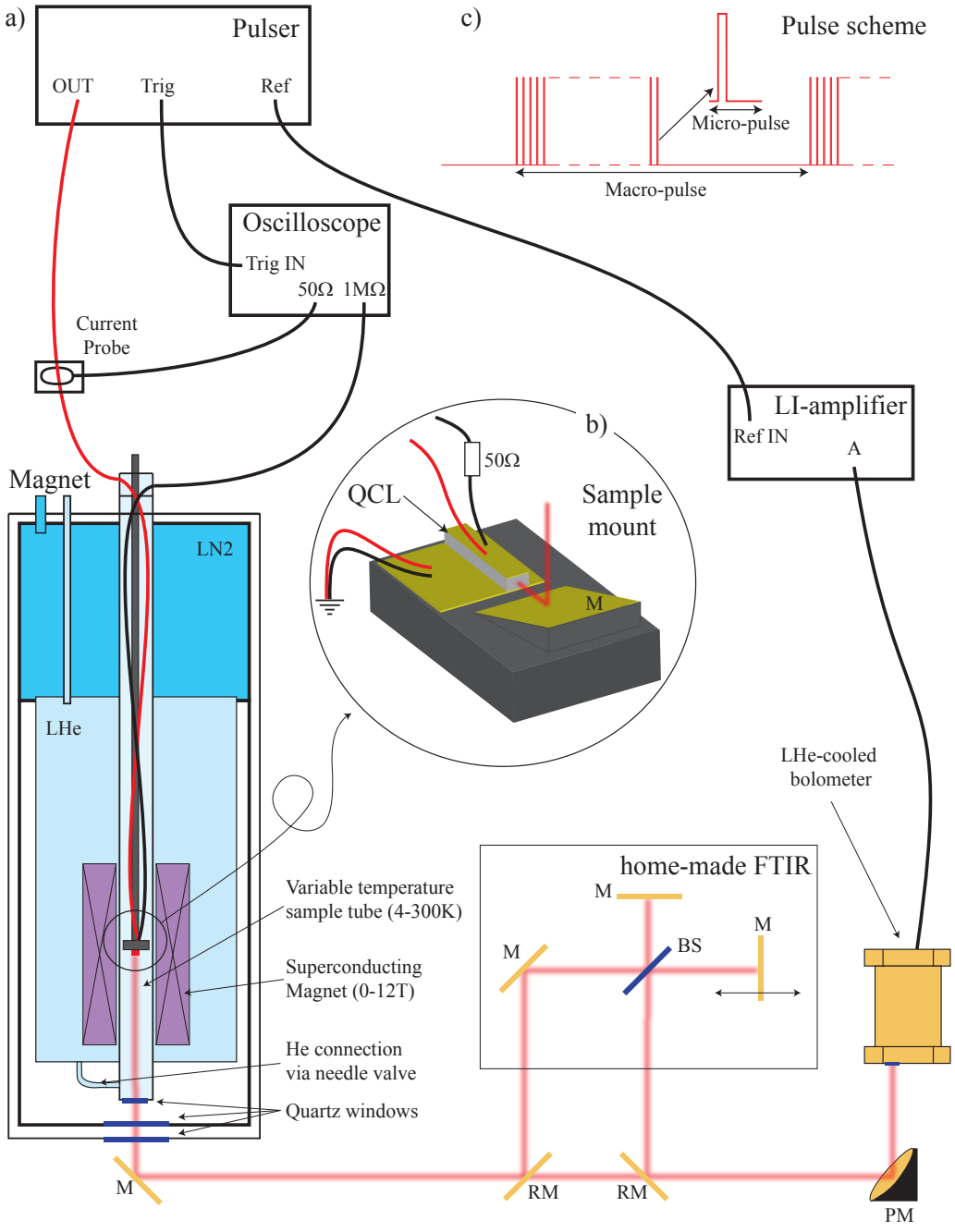

Figure 2.2 – QCL-magnetospectroscopy setup and scheme of measurements. a) The electrical circuit used to drive the lasers into the superconducting magnet and measure their output is explained in the text. b) The inset in the centre details the sample mount for electrical biasing and optical out-coupling. c) The top-right scheme shows the macro/micro-pulse concept. The optical measurement is performed via mirrors (M), some of which removable (RM), one parabolic (PM) and a beam splitter (BS).

of a liquid-He-cooled *Janis Research Company* superconducting magnet, allowing the magnetic field to vary in the range ±12 T. This is a vertical-solenoid magnet provided with bottom optical opening through quartz windows. The temperature of the sample can be set in the range 1.5 – 300 K because the superconducting magnet is built in such a way that the sample is placed in a "variable-temperature insert". This is thermically isolated from the He-bath and its temperature can be controlled with a combination of He-gas flow through the needle valve, pump-controlled under-pressure and PID-stabilised heater at the sample-holder and at the inner-most window.

In order to be able to extract the emitted radiation, while applying an orthogonal magnetic field (with respect to the sample's growth direction), the QCLs are placed horizontally, lasing towards a neighbouring 45°-oriented flat gold mirror (M) that reflects the light to the bottom windows, as sketched in the inset b) of Fig. 2.2. No additional optics is used inside the magnet because the 2-inches sample-tube, where the QCLs are placed, naturally acts as a metallic waveguide to the exterior. An optical board is placed immediately below the magnet and another 45° gold-coated 10×20 cm^2 flat mirror deviates the beam horizontally to another parabolic mirror focussing the light onto the liquid-He-cooled Ge-based thermistor of the *Infrared Laboratories Inc.* bolometer, unit 965. This, considering windows and diaphragm cut-offs, and thermistor response, is sensitive up to a maximum frequency of 11 THz (46 meV) with a noise-equivalent power as low as few pW/$\sqrt{\text{Hz}}$ and for operating frequencies up to 50 Hz. This is not directly compatible with the driving pulse frequency of the QCL (30 kHz), thus a macro-pulse/micro-pulse pumping scheme has to be used. This consists of superimposing a low-frequency square wave to the fast electric modulation so to meet the response time of the detector, as sketched in the top-left panel c) of Fig. 2.2. In the following experiment a macro-pulse frequency of 30 Hz was used. The voltage signal is then first pre-amplified at the bolometer and then fed into an *Eg&G 7260* lock-in amplifier, referenced to the macro-pulse low-frequency. This is then read by the Labview program and allows the measurement of the $J-V-L$ curves relating laser emission L to the QCL's $J-V$ characteristics.

The bolometer is a very sensitive detector whose output is proportional to the total incident power within the working spectral range. In order to extract the spectral information, a home-made Fourier-transform infrared spectrometer (FTIR) was placed between the flat mirror outside the magnet and the parabolic one focussing onto the bolometer. This FTIR operates on the principle of a Michelson/Morley interferometer: the light is split by a Mylar beam-splitter towards two flat mirrors, one of which can be displaced by a software-controlled sledge. The beam is then re-united at the beam-splitter and sent to the collecting mirror of the detector. Moving one of the mirrors, the optical path, and

thus the relative phase, of one of the two parts of the beam changes, resulting in a varying interference condition when they are overlapped again: an interferogram can be recorded when acquiring the detector's output as a function of the displacement of the mirror. A Fourier-transform converts the interferogram into the spectrum, relating the difference in travelling time (univocally connected to the displacement via the speed of light) to the frequency domain: the FTIR resolution is 0.045 cm^{-1} Another Labview software controls the mirror movement and performs the measurement and transformation, at fixed values of magnetic field and at specific points of the $J-V$ characteristic.

One last comment is needed concerning THz-frequency beams propagation in air. In the 0.5–5 THz range, the absorption coefficient of the water lines in air can reach 2.3×10^{-3} cm^{-1}, therefore usually the premises of the instrumentation for THz-related studies are purged with dry air or gaseous nitrogen. For the present measurements, inside the superconducting magnet no significant absorption takes place since the THz-beam propagates either in He-vapour or in very high vacuum, both transparent. Outside, instead the beam propagates for about one meter in unpurged free space: this slightly attenuates the beam but, because of the relatively high emitted power which will not be discussed, it does not pose problems.

2.3 Measurements & Analysis

With the setup described in the previous section, the $J-V$ characteristics of the QCLs were recorded along with the laser emitted power L as a function of the magnetic field B, applied along the growth axis, while the temperature of the sample could be varied in the range 4-200 K.

First, at $B = 0$ T, the maximum operating temperature of the lasers was determined and found to be 130 K for the Au-device[173] and 148 K for the Cu-device. This fact already testifies the benefits of using Cu-Cu DM-waveguides: for the present devices, an improvement of 18 K. At $B = 12$ T both could reach higher temperatures, namely $T_{max}^{Au} = 182$ K and $T_{max}^{Cu} = 195$ K.

Then the lasers were also tested in reverse bias: in spite of the fact that the structure is not symmetric, it lased at 14.7 meV (3.55 THz) up to $T_{max} = 70$ K at $B = 0$ T, reaching $T_{max} = 100$ K at $B = 10.6$ T, where the maximum emission takes place.

In the following sections the magneto-spectroscopy investigation is presented and discussed. Most of the results concern the forward (natural) biasing of the structure while the last section before the conclusions is dedicated to the reverse bias operation.

2.3.1 Forward bias maps

The results of the performed magneto-spectroscopy are reported in Fig. 2.3: the $B-J-L$ map for the Au-device is presented in panel a) on the top (measurement parameters: 1000 pulses per macro-pulse with width 95 ns, $T = 4.2$ K).

To be able to discuss the possible transitions between Landau levels, the fans for the involved upper state and lower miniband are plotted for the first few orders in panel c) below the maps, according to the non-parabolicity-corrected formula of Eq. (2.2). The bold lines mark the Landau index $n = 0$ of the upper state $|5, 0\rangle$ and of the lower-lying miniband $|(4, 3, 2), 0\rangle$. For the level $|5, 0\rangle$ broadening is taken into account according to Eq. (2.3). Equivalently, one could instead consider the un-broadened state $|5, 0\rangle$ interacting with a continuum of states delimited by $|4, n\rangle$ and $|3, n\rangle$. Thinner lines constitute the higher-index Landau levels while dashed lines indicate the B-field position of their crossings with $|5, 0\rangle$.

Upon inspection, two features stand out: the threshold current density decreases with magnetic field and the emission is interrupted by a 1.5 T-wide dark gap in the centre extending from $B = 5.1$ T to $B = 6.6$ T where the lasers switch off. Both features will be discussed in detail in the coming paragraphs and sections.

As already explained in section 2.1 and supported by the transport data discussed below, J_{th} strongly depends on the non-radiative depopulation paths for the upper-state electrons, as from Eq.s (1.1) and (1.3). These get progressively closed by the increasing magnetic field, resulting in an improved dynamic range. Nonetheless, the total emitted light decreases with B: this suggests an increase also in the lower state lifetime, partially balancing the previous improvements.

Having now discrete levels, at some magnetic fields, the lasing transition $|5\rangle \rightarrow |4, 3\rangle$ is resonant with the cyclotron energy. In such condition, elastic scattering opens a relaxation channel and the population inversion decreases: as a consequence the gain decreases and eventually falls below the losses' value, ceasing the lasing action. This is the case at 5.8 T (15.1 meV) where $|(4, 3), 1\rangle$ cross $|5, 0\rangle$.

In panel b) of Fig. 2.3 the $B - J - L$ map of the Cu-device is shown (1000 pulses per macro-pulse with width 345 ns, $T = 30$ K). One can immediately recognise that the central gap is narrower, extending for 1 T, vs 1.5 T for the Au-device. This directly points at a lower loss level for the Cu-Cu waveguide with respect to the Au-Au.[3]

Several oscillations in the threshold current density and consequent variations in the emitted light are present in the colour maps, especially for the low magnetic-field region.

[3]This is unrelated to the slight difference in temperature between the two measurements, as explained in Appendix B.

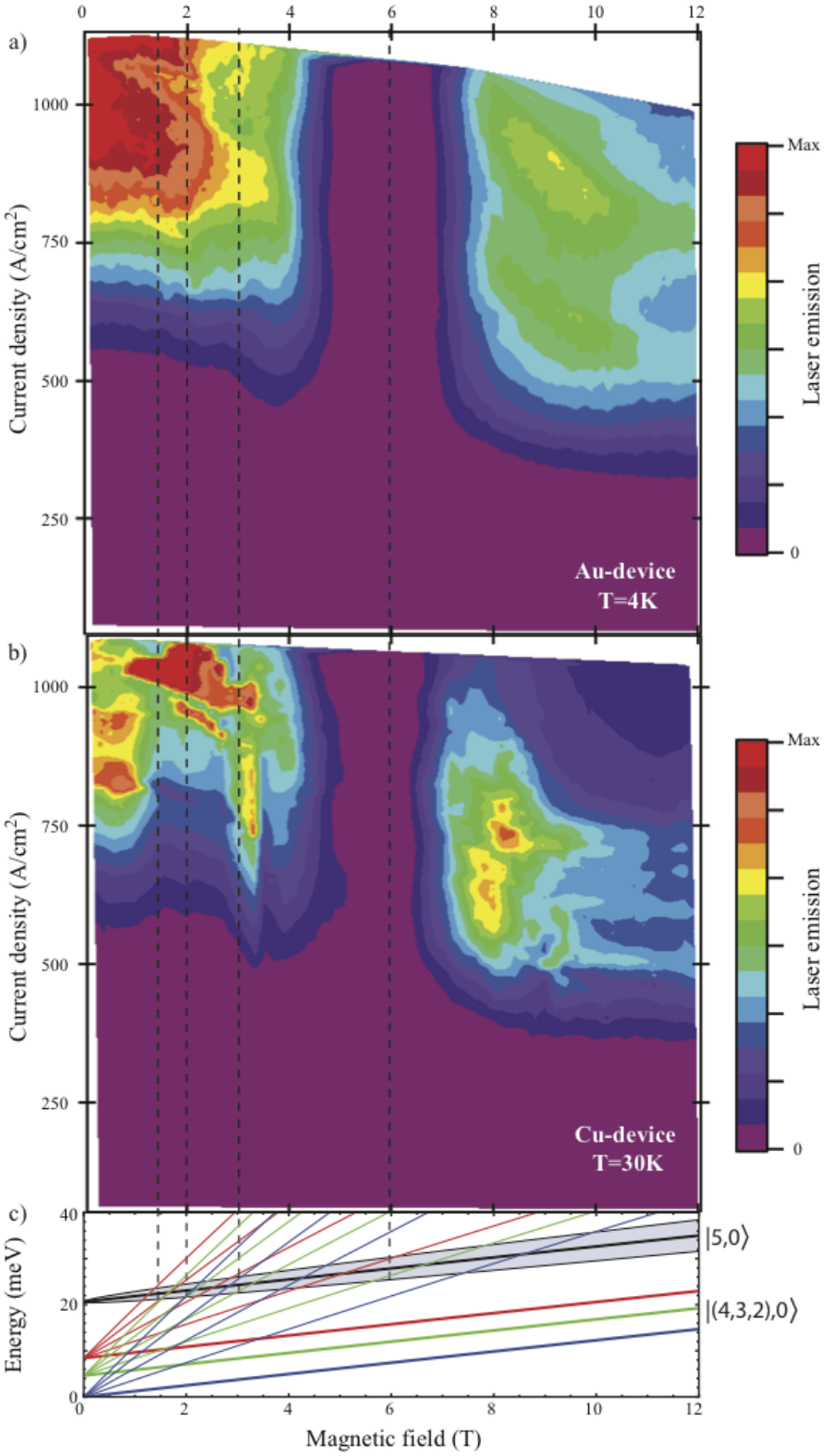

Figure 2.3 – QCL emission vs magnetic field and current density for a)the Au-device and b)the Cu-device. c)Landau fan of the involved states.

These features are particularly strong for the Cu-device. Most of them are related to the crossings of the higher-index Landau levels of states $|4\rangle$ and $|3\rangle$ with the upper lasing state $|5\rangle$, therefore modulating the levels of gain and population inversion.

As an additional remark, one would expect to see one gap per crossing of $|5,0\rangle$ with $|(4,3),n\rangle$, while we measure a gap in the optical emission only for $n = 1$ and see small modulations for $n = 2, 3, ...$ On the other hand electrically we see clear signatures of different strengths for all crossings, in the Cu-device, and they would be more and clearer if the device worked in continuous wave. This hints at the fact that all crossings modulate the lifetime of the transition, while only the first one induces strong reabsorption via polarisation mixing. In spite of the fact that, to the best of our knowledge, no theoretical investigation is available on the dependence of the inter-Landau scattering on the Δn between the levels, the experimental literature on similar structures also reports the same behaviour, i.e. only one broad gap in the emission for $\Delta n = 1$[201, 203]. Multiple gaps for several values of Δn were also reported[78], but these are measured on structures where the optical transition is vertical, i.e. it takes place within a single quantum well.

From the maximum current density it is then possible to derive the transport time of the carrier through one period according to Eq. (1.4). For the Au-device at $B = 0$ T, $J_{max} = 959$ A/cm^2 at 4 K corresponds to $\tau_{trans} = 8.1$ ps. Applying an increasingly strong magnetic field, the first roll-over of the light emission shifts to lower J_{max} down to 523 A/cm^2 at $B = 12$ T corresponding to 14.9 ps transport time. When increasing the temperature, instead, the J_{max} increases (cf. Fig. 2.5 on page 67): at $B = 12$ T $J_{max} = 769$ A/cm^2, corresponding to $\tau_{trans} = 10.1$ ps. Within the full range of magnetic fields and temperatures, these transport times are of the same order of magnitude as the expected effective upper-state lifetime at $B = 0$ T, $\tau_{eff} \simeq 10$ ps[173], meaning that the structure is able to maintain a good level of population inversion. The map of the Cu-device shows the roll-over points for slightly higher current density values at about 831 A/cm^2 ($B = 0$ T) and 489 A/cm^2 ($B = 12$ T) corresponding to transport times of 9.4 ps and 15.9 ps, respectively, also in the same range of values.

Finally, more than one maximum along J is present in the maps, as better seen in Fig. 2.4: this modulation could stem from different resonance conditions for the states in the miniband to be LO-phonon depopulated to the lowest state of the injector.

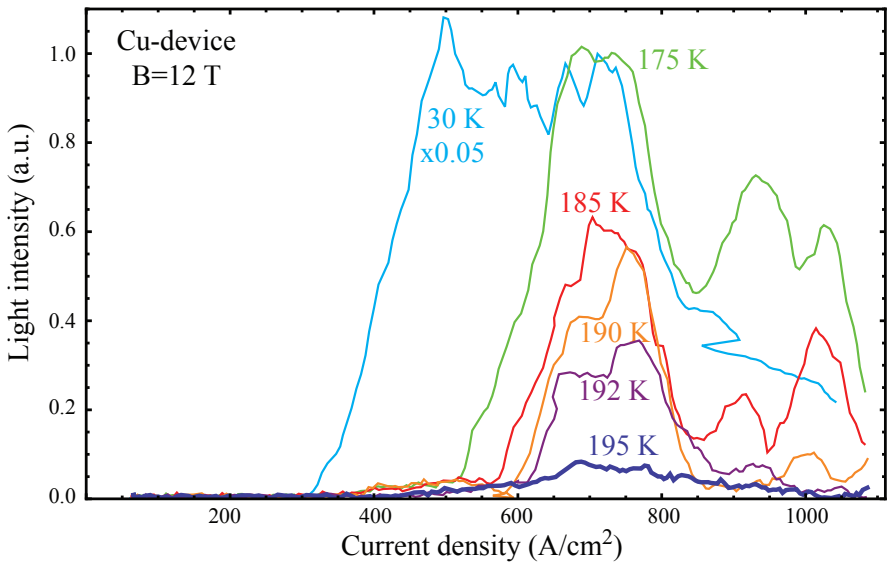

Figure 2.4 – $J-L$ curves for the Cu-device at $B = 12$ T for temperatures of 30 K (light blue), 175 K (green), 185 K (red), 190 K (orange), 192 K (violet) and 195 K (blue, thick).

2.3.2 Temperature performance and threshold current density analysis

The lasing performance of the QCLs were studied at different magnetic fields and temperatures. As discussed in section 2.1, the first benefit of the magnetic field-induced in-plane carrier confinement is the improvement of the maximum operating temperature of the lasers: when applying a magnetic field of intensity $B = 12$ T, the Cu-device raised its T_{max}^{Cu} from 148 K to 195 K while the Au-device raised its T_{max}^{Au} from 130 K to 182 K.[4] The $J-L$ curves of the Cu-device at selected temperatures at $B = 12$ T are presented in Fig. 2.4 and reveal the laser emission performance till $T_{max}^{Cu} = 195$ K (thick blue line), thus with an improvement of 45 K due to the magnetic confinement. The same experiment on the Au-device brought a similar improvement of 42 K.

The temperature behaviour of the threshold current density J_{th} could then be tracked at $B = 0$ T and $B = 12$ T and the collected points are shown in Fig. 2.5 for both devices. The 0 T-series is extracted from measurements performed in an external flow cryostat coupled to a bolometer (the small difference in the values of J_{th} for low temperatures between the maps and the points here reported might stem from a different alignment of the temperature sensor). Comparing the performance of the different devices at $B = 0$ T, one can see how the Cu-device has a lower threshold current density in the whole

[4]The devices whose measurements are here reported are the better performing ones in terms of temperatures, although the other ones perform worse by only 2 K. All discussed features were checked to be present in all the tested devices.

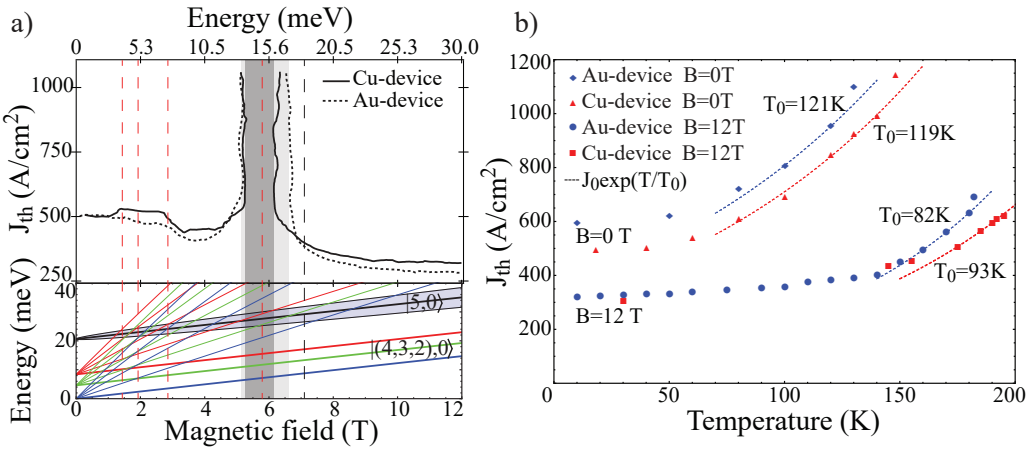

Figure 2.5 – a) Threshold current density J_{th} vs magnetic field for both device types showing a direct comparison of the non-lasing gaps and of the modulations. b) J_{th} vs temperature for both devices at $B = 0$ T and $B = 12$ T. The reported values of T_0 are fitted with Eq. (1.8).

temperature range that allows it to reach a higher T_{max}, in spite of the very similar T_0.

The values of T_0 were fitted with Eq. (1.8) and result to be $T_0^{Au} = 121$ K, $T_0^{Cu} = 119$ K at $B = 0$ T. The values fitted for the $B = 12$ T series are $T_0^{Au} = 82$ K and $T_0^{Cu} = 93$ K. The T_0-values get worse with magnetic field due to the fact that the dynamic range is reduced, and in particular J_{max} is almost halved (this point will be discussed in more details later in the section). The fitting curves are reported as dashed lines in panel b) of Fig. 2.5.

In the following we will discuss and compare the J_{th}-series and extract thereby information on the investigated QCLs with the help of Eq.s (1.3) and (1.6): recall

$$J_{th} = \frac{e\alpha_{tot}}{g_c \tau_{eff}} \quad \text{with} \quad \alpha_{tot} = \alpha_m + \alpha_w + \alpha_{ISB}.$$

It is important to note that, since all devices are processed from the very same heterostructure, we can assume that, *at a fixed magnetic field and temperature*, gain cross-section g_c (Eq. (1.2)), effective upper state lifetime τ_{eff} (Eq. (1.1)), re-absorption losses α_{ISB} (Eq. (1.7)) and doping density n_s are the same. Therefore a relation among the J_{th} directly reflects a relation among α_{tot} and in particular among the cavity losses $\alpha_m + \alpha_w$.

Considering first the series at $B = 0$ T, on the whole temperature range, they maintain approximately the same J_{th} ratio

$$\frac{J_{th}^{Cu}}{J_{th}^{Au}} = \frac{\alpha_{tot}^{Cu}}{\alpha_{tot}^{Au}} = 0.85 \pm 0.03 \quad \text{at} \quad B = 0 \text{ T},$$

showing a 15% total loss reduction. After Ohtani[173], the mirror and waveguide losses of the Au-device at 10 K amount to $\alpha_m^{Au} + \alpha_w^{Au} = (7.2 \pm 2.9)$ cm^{-1} with total losses $\alpha_{tot}^{Au} = (17.5 \pm 4)$ cm^{-1}. These values were determined for slightly different structures of a growth series but we can assume that all devices in Ref.[173] have similar re-absorption losses since the doping levels and the structures are very close to each other. This finally allows us to derive the Cu-device total losses to be $\alpha_{tot}^{Cu} = (14.9 \pm 3)$ cm^{-1}. Since the two device types have the same α_{ISB}, one can estimate a cavity loss of $\alpha_m^{Cu} + \alpha_w^{Cu} = (4.6 \pm 6)$ cm^{-1}, corresponding to a reduction of one third with respect to the Au-device.[5] The obtained result is consistent with the calculations reported in Ref. [121].

When operating the lasers subject to a magnetic field, the low-temperature J_{th} gets almost halved $J_{th}^{0T}/J_{th}^{12T} = 1.8$ and the lasers' performances in temperature change. Up to about 160 K, the J_{th} of both device types are very close and increase almost linearly in T, showing a very weak temperature dependence. This fact indicates that, in this range, J_{th} is not set by the losses any more: now J_{th} is dominated by a parasitic current needed to keep the structure aligned and the laser performance is voltage-limited. Such an effect has already been seen in previous studies of THz-QCLs.[210, 211] In order to take this fact into account, Eq. (1.3) can be complemented with an additional term[211]

$$J_{th} = \frac{e\alpha_{tot}}{g_c \tau_{eff}} + J_{par}.$$

Increasing the temperature, it is only above 160 K that the Cu-device outperforms the Au-device. At the highest temperatures, the J_{th} ratio for the two devices is consistent with the one without applied B-field, namely $J_{th}^{Cu}/J_{th}^{Au} = 0.87 \pm 0.05$, indicating once more that the Cu-losses are lower than the Au-losses, also at $B = 12$ T.

2.3.3 Emission spectrum study

A study of the emission spectra was performed on the Au-device.[6] Spectra, as the one shown in panel a) of Fig. 2.6, were taken at several points of operation of the lasers, for different values of magnetic field, injected current and temperature. When considering the strongest emission line of each recorded spectrum vs B-field, the emission energy chart in panel b) of Fig. 2.6 could be compiled.

The QCL is lasing predominantly at 14.3 meV, i.e. 3.46 THz, with the emission energy spanning the range 13.4–15.3 meV (3.24–3.70 THz). Approaching the non-lasing gap, the

[5] The large error is the result of a pessimistic error estimation via standard correlated error propagation and it remains valid that the possible range for the mirror and waveguide losses is bound to positive values

[6] The spectral emission was studied on both Au-devices, resulting in very similar spectra. The statistical analysis is performed combining data from both devices.

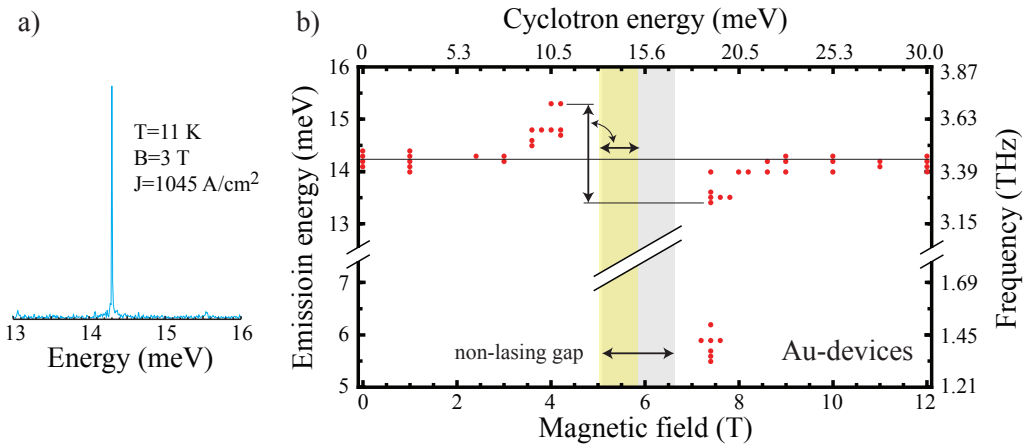

Figure 2.6 – a) Example of a spectrum showing single-mode laser emission. b) Emission energy chart for the Au-devices plotted against magnetic field. (500 pulses per macro-pulse with width 104 ns) The gray area indicates the extent of the non-lasing gap, while the yellow area reports onto the magnetic field axis the lasing interval, for comparison with the gap.

emission energy experiences a blue- (red-) shift coming from lower (higher) magnetic field values. This behaviour can be attributed to the Stark shift caused by the increasing voltage applied to the laser needed to reach the threshold current density while competing with the increasing non-radiative losses. This is also supported by the curves in panel b) of Fig. 2.8 where the normalized voltage at fixed J is shown. Here, two voltage shoulders are present on each side of the gap region (in grey, through Fig. 2.8). On the high-B-field side, the emission is also hampered by an additional depopulation channel giving rise to emission at lower energies.

The highest emission energy of 15.3 meV is met for B-field about 4.5 T (approaching the lower edge of the gap) and especially for temperatures above 15 K. The emission takes place at 13.4 meV at about 7.5 T (approaching the higher B-field edge of the gap) and the red-shift gets stronger for temperatures above 45 K. Such emission-energy shifts are nonetheless already present at lower temperatures. The energy extension of this lasing range is reported in panel b) of Fig. 2.8 and throughout the other panels as a vertical yellow band, to visually compare its extension with the non-lasing gaps. The discussion is carried out in the next section.

Additionally, at magnetic fields of about 7.5 T, the device is found to lase also in the range 5.5–6.3 meV (1.33–1.52 THz). Comparing the emission energy with the calculated levels and oscillator strengths reported in panels a) and b) of Fig.2.7, such emission is consistent with a transition from state $|3\rangle$ to the lower one $|2\rangle$ ($E_{32} = 4.6$ meV and $f_{32} = 17.1$).

We investigated this emission in current density and temperature: the resulting spectra

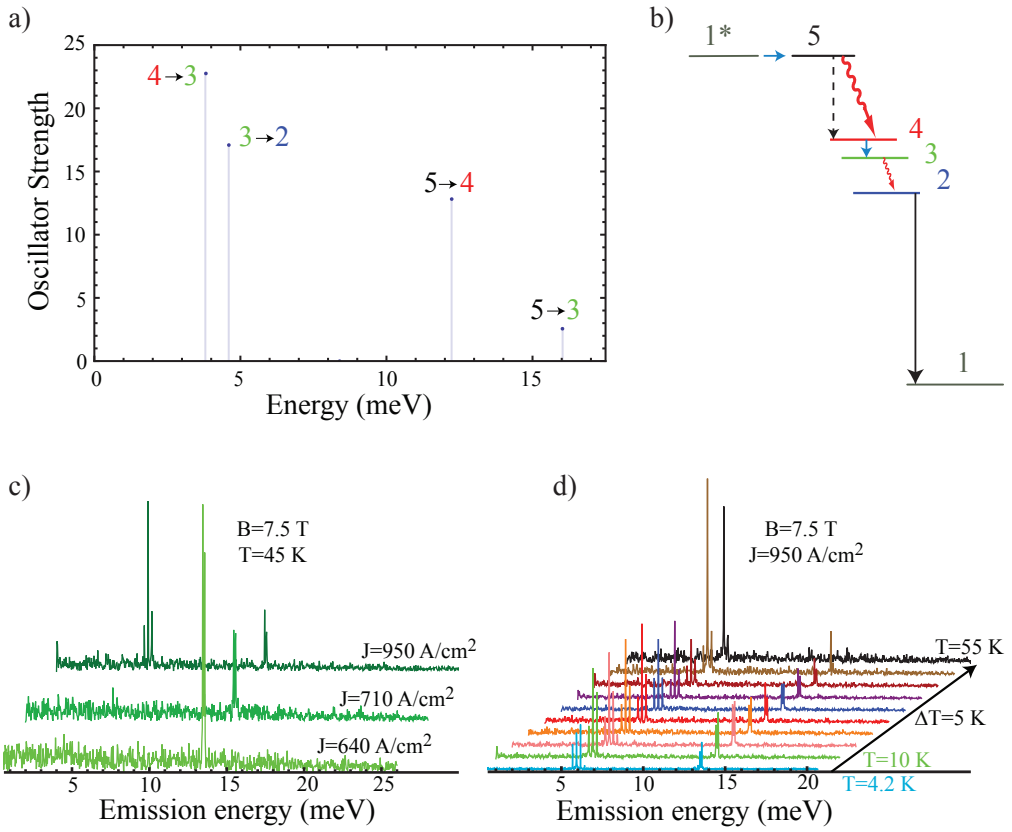

Figure 2.7 – a) Oscillator strength values for the main possible transitions. b) Level scheme showing the shortening of the main transition favouring the low-energy lasing. c) and d) show spectra from Au-devices clarifying the behaviour of the low-energy emission in J and T at a fixed magnetic field $B = 7.5$ T. (500 pulses per macro-pulse with width 104 ns)

are collected in panels c) and d) of Fig.2.7, respectively. The first series shows the current density dependence: the low-energy emission is not present immediately after threshold, but appears with increasing injected current, at the expenses of the high-energy one. This is most likely due to the fact that close to the non-lasing gap, the resonance between the photon and the cyclotron still depopulates state $|5\rangle$ in favour of $|4,3\rangle$ thus accumulating carriers in $|3\rangle$ that is then able to achieve population inversion and lase onto state $|2\rangle$. The same effect was found in similar structures.[208] Then, at fixed $J = 950$ A/cm^2, the temperature dependence is presented in the second series: the low-energy emission is present at 4.2 K and is of comparable intensity to the higher energy one (cyan spectrum). Increasing the temperature, the higher-energy emission, now at 13.5 meV, slightly decreases in intensity and coexists till 50 K. At 55 K the low-energy emission is the only one present and is much stronger than at lower temperatures. Further increment of the temperature brings back the system to the high-energy emission only.

2.3.4 Discussion

In Fig. 2.8 the emitted intensity and the normalized voltage $V(B)/V(B = 0\ \mathrm{T})$ are plotted as a function of the magnetic field as continuous and dashed lines for the Au- and Cu-device, respectively. In particular they allow a comparison between the optical and electrical characteristics.

Panel a) compares the emitted intensity at fixed injected current densities of 600, 800 and 1000 A/cm^2 (horizontal cuts of the maps in Fig. 2.3) while panel b) shows the normalized voltage $V(B)/V(B = 0\ \mathrm{T})$ at constant current density.

The curves in panel a) clearly show the difference in the extension of the non-lasing region between the two devices. The two regions are indicated with light and dark grey bands throughout the figure and, as already seen from Fig. 2.5, they are maintained over the whole explored current density range. As already noted, they take place about the main crossing of the upper laser level with the first Landau level of the lower ones at a cyclotron energy of 15.1 meV (right-most vertical dashed red line). This crossing is determined in the $V(B)$ curves in panel b) by the main broad central minimum present in most curves and identifies the energy of the electronic transition between the upper and lower laser levels. In fact when the resonance condition is met, a non-radiative channel opens for electrons to decay faster than the radiative transition, requiring less applied bias to sustain the same current density. Considering Eq.s (1.1) and (1.3), this means a strong decrease of $\tau_{eff} \simeq \tau_{up}$ resulting in a big increase in J_{th} creating the gaps shown in panel a) of Fig. 2.5.

When comparing this value with the energy of the "asymptotic" optical emission, i.e. 14.3 meV, it is clear that the optical transition is shifted with respect to the electronic one, derived from transport to be at 15.1 meV. Such discrepancy has already been seen in THz-QCLs[118, 212] and stems from the fact that the matrix elements ruling the transition from the upper to the lower subband have different expressions for the optical transition[206] and for electrical one (electron-electron scattering between the respective Landau levels)[204]. These then result in different energies when summed over the states of the miniband.

Additionally, several many body effects have been pointed out as responsibles for similar shifts in highly doped intersubband systems, the main of which is the depolarisation shift[206]. This effect influences the absorption spectrum by modifying the optical energy with respect to the bare electronic energy difference. Even though the depolarisation shift generally induces a blue-shift of the transition, it has been shown[213] that for an inverted

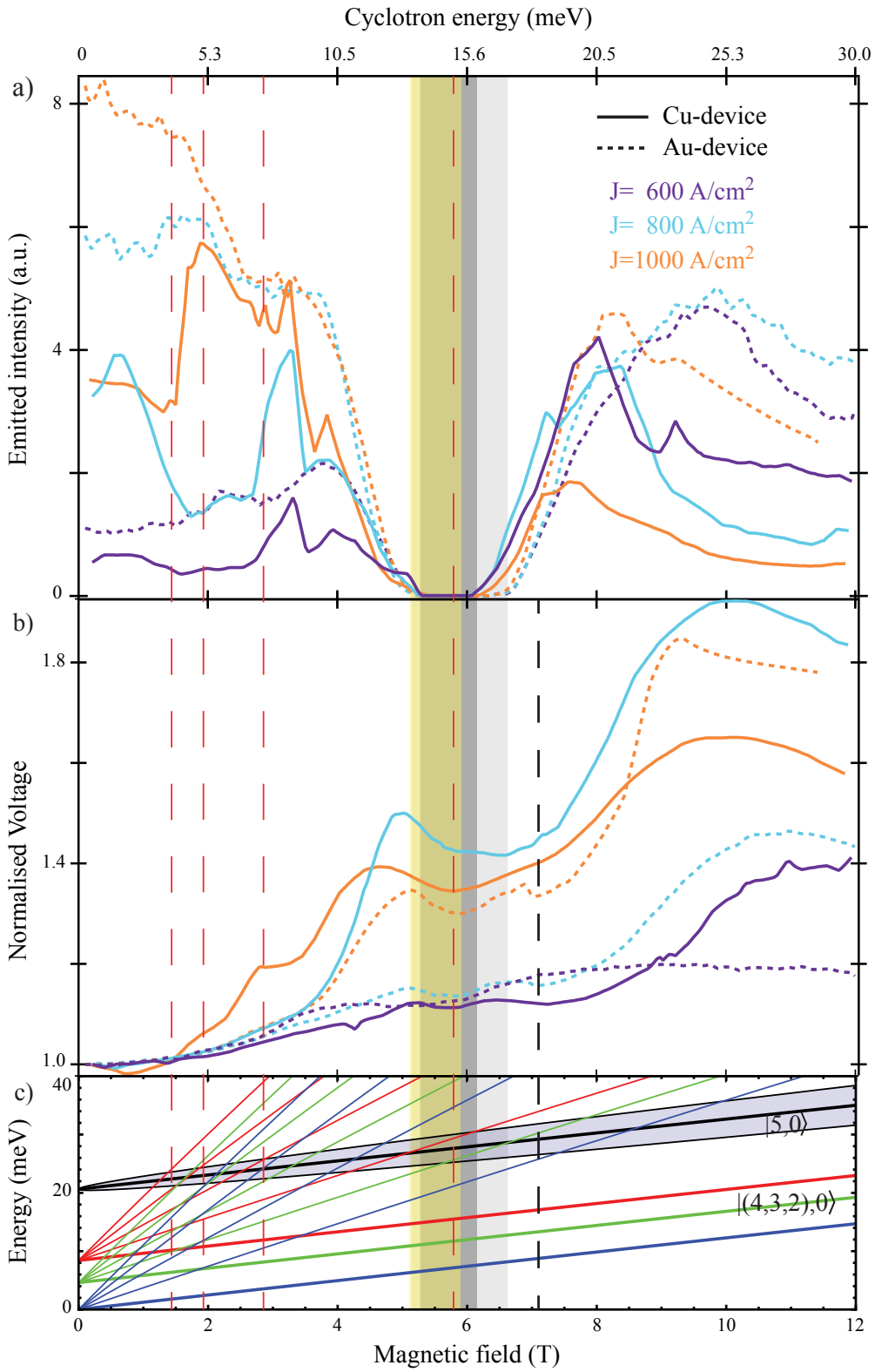

Figure 2.8 – a) Emitted intensity of the laser and b) normalized voltage $V(B)/V(B = 0\ \mathrm{T})$ plotted against magnetic field for the Au- and Cu-devices, displayed in dashed and full lines, respectively. The curves of panel a) and b) are taken at fixed current densities: 600, 800, 1000 A/cm^2 displayed in violet, light blue and orange, respectively. The Landau fan chart of the involved states is also plotted in panel c).

system, the sign is also inverted. The maximum energy shift can be evaluated from

$$\Delta E \simeq \frac{e^2 n_{up} S}{\epsilon_r \epsilon_0} \tag{2.4}$$

where n_{up} is the upper state population, ϵ_r/ϵ_0 the relative/vacuum permittivity. The depolarization integral was evaluated to be $S = 5/(9\pi^2)a$ in the approximation of a vertical transition in an infinite quantum well of width a.[206] In the present case, the transition does not take place within the same well and a was approximated by the transition dipole. With $\epsilon_r = 13.32$ and $a = 22$ nm and, assuming[137] $n_{up} = 10\% n_s = 4.86 \times 10^9$ cm^{-2}, one obtains $\Delta E = 0.08$ meV. This has to be compared with a measured energy difference of about 0.8 meV, showing that the depolarization shift has a sizeable influence (10%) on the transition energy shift but other effects are needed to account for the bigger energy difference.

Considering then the lower B-field range of the measurements in Fig. 2.8, several features are present both related to the emission intensity and to the transport. They are much stronger for the Cu-device, and take place close to the main crossings of $|5,0\rangle$ with $|(4,3),n\rangle$, as clearly seen also in panel a) of Fig. 2.5. In the high B-field region, the laser is in the strong confinement regime[207] where no relevant crossing takes place and the emission decreases with higher magnetic fields, due to the progressive misalignment of the states with increasing magneto-resistance.

Noteworthy is furthermore the fact that, in panel b) of Fig. 2.8, there is a minimum at about 7.1 T that appears in all curves with different strength and is especially evident for the Au-device (vertical thin dashed line). Since it is close to the magnetic field value for which lasing at low energy was detected, we attribute this minimum to photon-assisted transport from state $|3\rangle$ to $|2\rangle$ while lasing at about 5.9 meV. There might also be a small contribution of the crossing of $|3,1\rangle$ with $|5,0\rangle$, but it has to be noted that this minimum is quite narrow and well separated from the broad central one, supporting these facts the photon-assisted transport hypothesis.

Finally, we come to discuss the range of emission of the QCLs, 13.4–15.3 meV, reported throughout the figures as a yellow band, corresponding via the cyclotron energy to the range 5.1–5.9 T. This lasing interval has almost the same extension and almost overlaps with the non-lasing gap of the Cu-device (dark grey band). Instead the gap of the Au-device (light grey band) extends further towards higher fields for 1.5 T as better seen from panel a) of Fig. 2.5. This could be interpreted as follows: the gap of the Cu-device seems to be the narrowest possible, given the tuning of the emission. Instead the gap of the Au-device is broader due to additional losses in the QCL-structure. Interestingly, the

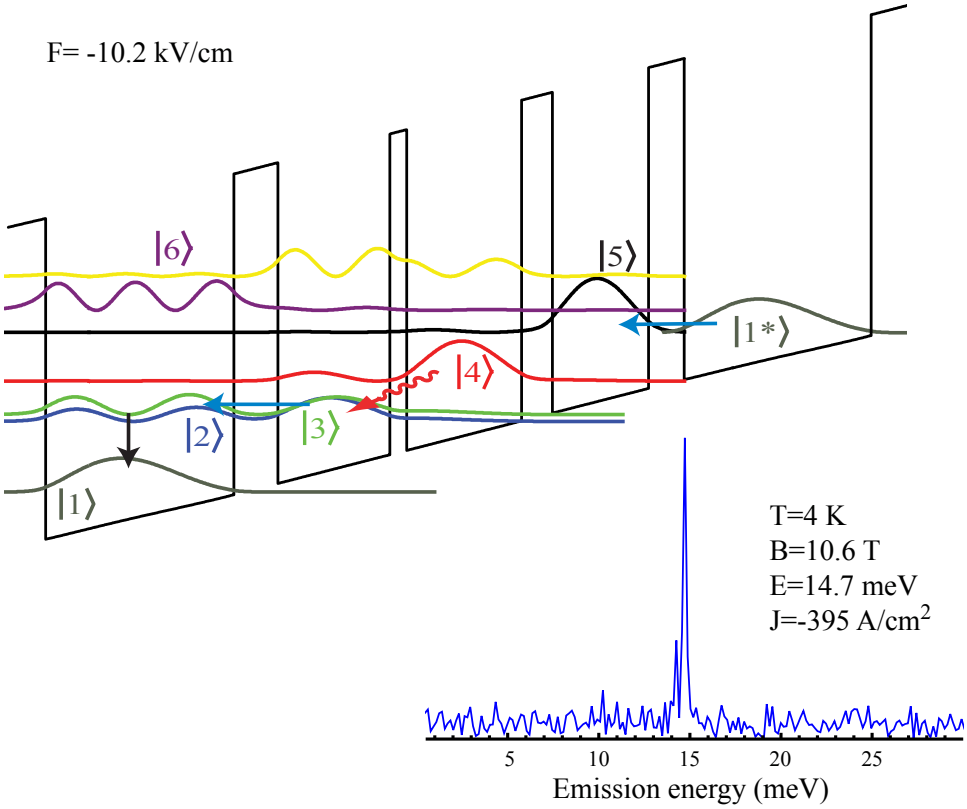

Figure 2.9 – a) Conduction band scheme and modulus of the relevant wavefunctions of the investigated active region upon reverse bias, at the calculated alignment field of $F = -10.2$ kV/cm. The injector fills state $|5\rangle$, that gets non-radiatively depopulated onto state $|4\rangle$ that lases onto the miniband $|3, 2\rangle$. This is resonantly depopulated into the injector $|1\rangle$, that funnels the electrons into the next period ($|1*\rangle$). b) Spectrum recorded for the best emission conditions of $B = 10.6$ T and $J = -395$ A/cm^2.

ratio between the gap extensions coincides with the ratio of the cavity losses:

$$\frac{\Delta B^{Cu}}{\Delta B^{Au}} = \frac{\alpha_m^{Cu} + \alpha_w^{Cu}}{\alpha_m^{Au} + \alpha_w^{Au}} = \frac{2}{3}. \tag{2.5}$$

Nonetheless, the two gaps are not centred with respect to each other, possibly due to the asymmetry of the modal gain function in magnetic field.

2.3.5 Reverse bias study

Although the structure of the active region is non-symmetric upon bias inversion, lasing action could be detected also in reverse bias. Its maximum lasing takes place at 14.7 meV (3.55 THz) for a magnetic field of 10.6 T. The moduli of the calculated wavefunctions at the alignment field of -10.2 kV/cm are shown in panel a) of Fig. 2.9, while panel b) shows the spectrum recorded at the point of maximum emission.

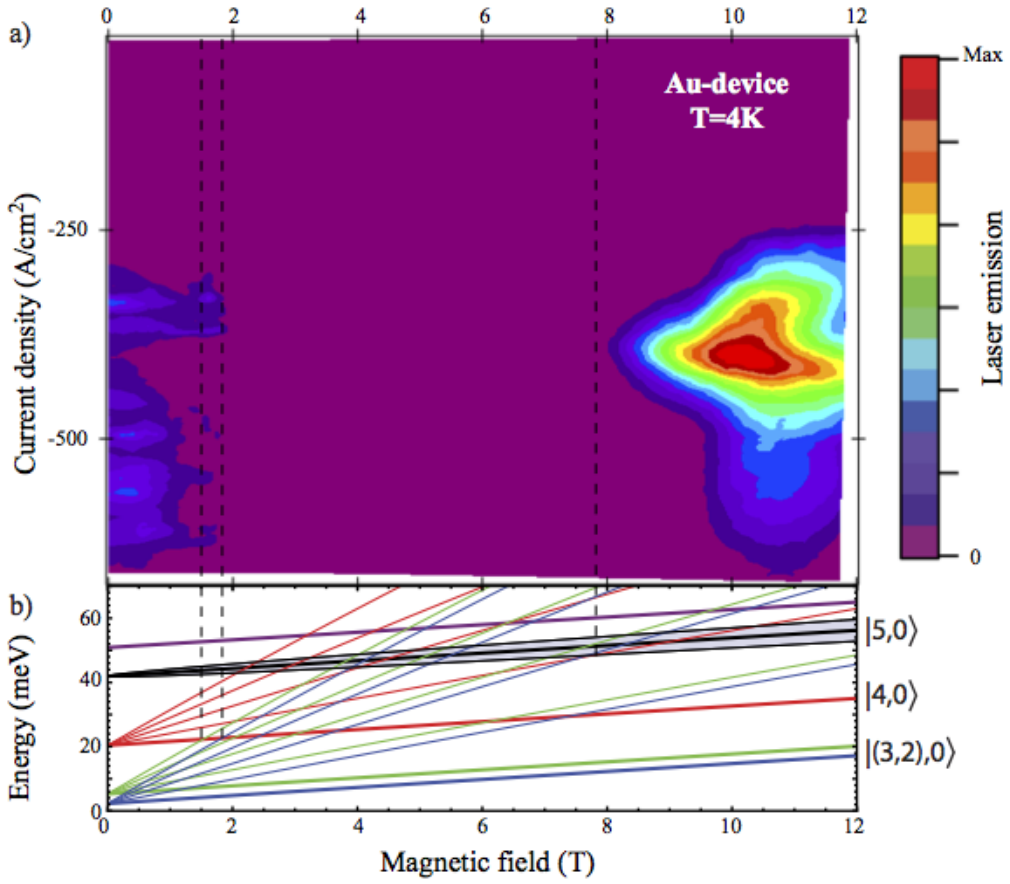

Figure 2.10 – a) QCL emission vs magnetic field and current density for the Au-device driven in reverse bias (500 pulses per macro-pulse with width 104 ns, $T = 4.2$ K). b) Landau levels' fans of the involved states.Note the negative sign of the vertical axes in panel a).

Since the structure is constituted by a wide injector followed by three thinner wells, upon inversion of the bias, the wavefunction scheme is similar to the one for direct bias. The calculated bandstructure shows that the injector still funnels the electrons into state $|5\rangle$. From there, at strong magnetic fields, they can non-radiatively transfer to the lower level $|4\rangle$ thanks to the Landau level crossing in the B-range 7.5–10.5 T, and then lase onto $|3\rangle$.

The measured $B - J - L$ map is reported in panel a) of Fig. 2.10 along with the calculated Landau level fans (panel b)). Again, two lasing regions are present, although with a huge dark gap in between ($\Delta B = 6$ T) and showing a small change in threshold current density.

At $B = 0$ T two different lasing regions are met for increasing negative current density, but the situation is less clear, since the Landau levels are not yet formed. An additional source of uncertainty comes from the fact that it was not possible to take the corresponding spectrum. What seems likely is that, initially the populated state $|5\rangle$ is lasing onto $|4\rangle$

(E_{54}=21.2 meV, z_{54}=3.21 nm). For increasing bias, it is not clear which scheme would lase, since both $|5\rangle$ and $|1^*\rangle$ raise in energy staying close to alignment while $|2\rangle$ is still in resonant LO-phonon condition to $|1\rangle$.

2.4 Conclusions and Outlook

At this point, let us summarise the main results of this study. We performed the magneto-spectroscopy of InGaAs/AlInGaAs THz-quantum cascade lasers, comparing two different DM-waveguide metals. We could show that the active region lases for most B-field values at frequencies about 14.3 meV and, for a small interval of magnetic fields and temperatures, low-energy emission is also present at 5.9 meV. The device processed in a Cu-Cu DM-waveguide could lase up to 148 K without magnetic field and up to 195 K with B=12 T. The maximum operating temperatures are 18 K and 13 K higher than those of Au-Au DM-waveguide devices, for the case without and with magnetic field, respectively. This confirms the better temperature performance of the devices with copper waveguide. Additionally, the maximum operating temperature of the presented devices are higher than the ones of the THz-QCLs realised in other InGaAs-based material systems, confirming the suitability of the quaternary barriers for THz-QCLs and opening new possibilities by varying their composition. Nonetheless, the maximum operating temperature is still far from the Peltier-cooler region, hindering practical utilisation of the lasers. Surprisingly, the lasers operated also in reverse-bias condition.

Finally, it is interesting to compare our results to all other material systems which have been studied with magneto-spectroscopy. The relevant quantities are summarized

Table 2.1 – Material system comparison for the THz-QCLs investigated also in strong magnetic field: for each system are given the metal constituting the waveguide (Wvg.), the maximum operating temperature with and without magnetic field with their difference $\Delta T_{max}= T_{max}(B) - T_{max}$, the photon and LO-phonon energies E_{phot} and E_{LO}. The ratio of the cyclotron energy calculated at the magnetic field where the maximum temperature was measured $E_c(B|_{T_{max}})$ with the previous energies is also reported. In order to have a fair comparison, all cyclotron energies in this table were computed in the constant-mass approximation. The results obtained in this thesis are marked in blue.

Well/Barrier material	Wvg. Metal	T_{max} (K)	$T_{max}(B)$ (K)	ΔT_{max} (K)	E_{phot} (meV)	E_{LO} (meV)	E_c/E_{phot}	E_c/E_{LO}	Ref.s
GaAs/AlGaAs	Cu	178	225 (19.3T)	47	13.0	36	2.6	0.93	[79, 121, 196]
InGaAs/InAlAs	Au	122	-	-	12.8	33	-	-	[144]
InGaAs/GaAsSb	Au	142	190 (11T)	48	14.8	33	2.0	0.90	[146, 203]
InGaAs/AlInGaAs	Au Cu	130 148	182 (12T) 195 (12T)	52 47	14.3	33	2.3	0.98	[173] [214]

in Table 2.1, leaving out the InAs-based THz-QCL that does not show the same level of maturity. All lasers emit at similar energies and strikingly their temperature performances improve by the same amount (approx. +48 K) independent of the material system. Three energies are relevant for the present comparison: the photon energy E_{phot}, the LO-phonon energy E_{LO} and the cyclotron energy in the wells at the magnetic field for which the maximum operating temperatures were recorded $E_c(B|_{T_{max}})$. When taking the ratios between them, one realizes that all maximum temperatures were recorded with the lasers in the ultra-strong confinement regime[207, 196] when $E_c(B|_{T_{max}})$ is greater than the photon energy and close to the phonon energy. This seems to underline some common operation regime/limitations and in fact it is consistent with the fact that all designs are based on resonant-phonon depopulation scheme that gets enhanced when the cyclotron is as well resonant. This might be interpreted as the current lasers having all about 50 K to gain in performance from the optimal depopulation of the lower level.

On the other hand, such an improvement would not be enough and the optimisation of the other parameters, like scattering mechanisms, transition type and band structure, is fundamental for THz-QCL aiming at operating close to room temperature. The inadequacy of the resonant phonon design for high-temperature operation has already been discussed[211] and different QCLs, relying on the so-called *scattering assisted* architecture, have already been investigated showing good-performances[151]. In such design, the upper state population is achieved by LO-phonon scattering instead than by resonant tunnelling, but in view of our results, this might still not be enough to bring THz-QCLs close to room temperature operation.

Part II

Near field coupling of terahertz split-ring resonators

Chapter 3

Terahertz split-ring resonators

The present chapter discusses the THz-split-ring resonator (SRR) that is the constitutive unit of the metasurfaces used in this thesis. One of their most exploited features is the ability to confine electro-magnetic fields into highly sub-wavelength volumes, increasing, in such a way, the strength of the interaction between field and material. This is of great importance first when dealing with 2-dimensional electron systems like 2DEGs or graphene, where radiation with wavelength of 30 µm – 1 mm interacts with systems nominally 0.3 – 30 nm thick. This is needed for any opto-electronics device but, when increasing the strength of the interaction, this is a key factor also to enter the field of quantum electro-dynamics and to access the (ultra-)strong coupling regime. These points will constitute the basis of the investigations reported in part III, concerning strongly coupled systems and THz-modulators.

Before that, the next chapter investigates the near-field interaction of dual THz-metasurfaces, resulting in broadband, approximately constant extraordinary transmission. The explanation of this phenomenon requires a more in-depth understanding of the metamaterial effective parameters and of their optical properties.

3.1 Design, characterisation and simulation of THz-SRRs

The analogy between a split-ring resonator and an *RLC*-series oscillating circuit has already been introduced in section 0.1.1 on page 4.

For a given SRR-structure, the *RLC*-series mapping is strictly true only for the resonance corresponding to the electric-field concentrated within the slit. This *LC*-resonance is the one showing the strongest field concentration for the given geometry while display-

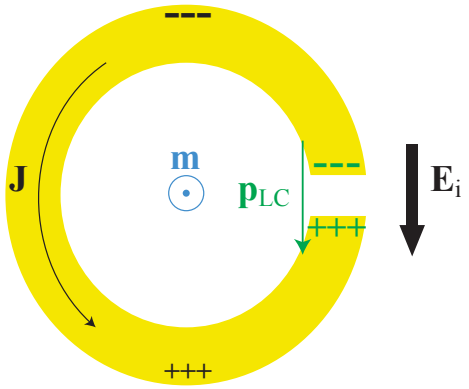

Figure 3.1 – Basic SRR-design with electric-LC-dipole p_{LC}, magnetic dipole m and induced current J. The accumulated charges are indicated by plus/minus signs, for the LC-mode (green) and the $\lambda/2$ mode (black).

ing the lowest resonance frequency[215]: the corresponding dipole is marked by the green signs and sketched as $\mathbf{p}_{LC}$ in panel a) in Fig. 3.1. Higher-order resonances are present or possible at higher frequencies and with a weaker field concentration. For instance, the same structure can also behave as an electric dipole: in such a case, the lowest-order resonance condition corresponds to the metallic side of the SRR being approximately equal to half of the radiation wavelength, along the direction of the illuminating electric field. Such resonance is then classified as a dipolar ($\lambda/2$) mode and corresponds to the charge accumulation marked by the black signs in panel a) in Fig. 3.1. Dipolar and higher-order modes show a weak field concentration due to the fact that charges of opposite signs collect far apart, at the edges of the metallic ring, while for the LC-one they are the closest possible, facing each other at the slit.

As a matter of fact, a line of research devoted to THz-field enhancement via nanogaps recently flourished for applications in sensing and non-linear optics.[216, 217, 218] The strong field-enhancement comes from the free charges in the metal that face each-other over nanometric distances.[219]

Several designs have been investigated in the past decades, more or less direct variations of the initial one.[220] All SRR-related work presented in this manuscript bases on a single design of SRR, shown in panel a) of Fig. 3.2. The design is constituted by two split rings connected back-to-back and it was taken from previous works on THz-SRRs[27] and it is a modification of a previously proposed SRR[26]. Schurig and coworkers pointed out that the design used has spatially-independent "inductive and capacitive elements, only one type of which is involved in coupling the fundamental mode to the desired external field".[26] It is the capacitive element, i.e. the SRR-slit, that couples to the electric field, whereas the two counter-propagating inductive loops give an effectively null total

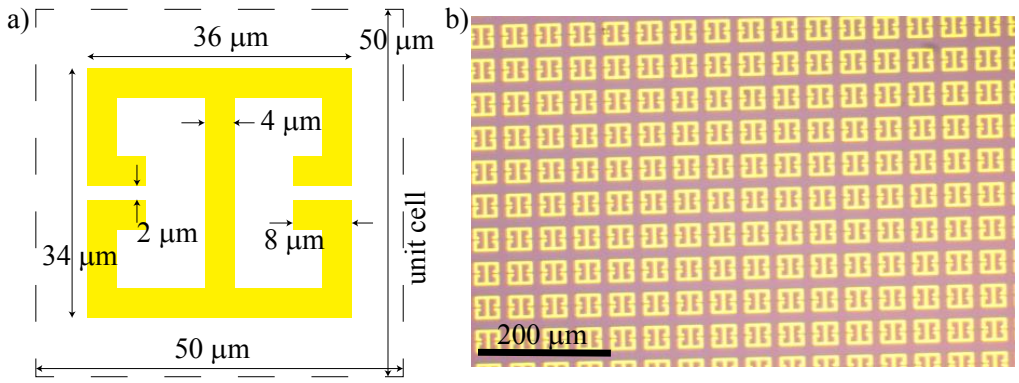

Figure 3.2 – a) Design of the used THz-SRR, with the dimension of its components and of the unit cell. b) Optical picture of an array of SRRs.

magnetic dipole.

When the SRR is illuminated by radiation linearly polarised across the slits, the two induced magnetic moments have opposite directions, therefore cancelling each other. Therefore, such geometry cannot couple to the magnetic field of the orthogonally incident radiation while, at the same time, does not allow a torque produced by a static B-field, making these structures suitable for experiments carried out in a magnet.[221]

The SRR structure was investigated with a THz-Time-Domain-Spectroscopy setup (THz-TDS) with a working bandwidth of about $0.2 - 3.0$ THz, described later in section 3.5. To this purpose, a two-dimensional array of split ring resonators was produced into a Gold layer of thickness ranging between 200 nm and 250 nm following the procedure reported in appendix H.1 on page 269. Note that these thicknesses are larger than Au's skin depth at the investigated frequencies, thus the metal behaves as such. The SRRs are placed with a periodicity of 50 µm in the two orthogonal directions and cover a squared area of 2.5×2.5 mm^2, a part of which is shown in panel b) of Fig. 3.2.

The spectral response of the THz-metasurface in the investigated range is constituted by two resonances, when the source, linearly polarised, is aligned across the slits, while only one absorption dip is present for the orthogonal polarisation, along the slits, as shown in Fig. 3.3 in red and blue, respectively. When the array is realised on a Si/SiO$_x$ substrate, the main resonance takes place at about 0.6 THz with a quality factor of 4.75 and corresponds to the LC-mode. The second, much broader, resonance has instead its minimum at about 2.35 THz and corresponds to the dipolar mode in the same polarisation (red trace). The blue trace presents a single broad resonance at about 1.25 THz and corresponds to the dipolar mode in the orthogonal polarisation.[222] Both measurement are normalised to the transmission through the bare substrate. Note that the exact value of the resonant frequency depends on the substrate used, and more in general on the

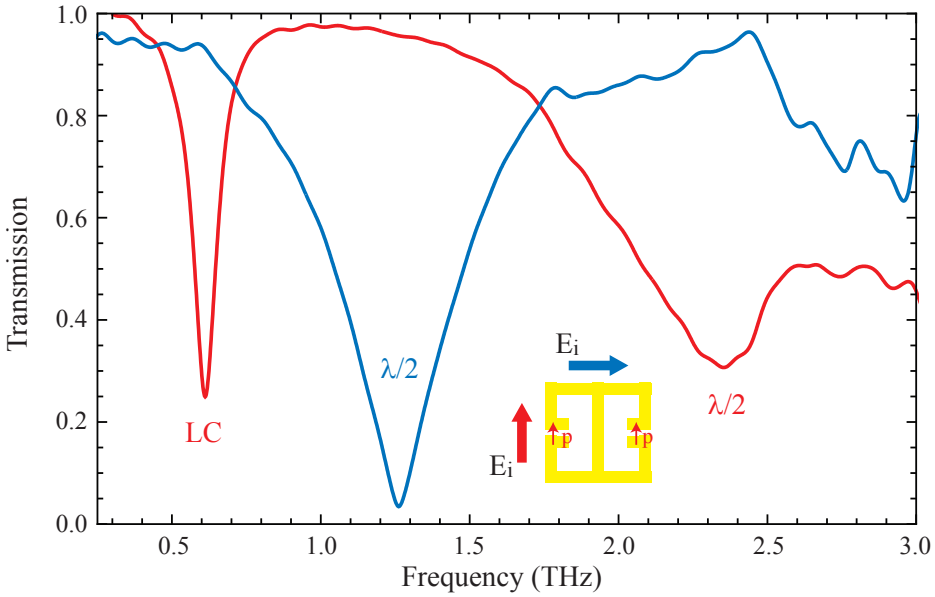

Figure 3.3 – Transmission of the direct-SRR metasurface in the two linear polarisations.

surrounding dielectric: hence different substrates will shift the resonance. For the work in this thesis, the described resonators were produced on top of both GaAs- and Si/SiO_x-substrates shifting the resonance from approx. 0.5 THz to 0.6 THz, consistent with the different permittivities. GaAs is the substrate used for the investigation in chapter 7 because it can host high-quality two dimensional electron gases, while the silicon-based substrate was used because of graphene in chapter 8.

In order to better investigate the resonant modes, FDTD commercial software was used to simulate the sample. Initially *COMSOL Multiphysics* was used, while later *CST Microwave Studio* was preferred due to its faster computation algorithm. The material parameters were taken from the built-in libraries. Moreover, such simulations allow parameter's studies without the need of producing a sample for each parameter value, investigating, e.g., different materials, dimensions, incident-radiation properties.

The simulated electric-field components for the three resonances previously discussed are presented in Fig. 3.4. The different rows present the simulations for the *LC*- and $\lambda/2$-mode for excitation linearly polarised in the vertical direction and for the $\lambda/2$-mode for excitation linearly polarised in the horizontal direction, respectively. Within each row, the colour maps show the distribution of E_x, E_y and E_z in the xy-plane (the one containing the metasurface). The E-field distributions corresponding to the dominant polarisation of each mode are framed in red: the SRR responds to the incident field E_i in the same polarisation.

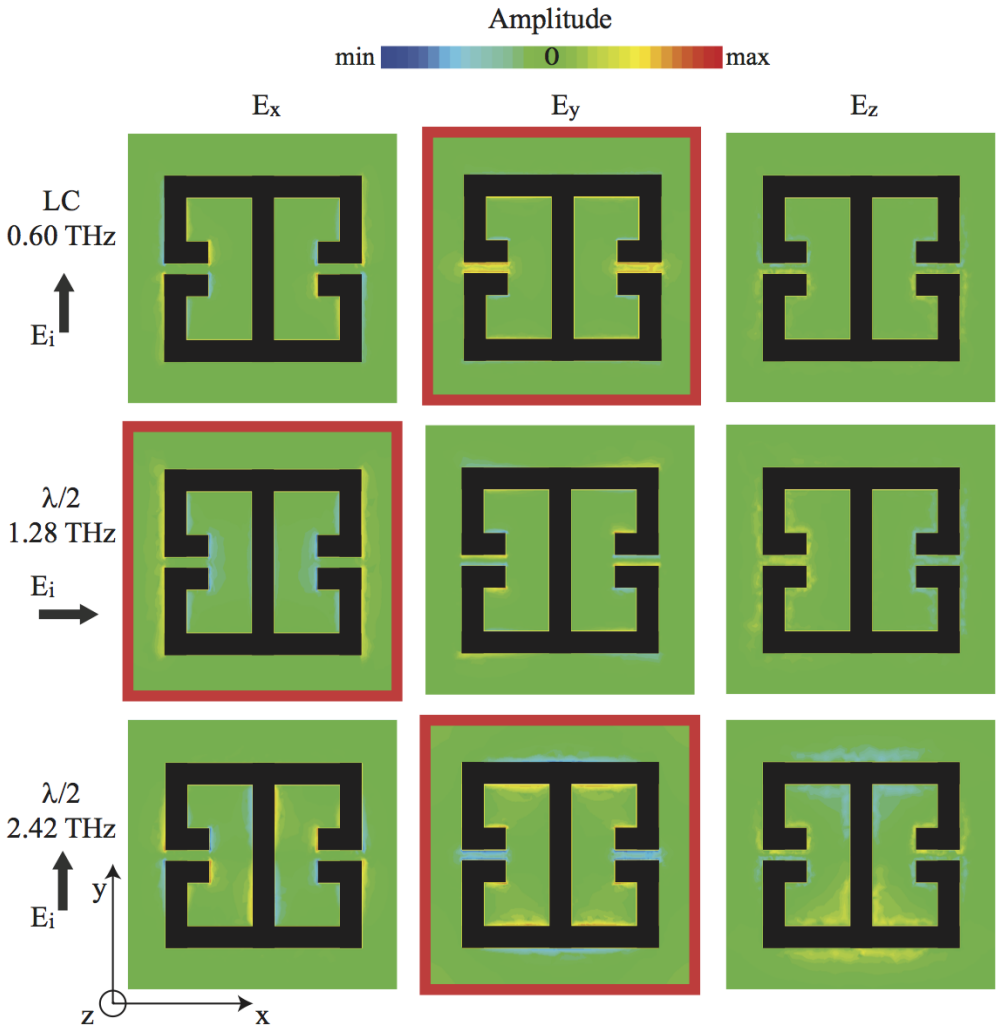

Figure 3.4 – Simulations of all electric field components for the three resonances of the direct-SRR. The red frames indicate the strongest field confinement for each resonance of the spectra in Fig. 3.3. The simulations were performed with CST Microwave Studio.

The *LC*-mode is the one with the best features. First, it shows an extreme field confinement by a factor 10^6, achieved by squeezing the electric field with a free-space wavelength of about 0.5 mm into a volume of the order of $8 \times 2 \times 4$ µm^3. Second, the field amplitude in the cavity gets enhanced by a factor of 20.

These favourable characteristics were already exploited, for example, to achieve one of the smallest lasers, so-called *LC*-laser.[223] In such device, a quantum cascade active region like the ones discussed in part I was filling the capacitor of the oscillating circuit, resulting in a device lasing at 1.5 THz.

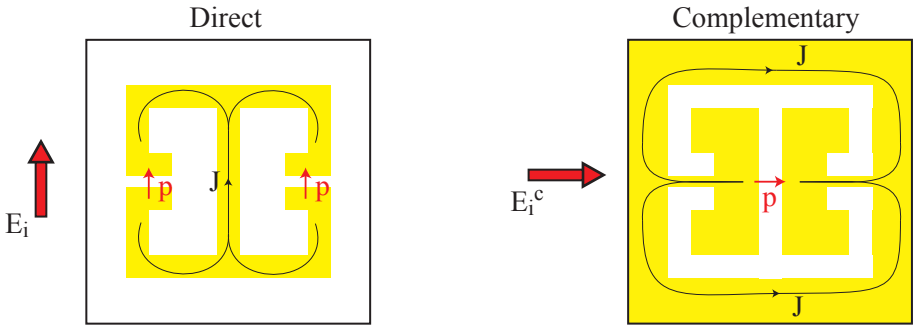

Figure 3.5 – Sketch of the dSRR with the dipole corresponding to the *LC*-mode (in red), excited in the proper polarisation. The cSRR, to show the complementary spectrum needs to be excited by the rotated polarisation to induce the marked dipole (in red). The induced currents are indicated by black arrows.

3.2 Direct and complementary SRRs

Babinet's principle is a useful tool to devise new optical objects. In the words of Jackson[224],

> A rigorous statement of Babinet's principle for electromagnetic fields can be made for a thin, perfectly conducting plane screen and its complement. [...] The original diffraction problem and its complementary problem are defined by the source fields and screens as follow:

Scattering problem	Electric field	Magnetic field	Screen
Original	E_i	B_i	S
Complementary	$E_i^c = cB_i$	$B_i^c = -E_i/c$	S^c

> The complementary situation has a screen S^c that is a complement of the original S and has source fields with opposite polarisation characteristics.

Let us highlight that the complementary problem requires a transformation of *both* objects *and* illuminating sources as shown in Fig. 3.5.

For the THz-split-ring resonator discussed in the previous sections one can therefore produce the complementary object by covering with metal the empty area in the unit cell and leaving free the area previously covered. The result is presented in Fig. 3.6. From here on, in the rest of the manuscript, complementary SRRs will be mentioned as "cSRRs". To make the distinction obvious and avoid confusion when comparing the two, the initial SRR will be denoted as "direct" dSRR, hence dSRRs vs cSRRs.

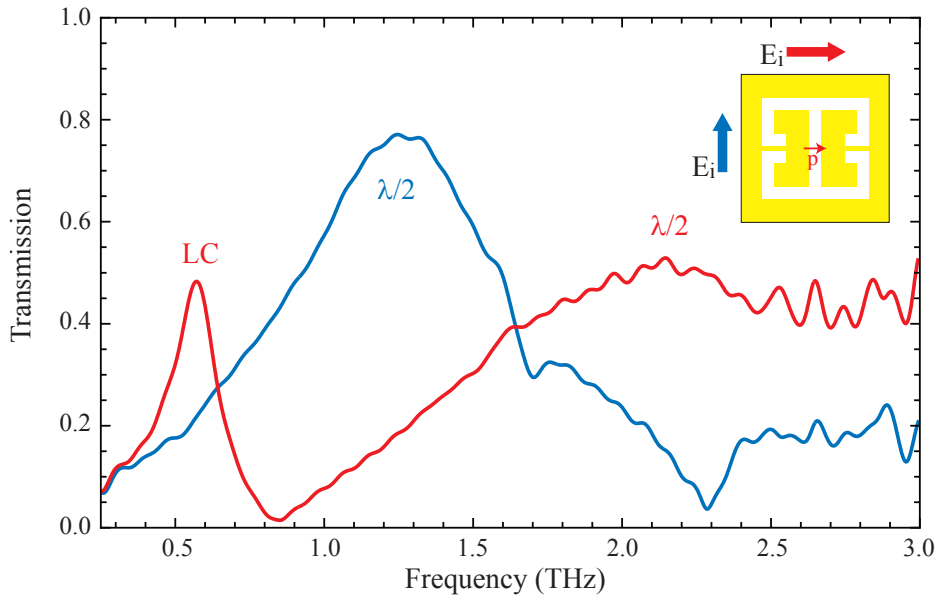

Figure 3.6 – Normalised transmission spectra of the cSRR sample in the two orthogonal polarisations.

The two structures resonate at the same frequency when illuminated with source polarisations orthogonal to each other, but they can be distinguished by their optical response. In fact the dSRR constitutes a band-stop filter, i.e. the resonance appears as an absorption in the background transmission, while the cSRR constitutes a band-pass filter, i.e. the resonance appears to be the transmittance of an otherwise dark screen. The spectra of the cSRR are shown in Fig. 3.6, to be compared with the corresponding spectra in Fig. 3.3.

It can be seen from the simulations in Fig. 3.7 that the *LC*-mode corresponding to the lowest-frequency resonance keeps the same character, despite being displaced in the two configurations. One can notice that the electric field and the electric current density distributions are exchanged.

Furthermore, one should note that the cSRR's lowest-frequency mode is now described by an *RLC*-parallel circuit and not any more by an *RLC*-series as for the dSRR's one, consistently with the complementarity of series and parallel configurations. This is the topic of the next section.

In the THz-frequency range, this kind of complementary resonators has been quite extensively investigated.[225, 226] It might nonetheless amuse the reader to know that, within this research work, its discovery was fortuitous, being the first cSRR sample the result of a processing mistake. In appendix H.1 on page 269 the recipes used for producing the samples are reported. One can notice, reading in detail, that few steps separate the

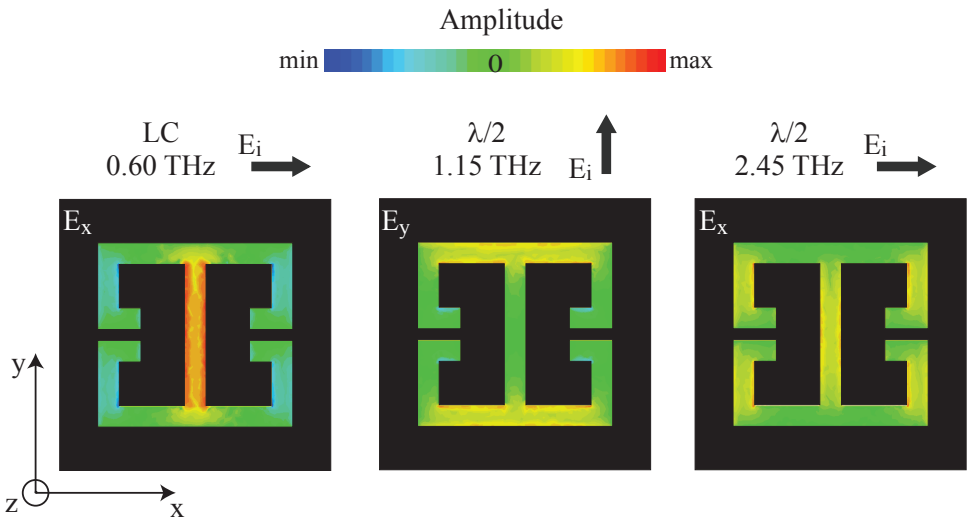

Figure 3.7 – Simulations of the in-plane electric field distribution for the resonances of the cSRR, in the respective exciting polarisations (cf. with the spectra in Fig. 3.6).

transposition of a positive or a negative image of the wanted structure onto the sample. Usually, the negative image was transferred so to obtain a metasurface of dSRRs. It happened once that a positive image was produced and the result was a cSRR sample.

3.3 Analytic circuital model of THz-SRRs

A way to easily model and get more insight into the THz-SRR properties is with the use of a transmission line model. This is even more pertinent recalling that the main SRR resonance is properly an *LC*-mode. The metasurface response can thus be reproduced by an analytical impedance-based model, taking advantage of the calculations in Ref. [27].

Let us consider first the case of a direct SRR metasurface. The complementary case will be readily treatable by a small modification of the discussion presented below.

For the purpose of the modelling, the metasurface is considered to be an infinitely thin layer sandwiched between vacuum (air) and the substrate. In the transmission-line representation in panel a) of Fig. 3.8, the metasurface impedance Z_{meta} shunts the line between the vacuum impedance Z_0 and the substrate impedance $Z_{subst} = Z_0/n_{subst}$. In this representation, the E-field of the wave impinging on the surface and propagating through the sample is represented by the voltage V_i.

The normalised transmission through a unit cell of the metasurface can therefore be written in terms of the materials' impedances as the product of the transmission from vacuum to metasurface, to substrate, to vacuum, divided by the transmission through the

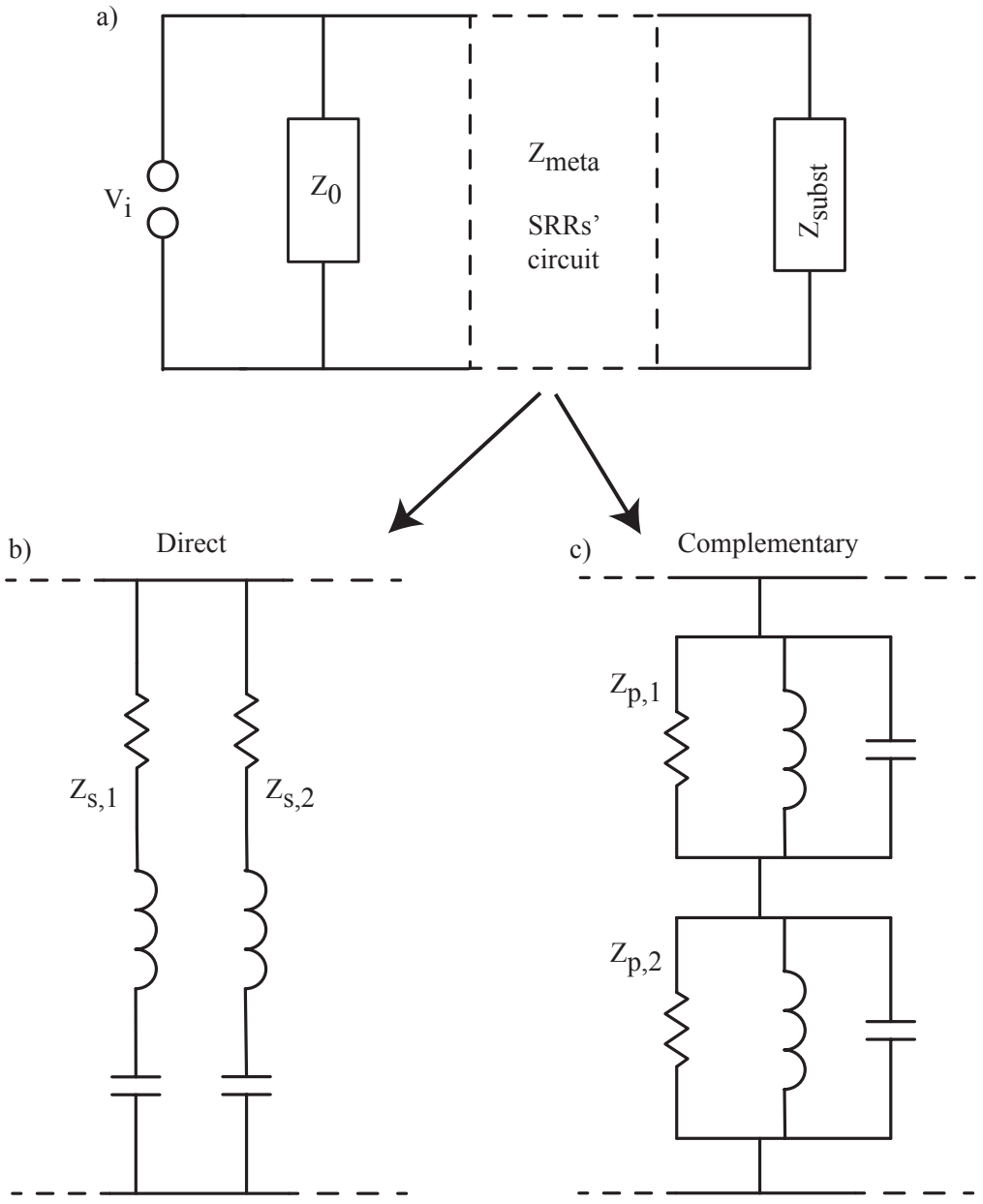

Figure 3.8 – a) Transmission-line model of the transmission through the sample: the incident radiation V_i impinges onto the sample constituted by SRRs Z_{meta} and substrate Z_{subst} from free space Z_0. b) Circuital schemes for the direct-SRR, represented by a parallel of RLC-series circuits $Z_{s,i}$. c) Circuital schemes for the complementary-SRR, is represented by a series of RLC-parallel circuits $Z_{p,i}$. $i = 1, 2$ indicate the different resonances.

substrate:

$$t_{meta}(\omega) = \frac{E_t(\omega)}{E_0(\omega)} = \frac{2Z_{meta}(\omega)}{Z_{meta}(\omega) + Z_0} \frac{Z_{subst} + Z_0}{2Z_{subst}}. \tag{3.1}$$

This procedure highlights the fact that the metasurface becomes actually the interface between vacuum and substrate.

At this point the frequency-dependent impedance of the metasurface needs to be determined. As already mentioned, the main resonance of the dSRR is a band-stop LC-resonance that can be modelled by an RLC-series circuit, hence with impedance

$$Z_s(\omega) = R + i\omega L + \frac{1}{i\omega C}. \tag{3.2}$$

The values R, L and C can be fitted or, sometimes, calculated. To account for the other resonances, since they have all a band-pass nature, a corresponding number of such RLC-series can be used. Panel b) in Fig. 3.8 shows the equivalent circuit needed to account for the LC- and $\lambda/2$-modes in the parallel polarisation. Concerning the orthogonal polarisation, a single circuit is enough to account for the $\lambda/2$-mode.

One should not forget that the metasurface is now the interface to the substrate and thus Z_{subst} needs to be put in parallel to the previous ones:

$$Z'_s(\omega) = \frac{Z_{subst} Z_s}{Z_{subst} + Z_s}, \tag{3.3}$$

Z_s is given by Eq. (3.2) and its ω-dependence is left implicit to have a light notation. The total response of the dSRR irradiated with source polarisation across the slit is hence given by

$$Z_{meta}^{dSRR,p}(\omega) = \frac{Z_{subst} Z_{s,1} Z_{s,2}}{Z_{subst}(Z_{s,1} + Z_{s,2}) + Z_{s,1} Z_{s,2}} \tag{3.4}$$

where $Z_{s,j}$ are the impedances of the j-th RLC-series circuit, $j = 1, 2$, in parallel to each another. An important point to highlight, implicitly contained in the above discussion, is that the response of the metasurface is substrate-dependent, both in amplitude and frequency, according to the complex material permittivity.

In Ref. [27] a coupling parameter is included to better fit the data, justifying it as a mutual-inductance coupling but without a specific physical explanation. In the present manuscript we neglect such coupling, arguing that the parameter is unnecessary and that physical coupling is excluded. This is connected to the absence of coupling between the two modes discussed in section 6.5 on page 153.

When considering instead the complementary SRR, the band-pass resonances can be

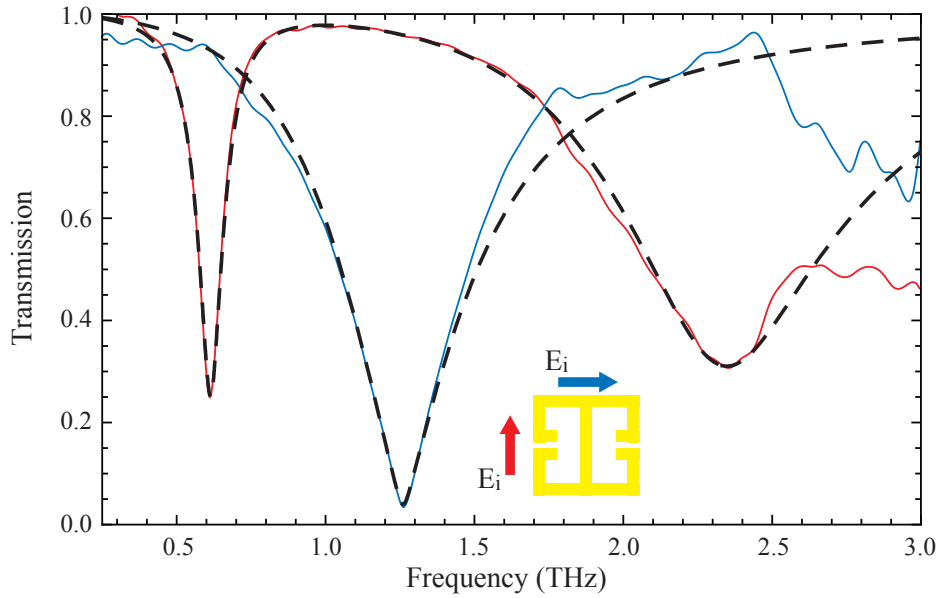

Figure 3.9 – Fit of the direct-SRR spectra with the *RLC*-series transmission-line model (black dashed lines). The parameters' values are collected in Table 3.1.

modelled as *RLC*-parallel circuits with impedance

$$Z_p(\omega) = \left(\frac{1}{R} + \frac{1}{i\omega L} + i\omega C\right)^{-1}. \tag{3.5}$$

The complementarity principle requires to exchange series and parallels in the circuits describing the two kinds of SRRs.[227, 228] This means that the modes of a cSRR resonator can be accounted for by two *RLC*-parallel circuits put in series one another as sketched in panel c) of Fig. 3.8 for the orthogonal polarisation. Its impedance is given by

$$Z_{meta}^{cSRR,o}(\omega) = \frac{Z_{subst}\left(Z_{p,1} + Z_{p,2}\right)}{Z_{subst} + Z_{p,1} + Z_{p,2}}, \tag{3.6}$$

with the same terms description as for Eq. (3.4). The superscripts p and o indicate the polarisation of the exciting THz-beam with respect to the SRR-structure and stand here for *parallel* and *orthogonal*, referred to the *LC*-dipole oriented across the slit. The two arrangements are highlighted in Figs 3.3 and 3.6 by the red arrows indicating the *LC*-dipoles.

The transmission spectra of the dSRRs and cSRRs can be reproduced by the presented model as shown in Fig. 3.9 for the dSRR case. The values extracted for the different circuital elements are reported in Table 3.1. One should notice the higher equivalent resistance values for the complementary resonators, indicating a lower quality factor.

Table 3.1 – Values obtained for R, L and C fitting the measured spectra in both polarisations for the direct and complementary resonators with the transmission-line model. The spectra are presented in Figs 3.3 and 3.6 and the resulting fitting curves are plotted in Fig. 3.9 for the direct SRR.

mode\par.s	R (Ω)	L (pH)	C (fF)
LC direct	120	300	0.225
LC compl	230	6.2	10
dipole direct	150	62.9	0.0817
dipole compl	520	7.54	0.6
direct orth	40	65	0.25
compl orth	5000	11.7	1.21

3.4 Refractive-index extraction for thin conductive sheets

The refractive index of the metasurface can be extracted from the transmission spectra under the approximation of a thin conductive sheet.[229, 230] Following Refs [229, 231], one can in fact write the normal-incidence transmission $E_s(\omega)$ through a homogeneous sample, e.g. the substrate used, as a function of the incident electric field E_i as

$$E_s(\omega) = t_v^s\, t_s^v\, e^{in_s\omega d/c}\mathrm{FP}_{vsv}E_i, \tag{3.7}$$

where $t_i^j = 2n_i/(n_i+n_j)$ are Fresnel's transmission coefficients from medium i to medium j and the exponential represents the phase accumulated while propagating within the material with thickness d and refractive index n_s. All refractive indexes are complex values and the indexes s and v denote substrate and vacuum, respectively. Note that to keep the notation light, in this section the substrate is indicated with the subscript s instead of *subst* as above. FP_{ijk} represents the Farby-Perot factor taking into account the multiple reflection undergone inside medium j, sandwiched between media i and k. Its formula is given by

$$\mathrm{FP}_{ijk} = \sum_{p=0}^{P}\left(r_j^k\, r_j^i\, e^{i2n_s\omega d/c}\right)^p = \frac{1}{1-r_j^k\, r_j^i\, e^{i2n_s\omega d/c}} \tag{3.8}$$

where $r_i^j = (n_i - n_j)/(n_i + n_j)$ are Fresnel's reflection coefficients from medium i to medium j at normal incidence and the last equality makes use of the property of the geometric series.

Let us now consider a sample that contains a conductive film f of thickness δ at the surface of the sample: its transmitted electric field is thus given by

$$E_f(\omega) = t_v^f \, t_f^s \, t_s^v \, e^{in_f \omega \delta/c} e^{in_s \omega d/c} \mathrm{FP}_{vfs} \mathrm{FP}_{fsv} E_i. \tag{3.9}$$

In TDS measurements, the multiple reflections within the substrate are usually removed by time-windowing the time-trace, i.e. by Fourier-transforming only the main pulse, cutting it before the appearance of the first echo. Thus one can set the connected Fabry-Perot terms to unity, $\mathrm{FP}_{fsv} = \mathrm{FP}_{vsv} = 1$. One needs instead to evaluate the term connected to the thin conductive layer FP_{vfs}. When the thickness of the layer is much smaller than the radiation wavelength, i.e. $\delta \ll \lambda$, one can disregard the phase accumulation for the single-path transmission while approximating the exponential in the Fabry-Perot term with its Taylor expansion, keeping only the first two terms. Such approximation is easily fulfilled by nanostructured layers at THz-frequencies: in the next chapters this will be used along with THz-metasurfaces, with and without graphene, with a thickness $\delta \simeq 200$ nm, much smaller than any wavelength probed by the setup $\lambda \simeq 100 - 1200$ µm.

Then, putting together the previous expressions and performing the mentioned thin-film approximation, the normalised transmission is given by

$$t = \frac{E_f}{E_s} = \frac{t_v^f \, t_f^s}{t_v^s} \frac{1}{1 - r_f^s \, r_f^v \, (1 + i 2 n_s \omega d/c)}. \tag{3.10}$$

At this point, substituting the formulae for Fresnel's coefficients, recalling that $n_v = 1$ and rearranging, one obtains

$$t = \frac{(1 + n_s)}{(1 + n_s) - i \frac{\omega}{c} \delta \, (n_f - 1) \, (n_f - n_s)}, \tag{3.11}$$

that, with the further approximation $n_f \gg n_s, 1$, becomes

$$t = \frac{(1 + n_s)}{(1 + n_s) - i \frac{\omega}{c} \delta n_f^2}. \tag{3.12}$$

Inverting with respect to n_f^2 gives

$$n_f^2 = i \frac{(1 + n_s)(t - 1)}{\frac{\omega}{c} \delta} \tag{3.13}$$

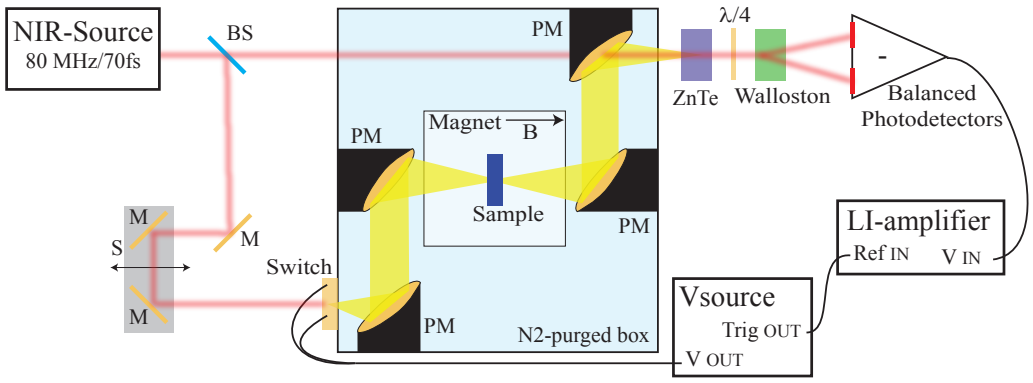

Figure 3.10 – Schematics of the used TDS-setups. The NIR beam is split at the beam splitter (BS). One part is sent with mirrors (Ms) to a delay line (S) onto the biased photo-conductive switch that generates the THz-beam (yellow). This is focussed via parabolic mirrors (PMs) first onto the sample, then in the ZnTe crystal where it overlaps with the rest of the NIR-beam. The NIR-beam goes than through a $\lambda/4$ plate and its polarisations are separated by a Wollaston prism and detected by a pair of balanced photodiodes. Most of the THz-beam travels in nitrogen-purged environment and the sample can be subjected to magnetic field. The signal is recorded via a lock-in amplifier, locked to the switch.

and, recalling that for a conductive medium, one can write the complex permittivity, and thus the refractive index $n_f^2 = \epsilon_f$ as

$$\epsilon_f(\omega) = \epsilon_s + \frac{i\sigma(\omega)}{\epsilon_0 \omega \delta}, \tag{3.14}$$

one can finally identify, substituting the free space impedance $Z_0 = (\epsilon_0 c)^{-1}$,

$$\sigma(\omega) = \frac{1+n_s}{Z_0 \delta}\left(\frac{1}{t(\omega)} - 1\right). \tag{3.15}$$

Equation (3.15) is used in the following chapters to derive the effective conductivity $\sigma_{eff}(\omega)$ of the metasurfaces from the measured transmission, allowing in some cases an effective medium discussion. In chapter 4 it is applied to a particular SRR-samples allowing to derive the phase of its dipoles, while in chapter 8 on page 207 it is applied to the graphene-SRR system, allowing an interesting discussion about the meaning of the thickness δ for monolayer materials.

3.5 THz-Time Domain Spectroscopy: basic principles and setup

All optical transmission measurements shown and discussed in this manuscript were performed with two similar THz-Time Domain Spectroscopy (TDS) setups, sketched in Fig. 3.10. In the setup, a Ti/Sapphire laser (*Maitai, SpectraPhysics*) produces light pulses at a wavelength of about 800 nm and with a length of 75 fs at a repetition rate of 80 MHz. The initial beam gets split into two, one of which impinges onto an interdigitated switch (*TERASED* by *Gigaoptics*, or by *Batop*, or from a collaboration with Dr. S. Dhillon at ENS in Paris) at an average power of 400 mW after going through a delay-line. The THz radiation is produced at the switch by photo-conductive generation. To such purpose, the switch is biased at 16 V with frequency 15.5 kHz and 50% duty cycle. The THz-beam is collected after generation, focussed onto the sample, re-collected after transmission and finally focussed onto a 110-oriented ZnTe crystal. The parabolic mirrors on either side of the sample are arranged in a confocal configuration and have f-number $f = 2$, while the other two parabolic mirrors have $f = 1$. All mirrors have diameters $d = 3$ inches.

Inside the ZnTe crystal, the THz-beam overlaps with the second part of the initial infrared beam: by Pockels effect, the electric field of the THz pulse induces birefringence in the ZnTe crystal that, in turn, changes the polarisation of the infrared beam. Such change is then detected by a pair of balanced photo-diodes (*Nirvana, Spectra-Physics, Newport*), illuminated by the beams created by the Wollaston prism after a $\lambda/4$ plate. This detection scheme is termed "free-space electro-optic sampling".[2] The time-domain measurement of the transmitted electric field amplitude is achieved by varying the delay between the THz and the near-infrared beams.

The THz beam travels continuously inside a nitrogen-purged environment to avoid water vapour absorption. The setup works generally in the bandwidth 100 GHz – 3.0 THz with a frequency resolution of 60 GHz and a minimum beam waist on the sample of about 1.5 mm (at the focal point, $F \simeq 0.5$ THz). The normalisation of the measured signal with respect to the empty holder hole or to the substrate ensures that the spectral characteristics of the setup are deconvolved from the sample's response.

An example of a time-trace measured with the used setup on a Si/SiO_x substrate is presented in Fig. 3.11, along with the Fourier-transformed spectrum, showing a SNR of about 10^3 in amplitude.

A parallel, conceptually identical setup was used for magneto-transmission measurements, where the beam path goes through a superconducting magnet (*Spectromag, Oxford Research Company*). The superconducting magnet is very similar to the one described

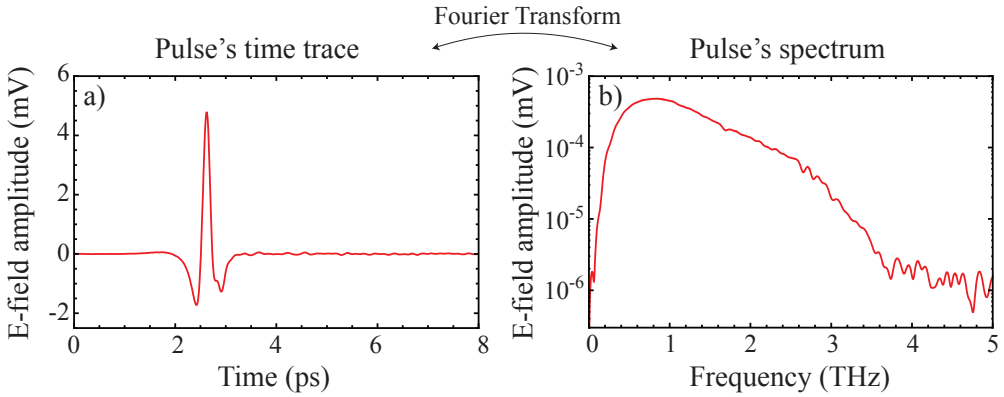

Figure 3.11 – Example of a) a time trace resulting from the measurement of a Si/SiO_x substrate piece and b) the corresponding spectrum, in log scale. The latter shows that the available maximum bandwidth of the setup is about 200 GHz – 3.5 THz for a signal-to-noise ratio in amplitude of about 100.

in section 2.2 on page 59, the main difference being that the superconducting coil is split into two and is arranged such that the magnetic field lies horizontally, collinear to the THz-beam path of the TDS. Two quartz windows on the opposite sides of the metallic shield allow the optical measurement. The focussing and collecting parabolic mirrors used for this setup have smaller diameter than the previous one ($d = 2$ inches) while the ones on either side of the sample have an f-number $f = 3.75$.

3.5.1 Cross-polarisation configuration

The described TDS setup produces linearly polarised light with polarisation axis along the bias applied to the photoconductive switch and detects the THz-radiation into the same polarisation. To such purpose, the normal axis of the ZnTe crystal is orthogonal to both the polarisation of the THz-radiation and of the probe beam.

As shown in Ref. [232], one can change the polarisation to which the detection scheme is sensitive by rotating by 90° the ZnTe crystal. Alternatively, one can leave the detection part of the setup fixed and rotate the switch. This configuration, called "cross-polarisation" allows the investigation of samples with circular polarisation properties. In fact, excitation and detection are linearly polarised and orthogonal, filtering each other, and any signal measured is the result of a polarisation rotation at the sample. This configuration will be used for the investigation of the closed-SRR in the next chapter and for transmission involving the cyclotron-transition in chapter 8.

Chapter 4

Extra-ordinary transmission and near-field interaction of dual terahertz metasurfaces

The idea of the present investigation came from an unexpected response of an unusual sample. When producing a complementary SRR sample, during the lift-off step, the metallic structures that should be removed fell instead back onto the substrate. This resulted in having the substrate completely covered by a layer of metal that is thick enough to be in principle opaque, uniform on the scale of the wavelength, but with periodical cuts shaped as the frame of THz-SRRs. This sample will be called, from now on, "closed-SRR sample" and the reason is clear from the optical and SEM images presented in Fig. 4.1.

When considering the closed-SRR sample from the optical point of view, one would expect to have no transmission because there is literally no area free from the metallic layer. Instead, unexpectedly, such sample displayed the non-negligible, featureless transmission, presented in Fig. 4.2. This and all subsequent measurements were performed in the THz-TDS setup described in section 3.5 on page 95. The curves in red and blue in Fig. 4.2 represent the normalised transmission of the sample for each of the two orthogonal polarisations aligned with the sides of the structure, whereas the black line, almost identically zero, is the trace corresponding to a continuous, homogeneous gold layer of the same thickness.

4.1 Quantifying the Extra-Ordinary Transmission

The spectra in Fig. 4.2 show first of all that the transmission is not due to leakage of the THz-radiation through the thin gold layer. In fact the latter is a factor of about 30

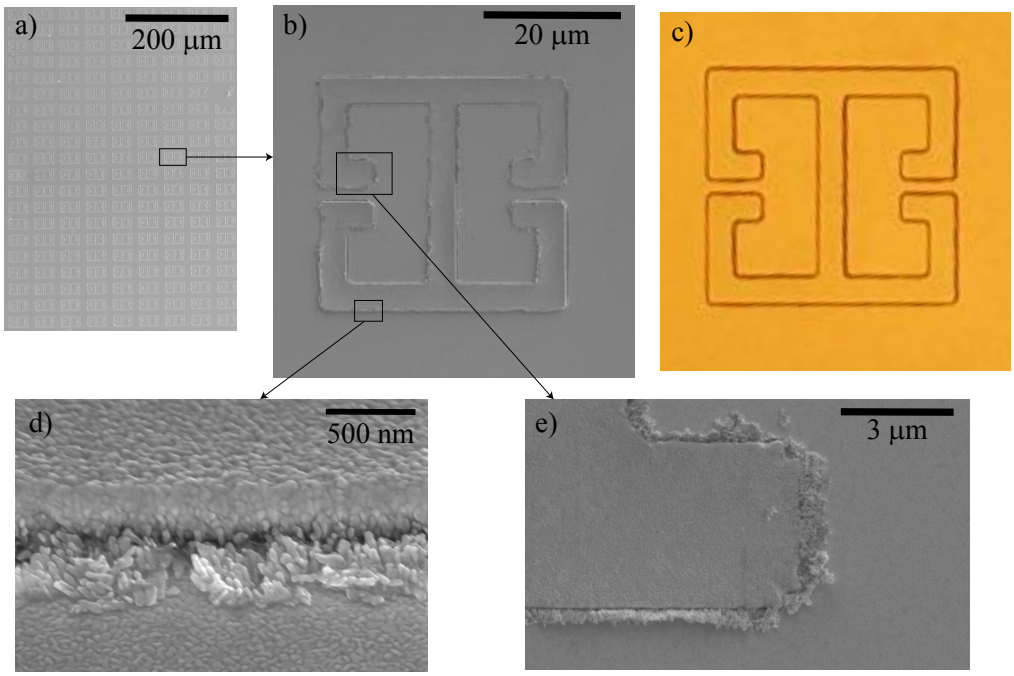

Figure 4.1 – a) SEM picture of a part of the closed-SRR field. b) Single closed-SRR and c-d) details of the contact points between he two layers. c) Optical image of a single closed-SRR. SEM images: courtesy of J. Keller and M. Süess.

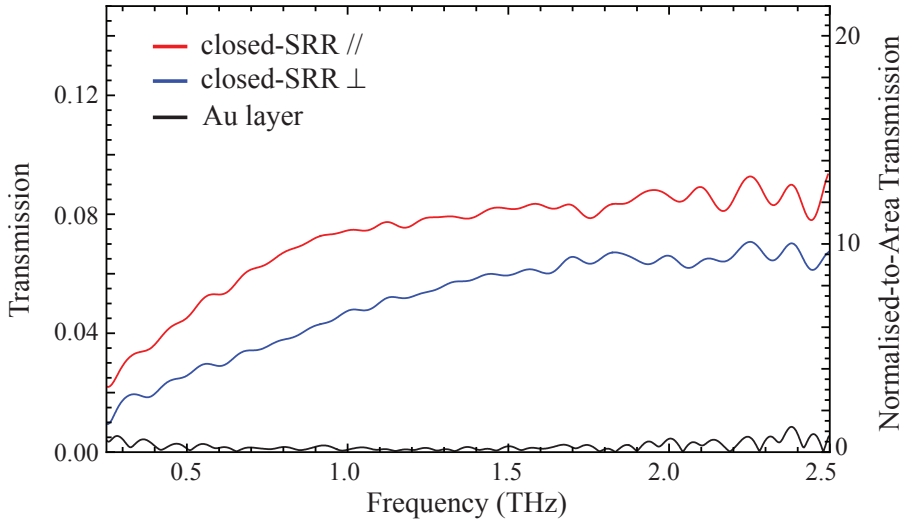

Figure 4.2 – Normalised transmission for the closed-SRR sample in the two polarisations.

smaller than the one through the closed-SRR area. We can thus look at the measured light as extra-ordinary optical transmission (EOT).

Extra-ordinary optical transmission was first reported by Ebbesen and coworkers in 1998[233], which showed EOT for an array of sub-wavelength holes in a metallic layer transmitting, at resonance, twice as much light as their area would allow them according to Bethe's theory[234]. This was explained with the coupling of light into surface plasmon modes that, thanks to their much tighter confinement, would propagate through the tiny holes and re-radiate on the other side of the screen.[235, 236] A big interest into plasmonics revived in the following decades, giving rise to both an experimental effort into mastering the phenomenon and a theoretical one for a deeper understanding.[237] More recently, also joining the research direction of transmission through narrow gaps, it was demonstrated that surface plasmons alone are not enough to explain the transmission but quasi-cylindrical waves are also needed for closely packed holes.[238]

In order to quantify the EOT for the investigated sample, the normalised transmission of the closed-SRR sample must be divided by the fraction of sample surface free from the metallic layer. The "free area" can be estimated by the product of the perimeter P of the SRR and the average distance s between the top and bottom layers due to imperfections and rough edges as seen from Fig. 4.1:

$$A_{free} = P \cdot s. \tag{4.1}$$

From the SEM pictures, one can estimate $s \simeq 50$ nm.

The fraction of "free area" can then be calculated by dividing A_{free} by the area of the unit cell: from Fig. 3.2 on page 83 the perimeter of the SRRs is $P = 332$ µm while the unit cell area is $A_{cell} = 50 \times 50$ µm^2, thus the free-area ratio is

$$A_n = \frac{A_{free}}{A_{cell}} \simeq 0.7\%. \tag{4.2}$$

Dividing the average transmission by A_n, one gets the following normalised-to-area EOT values for each of the two polarisations:

$$\frac{\langle t \rangle}{A_n} = \begin{cases} \frac{5.1\%}{0.7\%} \simeq 7 & \text{for } \langle T \rangle_\perp \\ \frac{7.3\%}{0.7\%} \simeq 10 & \text{for } \langle T \rangle_\parallel \end{cases} \tag{4.3}$$

These are of the order of 10, hence much greater than unity, showing that the sample displays extra-ordinary transmission.

Comparing the presented measurements with the EOT literature, one strong difference

is the absence of resonances.[237] This is the case in spite of the fact that the constituent elements are SRRs with specific resonant modes in this frequency range, as discussed in the previous chapter. In fact, one would expect such modes to be present in the spectrum, consistently with the basic interpretation of the EOT phenomenon: the THz radiation excites the subwavelength SRRs that re-radiate on the other side of the metallic plane. Instead a sizeable transmission is measured, about 30 times the one for a full continuous gold layer (black spectrum in Fig. 4.2) and, in particular, feature-less over the same range where the SRR would instead show three resonances (cf. Figs 3.3 and 3.6). This hints at the fact that a more complex explanation is needed to account for the whole behaviour of the closed-SRR sample.

As derived in section 3.4 on page 92, from the transmission spectrum it is possible

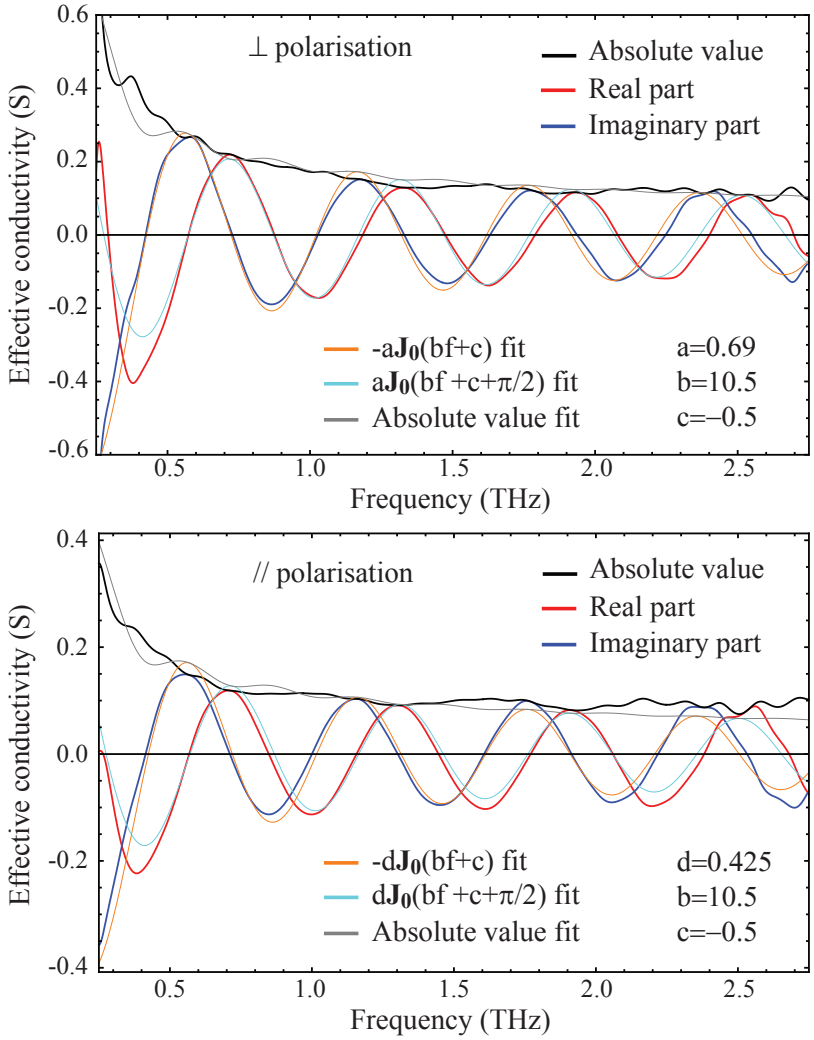

Figure 4.3 – Real and imaginary part of the effective conductivity of the closed-SRR sample, as derived from the transmission measurement and fits with the dephased Bessel functions.

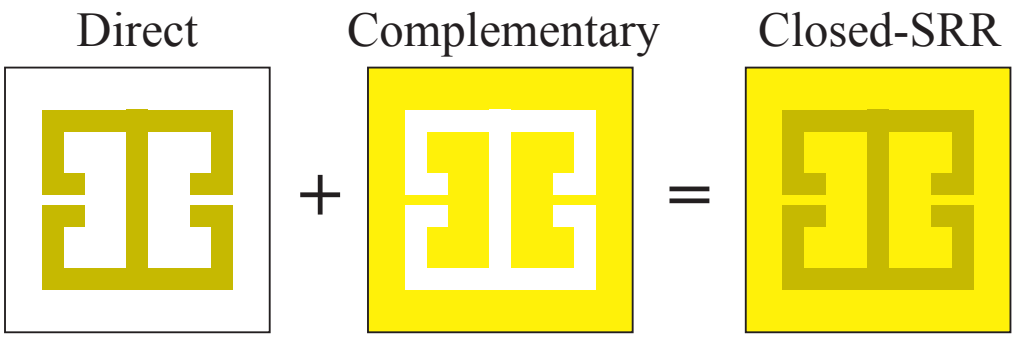

Figure 4.4 – Schematics of the composition of the closed-SRR unit cell.

to retrieve the effective conductivity of the measured sample, in the thin conductive film approximation. To this end, the complex transmission $t(\omega)$ in the parallel polarisation (obtained form the Fourier transform of the corresponding time-trace) was used to calculated the complex $\sigma_{eff}(\omega)$, making use of Eq. (3.15). The real and imaginary parts of σ_{eff}, along with it absolute value, are plotted as thick lines in Fig. 4.3.

It is interesting to note that the real and imaginary parts of the effective conductivity, giving rise to the flat transmission, are very similar oscillating functions and are dephased by $\pi/2$. Additionally, it is possible to fit the two curves with the zero-order Bessel functions $J_0(\omega)$: the thin lines superimposed to the data are obtained by fitting a rescaled Bessel function, namely $\pm aJ_0(b\omega + c)$, where a, b and c are fitting parameters. Interestingly, both real and imaginary part can be reproduced by the exact same function with a $\pi/2$-shifted argument, and just an overall rescaling (coefficient a is substituted by d) can account for the two different polarisations. The values of the coefficients are the following: $a = 0.69$, $b = 10.5$, $c = -0.5$ and $d = 0.425$.

At the point of writing, no theory was available for calculating the transmission and the conductivity of the investigated system, but we will point out that a zero-order Bessel function behaviour is also expected for the mutual inductance, and impedance, of a pair of very closed dipoles, as defined in Ref.s [239, 240] and calculated, e.g. for the conductance of coupled microstrip resonators, in Ref. [241]. Moreover, all display a $\pi/2$-shift between the real and imaginary part of the mutual impedance.[242]

In order to investigate further the phenomenon, we first conceptually decompose the closed-SRRs unit cell into its constituent structures as sketched in Fig. 4.4: the closed-SRR is the result of the overlapping of a direct SRR and a complementary SRR. In the next sections we present the measurements performed on a series of samples where the distance between the two constituting parts of the closed-SRR was varied in a control-

lable way. This gave information onto the interaction between the two parts at a highly subwavelength distance.

4.2 Tuning the near-field interaction

Further samples were produced, based on the same design as the closed-SRR sample. The first series consisting of three samples was realised in the same way as the closed-SRR ones, apart from the fact that in these the photoresist was not dissolved but it is still present in the sample, this resulting in a dielectric separation between the two layers. Within these samples, from now on called "spaced-SRR samples", the thickness of the photoresist was varied so to have the two layers at different distances but always within few micrometres, i.e. interacting in the near-field. A second series, instead, is produced by focussed-ion-beam (FIB) lithography by literally cutting the profile of the used THz-SRRs into a gold layer, thus called "FIBbed-SRR samples". We will see that these two kind of samples give the same results, the transmission spectra being spectrally identical.

4.2.1 Spaced THz-SRRs

The first series of samples is constituted by three samples produced in exactly the same way, only using photoresists with thicknesses of 340 nm, 1.06 µm and 1.63 µm. The precise values were determined with SEM pictures (courtesy of J. Keller) and the processing details can be found in appendix H.1 on page 269. It is clear that the two metasurfaces are spaced by a deeply subwavelength amount, namely $\lambda/1470$, $\lambda/472$ and $\lambda/307$, for a reference free-space wavelength of 500 µm. For comparison, the closed-SRR has a spacer equivalent to $10^{-4}\lambda$. An idea of the final structures can be gained from Fig. 4.5 where tilted SEM views of the samples are displayed.

The spectra obtained for the two orthogonal polarisations of each sample are presented in Fig. 4.6, the subsequent panels a), b) and c) displaying spaced-SRR samples with increasing spacing. For a general comparison, the spectra of the three spaced-SRR samples are compared within each other and with the ones for the closed-SRR sample, for each polarisation, in panels a) and b) of Fig. 4.7.

We start the discussion from the sample with the thickest spacer (panel c) in Fig. 4.6): its spectra in both polarisations show two resonant features, one at about 0.6 THz and one at about 1.5 THz. These are the frequencies where we would approximately expect the resonant features of the individual metasurfaces and present also a very similar shape: comparing with Fig. 3.6 on page 87, the LC-mode of the cSRR is at about 0.6 THz, while the $\lambda/2$-mode in the orthogonal polarisation is found at 1.25 THz. Note that the two

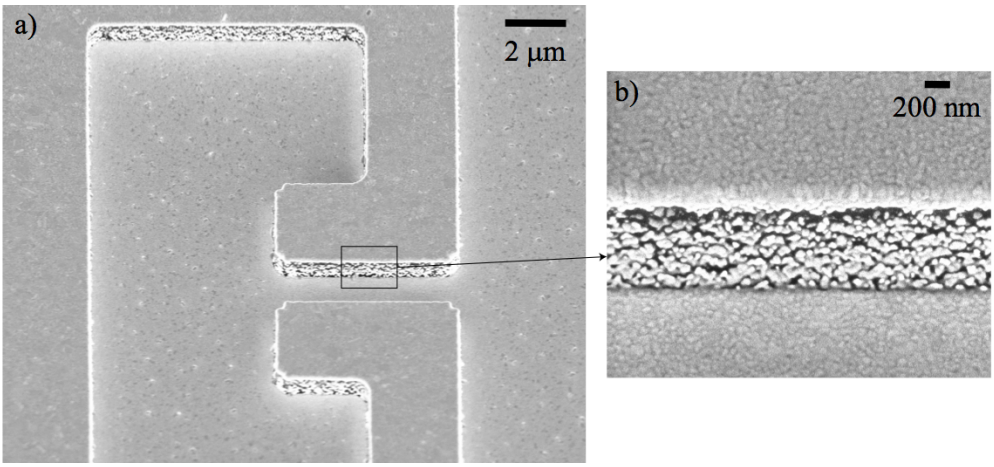

Figure 4.5 – SEM pictures of one of the spaced-SRR samples a) in a perspective overview and b) with a magnification of the side. Courtesy of J. Keller

samples were realised with the same substrate, hence its refractive index does not play a role in the frequency of the resonances. What then distinguish the spectra for the two polarisations is that at high frequencies the amplitude of one decreases while the other increases. This is also reminiscent of the the cSRR spectra for opposite polarisations.

This analysis highlights how the spaced-SRR sample response is connected to the one of the constituent cSRR, nonetheless showing in both polarisations features that were specific of only one of the two.

When considering the spaced-SRR sample with intermediate spacer thickness (panel b) in Fig. 4.6), the overall shape and the resonances present in the spectra are very close to the ones described above. The difference with the thickest spaced-SRR sample are found in the overall smaller transmission amplitude and in the small shift in frequency of all resonances. In particular, when comparing the *LC*-like peaks, their average amplitude decreases from 52% to 36% while the relative frequency-distance of each-other (frequency distance normalised to the average frequency) changes from 30% to 12.5%.

The decreased amplitude is probably the result of the thinner spacer, allowing less radiation to leak to the other side. The frequency distance of the two peaks can instead now be connected to the changed dielectric environment of the metasurfaces, probing different permittivities with changing resist thickness. This is a very large frequency shift for a resist-thickness change of about 570 nm, probed at a free-space wavelength of 500 µm. This point will be discussed further along to the FIBbed-SRR samples in the next section.

Moving to the thinnest spaced-SRR sample (panel a) in Fig. 4.6), the peaks disappeared leaving only a smooth spectrum with overall transmission amplitude and shape similar to the background of the previous ones.

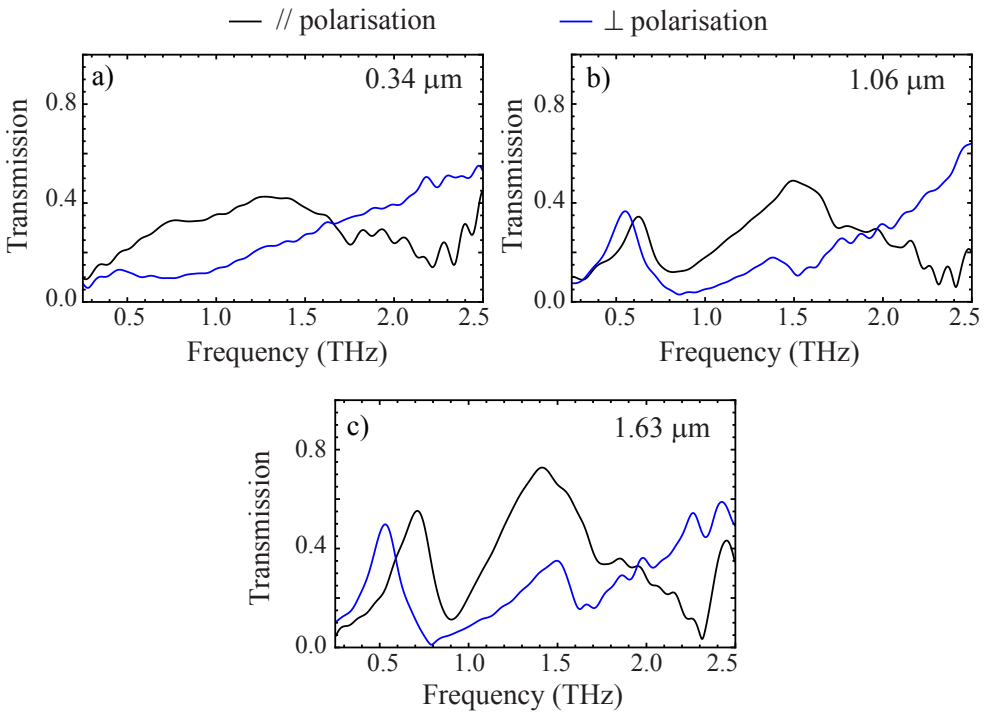

Figure 4.6 – Transmission spectra measured for the series of spaced-SRR samples in both polarisations. Each panel shows the spectra of a single sample: panel a) corresponds to a spacer thickness of 0.34 µm, panel b) to one of 1.06 µm and panel c) to one of 1.63 µm.

Now we can compare all measured samples: all spectra are collected in Fig. 4.7 according to the polarisation of the measurement.

Panels a) and b) show more precisely the relation between the spectra of the three samples of the spaced-SRR series, confirming the previous discussion. Comparing them to the spectra of the closed-SRR (in red), the latter are much weaker and flatter than the thinnest spaced-SRR (in black). Nonetheless, the closed-SRR sample is conceptually part of the series, in the direction of spacer reduction.

To support the measurements, the investigated structures were simulated with CST Microwave Studio and the spectra for two spacer thicknesses are presented in Fig. 4.8. The numerical calculation is able to reproduce all features in the spectrum of the thicker spaced-SRR, namely the tuning of the *LC*-like peak in the two polarisations and the position and shape of the additional peaks at higher frequencies as well as the overall background dependence (the spikes above 1.7 THz are artefacts and should be ignored).

The thinnest spacer allowed by the program was used to calculate the cyan and gray curves: these compare well with the closed-SRR traces in terms of the amplitude of the transmitted light, while, on the other hand, still showing faint resonant features in the low frequency range on a decreasing background, differently from what measured.

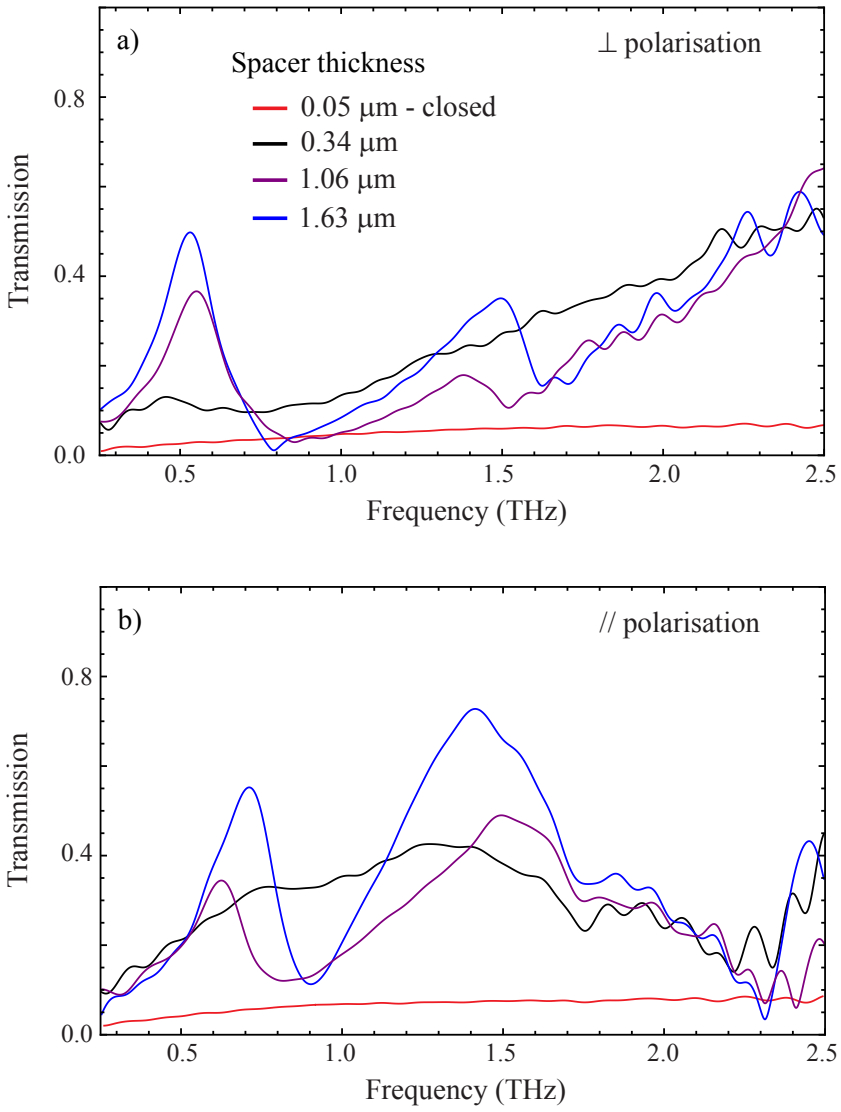

Figure 4.7 – Comparison of the transmission spectra of the closed-SRR and of the spaced-SRR samples, according to the two polarisations.

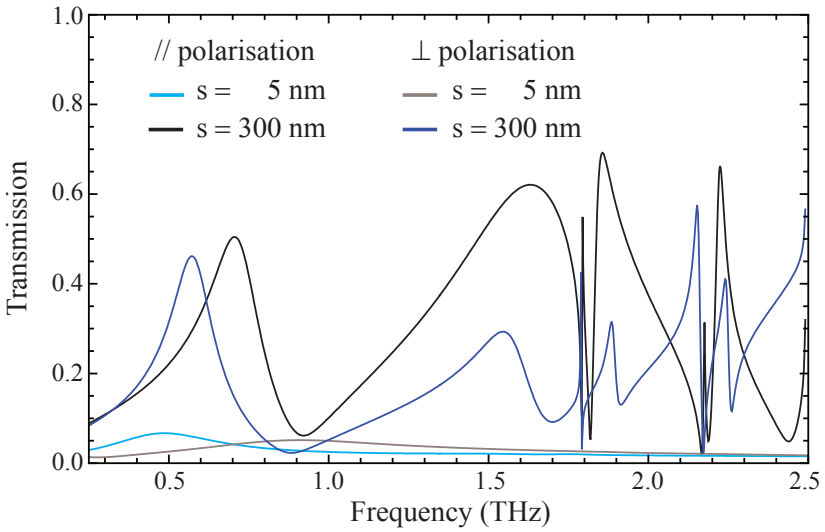

Figure 4.8 – FDTD-calculated spectra for spaced-SRR designs with different spacer thicknesses. Apart from some artefacts above 1.7 THz, the numerical spectrum shows similar features to the measured ones collected in Fig. 4.7.

Few caveat accompany the presented calculations. First, for computational time reasons, the structure is modelled as gold 2D-surfaces. Second, the spacer is then filled with vacuum because the refractive index of the used resists is not known at THz-frequencies. This hinders a direct comparison between the spacer thicknesses in the simulations and in the samples. Third, although the simulated spectra seem to reproduce well the amplitude of the transmission, the normalisation to the substrate is not included, as it is instead for the plotted measurements. Finally, from the SEM pictures of the closed-SRR sample most of the top metasurface seems to be into the gap of the other, probably touching the substrate. Unfortunately, this is a feature that cannot be implemented in the simulation, e.g. reducing further the spacer thickness, because of the already huge aspect ratio within the model (5 nm smallest features for a maximum wavelength of 1.2 mm).

In order to quantitatively compare the EOT properties of the samples, the transmission values at about 0.6 THz are plotted for all samples in Fig. 4.9, along with the calculated normalised-to-area EOT value t/A_n(cf. Eq. (4.2)). For the two thickest spaced-SRR samples the transmission amplitude of the *LC*-like peak was used, averaged among the two polarisations.

It is interesting to note that the transmission amplitude decreases almost linearly with spacer thickness and thus the EOT value increases accordingly. Moreover, in spite of the fact that all samples have highly subwavelength spacers (at least $\lambda/300$), features connected to the resonances of the individual metasurfaces disappear only for spacers of

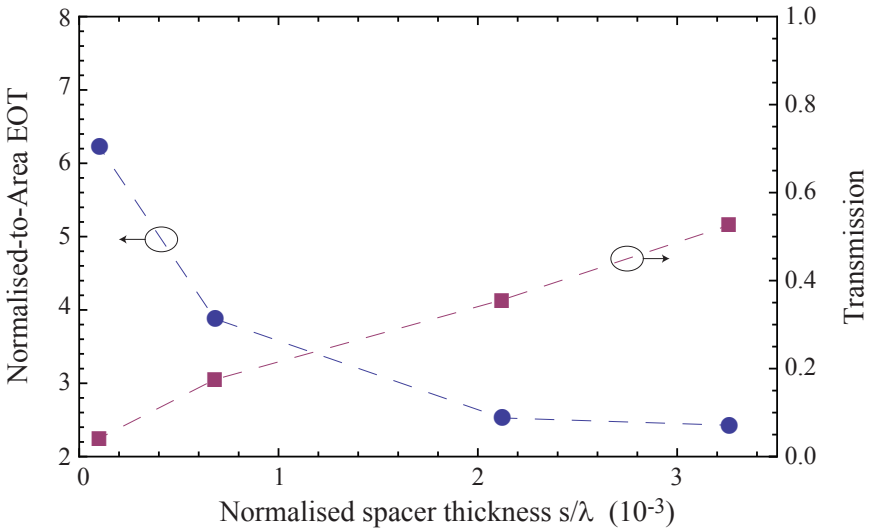

Figure 4.9 – Comparison of the normalised-to-area EOT values (left axis) and of the transmission values (right axis) of the closed-SRR and of the spaced-SRR samples for $f \simeq 0.6$ THz ($\lambda = 500$ µm).

340 nm or thinner.

4.2.2 FIBbed-SRR samples

A second series of samples was produced by focussed-ion-beam lithography[1]. This is a technique that accelerates Ga atoms, shooting them onto a target, resulting into the mechanical removal of the hit material. In such a way, the profile of the THz-SRRs was cut into a gold layer. Two samples were produced with different Ga-atoms beam waists onto the sample, resulting in different line widths of the milled structures. The first array was written with a line approx. 300 nm wide, the second being instead approx. 50 nm wide. Some SEM images of the samples can be seen in Fig. 4.10. In the pictures, the lightest tone of grey indicates the gold layer, the darkest the substrate, in this case low-doped Si.

The two FIBbed-SRR samples were then measured in transmission for the two polarisations and their spectra are collected in Fig. 4.11. By comparing the different spectra one can see that the relation between narrow and wide cut gaps is the same as the relation between thin and thick spacers in the spaced-SRR samples (cf. Fig. 4.7). In fact, the wide-gap sample shows multiple resonances similarly to the thick-spacer sample, while the narrow-gap sample shows no specific spectral feature but rather a uniform transmission, like the thin-spacer sample. Additionally, at the position of the main peaks, both thinnest spaced-SRR and narrow-FIBbed-SRR transmit about 3.5 times less than the

[1]The FIBbed-SRR samples were realised by M. Sueess. I am indebted to him for his skills with the machine in milling the samples and taking wonderful SEM pictures.

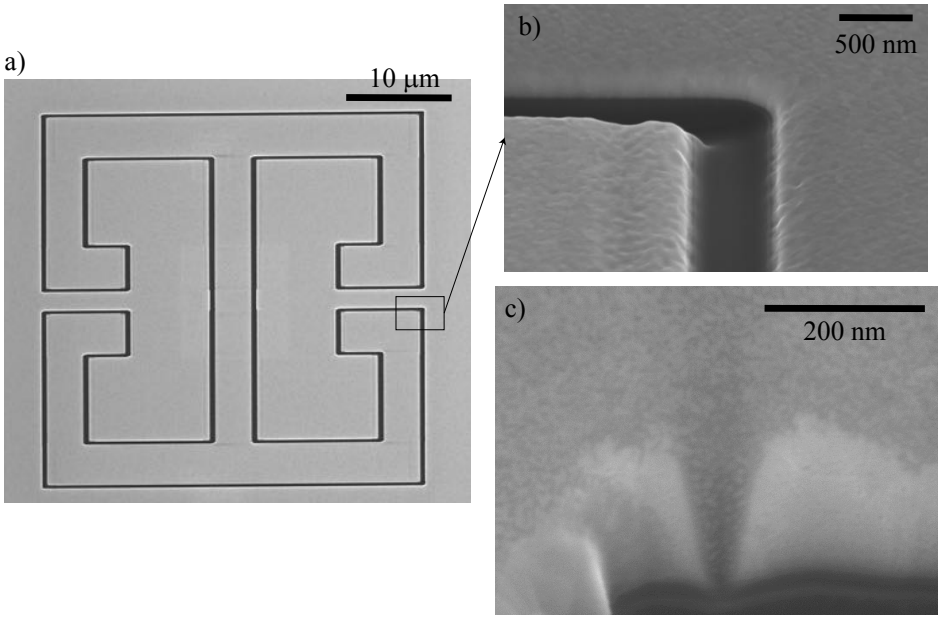

Figure 4.10 – SEM pictures of the FIBbed-SRR samples. a) Front view and b) detail of the wide FIBbed-SRR sample. c) Cross-section of the gap in the narrow FIBbed-SRR sample. Courtesy of M. J. Süess.

thickest spaced-SRR and the wide FIBbed-SRR. On the other hand the overall transmission amplitude is strongly reduced with respect to the spaced-SRR samples, at some frequencies almost by an order of magnitude.

One notable feature, shown in the enlarged inset of panel a), is that for the FIBbed-SRR, the frequency of the *LC*-like modes in the two polarisations is practically the same, contrary to what happens for the spaced-SRR samples. The normalised frequency distance amounts in fact to 3.5% of the average frequency. Following the previous line of discussion, this is due to the fact that the two metasurfaces share the same dielectric environment: here both metasurfaces are placed between air on one side and the substrate on the other.

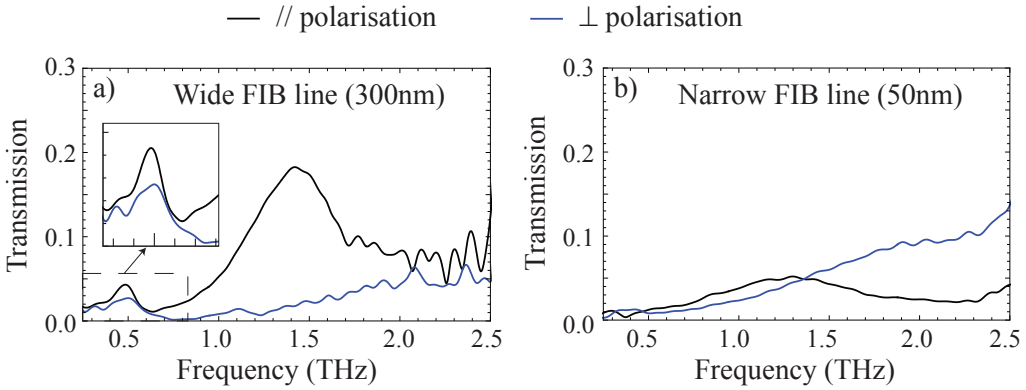

Figure 4.11 – Normalised transmission spectra of a) wide and b) narrow FIBbed-SRR samples.

Instead, in the spaced-SRR samples, the top metasurface is sandwiched between air and the resist while the bottom one is sandwiched between the resist and the substrate.

4.3 Ruling out far-field interactions

After all previous measurements and discussions, it seems clear that the measured transmission is not a far-field phenomenon. Given the geometry of the samples, we have the possibility to directly test this hypothesis. Considering again Fig. 4.4, we can use the reference dSRR and cSRR samples to directly test if their combined transmission matches that of the closed-SRR. Expressed in transmission coefficients, the equality to be investigated reads:

$$t^{subst}_{\text{closed-SRR}}\, t^{\text{closed-SRR}}_{air} \stackrel{?}{=} t^{subst}_{\text{cSRR}}\, t^{\text{cSRR}}_{\text{dSRR}}\, t^{\text{dSRR}}_{air}, \tag{4.4}$$

with t^j_i indicating the transmission at the interface from medium i to medium j. The phase change has been neglected assuming an infinitely thin SRR (double) layer that would not introduce phase changes during propagation.

To this end, the dSRR sample was placed on top of the cSRR sample, with the metasurfaces facing each other as in the previously mentioned sketch, at a distance that could be estimated to be of the order of 100 µm (thin plastic tape). The transmission was measured in the parallel polarisation and the spectrum is shown in red in panel a) of Fig. 4.12. It is consistent with the spectrum in black, resulting from the product of the transmission through the individual samples measured in the same polarisation (reported in panel b) of the same figure).

Comparing the spectrum of the stacked metasurfaces to the ones of the thickest spaced-

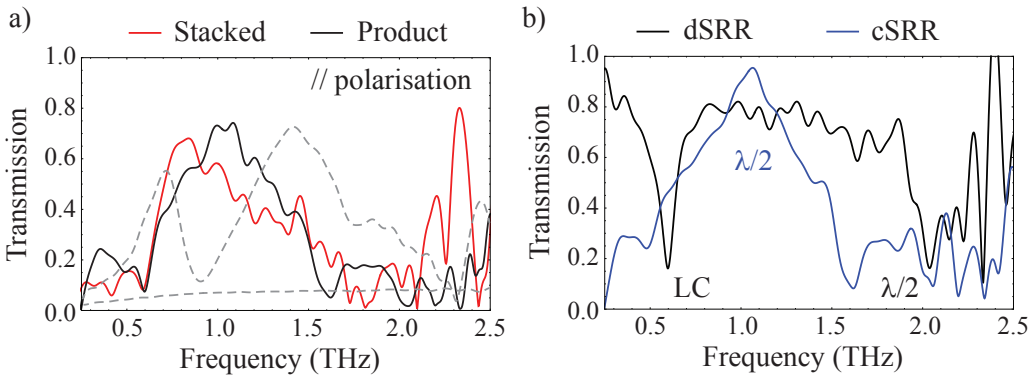

Figure 4.12 – a) Comparison of the transmission spectra of the stacked dSRR-cSRR with the product of the single ones, for the parallel polarisation. The single metasurface spectra are reported in b). For additional comparison, the corresponding transmission of the thickest spaced-SRR and of the closed-SRR samples are reported in a) as dashed gray lines.

SRR and of the closed-SRR samples, reported in panel a) as dashed gray lines, we can definitively exclude any relation among them. We therefore conclude that the transmission of the samples measured in the previous sections is governed by near-field interactions.

4.4 Polarisation response of the samples

In order to gain more information on the samples, the transmission was measured for the cSRR, for the spaced-SRR and for the closed-SRR samples, rotating the sample within its plane. In this way, we vary the angle between the polarisation of the incident electric field and the SRRs in the samples. This is particularly useful, having in mind the representation of the sample as (electric) dipoles.

The measurements are displayed in Fig. 4.13 for the cSRR sample and the spaced-SRR one, respectively in panel a) and b), and in Fig. 4.14 for the closed-SRR samples.

The sample-rotation measurements performed on the cSRR sample, in panel a) of Fig. 4.13, highlight the different symmetries and Q-factors of the three modes. The LC-mode gives rise to the oblated shape at about 0.5 THz, very narrow in frequency but quite extended in angle. This is typical of a well defined electric dipole to which the incident radiation couples as long as a component of the electric field is aligned to it. The other two dipolar modes are instead quite broad and round in the (f, α) plane, showing that, due to the approx squared shape of the SRR, a wide angle range is able to couple to the extended dipolar modes and the electric dipole for this modes is not as well defined as for the LC-one, as expected.

The sample-rotation measurements performed on the thickest spaced-SRR sample (in panel b) of Fig. 4.13) show two narrow oblate features for 0° and 90°. These are placed at close frequencies and at 45° merge, as better seen in the transmission spectra: these are the two LC-like peaks. The other peaks behave instead as $\lambda/2$ resonances.

The angular dependence of the LC-like peaks suggests that two electric dipoles are present in this sample, orthogonally placed with respect to each other.

Finally, the series of measurements of the closed-SRR starts with the source polarisation aligned across the dSRR gaps and ends orthogonally to it in steps of 15°.

Upon rotation, one can see that, apart from a small reduction of the overall transmission, the spectrum does not change and still shows no resonant features. This means that the illuminating radiation can couple with the same strength to the dipoles in the sample, no matter what is their relative orientation. Since the source is linearly polarised, this pattern suggests that the sample behaves similarly to a circularly polarised object. Nonetheless, cross-polarised measurements of the sample (cf. Fig. C.2 on page 242) show

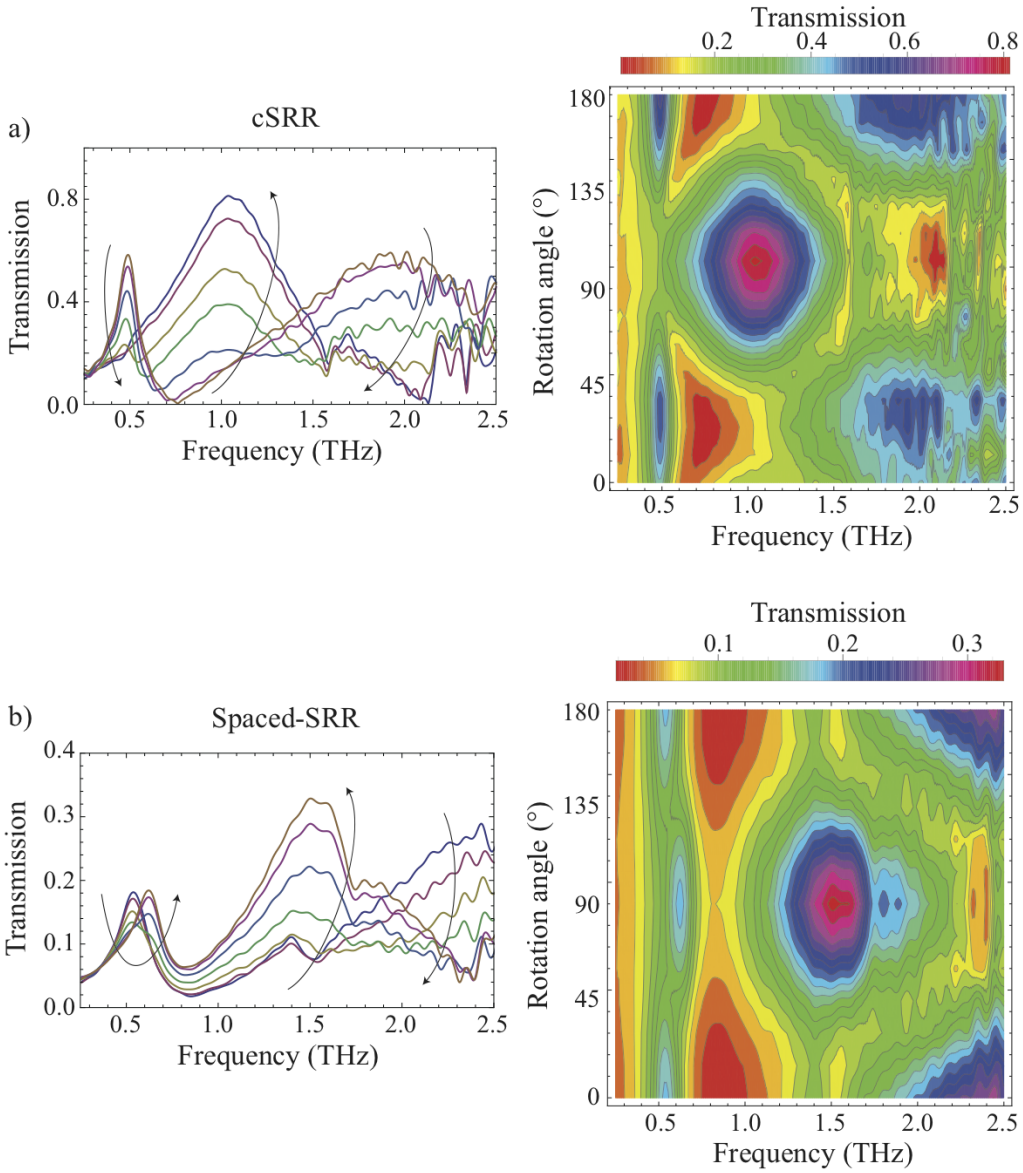

Figure 4.13 – Transmission spectra and contour plots for a) the cSRR-sample and b) the thickest spaced-SRR sample, taken at subsequent rotational steps of the sample with respect to the polarisation of the incident light.

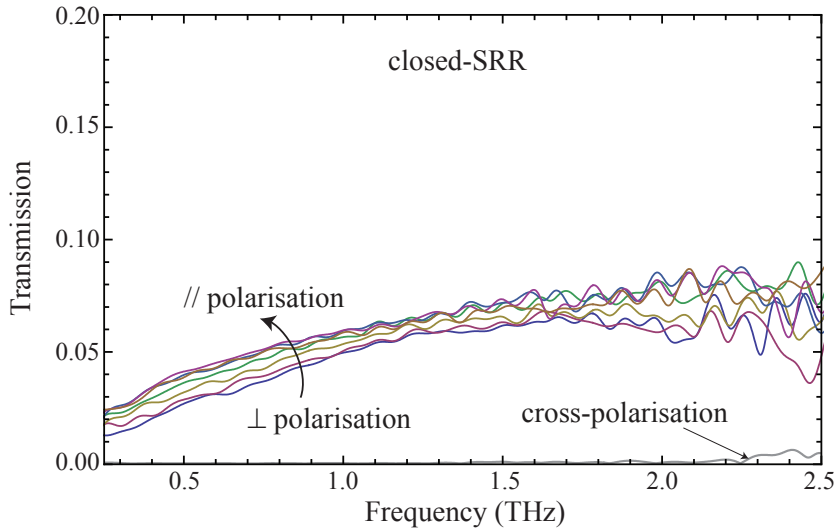

Figure 4.14 – Transmission spectra for the closed-SRR-sample taken at subsequent rotational steps of the sample with respect to the polarisation of the incident light. The crossed-polarisation transmission spectrum is also plotted in gray.

that the after transmission through the sample, no electric field component orthogonal to the incident one is present, in contrast to standard circularly polarised objects.

The comparison gets clearer in the polar plots in the top row of Fig. 4.15 where the average normalised transmission amplitude of the closed-SRR sample is compared to the one for the *LC*-mode of the other two samples. The polar plots of the expected angle-dependence of the field-sample couplings are plotted for comparison in the lower row.

As expected, the *LC*-mode of the cSRR has a shape typical of dipole coupling, with maximum amplitude when field and dipole are aligned and zero when they are orthogonal, hence behaving in a $\cos\theta$ fashion.

The polar plot of the transmitted amplitude for the spaced-SRR sample shows four identical lobes at $\pi/2$ from each other. This shape can be reproduced by the coupling pattern of two orthogonal dipoles, hence by the function $\cos\theta + \sin\theta$, as shown in the second row. For this shape to match the experimental one, a rotation by 45° is needed, indicating a dephasing of the two dipoles, either in time or in real space. This configuration corresponds to a turn stile antenna, investigated and used in electrical engineering for omnidirectional antenna capable of circularly polarised radiation.[242].

When coming to the closed-SRR transmission pattern, the polar plot is quite different from the previous ones and tends to a circular shape. A circularly polarised object can be represented by as a pair of 90° dephased dipoles, thus coupling to a linear polarisation as $\cos\theta + i\sin\theta$ and resulting in a circular pattern.

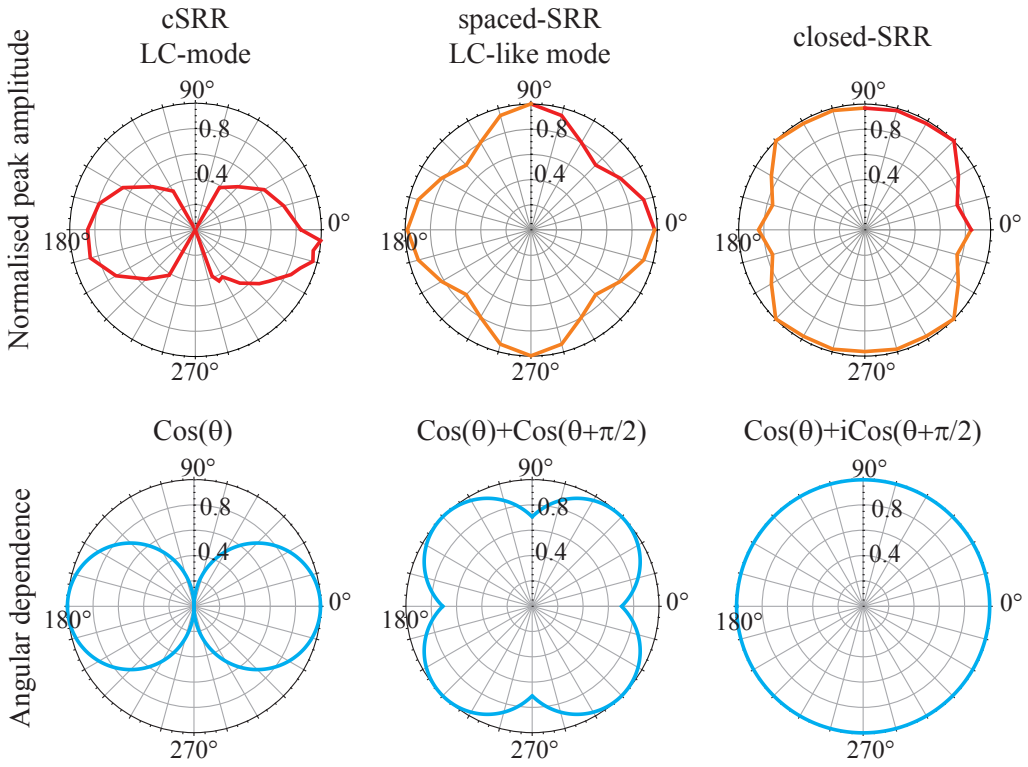

Figure 4.15 – Polar plots of the normalised peak amplitude of the *LC*-peak of the cSRR, of the *LC*-like peak of the thickest spaced-SRR and of the average transmission of the closed-SRR sample. These are compared to the coupling functions for single dipole, crossed equal dipoles and crossed dual dipoles.

4.5 Duality vs complementarity

When considering the non-resonant frequency response of the closed-SRR sample in spite of being constituted by two resonant structures, the one complementary of the other, one naturally thinks of self-complementary antennas.[243] Self-complementary antennas are constituted by a resonant structure that is its own complementary, and posses the nice property of having a flat constant impedance, whose value depends on the specific excitation arrangement.[244, 245] The best example of such class are maybe bow-tie and spiral antennas.[246]

From the point of view of antennas and impedance matching, it was experimentally found and later demonstrated that the impedances of two complementary objects are related. The impedance of a direct antenna Z_d and the one of its complementary Z_c are connected by[243, 246]

$$Z_d Z_c = \left(\frac{Z_0}{2}\right)^2, \tag{4.5}$$

where $Z_0 = \sqrt{\frac{\mu_0}{\epsilon_0}} = 377\ \Omega$ is the vacuum impedance. This assumes also that the antennas

are made of perfect conductors and that the voltage/current feedings are complementary to each-other.

For self-complementary structures then it holds $Z_d = Z_c \equiv Z_{self}$. Substitution into the previous equation gives

$$Z_{self} = \frac{Z_0}{2}, \tag{4.6}$$

revealing constant impedance, over the bandwidth for which the small electrical antenna approximation holds.[243] This is called Mushiake's relation, from the researcher that demonstrated it formally.

When attentively considering the closed-SRRs, in spite of the fact that they are constituted by a direct SRR and its complementary cSRR, they are not self complementary. In fact, the complementary of the closed-SRR structure would be a very narrow wire, shaped as the edges of the SRRs. We need then to consider with more attention the parts of the closed-SRR in Fig. 4.4 and the discussion on complementarity in section 3.2 on page 86. What differentiates the two is the fact that, although the screens are complementary to each other, the irradiating sources are not: for the complementary response the sources need to be rotated (hence complemented) as well, while the measurements on the closed-SRR sample probes both metasurfaces with the same polarisation.

The transformation performed on the single entities (screens, fields) is called *duality* and its action on the electromagnetic fields in free space can be determined by[247, 224]

$$\begin{pmatrix} \mathbf{E}_d \\ Z\mathbf{H}_d \end{pmatrix} = \begin{pmatrix} \cos\theta & -\sin\theta \\ \sin\theta & \cos\theta \end{pmatrix} \begin{pmatrix} \mathbf{E} \\ Z\mathbf{H} \end{pmatrix}. \tag{4.7}$$

Such transformation is a rotation by an angle θ. Maxwell's equations are invariant under such transformation when written in their generalised form, i.e. including (fictitious) magnetic charges and currents.[224] This system of equations reconciles with the complementarity relations of section 3.2 on page 86 upon setting $\theta = -90°$ and recalling that $c\mathbf{B} = Z\mathbf{H}$ and we can define the matrix performing a dual transformation as

$$D = R_{-\pi/2} = \begin{pmatrix} 0 & 1 \\ -1 & 0 \end{pmatrix}. \tag{4.8}$$

The result of the duality transformation onto the different entities we are considering is illustrated in Fig. 4.16; one should keep in mind that only the duality of both fields and sources determines complementarity.

If we then start from the direct SRR and associate to it an electric dipole, the duality

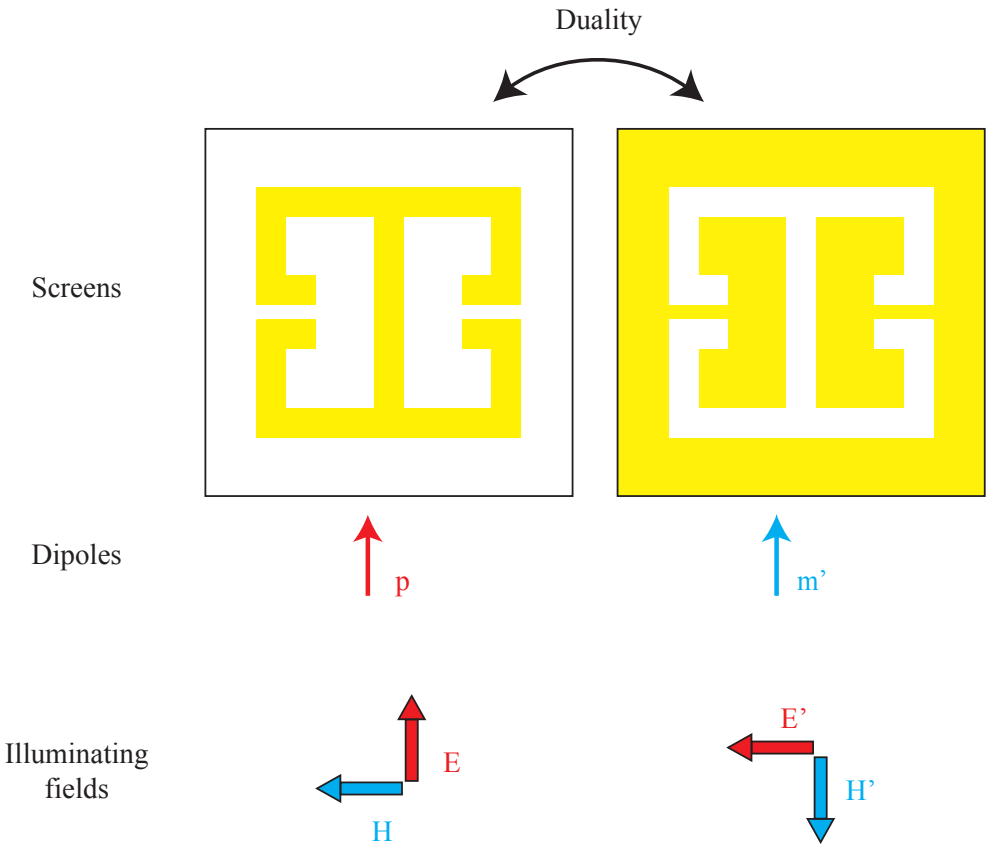

Figure 4.16 – Examples of screens, dipoles and propagating plane wave fields connected by the duality relation.

transformations tell us that we should associate a magnetic dipole to the complementary SRR. This was the conclusion also of Bethe, when considering the radiation scattered by a circular hole in a perfectly conducting plane.[234, 248] For more details onto the duality transformation and its effect on dipoles, see appendix C on page 239.

4.6 Electro-magnetic dipoles

According to the previous discussion, we can then schematise the closed-SRR sample as a pair of electro-magnetic dipoles, the one dual of the other. Conceptually similar structures have already been investigated and used in electrical engineering to achieve unidirectional broadband antennas. Several reports made use of a dipolar antenna overlapping with a slot antenna to achieve a so-called cardioid emission pattern with large bandwidth.[249, 250, 251, 252, 253, 254, 255]

The intuitive explanation of this behaviour, given in the cited literature, is that the

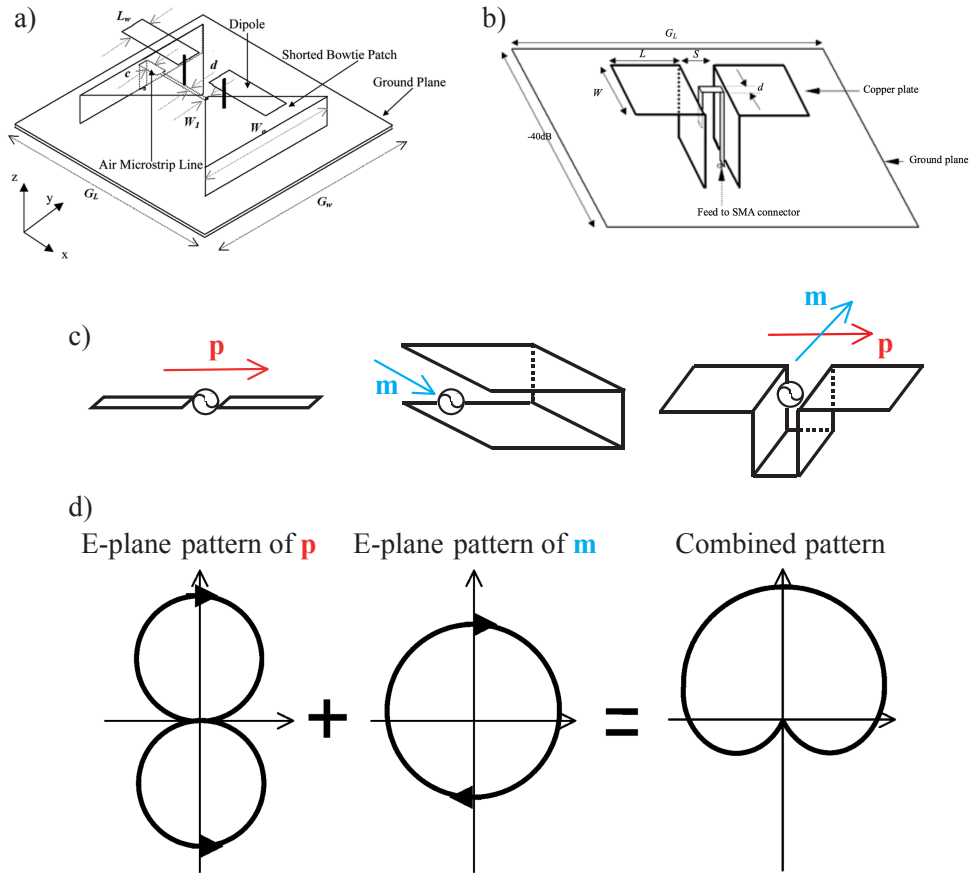

Figure 4.17 – Examples of crossed-dipole based transmitters from the literature. a-b) Each transmitter is constituted by an electric dipole and an equivalent slot antenna, hence c) they can be equivalently considered as crossed electro-magnetic dipole. d) They emit broadband radiation in a single half-space Adapted from Refs [255, 253].

electric-field radiation pattern of the electric dipole (two lobes in the plane orthogonal to the dipole direction) and the one of the slot antenna (circles around the long axis of the slot) cancel in one half-space while sum in the other. Such structure is schematised by an electric dipole crossed to a magnetic dipole and it is sometimes referred to as "Huygens' surface".[256, 257, 258]

Considering the closed-SRR and its constituent from the mentioned point of view, it is clear that an electric dipole can be associated to the dSRR, oriented across the gaps. Less clear is how to orient the magnetic dipole that should be connected to the cSRR and what is its phase relation to the previous one. In recent years several investigations gave a more complete picture of the dipoles that can be induced in a single slot, showing that magnetic and electric dipoles coexist and can participate to the emitted radiation.[259, 260, 261, 262] This is true also for split-ring resonators.[263, 264] Moreover, studies of dielectric resonating particles possessing both an electric and a magnetic dipole were also performed and displayed high broadband transmission and the possibility of controlling the phase of the transmitted light.[265, 266] These results provide a rather complex picture and, despite believing that this is the right direction for the interpretation of the measured phenomenon, a bigger theoretical effort is needed to model the structure and provide a counterpart to which compare the measurements.

4.7 Conclusion and Outlook

The closed-SRR sample shows a very peculiar behaviour: despite being constituted by two dual metasurfaces that leave almost no free area on the sample surface, a sizeable flat transmission was measured. This phenomenon was discussed in the frame of extraordinary optical transmission, showing relatively high normalised-to-area EOT values up to 10.

We fabricated additional samples where we controllably vary the distance between the metasurfaces at a highly subwavelength scale ($\simeq \lambda/300 - \lambda/1500$) and we showed that the measured behaviour cannot be accounted for by far-field interaction of the two metasurfaces. Nonetheless, in spite of the highly subwavelength spacing, resonant features associated to the far-field response of the independent dSRRs and cSRRs are present in the spectra of samples with spacing larger than $\lambda/500$.

Our measurement have aspects in common with three different phenomena, namely, extra-ordinary transmission, self-complementary antennas and crossed electromagnetic dipoles (Huygens surfaces). Nonetheless, none of the theories underlying the previous phenomena can be directly applied to the present investigation. In fact, first, the EOT transmission we measured is not resonant with a plasmonic mode, second, the comple-

mentary structure of the closed-SRR is not the structure itself and, third, it is not clear which dipoles can represent the sample and how they are oriented with respect to each other.

Part III

Coupling of Terahertz Metamaterials to 2DES for studying the USC regime

Chapter 5

Graphene: a particular two-dimensional electron system

Two-dimensional electron systems (2DESs) are mesoscopic systems that can be theoretically treated as a plane of free electrons. The term is meant as a broader class than the one of 2-D Electron Gases (2DEGs). The first such structures were identified in the 1960s at the interface between silicon and its oxide in MOSFET structures[267] and they immediately attracted interest for the high mobility of the carriers therein.[45] Since then, accumulation and depletion layers have been studied extensively, used in a large amount of devices and realised in several different systems. The term 2DEGs came then to mean the electron gases realised into solid state systems at the interface between two semiconductors, or two oxides or a semiconductor and an oxide.[35] Nonetheless, 2DESs were also found quite soon above the surface of liquid helium[268] and, more recently, in 2D monolayer-systems like graphene[269] or transition-metal-dichalcogenides[270]. The term 2DES encompasses this whole group of systems.

This chapter presents both a theoretical and experimental introduction on graphene, that in a decade became one of the most studied solid state systems.[271, 272]

5.1 Theoretical basics

Graphene, a single-layer of hexagonally arranged carbon atoms[269], is one of the most studied electronic systems since 2004 because of its high charge carrier mobility, up to 2.3×10^5 cm^2/Vs at room temperature at $n_s \simeq 10^{12}$ cm^{-2}[273] and 10^7 cm^2/Vs at $T = 25$ K[274]. It can be regarded as the first truly bi-dimensional material, since its transverse dimension was measured to be 0.33 nm, such being the extension of its out-of-plane molecular p_z-orbitals. Additionally, it behaves as a 2DEG displaying the quantum

Hall effect.[275, 276]

Few-layers and monolayer graphene were first reported by German chemists in 1948[277] and in 1962 [278], while its band structure had already been calculated in 1947 within the efforts for understanding graphitic materials[279]. Each carbon atom belonging to the honeycomb lattice is covalently bonded to three neighbours via the s- and p_x, p_y-orbitals forming high-energy σ bands. The p_z-orbitals instead are oriented orthogonally to the plane and form the π-bands which control the electronic properties of graphene. The energy dispersion of these π-bands, which form the conduction and valence bands of graphene, was derived to be, in the tight-banding approach and assuming only nearest-neighbour interaction with energy $\gamma_0 = 3.2$ eV,

$$E_{CB,VB}(\boldsymbol{k}) = \pm\gamma_0\sqrt{1 + 4\cos\left(\frac{k_x a}{2}\right)\cos\left(\frac{k_y a\sqrt{3}}{2}\right) + 4\cos^2\left(\frac{k_x a}{2}\right)}, \tag{5.1}$$

where $a = 2.46$ Å is the lattice constant, a factor $\sqrt{3}$ bigger than the nearest-neighbour distance. The resulting band structure can be seen in Fig. 5.1: at Γ there is an energy gap of about 20 eV while the bands touch in six non-equivalent points making graphene a zero-gap semiconductor. These points, often called *charge-neutrality points* (CNPs), are subdivided into two groups related to each of the two identical atoms constituting the lattice basis and are labelled K and K'. Such degeneracy can be useful for investigating many-body and topological phenomena and can be treated from the quantum mechanical point of view as a pseudo-spin degree of freedom.[280, 281]

A very peculiar feature is that, close to the K- and K'-points, where the bands touch, the dispersion has a linear behaviour[279]

$$E_{CB,VB}(\boldsymbol{k'}) = \pm\hbar v_F|\boldsymbol{k'}| \tag{5.2}$$

where the wavevector $\boldsymbol{k'}$ is defined with respect to the K-points and the proportionality constant depends on the Fermi velocity $v_F = \frac{a\gamma_0\sqrt{3}}{2\hbar} \simeq 10^6$ m/s (cf. Fig. 5.1).

It was realised that the physics in the linear-band regime can actually be described by the Weyl Hamiltonian for relativistic massless particles (originally, neutrinos), derived from the Dirac equation in the limit of vanishing mass,[282]

$$\hat{H}_{Weyl} = \hbar v_F \begin{pmatrix} 0 & \hat{k}'_x - i\hat{k}'_y \\ \hat{k}'_x + i\hat{k}'_y & 0 \end{pmatrix} = v_F \hat{\boldsymbol{\sigma}} \cdot \hat{\boldsymbol{p}} \tag{5.3}$$

where $\hat{\boldsymbol{\sigma}} = (\hat{\sigma}_x, \hat{\sigma}_y)$ is the Pauli-matrix vector in the plane and corresponds to the pseudo-

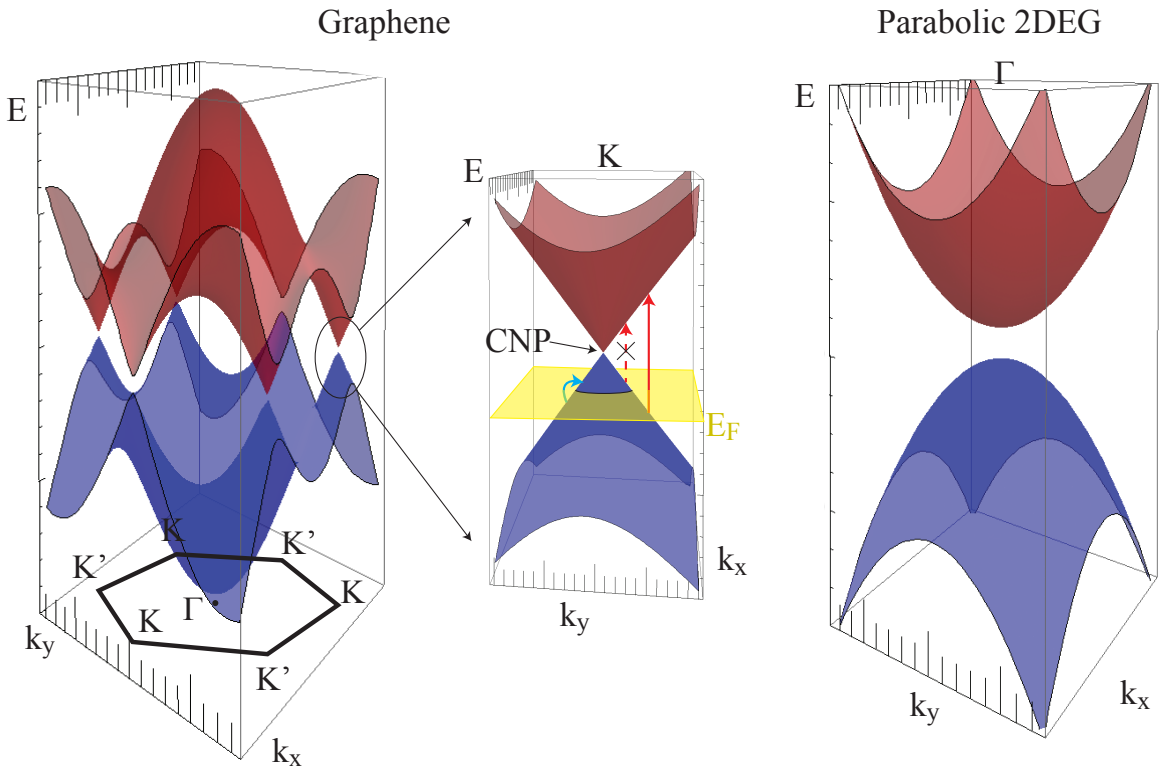

Figure 5.1 – Comparison of the band structure of graphene (left) and of a parabolic semiconductor (right). The valence bands are in blue and the conduction bands in red. The close-up to one of graphene's cones (centre) shows the linear dispersion, the always-allowed intraband transition (cyan arrow) and the interband transitions (red arrows) with a cutoff of $2E_F$.

spin connected to the degenerate K-, K'- points. In the same way as for ordinary spins, the concept of *chirality* can be introduced with all connected topological consequences. Since these are outside the scope of this thesis, the interested reader is referred to Ref.s [283, 284] and references therein for more information on this regard.

Because of such description, the CNPs are often also termed *Dirac points* and the bands themselves *Dirac cones*. A further direct consequence of such description is that, at the CNP, graphene holds $m^* = 0$[285], since

$$m^* = \frac{E_F}{v_F^2} = \frac{\hbar}{v_F}\sqrt{\pi n_s}, \tag{5.4}$$

being n_s the sheet carrier density and $E_F = \hbar v_F \sqrt{\pi n_s}$ the Fermi energy.[1] Therefore

[1]This is in contrast with what one would derive substituting a linear k-dependence in the usual formula with the second-order k-derivative for the effective mass: this would give a diverging effective

graphene carriers close to the CNP behave as massless relativistic particles and allow the study of interesting phenomena in solid state systems.

From the point of view of devices, the absence of a gap between conduction and valence bands has huge drawbacks and hinders the direct transposition of most electronics/photonics schemes from more ordinary semiconductors to graphene-based architectures. For that purpose, soon after its discovery, researchers found ways to create or induce a gap either by etching nanoribbons[286, 287, 288], or stacking two layers[289, 290] or using the selective influence of the boron-nitride substrate[291]. In general a gap of up to 250 meV (60 THz) can be opened, therefore covering the whole THz-range and most of the MIR-one. In principle photonics devices in these frequency-ranges could be realised. The practical issue lays in the difficulty of achieving a homogeneous gap over dimensions comparable with the radiation wavelength, especially towards the THz-range. In fact the gap is very sensitive to any kind of unintentional doping (processing residuals, adsorbed molecules), to substrate morphology, to lattice imperfections, etc., that strongly reduce its actual size, eventually closing it.[292]

5.2 Electro-optical properties of graphene with and without magnetic field

Due to its peculiar, conical dispersion relation, graphene can sustain both intraband and interband optical transitions $\sigma(\omega) = \sigma_{intra}(\omega) + \sigma_{inter}(\omega)$ in the same frequency-range, provided the Fermi level is suitably set. As sketched in Fig. 5.1, intraband transitions (cyan arrow) that connect two states within the same band are always possible for small photon energies (excluding the singularity at $E_F = 0$ eV) while interband transitions (red arrows) that transfer electrons from the valence band to the conduction band are possible only for photon energy above twice the Fermi energy, $E_{phot} > 2E_F$.

The magneto-optical AC-conductivity tensor of graphene can be calculated from the Kubo formula[293, 294]

$$\sigma_{ij}(\omega) = \frac{\Pi^R_{ij}(\omega + i0)}{i\omega}, \tag{5.5}$$

where $\Pi^R_{ij}(\omega)$ is the retarded current-current correlation function.

The tensor elements were calculated for the spectrum of graphene's Landau levels and,

mass. The apparent contradiction comes from the fact that the latter formula is derived *assuming* a parabolic dispersion.

in the limit of small magnetic fields $B \to 0$ and negligible excitonic energy, they are[293]

$$\sigma_{xx}(\omega) = -\frac{2ie^2(\omega + i/\tau)}{h}\left[\frac{1}{(\omega + i/\tau)^2}\int_0^\infty d\omega\,\omega\left(\frac{\partial f_{FD}(\omega)}{\partial\omega} - \frac{\partial f_{FD}(-\omega)}{\partial\omega}\right) - \int_0^\infty d\omega \frac{f_{FD}(-\omega) - f_{FD}(\omega)}{(\omega + i/\tau)^2 - 4\omega^2}\right] \tag{5.6}$$

and

$$\sigma_{xy}(\omega) = \frac{e^3 v_F^2 B}{\pi c}\int_0^\infty d\omega\left(\frac{\partial f_{FD}(\omega)}{\partial\omega} + \frac{\partial f_{FD}(-\omega)}{\partial\omega}\right) \times \left[\frac{1}{4\omega^2 - (\omega + i/\tau)^2} - \frac{1}{(\omega + i/\tau)^2}\right], \tag{5.7}$$

where τ indicates the carrier scattering time, $f_{FD}(\omega) = \left(e^{(\hbar\omega - E_F)/K_BT} + 1\right)^{-1}$ the Fermi-Dirac distribution, k_BT the thermal energy and E_F the energy of the Fermi level. The term with the first integral in Eq. (5.6) represents the intraband conductivity, while the second one represents the interband conductivity.

In the limit $B = 0$ T, $T = 0$ K and $E_F = 0$ meV, the intraband conductivity can be written as[294]

$$\sigma_{intra}(\omega, E_F, \tau, T) = -i\frac{e^2 k_B T}{\pi\hbar^2(\omega - i/\tau)}\left(\frac{E_F}{k_BT} + 2\ln\left[\exp\left(-E_F/k_BT\right) + 1\right]\right). \tag{5.8}$$

The first term of Eq. (5.8) represents the Drude-like conductivity, the second one accounting for the non-zero conductivity at the CNP. It has to be noted that the real part of the conductivity, responsible for the absorption, is positive.

The interband conductivity, instead, can be evaluated analytically, in the approximation of high Fermi energy with respect to the thermal energy ($E_F \gg k_BT$ or $T = 0$ K), as[294]

$$\sigma_{inter}(\omega, E_F, \tau, 0) = \frac{-ie^2}{4\pi\hbar}\ln\left(\frac{2E_F - \hbar(\omega - 2i/\tau)}{2E_F + \hbar(\omega - 2i/\tau)}\right). \tag{5.9}$$

For long carrier lifetime ($1/\tau \to 0$), the energy cut-off appears, the real part of the conductivity being non-zero and constant $\mathrm{Re}[\sigma_{inter}] = \frac{\pi e^2}{2h}$ for $E_{phot} > 2E_F$. This results in a frequency-independent absorption quantum $A_q = \pi\alpha \simeq 2.3\%$, where α is the fine structure constant: the calculation was confirmed by experiments.[295, 296] This behaviour is similar to more ordinary 2DEGs, for which the general formula includes a correction factor coming from the not-unitary refractive indexes of the surrounding materials: $A_q = \pi\alpha/n_c^2$ with $n_c = (n_1 + n_2)/2$.[297] For a free-standing 2DEG, as graphene can be, $n_c = 1$.

For moderate magnetic fields B, perpendicular to the graphene layer, the diagonal elements of the conductivity tensor can be simplified into the semi-classical formula[298, 299]

$$\sigma_{\pm}(\omega, B) = \sigma_{DC} \frac{i\Gamma}{\omega \pm \omega_{cyc} + i\Gamma}, \tag{5.10}$$

where σ_{DC} is the zero-field DC-conductivity, $\Gamma = 1/\tau$ the scattering rate, ω_{cyc} the graphene's cyclotron angular frequency that provides the B-dependence and the sign refers to the handedness of the radiation.

The zero-field DC-conductivity σ_{DC} can be derived from the previous σ_{ω}, given by Eqs (5.8)-(5.9), and in the limit of $k_B T \ll E_F$ and for small energies involving only intraband transitions, it reads

$$\sigma_{DC} = \frac{2e^2}{h} \frac{E_F}{\hbar\Gamma}, \tag{5.11}$$

where the prefactor is the conductance quantum for a doubly degenerate channel. In the literature one finds it often expressed through the Drude weight $D = (v_F e^2/h)\sqrt{\pi n_s}$ as $\sigma_{DC} = D/(\pi\Gamma)$.[300, 230]

Increasing the strength of the magnetic field, the free particle Hamiltonian describes the system when performing the minimal coupling for Eq. (5.3).[283] The diagonalisation of the system quantises the Dirac cones into a fan of Landau levels described by[2][303]

$$E_n = \mathrm{sign}(n) v_F \sqrt{2e\hbar B|n|} = \mathrm{sign}(n)\hbar\omega_{cyc}\sqrt{|n|} \tag{5.12}$$

$$\omega_{cyc} = v_F \sqrt{\frac{2eB}{\hbar}}, \tag{5.13}$$

with quantum number $n \in \mathbb{Z}$, referring to electrons for $n > 0$ and holes for $n < 0$. A particular consequence of the Landau fan of graphene is the presence of a $n = 0$ Landau level where both carrier types coexist. (Note that, with respect to 2DEGs, the level degeneracy is doubled due to the pseudo-spin degree of freedom.) The most peculiar properties described by Eq. (5.13) are that the Landau levels are proportional to the square root of the magnetic field, as in topological insulators[304, 305], instead of being linear in B as in Eq. (0.23), while depending only on a single, not-tunable material parameter, namely the Fermi velocity v_F. The $n = 0$ level gives rise to the anomalous integer quantum Hall effect in graphene, for which, at high magnetic fields, a Landau

[2]Since graphene was not extensively investigated under magnetic field within the present work, only the relevant discussion of its properties in presence of B is given. The interested reader can learn more, e.g., in Refs [301, 302].

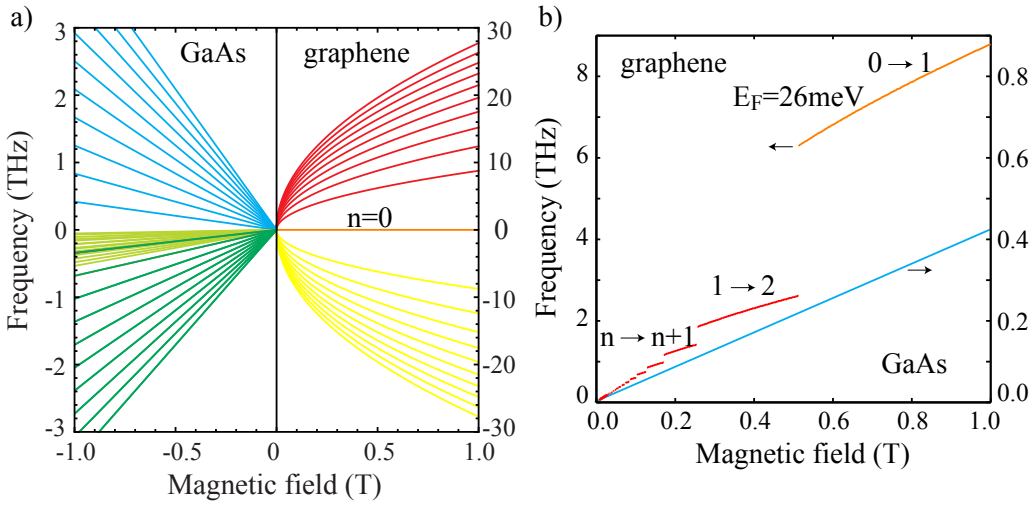

Figure 5.2 – Comparison of a) the Landau fans and of b) the cyclotron transition of graphene and GaAs. Note the symmetry of the fan of graphene, including the $n = 0$ level, while GaAs has different slopes for the different carriers ($m_e^* = 0.067m_e$ cyan, $m_{hh}^* = 0.51m_e$ light green, $m_{lh}^* = 0.082m_e$ dark green). The dashed purple line indicated the Fermi level in graphene. In b) only the $n \to n+1$ transitions are plotted for graphene (red and orange). Note the factor ten in the vertical energy scale between graphene and GaAs, for the same magnetic field value.

level appears where no level was present at $B = 0$ T.[285]

A comparative plot for the Landau levels in graphene and in GaAs is presented in panel a) of Fig. 5.2. Apart from highlighting the parabolic vs linear behaviour, an important difference is that graphene's Landau levels are placed at tenfold higher energies than the corresponding GaAs ones, for comparable magnetic field strengths. Otherwise said, the Landau level in graphene for a given energy value can be found at a field that is 1/10 than the one for which a Landau level with the same energy is found in GaAs. When considering the cyclotron transition from the last filled Landau level to the next empty one, at a given Fermi energy GaAs displays a continuous straight line (cyan line in panel b), left-hand side axis). Instead, the square-root dependence in graphene results in the cyclotron transition curve shown in red/orange in panel b) for a $E_F = 26$ meV (right-hand side axis). This is approximately linear for low magnetic fields, i.e. high filling-factors, while it turns into parabolic segments when the subsequent Landau levels are better separated, i.e. low filling-factors. In the limiting case of a Fermi level at the CNP $E_F \simeq 0$ meV, the curve corresponds to the first parabolic Landau level.

Experimentally, for intrinsic graphene layers naturally found onto graphite crystals, extremely high mobilities were deduced from the measured Landau levels detected down to 1 mT.[274]

Following the same reasoning as for Eq. (0.28), the allowed optical transitions in

graphene are governed by the interaction Hamiltonian[306]

$$\hat{H}_{int}^{graph} = 2ev_F\hat{\boldsymbol{\sigma}} \cdot \hat{\boldsymbol{A}}_{em}, \tag{5.14}$$

with $\hat{\boldsymbol{A}}_{em}$ still defined by Eq. (0.29).

Given the form of the Hamiltonian (5.3), it is convenient to work in the circular basis $|\pm\rangle = (|x\rangle \pm i|y\rangle)/\sqrt{2}$ for the Pauli matrices $\hat{\sigma}_\pm$ and for the polarisation vectors $\hat{\varepsilon}_\pm$. The matrix element for transitions between Landau levels is therefore given by[307, 302]

$$\langle n'|\hat{\sigma}_\pm \cdot \hat{\varepsilon}_\pm|n\rangle \propto \delta_{|n|,|n'|\mp 1} \tag{5.15}$$

This means that, in general, three kinds of transitions are allowed:

- interband transitions $|-n\rangle \to |n+1\rangle$ and $|-n-1\rangle \to |n\rangle$ with energy $(\sqrt{n+1} + \sqrt{n})\hbar\omega_{cyc}$,
- intraband transitions $|n\rangle \to |n+1\rangle$ and $|-n-1\rangle \to |-n\rangle$ with energy $(\sqrt{n+1} - \sqrt{n})\hbar\omega_{cyc}$,
- $n = 0$ Landau-level transitions $|-1, 0\rangle \to |0, 1\rangle$ with energy $\hbar\omega_{cyc}$.

Strictly speaking only intraband transitions are cyclotron transitions and appear at lower energies than interband transitions. Each transition pair is degenerate in energy but can be resolved with circularly polarised light. This is again in strong contrast with the case for a conventional 2DEG (cf. Eq. (0.34)) where cyclotron transitions take place between neighbouring states only and no $n = 0$ state is present. Nonetheless, narrow-gap materials like an inverted HgTe/CdTe quantum well show similar features.[308]

Experimentally, magneto-optical investigations on graphene were performed mainly on epitaxial graphene on the C-face of SiC, since this kind of samples allow relatively large area and show good mobilities and low doping.[307] On these, cyclotron absorption could be detected down to $B = 0.4$ T and $E \simeq 10$ meV. Also exfoliated samples were investigated but at much higher photon energies and magnetic fields: the smallest feature was detected for $B = 6$ T and $E \simeq 100$ meV.[309] This was due to quite low mobilities and small sample dimensions. Finally, more recently, similar measurements could be performed onto CVD-based samples. The first attempt[310] employed fields up to 120 T to compensate for the quite low mobility, even if Landau level transitions could be detected for $B = 10$ T and $E \simeq 117$ meV. Higher mobilities allowed the detection of Landau-level transitions in CVD-graphene down to $B = 5$ T and $E \simeq 85$ meV.[311] The improvements in the quality of CVD-graphene will favour this kind of samples for future studies in the full THz-range.

More recently, studies on the plasmonic and optical properties of graphene have been and are being pursued.[271, 272] The linear dispersion relation near the CNP with the absence of a sizeable band-gap gives rise to a scenario different from the case of usual semiconductors. In particular two types of optical transitions can be considered, corresponding these to different contributions into the conductivity tensor: intra-band and inter-band transitions.[312] For the latter, a cut-off energy of twice the Fermi energy applies and, being E_F typically of some hundreds meV (infrared spectral region), they become dominant on the intra-band transitions at THz frequencies. These combined electro-optic characteristics reveal graphene as a promising material for optoelectronic and plasmonic applications.[313] In the quest for decreasing the THz gap, useful applications of graphene reside particularly in detectors[314] and modulators[83].

As a last remark, the fact that graphene's Landau levels are not equally spaced had some researcher thinking of its optical exploitation possibilities: from the proposal for a graphene-based Landau-level laser in the MIR/THz-frequency range[315] to coherent THz generation from four-wave mixing[306] to generation of entangled photons[316].

5.3 Production

In the time-frame of this thesis, graphene from different sources and produced with different methods was used. Here we give a brief introduction of the different graphene types and try to compare them explaining their advantages and disadvantages[317] for the purposes of this work.

Mechanically exfoliated graphene (plastic-tape method)

This is the "historical" method for the production of layered materials: it consists in using a sticky tape to remove the superficial layers of a crystal, hence the colloquial name. Originally, it was used for cleaning crystals to have a clean, fresh surface for subsequent experiments like, e.g., x-ray diffraction or chemical analysis. Nowadays crystalline graphite can be purchased in small crystals with dimensions of some millimetres cube. The one used for the flakes in the studied samples was purchased by *Graphene Supermarket*.

One then takes a piece of adhesive tape and places on it one of the graphitic crystals. The crystal is then removed leaving behind a, usually thick, stack of graphitic material. The plastic tape is held at its extremities and folded in half so to stick the material on both sides. The tape is then opened and the result is that there are now two regions covered with graphitic material, one being (most of) the initial stack, the other what has been ripped from it. The plastic tape is then folded again along different axes several

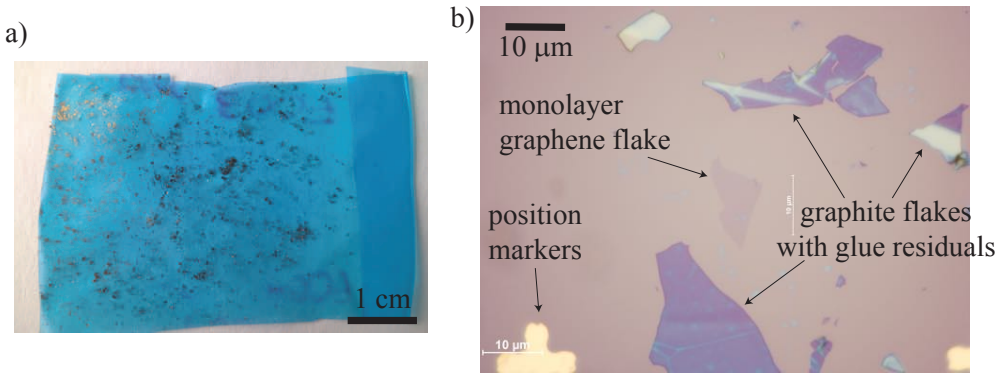

Figure 5.3 – a) Scotch tape used for graphite exfoliation and b) produced graphene flake. The monolayer graphene flake is surrounded by thicker multilayers, some containing glue residuals from the tape.

times till a good portion of the tape is covered by a multitude of thin layers of graphitic material, as shown in panel a) of Fig. 5.3. At this point, a substrate, that had been previously cleaned and prepared, is placed, face-down, on the tape. After some time and after eventual procedures to enhance the contact and the sticking between the graphitic material and the substrate surface, the latter is removed from the tape. The substrate is constituted by a low conductivity silicon wafer covered with 285 nm of silicon oxide. More details on the substrate can be found in the corresponding paragraph later in this section. Different procedures can be used to enhance the sticking like

- pressing the substrate on the plastic tape from the substrate side for a more or less prolonged time;
- pre-heating the substrate on a hot plate slightly above 100°C, compatibly with the used plastic tape, to remove any residual absorbed H_2O;
- placing the pair substrate/plastic-tape on the hot plate at about 60°C on the plastic-tape-side, compatibly with the used plastic tape, for a more or less prolonged time;
- a combination of the previous ones.

Due to the small number of samples produced, no statistic is available on whether at all and which of the listed method actually enhances the graphene flakes yield in number and/or size. Panel b) of Fig. 5.3 shows an example of a produced graphene flake with the plastic tape in panel a).

Usually some graphitic material with a variable number of layers sticks to the substrate via van-der-Waals interaction: the yield was of few usable monolayer graphene flakes per substrate, with a slightly higher amount of bilayer flakes and much larger presence of tri-

and multi-layer flakes. These can be identified and characterised with Raman spectroscopy and field-effect-transistor- (FET-)like measurements as explained later in this section. This method allowed the production of graphene flakes with typical dimensions of the order of 10×5 µm^2. The mobility is expected to reach 10^5 cm^2/Vs, when the samples don't have too many glue residuals. The produced flakes were used for the samples described in section 8.3 on page 229.

CVD-grown graphene

Chemical Vapour Deposition (CVD) is a technique that uses gaseous precursors to synthesise materials via a catalyst, usually at high temperature. After initial studies with transition metals[318], it was soon discovered that graphene can be synthesised via CVD on large-area copper or nickel surfaces.[319, 320, 321] These metals act as catalysers for methane that dissociates at high temperatures leaving behind a layer of carbon atoms, while the residual hydrogen atoms form gas molecules that are pumped away. The layer formation starts from a nucleation point and expands radially till another layer is met, forming a grain boundary. At this point carbon atoms get further catalysed and start forming a second layer from the nucleation point, and the process can continue iteratively. Panel a) of Fig. 5.4 presents an SEM picture of CVD-grown graphene grains with the darker nucleation points where the second layer started to form. The challenge for growing a good graphene monolayer relies in knowing the right moment to stop the growth, on the one hand maximising the monolayer coverage while, on the other hand, keeping small the amount of bilayer. Nevertheless, this method can grow graphene layers of any extension, provided the oven and the substrate are of the needed dimension. The main disadvantage of such kind of graphene is that the routine mobility often does not exceed 5000 cm^2/Vs, hindering its use in transport experiment and whenever the carrier mean free path has to be long.

Once grown, the graphene needs to be transferred to a suitable substrate: this is usually done by performing the following steps[319]:

1. the graphene is covered with a polymeric layer for protection and structural stability;

2. the substrate is removed by chemical etching in a liquid solution leaving the pair graphene/polymer floating;

3. the pair is placed in fresh water to rinse away the etching solution, repeating the procedure at least two times;

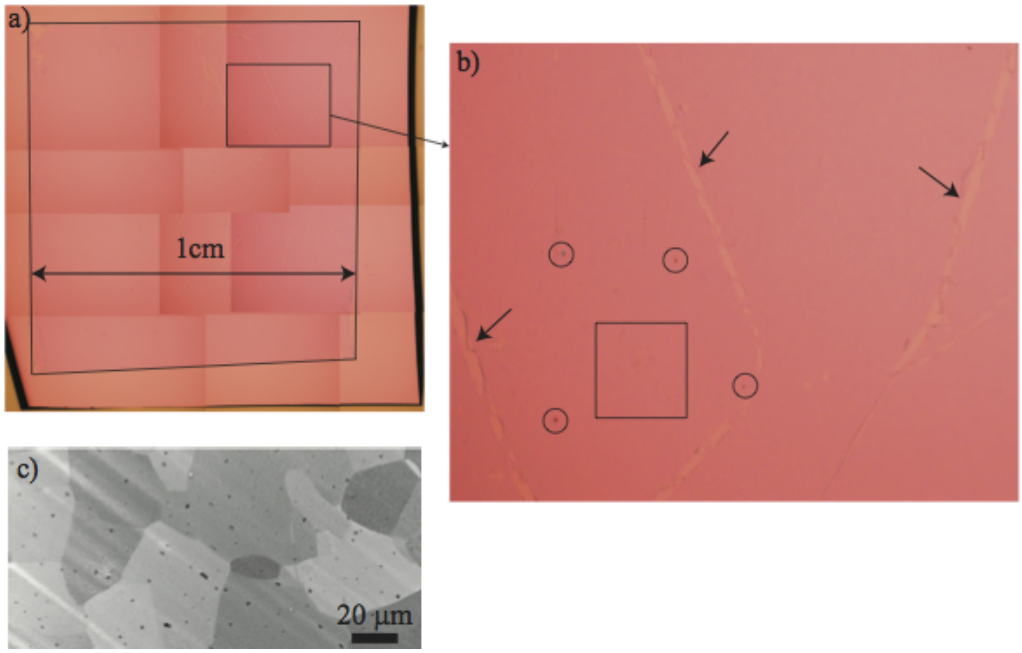

Figure 5.4 – a-b) Optical and c) SEM pictures of CVD graphene. a) Macroscopic transferred layer. b) Detail showing the transfer's issues: metallic residuals (circles), cracks (arrows) and polymeric residuals (square). c) The granular structure of the CVD-layer can be seen at the SEM; the black dots are the nucleation points surrounded by multiple graphene layers, while the overall wiggles come from the Cu foil on which it was grown and onto which the graphene still resides.

4. the wanted substrate, previously arranged and cleaned, is used to "fish" the pair from the water side. It therefore helps if it is not too much hydrophobic, since the pair needs to be lifted from below, taking care of trapping the smallest amount possible of water below the graphene;

5. the sandwich, substrate-graphene-polymer, needs to dry, usually at room temperature, to complete the adhesion of the graphene to the substrate;

6. the polymer can be removed, usually by a solvent but also by thermal annealing when possible, and the sample is ready for characterisation.

As for graphene flakes, the standard substrate is constituted by a low conductivity silicon wafer covered with 285 nm of silicon oxide. More details on the substrate can be found in the corresponding paragraph later in this section.

The first factor limiting the quality of CVD-graphene is the transfer procedure. This sets the graphene layer, although protected by the polymer, under big stress: the graphene often suffers cracks and ripples while any chemical used, from the etching solution to ions in the rinsing water to the polymer itself to the solvent, can finally dope the layer. These usually place the Fermi level of graphene into the valence band (p-doping) more or less

far from the CNP. The CVD-graphene quality was nonetheless soon improved with larger grain dimensions and cleaner transfers but this did not improve much its mobility.[322, 323] Initially, the reason was believed to be the presence of grain boundaries[324, 325, 326] that act as potential barriers for the transport carriers. Recently, it was instead demonstrated that CVD-graphene can show a mobility of 3.5×10^5 cm^2/Vs, i.e. comparable with good exfoliated flakes, provided that chemicals and polymers are avoided during the transfer process and that a better substrate is used (hBN).[327] The CVD-graphene was dry-transferred with a pick-up procedure that relies on van-der-Waal interaction with the recipient boron nitride layer.

The CVD-graphene used for the samples of section 8.1 on page 208 was grown in the groups of Prof. Schönenberger at the University of Basel and of Prof. Park at ETHZ. The specific parameters, along with the transfer procedure, are reported in appendix H.2 on page 270.

SiC-graphene

Silicon carbide (SiC) is a compound material with a large band gap, very resistant to high temperatures and voltages, used since long time in the electronic industry. During the growth of epitaxial layers in the MBE, researchers realised that, when heating up the SiC-crystals above 1000°C in ultra-high vacuum, graphite would form at the surface by decomposition of the substrate[328] and could result in single epitaxial graphene layers[329]. In the subsequent decades the growth method was improved till reaching a full coverage with a controlled yield and it was finally possible to show that the layer behaves as a 2DEG displaying Shubnikov-de Haas oscillations in magneto-transport.[330] In general, the hexagonal single crystal $6H - SiC$ is chosen as starting material and graphene can be grown on the two different terminations of the SiC-surface. The Si-face allows the growth of up to few continuous layers of graphene, electrically insulated from the rest of the sample, the top-most being quite negatively doped. On the C-face, instead, a stack of disconnected but ordered monolayers can be grown, they being electrically insulated from the substrate, too. The latter kind of graphene is the one possessing the best mobility of the two, few tens of thousands of cm^2/Vs, superior to the CVD-graphene and comparable to medium quality flakes.[331, 332]

Despite being SiC-graphene promising for the realisation of large-area, high-quality devices, it brings along several disadvantages, mainly related to the substrate. The first disadvantage is that the graphene cannot be gated via the substrate and therefore one needs to process the sample to realise top gates. Second, despite the fact that the graphene layer seems continuous, for sure from the electrical point of view, it rests on a terraced

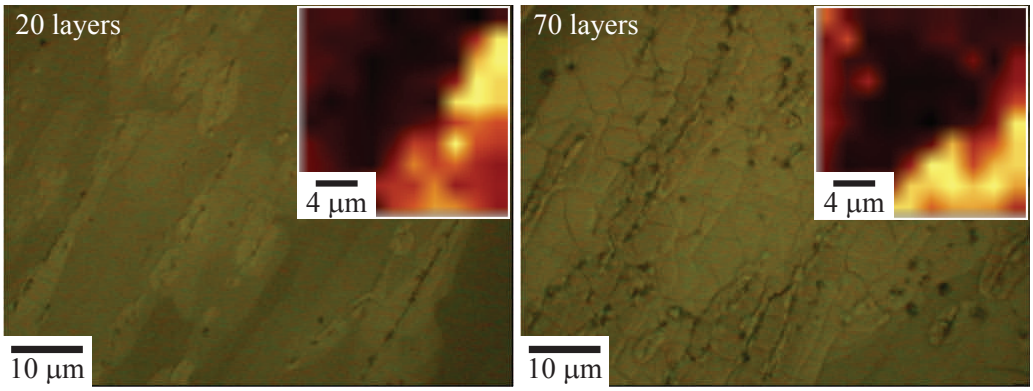

Figure 5.5 – Optical and Raman pictures of SiC-graphene samples with 20 and 70 layers. The graphene layers are very inhomogeneous and clearly follow the SiC terraces.

substrate with step of some nanometres in height and some micrometres in length, that create ripples and folds in the layers, when not breaking it up into islands. This fact creates inhomogeneities, relevant from the optical point of view, that were shown able to excite THz-plasmons.[299]

For the present work, SiC-graphene samples with about 20 and 70 layers on the C-face were bought by Graphene Works Inc.. Such samples have been shortly investigated till realising that no cyclotron transition is visible in the low THz range. The measurements are reported in section 8.2 on page 227. An optical micrograph of such a sample is shown in Fig. 5.5, highlighting the granularity of the surface.

Other methods for graphene production

Alternative methods have been investigated and demonstrated for graphene production, but since graphene produced in such ways was not used in this work, only a very short description of the most used will be given, referring the interested reader to the literature.[333]

- *Liquid-phase exfoliation* The graphite crystal is placed in a solvent, usually non-aqueous or with surfactants, and then sonicated for long time. The solvent is chosen with a surface tension such that the graphite tends to increase the exposed surface and favouring the breaking of the crystal into planes under sonication.[334, 335]

- *Graphite oxide reduction* Similar to the previous method, it relies on the oxidisation of graphite, subsequently exfoliated in aqueous solution per sonication and centrifugation. The solution is then used to cover the wanted substrate and the produced film gets then reduced in situ to graphene.[336, 337]

- *Surface-assisted coupling* This bottom-up approach produces (aromatic) graphene ribbons from initial precursors monomers. These halogens-functionalised monomers stick to a gold surface and, once heated to 200°C undergo dehalogenation and bind covalently together forming a linear polymeric chain. Providing further thermal energy produces cyclodehydrogenation, i.e. the monomers release the hydrogen atoms when close to the next monomer and bind covalently till forming a graphene nanoribbon, terminated with hydrogen.[338]

Substrates and gating schemes for graphene

The quest for the best substrate is one of the biggest challenges of graphene research. Being graphene a monolayer, almost a pure interface, its properties are extremely influenced by the surrounding environment, and thus by the substrate, on the one side, and the atmosphere, on the other.[339] A first tempting option is to remove everything: remove the substrate by etching, i.e. suspend the graphene like a bridge, and place it in vacuum. This is the route taken by several groups investigating transport phenomena.[340, 341] They suspend graphene by the electrical contacts, perform electrical annealing to desorb eventual adatoms and measure the sample in high vacuum. Unfortunately, such option is most of the time not possible when one would like to integrate graphene into a device, or needs a large area, or uses it for a chemical sensor, etc. A substrate is indeed needed; and it is in fact thanks to what became its conventional substrate that graphene became so popular. In fact one of the reasons for graphene being present in almost every solid-state lab in the world, apart from its low cost, is that we can see it, when placed on the "right" substrate, allowing a relatively easy manipulation.

The conventional substrate for graphene, used for the samples in section 8.1 on page 208, is a 500-µm thick, low-doped silicon wafer ($\rho = 50\ \Omega\,\mathrm{cm}$) covered by 285 nm of thermal silicon oxide from *NovaElectronics*. The result is that when graphene is placed on it and changes the surface impedance, the oxide layer becomes a cavity for visible light, building up enough contrast to see it, although faintly, at the microscope.[342]

The oxide has also a second function that is to electrically insulate the graphene layer from the silicon substrate that is usually doped and used as a gate electrode. This is in fact the standard arrangement for graphene in samples/devices: (even bad) conductor/insulator/graphene, both in bottom-gate and top-gate geometry. Thermally grown silicon oxide is particularly suitable because of its high breakdown voltage that allows gating up to about 100 V.

Improving the quality of graphene, it became clear that the substrate was the limiting factor for the mobility (neglecting for the moment the atmosphere, assuming it to be

vacuum): the research community moved then to hexagonal boron nitride (hBN), an insulator with the almost the same crystallographic arrangement of graphene, with a lattice mismatch of less than 2%.[343, 344] This material became the fixed partner for graphene for two reasons: (i) as a substrate it constitutes the smallest disturbance possible to the similarly arranged C-atoms while being insulating; (ii) it can also be exfoliated as graphene and used to cover and protect the latter from the atmosphere. These are the reasons for the hBN-graphene-hBN sandwich, being this process referred to as *encapsulation*.[345]

Our purposes put an additional constraint on the substrate: we want to measure the samples in transmission in the THz-frequency range. This means that the substrate should be as little doped as possible to have transmitted radiation. On the other hand, some measurements need to be performed at low temperatures and a not enough doped substrate will experience carrier freeze-out and will not act any more as a gate for the graphene. This was in fact the case for the substrate of the sample discussed in section 8.1 on page 208. Therefore a suitable substrate had to be developed for the subsequent samples.

The developed substrate is based on a low-doped wafer with an implanted layer of P-donors at a high concentration. In such a way most of the substrate, several hundreds of micrometres thick, is almost transparent to the THz-radiation, while the highly doped donor layer does not attenuate much the radiation due to its very limited transversal extension, below the radiation skin depth. Instead, due to its very high carrier concentration it still acts as a gate for the graphene layer. The best substrate was determined by testing a sample wafer, implanted at a very high density. It was etched for different etching times so to investigate gradually reducing doping densities. This is possible thanks to the exponential distribution of the implanted donors away from the surface: etching away, from the surface down, a certain amount of material results in changing the donor density by a large amount. The best substrate was found to correspond to the following parameters: implant with density 2×10^{19} cm^{-3} resulting in a surface charge density of 10^{14} cm^{-2} for the most doped layer, located approximately at a depth of about 100 nm from the surface. Then the sample was thermally oxidised to grow the wanted top oxide layer. Such substrates were used to produce the samples discussed in section 8.3 on page 229. More details can be found in appendix I on page 273.

One must also mention that graphene can be transferred to virtually any substrate, according to the specific industrial or scientific use. For example, polymeric substrates are used for flexible electronics, where graphene plays the role of a bendable transparent electrode[346, 347]. Alternatively, it was integrated into GaAs structures to investigate hybrid-materials transport structures.[348, 349]

Finally, also top-gate schemes are extensively used in the community, in combination with or in substitution of back-gating. They were not used for graphene in the present work, but few words will be spent, for completeness. In transport experiments, the top-gated sample is usually covered by an insulator (SiO_x, Al_2O_x, hBN, etc.) and a metallic layer is evaporated above.[350, 351] This is obviously problematic for optical experiments where one needs to access the sample with propagating radiation. A first alternative, at THz-frequencies is to use Cr-thin layers as top-gate electrode, because it is at the same time conductive and transparent for long wavelengths.[352] Another solution, are instead ion-gels.[353, 354, 355, 356] These are a viscous compounds of an electrolyte and a polymer: the first gets polarised when a bias is applied at two arbitrary points of the casted material, creating a very thin, highly capacitive layer facing the electrodes, one being the contact, the other being the graphene layer. The main advantage of this method is the possibility of non-local gating, for instance placing the gating contact on the side of the sample.

5.4 Characterisation: Raman spectroscopy and FET-measurements

Because of the intrinsic uncertainties and difficulties in obtaining high-quality graphene from the methods described in the previous section, it is important and necessary to characterise the material when producing samples. This is usually done combining different kinds of methods, the two mandatory ones being the Raman spectroscopy and the field-effect-transistor-like electrical characterisation.

Raman spectroscopy is a widely used technique of optical characterisation that allows the determination of the phononic modes of the sample's superficial layers. Usually a visible monochromatic source is shone onto the sample and the reflected signal is collected and dispersed by a grating. The spectrum is constituted by (several) peaks corresponding to the Stokes/anti-Stokes states identified by addition/subtraction of the energy of one phonon from the one of the illuminating photons.

For the case of graphitic materials, the following phononic energies are characteristic of the material and give specific information[357, 358]: the attention is usually concentrated on the three peaks at about 1350 cm^{-1} (D peak), 1600 cm^{-1} (G peak) and 2700 cm^{-1} (2D peak or G'-peak) from the pumping signal, shown in an exemplary spectrum in Fig. 5.6. The G peak is typical of graphitic materials and is connected to the doubly degenerate zone centre mode in the hexagon, so it is always present and quite intense. The D peak, at slightly lower energy, identifies the phonons caused by imperfections in

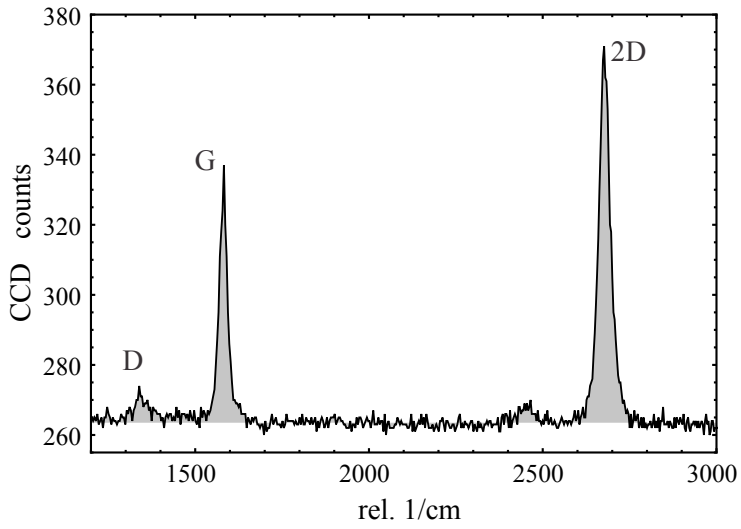

Figure 5.6 – Raman spectrum of CVD-graphene: the 2D peak is taller and as narrow as the G peak, indicating that the sample is constituted by a single layer.

the hexagonal structures usually due to cracks or grain boundaries, therefore it is often regarded as the defects' peak. Finally, the most important is the 2D peak at about twice the energy of the previous one. It originates from a second-order process involving two in-plane transverse-optical phonons with wavevector q from the K-point, that couple to electronic states in the Dirac cones with wavevector $k = q/2$.[359]

The substrate on which the graphene layer is resting slightly influences the specific value at which the peaks are found and the standard values are given for graphene on Si/SiO_x substrates.[360] Increasing then the number of layers, the electronic band structure hybridises splitting the monolayer-graphene 2D-peak into several close ones of smaller intensity. It is therefore possible, for a stack of few-layers, to identify the number of layers constituting the measured region, when its amplitude and full width at half maximum (FWHM) are compared to the ones of the G peak. In particular, if the 2D peak is narrower and with a bigger amplitude, it indicates that the illuminated area of the sample is constituted by monolayer graphene. If instead the 2D peak is as high as the G peak and comparably/slightly more wide, the sample is constituted by bilayer graphene. Increasingly smaller amplitudes and wider FWHM identify multilayers with an increasing number of layers.[357, 358]

An additional comment is due concerning the generalisation of such analysis: the discussed conclusion based on the Raman spectrum are valid for the part of the sample illuminated by the pumping spot, generally less than 1 µm in diameter. Therefore the measurement should be performed on several points of the sample, taking care that they are representative for the whole area. In this respect, especially the conclusions on the

disorder drawn from the D peak are not very significant for single sampling points.

When the Raman characterisation is not able to univocally identify the number of layers, or in any case when an additional confirmation is needed, atomic-force microscopy (AFM) is used to determine the exact thickness of the stack with respect to the substrate, to be compared with a monolayer thickness of 0.335 nm.

The Raman spectroscopy setup used for the characterisation of the samples in the present thesis is a confocal Raman microscope CRM200 by WiTec, working at room temperature with a green laser-diode source at 532 nm. The sample is illuminated by a 1 mW linearly polarised light-beam through a 100× microscope objective with a numerical aperture of 0.8, producing a spot diameter on the surface of the sample of about 400 nm. The reflected signal is brought, after notch-filtering the excitation wavelength till 50 cm^{-1}, to a 600 grooves/mm grating that disperses the different colours and is recorded by a Peltier-cooled charge-coupled detector. The setup is also able to record 2D-maps like the one presented as insets in Fig. 5.5.

After having determined a suitable graphene layer, the electrical characterisation is also needed, before (or in parallel to) producing the actual sample. This allows the determination of two important parameters of the material: mobility and density of the carriers, respectively given by slope and position of the Dirac cones. This can be done in the FET-like configuration.[361, 362]

To such purpose, the graphene layer is provided with Ti/Au 5/500 nm source (S), drain (D) and gate (G) contacts[363], under all aspects resembling an FET. Changing the gate voltage with respect to the graphene layer moves the Fermi level up and down in the Dirac cones, eventually passing also through the CNP. At the same time, the source-drain voltage at a fixed current (or current at a fixed voltage) is monitored.

This is done with the setup in Fig. 5.7: two *Keithley* sourcemeters are used as voltage sources for both V_{SD} and V_G. The first one is usually set to $V_{SD} = 10$ mV while the gate bias varies in the range ±100 V. Both sourcemeters monitor at the same time the current flowing into the circuit, hence the SD-current from which to derive the graphene resistivity (cf. Eq. (5.18) in the following) and the possible leakage current through the oxide. Throughout the thesis, for each sample, the gating voltage was varied in a suitable range, in order to keep the leaking current through the oxide below 5% of the S/D one, when present. With very sensitive samples, an *EG&G* lock-in amplifier was used as AC-source for the SD-current by setting the voltage source of the internal oscillator and closing it onto the series of a 10 MΩ resistor and the sample. Since the sample has a lower resistance, of the order of few kΩ, one can assume that a constant current is flowing into

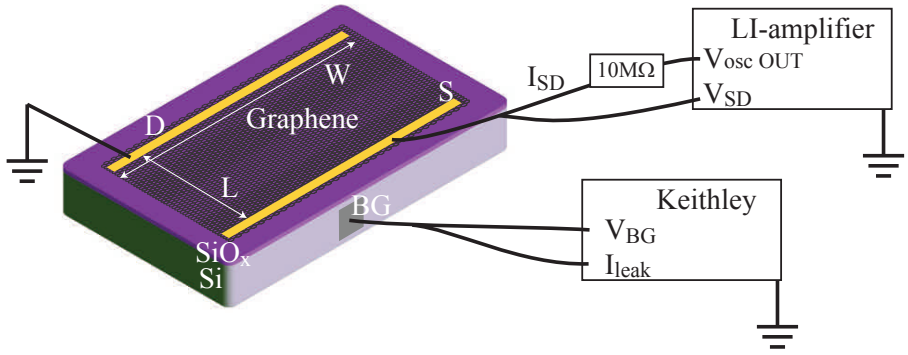

Figure 5.7 – FET-charcaterisation scheme: the SD-voltage V_{SD} is measured at a constant current I_{SD} while sweeping the backgate voltage V_{BG} and monitoring I_{leak}. The mobility is derived thanks to the geometrical factor W/L.

the circuit. The measurements were run and controlled by Labview programs written for the specific purpose.

Assuming a constant density of states in the contacts, the changing resistance measured through the graphene layer directly reflects the density of states into the monolayer. An indication of the good quality of the graphene is then a narrow, sharp peak revealing a high mobility and a low concentration of residual charges. The latter is also an important parameter, especially when wanting to probe graphene in the limit of zero charge density and negligible carriers' effective mass. Residual charges at the CNP are always present due to thermal excitations of electron-hole pairs and to the layer inhomogeneities that create electron-hole puddles.[364] The latter are unfortunately particularly pronounced for CVD graphene layers: in fact the mobility is usually low and especially the transfer procedure produces several defects in the layer that result in a finite residual charge density at the CNP. Additionally the chemicals used in the transfer procedure usually leave the CVD graphene p-doped with the Fermi level placed about 100 meV into the valence band.[319] Graphene flakes have often higher quality, especially if not much processed, with a lower residual charge density, higher mobility and small environmental doping.[361, 362] SiC-graphene has similar properties as graphene flakes but usually its environmental doping is relatively high (about 400 meV) while the gating results difficult when keeping the SiC substrate.[274]

To extract the value of the mobility from such electrical measurements, one takes advantage of the fact that the graphene constitutes one plate of a planar capacitor, the other one being the gating substrate, spaced by the insulating oxide. Knowing the capacitance C of the parallel-plate capacitor one can then use the definition of capacitance to derive the amount of induced charge at a given applied voltage $Q = CV$. Since we are dealing with a 2D material, it is convenient to divide both sides by the area, while introducing

the formula for the capacitance of a parallel plate capacitor and write the induced charge density change as

$$\Delta n = \frac{C}{eS}\left(V_G - V_{CNP}\right) = \frac{\epsilon_0 \epsilon_r}{et}\left(V_G - V_{CNP}\right), \tag{5.16}$$

where $\epsilon_r = 3.85$ and $t = 285$ nm are the relative permittivity and the thickness of the silicon oxide layer, while $(V_G - V_{CNP})$ is the applied back-gate voltage with respect to the position of the CNP. The calculation for $V_G = 0$ V gives the initial doping of the graphene layer Δn_0 that, for CVD-graphene at room temperature and ambient conditions, is usually negative, indicating p-doping, and of the order of 10^{12-13} cm^{-2}.

One can then derive the mobility by using the semi-classical formula from the Drude model

$$\mu = \frac{1}{n_s e \rho_S}, \tag{5.17}$$

where n_s is the charge density derived via Eq. (5.16) and ρ_S is the sheet resistance of the graphene layer (resistivity per unit thickness). The latter is given by the resistance measured between source and drain, corrected by a geometrical factor containing length L and width W of the current-carrying channel:

$$\rho_S = \frac{W}{L} R_{SD} = \frac{W}{L}\frac{V_{SD}}{I_{SD}}. \tag{5.18}$$

Since the formula for the mobility is inversely proportional to Δn, for ideal conditions the value diverges at the CNP: for such reason, the value reported is usually the one fitted "far enough" from the CNP.

Additionally, Eq. (5.16) allows the derivation of the Fermi energy according to the formula[354]

$$\Delta E_F = \hbar v_F \sqrt{\pi \Delta n}. \tag{5.19}$$

An example of an FET-curve for a graphene flake is shown in panel a) of Fig. 5.8, measured with the setup in Fig. 5.7. A clear CNP is present at slightly negative back-gate voltage V_{BG}, showing that the layer is slightly n-doped. The FET-curve shows a quite marked hysteresis, often associated to charge trapping in the substrate. Panel b) shows the absence of leakage current through the back-gate oxide.

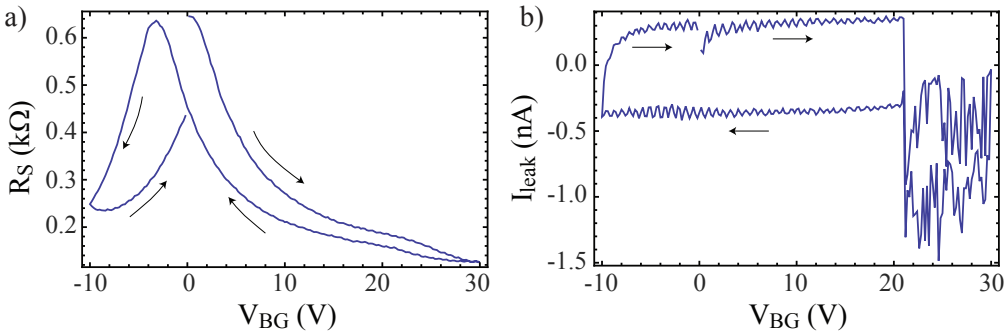

Figure 5.8 – Example of FET-characterisation on a graphene flake: a) FET-curve displaying a clear CNP, with hysteresis. b) Negligible leakage current through the gate oxide. Sample: courtesy of P. Li.

Chapter 6

The ultra-strong light-matter coupling regime

In this chapter we will discuss the physics of the interaction of the cyclotron transition in 2DESs with the THz-cavity created by the split-ring resonators.

We will discuss further the minimally coupled Hamiltonian, already seen in section 0.2.2 on page 18. In the second quantisation formalism, it is written

$$\hat{H}_{tot} = \hat{H}_{mat} + \hat{H}_{cav} + \hat{H}_{int,1} + \hat{H}_{int,2} \tag{6.1}$$

$$\hat{H}_{mat} = \sum_{\boldsymbol{k}} \hbar\omega_{cyc} \left(b^{\dagger}_{\boldsymbol{k}} b_{\boldsymbol{k}} + \frac{1}{2} \right) \tag{6.2}$$

$$\hat{H}_{cav} = \sum_{\boldsymbol{k}} \hbar\omega^{cav}_{\boldsymbol{k}} \left(a^{\dagger}_{\boldsymbol{k}} a_{\boldsymbol{k}} + \frac{1}{2} \right) \tag{6.3}$$

$$\hat{H}_{int,1} = \sum_{\boldsymbol{k}} i\hbar\Omega_{\boldsymbol{k}} \left[a_{\boldsymbol{k}} \left(b^{\dagger}_{\boldsymbol{k}} - b_{-\boldsymbol{k}} \right) + a^{\dagger}_{\boldsymbol{k}} \left(b^{\dagger}_{-\boldsymbol{k}} - b_{\boldsymbol{k}} \right) \right] \tag{6.4}$$

$$\hat{H}_{int,2} = \sum_{\boldsymbol{k}} \hbar D_{\boldsymbol{k}} \left(a^{\dagger}_{\boldsymbol{k}} a_{\boldsymbol{k}} + a_{\boldsymbol{k}} a^{\dagger}_{\boldsymbol{k}} + a^{\dagger}_{\boldsymbol{k}} a^{\dagger}_{-\boldsymbol{k}} + a_{\boldsymbol{k}} a_{-\boldsymbol{k}} \right). \tag{6.5}$$

The hat on the creation and destruction operators was dropped to keep a lighter notation and the Hamiltonians are written for a closed system, i.e. neglecting the loss terms.

The matter Hamiltonian $\hat{H}_{mat}$ corresponds to the quantisation of Eq. (0.22) and, despite being a fermionic system, the operators $b^{\dagger}_{\boldsymbol{k}}$, $b_{\boldsymbol{k}}$ are meant to be bosonic operators after a suitable transformation.[48, 365] Such approximations is allowed when one considers an *ensemble* of two-level systems coupled to the same optical mode, such that the ensemble is far from saturation. Instead, this is not possible any more when dealing with very intense excitations or with a small number of two-level systems, both cases bringing the system towards saturation and thus requiring a fermionic treatment.[366] The energy

of the electronic transition is given by $E_{cyc} = \hbar\omega_{cyc}$ and it has the advantage that it can be tuned with the applied magnetic field B according to Eq. (0.12).

The cavity Hamiltonian $\hat{H}_{cav}$ is written in the approximation of a *photonic* cavity of volume $V = S \times L_z$ with allowed angular frequencies $\omega_{\boldsymbol{k}}^{cav}$. The present discussion follows Refs [48, 49] in neglecting that we are in fact dealing with a plasmonic cavity, the split-ring resonator. Nonetheless the behaviour of the system, in which we are interested, stays the same and the coupling constants change by some prefactors.[1]

When the degree of coupling increases, the interaction cannot any more be treated as a perturbation and different approximations can be made on the total Hamiltonian $\hat{H}_{tot}$, to be diagonalised. In the following, we will briefly analyse the case of the *strong light-matter coupling* before coming to the description of the *ultra-strong light-matter coupling*.

The present discussion is carried out, following Refs [48, 49, 60], in the $\hat{\boldsymbol{p}} \cdot \hat{\boldsymbol{A}}$ formalism. Additionally, the specific formulae are derived having in mind a system where the matter transition is given by the cyclotron transition in a 2DEG. Nonetheless, the same discussion can be equivalently written in the $\hat{\boldsymbol{d}} \cdot \hat{\boldsymbol{E}}$ formalism, more suitable to describe the phenomenon when involving intersubband transitions.[46, 365]

6.1 The strong light-matter coupling regime

The interaction Hamiltonian linear in the cavity operators $\hat{H}_{int,1}$ is the one derived from the $\hat{\boldsymbol{p}} \cdot \hat{\boldsymbol{A}}$-term and contains the paramagnetic terms. The coupling constant for the discussed system can be written as

$$\Omega_{\boldsymbol{k}} = \sqrt{\frac{e^2 N_{QW} \rho_{2DEG} \omega_{cyc}}{4\epsilon_0 \epsilon_r m^* L_z \omega_{\boldsymbol{k}}^{cav}}} \tag{6.6}$$

where N_{QW} is he number of quantum wells, i.e. 2DEGs, inside the cavity, ρ_{2DEG} and m^* are the 2DEGs' density and effective mass, ϵ_r is the relative (effective) permittivity of the material in the cavity.

When $\Omega_{\boldsymbol{k}}$, which represents the exchanged energy between the matter and light part is small but non-negligible with respect to the energy of the states themselves and higher than the loss rates, the system is said to be in the *strong light-matter coupling* regime. In this case the quadratic part of the Hamiltonian can be neglected and the system is

[1] For a more detailed discussion on this point the reader is referred to Refs [367, 365]. The two treatments lead to slightly different, but consistent, forms of the coupling constants.

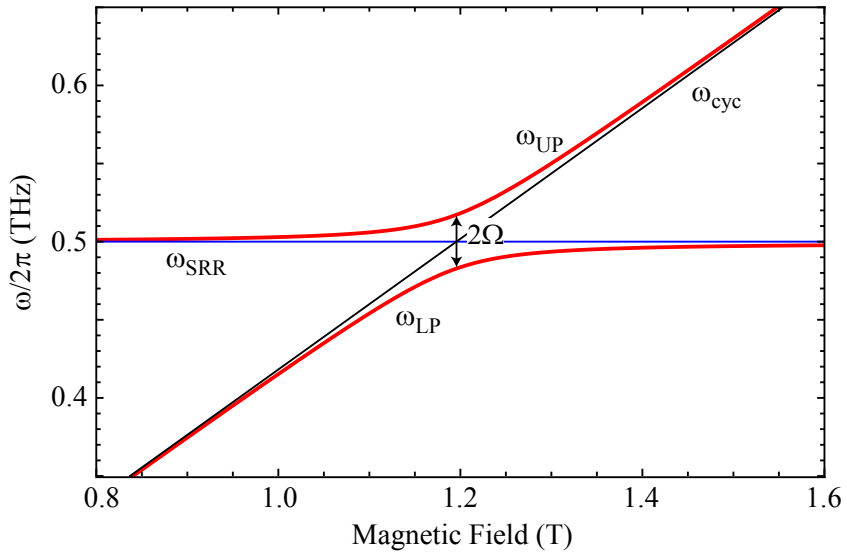

Figure 6.1 – Schematics of the strong light-matter coupling regime, showing the polaritonic branches.

described by the so-called Jaynes-Cummings Hamiltonian[50]

$$\hat{H}_{JC} = \hat{H}_{mat} + \hat{H}_{cav} + \hat{H}^{RWA}_{int,1}, \tag{6.7}$$

where additionally the rotating-wave approximation has been performed,

$$\hat{H}^{RWA}_{int,1} = \sum_{\boldsymbol{k}} i\hbar\Omega_{\boldsymbol{k}} \left(a_{\boldsymbol{k}} b^{\dagger}_{\boldsymbol{k}} - a^{\dagger}_{\boldsymbol{k}} b_{\boldsymbol{k}} \right), \tag{6.8}$$

leaving only the resonant terms in $\boldsymbol{k}$.

In this regime, when the light and matter part of the system are brought into resonance at ω_{res}, they hybridise and an anti-crossing pattern is formed as plotted in Fig. 6.1, with reduced Rabi splitting given by $\Omega_{\boldsymbol{k}}/\omega_{res}$.

Noteworthy is that the asymptotes of the polaritonic branches coincide with the uncoupled parts, far from the interaction region, while at the anticrossing the distance between polaritons depends linearly on $\Omega_{\boldsymbol{k}}/\omega_{res}$ as plotted in Fig. 6.3 on page 149.

6.2 Increasing the interaction until ultra-strong light-matter coupling

When the degree of strong coupling is particularly accentuated, the second order terms in the coupling constant, in $\hat{H}_{int,2}$, and the counter rotating terms, in both $\hat{H}_{int,1}$ and

$\hat{H}_{int,2}$, cannot be neglected any more: the full Hamiltonian of Eqs (0.35)–(0.39) is needed. This increased degree of strong coupling is thus termed *ultra-strong coupling* (USC).[48]

Recall that the coupling constant of $\hat{H}_{int,2}$ is $D_{\boldsymbol{k}} = \frac{\Omega_{\boldsymbol{k}}^2}{\omega_{cyc}}$, of second order in $\Omega_{\boldsymbol{k}}$.[2]

The matrix describing the USC-system, to be diagonalised to derive eigenvectors and eigenvalues, is then[49]

$$M_{\boldsymbol{k}} = \begin{pmatrix} \omega_{\boldsymbol{k}}^{cav} + 2D_{\boldsymbol{k}} & i\Omega_{\boldsymbol{k}} & 2D_{\boldsymbol{k}} & i\Omega_{\boldsymbol{k}} \\ -i\Omega_{\boldsymbol{k}} & \omega_{cyc} & i\Omega_{\boldsymbol{k}} & 0 \\ 2D_{\boldsymbol{k}} & i\Omega_{\boldsymbol{k}} & \omega_{\boldsymbol{k}}^{cav} - 2D_{\boldsymbol{k}} & i\Omega_{\boldsymbol{k}} \\ i\Omega_{\boldsymbol{k}} & 0 & i\Omega_{\boldsymbol{k}} & \omega_{cyc} \end{pmatrix}. \tag{6.9}$$

The four-dimensional eigenvector is $\left(w_{\boldsymbol{k}}^j, x_{\boldsymbol{k}}^j, y_{\boldsymbol{k}}^j, z_{\boldsymbol{k}}^j\right)^T$ defines the creation and destruction operators of the polaritonic system for the upper polariton ($j = UP$) and lower polariton ($j = LP$) as

$$\hat{p}_{\boldsymbol{k}}^j = w_{\boldsymbol{k}}^j \hat{a}_{\boldsymbol{k}} + x_{\boldsymbol{k}}^j \hat{b}_{\boldsymbol{k}} + y_{\boldsymbol{k}}^j \hat{a}_{-\boldsymbol{k}}^\dagger + z_{\boldsymbol{k}}^j \hat{b}_{-\boldsymbol{k}}^\dagger, \tag{6.10}$$

where the operator symbol has been temporarily re-introduced to distinguish the operators from the coefficients. The normalisation condition now reads

$$\mid w_{\boldsymbol{k}}^j \mid^2 + \mid x_{\boldsymbol{k}}^j \mid^2 - \mid y_{\boldsymbol{k}}^j \mid^2 - \mid z_{\boldsymbol{k}}^j \mid^2 = 1, \tag{6.11}$$

and noteworthy is the presence of the anti-resonant creation operators in the definition of the polaritonic destruction operator. This description reconciles with the strong coupling regime when the last $-\boldsymbol{k}$-terms are negligible ($y_{\boldsymbol{k}}^j \simeq 0$, $z_{\boldsymbol{k}}^j \simeq 0$).

The polaritonic branches are then derived as eigenvalues of the matrix (6.9) and are plotted in the top graph of Fig. 6.2. The most notable feature that differentiates it from Fig. 6.1 is the presence of a gap, that separates the left and right asymptotes of the, otherwise constant, cavity frequency. This is the direct outcome of the $\hat{\boldsymbol{A}}^2$-term.

From a semi-classical perspective, it was shown that such gap can be justified and reproduced by writing a suitable complex dielectric function for the medium filling the cavity and containing the matter part.[365, 28, 368]

A direct consequence of this regime is the difficulty of defining the *anti-crossing point*: it is defined as the point of minimum distance between the lower and the upper polaritonic branch and, in the strong coupling regime, it corresponds automatically to the 50% mixing of matter and photonic parts in the polariton. From Eq. (6.10) it is clear that the two

[2] Todorov and coworkers showed that the self-interaction of the polaritonic states, coming from the $\hat{\boldsymbol{A}}^2$-term, is connected to the depolarisation shift of the intersubband transitions, acting collectively on the electrons of the 2DEG, more evident when working in the dipole gauge.[367, 365]

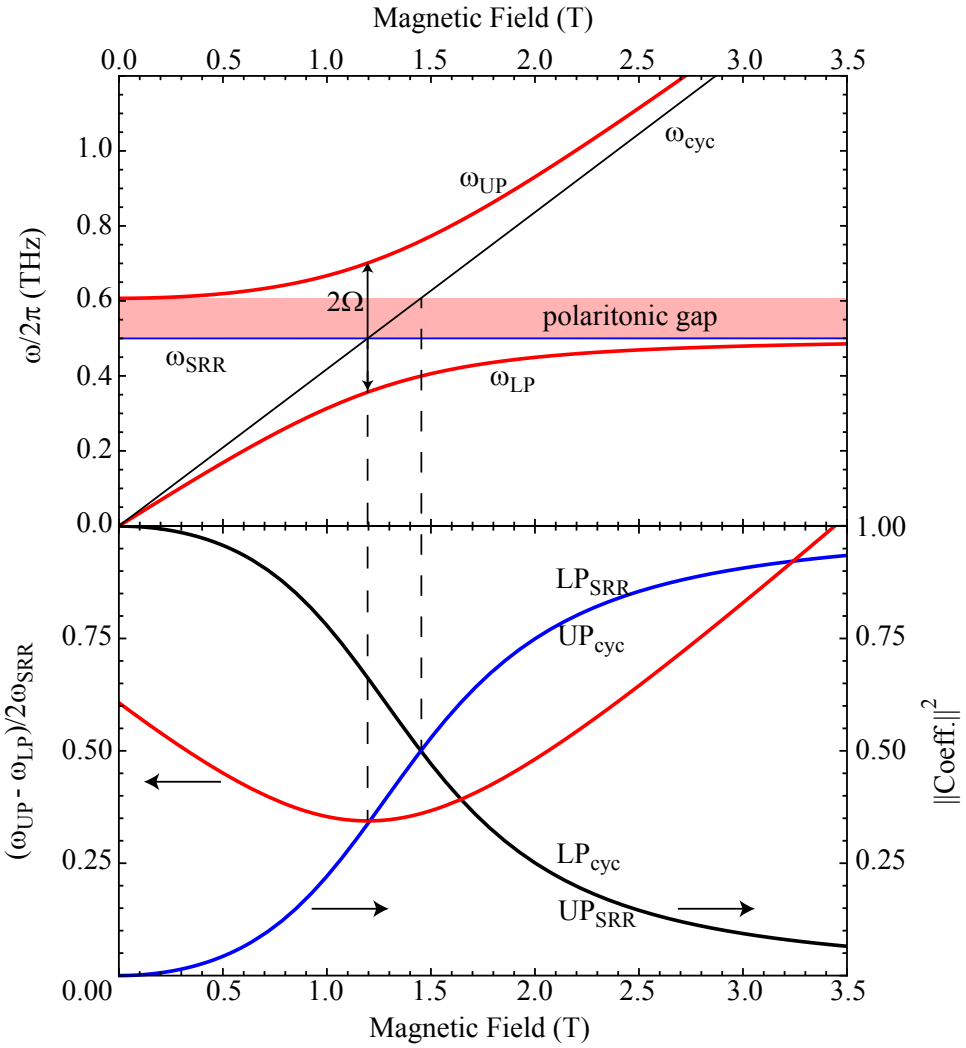

Figure 6.2 – a) Polaritonic branches and gap in the ultra strong coupling regime. The two definitions of the anticrossing point are not any more equivalent: the minimum distance point (from the red curve in b)) does not coincide with the 50% mixing of the matter and light part (blue and black curves in b)).

conditions do not identify the same point any more. Instead they correspond now to the two possible resonance conditions between the tunable matter frequency and the two edges of the gap identifying the loaded and unloaded cavity. This can be understood from Fig. 6.2. The reduced Rabi frequency can thus be written

$$\frac{\Omega_{Rabi}}{\omega_{cav}} = \sqrt{\frac{e^2 \rho_{2DEG}}{4\epsilon_0 \epsilon_r m^* L_z \omega_{cyc} \omega_{cav}}}. \tag{6.12}$$

As discussed extensively in the related literature, this can be enhanced by acting on the different factors, in particular by increasing the number of electrons, using materials with lower effective mass or working at lower frequencies.[368, 48, 49] Some examples will be given in section 6.4.

Finally it is interesting to discuss the behaviour of the polaritonic branches for an increasing degree of strong coupling. In the strong coupling regime, at resonance, the polaritonic branches are symmetrically pushed away from the crossing point $\omega_{UP,LP} = \omega_{res} \pm \Omega_{Rabi}$, as shown by the straight black lines in Fig. 6.3. This means that, for normalised Rabi splittings equal or greater than 1, the lower polariton energy should vanish or even become negative. This is a non-physical consequence of using a model beyond the validity of its approximations. In fact, in the ultra-strong coupling regime the presence of the gap results in a different relation for the polaritonic branches on the Rabi frequency,

$$\omega_{UP,LP} = \sqrt{\omega_{res}^2 + \Omega_{Rabi}^2} \pm \Omega_{Rabi}, \tag{6.13}$$

keeping the lower polaritonic branch always positive as shown by the red lines in Fig. 6.3.

One of the main features of such a USC state is the presence of photons in the ground state of the system[48], a fact linked to different quantum optical features. For instance, it was predicted that such a system can generate correlated photons from squeezed vacuum states[48], that virtual photons can be converted into real ones and released by the system[369], that a thermal cavity in the USC regime can emit bunched and anti-bunched photons[370] or show photon blockade[371]. Experimental work was pursued in such direction, showing non-adiabatic switching of the USC interaction between intersubband transitions and plasmonic cavities[372] or observing the dynamical Casimir effect in a superconducting LC-circuit in the USC regime[373].

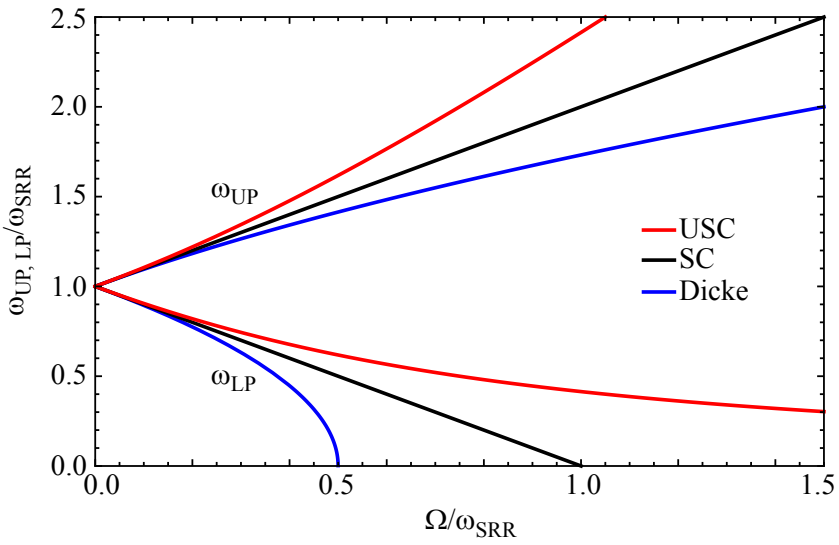

Figure 6.3 – Frequency behaviour of the polaritonic branches vs reduced Rabi frequency for a system in ultra strong coupling (USC, red), for one in strong coupling (SC, black) and for one described by the Dicke Hamiltonian (Dicke, blue).

6.3 Ultra-strong coupling for massless particles

If one considers a system in which the particles are massless, the description of its interaction with light would not contain the $\hat{\boldsymbol{A}}^2$-term. This is a well known case in particle physics and is described by the Dicke Hamiltonian

$$\hat{H}_{Dicke} = \hat{H}_{mat} + \hat{H}_{cav} + \hat{H}_{int,1} \tag{6.14}$$

If the system is in the ultra-strong coupling regime, one would have to diagonalise the same Hamiltonian as for the strong coupling case, but this time including the counter-rotating terms. The result is shown by the blue lines in Fig. 0.10: the lower polaritonic branch bends towards negative energies and eventually dies out with infinite first derivative at $\omega = 0$ with a behaviour proper of a second-order phase transition. This fact results into the so-called superradiant Dicke phase transition[59], yet another regime different from both the strong coupling and the ultra-strong coupling, previously discussed, where the ground state contains photons and the atomic polarisability is coherent.

The first question to pose is whether the Dicke Hamiltonian can be realised in any solid-state system. In order to have an interaction Hamiltonian linear in the vector potential, one needs to perform the minimal coupling substitution, as shown in Eq. (5.14), for a linear momentum term. The natural candidate is then graphene: the previous line of discussion can be repeated for the massless-particle Hamiltonian of Eq. (5.3), $\hat{H}_{Weyl} = v_F \hat{\boldsymbol{\sigma}} \cdot \hat{\boldsymbol{p}}$.

Nonetheless, one has to remember that, for graphene, the massless-particle Hamilto-

nian is an approximation valid for small energies close to the Dirac point, with nearest-neighbour interaction. It would be an exact description only in an ideal system at the CNP itself. Therefore one needs to consider the bigger picture with fewer simplifications and check the relative magnitude of the eventual $\hat{\boldsymbol{A}}^2$-term.

Hagenmüller and Ciuti[60] calculated that the massless-particle approximation for graphene near the CNP is valid also for higher orders of atomic interaction. These indeed create an $\hat{\boldsymbol{A}}^2$-term but it can be proved negligible with respect to the other interaction terms ($D \ll \Omega$). They derived the following normalised Rabi angular frequency for the coupling of graphene's cyclotron transition to the cavity:

$$\frac{\Omega_{Rabi}}{\omega_{res}} \propto \sqrt{\nu}\sqrt{\frac{\alpha g_s}{\pi\sqrt{\epsilon_r}}}, \tag{6.15}$$

where $\nu = \frac{\rho hc}{g_s eB}$ is the filling factor of the graphene's Landau levels for a carrier density ρ at a magnetic field B with spin and valley degeneracy $g_s = 4$, α the fine-structure constant and ϵ_r is the relative permittivity of the material surrounding the graphene. The formula shows that, for high filling factors, it is possible to enter the ultra-strong coupling regime with graphene (e.g. $\Omega_{Rabi}/\omega_{res} \gtrsim 0.5$) without the presence of the gap.

Their treatment reveals then the appearance of a quantum critical point at which the lower polaritonic branch vanishes, making the ground state of the system unstable and undergoing a phase transition. The order parameter is given by the carrier density that has its critical value at $\rho_c = 1.4 \times 10^{11}$ cm^{-2}.

The topic is nonetheless debated: Chirolli et al.[61] and Pellegrino et al.[62] argued that indeed an $\hat{\boldsymbol{A}}^2$-term has to be included in the treatment of such system, coming from the interband transitions available among the Landau levels of a doped graphene sheet. Such transitions are instead neglected when dealing with neutral graphene or when restricting the discussion to interband transitions. The presence of the quadratic interaction term brings the system back to the ultra-strong coupling regime eliminating the possibility of achieving a superradiant phase transition.

Either way, it is important to realise the system and perform the measurements to help understanding which model is valid and which approximations allowed. Additionally, graphene is in any case interesting for its peculiar, unevenly spaced Landau levels, that place it in direct contrast to the cyclotron behaviours in 2DEGs. For example, such difference opens the possibility of reaching population inversion by optical pumping, foreseen as a good candidate for a Landau-level laser.[315]

The implementation of such system and the measurement thereon performed are the subject of chapter 8 on page 207.

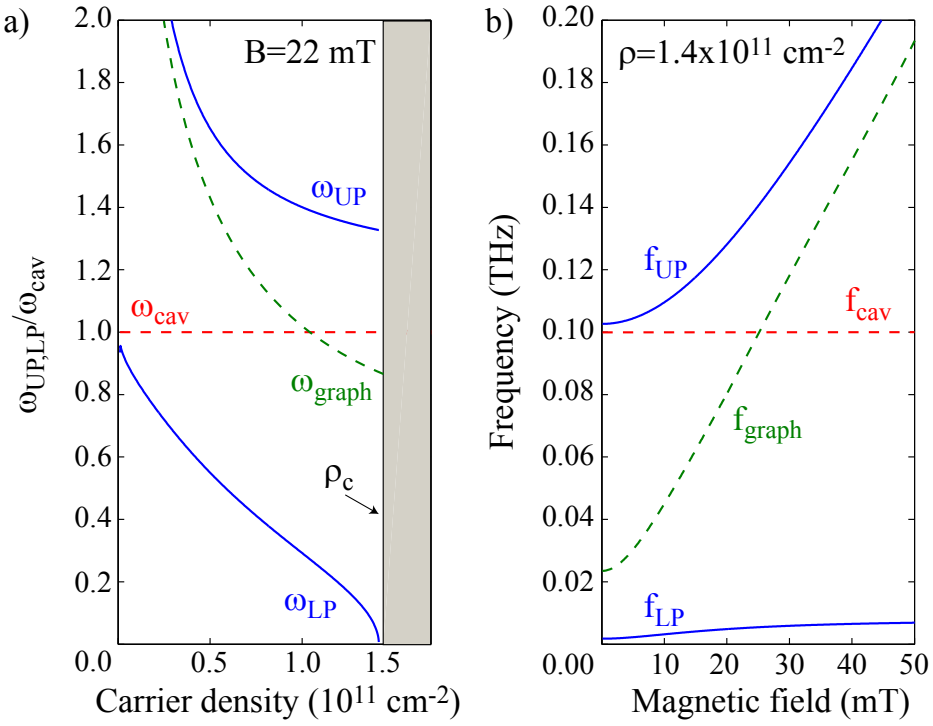

Figure 6.4 – Ultra strong coupling for the cyclotron transition in graphene and a photonic cavity. The Dicke phase transition takes place at the critical density ρ_c. a) Normalised frequency of the polaritonic branches as a function of the graphene's carrier density at fixed magnetic field, close to the anticrossing. b) Frequency of the polaritonic branches as a function of magnetic field at a fixed graphene's carrier density, shortly before ρ_c. Adapted from Ref [60]

6.4 Ultra-strong coupling of the cyclotron transition of a 2DEG to THz-resonators

The system described in the previous sections was realised by Scalari and coworkers with an array of the direct split-ring resonators of chapter 3 on page 81 on top of the heterostructure *EV*1452 containing a 2DEG (the growth sheet can be found in appendix A.2 on page 235) and measuring the sample in transmission while applying an orthogonal magnetic field. The presence of the gap together with a normalised Rabi splitting $\Omega_{Rabi}/\omega_{res} = 34\%$, confirms that the system is in the USC regime.[47, 374, 368] The measurement map is presented in Fig. 6.5. The map shows how the transmission through the sample changes with increasing magnetic field for the frequency range $0.2 - 2.5$ THz. Starting from low magnetic fields and low frequencies, three main lines can be easily identified:

- First the cyclotron transition cuts obliquely the plane as a straight line, whose slope is consistent with the effective mass of the material hosting the 2DEG. This also

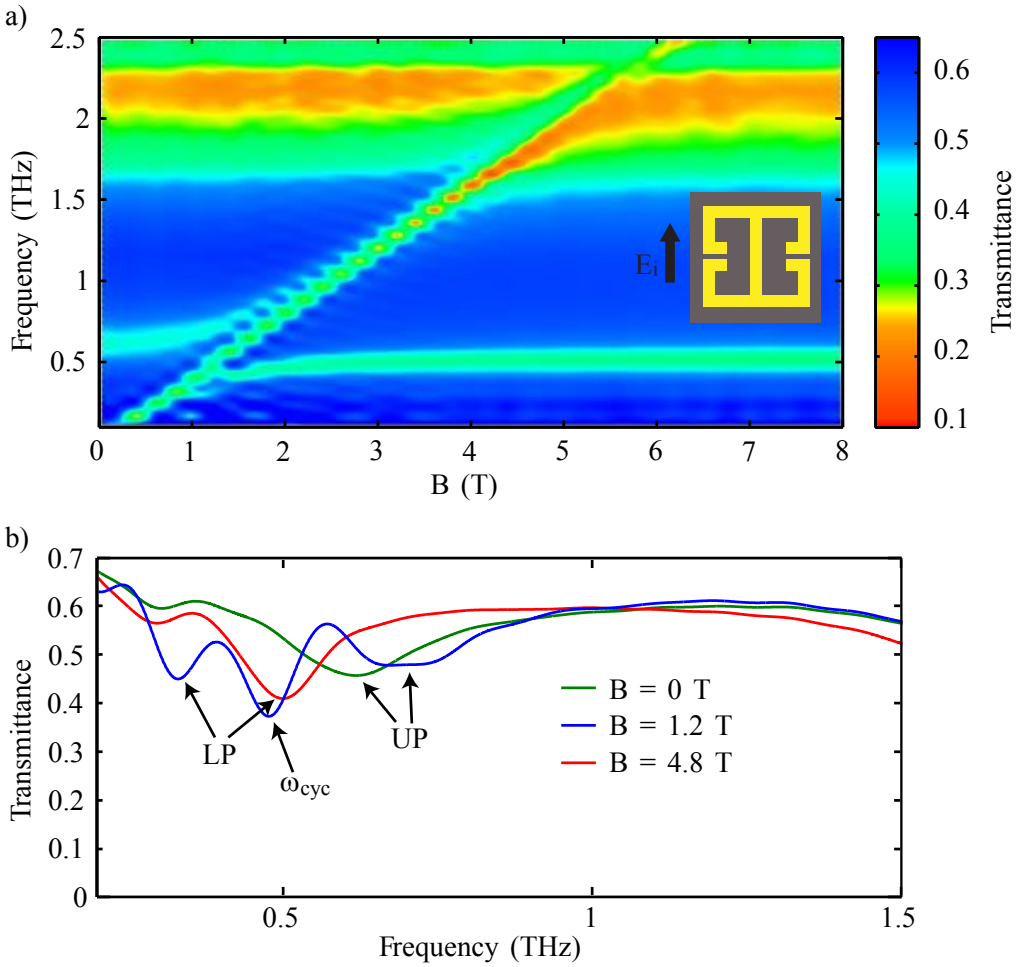

Figure 6.5 – a) Transmission map for direct THz-SRRs in ultra strong coupling to the cyclotron transition in a single GaAs/AlGaAs 2DEG. b) Spectra (vertical cuts of the map) for no applied magnetic field (green), at the anticrossing point (blue) and for strong magnetic confinement (red). Adapted from Ref. [368].

defines the asymptote of the lower polariton for low magnetic field and of the upper polariton for high magnetic fields. This feature is present because, although many electrons in the 2DEG are coupled to the dSRRs, a part of them is still uncoupled and absorbs the THz-radiation, when in resonance.

- Then the lower polaritonic branch starts, at low magnetic fields, from the cyclotron line and later bends asymptotically towards the frequency of the magnetic-field independent, uncoupled dSRR, 0.5 THz in this case.

- The upper polariton, instead, tends asymptotically to the cyclotron line for high magnetic fields, while it bends horizontally towards zero B-field, following the behaviour of the magnetic-field independent, uncoupled dSRR. In spite of this, the

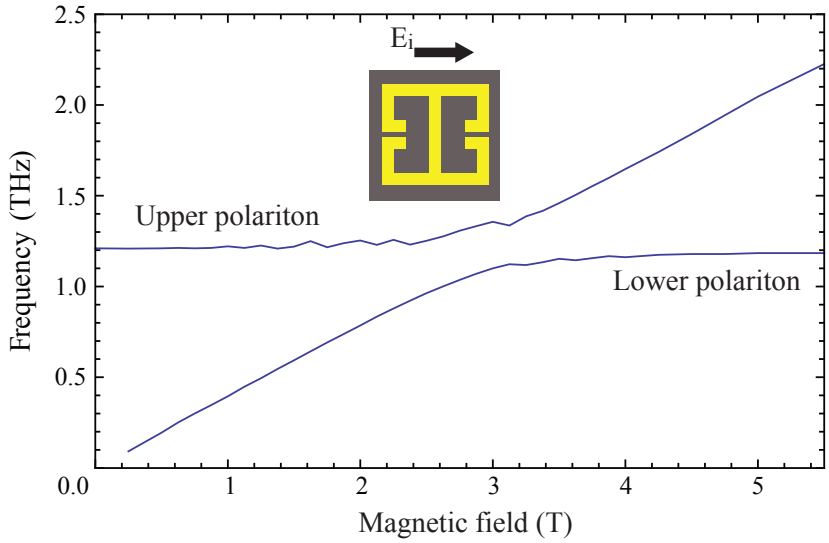

Figure 6.6 – Polaritonic branches extracted from the magneto-transmission measurements of the same sample as in Fig. 6.5 but for the orthogonal polarisation.

frequency of the upper polaritonic resonance at $B = 0$ T is higher than the one of the uncoupled SRRs, their difference quantifying directly the extent of the polaritonic gap.

6.5 Coexisting strongly coupled system for the different optical modes

It is interesting to note that at higher frequencies (approx. 2.2 THz), the features described above are doubled, creating an additional anti-crossing in Fig. 6.5. These reveal that the higher-frequency dipolar mode of the SRR is also in strong coupling with the cyclotron transition, but no gap is seen, ruling out ultra-strong coupling. This is consistent with the smaller concentration of the E-field distribution, as revealed by the FDTD simulations in Fig. 3.4 on page 85.

When considering the general properties of the THz-SRR used, described in chapter 3, one recalls that in the bandwidth of the used setup another optical mode is present. This is the dipolar mode excited by the orthogonal polarisation, with respect to the previous one (cf. Fig. 3.3 on page 84).

To confirm that also this mode can couple strongly to the cyclotron transition of the 2DEG, we measured the transmission of the sample for increasing magnetic field, with the polarisation of the incident THz-radiation along the slits of the dSRR. The extracted minima are plotted as a function of magnetic field in Fig. 6.6.

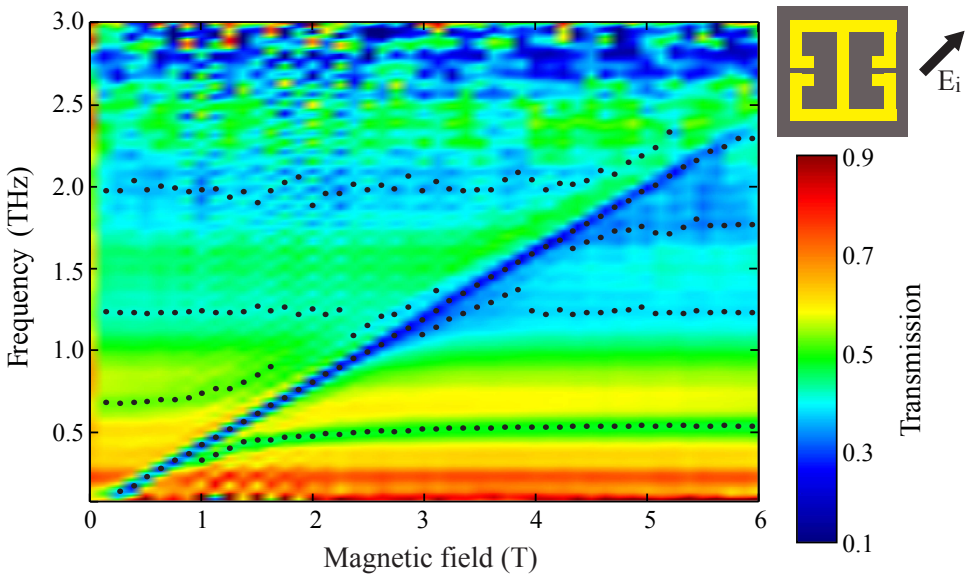

Figure 6.7 – Transmission map measured for the sample oriented at 45° with respect to the incident polarisation. The anticrossing of the THz-modes in both polarisations are present.

The dipolar mode at about 1.2 THz participates to the strong coupling with a normalised Rabi frequency $\Omega^{\perp}_{Rabi}/\omega^{\perp}_{\lambda/2} = 11\%$. This is a relatively good vale but still one third of the one for the LC-mode ($\Omega^{\parallel}_{Rabi}/\omega^{\parallel}_{LC} = 34\%$). In fact no clear gap is present and the the extremal values differ only by few percents, confirming that this system does not display ultra-strong coupling.

At this point, two natural questions come up: (i) are the two anticrossings in the same polarisation interacting? (ii) can we mix them with the one in the orthogonal polarisation?

The questions are legitimate because the constituents of the single systems are not isolated: in fact all optical modes are produced by overlapping currents in the same gold stripe forming the THz-SRR, while they also partially overlap concerning the spatial distribution. This latter fact also means that also the electrons of the common 2DEG areas can take part in multiple strong coupling events.

The questions are relevant, because, if two or more systems were coupled together, one could act on one of them non-perturbatively through the others.

From Fig. 6.5 the strongly coupled systems connected to the LC- and to the dipolar modes do not seem to interact, possibly also because of the large distance in frequency. Then, the sample was mounted at 45° with respect to the incident polarisation and the transmission map in Fig. 6.7 was recorded.

The black dots mark the positions of the minima extracted from the single spectra and help to identify the anticrossings, especially for the two dipolar modes where the signal contrast is much lower. All three modes are visible and all anticross with the

cyclotron transition approx. as strongly as for the measurements performed in the single polarisations (cf. Figs 6.5 and 6.6). The extracted minima for the highest-frequency dipolar mode seem to show a polaritonic gap, but this is an artefact due to the very low signal and to the very broad resonance.

When looking for an interaction between the anticrossings, they seem to just overlap, without ever crossing the cyclotron transition. In fact, were they coupled, the upper polariton of the lower-frequency system should continuously turn into the lower polariton of the next one at higher frequency. Instead all polaritonic branches with enough contrast seem to tend asymptotically to the cyclotron transition and to the respective optical modes, without interaction.

This is partially confirmed by the measurements with very high normalised Rabi splitting reported in Ref. [368], where the upper polariton connected to the *LC*-mode crosses the polaritonic gap of the USC of the dipolar mode without coupling to it. Vice versa, the lower polaritonic branch of the USC of the dipolar mode crosses the polaritonic gap at the *LC*-frequency.

These characteristics, that can be seen as a polarisation-resolved (ultra-)strong coupling, could be exploited to work in parallel on different USC-systems on the same sample. Additionally, one could think of using the real-space rotation degree of freedom to interact with the system, possibly with outlook in optomechanics.

6.6 A broadly tunable system

Starting from the initial system, described in the previous sections, in order to increase the degree of USC of the *LC*-mode Scalari and coworkers investigated extensively the connected parameter space, as from Eq. (6.12).[28, 368] For instance, complementary SRRs were preferred to direct ones (cf. section 3.2 on page 86), although they decrease the coupling strength at constant frequency and with the same 2DEG ($\Omega_{Rabi}/\omega_{res}$ =27% vs 34%), because they make the measurements easier and clearer, hiding the uncoupled part of the cyclotron.

Then the total number of electrons taking part in the USC was increased by growing stacked 2DEGs: $\Omega_{Rabi}/\omega_{res} = 57\%$ was achieved with 4 stacked GaAs-based 2DEGs and raised to $\Omega_{Rabi}/\omega_{res} = 72\%$ with 20.

Another knob comes by using materials with with lower effective mass: a single InAs-based 2DEG showed $\Omega_{Rabi}/\omega_{res} = 69\%$, resulting equivalent to a stack of 20 GaAs-based 2DEGs. The difference cannot be addressed only to the different electronic effective mass but also to a certain degree of screening of the *E*-field by the thicker charged stack.

A sample with THz-SRRs realised into superconducting Nb and resonating at a lower frequency ($f \simeq 300$ GHz) onto 4 stacked GaAs-based 2DEGs showed $\Omega_{Rabi}/\omega_{res} = 87\%$. The use of the superconductor paves the way towards ultra-fast, non-adiabatic switching for quantum optical experiments.[373, 370]

The highest degree of USC presently attained in the presented system has a normalised Rabi frequency reaching 110% and was measured for a metasurface of golden cSRRs resonating at $f \simeq 250$ GHz in USC with 20 stacked GaAs-based 2DEGs.[375]

USC is not a phenomenon belonging to the THz-frequency range alone: it was shown in several systems for different frequency ranges in the last years. They range from intersubband transitions/plasmons in quantum wells in the THz- and MIR-frequency range coupled to plamsonic cavities[372, 376, 377, 378], to superconducting LC-circuits or magnetoplasmonic modes in coplanar waveguides for the GHz-frequency range[379, 373, 380], to organic molecules in metallic cavities in the visible[381] and NIR[**?**]. Recently, USC with normalised Rabi coupling of 1.34 was reported for superconducting qubits in the GHz-frequency range.[382]

The following step was and still is to integrate such systems into opto-electronic devices or, from a more basic-science point of view, with transport systems. Concerning the first point, strongly-coupled systems have already been used for the realization of optoelectronic devices, showing that the strong-coupling regime is reflected onto the electrical output of photodetectors[55, 56] or onto the light output of electrically pumped structures[58, 57]. Instead, concerning transport, in the past few years, a lot of theoretical effort was put into the subject, concluding that the transport properties of dressed electrons could improve with respect to the uncoupled case.[383, 384, 385, 386] A first, debated, experimental result following these ideas reported a conductivity improvement for an ensemble of organic molecules coupled to a plasmonic visible mode.[387]

Following suit, aiming at measuring the transport properties of our system in presence of USC, we etched the 2DEG into Hall-bars that were covered with THZ-SRRS and took advantage of the phenomenon of microwave-induced resistance oscillations (MIROs) to optically excite the system. The specific system, the MIRO phenomenon and the results are the topic of chapter 7. The implementation of the THz-SRR/2DEG system in graphene, aiming at observing the Dicke phase transition is instead the topic of chapter 8.

Chapter 7

Microwave-induced resistance oscillations in the USC regime

This chapter presents the efforts made towards the realisation of a hybrid system where the ultra-strongly coupled system discussed in chapter 6 could be investigated also electrically via basic transport measurements. The aim is then to be able to act on the electro-optical device and manipulate the hybridised states: given the predicted quantum optical features, this would be another important realisation of quantum optics in a solid-state device.

Since the used ultra-strongly coupled system relies on the cyclotron transition of a 2DEG, the natural choice towards transport was to etch the 2DEG into a Hall-bar and investigate its magneto-transport, as introduced in section 0.1.2 on page 9. In order to be sure that the performed measurements are directly connected to the state of the system, we made use of the phenomenon of microwave-induced resistance oscillations (MIROs), where the system is optically pumped in the low-THz-region and the magneto-electrical trace displays features connected to the photoresponse of the Hall-bar.

Such investigation required the fabrication of several Hall-bars with different characteristics and allowed, in particular, a study of the dependence of the MIRO phenomenon on the width of the Hall-bar channel, that could also help in shining more light on the unclear origin of the phenomenon.

7.1 Microwave-induced resistance oscillations

Microwave-irradiated 2DEGs in magnetic field have been studied since the mid 1980s, either on large area samples[388] or in etched Hall-bars[389], with and without additional plasmonic structures, e.g. (anti-)dot arrays[390, 391]. The aim of such investigations

was the magneto-optical characterisation of the cyclotron transition and of the magneto-plasmon resonance (MPR). The MPR studies in Hall-bars were of particular interest because they also allowed the link and the comparison between the optical transmission (reflection) of a GHz beam through (off) the sample and the electrical longitudinal resistivity.

When performing magneto-transport measurements on a high-mobility Hall-bar, the transverse resistivity displays the quantum Hall effect while the longitudinal trace shows the Shubnikov-de Haas (SdH) oscillations; both effects were briefly introduced in section 0.1.2 on page 11. If one repeats the same measurements while shining microwave radiation on the sample, the transverse resistivity does not change while the longitudinal trace acquires additional features.

Initially microwave irradiation would make a peak appear in the, otherwise smooth, low-B-field longitudinal resistivity trace.[388] The first investigations of microwave-irradiated 2DEG structures dealt with resonant excitation of the cyclotron resonance[392], and soon the interest shifted mainly to plasmons.[393, 388] This was due to the possibility to study collective interactions of charges in a system where the dimensionality and the charge density can be tuned. Such ideas stemmed from the interest in semiconductor plasmonics after the first optical experiments with metals by Otto[394] and Kretschmann[395].

After initial investigations performed in transmission[396], photo-conductive measurements were employed, where the radiation modifies the conductivity of the system, measured in transport[397, 398].[1] When performing such photo-conductive experiments onto Hall-bars, a peak compatible with resonant absorption of the microwave radiation was measured in the resistivity trace.[389] It could be explained by radiation-induced heating that would enhance resonantly the resistance of the sample. Furthermore, while expecting a peak at the cyclotron frequency, moving linearly in magnetic field, as it would be for an infinite 2DEG, the feature was at a shifted frequency-value and depended quadratically on B.

The measured magneto-plasmon resonance was found to be a mixing between the cyclotron resonance ω_c given by Eq. (0.12) and the plasma excitation ω_p given by[402]

$$\omega_p^2 = \frac{n_s e^2}{2m^* \epsilon_0 \epsilon_r} q, \tag{7.1}$$

where n_s and m^* represent sheet density and effective mass of the 2DEG, the relative permittivity is averaged between the surrounding dielectrics $\epsilon_r = (1 + \epsilon_{GaAs})/2$, while q

[1] Similar measurements were previously used to study Si-based MOSFETs[392, 399] and electron-spin resonance[400, 401].

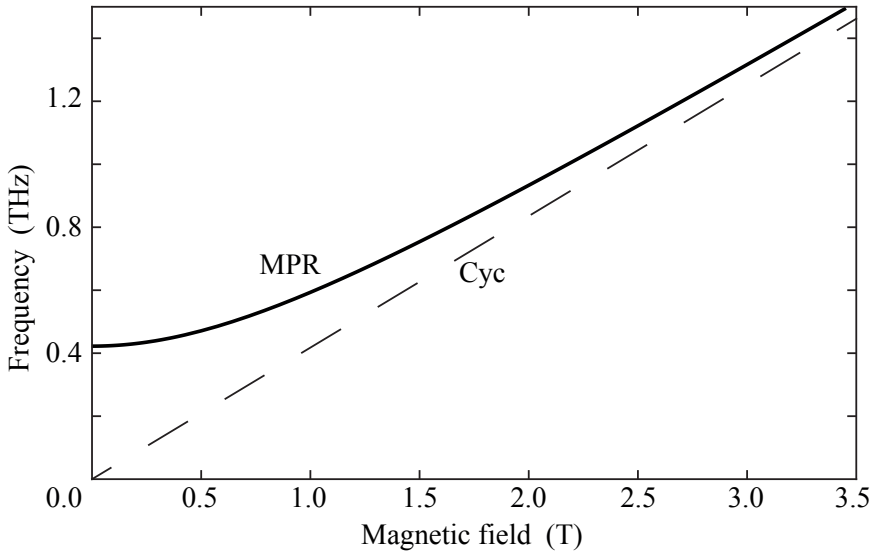

Figure 7.1 – Magneto-plasmon resonance (MPR) compared to the corresponding cyclotron resonance (Cyc). Both have been calculated for a 2DEG stripe 4 µm wide, with parameters' values taken from the measurements.

is the plasmon wavevector. The latter can be approximated, for standing waves across the Hall-bar channel, by the formula $q = j\pi/w$ with $j = 1, 3, 5, \ldots$, w being the channel width. Such formula assumes an ideal potential, e.g. like an infinite quantum well, and it was found numerically that, for standard samples characteristics, ω_p needs to be reduced by 15% to account correctly for the measured frequency. One must therefore substitute $q = 0.85^2 j\pi/w$.[403] The mixed MPR dispersion follows then the formula

$$\omega_{MPR}^2 = \omega_p^2 + \omega_c^2 \tag{7.2}$$

and it is plotted in Fig. 7.1.

Finally, for large samples one must also check whether retardation plays a role: this can be done by evaluating the coefficient A given by[403]

$$A = \sqrt{\frac{n_s e^2 w}{2\pi\epsilon_0 m^* c^2}}. \tag{7.3}$$

For $A \geq 1$, the dispersion is modified from the one given by Eq. (7.2).[404] This is not the case for the investigated samples, for which $A \simeq 0.1$, therefore requiring no correction.

This kind of measurements were pursued further over the years on samples with increasingly higher mobility. Shortly after the year 2000, in a high-mobility Hall-bar, irradiation produced the appearance of a series of additional oscillations in the longitudinal resistivity trace, whose periodicity is connected to the cyclotron transition: they were

termed MIROs and, when reaching vanishing resistivity, re-named zero-resistance states (ZRSs).[405, 406] The first reported measurements are shown in Fig. 7.2.

Initially, ZRSs were observed in the ρ_{xx} traces of irradiated samples where MPR was not detected.[406] On the other hand, on geometrically similar samples, but with lower mobility, a decade earlier MPR was measured but no MIRO.[389] This initially lead to think that MPR and MIRO would be mutually exclusive, or even that they could be two sides of a similar phenomenology for different sample parameters, especially mobilities.[407]

Phenomenologically, it is clear that the periodicity of the MIRO is related to the cyclotron frequency of the material, since the magnetic field B_j, at which the j-th minimum of the MIROs takes place, is related to the cyclotron transition according to the formula

$$B_{\pm j} = \frac{\pm B_f}{\mid j \mid + \frac{1}{4}} \quad j \in \mathbb{Z}. \tag{7.4}$$

B_f is the magnetic field for which the irradiating microwave frequency f_{MW} is resonant with the cyclotron transition,

$$B_f = \frac{2\pi m^*}{e} f_{MW}, \tag{7.5}$$

j is the order of the sub-harmonic and $1/4$ is a phase shift that appears to decrease for increasing j. The specific value of the phase shift is still debated[408, 409], but Eq. (7.4) can be considered correct at least for the first sub-harmonics.[410, 411]

The measurements in Fig. 7.2 show both MIRO/ZRS and MPR. They were often recorded together in Hall-bar-shaped samples, when the irradiation frequency is above the MPR minimum, proving that the two phenomena can coexist. Moreover, MIRO were detected also when the irradiation frequency is lower than the MPR minimum (several data from the literature have been collected in appendix E on page 247). These facts hints to the independence of the two phenomena. Hatke and coworkers took advantage of this independence between the two phenomena to investigate the lowest value of resistivity for a ZRS: by fitting the MPR peak, first alone and then tuned into a ZRS, they hint to the fact that ZRS are not states where the system posseses no resistance, but they are the result of instabilities in the sample trying to avoid a state with negative resistivity.[412].

Another interesting observation can be made on the interplay between CR and MPR. Despite the fact that the for low B-fields MPR and CR were never measured together, being the first an electrodynamical correction of the second, the MIRO were always measured with minima connected to the CR-value and not the MPR-one. This might point at the fact that, due to the lateral confinement, the MPR becomes preponderant over the CR but the latter does not disappear, but just weakens.

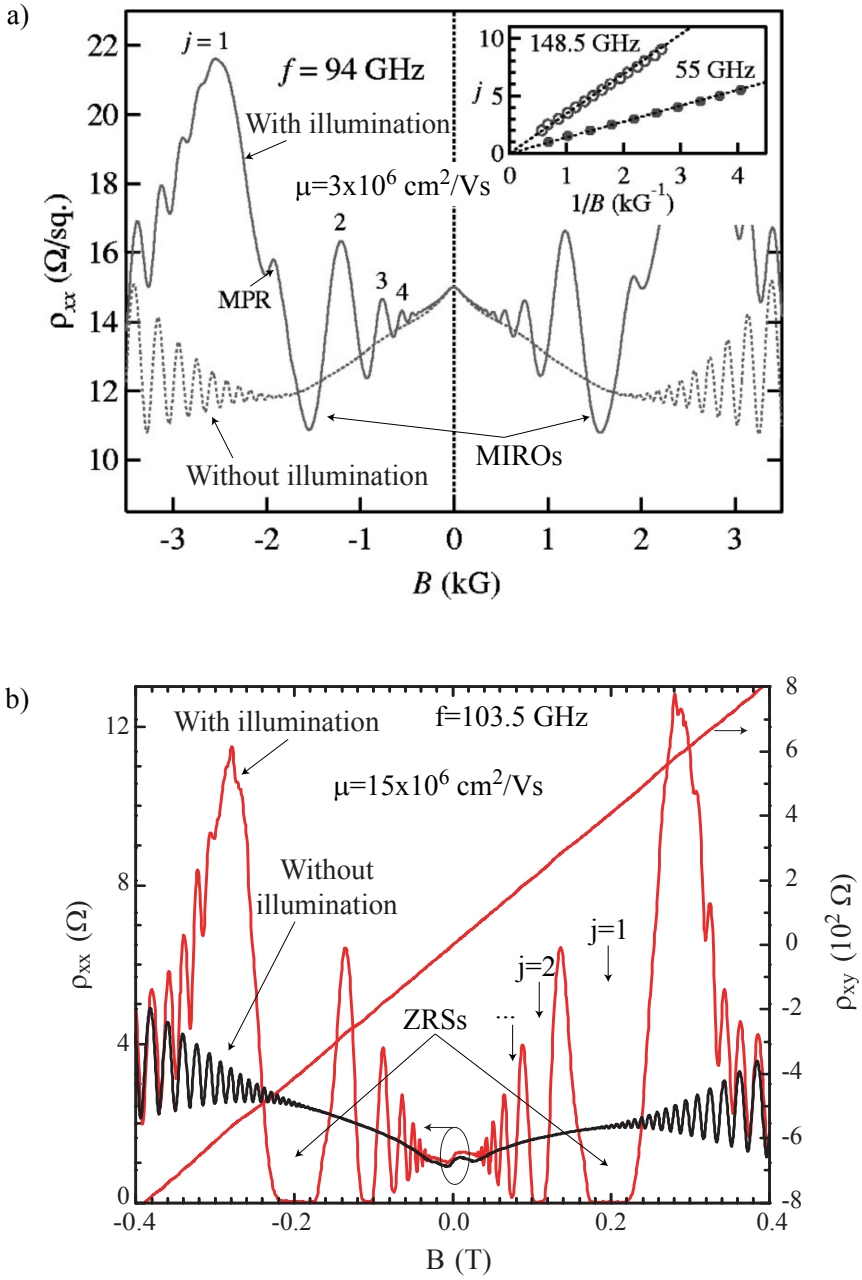

Figure 7.2 – a) First reported MIRO measurement, adapted from [405]. The index j indicates here the MIRO maxima. b) First reported ZRS measurement, adapted from [406]. The index j indicates here the MIRO minima, the first two developed into ZRSs. The transversal resistivity is also plotted and it is unchanged under irradiation. Note that the main difference lies in the mobility, 5 times higher for the sample displaying ZRSs.

After the first reports[405, 406], MIROs have been investigated extensively spanning a large range of parameters. The results on the appearance of the MIROs are collected below for the GaAs/AlGaAs material system from several publications.[390, 391, 412, 413, 414, 415, 416, 417, 418, 419, 420, 421, 422, 423, 389, 424, 425, 426, 427, 422, 428, 429, 430, 431, 432, 433, 434, 435, 436, 437, 438, 439, 440, 441, 442] The complete information is collected in appendix E on page 247.

Source frequency MIROs were observed, on different systems, for a wide range of frequencies spanning from 2 GHz to 1.6 THz.[439, 425] Often the effect vanishes at the edges of the interval and it is therefore mostly studied for frequencies approximately in the range $30 - 150$ GHz.

Source power When varying the power of the microwave source, the amplitude of the oscillations varies accordingly, often showing a linear dependence for low intensity, that becomes sublinear for higher powers.[412] Most investigations were carried out with a source power of the order of 1 mW, nonetheless spanning a big range from few microwatt to several tens of milliwatt.[409, 437] Eventually, the amplitude saturates for very intense irradiation.[435]

Source polarisation Frequency and phase of the MIROs were shown to be insensitive to the polarisation of the microwave radiation.[419] On the other hand, the amplitude of the oscillations seems to be maximal for microwave polarisation parallel to the current flow in the Hall-bar and minimal in the orthogonal configuration, while it is insensitive to a variation of angle for circularly polarised light.[419, 443] Additionally, it was shown insensitive to the handedness of the circular polarisation.[444]

Sample mobility Maybe the most important parameter, the carrier mobility is tightly connected to the scattering time and it is used to estimate the magnetic field for which the 2DEG gets quantised. MIROs were reported for GaAs/AlGaAs samples with mobility starting at about 2×10^6 cm^2/Vs, whereas ZRSs were often, but not always, reported for much higher mobilities of about 10×10^6 cm^2/Vs.[439, 442, 427, 418] important to note that this is the key parameter that enabled the discovery of the MIRO/ZRS phenomenon, since researchers from the same group performing the same kind of measurements in the same conditions, with samples with the same geometry *but* different mobilities, for the low mobility sample (1.2×10^6 cm^2/Vs) reported MPR[389] while for the high-mobility sample (15×10^6 cm^2/Vs) ZRS were discovered[406]. The lowest reported mobility for a sample displaying MIRO in a GaAs/AlGaAs system is 0.56×10^6 cm^2/Vs.[440]

2DEG density The phenomenon is expected to disappear for too high carrier densities, being most investigations performed at about 5×10^{11} cm^{-2} electronic charge density. Nonetheless the investigated samples range from 1.3 to 10×10^{11} cm^{-2}.[413, 427]

Sample temperature MIROs appear below 10 K, being best visible about 1.5 K, with reports in the range $0.05 - 2$ K.[438, 405]

Sample geometry and dimensions MIROs have been mainly detected in Hall-bar- and van-der-Pauw-shaped samples with relatively large dimensions: the smallest dimension was always above 50 µm, often reaching several hundreds of microns or even several millimetres.[406, 426, 412] Corbino disks are also a common geometry for magneto-resistance measurements and systems with such shape also showed MIROs.[445, 441] To the best of our knowledge, only Bykov reported a measurement onto a single 5×10 µm^2 Hall-bar.[446] This result will be discussed more extensively later in the chapter. Finally, another system for the study of magneto-plasmon excitations are anti-dot lattices etched into a 2DEG: the reported attempts seem to not influence the MIRO but rather the MPR.[391, 423, 429, 430]

2DEG type As already mentioned, most investigations were performed onto the GaAs/AlGaAs material system, whose 2DEG is either formed in the triangular well at the interface or into a GaAs quantum well created between AlGaAs barriers.

Soon after, alternative two dimensional systems were investigated. Two dimensional hole gases (2DHGs) in the same GaAs/AlGaAs material system were measured displaying no MIRO.[447, 448] No MIROs were also reported for 2DEGs in Hg/CdHgTe[449], SiC-graphene[450], Si/SiGe[451] and for the first attempt in MgZnO/ZnO[452]. The last two systems showed nonetheless MPR. MIROs were instead successfully measured in a 2DHG in strained Ge/SiGe[453] and in a subsequent attempt on MgZnO/ZnO[454]. Additionally, very similar oscillations were measured for the 2DEG on the surface of liquid helium[455, 456].

Concomitantly with the discovery of the MIRO, several different kinds of oscillations of the longitudinal resistivity of a 2DEG were reported. Two of the most studied are the Hall field-Induced Resistance Oscillation (HIRO) and the (acoustic-)Phonon-Induced Resistance Oscillation (PIRO). The HIROs are present in the differential resistance trace when driving a current through the Hall-bar[457], while the PIROs are due to resonant interaction of the 2D electrons in high Landau levels with the acoustic phonons[458].

These results hint at the fact that a general mechanism should be present to encompass all experimental observations.

7.1.1 A brief review of the different theories

In order to explain and understand the MIRO phenomenon, different theoretical models have been and are being developed to account for the oscillations in the magneto-conductivity of the sample starting from the microscopical effects.[2]

Most of the proposed theories associate the phenomenon to non-equilibrium phenomena in high-filling-factor Landau levels.[410]

The biggest class of theories, which relies on the so-called "displacement" mechanism, connects the MIROs to the spatial displacement of semiclassical electronic cyclotron orbits that would result into the breaking of the Landau-levels transition selection rule (Eq. (0.34)), taking advantage of disorder-, impurity- or phonon-scattering.[459, 460, 461, 462] As sketched in Fig. 7.3, the photon ω would promote in energy the electron into the landscape of electric-field-tilted Landau levels and the scattering would help the electron reaching the closest level, up- or down-stream, according to the photon frequency. Depending on whether the electron increases or decreases the electrostatic field, one measures an effective enhancement or reduction of the magneto-conductivity of the sample.

Another very strong theory class relies on the "inelastic" mechanism, which proposes that MIROs originate from a modification of the non-equilibrium electronic population of the Landau levels, broadened by disorder, as sketched in Fig. 7.4.[463, 442] In fact the total longitudinal conductance of a Hall-bar is proportional to the derivative of the distribution function, usually positive for equilibrium conditions Under irradiation, this quantity changes sign due to the presence of areas with inverse filling in the momentum-symmetric part, leading to oscillating magneto-conductance.

Another theory addressed the phenomenon to semi-classical microwave-driven electron orbits.[464] This theory treats perturbatively the effect of elastic scattering due to randomly distributed charged impurities on the exact solution for the harmonic oscillator wave function in the presence of radiation. The MIROs/ZRSs are then explained as the result of the interplay of the electron microwave-driven orbit dynamics with the Pauli exclusion principle, as sketched in the panels of Fig. 7.5.

One should note that all previous theories, relate the MIROs to phenomena taking place *inside the bulk of the 2DEG*. The down-side of this is that they have troubles explaining ZRSs. In fact those theories consequently predict the presence of negative-resistance states that would be measured as ZRSs only thanks to a out-of-equilibrium

[2]The most articulated and relevant theories are briefly discussed here, but, for a more complete discussion, the interested reader is invited to consult the referenced and citing articles of the references, as well as subsequent work from the same authors.

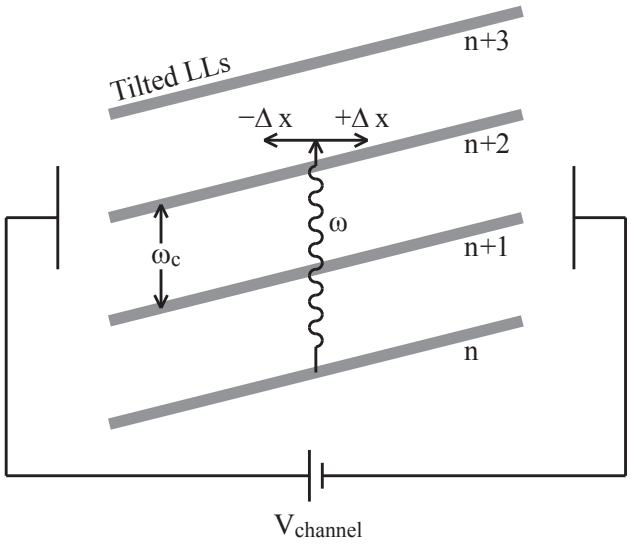

Figure 7.3 – Representation of the displacement mechanism for the origin of the MIRO: $V_{channel}$ indicates the voltage applied to the Hall-bar, n indexes the Landau levels while ω indicates the absorbed photon. Further explanation can be found in the text. Adapted from [459].

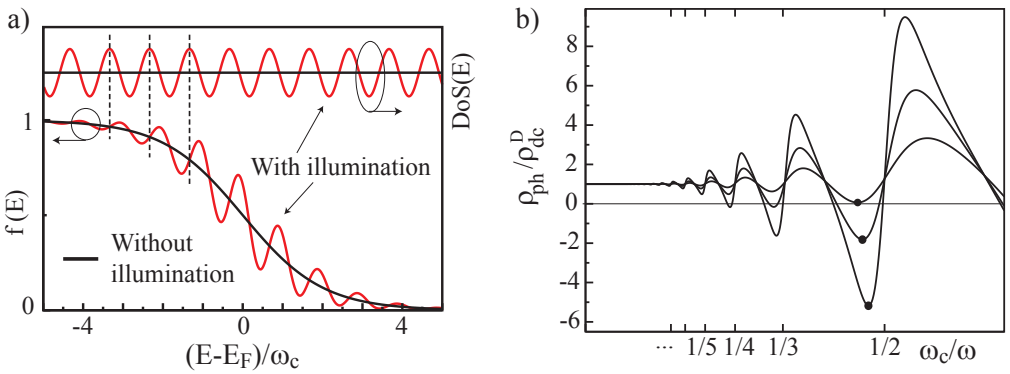

Figure 7.4 – Representation of the inelastic mechanism for the origin of the MIRO. a) Distribution function $f(E)$ and density of states $DoS(E)$ under microwave irradiation (red) and unperturbed (black). b) Calculated effect on the normalised resistivity. Adapted from [463].

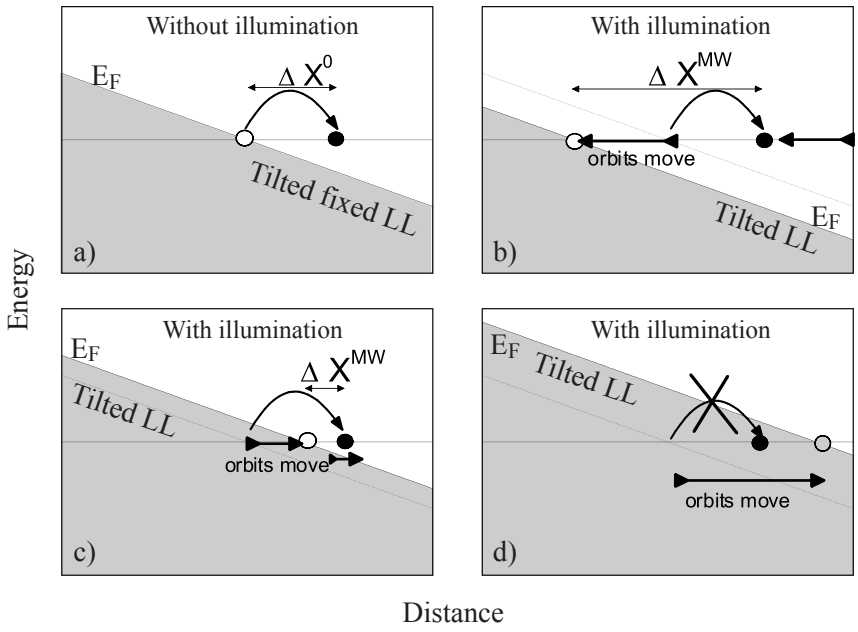

Figure 7.5 – Representation of the semi-classical microwave-driven electron orbits theory for the origin of the MIRO. a) An electron would scatter by ΔX^0 due to some impurity. Because of the microwave field, the tilted Landau levels oscillate (bold horizontal arrows) and, depending on the relative phase, the electron scattering is b) enhanced, c) reduced or d) quenched. Adapted from [464].

compensation of all currents with the formation of domains.[412] In order to overcome these issues other theories where developed focussing the attention on the edges of the samples.

Another extensive theory explains the MIRO oscillations as resulting from plasmonic excitations of near-contact regions that get depleted of, or filled with, electrons, as sketched in Fig. 7.6.[465, 411] When the 2DEG in front of the contact is depleted, the electrons propagating along the edges in skipping orbits cannot enter the contact and a lower resistivity is measured. These conductivity oscillations are explained via a "ponderomotive force". Mikhailov observes that MPR and MIROs are present independently in the irradiated measurements and that the MPR is a bulk phenomenon. He hence concludes that the MIRO could not be of the same kind, resulting in a phenomenon of a lower dimensionality (edge/surface).[407] One consequence of this theory is also that the same arrangement of contacts should produce the same MIROs, irrespectively of the Hall-bar shape. This also sparked quite some unresolved discussion.[466, 467]

Finally, another theory attributes the MIRO phenomenon to microwave-stabilised edge transport.[468, 469] The theory was developed noticing the parallelism with magneto-transport at low filling-factors. In fact, for strong magnetic fields, the Landau levels are

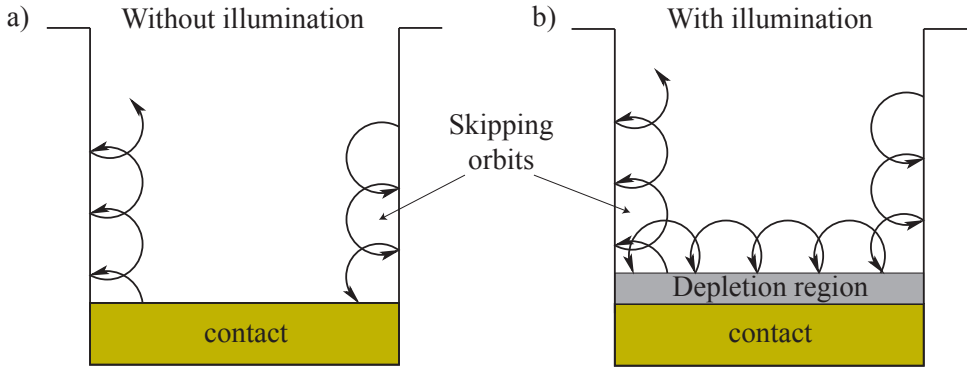

Figure 7.6 – Representation of the ponderomotive force theory for the origin of the MIRO: a) without illumination, the electrons propagate along the edges into the contacts. b) Under microwave-irradiation, a depletion region can form that detaches the contact from the channel, resulting in lower measured resistivity. Adapted from [465].

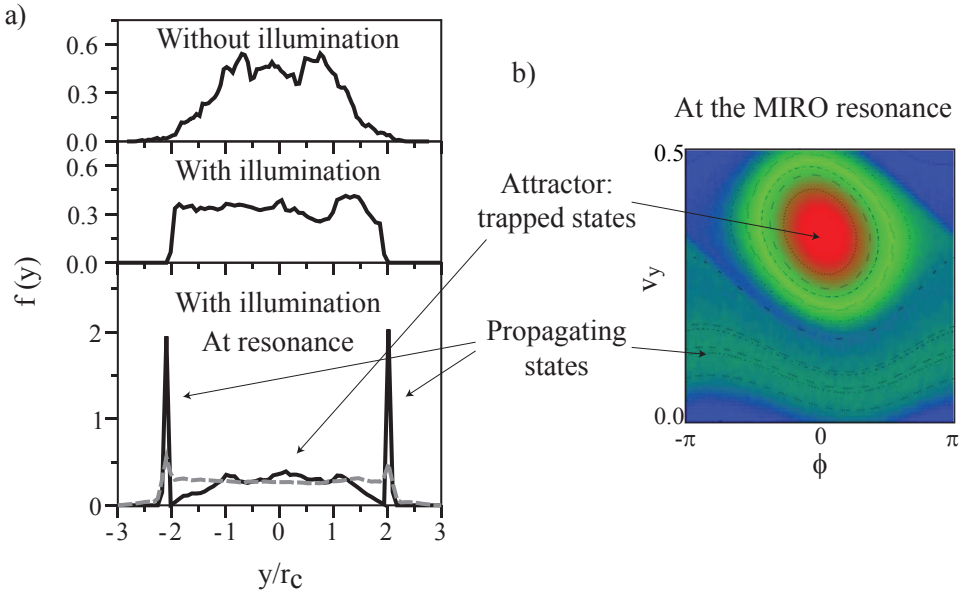

Figure 7.7 – Representation of the microwave-stabilised edge transport theory for the origin of the MIRO. a) The electrons in a Hall-bar are more present in the centre of the channel than at the edges (top graph). When microwaves illuminate the sample, the distribution function across the channel $f(y)$ is more homogeneous (middle graph). If the radiation is tuned at resonance with the phase-shifted cyclotron transition (MIRO resonance), the electrons accumulate at the edges of the channel (bottom graph). b) This corresponds to the formation of an attractor in the Hall-bar channel for electrons with strong orthogonal components of the velocity v_y, while edge electrons are free to propagate. Φ is the phase difference between the microwave radiation and the cyclotron transition.[468, 469]

well separated in energy and electron propagation occurs along the sample edges that become ballistic (cf. section 0.1.2 on page 11). This is connected to the fact that the cyclotron radius becomes much smaller than the electron mean free path. This would not be the case for the low-B-field, high filling-factors condition at which the MIROs occur. Instead, with methods similar to the ones used in chaos theory, it was calculated that, for certain irradiation frequencies, an attractor is formed that allows edge electrons to propagate almost ballistically also at low B-fields, as shown in Fig. 7.7 (more details in the legend).

For one decade now, a big effort, both experimental and theoretical, has been put into understanding such effect, nonetheless, there is no agreement on which could be the true origin of the MIROs and additional investigations are needed. The results presented in this manuscript will be able to shine some more light onto some of these aspects.

7.2 Idea underlying the performed investigation

The idea underlying the present investigation relies on the fact that the USC between the SRR modes and the cyclotron transition creates polaritonic states as discussed in chapter 6. These mixed states can be seen as effectively shifted cyclotron transitions and photonic modes. This is illustrated by the anticrossing in Fig. 7.8, that will be discussed in detail in section 7.6.1.

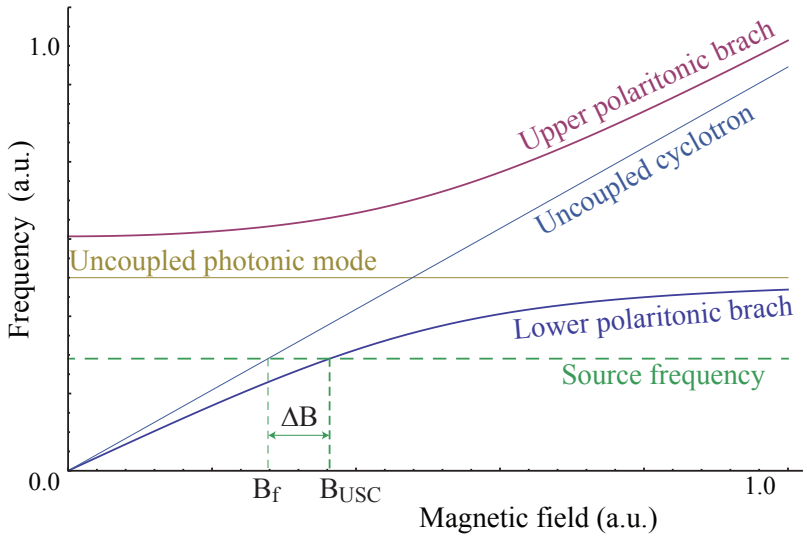

Figure 7.8 – Principle of USC-detection via the MIRO phenomenon: the thick lines show an anticrossing due to ultra-strong coupling. If the sample in such condition is illuminated by radiation of a given frequency (dashed green line), lower than the uncoupled photonic mode (yellow line), it crossed the lower polaritonic branch at B_{USC}. In a sample without USC, the crossing would take place at B_f. The two values create two different MIRO sets, according to Eq. eq:miro:shifted-minima.

At this point, let us only state that the MIROs measured on the ultra-strongly coupled system should then be correspondingly shifted with respect to the ones measured on the uncovered Hall-bars. In fact, if the cyclotron is resonant with the GHz-source at B_f according to Eqs (7.4)-(7.5), one of the polaritonic branches will be resonant with the same source at a shifted magnetic field $B_{USC} = B_f + \Delta B$. Using the quarter-phase-shift formula, the shifted minima corresponding to the SRR-covered Hall-bar should take place at

$$B_{\pm j}^{USC} = \frac{\pm B_{USC}}{\mid j \mid + \frac{1}{4}} = B_{\pm j} + \Delta B_{\pm j}^{USC} \quad j \in \mathbb{Z}. \tag{7.6}$$

This is visualised in Fig. 7.8 as the crossing points between the "source frequency" line and the "uncoupled cyclotron" and the "lower polaritonic branch" lines.

This might point at the fact that, due to the lateral confinement, the MPR becomes preponderant over the CR while the latter does not disappear, but just weakens. Supporting data in this directions were measured for USC-samples where the SRR-frequency is below the MPR-minimum, i.e. where no matter excitation should be present any more.[470] They show an interaction between the cavity mode with an unexpected resonance consistent with the CR, despite the system being etched such that the MPR minimum lies at higher frequencies.

7.3 Setup for MIROs

The measurements were performed with a liquid-He-cooled *Janis Research Company* superconducting magnet, allowing the magnetic field to vary in the range ±12 T (cf. section 2.2 on page 59). This is a vertical-solenoid magnet provided with bottom optical opening through quartz windows. The temperature of the sample can be set in the range 1.5 – 300 K because the superconducting magnet is built in such a way that the sample is placed in a "variable-temperature inset". This is thermally isolated from the He-bath and its temperature can be controlled with a combination of He-gas flow through the needle valve, pump-controlled under-pressure and PID-stabilised heater at the sample-holder and at the inner-most window.

In order to perform the presently discussed transport measurements, the magnet was cabled with 24 high-resistance constantane woven loom wires (*CMR direct*): each wire has a diameter of about 110 µm and a resistance of 66 Ω/m, constant in temperature. The high resistance helps keeping the sample thermally insulated from the room-temperature instrumentation, while the fact the wires are weaven in pairs helps avoiding pick-up signal induced from oscillating sources.

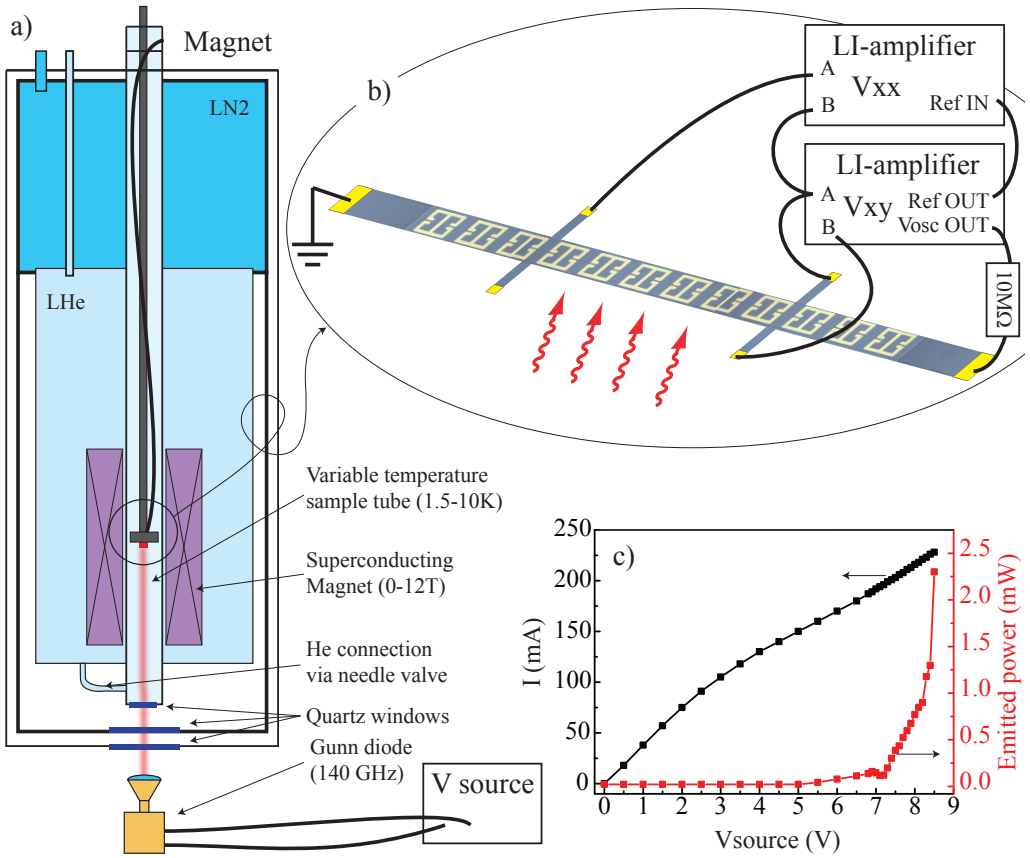

Figure 7.9 – a) Setup used for the MIRO measurements: the sample is placed in the sample tube and is illuminated by the radiation emitted by the Gunn diode. b) The longitudinal and transverse voltages of the Hall-bar are measured with two Lock-in amplifiers, one of which is also used as voltage source. c) Calibration of the emitted power by the Gunn-diode as a function of the bias V_{source}.

On the one end, the wires of the cable were soldered to the pins of the chip socket, where the chip carrier is fixed during the measurements (*E-tec interconnect*, LCC-series). The socket is a plastic housing with 32 pins that accommodates and electrically contacts the ceramic sample carrier. The latter has gold-plated little pads from which the sample can be wire-bonded, once glued to its base. At the other end of the cable, a 24-pins connector (*Fischer*) allows electrical access to the sample in the middle of the superconductive solenoid.

At the external connector a self-made box is plugged where the different lines are brought to individual BNC-connectors, each of them provided with a switch to keep the line grounded while changing the cables. These are in turn connected to several *EG&G* lock-in amplifiers and some *Keithley* sourcemeters. One lock-in amplifier is needed per measured voltage in the sample (V_{xx} and V_{xy}). The setup varied from two instruments for the measurement of a single Hall-bar to four for measuring two together. The AC-current is sourced by one of the lock-ins by setting the voltage source of the internal oscillator

and closing it onto the series of a 10 MΩ resistor and the sample, as sketched in panel b) of Fig. 7.9. Since the sample has a lower resistance, of the order of few kΩ, one can assume that a constant current is flowing into the Hall-bar channel, usually in the range 10–200 nA, and the resistivity is derived by dividing the measured voltages by the current, eventually corrected by the form factor as shown in section 0.1.2 on page 11. When needed, one DC-sourcemeter is used to apply a DC-bias to the gate with respect to the Hall-bar channel, measuring at the same time the leakage current. All these measurements are controlled by labview programs written for the specific purpose.

Microwave radiation is produced by a Gunn-diode oscillator at 140 GHz (*SAGE millimetre*) and is linearly polarized with 95% suppression. This is provided with a 2-inches horn antenna on top of which a lens with 15 cm-focal distance is mounted. This emits towards the bottom window of the cryo-magnet, using the 2-inches VTI as a waveguide. For some measurements, an additional 9 mm-diameter light-guide was installed to bring the light closer to the sample surface but no improvement was detected. The power transferred into the sample compartment by such arrangement was measured via a Thomas Keating absolute power-meter to be about 2.3 mW when the Gunn-diode is biased at the maximum voltage. The biasing is performed with an *HP* current source that is controlled manually. A sketch of the set-up is given in panel a) of Fig. 7.9 while panel c) shows the dependence of the emitted power on the bias applied to the device. The calibration is used to convert the applied voltage into emitted power when performing the power-dependence studies discussed in section 7.6.1.

7.4 Investigated samples

Two series of samples were investigated. The first series[3] is constituted by samples $A1452$, $B1452$, $C1452$, $D1452$ that are the transport counterpart of the samples displaying ultra-strong coupling in Ref.s[47, 374, 368], some of which were discussed in section 6.4 on page 151. The samples are constituted by a Hall-bar etched into the 2DEG $EV1452$ (growth sheet in appendix A.2 on page 235) and covered with direct SRRs of the kind of the ones discussed in chapter 3. In particular, samples $A1452$, $B1452$ contain dSRR exactly as the ones sketched in Fig. 3.2 on page 83 but for the vertical side that is 36 µm long instead of 34 µm. This results in a small reduction of the resonant frequency but without affecting any other characteristic of the dSRR, as shown in appendix F on page 251. Pictures of the samples can be found in Fig. 7.15.

[3]Samples $A1452$, $B1452$, $C1452$, $D1452$ were processed by C. Rössler in the group of Prof. Ensslin at ETHZ and in the clean room facility FIRST.

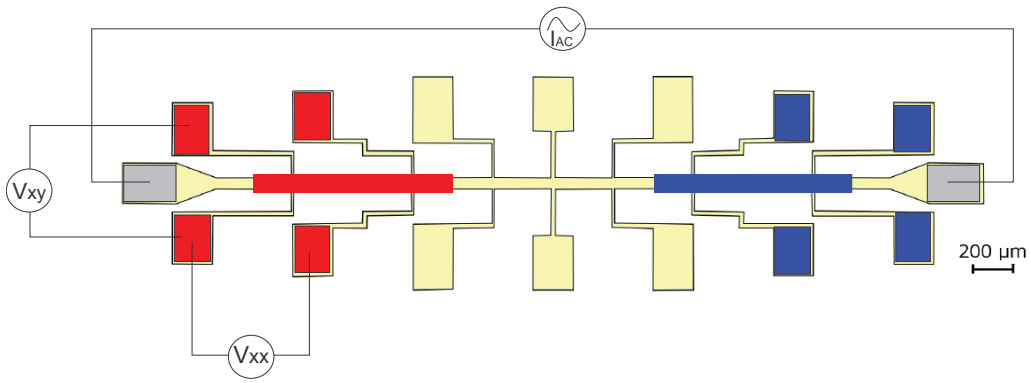

Figure 7.10 – Sketch of the samples investigated for the MIRO measurements. Three Hall-bars (red, yellow and blue) are identified onto a single channel. The transport measurements are performed as drawn, for each single Hall-bar. The drawing represents exactly samples of the first series −1452. Samples of the second series are similarly conceived, but usually contain four Hall-bars and have the contacts further apart, as shown in Fig. 7.25.

The second sample series[4] is constituted by samples $A2109a$, $A2109b$, $C2124$, $G2124$, $K2124$ which employ a single complementary-SRR (cSRR, cf. section 3.2 on page 86), whose central gap can allocate either an entire side or the whole of the Hall-bar channel. The contact lines used to measure the longitudinal voltage join the channel within the cSRR's gap, leaving no part of the Hall-bar channel side uncoupled. These samples were realised with the 2DEGs $EV2109$ and $EV2124$ (growth sheet in sections A.4 and A.3 of appendix A on page 233). Pictures of the samples can be found in Fig. 7.25.

The main difference between the 2DEGs is the electron mobility: $EV1452$, $EV2109$ and $EV2124$ showed $\mu = 0.8 \times 10^6$ cm^2/Vs, 0.6×10^6 cm^2/Vs and 1.7×10^6 cm^2/Vs, respectively at electron carrier densities of approx. $n_s = 3 \times 10^{11}$ cm^{-2}.

All samples contain at least an SRR-covered- and an uncovered-Hall-bar realised by placing multiple sets of contacts along the same channel, as sketched in Fig. 7.10, but separated enough to avoid cross-talks. The specific placement of the SRRs on the Hall-bars will be discussed later concomitantly with the respective MIRO measurements. The next section deals instead with the MIRO measurements on the uncovered Hall-bars. Thus, the relevant parameters distinguishing the different samples are the 2DEGs' density and mobility of the specific heterostructures/samples and the width of the etched Hall-bar channels.

[4]The samples $G2124$, $A2109a$, $A2109b$, $K2124$, $C2124$ were processed by G. L. Paravicini Bagliani in Prof. Faist's group at ETHZ and in the clean room facility FIRST.

7.5 MIROs in uncovered Hall-bars

In this section we present the MIRO investigation performed on Hall-bars with different channel widths. These results will allow us to introduce experimentally the phenomenon and to discuss the measurements that will be the reference for the SRR-covered samples discussed in the next sections.

Let us start by discussing the measurements performed on sample $B1452$. The longitudinal (V_{xx}) and transverse (V_{xy}) voltages were measured at the contacts as shown in Fig. 7.10 while sweeping the perpendicular magnetic field, the sample being at a temperature $T \simeq 2$ K. An oscillating current of 200 nA at 74.7 Hz was applied between source and drain and V_{xx} and V_{xy} were detected with lock-in amplifiers while all other contacts were floating. V_{xx} and V_{xy} were then converted into the longitudinal and transverse resistivities ρ_{xx} and ρ_{xy} according to Eqs (0.14).

The resistivities ρ_{xx} and ρ_{xy} were first measured for the sample in the dark, producing the black curves in Fig. 7.11. The ρ_{xx} trace shows Shubnikov-de Haas (SdH) oscillations starting from $B = 0.3$ T. In this low magnetic field range, the ρ_{xy} trace is a straight line with no plateaux from the quantum Hall effect. From the two curves one can extract a total (Hall) sheet electron density of about 5.35×10^{11} cm^{-2} and a mobility of 814000 cm^2/Vs. The periodicity of the SdH oscillations corresponds to a sheet carrier density of 3.0×10^{11} cm^{-2}. This value is almost 2 times smaller than the one derived from the transversal resistivity, denoting that almost half of the total charge is not contributing

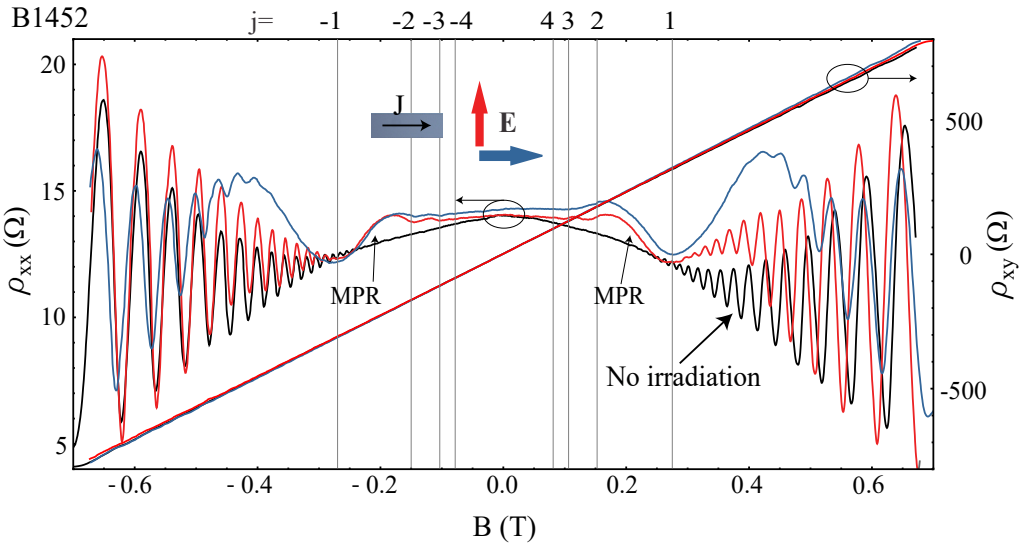

Figure 7.11 – ρ_{xx} and ρ_{xy} traces measured on the bare Hall-bar of sample $B1452$, for microwave irradiation in the two orthogonal polarizations (red and blue, correspondence with the arrows in the inset) and with no irradiation at all (black). Clear MIRO minima are present while the Hall resistance shows no feature.

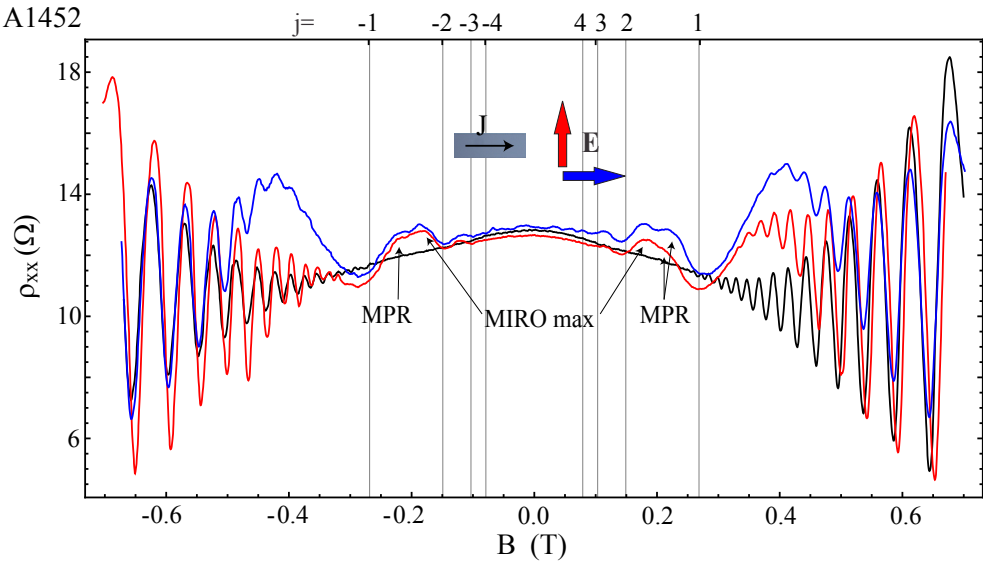

Figure 7.12 – ρ_{xx} traces measured on the bare Hall-bar of sample $A1452$, for microwave irradiation in the two orthogonal polarizations (red and blue, correspondence with the arrows in the inset) and with no irradiation (black). Clear MIRO minima are visignle up to $j = 3$.

to the longitudinal transport. The reason is unclear, but the measurements do not show any evidence of parallel conduction. Additionally, the calculations predict correctly the position of the observed MPR peaks, when using the sheet density obtained from the SdH oscillations. This will hence be the one considered in the following.

After the first measurement in the dark, the Gunn-diode is switched on with beam polarization orthogonal to the Hall-bar channel and the same measurement performed again: the red curves result. The sample is then rotated by 90° so that the beam polarization is now parallel to the Hall-bar channel: the measurements are shown in blue.

In the irradiated ρ_{xx} traces, oscillations appeared in the low-B-field region $[-0.4, 0.4]$ T, superimposed to the SdH oscillations. In ρ_{xy} instead, no relevant modification is detected. The vertical lines and the values displayed on the top of the frame identify the expected position of the first four minima of the MIROs, according to the empirical formula of Eq. (7.4), $B^j_{min} = 0.33\text{T}/(\mid j \mid +\frac{1}{4})$=0.27 T, 0.15 T, 0.10 T, 0.08 T. We can therefore conclude that the measured oscillations are MIROs.

Considering in more details the ρ_{xx} traces, a small increase in the resistivity at zero magnetic field is present in the blue irradiated curve, the one for the polarization along the channel, consistent with an expected better absorption in this configuration. Applying then an increasing magnetic field in either direction, the resistance starts to oscillate showing up to 3 or 4 minima with the values close to the expected MIRO B-field positions. The two polarizations show on-sets of the SdH oscillations at higher B-fields than the non irradiated trace, confirming some heating in the 2DEG, once again more pronounced for

polarisation along the Hall-bar channel. Nonetheless all SdH oscillations have a close phase and almost overlap at the edge of the displayed B-field range, denoting a very small change in the carrier density. Interesting is also the fact that the first maximum at about ± 0.435 T is absent in the red curve, the same curve that reconcile with the black one faster than the blue one. This could be again addressed to less radiation coupling.

Moreover, a very faint shoulder appears between the first two minima at about ± 0.235 T and it is consistent with the expected magneto-plasmon resonance given by Eq. (7.2). This feature is better seen at about $B = \pm 0.23$ T for sample $A1452$, whose measurements are reported in Fig. 7.12.

7.5.1 Channel-width dependence of the MIROs in uncovered Hall-bars

For each sample of the series, an SRR-covered Hall-bar was realised along to the corresponding uncovered-Hall-bar. Specifically, the channel widths are ranging from 4 µm to 60 µm allowing a quite extensive study of the MIROs with respect to this parameter. Additionally, for some pairs of samples, the ones showing MIROs the others not, this is the main difference, confirming the fact that it is a relevant dimension that a MIRO theory must take into account.

Therefore, in the following we discuss the aggregated data from the MIROs on the uncovered Hall-bars. This is based on the presence/absence of the MIRO minima in the measured irradiated trace and on the amplitude of the MIROs, averaged between the first minimum at $B_1 \simeq 0.27$ T and the following maximum at about $B_{1,2}^{max} \simeq 0.20$ T. The single measurements are reported throughout this chapter and appendix G on page 253, where they are used as reference for the traces on the SRR-covered Hall-bars.

The average amplitude of the MIRO oscillations is plotted against channel width in Fig. 7.13, for all investigated uncovered Hall-bars, averaged also between positive and negative B-fields. The Hall-bars with width smaller than 20 µm show no MIROs, while they are present in wider samples. Specifically, the samples with channel width of 4 µm are $A2109$ (measurements plotted in Fig. 7.26) and $G2124$ (Fig. 7.31) while sample $K2124$ (Fig. 7.27) has a channel width of 15 µm. Instead all samples of the first series, $A1452$ (Fig. 7.12), $B1452$ (Fig. 7.11), $C1452$ (Fig. G.9), $D1452$ (Fig. G.10), and sample $C2124$ (Fig. 7.28) have channel widths equal to or wider than 38 µm and all show MIROs with different amplitudes.

From the available points, it is reasonable to conclude that the presence of the MIRO oscillations depends on the width of the channel. The dashed blue line interpolating the

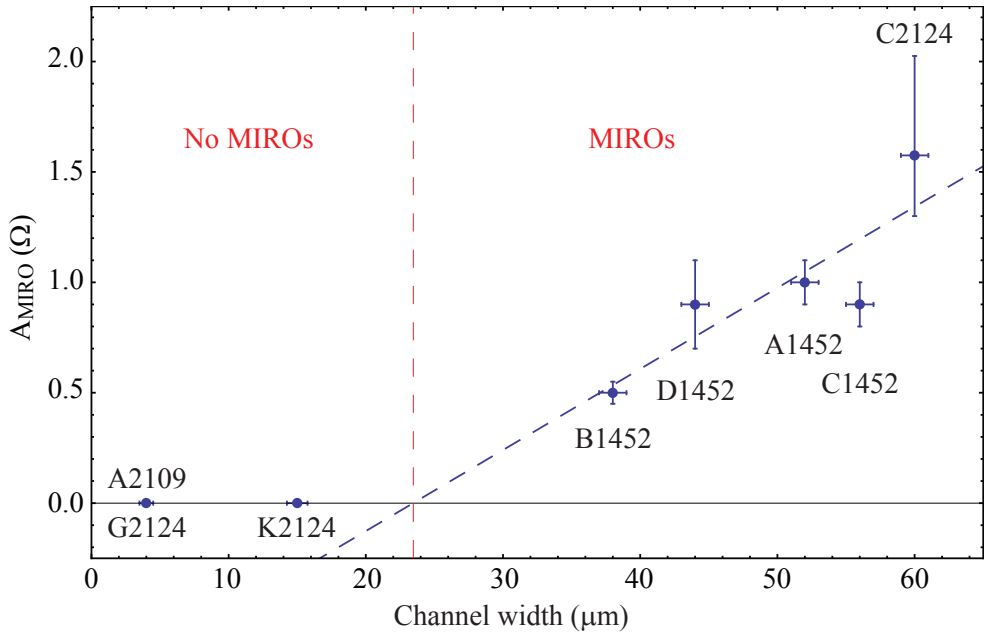

Figure 7.13 – The average amplitude of the MIRO oscillations is plotted against channel width for all investigated uncovered-Hall-bar samples. This shows a clear threshold in channel width to see the phenomenon.

points in Fig. 7.13 is a linear fit, but in absence of a defined MIRO theory it is meant as a guide to the eye. Additionally, note that the data are extracted from measurements performed under the same conditions of irradiation, current density and temperature, on samples realised in the same material system but with different channel lengths. In a final MIRO theory the oscillation amplitude might depend on these latter values, thus requiring some normalisation procedure to quantitatively compare the points, nonetheless leaving valid our qualitative comparison.

The fact that Hall-bars realised with the same heterostructure but with different channel widths respond differently to GHz-irradiation already allows us to rule out some of the proposed MIRO theories. In fact, the "displacement" theory, the "inelastic-mechanism" theory and the "driven semiclassical-orbits" theory (cf. section 7.1.1) treat the MIRO as a "bulk" phenomenon or, in any case, describe it from an infinite-sample perspective, as if the reduction of the sample area would have no consequences.

One might argue that reducing the sample area reduces also the radiation-2DEG coupling, thus naturally reducing the effect. Instead the effect on the samples does not seem to depend on the polarisation of the incident radiation, maybe also due to some polarisation mixing inside the sample compartment in the magnet. In any case, no MIROs are observed for samples with narrow channels, in spite of the fact that the length of their channel (41 µm) is up to one order of magnitude larger than the width. In samples with

width of such dimensions MIROs were measured. To sum up this point, the mentioned "bulk" theories cannot explain this behaviour and should be put aside or modified.

Two theories, instead, take into account the finiteness of the sample: the "ponderomotive-force" theory and the "stabilised edge-transport" theory.

The "ponderomotive-force" theory addresses the MIRO to plasmonic oscillations at the contacts and concludes also that similar contact arrangements should give the same effect.[411] We can then exclude also this theory because all investigated samples use the same design of contact pad. Additionally sample $C2124$, displaying MIRO, has exactly the same contacts arrangement as samples $A2109$, which show no MIRO.

At this point we move on to discuss the presented measurements with respect to the last of the considered theories. To gain some insight into the physics, the width of the Hall-bars is compared to the following, relevant lengths for a 2DEG in magnetic field: the electronic mean free path, the phase-coherence length, the magnetic length, the cyclotron radius, and the width for which the MPR is resonant with the used source at $B = 0$ T. The data are collected in Table 7.1 and plotted in Fig. 7.14.

The electron's mean free path is the distance travelled by an electron between two scattering events and is defined as the product of Fermi's velocity and the Drude scattering time τ_D

$$l_{mfp} = v_F \tau_D. \tag{7.7}$$

Fermi's velocity can be estimated, for a 2DEG, from the geometrical 2D-density of states as

$$v_F = \frac{\hbar\sqrt{2\pi n_S}}{m^*}, \tag{7.8}$$

where $k_F = \sqrt{2\pi n_S}$ is Fermi's wavevector and n_S the electron density. Instead τ_D can be calculated from the derived sample mobility μ as

$$\tau_D = \frac{\mu m^*}{e}. \tag{7.9}$$

This gives $l_{mfp} \simeq 8 - 15$ µm.

The scattering events can anyhow conserve the phase of the electron, being the phase-coherence length l_ϕ, defined as the length the electrons can travel before their coherence is lost, better suited for discussing the electrons' "memory". This can be calculated from the dephasing time τ_ϕ. Since for the parameters of the present investigation the thermal broadening of the levels is still bigger than the scattering broadening, τ_ϕ is given by[44]

$$\frac{1}{\tau_\phi} = \frac{\pi}{2}\frac{(k_B T)^2}{\hbar E_F} ln\left(\frac{E_F}{k_B T}\right), \tag{7.10}$$

where $E_F = \frac{1}{2}m^* v_F^2$. For the given situation, one obtains $\tau_\phi \simeq 50$ ps to be compared to $\tau_D \simeq 20 - 65$ ps, depending on the specific sample mobility and carrier density. In such a situation l_ϕ can be estimated as $v_F \tau_\phi$ to be approx. 12 µm. Therefore for the given samples characteristics $l_\phi \simeq l_{mfp}$.

The magnetic length is function of the magnetic field only

$$l_B = \sqrt{\frac{\hbar}{eB}} \tag{7.11}$$

and corresponds to length scale at which a specific B-field value confines the Landau levels. At $B = 0.33$ T, the field for which the microwave source is resonant with the cyclotron transition, $l_B = 0.044$ µm.

The cyclotron radius of the semiclassical orbits is given by

$$r_{cyc} = \frac{\hbar}{eB}\sqrt{2\pi n_S} \tag{7.12}$$

and at $B = 0.33$ T one gets $r_{cyc} = 0.27$ µm.

Finally, the zero-field MPR given by Eq. (7.1) is resonant with the used source and the measured carrier densities for channel widths about 30 µm.

All values calculated for the specific samples characteristics are collected in Table 7.1.

Table 7.1 – Collection of different important lengths in the investigated samples. All length are in µm and are plotted in Fig. 7.14.

Sample	w	l_ϕ	l_{mfp}	l_B	r_{cyc}	w_{MPR}	MIRO?
*A*1452	52	12.0	7.89	0.04	0.28	31.4	Y
*B*1452	38	11.7	7.36	0.04	0.27	30.2	Y
*C*1452	56	12.0	7.73	0.04	0.28	31.6	Y
*D*1452	44	12.0	10.7	0.04	0.28	31.6	Y
*A*2109	4	10.3	4.52	0.04	0.24	23.1	N
*K*2124	15	11.7	15.4	0.04	0.27	30.2	N
*C*2124	60	11.7	15.4	0.04	0.27	30.2	Y
*G*2124	4	11.7	15.4	0.04	0.27	30.2	N

The comparison is visualised in Fig. 7.14.

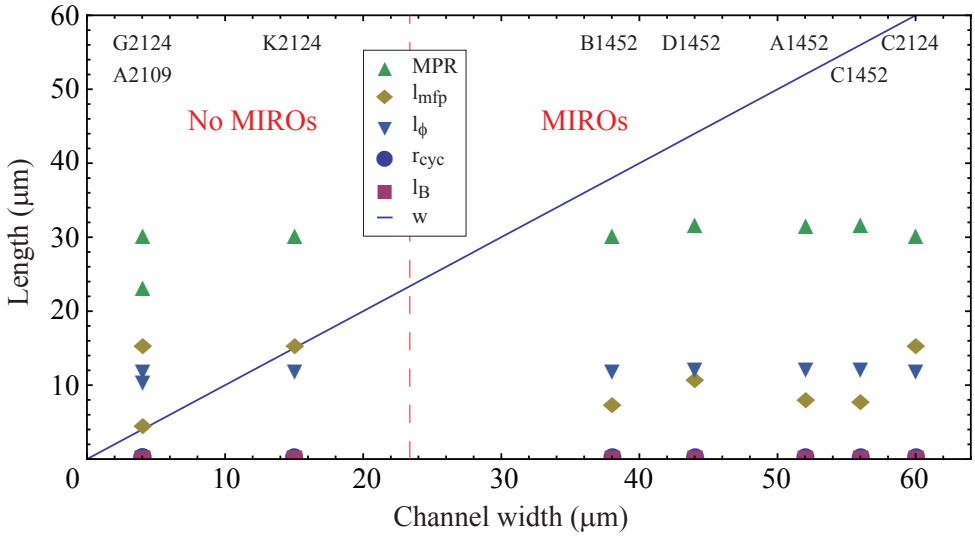

Figure 7.14 – Comparison of the relevant physical lengths (vertical axis) with the channel width for each investigated sample (blue line). The numerical data are reported in Table 7.1.

We can start the discussion by first disregarding completely the magnetic length l_B since it is always at least two orders of magnitude smaller than the relevant dimensions of the samples and it is the same for all samples, at a given magnetic field.

Instead, the cyclotron radius r_{cyc} plays a role when the magnetic confinement is such that the transport takes place by skipping orbits at the edges of the sample. At the low magnetic fields with which we work, it might not be completely the case, at least for the samples with lower mobility. In any case, the contact lines at the Hall-bar channel are 3 µm wide, thus one order of magnitude bigger than r_{cyc}. In such a case, the sample is not disconnected from the contacts and we can disregard also r_{cyc}, for the present discussion.

The correlation between the samples displaying MIRO and the ratio l_{mfp}/w between the mean free path l_{mfp} and the channel width w, shows that no oscillations are seen for samples where $l_{mfp}/w \geq 1$, while all samples showing MIRO have a ratio $l_{mfp}/w \leq 0.25$. This physically means that MIROs are not displayed by sample that are ballistic across the channel. This fact would support Chepelianskii's theory because, for the case of a ballistic channel in the width dimension, the edge channels would be shorted by electrons escaping from one side to the opposite.[468] On the other hand, it would contraddict the measurements performed on samples with very high mobilities, showing MIRO and ZRS.

A similar effect has been already reported by Bykov in Ref. [446], where the author compares MIROs measured on two Hall-bars with different channel dimensions, one with length times width of 450×50 µm^2 and one with 10×5 µm^2, where the electrons' mean free path in the 2DEG is $l_{mfp} = 25$ µm. The author showed a weakening of the MIRO's amplitude in the second Hall-bar addressing it to the fact that the electrons in the channel

are ballistic in both directions. Nonetheless no quenching of the MIRO phenomenon was seen. The present investigation, instead, shows the disappearance of the MIRO oscillations for Hall-bars that differ from others only in the width of the channel.

The same discussion can be done for the phase-coherence length l_ϕ, but with a deeper meaning in the present context. In fact, in general l_ϕ and l_{mfp} are not identical and, in view of detecting a coherent effect, the first is more important than the second. Note that assuming l_ϕ were the relevant length scale for observing the MIRO phenomenon in these samples, the sample with $w = 15$ µm could display MIRO because $l_\phi \lesssim w$ while all samples with $w = 4$ µm fulfil $l_\phi/w \simeq 3$. This would also solve the previously mentioned contraddiction, because samples with higher mobility do not present automatically large l_ϕ. This point will be discussed further at the end of the chapter.

Finally, it is interesting that the width separating samples displaying or not MIROs corresponds to the minimum width for which the MPR can be excited for the used source frequency: for a 2DEG system with an electron sheet density as in the samples, an MPR can be excited at 140 GHz if the channel width is about 30 µm. This correlation seems nonetheless fortuitous because in the literature no connection has been reported between the two phenomena, as shown also in appendix E on page 247.

7.6 MIROs in SRRs-covered Hall-bars

The rest of the chapter is now devoted to the investigation of the MIRO phenomenon in SRR-covered Hall-bars. All of the previously discussed Hall-bar types were covered by SRRs of different kinds, direct-SRR or complementary-SRR and with frequencies ranging from 100 to 500 GHz, in an attempt to detect the USC between the SRRs and the cyclotron transition in the 2DEGs.

7.6.1 First sample series with direct-SRRs

This section presents the measurements performed on samples $B1452$ and $A1452$. The sample $B1452$ is designed such that the 36×500 µm^2 Hall-bar channel is just wide enough to accommodate a single row of SRRs, with the same spacing as for the optical USC-sample discussed in section 6.4. Sample $A1452$ contains instead two rows of SRRs onto the 52×500 µm^2 channel, arranged so to focus the radiation on the Hall-bar edges. Some photographs of the samples are shown in Fig. 7.15. As shown in picture b), each Hall-bar is part of a 3.4 mm channel where two other reference Hall-bars find place with dimensions identical to the previous one. The difference consists in the fact that the first Hall-bar is the one containing the SRRs, the second Hall-bar is left uncovered, while the

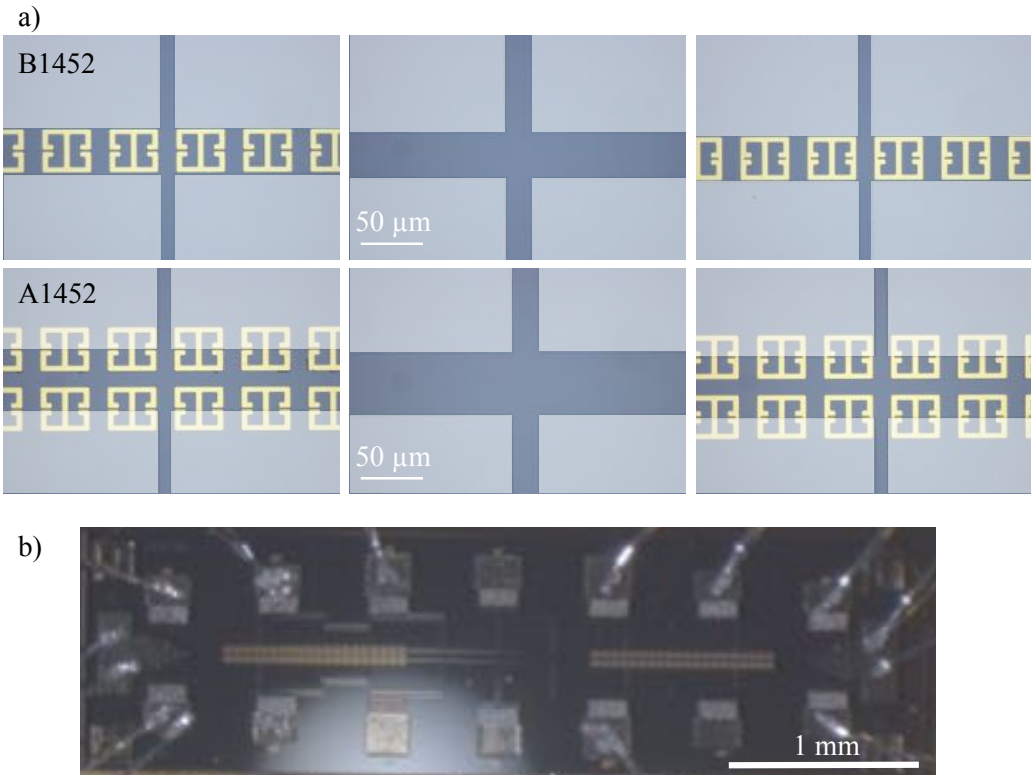

Figure 7.15 – a) Optical micrographs of the different measured Hall-bars in samples $B1452$ and $A1452$. Each row shows a single sample, with the single pictures taken from the three Hall-bars therein defined. b) Picture of the whole sample $A1452$, showing also the contacts.

third is covered by metallic structures almost identical to the SRRs but with shorted gaps. In this way, we have a reference for the effect the metal, decoupled from the USC itself. Each Hall-bar is spaced by few hundreds of micrometres from the neighbouring ones to avoid any coherent interaction.

Two additional samples ($C1452$ and $D1452$) with higher-frequency SRRs were also realised. Their investigations can be found in appendix G on page 253.

Measurements on sample $B1452$

Let us first briefly discuss the transport measurements performed on the Hall-bars of sample $B1452$. The resistivities ρ_{xx} and ρ_{xy} were measured for each of the three different Hall-bars in the sample: they are collected in Fig. 7.16. The trace corresponding to the uncovered-Hall-bar has already been discussed in the previous section along with Fig. 7.11. Apart from a slight asymmetry in magnetic field, the SdH-oscillations on the SRR- and shorted-SRR-covered Hall-bars look quite similar to each other and very different from the uncovered Hall-bar. Although the SdH oscillations of covered and uncovered Hall-bars are almost in phase and have $B = 0.3$ T as a common on-set, the general behaviour is

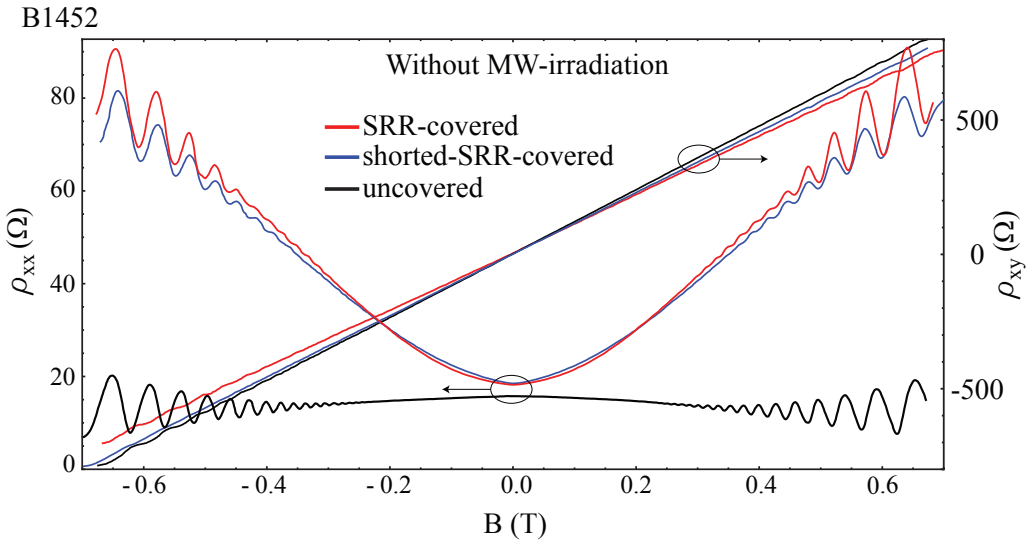

Figure 7.16 – ρ_{xx} and ρ_{xy} traces measured on all Hall-bars within sample $B1452$, without illumination. The SdH oscillations of SRR-covered (red), shorted-SRR-covered (blue) and uncovered (black) Hall-bars are in phase, while the metallic structures increase the background of the measured traces. Very small differences were measured in the Hall-resistivity.

different, showing, first, an increase in the resistivity at zero magnetic field, denoting a decrease in mobility, and, second, a positive curvature away from $B = 0$ T, opposite to the trace for the uncovered one. Both effects can be addressed to the metallic structures deposited on top of, and very close to, the 2DEG, acting as local floating gates and thus additional scattering centres.

Considering the ρ_{xy} traces in the low magnetic field range, all curves are very close to each other. This reveals almost no change in the total (Hall) carrier density.

From the complete set of traces it is possible to extract a total (Hall) sheet electron density of about 5.35×10^{11} cm^{-2} within 2% for all three Hall-bars and a mobility of 814000 cm^2/Vs, 702000 cm^2/Vs and 683000 cm^2/Vs for the samples with free surface, with shorted SRRs and with SRRs, respectively. Instead from the periodicity of the SdH oscillations, it is possible to derive the sheet density of the electrons participating in the longitudinal transport to be 3.0×10^{11} cm^{-2} within 1% for all Hall-bars.

In order to discuss the photoresponse of samples $B1452$ and $A1452$, let's first recall the optical behaviour of the resonators and their coupling to the cyclotron transition of the 2DEG.

As discussed in chapter 3 on page 81, the used SRRs show the main LC-mode at about 500 GHz, insensitive to magnetic-field, when optically excited with beam-polarization across the SRR slits. In such configuration, the e.-m. field gets concentrated within the

slits increasing its amplitude by a factor 20. Other two dipolar modes are present at higher frequencies, at about 2.3 THz for the same polarisation and at about 1.1 THz for the orthogonal one. Note that these resonant frequencies are slightly lower than the ones reported in chapter 3 on page 81 because here the SRRs are realised onto a GaAs-based substrate and not a Si-based one.

As shown in section 6.5 on page 153, all these resonances couple strongly to the cyclotron transition: the dipolar modes are also in ultra-strong coupling with the cyclotron transition, although with a smaller normalized Rabi frequency than the LC-one, consistently with the definition of Eq. (6.12).[47, 368] Hence at 140 GHz their lower polariton is indistinguishable from the cyclotron and, furthermore, they do not interact with the LC-mode as also shown in section 6.5 on page 153. Therefore we can safely ignore both of them for the present low-frequency investigation and focus the attention on the LC-mode alone.

Concerning the shorted resonators, they all show only dipolar resonances with frequencies above 1.0 THz, once again far enough to be disregarded as a coupled systems. The analysis and discussion of their calculated transmissions and E-field distributions are reported in appendix G on page 253.

The normalized Rabi splitting of the LC-mode amounts to 34%[374, 368], that corresponds to 97.2% matter part and 2.8% photonic part in the lower polaritonic branch at the source frequency. The lower branch resonates at 140 GHz for magnetic fields B_{USC} =0.41 T, which have to be compared with a cyclotron magnetic field B_f =0.33 T at the same frequency. Figure 7.17 shows the behaviour of the anti-crossing as fitted from the transmission measurements performed on a large-area optical sample (Fig. 6.5 on page 152) with the theory from section 6.2 on page 145, thanks to which the Hopfield coefficients can also be calculated. As a side note, the used optical setup has a lower bandwidth edge at about 200 GHz, therefore the positions of the polaritonic branches at the Gunn-diode frequency are an extrapolation of the fits.

Using the quarter-phase-shift formula, the shifted minima corresponding to the SRR-covered Hall-bar should appear at $B_{\pm j}^{USC}$ = 0.33 T, 0.18 T, 0.13 T, etc., according to Eq. (7.6). Therefore the wanted feature, confirming the assumptions, will be a shift in magnetic field of the MIRO minima. For the first one $j = 1$ this amounts to $\Delta B = B_{\pm 1}^{USC} - B_{\pm 1} = 0.06$ T, i.e. a shift of 18%, small but resolvable with the used set-up.

Coming to the measurements, Fig. 7.18 presents the complete series of the ρ_{xx} traces for all the studied Hall-bars. For each Hall-bar, the ρ_{xx} traces are shown first without irradiation (black) and then under microwave irradiation with electric field orthogonal

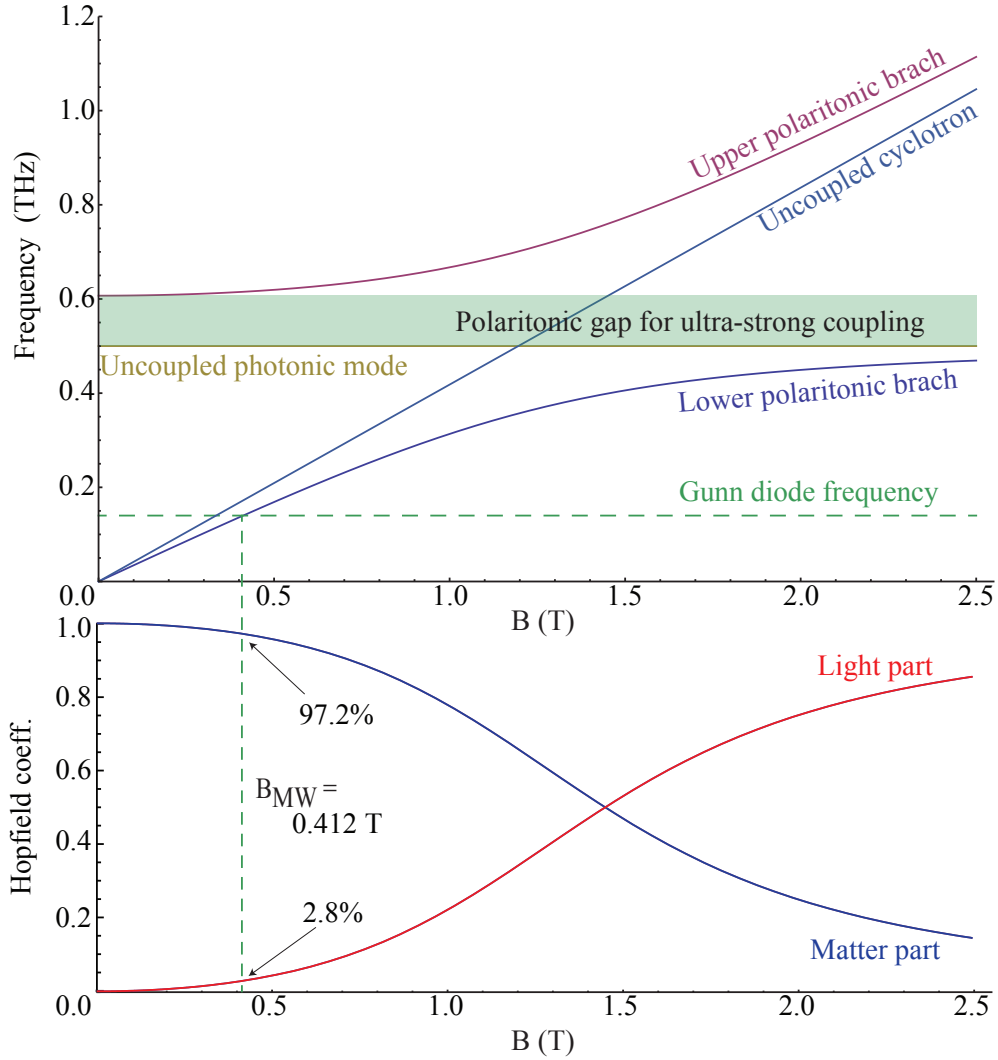

Figure 7.17 – Fit of the measured anticrossing, reported in Fig. 6.5 on page 152. In blue and purple are displayed the lower and upper polaritonic branches for the strong coupling between the LC-mode (thin yellow line) and the cyclotron transition (thin blue line). The green shaded area indicates the polaritonic gap, witness of the ultra-strong coupling condition of the system. The dashed green line indicates the Gunn diode frequency: its absorption by the lower polariton should allow the detection of the USC in the transport measurement as explained in Fig. 7.8. Below, the Hopfield coefficients show the mixing of matter and light part.

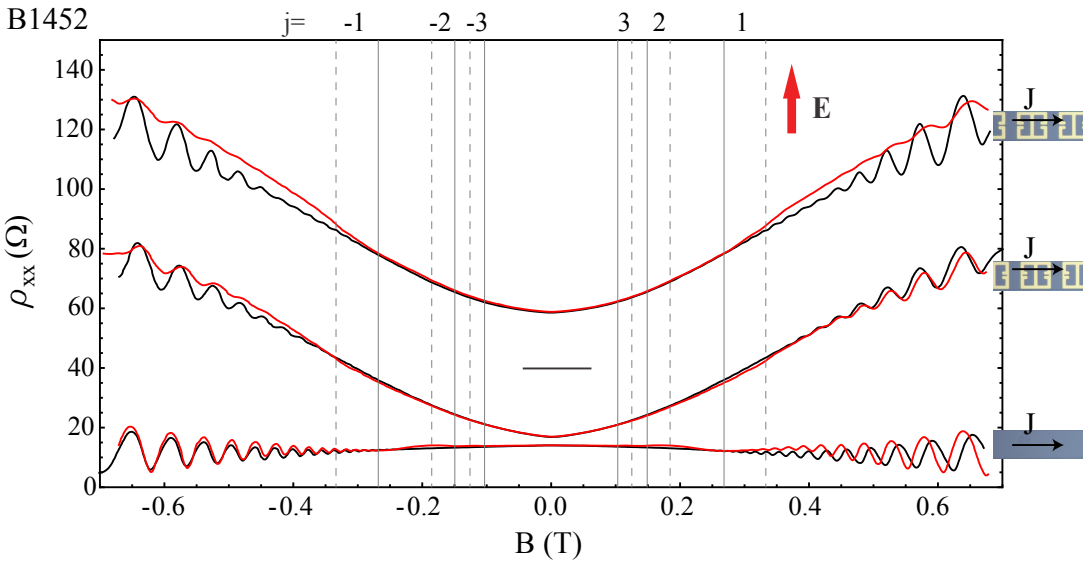

Figure 7.18 – ρ_{xx} for sample $B1452$ for uncovered (lowest pair), shorted-SRR-covered (middle pair) and SRR-covered (top pair) Hall-bars, without irradiation (black) and with orthogonally polarized radiation (red). The up-most group has been off-setted for clarity.

(red) to the Hall-bar axis along which the current flows, i.e. able to excite the LC-mode of the SRRs. For clarity the SRR-covered traces were plotted off-setted as the up-most set, the central segment indicating their referential zero-resistivity. The vertical lines show the expected positions of the MIRO minima for the uncovered Hall-bar (continuous lines) and for the Hall-bar in USC (dashed lines).

The traces of all Hall-bars without irradiation are here shown in black and were discussed in Fig. 7.16, while the uncovered Hall-bar traces were discussed in Fig. 7.11. Comparing the traces of the covered Hall-bars with the uncovered one, one sees that, apart from the already-discussed much higher resistivity, all SdH oscillations, when still present, are almost in phase with each other and only small deviations are present, possibly due to small temperature instabilities. This denotes almost no variation in the 2DEG density across the samples. All irradiated traces of the Hall-bars have a higher SdH on-set than the corresponding non-irradiated. Comparing the traces with orthogonal polarization, the covered Hall-bars have higher SdH on-set, showing a stronger heating consistent with a stronger light-focus by the SRRs.

Looking for MIRO minima into the SRR-covered Hall-bar red trace of Fig. 7.18, no feature seems present. One can extract more information on the photo-response by subtracting the bare electrical trace: Figure 7.19 shows the difference between the irradiated and non-irradiated traces for the uncovered and SRR-covered Hall-bars.

Let's first consider the black curve, showing the difference between the traces for the uncovered Hall-bar: it highlights the first maxima and minima, while smearing out more

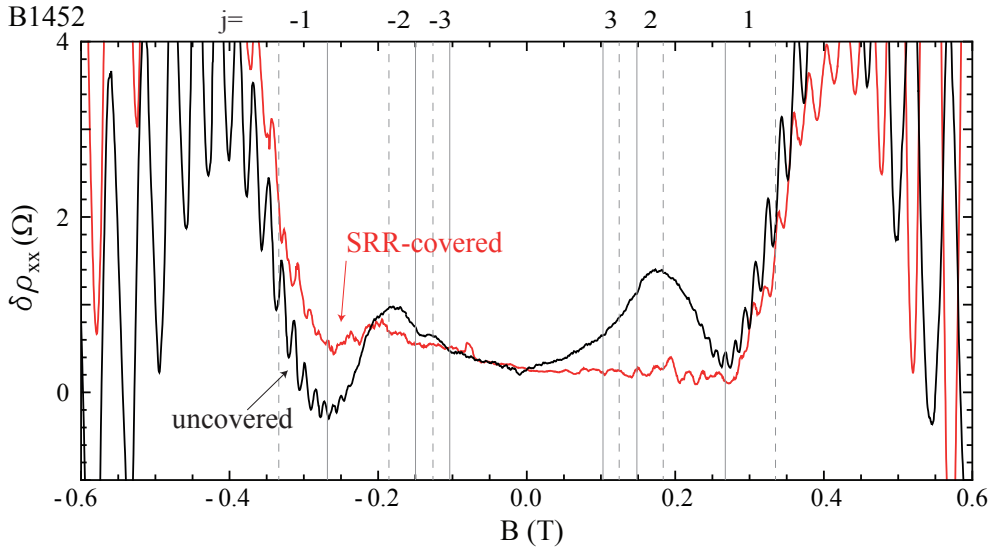

Figure 7.19 – $\delta\rho_{xx} = \rho_{xx}^{MW} - \rho_{xx}^{dark}$ for uncovered and SRR-covered Hall-bars in $B1452$
$\delta\rho_{xx} = \rho_{xx}^{MW} - \rho_{xx}^{dark}$ for uncovered and SRR-covered Hall-bars in $B1452$, showing no shift in the observed MIRO minima.

the additional oscillations already seen in Fig. 7.11. The $j = \pm 1$ minima fall exactly at the expected field $B_{\pm 1} = \pm 0.27$ T. The red curve, difference between the traces of the SRR-covered Hall-bars, shows the first maxima to be consistent in extension and amplitude with the ones in the black curve. The signal then decreases, going to smaller B-field values, till showing kinks that for negative magnetic fields develops into a full minimum, also located at $B_{\pm 1}$. No clearer and/or additional oscillations are present, as well as no feature that could be consistent with shifted minima, the first one expected at $B_{\pm 1}^{USC} = 0.33$ T.

Given the fact that in the optical measurement (cf. Figs 7.17 and 6.5 on page 152) both the polaritonic branches and the cyclotron absorption are present due to uncoupled areas of the 2DEG, rather than a shifted set of minima, one would expect two separate minima sets, eventually merging into a broader one. When bearing in mind either of these pictures, none of them can be associated to the red trace of Fig. 7.19.

Additionally, the fact that a relevant, and optically active, part of the 2DEG's electrons are coupled to the SRR is confirmed and quantified by the magneto-transmission measurement presented in panel b) of Fig. 6.5 on page 152. Considering the curve taken at the anti-crossing one can estimate the ratio between hybridised and not-hybridised electrons from the ratio of the absorption dip amplitudes of cyclotron and polaritons. Such ratio amounts approximately to 40%, certifying that the signal due to the coupled part of the system is commensurate to the uncoupled part and one would expect both to contribute to the effect. Actually, in sample $B1452$, the extent of the unit cell in the

direction across the gap was reduced, decreasing the amount of free 2DEG surface and increasing the relative weight of USC electrons.

Two other import points to discuss concern the geometry of the sample. First, we need to compare the arrangement of the SRRs with the phase coherence length of the sample $l_\phi = 12$ µm (cf. Table 7.1). Instead the USC-regions are distributed periodically in the middle of the Hall-bar channel with a separation of about 18 µm, when they belong to the same dSRR, and 12 µm, when they belong to neighbouring dSRRs (cf. panel a) of Fig. 3.2 on page 83). Therefore, it is possible, in spite of the fact that the sample is not in the best condition, that electrons flowing along the channel between two USC areas keep their coherence properties.

Second, in sample $B1452$ the SRRs are placed within the Hall-bar channel, focussing the GHz-light at its centre. After the investigation described in the previous chapter, the only theory that our data support predicts microwave-stabilised edge transport[468]. Therefore the present arrangement would be removing light from the flowing electrons instead of coupling light to them.

The next step is then to move the SRRs to the edge of samples and repeat the MIRO investigation.

Focus on the edges: sample $A1452$

In order to better investigate the case for edge-transport, sample $A1452$ was investigated. In it two rows of SRRs are placed so that their gaps find place at the edge of the channel as shown in Fig. 7.15. The channel is here 52 µm wide, approximately as the unit cell of the SRRs.

The full set of traces for the three Hall-bars in sample $A1452$ is shown in Fig. 7.20 while the uncovered-Hall-bar set is plotted alone in Fig. 7.12. In all irradiated traces, both on SRR-covered and shorted-SRR-covered Hall-bars, minima are present, at the uncoupled MIRO positions. This is more evident when performing the subtraction of the spectra, whose result is shown in Fig. 7.21. As for sample $B1452$, these features are incompatible with USC-shifted MIRO minima.

Additionally, for this sample it is difficult to quantify the amount of ultra strong-coupling because the 2DEG material is not completely filling the SRR-cavities. A similarly shaped sample produced for optical measurements showed a halved normalised Rabi splitting compared to that in an extended sample. If this is indeed the case also for the transport sample, the expected shift between cyclotron and lower polariton at 140 GHz (ΔB in Fig. 7.8) would be smaller than the broadening of the MIRO minima, preventing

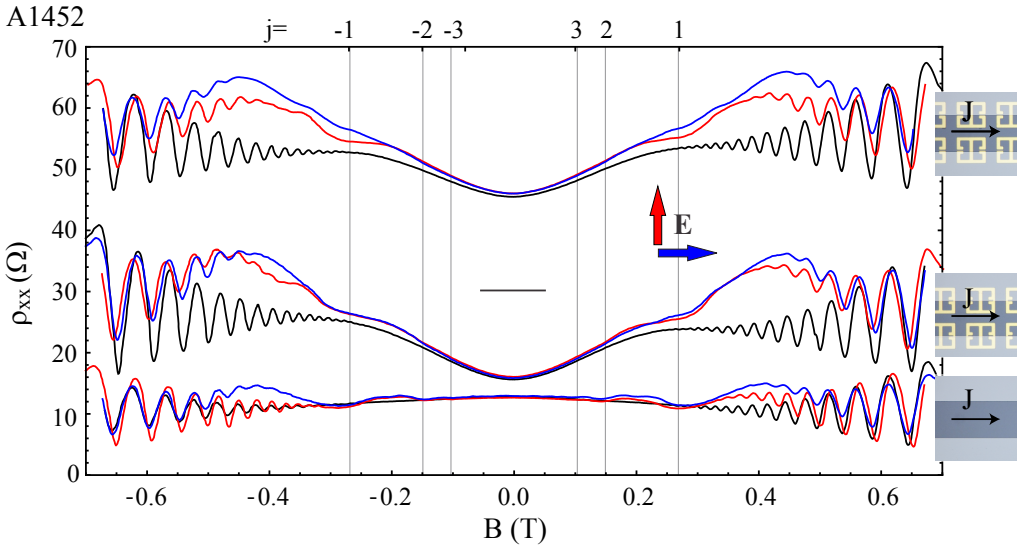

Figure 7.20 – ρ_{xx} traces for sample $A1452$ for all three Hall-bars, without irradiation (black) and with longitudinally and orthogonally polarized irradiation (blue and red, respectively). The up-most group has been off-setted for clarity.

one from detecting a difference in their positions, if present.

The difference traces for sample $A1452$, as well as all the ones for the remaining samples reported in appendix G, do not display symmetric oscillations about a barycentre but rather stay above the non-irradiated trace. A similar feature was discussed in Ref. [446], where it was argued that it should be connected with the regime of a ballistic channel in the orthogonal direction. This is not the condition for the present samples, where instead it seems connected to a more general heating generated in the samples by the strong irradiation that increases the background resistivity. This perspective is one of the basis for the power-dependence investigation discussed in the next section.

Finally, a short comment is due to the different shape of these traces with respect to the ones of sample $B1452$: for comparison they are plotted together in Fig. 7.22. The ρ_{xx} traces taken on sample $A1452$, where two rows of SRRs are present, show an initial parabolic growth when increasing the magnetic field, reaching soon a stable resistivity value around which they oscillate. The ρ_{xx} traces taken on sample $B1452$ instead, where a single row of resonators spans the whole channel width, show a steeper parabolic behaviour in the entire investigated B-range. When compared to the measurements on the uncovered Hall-bars, they both show an opposite curvature at low magnetic field. In the higher-field range instead, the traces of the double row of resonators look similar to the uncovered ones. This can be tentatively explained with the fact that the two rows of resonators leave a free channel in the middle behaving like an uncovered Hall-bar, and thus it displays features belonging to regions with two different resistances. Instead, the single row of SRR forces

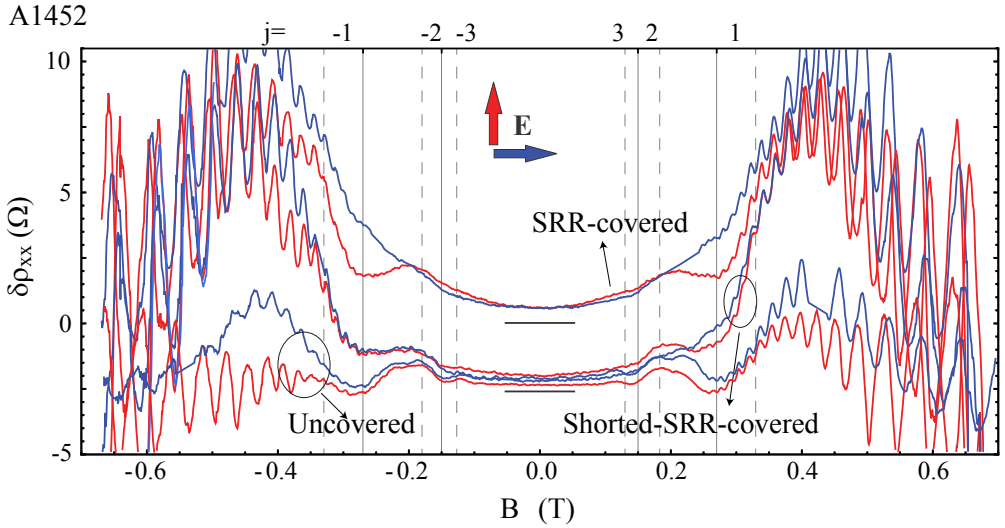

Figure 7.21 – $\delta\rho_{xx} = \rho_{xx}^{MW} - \rho_{xx}^{dark}$ for all Hall-bars in sample $A1452$. No shift of the MIRO minima is seen for the SRR-covered Hall-bar.

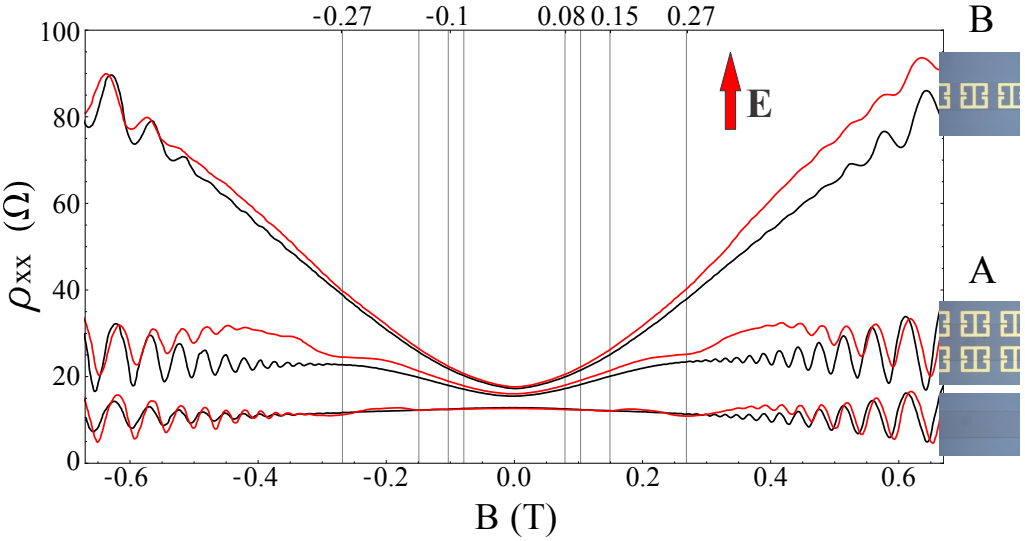

Figure 7.22 – Comparison of ρ_{xx} traces for the SRR-covered Hall-bars of samples $A1452$ and $B1452$, recorded with and without illumination. The traces of the uncovered Hall-bar of sample $A1452$ is also displayed as reference.

the electrons to flow into a similar electric landscape, nonetheless, more resistive than the previous ones.

Given the inconclusive situation, a power-dependence study was performed on sample *A*1452 to assess the influence of the SRRs on the strength of the unshifted MIRO features: this is the topic of the next section.

Power-dependent effect of the SRRs on the unshifted MIRO

The power-dependence study presented in this section wants to determine whether the presence of the SRRs is changing the photoresponse of the Hall-bars to the irradiation, despite the fact that the MIRO minima are not shifted. To do so, the ρ_{xx} traces of all Hall-bars in sample *A*1452 were recorded for different irradiation powers ranging from 20 µW to 2.3 mW: the ones of the SRR-covered Hall-bar for polarisation orthogonal to the channel are collected in Fig. 7.23. The radiation power was changed by applying different biases to the Gunn-diode according to the calibration curve plotted in panel b) of Fig. 7.9. The corresponding plots for the SRR-covered and shorted-SRR-covered Hall-bars can be found in Fig. G.7 of appendix G.

This power series displays clearly the MPR peaks growing strongly for increasing power till even lifting and shifting the first MIRO minimum. Nonetheless, at the lowest power when no MPR seems present but only the MIROs, these oscillations do not cross the dark (black) line, i.e. in the present samples the MIROs do not oscillate about the non-irradiated trace but rather above it.

The dark trace was subtracted from the illuminated ones, $\delta\rho = \rho_{xx}^{rad} - \rho_{xx}^{dark}$, for

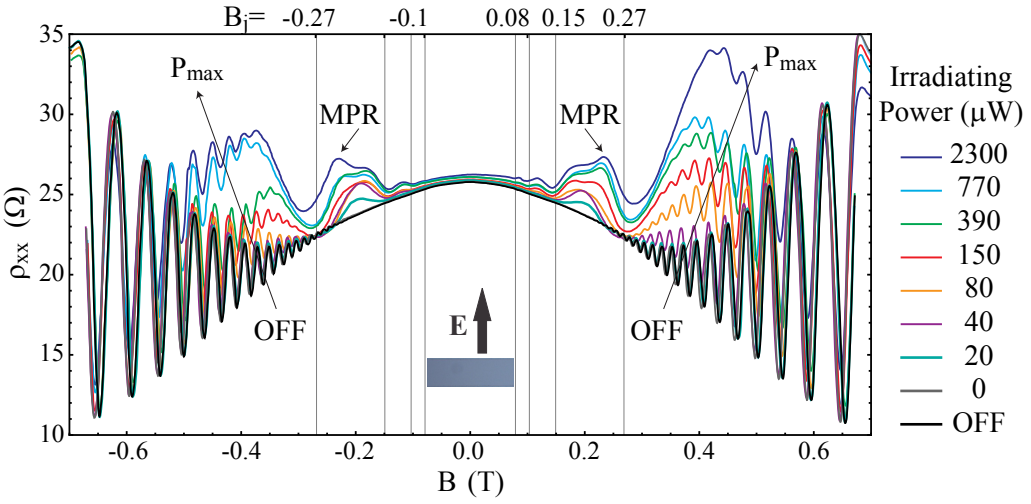

Figure 7.23 – Power dependence of the low-B-field region of ρ_{xx} for the uncovered Hall-bar in sample *A*1452 with illumination polarization orthogonal to the Hall-bar axis.

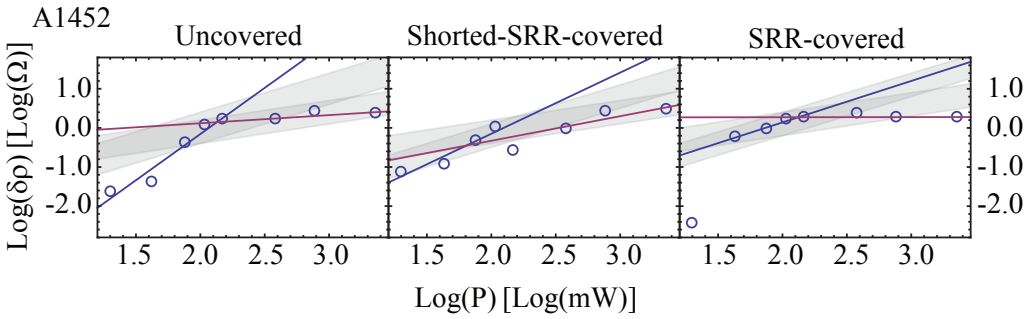

Figure 7.24 – Double logarithmic plot of the MIRO amplitude vs power for the first two minima of sample *A*1452 (empty circles). The lines are fit to the data (cf. Table 7.2), while the gray-shaded bands are the expected behaviour according to the theories.

the different irradiation powers. To remove additional possible heating effects and the unknown background, the amplitude of the MIRO oscillations is extracted by averaging the amplitude of the first minimum and the first maximum. The resistivity values of the minima and maxima were tracked for the different powers, averaging between positive and negative magnetic fields, for each of the uncovered, SRR-covered, shorted-SRR-covered Hall-bars. Figure 7.24 shows the log-log plots of the average amplitude of the first MIRO oscillation for the three Hall-bars vs power.

The literature often reported, supported by both the displacement and inelastic theory, the dependence of the MIRO amplitude $\delta\rho$ on the power P as a single-exponent power law, with $\delta\rho \propto P^1$ for low powers changing to $\delta\rho \propto P^{0.5}$ for bigger P values. These two power-law dependences are reported in Fig. 7.24 via the grey-shaded areas, for comparison. Each dataset shows different low- and high-power behaviours, though not always following the expected ones.

When fitting the data, the lines in Fig. 7.24 result: they correspond to the exponents reported in Table 7.2. By considering the different low-power exponents, one can see that indeed the presence of the SRRs on the channel has a strong effect on the MIRO response. Although the MIROs are neither shifted, nor amplified, the lower exponents for the power laws of the SRR-covered Hall-bar indicates that a stronger effect takes place, consistent with the function of the SRRs as light-concentrators.

The high-power exponent, being almost zero, indicates that the SRR-covered sample photoresponse is soon saturated, contrary to the uncovered-Hall-bar sample where it still increases for the studied power range.

An important remark to make is that the difference traces do not show an oscillation symmetric about the abscissa because a background is present. It increases with magnetic field and could be related to heating in the sample.

Table 7.2 – Power-law fit of $\delta\rho(P) \propto P^x$ for the three Hall-bars in $A1452$.

Hall-bar	low-power exponent	high-power exponent
theory	1	0.5
bare	2.36	0.21
shorted-SRR	1.56	0.63
SRR	1.06	0.003

The Hall-bars can thus be seen as detectors of radiation and their responsivity, derived as the slope of the linear fit of the low-power data till $P \simeq 150$ µW, can be analysed accordingly. To such purpose, the resistivity values at specific points of the difference traces are extracted for increasing irradiation power: this was done for $B = 0$ T and for the B-ranges identifying the first and second MIRO maxima. The last two ranges take therefore into account a combined effect of the MIRO and of the background. The ratio of the extracted responsivities between the three Hall-bars for the different ranges are reported in Table 7.3, compared with the ratio of the integrated simulated field intensities at the 2DEG position for the polarisation for which the LC-resonance is excited, at 140 GHz, but not in the ultra-strong coupling condition (CST Microwave Studio).

What the data show is that the responsivity of the SRR-covered Hall-bar is always better than both the bare Hall-bar and the shorted-SRR-covered one. The latter is in turn better than the bare one. This means, first, that the metallic structures help coupling the radiation into the 2DEG. On the other hand, this cannot be addressed to the presence of the metal only or to the optical mode of the uncoupled SRR. In fact the latter is quantified by the last column in Table 7.3: the simulations tell us that the shorted-SRR concentrate the electric field at 140 GHz in the best way, slightly better than the SRR-structure for the given frequency. The fact that instead the SRR-covered covered still performs

Table 7.3 – Responsivity comparison for the three Hall-bars in $A1452$ at three different B-field values. The last columnpresents the field enhancement at the 2DEG position at 140 GHz in the LC-polarisation.

Ratio \ B-field range	$B = 0$ T	2nd max	1st max	E-field
SRR/bare	+21%	+2.7%	+3.7%	+39%
SRR/shorted	+1.7%	+1.4%	+2.0%	+3.1%
shorted/bare	+12%	+2.0%	+1.8%	+44%

better, means that another mechanism has to be responsible for the differences. This points towards a relevance of the ultra-strong coupling condition for the better radiation coupling.

Therefore, despite the fact that the expected shift in the MIRO features is not seen, one can conclude that the presence of the SRRs could increase the effect of the MIRO phenomenon, while the ultra-strong coupling condition of the SRR-covered Hall-bar still favours the coupling of the radiation with the 2DEG, measured in transport.

Aiming at detecting a big effect of the USC, a second set of samples was produced where the entire channel side fits into the gap of a single complementary SRR. Its investigation is the topic of the next section.

7.6.2 Second sample series with complementary-SRRs

The idea is to use a single complementary-SRR (cSRR, cf. section 3.2 on page 86 in chapter 3), whose central gap can allocate (part of) the Hall-bar channel.[5] The contact lines used to measure the longitudinal voltage join the channel within the cSRR's gap, leaving no part of the Hall-bar channel side uncoupled. The photographs of two examples of such arrangements are shown in Fig. 7.25.

The used cSRRs were designed with a central gap about 5 µm wide and with a variable length ranging from 58 µm to 150 µm to tune the resonant frequency. More details on the cSRRs used can be found in appendix D on page 245. In an attempt to go closer to the Gunn-diode frequency and thus increase the B-field distance between cyclotron resonance and lower polariton, cSRRs with resonant frequencies f_{cSRR} = 110 GHz, 190 GHz and 300 GHz were investigated. The resonant B-field increases for f_{cSRR} approaching 140 GHz. The case of the 110 GHz resonator, for which the Gunn-diode frequency falls into the polaritonic gap, is also interesting.

The resonators were realised onto different Hall-bars etched into wafers $EV2124$ and $EV2109$, GaAs/AlGaAs 2DEGs with mobilities of 1.7×10^6 cm^2/Vs and 0.57×10^6 cm^2/Vs at an electron concentration of 3×10^{11} cm^{-2} and 2×10^{11} cm^{-2}, respectively. Their growth sheets are reported in appendix A on page 233.

All subsequently discussed Hall-bars have a length of 41 µm, therefore fitting into any of the cSRRs. Three Hall-bar widths have been investigated: 4 µm, 15 µm and 60 µm. The narrowest fits completely into the cSRR's gap leaving few hundreds of nanometres

[5] The samples $G2124$, $A2109a$, $A2109b$, $K2124$, $C2124$ were processed by G. L. Paravicini Bagliani in Prof. Faist's group at ETHZ and in the clean room facility FIRST, who also designed the processing mask.

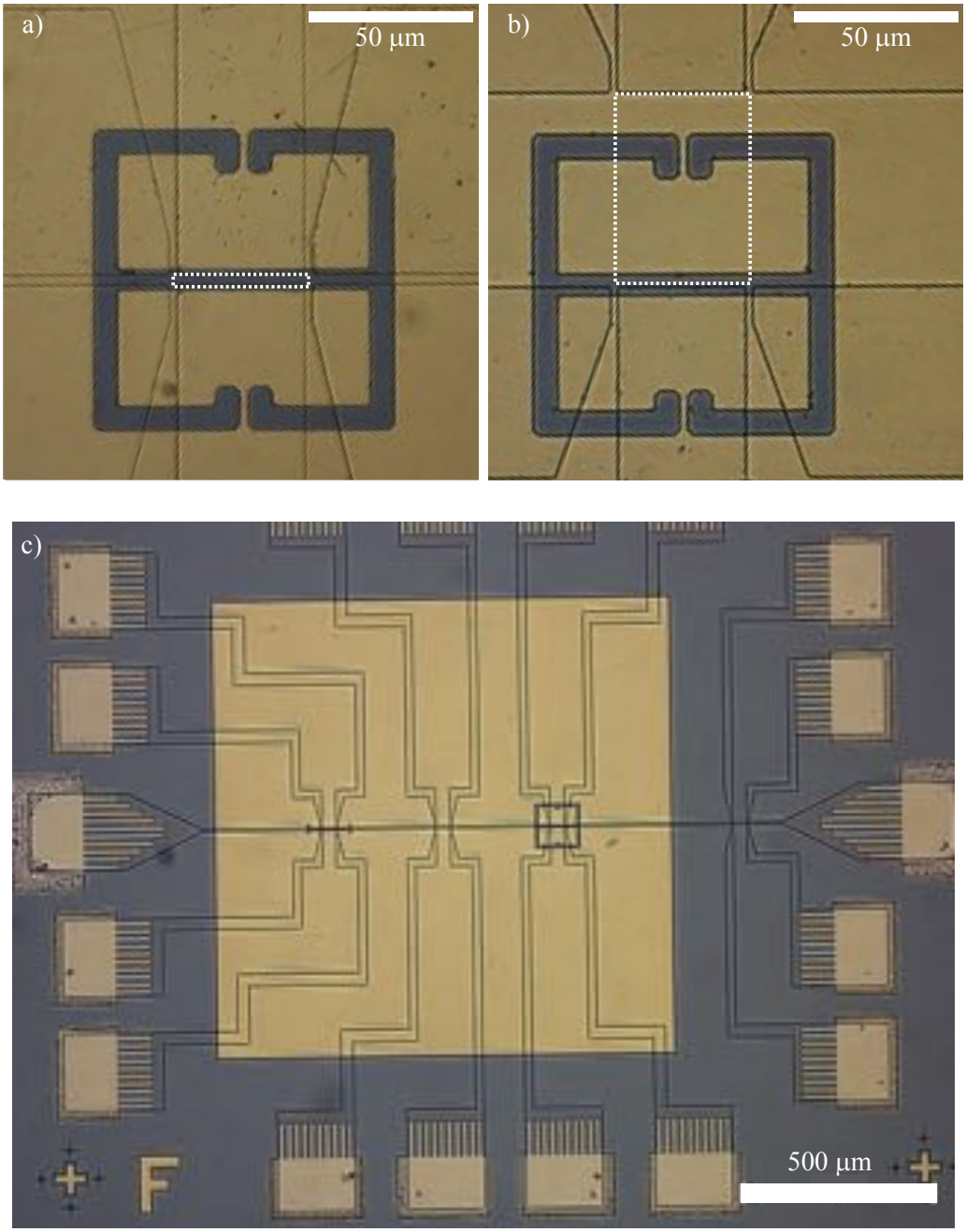

Figure 7.25 – Optical micrographs of some samples of the second series. a) cSRR placed onto a 4 µm wide Hall-bar, filling the gap of the resonator. b) For a 60 µm wide Hall-bar, the cSRR is aligned onto one side. The Hall-bar channel is identified by the white dashed rectangle and the contacts define its length completely within the cSRR gap. c) Picture of a whole sample, showing four Hall-bars in series, one of which uncovered. The patch where the cSRR is produced and the contacts' arrangement are clearly visible. Courtesy of G. L. Paravicini Bagliani.

Table 7.4 – Summary of the characteristics and of the results of MIRO investigation on the cSRR-covered samples: 2DEG growth, channel width, cSRR frequency and contacts arrangement are reported, along to whether MIRO minima were detected.

Sample	w (µm)	f_{SRR} (GHz)	patch	MIRO?	
				uncovered	cSRR-covered
*A*2109*a*	4	190	small	N	N
*A*2109*b*	4	300	small	N	N
*K*2124	15	300	big	N	Y
*C*2124	60	190	small	Y	Y
*G*2124	4	110	big	N	N

of free space on the sides. The other two are instead arranged in such a way that the cSRR's gap is filled, being the channel and the cSRR's gap aligned on one side, as shown in picture b) of Fig. 7.25. By measuring the longitudinal resistance via the contacts on the same side, one maximises the possible USC-effect on the measured trace. Moreover, every sample features also an uncovered Hall-bar nearby, with exactly the same dimensions as the cSRR-covered one.

The usage of cSRRs has some specific features to be dealt with. The first, positive one, is that the Hall-bar channel is free from metal therefore it retains its unperturbed potential landscape, contrary to the samples of the first series. On the other hand, this is not true for the rest of the sample, partially covered by the extended metallic layer. This fact was counterbalanced by gating the 2DEG, i.e. applying a voltage between the gold layer where the cSRR is realised and the Hall-bar to bring the electron density below the metal to match the one in the uncovered parts. This often resulted in biasing the sample with few hundred millivolts till the maximum possible value before the insulating capping layer would start to leak. The metallic patches, into which the cSRRs are realised, have an area of either 1.2×1.2 mm^2 (small patch) or 1.2×3 mm^2 (big patch) and cover most of the sample, stopping before the contacts. These allow an easy bonding for electrical biasing, while they can also act as patch antennae. Fortunately, their side corresponds to much longer wavelengths than the one used, avoiding any resonant optical response.

The characteristics of the samples are collected in Table 7.4.

The ρ_{xx} traces for the investigated samples are collected in Fig.s 7.26-7.31. Below each top panel showing the measured traces, a second one containing the difference $\delta\rho_{xx}$ between the irradiated and the dark ones is reported to give further insight into the consequences of the irradiation.

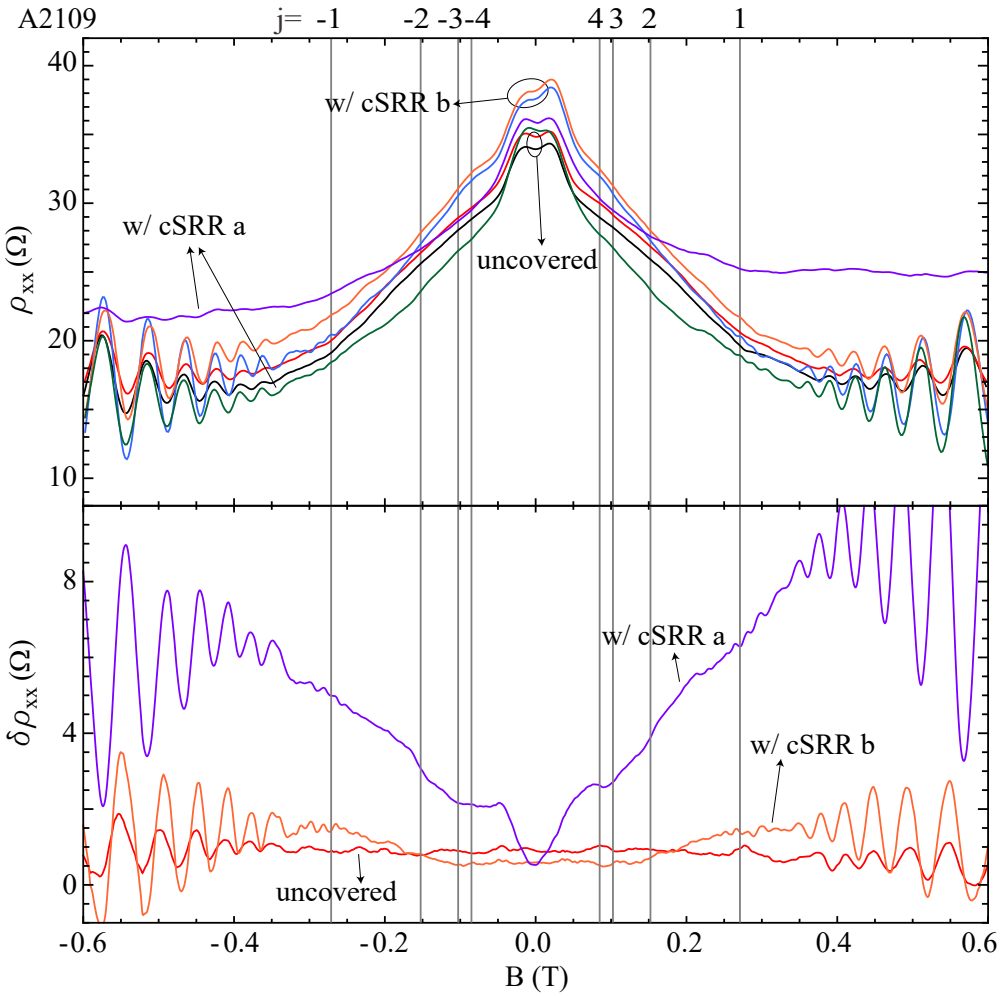

Figure 7.26 – Top: SdH measurements on samples *A*2109*a* and *A*2109*b*, performed with and without irradiation, resulting in the red/violet/orange and black/green/blue traces, respectively, for the uncovered and the cSRR-covered Hall-bars. Bottom: subtraction of the non-irradiated trace from the irradiated one, showing that no MIRO minima could be detected for the investigated Hall-bars. T=1.5 K. More details in the text.

The SdH traces of samples *A*2109*a* and *A*2109*b*, in Fig. 7.26, do not show any feature consistent with MIROs, both in the uncovered and cSRR-covered Hall-bars. Only the trace for the cSRR-covered Hall-bar in *A*2109*a* shows strong heating upon illumination, possibly the result of the stronger field concentration.

Sample *K*2124 shows no clear MIRO minima in the traces of the uncovered Hall-bar in Fig. 7.27. The trace of the cSRR-covered Hall-bar displays instead few very clear oscillations, taking place at the expected uncoupled positions. This confirms that the field-concentration effect of the SRR helps in the appearance of the MIRO, despite no

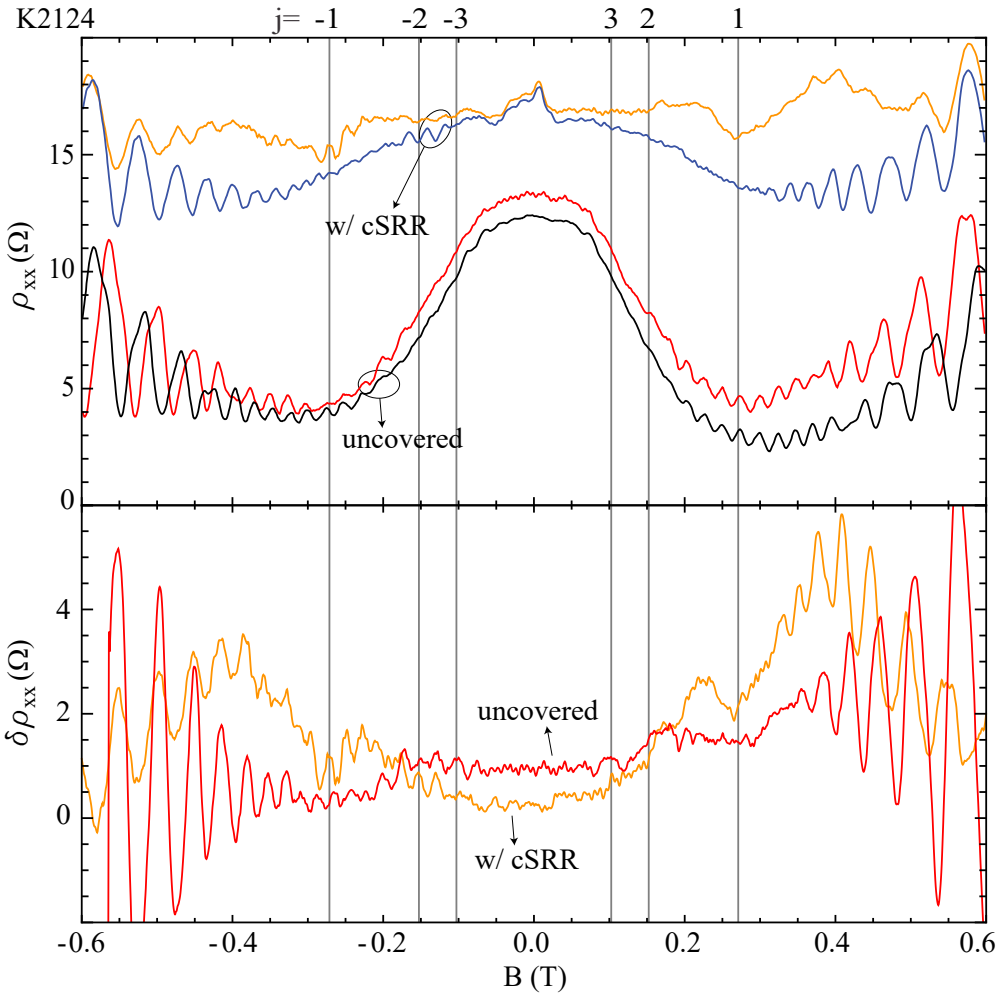

Figure 7.27 – Top: SdH measurements on sample $K2124$, performed with and without irradiation, resulting in the red/orange and black/blue traces, respectively, for the uncovered and the cSRR-covered Hall-bars. Bottom: subtraction of the non-irradiated trace from the irradiated one, showing almost no feature, apart from a very broad faint first minimum for the bare Hall-bar. MIRO minima at the uncoupled positions are already well visible in the measurement trace of the cSRR-covered one. T=1.5 K. More details in the text.

shift connected to the eventual ultra-strong coupling regime in which the sample should be.

The traces of sample $C2124$, in Fig. 7.28, show very clear minima at the expected position for the uncovered Hall-bar, while similar oscillations but at different magnetic field values are present in the traces of the cSRR-covered Hall-bar. Three minima, two on the negative B-field side and one on the positive side, are identifiable in the irradiated trace (orange), all three not consistent with the uncoupled MIRO minima. The two outmost minima in the opposite B-field orientations take place at the same magnetic field value

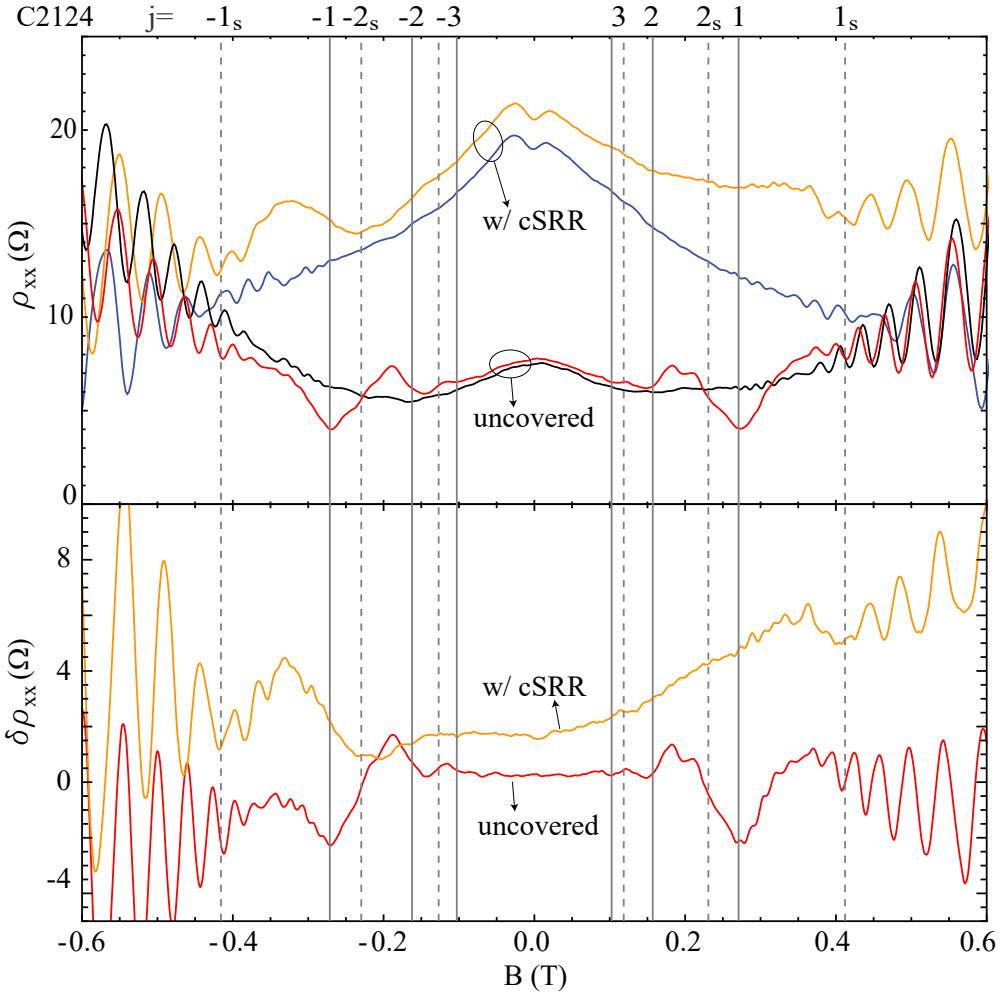

Figure 7.28 – Top: SdH measurements on sample $C2124$, performed with and without irradiation, resulting in the red/orange and black/blue traces, respectively, for the uncovered and the cSRR-covered Hall-bars. Bottom: subtraction of the non-irradiated trace from the irradiated one, showing the first MIRO minima at the uncoupled positions for the bare Hall-bar (solid vertical line), while few oscillations are present in the cSRR-covered trace at j_s, displaced from the uncoupled minima (dashed vertical lines). Additional features are present in the red trace at about ± 0.21 T consistently with the magneto-plasmon resonance across the channel of the Hall-bar.[389, 403] T=1.5 K. More details in the text.

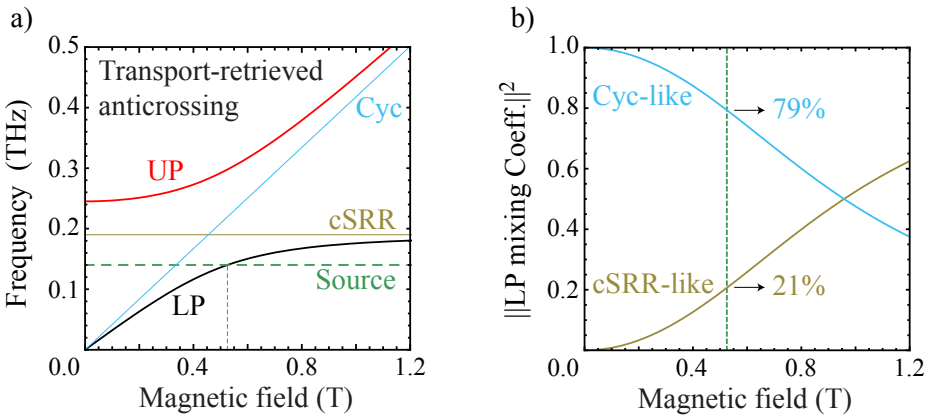

Figure 7.29 – a) Calculated anticrossing for the sample $C2124$ obtained by fitting the Rabi splitting to the wanted resonance between lower polariton and Gunn diode emission. The fit provides a normalised Rabi frequency of 43%. The displaced MIROs allow the retrieval of the degree of USC in the sample once also the resonant frequency of the cSRR is known. b)The mixing coefficients of the lower polariton at resonance with the source, show that the character of the polaritonic branch is still cyclotronic (79%, 21% photonic-like), despite being at B-fields higher than the bare cyclotron-cSRR resonance, clear feature of the USC.

$B_{\pm 1}^{USC} = \pm 0.42$ T while the second minimum at about $B_{-2}^{USC} = -0.23$ T. These values are consistent with MIROs generated by a shifted cyclotron, i.e. lower polariton, that is resonant with the source at $B_{LP}^{140GHz} = 0.52$ T. This, in turn, corresponds to an ultra-strongly coupled system with normalised Rabi frequency of $\Omega_{Rabi}^{MIRO}/\omega_{SRR} = 43\%$. The calculated anticrossing corresponding to such system is shown in panel a) of Fig. 7.29. The calculation code is the same used for the fitting of the transmission measurements[48, 49], that gets as inputs the resonator frequency and the normalised Rabi frequency. The first was determined by FDTD simulations and reference measurements to be 190 GHz (cf. appendix D on page 245) while the second was estimated by the shift of the MIRO minima. The calculated mixing coefficients of the lower polariton are plotted in panel b) and confirm the strong hybridisation of the cyclotron transition with the photonic mode: the amount of cyclotronic and photonic transitions at the source frequency are estimated to be 79% and 21%, respectively. Being at B-fields higher than the bare cyclotron-cSRR resonance, the fact that the cyclotronic part is still predominant is a clear feature of the USC.

In order to confirm beyond any doubt the presence of a transport signature of the USC regime in the sample, the optical spectroscopy of the USC sample, as carried out in Ref.s [47, 368] was performed.

The sample itself is not suitable for this because the available transmission setup does not have a high enough SNR to measure a single cSRR. Therefore, an optical sample was

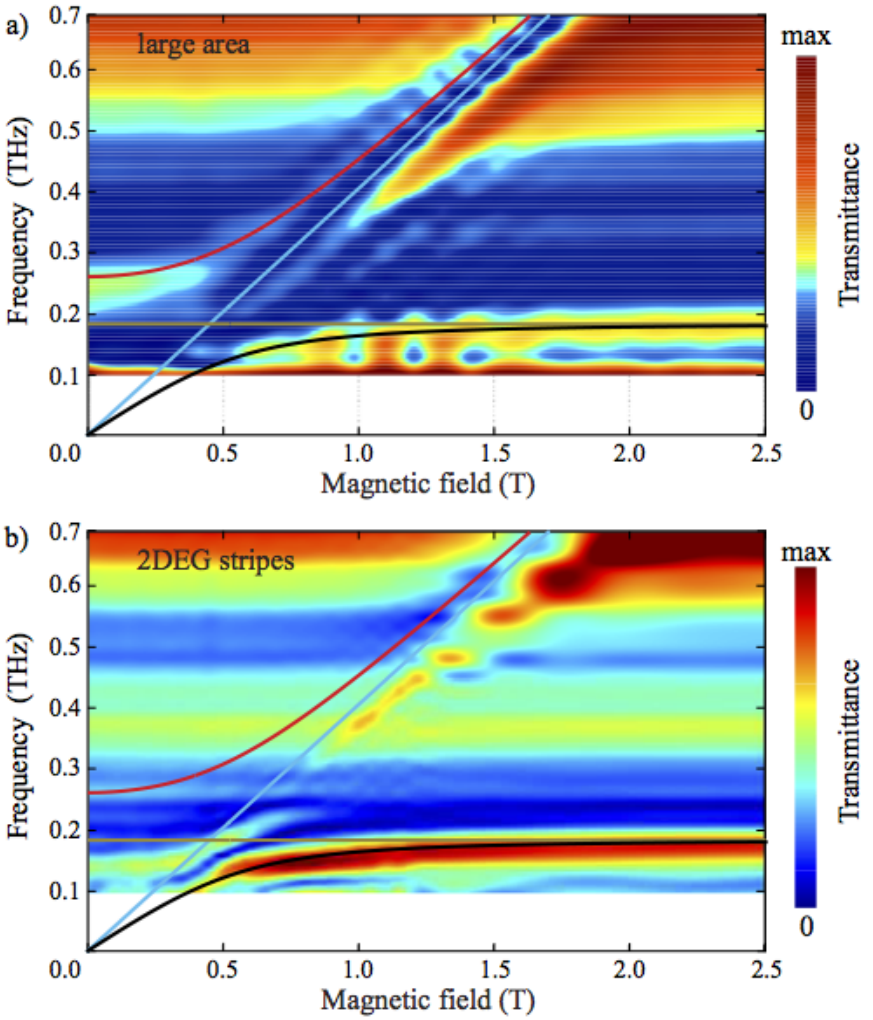

Figure 7.30 – a) Optical magneto-transmission measurements on the array of THz-cSRRs realised onto a large-area piece of 2DEG: just within the setup bandwidth, a clear anti-crossing is detected. The lines show the calculated anticrossing best matching the data. b) Optical magneto-transmission map measured onto the THz-cSRR array realised onto 2DEG stripes with width equal to the Hall-bar channel. For comparison, the calculated anti-crossing from panel a) is overlayed to the map, showing almost no change in the lower polaritonic branch.

produced where an array of cSRRs, identical to the one onto sample $C2124$, is realised onto a piece of the 2DEG coming from the same epitaxial growth as the one constituting the Hall-bars.[6] The sample transmittance measured for increasing applied magnetic field is presented in the color map of panel a) in Fig. 7.30 and confirms the high degree of USC in the system.

The color map is overlayed with the fit of the maxima, clearly showing the large anticrossing with a normalised Rabi frequency $\Omega^{opt}_{Rabi}/\omega_{res} = 51\%$ and confirming the previous analysis.

[6]The optical samples were processed by and measured in collaboration with G. L. Paravicini Bagliani.

Towards transport experments, the 2DEG of a second sample was etched in stripes, as wide as the Hall-bar channel and with one side aligned to and completely filling the gap of the THz resonators where the electric field is concentrated (cf. Fig. 7.25b)). The corresponding color map, in Fig. 7.30b), shows the same lower polaritonic behaviour, confirming no change in the degree of coupling. The upper polariton is too weak to be clearly detected while a lower frequency feature is present, possibly due to magneto-plasmonic effects[403].

Ω_{Rabi}^{trans} and Ω_{Rabi}^{opt}, obtained from the transport and from the optical measurements, can be considered consistent. In fact, the transport sample, because of its geometry, leaves a part of the fringing field on the side of the cSRR-central gap uncoupled, thus slightly reducing the width of the anticrossing.

The calculated mixing coefficients of the lower polariton, corresponding to Ω_{Rabi}^{trans}, are plotted in panel d) and confirm the strong hybridisation of the cyclotron transition with the photonic mode: the amount of cyclotronic and photonic transitions at the source frequency are estimated to be 79% and 21%, respectively.

Finally, the traces of sample $G2124$ are shown in Fig. 7.31. They show no feature for the uncovered Hall-bar (red trace), consistently with the measurements on samples $A2109$ that has uncovered Hall-bars with the same dimensions. Instead, the trace of the cSRR-covered Hall-bar (orange trace) shows strong heating with the appearance of weak kinks in correspondence to the uncoupled MIRO positions. This would be peculiar if the sample were in USC because the irradiation frequency would fall into the polaritonic gap separating the two polaritonic branches, for the expected degree of ultra-strong coupling. Nonetheless, optical studies on magneto-plasmonic samples showed that when the SRR-resonant frequency lies higher than the plasmon frequency, no coupling is present between the two instances, while some residual, non-plsmonic cyclotron is strengthened.[470] This picture is consistent with the MIRO results.

The results of the MIRO investigation on the cSRR-covered samples are summarised in the last two columns of Table 7.4. At this point, one comment is due about the patch size reported in the table. The terms “big” and “small” refer to two different designs used to place the contact pads around the Hall-bars, being the shape of the contact pads the same for each contact in all samples. This is relevant because the ponderomotive-force theory concludes that samples with the same contacts should display the same MIRO oscillations.[465] This is not the case for the investigated samples, since the samples not displaying any feature have the same contact arrangement as either sample $K2124$ or $C2124$, the main difference being the channel width.

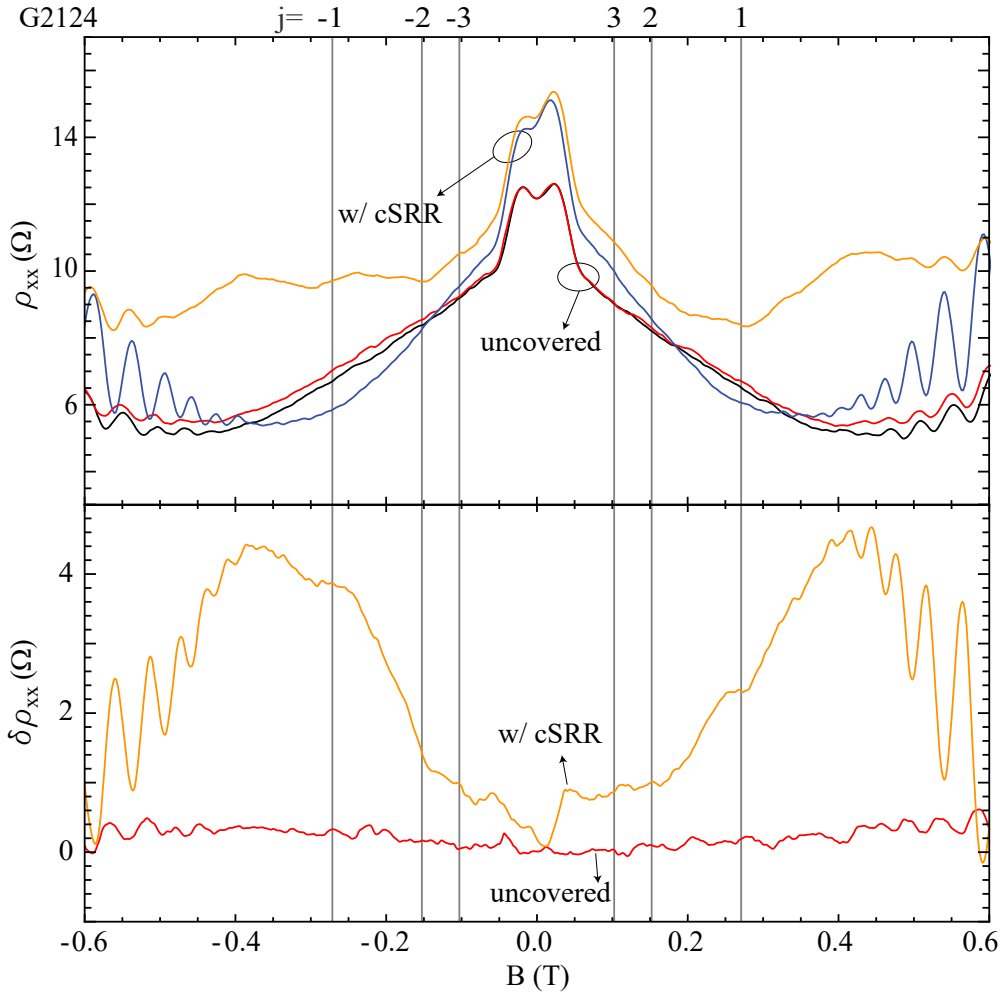

Figure 7.31 – Top: SdH measurements on sample *G*2124, performed with and without irradiation, resulting in the red/orange and black/blue traces, respectively, for the uncovered and the cSRR-covered Hall-bars. Bottom: subtraction of the non-irradiated trace from the irradiated one, showing no MIRO minima for the bare Hall-bar, while some kinks consistent with the uncoupled MIRO minima are present in the trace of the cSRR-covered one. T=1.5 K. More details in the text.

7.7 Conclusions

The first important conclusion of the performed investigation concerns the results about sample $C2124$ (Figs 7.28-7.30). These confirm that transport measurements provide insights into the amount of ultra strong coupling of the sample. We demonstrated a system in the USC regime in the terahertz frequency range based on the quintessential transport device, the Hall-bar, and we showed that its USC status is reflected onto low-frequency transport measurements, making use of the phenomenon of microwave-induced resistance oscillations. This is an important step towards the exploitation of the USC regime for optoelectronics in general and for quantum optics in the terahertz frequency range.

Strongly-coupled systems have already been used for the realization of optoelectronic devices, showing that the polaritons can influence the energy spectrum of the device both electrically and optically[55, 56, 58, 57]. The ultra strong coupling regime, with its much stronger interaction, can deeply improve the systems' coherence, a fundamental property on which researchers and devices rely.[471, 472, 473, 474] This is important also in the direction of inversionless polaritonic lasing[475] and to reach the level of vacuum field fluctuations. In spite of demonstrations of USC in several different systems[476, 367, 379, 381, 47], the access to it and its exploitation are still limited and more studies and realisations of transport/electrical interfaces are needed.

Additionally, the electrical properties of strongly coupled transport-optical systems are expected to improve significantly due to the larger range coherence of the photonic part of the system[383, 384, 385, 386]. Recently, first results on the enhanced conductivity of hybridised organic semiconductors were also reported[387]. The presented system represents a quintessential step in this direction, because it encompasses an Hall-bar, the reference system for any transport investigation. Furthermore, in this investigation we took advantage of the MIRO phenomenon thus interrogating the system at a specific frequency, but already the vacuum field fluctuations are expected to bring the system in USC and affect the transport. They stay as an important outlook for such system, at the same time requiring more theoretical work.

Finally, the investigated system represents an important playground for THz quantum optics. Quantum optics in the terahertz frequency range is a new area of research where reliable and well performing setup components are still under development and few initial results are available.[477, 478, 479, 480] The presented system, while carrying along the quantum optical potential of any USC system, adds a transport interface to the THz-quantum optics toolbox and will allow new experiments in this young, promising field.

The second conclusion comes from the discussion of the measurements on all Hall-bars,

with and without the SRRs, reconsidering the whole set of samples. In section 7.5 only the uncovered Hall-bars were discussed and the results were collected in Figs 7.13 and 7.14: now we can compile a more complete one, in Fig. 7.32.

Considering first the results on the first sample series −1452 (cf. section 7.6.1), these support the initial picture: in fact all uncovered Hall-bars showing MIROs, showed oscillations at the same B-field values also when covered with dSRRs. Eventually the oscillations were weaker.

The results on the second sample series (cf. section 7.6.2), collected in Table 7.4, instead, offer additional insights. In fact, two SRR-samples behave differently from their uncovered counterpart: $K2124$ and $C2124$. The latter, $C2124$, is the only sample showing USC-MIRO, shifted with respect to the uncovered-Hall-bar (cf. Fig. 7.28). This confirms the fact that only wide-channel Hall-bars show MIRO in the first place.

Sample $K2124$, instead, is important for the fact that its channel width is in the region where quenching of the MIROs is observed: in fact the uncovered-Hall-bar showed no MIROs. The corresponding cSRR-covered Hall-bar, on the contrary, showed unshifted MIROs (cf. Fig. 7.27), demonstrating that a stronger radiation concentration was beneficial for the phenomenon, while this was not the case for narrower samples. This seems consistent with the discussion on the phase-coherence length in section 7.5.1. In fact, sample $K2124$ is the one with $l_\phi \simeq w$. Nonetheless, a more detailed theory is needed to support this picture from a microscopical point of view.

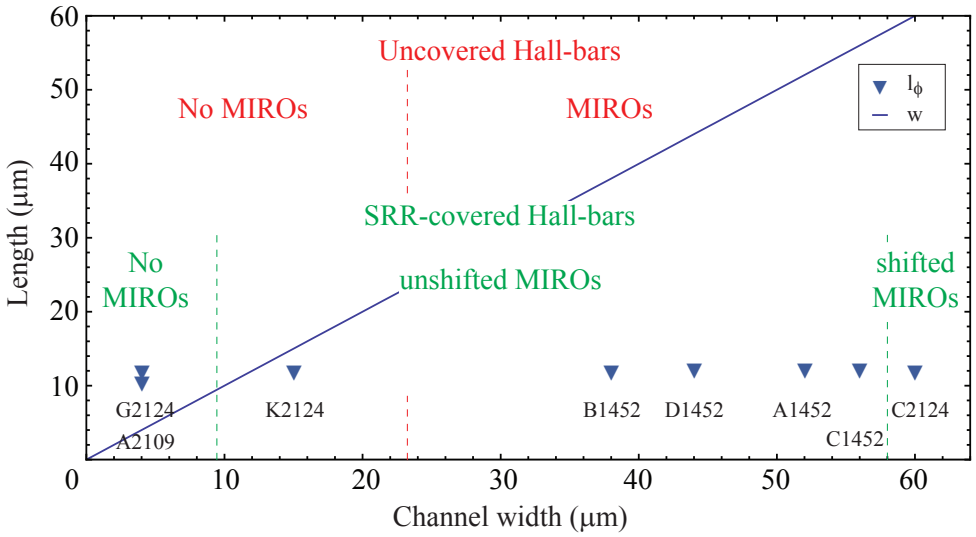

Figure 7.32 – Comparison of the phase coherence length in the different 2DEGs with the channel width for each investigated sample. Their relation seem consistent with the presence of the MIROs in their longitudinal resistivity traces, both with and without SRR.

In conclusion, this chapter described the efforts undertaken to measure in transport the ultra-strongly coupled state of THz-split-ring resonators-covered Hall-bars, taking advantage of the phenomenon of microwave-induced resistance oscillations. First results were presented, while the overall performed measurements on the two series of samples allowed to discuss the different proposed theories for the MIRO phenomenon, supporting the edge-stabilisation theory and ruling out some of the others.

Chapter 8

A graphene-based THz-modulator on the way to the Dicke phase transition

The present chapter describes the efforts undertaken towards ultra-strong coupling between the cyclotron transition in graphene and THz-split-ring resonators.[1] This target was not yet achieved and remains as an outlook to the work presented here, the main limitation being the difficulty in obtaining a cyclotron transition in graphene in the THz-frequency range.

Nonetheless, several types of graphene were characterised and different samples produced, coupling graphene to the SRRs presented in chapter 3. The investigation of such samples without magnetic field revealed the sample's capabilities as THz-modulator: this is presented in the next sections. Later, the samples studied in B-field are discussed.

Graphene is a particularly interesting material for the THz-frequency range. Its linear dispersion relation near the CNP with the absence of a sizeable band-gap gives rise to a scenario different from the case of usual semiconductors, concerning optical transitions. When considering inter-band transitions, a cut-off energy of twice the Fermi energy applies, E_F being typically some hundreds meV (infrared spectral region). This fact, therefore lets intra-band transitions become dominant at THz-frequencies. Such electro-optic characteristics reveal graphene as a promising material for optoelectronic and plasmonic applications.[313] In the THz-frequency range, useful applications of graphene reside particularly in detectors[314] and modulators[83, 481], but also sources have been

[1] Some parts of this chapter appeared, sometimes *verbatim*, in F. Valmorra et al., Nano Letters **13**, 3193 (2013)

foreseen[482, 483, 315].

When considering graphene in view of the THz-spectroscopy we want to perform with it, the relation between different dimensions needs to be considered. First, the THz-beam will contain wavelengths in the range 100 µm – 1.5 mm and can be focussed down to a spot with waist comparable to the longest wavelength. These dimensions create immediately concerns when considering that a monolayer of graphene is approx. 0.335 nm in thickness, hence with a mismatch of six orders of magnitude along the propagation direction. Such incommensurability is mitigated by the use of SRRs. They, in fact, concentrate the light to subwavelength volumes, thus enhancing the interaction. The second issue stems from the lateral dimension: the beam-waist, focussed onto the sample surface by parabolic mirrors is of the order of 1 millimetre and aperture screens cannot be used because they would Fourier-filter the source, reducing its bandwidth.

Therefore, of the different kinds of graphene available for this work, all described in section 5.3 on page 129, we can directly exclude flakes because their very small area (approx. 100 µm^2) will not allow for enough contrast in the transmission measurement. Thus we are left with SiC- and CVD-graphene. The choice fell on CVD-graphene because it can be gated directly from the substrate, while SiC-graphene would need to be provided with a top gate, further complicating the sample structure and the features of the THz-response.

Note that the SRRs concentrate the electro-magnetic radiation also laterally and they can indeed be used for smaller graphene surfaces. Nonetheless other issues come then into play: this possibility and its limitations will be discussed later in section 8.3.

8.1 THz-metasurface onto CVD-graphene: amplitude modulation of THz-waves

The sample discussed in this section is constituted by monolayer CVD-graphene (cf. section 5.3 on page 129) interacting with an array of direct SRRs of the same kind of those described in chapter 3. Monolayer CVD-graphene was grown on commercial Cu-foil and a piece of about 1×1 cm^2 was then PMMA-transferred onto a high-resistivity Si/SiO_x substrate, according to the procedures detailed in appendix H.2 on page 270. The dSRR array and the S/D contacts were defined onto the transferred CVD-graphene via standard photolithographic technique and produced by e-beam evaporation of Ti/Au with a thickness of 4/200 nm in a UHV-chamber. The processing details can be found in section H.1 on page 269 of the appendix. A picture and a cross sectional sketch of the sample are shown in Fig. 8.1.

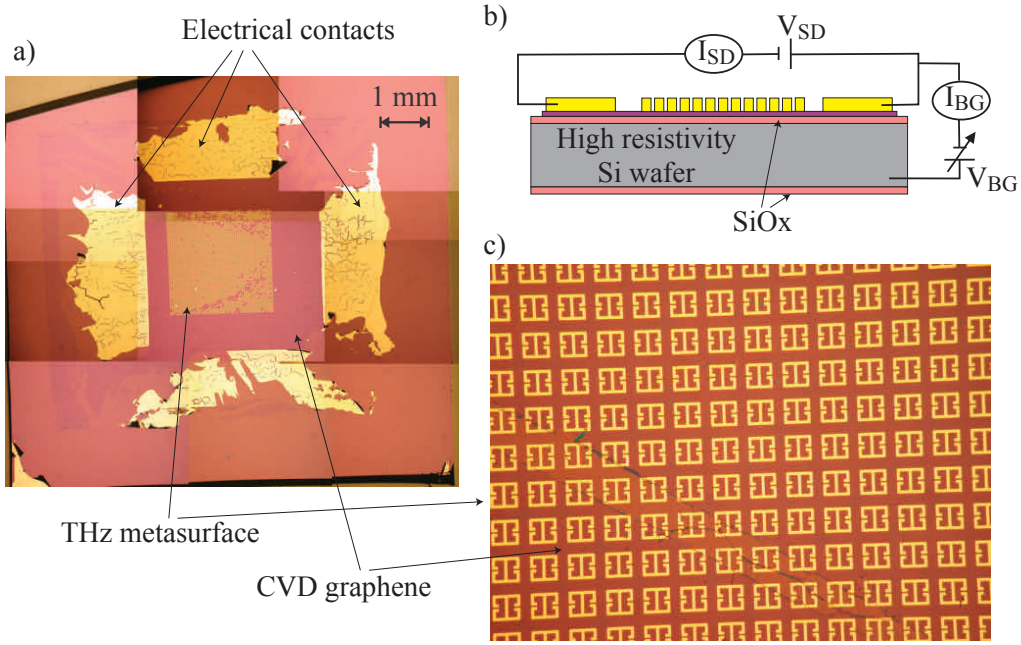

Figure 8.1 – a) Optical picture of the sample employing a THz-metasurface onto CVD-graphene. b) Scheme of the cross-section of the sample and of the electrical arrangement for the gated measurements. c) Detail of the active area of the sample.

Graphene was then characterised by Raman spectroscopy and by FET-measurements. Confirmation of dealing with monolayer was obtained by Raman spectroscopy showing in general a narrow intense 2D-peak and a low intensity D peak (D/G$\simeq$0.10) (cf. section 5.4 on page 137 for the explanation of the results of Raman spectroscopy). Panel a) of Fig. 8.2 shows the picture of unitary cell containing a single dSRR evaporated onto the graphene layer. The same area was scanned by the beam of the Raman microscope and the map in panel b) was compiled from the intensities of the 2D-peaks at the different points. Their intensity results to be quite homogeneous across the graphene layer, while no signal comes from the gold and from the polymer residual in the centre.

The FET-characterization of the CVD-graphene allowed to retrieve the graphene square resistance plotted in panel c) of Fig. 8.2. The square resistance displays a clear maximum, situated at $V_G^{CNP} = 10.6$ V, that constitutes the charge neutrality point (CNP) of the investigated CVD-graphene layer in the device, revealing its natural p-doping. The CNP maximum has a very broad shape when compared to the corresponding curve for exfoliated graphene flakes: as discussed in section 5.3 on page 129, this can be attributed to the macroscopicity of the system (5 mm vs $\simeq$10 µm) that includes inhomogeneities into the current path, such as residuals and cracks from the transfer procedure. The asymmetry between $p-$ and $n-$region is also regularly seen[484, 485] but in the present case was also strengthened by some current leaking through the gate oxide. In fact, despite the fact

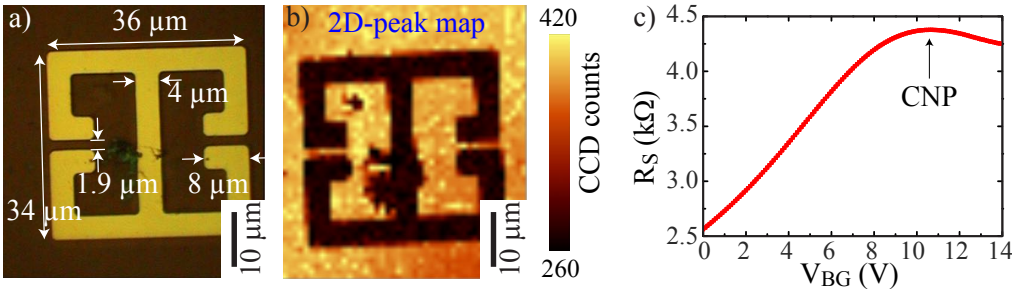

Figure 8.2 – a) Optical picture of the split ring resonator constituting the unit cell of the two-dimensional THz-metamaterial. b) Raman map of the 2D-peak intensity across the metamaterial unit-cell of panel a). c) FET-characteristic of the sample.

that the breakdown voltage of 285 nm of thermally grown SiO_x is higher than 100 V, in the present sample the gating bias was stopped at 14 V when the leaking current through the oxide layer reached 5% of the S/D current. The measured leakage is shown in panel c) of Fig. 8.2. The linear fit of the p-side gives a hole mobility of about 2050 cm^2/Vs, taking into account the sample geometrical factor $L/W = 1.1$. This factor is derived as the ratio of the distance between source and drain to the current-path width but the cracks in the transferred graphene layer reshape the current path leading to a possibly lower carrier mobility. The standard parallel-plate capacitor model allows one to estimate the initial p-doping of the graphene to be $p \simeq 8 \times 10^{11}$ cm^{-2}, corresponding to a zero-bias Fermi level of $E_F \simeq -104$ meV (cf. Eq.s (5.16) and (5.19)).

The metasurface is constituted by a 2.5×2.5 mm^2 array of dSRRs with a unit cell of 50×50 μm^2, whose structure is described in section 3.1 on page 81, pictured in panel a) of Fig. 8.2. Let us recall that the dSRR responds to a linear excitation across the slits by concentrating most of the electro-magnetic field into the gaps, in the LC-mode, while a broader dipolar mode with higher frequency is located at the edges of the structure. In the orthogonal polarisation another dipolar mode is present at intermediate frequencies. All modes have a z-direction extension of approx. 2 µm, hence fully overlapping with the graphene layer onto which the metasurface is deposited.

Panels a) and b) of Fig. 8.3 show the simulated in-plane E_{xy} and out-of-plane E_z electric field amplitude distributions in the plane of the graphene layer, at the LC-resonance when exciting the resonators with THz-waves polarised in the y-direction. Panel c) shows the vertical distribution of E_{xy}, being the cut performed at the gaps. E_z will be disregarded in the present discussion because it is not significantly interacting with the graphene layer[486]. This statement will be supported and discussed later in section 8.1.2. As clear from panels b) and c), the exciting THz-electric field gets concentrated mostly into

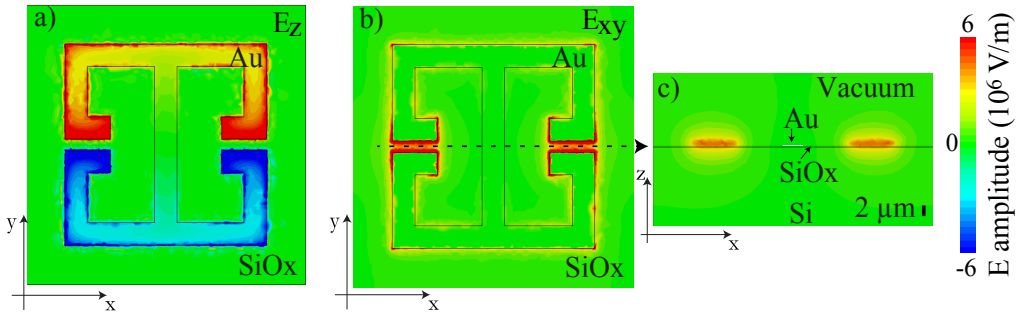

Figure 8.3 – Finite-elements simulation of the electric field amplitude at the *LC*-resonance. The exciting wave is linearly polarized in the y-direction. The distribution of the E_z and E_{xy} components in the plane of the SRR are plotted in panels a) and b), respectively. c) Distribution of E_{xy} in the orthogonal plane, set at the position of the dashed line in b).

the SRR-gaps, confining a wavelength of 0.5 mm into a maximum volume of $8 \times 2 \times 4$ µm^3, i.e. shrinking its volume by a factor 10^6. In other terms, such concentration corresponds to a confinement along the beam direction of $\lambda/125$ in vacuum, deep into the sub-diffraction region and about 60 times more than in photonic cavities (e.g. Fabry-Perot) limited to $\lambda/2$. We therefore argue that only the graphene residing within the dSRR-gaps is effectively taking part in the interaction. Additionally, the *LC*-resonance is the one displaying a direct correspondence to the sample geometry and allowing a physical discussion of the *RLC*-circuit model of the dSRRs (cf. section 3.3 on page 88). Therefore, in the following discussion the attention will be focused onto the spectral region $0.25 - 1.75$ THz.

8.1.1 Measurements without magnetic field

Alongside to the sample already introduced, a reference sample was produced: this is in all respects identical to the previous one, apart from not containing the graphene layer. The two samples were measured in the same configurations and the resulting spectra, normalized to the substrate, are reported in Fig. 8.4.

The measurements clearly show the strong effect of graphene onto the spectra of the metasurface. This confirms the interaction of the THz-beam with the graphene layer thanks to the dSRR's field concentration. In fact, transmission through the plain graphene layer alone would not show a sizeable absorption, consistently with the literature[487]. As expected, the effect is particularly evident for the *LC*-mode, whereas the other modes show similar but weaker influences. Thus, this suggests, once more, that we can carry on the analysis and discussion focussing onto the *LC* mode.

Let us thus first discuss the measurements in Fig. 8.4. The oscillations above 2 THz stem from the normalization of a low intensity signal, whereas the overall wiggling is due to the Fourier transformation of a signal with a finite extension in the time domain.

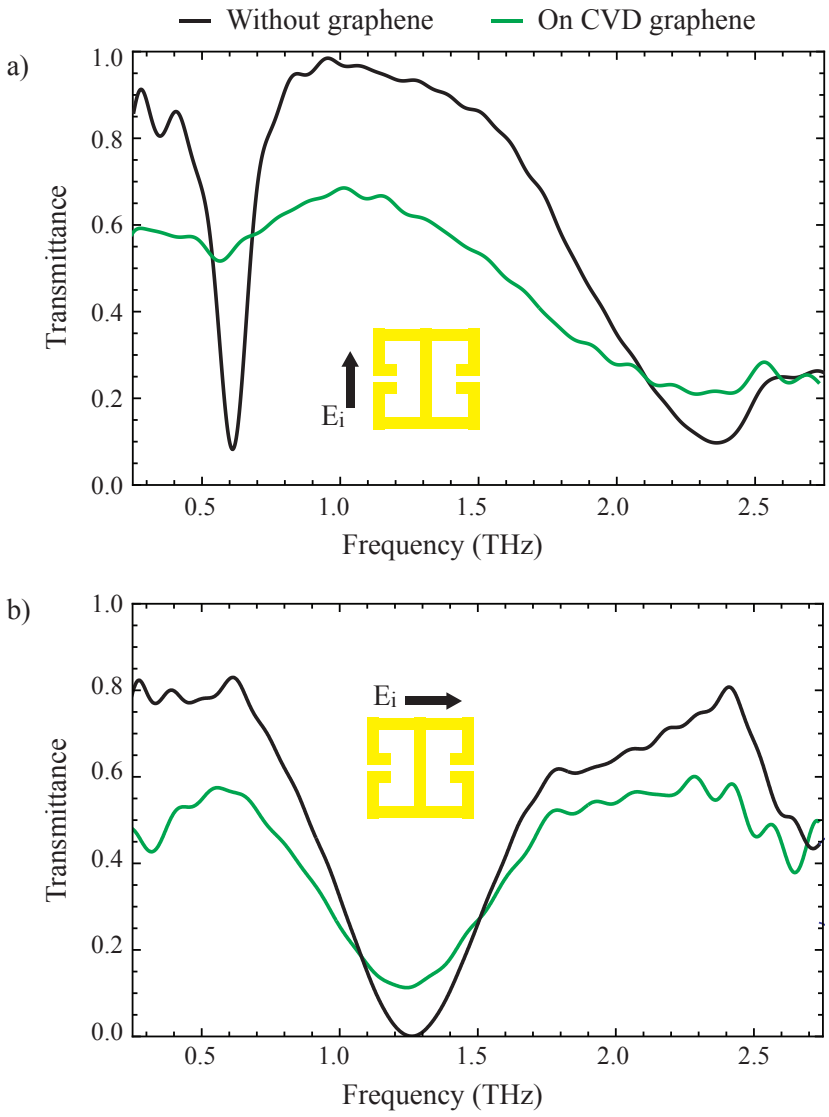

Figure 8.4 – Visualisation of the effect of the graphene layer onto the transmittance of the dSRRs in the two polarisations.

In the measured spectra, the presence of the graphene strongly affects the whole system response: the overall transmittance is decreased whereas the two metamaterial resonances are still present but with different characteristics. The transmittance of the unbiased sample, for the polarisation exciting the LC-mode, reveals an increased transmission at the now broader resonances, accounting to 9.9 dB. The frequency of the LC resonance red-shifts by about 45 GHz (approx. 7%) while its Q-factor degrades from Q_{ref}=4.75 to Q_g=2.6. The dipolar mode also degrades in a similar way (transmission increase by 4.5 dB) while the shift is only half as much (approx. 22 GHz, 1%). Precise values for the latter quantities are more difficult to assert, due to the fact that it is at the limit of the setup bandwidth. Moreover, the resonance shifts can be determined by numerically enhancing the resolution of the Fourier-transform, hence the values should be considered from a qualitative point of view.

The different behaviours of the two modes result from their nature: the presence of a (bad) conductor, the graphene, within the capacitors changes the resonance of the LC-circuit in a much stronger way than for the dipolar resonance. The latter depends more on the size of the SRRs' edge which is less influenced by the graphene, whereas the change in intensity is due to the degree of screening. The measured sample behaviour is in agreement with results on similar systems published in the past few years.[488, 486, 489, 481, 490, 491]

The measurements presented in Fig. 8.4 were performed without gating the sample, i.e. they correspond to the calculated residual p-doping, this being identified by the leftmost point in the square-resistance curve in panel c) of Fig. 8.2. The effect of gating on the transmission spectra was investigated by taking subsequent measurements for increasing back-gate voltages. They are presented in Fig. 8.5 where the curves from green to blue correspond to increasing back-gate voltages, as colour-coded in the inset. The transmittance without graphene is also plotted for comparison (black spectrum).

The gating of the graphene layer, by increasing V_G towards the CNP, tends then to deepen and sharpen the resonances. Concurrently, the transmittance in the frequency range in-between the two resonances increases. At higher voltages than the CNP the quite flat square-resistance of the graphene results in almost no change in the spectra beyond that point.

A clearer way to visualise these effects is by plotting the normalized transmission difference with respect to its value near the CNP where the resonance is the sharpest. The quantity $-\Delta T/T_{CNP} = (T_{CNP} - T_G)/T_{CNP}$ is displayed in Fig. 8.6. At resonance the transmission linearly decreases for increasing negative gate voltage, i.e. for increasing hole carrier density. Entering the n-doped region the transmission stays almost constant due to the asymmetry in the square-resistance curve in panel b) of Fig. 8.2. The gating

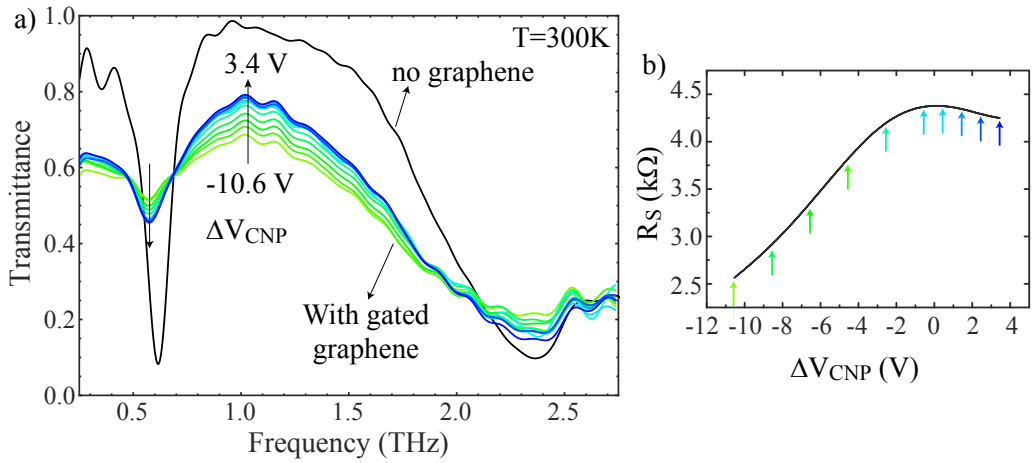

Figure 8.5 – a) Room temperature transmittance spectra of the gated CVD-graphene/THz-metamaterial device for back-gate voltages V_G=(0,2,4,6,8,10,11,12,13,14) V, from green to blue, with $\Delta V_{CNP} = V_G - V_{CNP}$. Compare with b) to relate ΔV_{CNP} to the variation in the graphene square resistance. The reference spectrum of the THz-metamaterial directly evaporated onto the substrate without the graphene is shown in black. All spectra are normalized to the bare substrate.

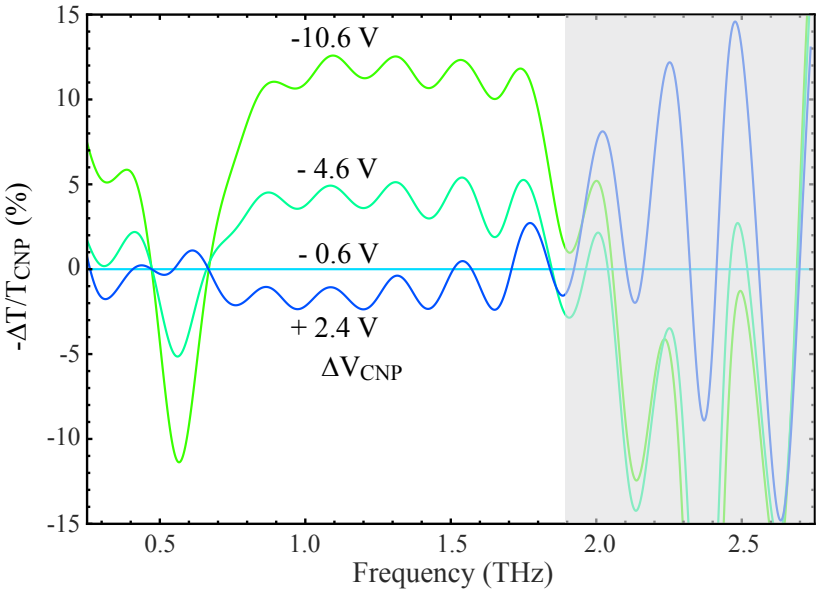

Figure 8.6 – Relative transmittance normalized to the value near the CNP for a selection of spectra. Maximum modulation depths of -11.4% and 11.5% at -10.6 V from the CNP are derived at the *LC*-resonance (610 GHz) and for the region 0.8 – 1.75 THz, respectively. In correspondence to the cut-wire resonance (gray-shaded region) the difference between the spectra is too small to give a meaningful normalized value, still showing similar behaviour as for the *LC*-one.

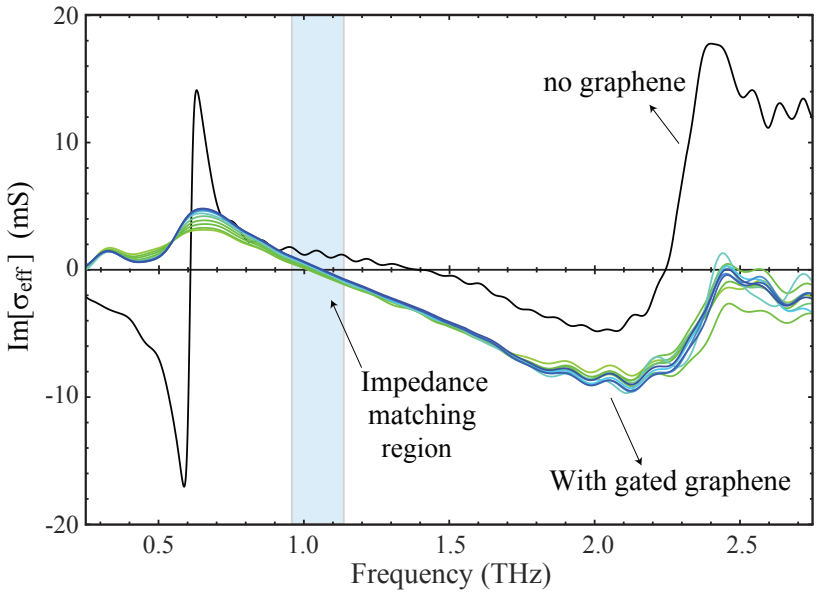

Figure 8.7 – Imaginary part of the extracted effective conductivity. At the crossing with the horizontal axis, the graphene-metamaterial system is impedance-matched to the substrate.

results in a maximum modulation depth at resonance of -11.4% at -10.6 V from the CNP and in a similar modulation depth of 11.5% in the region $0.8 - 1.75$ THz. The presented device has the advantage of working at low bias, while being purely planar. A more complete discussion of the performance as amplitude modulator and the comparison with the literature will be carried on in section 8.1.4 on page 222.

It is interesting to notice that the same amount of modulation is achieved both at resonance and at the high-transmission point, in the tails of both modes. More insight into this can be gained by the plot of the imaginary part of the effective conductivity σ_{eff} shown in Fig. 8.7. This is obtained from the transmission via Eq. (3.15) from chapter 3 on page 81 and it is connected to the real part of the effective refractive index ϵ_{eff} according to Eq. (3.14). The modulation in the large absolute modulation in the tails of the resonances corresponds to the region for which the imaginary part of σ_{eff} is close to vanish, hence meaning that $\epsilon_{eff} = \epsilon_{SiO_x}$ and impedance-matching is achieved. Furthermore it is interesting also to note that the sign of the modulation is related to the derivative of $Im\,[\sigma_{eff}]$, as expected from Eq. (3.14), and the frequencies for which no modulation is detected correspond to the maxima and minima of the curves.

By retrieving the quality factor of the LC-resonance (red points in Fig. 8.8) it is evident that it reaches its minimum value deep into the p-doped region. The Q-factor then improves by gating the graphene towards the CNP, showing the same qualitative behaviour as the square resistance, changing more than 35% with respect to its maximum value. A small blue-shift of 4.6 GHz for the minimum of the LC-resonance, initially

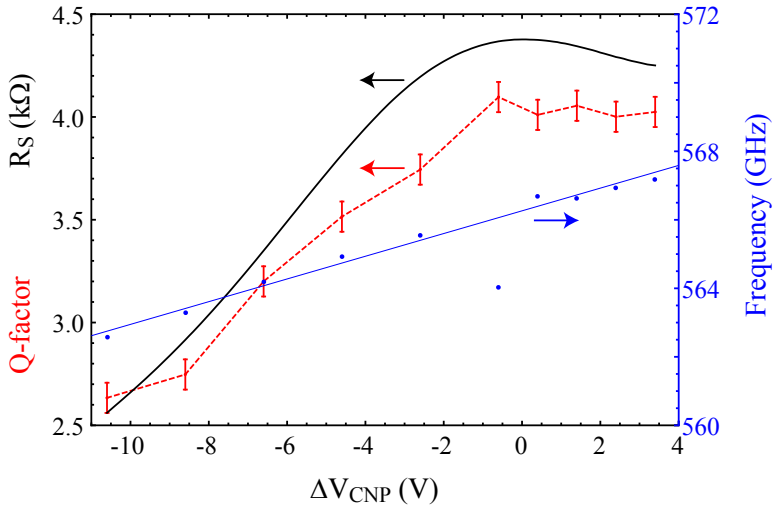

Figure 8.8 – Square resistance of the CVD-graphene layer (black curve, left axis), Q-factor of the LC-resonance (red points, left axis) and *LC*-resonance frequency (blue points, right axis). The horizontal axis expresses the voltage difference from the CNP, $\Delta V_{CNP} = V_G - V_G^{CNP} = V_G - 10.6$ V for $V_G = (0, 2, 4, 6, 8, 10, 11, 12, 13, 14)$ V. The square resistance is obtained from the S/D current with $V_{SD} = 10$ mV (contact resistance not taken into account). The curve was measured with the sample in nitrogen-purged environment and does not change under THz irradiation or for longer nitrogen exposure time. The blue line is a linear fit of the LC-resonance frequency minima.

red-shifted from the bare metamaterial value (610 GHz) because of the presence of the graphene by 45 GHz, is also present. By fitting the data a blue-shift-rate of 332 MHz/V over the whole measurement range (with exception of one point) can be extracted and is displayed by the blue line in Fig. 8.8. This can be qualitatively explained as follows: the capacitor gets first loaded by charges, that shift and broaden the resonance. Gating the graphene towards the CNP removes charges from layer, progressively restoring both resonant frequency and quality factor. Due to the quality and type of graphene used, at the CNP a consistent amount of charges is still present, limiting the modulation depth of the device. In perfect ideal conditions, the spectrum at the CNP should almost coincide with the one without graphene.

8.1.2 The vertical component of the electric field E_z

In the previous discussion, the whole analysis was relying onto the distribution of the in-plane electric field E_xy. But, as seen from the simulations reported in Fig. 8.3, the orthogonal component E_z is comparatively strong and covers a much larger area, where graphene is also present. In this section we want to support and discuss the negligibility of E_z with respect to E_{xy} in the analysis of the performed measurements.

Recalling that the golden resonators are evaporated directly onto the graphene layer,

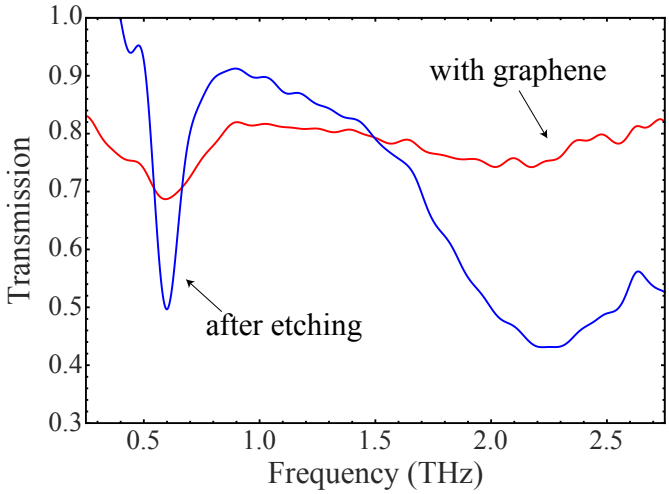

Figure 8.9 – Spectra measured onto the second sample, before (red) and after (blue) dry-etching of the exposed graphene. Compare to Fig. 8.4 on page 212.

it is evident that only the graphene buried below the gold could interact with E_z. In order to study such interaction, THz-TDS transmission measurements were performed on a second sample. The sample was produced in the same way as the one presented in the main text and contains CVD-graphene from the same growth-run. Differently from the first one, this sample does not contain ohmic contacts on the graphene and due to processing casualties contains about 20% of the initial number of resonators with unregular dilution on the same total area. These differences are anyhow not relevant for the present discussion.

The sample was first measured, then dry-etched and finally measured again. The oxygen-based dry-etching removes all the exposed graphene, as confirmed by subsequent microscopical inspection, leaving the gold-SRRs unaffected. After such process, the only graphene left is therefore the one buried below the gold of the resonators. The sample transmittance before and after the etching step, i.e. with and without graphene in the exposed surface, is presented in Fig. 8.9 in red and blue, respectively. The relevant feature of the presented curves is the Q-factor of the LC-mode. For the spectrum taken before the etching step, it accounts to about 2.1, whereas it improves till about 4.8 after the etching step. Comparing these values with the ones extracted from the measurements in the main text, the lowest Q-factor value (and also the overall spectral shape) is close to the one corresponding to the unbiased sample ($Q \simeq 2.65$) whereas the second one is practically equal, within the error bar, to the Q-factor of the reference sample without graphene ($Q = 4.75$). Similar, even stronger, behaviour can be seen for the second resonance. This fact strengthens the conclusion that the interaction of the graphene with E_z is negligible with respect to the interaction with E_{xy}, consistently with what

has also been shown in the literature for simulations of different metamaterial geometries interacting with graphene.[486] Therefore, we can analyse the sample focussing on the strongest interaction between E_{xy} and the graphene in the SRR-slits: this is the topic of the next section.

8.1.3 Circuital modelling of the gated measurements

In order to get more insight into the device properties, the simple electrical model described in section 3.3 on page 88 of chapter 3 can be used. As previously explained, taking advantage of the calculations in Ref. [27], the transmission of the device can be written in terms of the materials' impedances (cf. Eq. (3.1)) and in particular of $Z_{meta}^{graph}(\omega)$. This represents the complex impedance of the graphene-metamaterial system that we want to derive. To do so, we can start from the impedance of the metasurface alone, $Z_{meta}^{dSRR,n}(\omega)$, as from Eq.s (3.2)-(3.4). Writing each of the two resonances as an RLC-series circuit, the transmission spectrum can be calculated as a function of the effective parameters R, L, C. The parameters' values for the two modes are reported in Table 8.1 and agree with what was reported in the literature[27] from similar fittings and from finite-element simulations of the used golden resonators.

In order to get more insight into the modulation behaviour of the graphene-SRR system, a physical discussion can be set considering that the LC-mode concentrates the in-plane electric field within the gaps. Therefore, the fictitious capacitance used in the model can indeed be related to the physical capacitor. The presence of the graphene can then be accounted for by introducing in the model its impedance in parallel to the capacitance of the bare metamaterial[492], as sketched in the first circuit in Fig. 8.10.

The impedance of the graphene can be written via its complex sheet-conductivity as $Z_g^{-1} = \frac{W}{L}\sigma_g$, where W/L is the effective aspect ratio of the graphene interacting with the SRR-capacitor, needed to convert the sheet conductivity into a (3D) impedance. The equivalent impedance can then be derived as $Z_{eq}^{-1} = Z_C^{-1} + Z_g^{-1}$ and it corresponds to the total impedance of the capacitor formed by the SRR-slit including the graphene within

Table 8.1 – Extracted circuital values for the effective parameters (par.s) using the transmission-line model, for the two modes in the parallel polarisation.

mode par.s	R (Ω)	L (pH)	C (fF)
LC-mode	50	190	0.36
dipolar mode	57	24	0.19

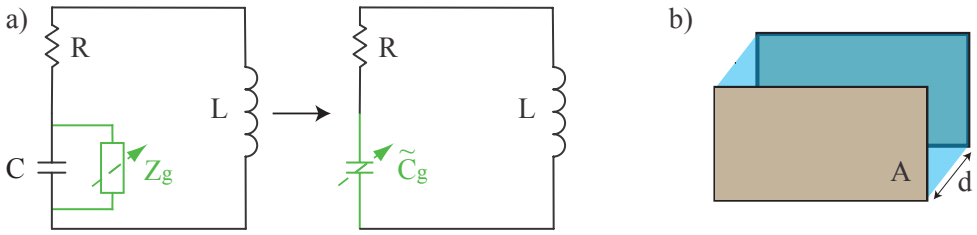

Figure 8.10 – a) Equivalent circuits of the graphene-metamaterial coupled system, considering at first the graphene impedance Z_g in parallel to C, then a complex capacitance $\tilde{C}_g$. b) Definition of symbols for the parallel-plate capacitor.

its expansions, as shown in panel a) of Fig. 8.10.[492] For such reason it is natural to write it as $Z_{eq}^{-1} = i\omega C_g$, where now the graphene-corrected capacitance is a complex quantity. Comparing the two formulae for the equivalent impedance, one can derive the following expression for C_g:

$$C_g = C + \frac{\sigma_g}{i\omega}\frac{W}{L}, \tag{8.1}$$

where $Z_C^{-1} = i\omega C$ was used to simplify the expression.

Unfortunately, in the given sample configuration, the factor W/L cannot be directly taken from the geometrical size of the gap. This is mainly due to edge effects in the small capacitor. To determine the needed value, the capacitor's geometry was simulated using COMSOL Multiphysics. The dSRR's extensions forming the gap were simulated as metallic contacts placed onto an homogeneous layer, the graphene, with a constant sheet resistance given by the values reported in the measured FET-curve in panel c) of Fig. 8.2. The W/L factor was then derived from the $I(V)$ current propagating from one contact to the other through the graphene layer. This procedure was repeated for the different sheet-resistance values of the gated graphene and its average value accounts to 7.45.

The present discussion allows an additional, very interesting, consideration about the issue of assigning a thickness t_g to the graphene layer, unavoidable to convert its sheet conductivity into a dielectric function, but not well defined from basic principles.Within the present discussion, instead, we can physically define t_g as follows.

Considering the simplest form of the SRR-capacitance, it can be written for the parallel-plate capacitor as $C = \epsilon_0\epsilon_{die}A/d$, where ϵ_0 and ϵ_{die} are the vacuum permittivity and the relative permittivity of the dielectric, A the plate area and d the distance between the plates, as schematised in panel b) of Fig. 8.10. By substituting the formula in Eq. (8.1) and rearranging the terms, one can write the graphene capacitance as

$$C_g = \epsilon_0\frac{A}{d}\left(\epsilon_{die} + \frac{\sigma_g}{i\omega\epsilon_0}\frac{W}{L}\frac{d}{A}\right). \tag{8.2}$$

By comparison, the term in brackets must correspond to the relative permittivity of the graphene layer. Indeed, this has the form of the standard expression for the complex relative permittivity of a conductive material[38], namely

$$\epsilon_g = \epsilon_{die} + \frac{\sigma_g}{i\omega\epsilon_0}\frac{1}{t_g} \tag{8.3}$$

when identifying

$$t_g^{-1} = \frac{W}{L}\frac{d}{A}. \tag{8.4}$$

The derived relation defines the "optical" graphene thickness to be derived from the aspect-ratio of the current path through the capacitor and the capacitor dimensions (cf. section 3.4 on page 92).

At this point one can substitute into Eq. (8.1) the formula for the AC-conductivity of graphene. As shown in section 5.2 on page 124, this is usually presented with two terms, separating the intra- and inter-band transitions. In the present situation, the cutoff energy for inter-band transitions is set by a Fermi energy of $\mid E_F \mid = 104$ meV, leaving only intra-band transitions relevant in the investigated energy range. In such a case, reporting Eq. (5.9), the graphene AC-conductivity is written as

$$\sigma_{intra}\left(\omega, E_F, \tau, T\right) = -i\frac{e^2 k_B T}{\pi\hbar^2\left(\omega - i/\tau\right)}\left(\frac{E_F}{k_B T} + 2\ln\left[\exp\left(-E_F/k_B T\right) + 1\right]\right), \tag{8.5}$$

where $k_B T$ indicates the thermal energy of 26 meV, being the measurements performed at room temperature. Note that the only other parameters are the Fermi energy E_F and the carrier scattering time τ.

The back-gate voltage applied to the sample acts experimentally on the graphene's Fermi level E_F in a fashion described by

$$E_F\left(\Delta V_{CNP}\right) = \hbar v_F\sqrt{\pi a \Delta V_{CNP}} \tag{8.6}$$

where $\Delta V_{CNP} = V_G - V_{CNP}$ is the voltage distance from the CNP of a given gating voltage V_G, $v_F = 10^6$ m/s is the Fermi velocity and $a = 7.56\times10^{14}$ m^{-2} V^{-1} is the capacitance per unit area per charge of the SiO_x oxide. Equation (8.6) follows directly from Eq.s (5.19) and (5.16).

Substituting Eq. (8.6) into Eq. (8.5), it is possible to calculate the graphene intra-band conductivity as a function of ω for a given applied back-gate voltage, leaving the scattering time as the only free parameter. A complex valued function results that, once inserted into the formula for $Z_{meta}^{graph}(\omega)$, will modify both the real and imaginary part of

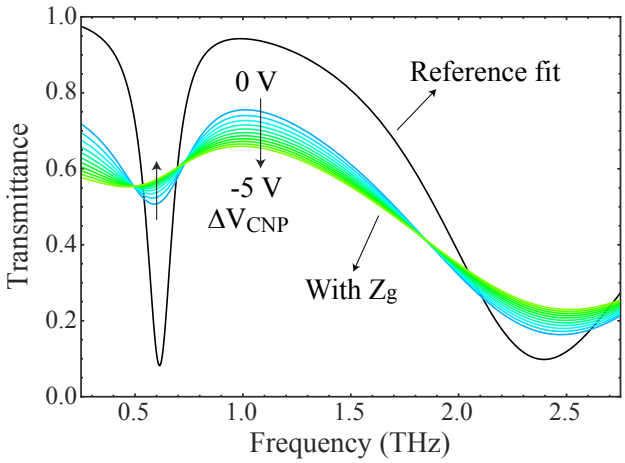

Figure 8.11 – Calculations of the THz-modulation with the transmission line model. The *RLC*-series circuit used is shown in Fig. 8.10. The black curve is obtained adjusting R, L, C till best agreement with the reference spectrum. The effective parameters' values for the two modes are given in Table 8.1. The green-to-blue spectra were calculated for decreasing values of ΔV_{CNP}, in good agreement with the measurements of Fig. 8.5.

the total circuital impedance, i.e. affecting both resistance and reactance of the system.

To summarise the logical sequence, each resonance will be described by an impedance of the form $Z_g(\omega) = R + i\omega L + \frac{1}{i\omega C_g}$, with effective parameter values from Table 8.1. The two resonances and the substrate are then put in parallel to obtain the metamaterial/graphene impedance $Z_{meta}^{graph}(\omega)$. Finally, substituting $Z_{meta}^{graph}(\omega)$ into the transmission-line formula Eq. (3.1) and fitting τ, it is possible to calculate the transmittance of the sample. The series of calculated spectra is shown in Fig. 8.11 and show the curves calculated by varying ΔV_{CNP} between 0 and -5 V in steps of 0.5 V using the best value found for the scattering time, $\tau \simeq 15$ fs. Only negative gate voltages are reported, because the used formulae are symmetric in ΔV_{CNP}, not taking therefore into account the different behaviour of the sheet-resistance in the n-doped region.

The derived value of τ can here be considered as an average scattering rate resulting from the whole graphene-material within the gaps of all resonators into the measurement beam, and it is in very good agreement with what reported in the literature[481, 493, 494, 274]. It can be also compared to the DC-scattering rate derived from the mobility measured during the FET-characterisation ($\mu = 2050$ cm^2/Vs) by using the relation[275, 276]

$$\tau_{DC} = \frac{e\mu E_F}{v_F^2}. \tag{8.7}$$

It gives $\tau_{DC} = 21$ fs, fairly close to the fitted value.

Considering the calculated spectra, the used model is in good agreement with the measurements of Fig. 8.5 on page 214, qualitatively reproducing all relevant characteristics

of the transmittance, and mostly also quantitatively. The transmitted intensity is correctly predicted over the whole frequency range with a calculated modulation of about 16% for both the LC-mode and the intra-resonances region. An initial shift of about 22 GHz is predicted for the LC-mode, close to the measured 45 GHz. The gating also red-shifts the resonance and broadens its shape but with much stronger effects than measured: in the calculated voltage range the gate-induced shift is bigger than 60 GHz (vs 4.6 GHz) and the Q-factor is always below 2 (vs $Q_{min} = 2.6$). Finally, the calculated dipolar mode is being predicted with a close absolute intensity and similar modulation, although a blue-shift is present. This small difference can be attributed to the fact that the calculation also considers this mode as an RLC-resonance. It is done for analytical purposes but, whereas for the LC-mode there is a concrete physical counterpart of the model, for the dipole-mode there is no real capacitor and the physical effect of the graphene might reside more in the resistive term rather than into the reactive one.

8.1.4 Discussion and Outlook as a THz-modulator

The measured sample behaviour is in agreement with results on similar systems published in the past few years, studying amplitude modulation of THz-waves.[488, 486, 489, 481, 490, 491]

In particular, the reported modulation has to be compared with previously published results on similar systems featuring graphene in an optical cavity, in order to show the advancement achieved. Afterwards, developments of this system into better amplitude-modulation and frequency-modulation will be shortly discussed.

THz-amplitude modulation

When our results were published, the highest amplitude-modulation of THz-waves making use of graphene amounted to 90% at 850 V of gating bias.[481] The device in Ref. [481] relies on CVD-graphene, transferred onto an array of metallic rings and sandwiched between bendable polymer layers that ensure mechanical stability while acting as a gate dielectric for an additional grid of gating electrodes. Despite having the advantage of demonstrating a bendable modulator with a big modulation depth, this device works at unpractical high voltages without the possibility of down-scaling, contrary to ours.

In fact, the main difference comes from the gating modality. The presented device is based on standard Si-processing technology, where the substrate is the gate electrode and the thermally-grown oxide is the dielectric. Silicon dioxide has a gate capacitance per electric charge of 7.56×10^{10} cm^{-2} V^{-1} with respect to 8.54×10^{9} cm^{-2} V^{-1} for the

4.22 µm thick polymer layer (parameter a in Eq. (8.6)). This means that there is an order of magnitude difference in the achievable Fermi-level shift at a given gate bias.

Reference [481] also showed that the bias scales linearly with the polymer thickness, but a 10 times thinner polymer layer would be most likely too thin to be self-standing. Additionally it can be argued that the Si-substrate performs a more homogeneous gating than the complicated multi-layered gating structure composed by two metallic grating, a further framing electrode and four polymer layers.

A further improvement comes from the fact that we use the LC-mode of THz-SRRs, the one giving the strongest field confinement[11], in contrast to dipolar or quadrupolar modes.

A second article[495] instead showed a modulation depth of 64% for a potential drop of 30 V by placing the graphene as one of the mirrors of a Fabry-Perot cavity realised around a 500 µm thick silicon wafer, the other mirror being constituted by a gold layer on the opposite side. A more extended study on this configuration for a THz-modulator is published in Ref. [495].

The device shows very good modulations, even though in a quite narrow frequency range (approx. 50 GHz). The main disadvantage is the use of a Fabry-Perot cavity, which is the prototype of a *photonic* cavity, thus limited by diffraction. Because of the photonic intrinsic limitation, this dimension cannot be smaller than $\lambda/2$ (diffraction limit). On the contrary, we rely on an *electronic* cavity, constituted by the LC-resonance of the dSRRs, which allows us to present a purely bi-dimensional system, whose thickness along the beam propagation direction can in principle be reduced to $\lambda/50$. In fact, both the thermal oxide and the substrate could be made thinner in an improved version of the device: low bias allows for a thinner oxide, whereas the only constrain for the Si-substrate thickness are the robustness of the sample and the maintenance of good conductive properties. This is an important improvement considering device integration.

The presented device architecture was independently optimised in Ref. [496]. The work reports on a top-gate scheme where the dSRRs act as a gate to the graphene layer placed below them after 35 nm of SiO_x. The device showed 18% amplitude modulation for a bias of 0.5 V. Again, as discussed previously, the reduction of one order of magnitude of the gate oxide, results in a comparison improvement of the modulation amplitude.

Finally, on the same line, the widest amplitude modulation was achieved with the ultimate gate dielectric from the point of view of thickness: ion-gels (cf. section 5.3 on page 129): 99% THz-modulation showed at 3 V.[497] Such gating scheme shows a gate

capacitance per electric charge of the order of 10^{13} cm^{-2} V^{-1}[354], much higher than the values reported above for the other schemes.

A last comment is due about amplitude-modulation: Ref. [498] calculated the achievable modulation as a function of the different material parameters and concluded confirming that the limiting factor is the mobility of graphene. A higher mobility value would be desired because it decreases the losses, while then requiring an impedance-matching mechanism to reduce wave-reflection. Without any impedance-matching they predict 100% modulation only above 10 THz.

Frequency modulation

Most of the previous results reported amplitude modulation of continuous THz-wave. In some cases the frequency modulation capabilities were investigated and they usually show a cutoff about 100 kHz.[481] No systematic investigation was performed on our own device from this point of view, but preliminary measurements showed frequency modulation of few tens of kHz. This is limited by the RC time constant of the circuit that suffers, on the one hand side, from the large area of the device contributing a huge capacitance $C \simeq 3$ nF, while, on the other hand side, a very high resistance is due to the badly-conductive, large graphene layer $R_{SD} \simeq 4$ kΩ. These values predict a maximum modulation frequency $f_{max} = 1/(RC) \simeq 80$ kHz.

To address such issue, a similar device was investigated where the modulation of the metasurface transmission was due to its interaction with graphene microribbons, tuned into resonance.[499] We had already reported in different publications that graphene ribbons, or more generally confined structures, are able to sustain plasmonic oscillations in the THz-spectral range.[500, 501] Since this is a resonant interaction, the effect is much stronger than for the case of a continuous graphene layer, that corresponds to the highly detuned system. In fact, a device featuring complementary SRRs with embedded graphene microribbons, both resonating about 4 THz, showed an amplitude-modulation depth of 60% for a bias of 135 V and a frequency modulation of 41 MHz for a device with an area of 0.5×0.5 mm^2 and parallel electrical connections among the different unit cells.

Interestingly, a second sample with exactly the same structure, but resonant at about 10 THz displayed also strong coupling with a normalised Rabi frequency of 10%.[499]

8.1.5 Measurement with magnetic field and discussion

The discussed CVD-graphene/THz-dSRRs sample was then measured immersed in magnetic field. Preliminary scans showed no anti-crossing and, in order to enhance the

signal-to-noise ratio, the cross-polarisation configuration was used (cf. section 3.5 on page 95). Recall that such configuration means that the sample is excited with a given linear polarisation while the detection is performed in the orthogonal one. This configuration cannot detect the linearly polarised SRR, but takes advantage of the fact that the uncoupled cyclotron transition is circularly polarised, hence can be excited and detected in both linear polarisations while having the additional benefit of automatically filtering the exciting beam. The map showing the cross-polarised transmission for low B-fields is shown in panel a) of Fig. 8.12, to be compared with the calculated cyclotron transitions in such frequency range, reported in panel b) for $E_F = 50$ meV and $E_F = 100$ meV. Unfortunately, the map does not show any feature moving in magnetic field. Additionally, no gating was possible because of carrier freeze-out in the substrate at T=7 K, therefore the map corresponds to $V_G = 0$ V and presumably still $\mid E_F \mid \simeq 100$ meV (this is not sure because, for the same reason, no FET-characterisation was possible), hence expecting an intermediate cyclotron absorption line between the two calculated in panel b).

Higher magnetic fields were then applied on an identical sample apart from the fact that the metasurface array is constituted by an array of complementary SRRs. The map of the transmission for a single polarisation, namely the one exciting the cSRRs, is reported in panel c) of Fig. 8.12. Again, unfortunately, no anticrossing coming from the hybridised cyclotron transition/cSRR-mode is detected, whereas a modulation of the resonance of the cSRRs is present. This latter phenomenon was not studied in the present work but it is in all respects identical to the work of Zanotto et al. that later reported on a very similar sample.[502] They showed that such a modulation is indeed the result of an interaction of the SRRs with the graphene at high magnetic fields, but not involving any strong coupling. Instead, the semi-classical modulation of the magneto-conductivity of graphene, given in Eq. (5.10), is responsible for the small tuning, counterpart of the electrical modulation previously discussed.

The probable cause of the absence of graphene's cyclotron transition and of its strong coupling with the SRRs is the low mobility of the investigated samples. In fact, first, the minimum confinement field for having defined Landau levels can be estimated in the present case to be $B_{min} \simeq \mu^{-1} \simeq (0.2\ \mathrm{m^2/Vs})^{-1} = 5$ T. Additionally, strong coupling requires that the two involved resonances have comparable losses.[503] Given a quality factor of approx. $Q = \omega_{res}/2\gamma \simeq 4$ for the investigated LC-mode of the SRRs (cf. Fig. 8.8), one can estimate the damping term of the cyclotron transition. In turn, this allows the estimation of the damping time $\tau = 2\pi/\gamma$ and, assuming it is entirely due to scattering processes, an order of magnitude for the mobility can be derived making use

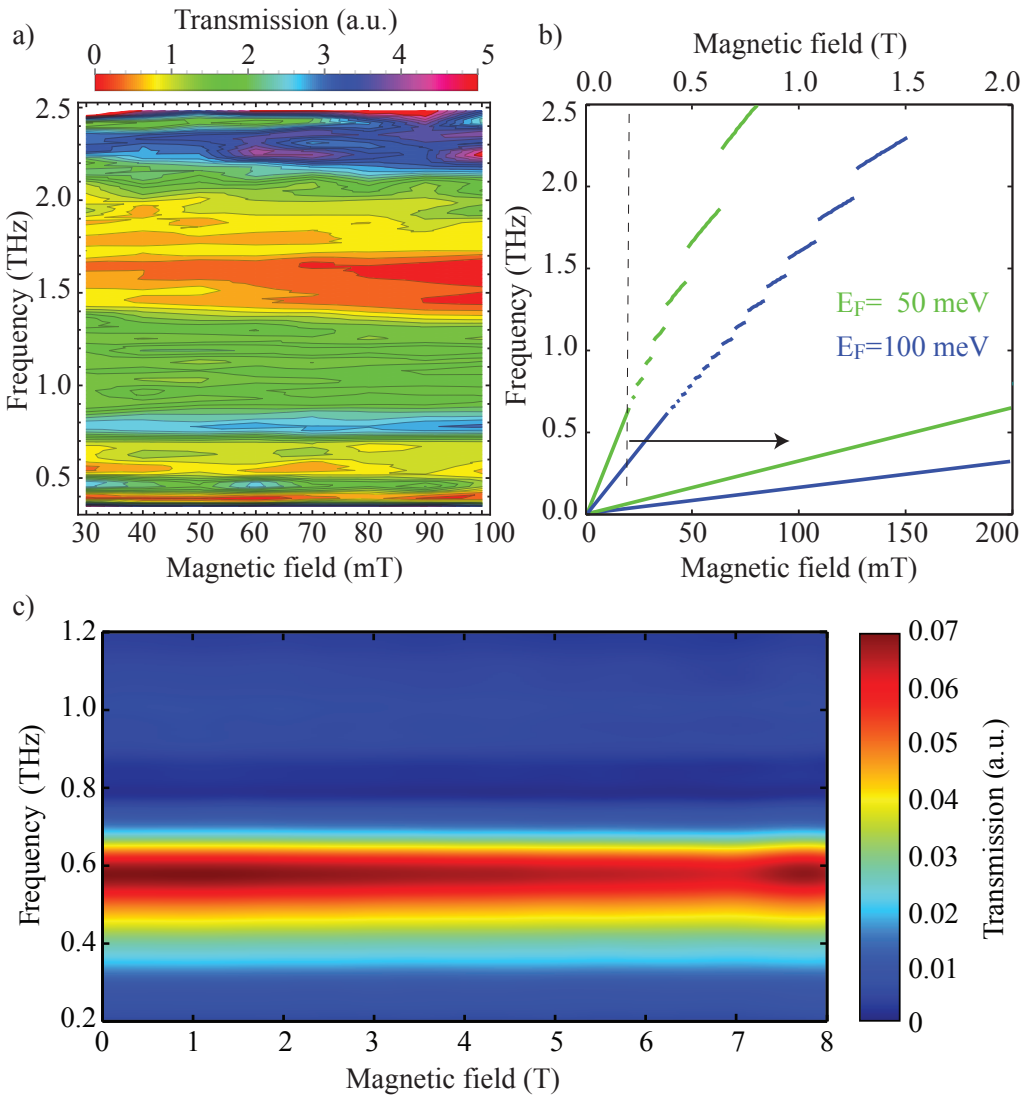

Figure 8.12 – a) Contour plot of the cross-polarisation transmission for low B-fields of the CVD-graphene/THz-dSRR array sample. b) calculated cyclotron transitions for $E_F = 50$ meV and $E_F = 100$ meV. c) Single-polarisation transmission map for a larger B-field range of the CVD-graphene/THz-cSRR array sample, showing magnetic-field-induced modulation of the LC-mode.

of Eq. (8.7):

$$\mu_{min} = \frac{2ev_F^2}{E_F}\frac{Q}{f_{res}}. \tag{8.8}$$

For the parameters of the discussed samples one derives $\mu_{min} \simeq 1.28 \times 10^6$ cm^2/Vs.

This estimation confirms the suspicion about the mobility: a fairly high mobility is needed to resolve the cyclotron transition at these frequencies, about two orders of magnitude higher than what commercially available for CVD-graphene.[2] This brought us to shift our efforts towards other types of graphene, where higher mobilities are routinely available. Magneto-transmission measurements for SiC-graphene are discussed in the next section. Another alternative is to use exfoliated graphene flakes, but with the disadvantage that, at THz-frequencies, their dimensions are usually subwavelength, hindering a direct investigation.

On the other hand, Eq. (8.8) provides also some more insight into the strong coupling conditions, suggesting that an investigation at higher frequencies will mitigate the requirements on the mobility (e.g. $\mu_{min} \simeq 0.38 \times 10^6$ cm^2/Vs for $f_{res} = 2$ THz). This offers an additional chance to investigate yet a different sample. Taking advantage of the field concentration of complementary SRRs, high-frequency cSRRs were produced directly onto exfoliated flakes, at the same time circumventing the size/wavelength mismatch issue. Their magneto-investigation is presented in section 8.3 on page 229.

8.2 Magneto-THz-transmission of SiC-graphene

SiC-graphene provides a large-area alternative to CVD-graphene, despite some disadvantages discussed in section 5.3 on page 129, while showing routinely higher mobilities. Two samples with about 20 and 70 layers on the C-face of SiC, bought by Graphene Works Inc., were measured in transmission, hoping for a stronger absorption because of the many stacked, high-mobility layers. No processing was performed on those, hence the layers are as-grown, unpatterned but also without the possibility of gating them or of determining their electronic mobility. In general, though, one expects relatively high Fermi energies $E_F = 100 - 400$ meV.[274]

The magneto-transmission maps through the two samples, normalised to the empty hole at $B = 0$ T, are reported in Fig. 8.13. The low-B-field map in panel a), measured on the sample with 20 layers, shows two minima, horizontally stretched and inconsistent with the expected cyclotron absorption calculated for a set of Fermi energies and plotted

[2] The recent report by Banszerus and coworkers of encapsulated CVD-graphene with mobility comparable to exfoliated flakes[327] opens another chance for this same kind of samples, provided the reported material is available.

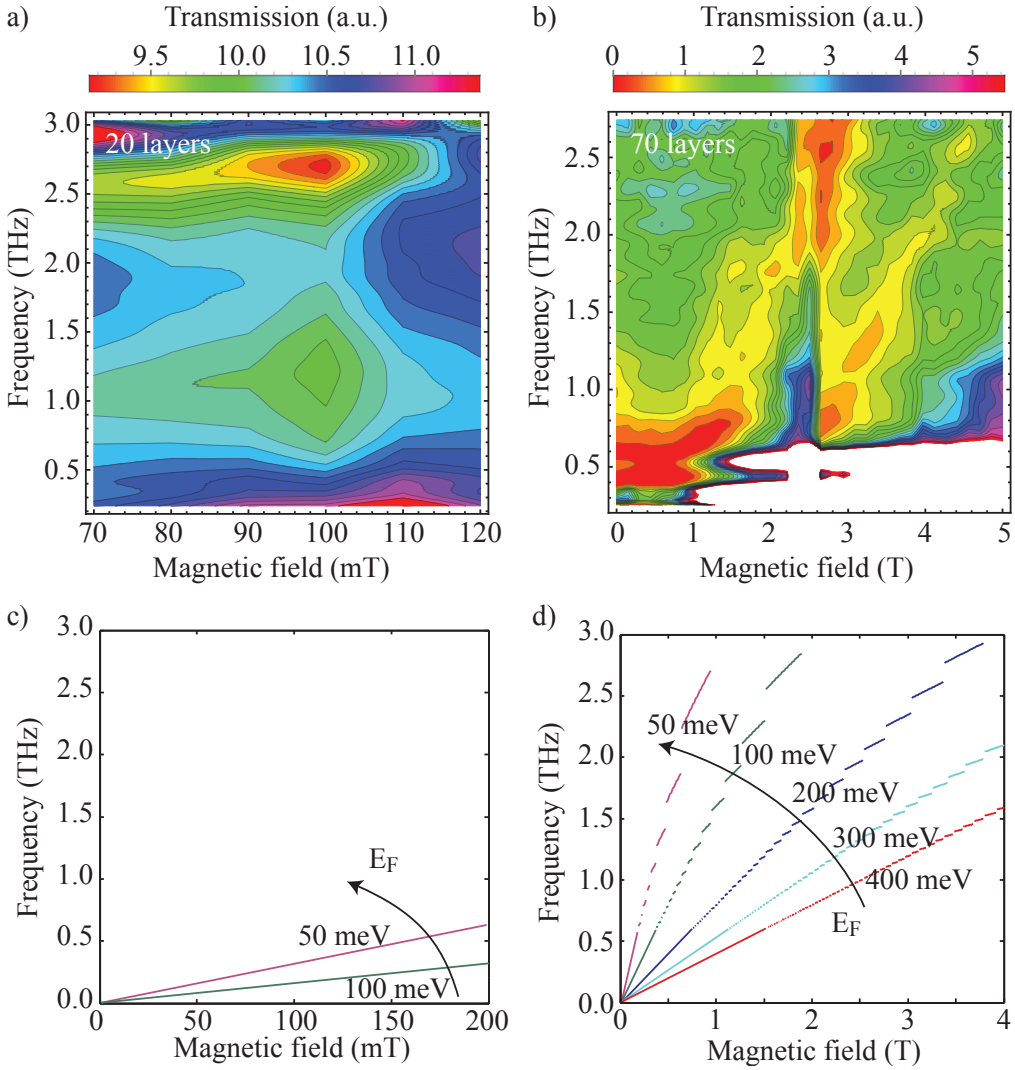

Figure 8.13 – B-field investigation of the SiC-graphene multilayered samples. a) Contour plot of the transmission of the SiC-graphene sample with 20 layers. b) Contour plot , for a wider B-range, of the SiC-graphene sample with 70 layers. c),d) Calculated cyclotron transitions for E_F = 50, 100, 200, 300, 400 meV for a comparable parameter space.

in panel c). It is nonetheless an unclear situation because they are expected at the edge of the measurement frequency range.

The sample with 70 layers was investigated for a wider B-field range and the map is shown in panel b). In the middle of the map, the alignment of the setup was adjusted to compensate for a magnetic-field drift in the detection beam-line. This is responsible for the artefact appearing as a vertical step at $B \simeq 2.6$ T. The map interestingly shows two minima at low frequencies, moving in B-field towards higher values, as expected for the cyclotron transition (cf. calculations in panel d)). On the other hand, these two features are almost identical to each other and the second one appears after the setup-adjustment step, hinting at the fact that they could be some drift artefacts.

Moreover, on this same kind of samples and for the same (f, B)-range Ref. [299] reported the detection of terraces-induced THz-plasmons. We detect no such features, probably due to the lower sensitivity of our setup compared to their Faraday-rotation detection scheme. A more sensitive setup and a gating scheme allowing control over E_F are needed for further investigations on this kind of samples.

8.3 High-frequency complementary SRRs onto exfoliated graphene flakes

As discussed concomitantly with Eq. (8.8), at higher frequencies the constraint on the graphene mobility to detect the cyclotron transition and achieve strong coupling would be looser. With this in mind, complementary SRRs were designed to work at about 1.9 THz, still within the bandwidth of the setup but at its higher edge, modifying the basic cSRR-structure discussed in chapter 3. Their dimensions, simulated electric-field distribution and transmission spectrum for the excited LC-mode are reported in Fig. 8.14.

At the same time, graphene flakes were exfoliated according to the procedure discussed in section 5.3 on page 129, onto the implanted substrate characterised in appendix I on page 273. Onto the chip, several flakes with different numbers of layers were found and cSRRs were produced on top of them via electron-beam lithography with subsequent evaporation and lift-off of a 150 nm thick gold layer.[3] This task is non-trivial because the flakes are randomly scattered, small in dimensions and show weak contrast, hence it is difficult to locate them to place precisely the cSRRs. Some pictures of one resonator of the realised sample are shown in Fig. 8.15: they show the realised cSRR in the PMMA-resist

[3]The part of the sample production involving the realisation of the cSRRs (electron-beam lithography, gold layer evaporation and lift-off) was performed by Dr. F. Mattioli, Dr. S. Cibella and Dr. R. Leoni at the laboratory of the Istituto di Fotonica e Nanotecnologie of the CNR in Rome, Italy.

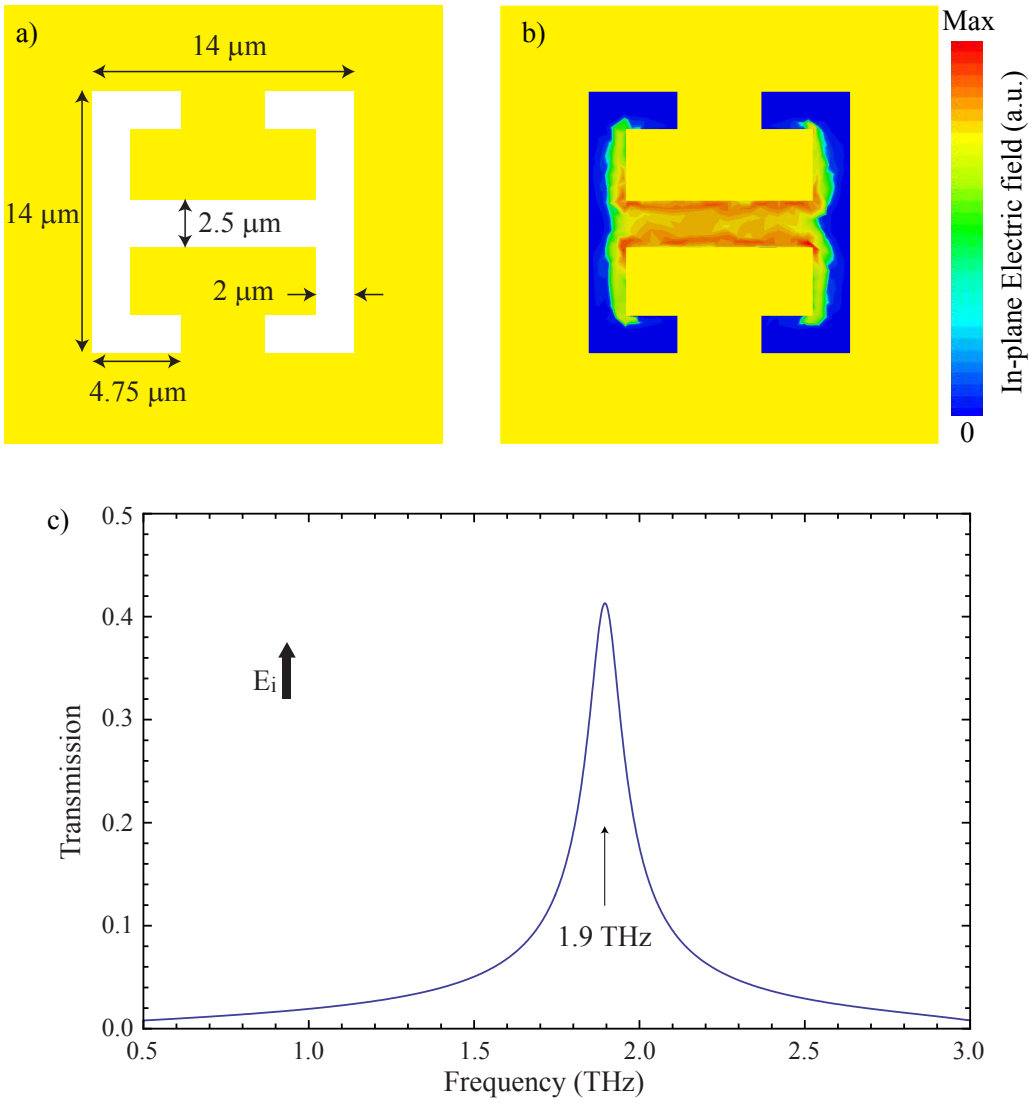

Figure 8.14 – a) Dimensions, b) simulated in-plane electric-field distribution and c) simulated transmission spectrum for the excited *LC*-mode of a cSRR at 1.9 THz for the investigations of graphene flakes.

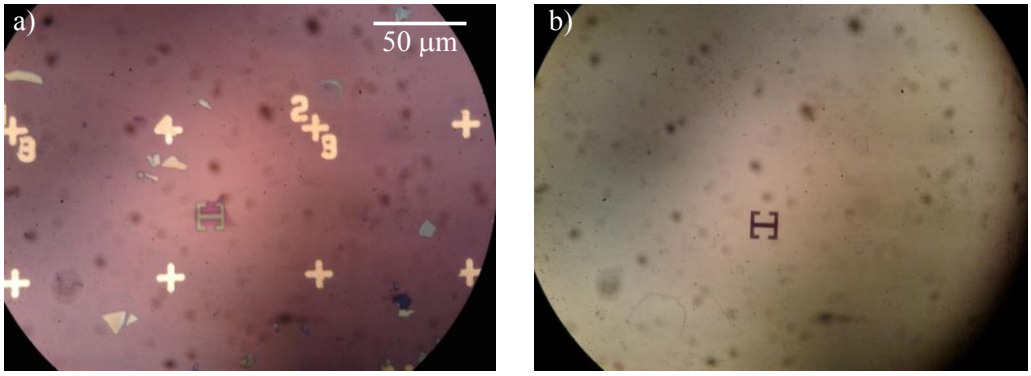

Figure 8.15 – a) Realised cSRR in the PMMA-resist and b) resulting structure after evaporation and lift-off of 150 nm of gold. Note the graphene flake below the resist in panel a). Courtesy of Dr. F. Mattioli.

and the resulting structure after evaporation and lift-off.

Note that the use of cSRRs in the present case is the only way to attempt THz-spectroscopy onto graphene flakes, because it concentrates the light onto a small region, the gap, that is placed onto the flake, while blocking the radiation from the rest of the sample. The challenge is instead the fact that the measurement of a single resonator is required and the magnet-coupled THz-TDS setup is thus at its limit.

An additional point to be considered is that the used cSRR-design facilitates electrical gating of the graphene flake (even though with the drawback of a huge capacitance area) but it does not allow electrical FET-characterisation, being no source/drain contact available.

The magneto-spectroscopy investigation performed on the sample is reported in panel a) of Fig. 8.16. The measurement was aligned in such a way that two cSRRs, aligned in the same direction and covering two few-layers graphene stacks, were excited by the THz-beam. Unfortunately, again, no feature is moving in the plane for varying magnetic field and frequency (cf. panel b) in Fig. 8.12). In order to better check this result, the map in panel b) shows the subsequent time traces corresponding to the spectra of panel a): it seems that no significant change is present in the phase and amplitude of the signal that could hint at the cyclotron transition or at its anticrossing with the mode of the cSRR.

This does not mean automatically that the effect we are tackling is not present, but it confirms instead that the setup in its present configuration is not sensitive enough for such a measurement. In fact, no peak about 1.9 THz is present, meaning that more than a single cSRR would be needed. Different measurement schemes can still be used to investigate the same sample, like cross-polarisation detection with the aid of THz-lenses

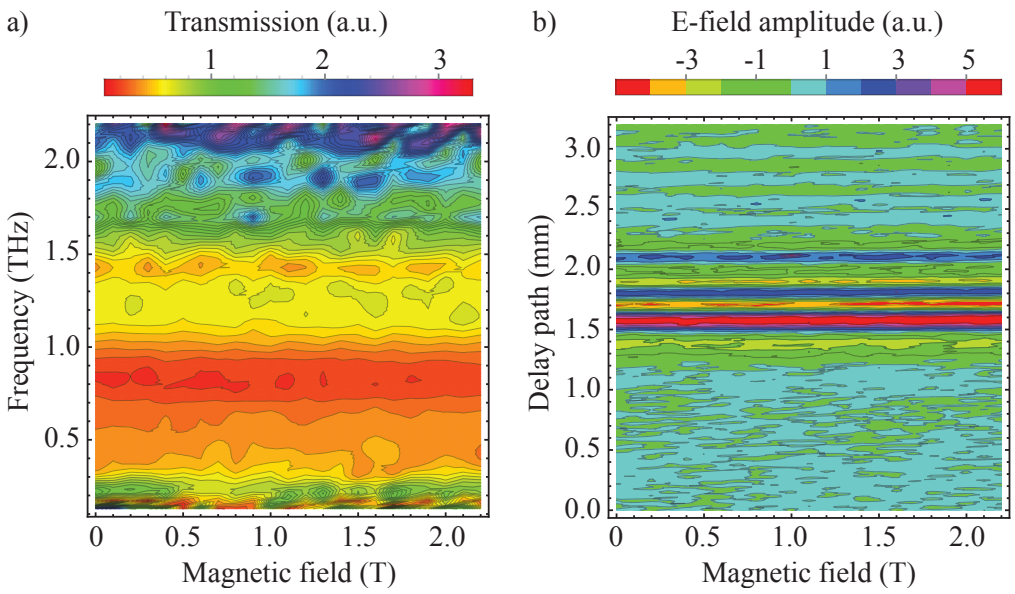

Figure 8.16 – a) Contour plot of the transmission of the single graphene-flake/cSRR sample. b) Contour plot of the measured time-traces, raw data used to calculate the map in panel a).

or double-modulation technique (cf. section 3.5 on page 95).

8.4 Final conclusions and outlook

The light-matter interaction of THz-SRRs and graphene was studied from several different point of views. The motivation for starting this investigation was the Dicke-phase transition in the ultra strong coupling regime for graphene (cf. chapter 6). Several samples were realised, of the same kind as the ones presenting USC with 2DEGs, but the simple substitution of the latter with graphene was not enough. In fact, the first, main challenge is the observation of the cyclotron transition in graphene, problematic because of the low mobility usually possessed by samples of large enough dimensions. Nonetheless, the realised samples allowed us to investigate the interesting physics of THz-modulation. The electro-optic interaction in samples containing CVD-graphene proved to realise a well-performing device that could be modelled by the analytical transmission-line model.

The initial motivation stays as an outlook to present work. Setup improvements are needed to be able to increase its sensitivity and thus measure single THz-SRRs onto graphene flakes. Improvements are planned also on the sample. The cSRR can be split into two parts, which do not disturb the optical mode while allowing one to perform the FET-characterisation to determine mobility and doping. To have the highest mobility possible, instead, graphene flakes suspended and/or sandwiched between hBN-layers should be investigated.

Appendix A

Growth designs of the used heterostructures

A.1 Growth design of EV1894

The investigated quaternary-barrier THz-QCLs were grown in the $In_{0.53}Ga_{0.47}As/Al_{0.17}In_{0.52}Ga_{0.31}As$ material system, according to the following growth design.

Table A.1 – Growth design of EV1894. i=intrinsic.

Part	Composition	Thickness (Å)	Doping (cm^{-3})
Top contact	InGaAs	600	3.00 $\times 10^{18}$
Upper cladding	InGaAs	10	i
	AlInGaAs	52	i
	InGaAs	400	i
	AlInGaAs	52	i
Active Region	InGaAs	131	i
$\times 150$	AlInGaAs	20	i
	InGaAs	135	i
	AlInGaAs	36	i
	InGaAs	113	i
	AlInGaAs	44	i
	InGaAs	221	2.20 $\times 10^{16}$
	AlInGaAs	52	i
Lower cladding	InGaAs	400	i
	AlInGaAs	52	i
	InGaAs	10	i
Bottom contact	InGaAs	600	3.00 $\times 10^{18}$
2" InP:Fe Wafer			

The grown heterostructure has a total thickness of 11.6 µm and is lattice-matched to the wafer substrate. The doping is achieved with silicon as volume-doping in the injectors (doped widest InGaAs well) and corresponds to a sheet density of $n_s \simeq 4.86 \times 10^{10}$ cm^{-2}.

After growth, the heterostructure was controlled with X-ray diffraction that revealed a -3%-deviation from the design. The band structure calculations presented in the main text were therefore performed with the corrected thicknesses.

A.2 Growth design of EV1452

The first of the used 2DEGs was grown in the GaAs/$Al_{0.3}Ga_{0.7}As$ material system, according to the following growth design.

Table A.2 – Growth design of EV1452. i=intrinsic.

Part	Composition	Thickness (Å)	Doping (cm^{-3})
Cap	GaAs	100	1.44×10^{18}
Doped Barrier	AlGaAs	500	1.01×10^{18}
	AlGaAs	400	i
Channel & Buffer	GaAs	10000	i
2" Semi-Insulating GaAs Wafer			

Typical carrier densities at $T = 1.5$ K were found to be $n_s = 3.1 \times 10^{11}$ cm^{-2} with a mobility $\mu = 8 \times 10^5$ cm^2/Vs, measured on the samples discussed in chapter 7 on page 157.

A.3 Growth design of EV2124

The second of the used 2DEGs was grown in the GaAs/$Al_{0.3}Ga_{0.7}As$ material system, according to the following growth design.

Table A.3 – Growth design of EV2124. i=intrinsic.

Part	Composition	Thickness (Å)	Doping (cm^{-2})
Cap	GaAs	50	i
Barrier	AlGaAs	450	i
Doping	GaAs	6	i
	Si δ-doping	0	3.53×10^{12}
	GaAs	6	i
Spacer	AlGaAs	400	i
Channel & Buffer	GaAs	5000	i
Superlattice	AlAs	25	i
$\times10$	GaAs	25	i
Buffer	GaAs	5000	i
3" Semi-Insulating GaAs Wafer			

Typical carrier densities at $T = 2$ K were found to be $n_s = 3 \times 10^{11}$ cm^{-2} with a mobility $\mu = 1.7 \times 10^6$ cm^2/Vs, measured on the samples discussed in chapter 7 on page 157.

A.4 Growth design of EV2109

The third of the used 2DEGs was grown in the GaAs/$Al_{0.3}Ga_{0.7}As$ material system, according to the previous growth design, the only difference being the substrate supplier.

Typical carrier densities at $T = 2$ K were found to be $n_s = 2.0 \times 10^{11}$ cm^{-2} with a mobility $\mu = 0.57 \times 10^6$ cm^2/Vs, measured on the samples discussed in chapter 7 on page 157.

Appendix B

Comparability of QCL measurements for different duty cycles and temperatures

The QCL devices discussed in part I were driven and measured at close, but different duty cycles and temperatures. The present section wants to clarify why the measurements are still absolutely comparable thus allowing the presented discussions.

The QCLs were always driven with a pulser with micro/macro-pulse scheme and a very small duty cycle so not to heat the device and at the same time to have a good signal on the bolometer (cf. section 2.2). When driving a QCL with low duty cycles (for instance below 10%), the emitted power is directly proportional to the duty cycle percentage and the temperature increase of the active region with respect to the substrate temperature can be estimated with the formula[97, 32]

$$T_{act} = T_{sub} + R_{th} I V \delta \tag{B.1}$$

where I and V are the driving current and voltage, δ is the duty cycle percentage and R_{th} the device thermal resistance. From the literature on similar THz-QCLs with DM-waveguides, one can set an upper value for the thermal resistance $R_{th} = 25$ K/W.[120, 504] Therefore, for an indicative electrical power of 10 W=1 A×10 V, a change in duty cycle from 0.5% to 2% gives a change in the temperature of the active region $\Delta T_{act} = 3.75$ K. This is almost negligible considering that the electron temperatures were found to be 50-to-100 K higher than the lattice temperature for QCLs operating at low temperature.[505, 506]

Most of the discussion in part I is focussed on devices measured at different temper-

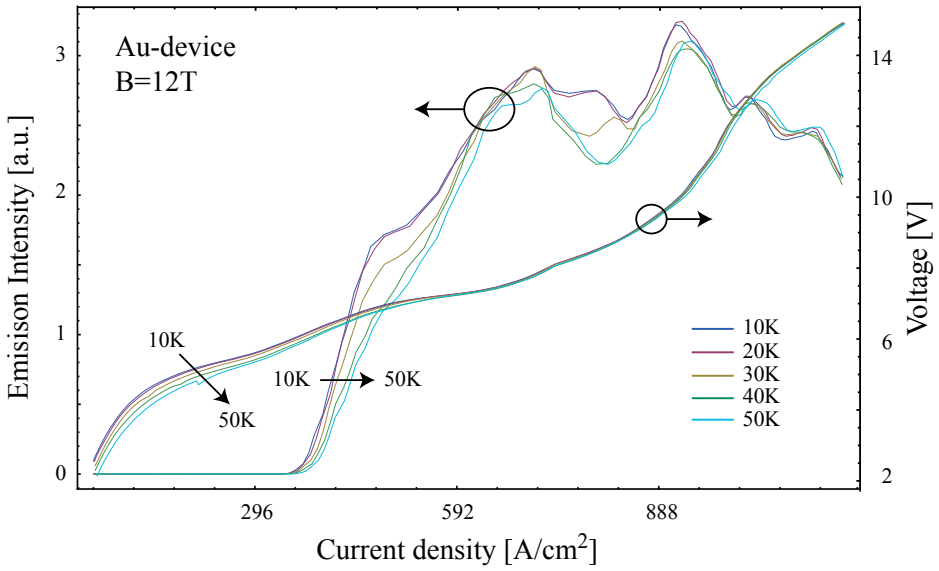

Figure B.1 – Comparison of $J-V$ and $J-L$ curves plotted for the Au-devices at $B = 12$ T for temperatures of $T = 10$ K, 20 K, 30 K, 40 K, 50 K.

	B=0T	B=12T
Au-device	0.11%	0.09%
Cu-device	0.08%	-

Table B.1 – Relative change in temperature of J_{th} for the range 4-50 K.

atures, namely 4.2 K for the Au-devices and 30 K for the Cu-devices. This was due to experimental reasons when trying to measure the device at high temperature within a liquid-He-cooled superconducting magnet. Fig. B.1 shows the $J-V$ and $J-L$ curves for the Au-device at $B = 12$ T for temperatures in the range $T = 10$–50 K. All curves are very similar. In particular the $J-V$ despite some small differences in the low-voltage region, then overlap almost completely. The $J-L$ curves are also very similar in what concerns the threshold current density, the maximum output and almost all of the main features.

To quantify and sustain the previous statements, the normalized change of J_{th} was calculated as

$$\frac{dJ_{th}}{dT}\frac{1}{J_{th}} \tag{B.2}$$

from the data points in panel b) of Fig. 2.5 in the temperature range 0-50K. The values are collected in the following Table B.1 and show a maximum relative change of 0.11%, both at $B = 0$ T and $B = 12$ T. Being most of our analysis based on the behaviour of the J_{th}, we believe we can safely compare the measurements. Additionally, we come to quantitative statements only when the data are directly comparable.

Appendix C

Electromagnetic duality and further characterisation of the closed-SRR sample

A brief discussion of electromagnetic duality is first reported, mainly following the thesis of Fernandez-Corbaton[507].

C.1 Dual dipoles

The direct and complementary SRRs used in the investigation of chapter 4, are metallic structures and therefore do not posses a permanent dipole while they can develop induced ones. Thus, in the most general form, we can write the polarisability matrix A, describing the response of the screen S to the illumination as

$$A = \begin{pmatrix} \alpha_{pE} & \alpha_{pH} \\ \alpha_{mE} & \alpha_{mH} \end{pmatrix}, \tag{C.1}$$

where the α_i, j are 3×3 tensors that connect the induced dipoles $i = p$, m to the inducing fields $j = E$, H as

$$\begin{pmatrix} \mathbf{p} \\ \mathbf{m} \end{pmatrix} = \begin{pmatrix} \alpha_{pE} & \alpha_{pH} \\ \alpha_{mE} & \alpha_{mH} \end{pmatrix} \begin{pmatrix} \mathbf{E} \\ Z\mathbf{H} \end{pmatrix}. \tag{C.2}$$

These are the general constitutive relations for the induced dipoles, including cross-polarisabilities. The relation holds also for SRRs meaning that they in general possess both and electric and magnetic dipole, but specific values can be calculated only for defined structures.[508, 509]

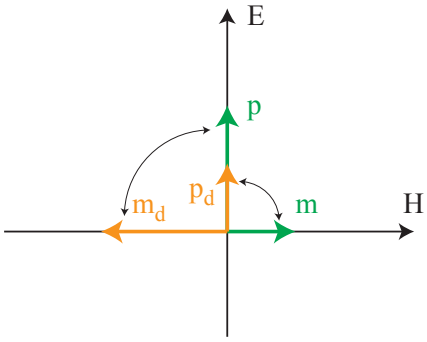

Figure C.1 – Dipoles induced in dual structures, for a fixed illumination.

The dual screen S_c would respond to the illumination with polarisabilities described by a matrix A_d, dual of matrix (C.1), i.e.

$$A_d = DA = \begin{pmatrix} \alpha_{mE} & \alpha_{mH} \\ -\alpha_{pE} & -\alpha_{pH} \end{pmatrix}. \tag{C.3}$$

Thus the dipoles induced by the same illuminating field, i.e. for a constant polarisation, onto the dual screen are given by

$$\begin{pmatrix} \mathbf{p}_d \\ \mathbf{m}_d \end{pmatrix} = A_d \begin{pmatrix} \mathbf{E} \\ Z\mathbf{H} \end{pmatrix} = \begin{pmatrix} \mathbf{m} \\ -\mathbf{p} \end{pmatrix}. \tag{C.4}$$

This means that the dual structure, under the same irradiation, is characterised by a dual electric dipole along the positive E-direction and with amplitude equal to the magnetic one. The dual magnetic dipole is aligned instead along the negative H-direction and with amplitude equal to the electric one. This situation is sketched in the (E, H) plane in Fig. C.1, where the direct dipoles p, m are indicated by green arrows, while the dual dipoles p_d, m_d are indicated by orange arrows. This shows that, in general two pairs of crossed electro-magnetic dipoles would be needed to represent closed-SRR structures, as indicated by the thin black arrows. These have opposite handedness, i.e. with the magnetic dipoles on the opposite sides of the respective electric dipoles: each pair of equally intense dipoles of opposite kind could then be interpreted as a Huygens' surface.

C.2 Duality group generator

From the point of view of group theory, each invariance is connected to a generator of the group that indicates the conserved physical quantity (and vice versa). For instance, the rotational invariance is connected to the fact that the total angular momentum is

conserved. For the case of electromagnetic duality, the generator of the group and the conserved quantity is helicity.[247, 510, 511]

Helicity is defined as

$$\Lambda = \frac{\mathbf{J}\cdot\mathbf{P}}{|\mathbf{P}|} \;\rightarrow\; \Lambda = \frac{\nabla\times}{k}, \tag{C.5}$$

where $\mathbf{J}$ is the total angular momentum, $\mathbf{P}$ is the linear momentum and k the wavevector. The definition means that helicity can be understood as the projection of $\mathbf{J}$ onto the direction of $\mathbf{P}$ and the second formulation is valid for monochromatic fields. For plane waves, therefore, helicity coincides with the handedness of the light in the plane perpendicular to the momentum vector, i.e. their circular polarisation state. The electromagnetic field has two possible helicity states: left and right circular polarisation. Then one can build a new field vector the clearly express this property by mixing $\mathbf{E}$ and $Z\mathbf{H}$:

$$\mathbf{G}_{\pm} = \frac{1}{\sqrt{2}}\left(\pm\mathbf{E} + iZ\mathbf{H}\right), \tag{C.6}$$

$$\Lambda\mathbf{G}_{\pm} = \pm\mathbf{G}_{\pm}. \tag{C.7}$$

Therefore the $\mathbf{G}_{\pm}$ will be eigenvectors of any system that preserves helicity. This is called Riemann-Silberstein formalism and it can be shown that this representation completely decouples the generalised Maxwell's equations for the two helical states.[512, 513]

Considering now one pair of crossed dipoles at a time, $m = \pm ip$ (where the imaginary unit represents the 90—degree angle and its sign the rotation direction), their fields are related as follows:[224]

$$\mathbf{E}_m = \mp iZ\mathbf{H}_p, \qquad \mathbf{H}_m = \pm\frac{i}{Z}\mathbf{E}_p. \tag{C.8}$$

Thus, when considering the helicity of the dual system, we need to evaluate the $\mathbf{G}_{\pm}$ from the total electric and magnetic fields, given by the sum of the fields created by the single dipoles

$$\mathbf{E}_{tot} = \mathbf{E}_p + \mathbf{E}_m, \qquad \mathbf{H}_{tot} = \mathbf{H}_p + \mathbf{H}_m. \tag{C.9}$$

Hence, substituting Eqs (C.8) into Eq. (C.9) and then into Eq. (C.7)

$$\sqrt{2}\mathbf{G}_{+} = +\left(\mathbf{E}_p \mp \mathbf{E}_p\right) + iZ\left(\mathbf{H}_p \mp \mathbf{H}_p\right), \tag{C.10}$$

$$\sqrt{2}\mathbf{G}_{-} = -\left(\mathbf{E}_p \pm \mathbf{E}_p\right) + iZ\left(\mathbf{H}_p \pm \mathbf{H}_p\right). \tag{C.11}$$

This means that for a given handedness of the dipole pair, the total produced field has a well defined helicity, respectively ∓ 1. To this end, the following conditions are needed: (i) both dipoles must be present, (ii) they must be placed at the same position in space and

(iii) they must be dual of each other.[511] In such a case, impinging radiation with helicity matching the dipole-pair handedness would be completely transmitted, while radiation with opposite helicity would be completely reflected. This property was termed *maximal electromagnetic chirality* and applications for it have been foreseen in circular dichroism measurements and in angle-independent circular-polarisation filtering.[514]

C.3 Chirality investigation

The measurements in the main text and the discussion in the previous section suggest that the sample might have properties of a circularly polarised object.

To check this point with the TDS setup, where both source and detector are linearly polarised, the samples were measured in cross-polarisation (cf. section 3.5.1 on page 96). This means that the sample was illuminated with one polarisation and the detection was sensitive to the orthogonal one: the measured spectra are reported in Fig. C.2 for the thickest spaced-SRR sample and in Fig. 4.14 on page 112 for the closed-SRR one. Both show that the cross-polarised transmission is suppressed by a factor of at least 20, hence the polarisation of the transmitted light is the same as the illumination and the samples do not turn it.

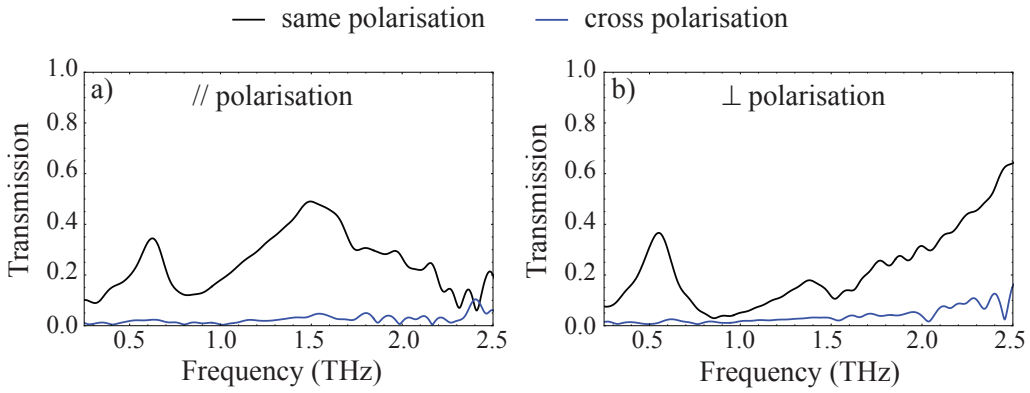

Figure C.2 – Cross-polarisation transmission spectra for the thickest spaced-SRR sample in the two polarisations, compared to the ones measured in the same polarisations.

C.4 Closed-SRR transmission at higher frequency

To further investigate the extension of the sample transmission, the closed-SRR sample was measured with a commercial FTIR able with a working frequency range from 12 THz up to the visible. The measured spectrum is presented in Fig. C.3 and shows that the

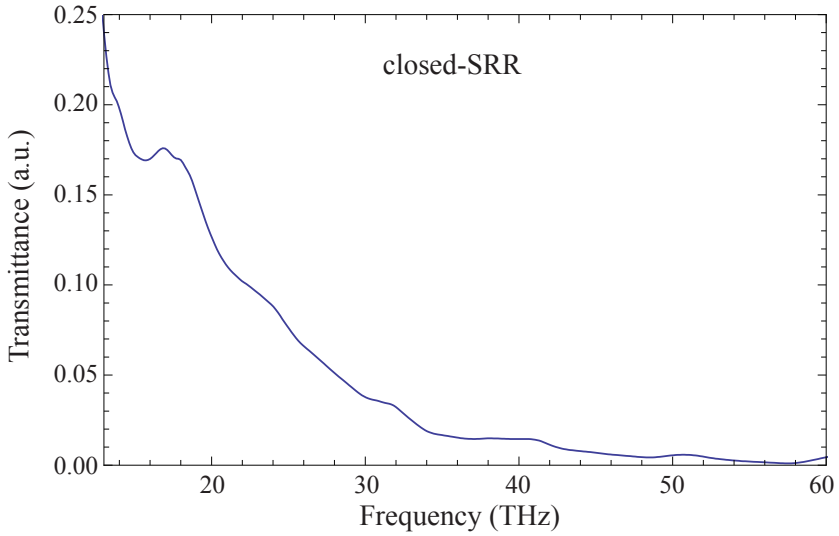

Figure C.3 – High-frequency limit of the transmittance of the closed-SRR sample. The normalised transmittance is obtained by long integration of the sample transmission, corrected for the long wavelength leakage through the full gold layer and normalised to the globar emission spectrum.

closed-SRR sample is still transmitting at 12 THz, halves its transmission at about 20 THz ($\lambda = 15$ µm) and it decreases by a factor 10 at about 34 THz ($\lambda = 9$ µm).

This is interesting because this value is smaller than the size of the used SRRs ($\simeq$ 40 µm) but still some orders of magnitude larger than the spacer thickness.

On the low-frequency side, instead, the transmission is seen slowly decreasing already at the edge of the TDS bandwidth (250 GHz, cf. Fig. 4.14). No setup is available to investigate the sample at lower frequencies, but increasing the wavelength one reaches soon the limit for which the radiation wavelength is bigger than the whole measured closed-SRR array, in fact 3 mm corresponds to a free space frequency of 100 GHz.

Appendix D

Complementary SRRs for the second series of MIRO samples

For the second series of MIRO samples, three different SRR frequencies were investigated, namely $f = 110$, 190, 300GHz. The correspondence between those, the side length and the sample they were used for are indicated in Table D.1. The simulated spectra for the cSRRs are presented in Fig. D.1 and were simulated with CST Microwave Studio designing the cSRRs in thin lossy gold layers on thick insulating GaAs substrates in air. The spectra show the LC-mode for the three different cSRR geometries, sketched in Fig. D.2.

The cSRRs also have $\lambda/2$ modes at higher frequencies (one is present in the plotted range of Fig. D.1), in the same polarisation, but only the LC-modes correspond to the field concentration into the central 5 µm gap, where the Hall-bar channel is placed.

Table D.1 – Summary of the frequencies and corresponding side length for the cSRRs of the second series of samples for the MIRO investigation.

f_{SRR} (GHz)	Side L (µm)	Samples
110	150	$G2124$
190	90	$A2109a$ $C2124$
300	58	$A2109b$ $K2124$

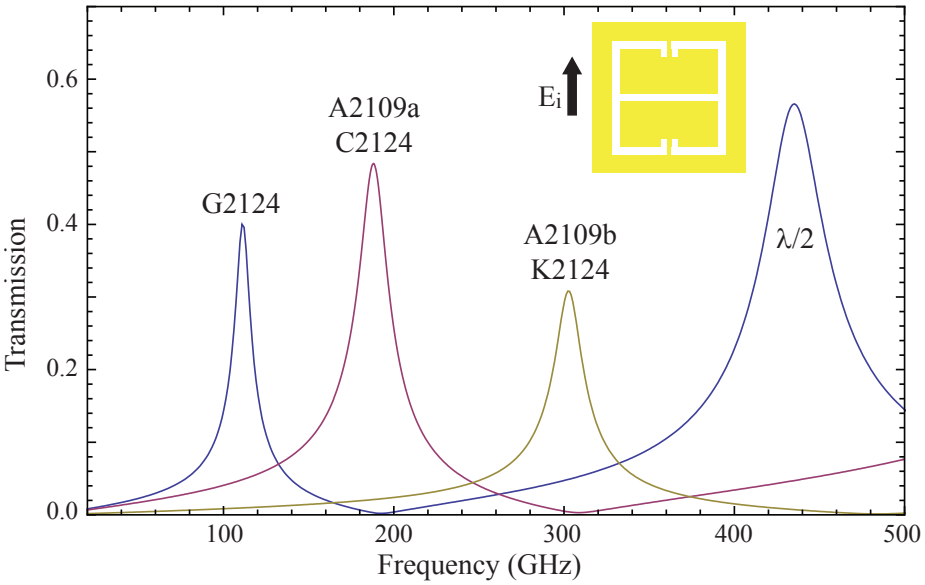

Figure D.1 – Simulated resonant peaks for the *LC*-mode of the cSRRs used for the second series of MIRO samples.

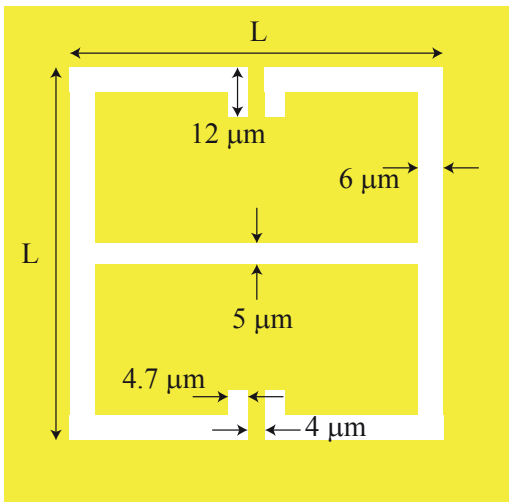

Figure D.2 – Design with dimensions of the cSRRs used for the second series of MIRO samples. The different square lengths L correpsond to the different frequencies as from Table D.1.

Appendix E

Comparison of MIRO's results in the literature

This appendix collects several literature data onto MIRO and ZRS investigations. The specific aim was to identify the different parameters ranges in which the phenomenon has been recorded. Particular emphasis is put onto the correlation of the presence and/or frequency of the magneto-plasmon resonance (MPR) with the presence of the MIROs and the frequency of the irradiation.

Legend:

Sample geometry: H=Hall-bar, D=dot lattice, AD=anti-dot lattice, C=Corbino, vdP=van der Pauw

$D1$ and $D2$ indicate the dimensions of the etched structures: they represent width and length of rectangular shapes (H, vdP) or dot diameter and lattice period for (anti-)dot lattices, or inner and outer radii for Corbino geometries.

Mobility μ and sheet carrier density n_s of the 2DEG are also reported.

The measurements were performed at the temperature T with a source frequency f_S, with power P_S and polarisation Pol: linear along $D1$, $D2$ ('l1', 'l2', resp.) or circular ('c').

The presence ('y') or absence ('n') of the different effects (MPR, MIRO, ZRS) is indicated.

The frequency relation between the illuminating radiation at f_{MW} and the MPR at $B = 0$ T f_{MPR} is indicated by: Y=yes, N=no, answering to the question $f_{MW} > f_{MPR}$?

Finally, question marks indicate quantities for which the referenced article provides no/an unclear value.

The first table collects data on Hall-bars etched in single 2DEGs in the GaAs/AlGaAs material system. The second one, instead, collects data on different structures etched in the same material system and on several structures realised in other materials systems, as well.

Ref.	Sample geometry	Material System	$D1$ (µm)	$D2$ (µm)	μ (10^6 cm^2/Vs)	n_s (10^{11} cm^{-2})	T (K)	Source f_S (GHz)	Source P_S (µW)	Source Pol	Effect? MIRO	Effect? ZRS	Effect? MPR	$f_{MW} > f_{MPR}$?
this work	H	GaAs/AlGaAs	4	40	0.8	3	1.5	140	20	l1	n	n	n	N
			60	500	1.5	2			2000	l2	y	n	y	Y
[391]	H	GaAs/AlGaAs	100	200	3.5	2	1.3	60	?	?	n	n	y	N
	H+AD		0.08	0.4	1.9			180						Y
[412]	H	GaAs/AlGaAs	50		13	2.9	0.65	160	?	?	y	y	y	Y
[413]	H+coplanarWG	GaAs/AlGaAs	800	1400	6 -15	1.3 -2.8	1.5	40-140	0.1	y?	y	n	y	Y
[414]	H	GaAs/AlGaAs	400	2600	1.2-3.9	1.5-2.5	1.8	20-80	1000	?	n	n	y mult.	N -Y
	luminescence		400			2.13			1000	?	n	n	y mult.	
[406]	H	GaAs/AlGaAs	200 - 50	?	15	3	1.3	27-115	1000	l1,l2	y	y	n	N
	vdP		3000	3000										
[416]	vdP	GaAs/AlGaAs	2000	5000	10	1.9	1.5	50	1000	?	y	n	n	Y
[417]	H	GaAs/AlGaAs	50	350	1.75	9	1.9	700-1630	5-80 $\times 10^3$	?	y?	n	?	Y
[419]	H	GaAs/AlGaAs	400	?	10	2.4-3	1.5-0.5	48	320-3200	?	y	y	n	Y
[420]	H?	GaAs/AlGaAs	?	?	?	?	0.5	30-117	10-3000	?	y	y	n	
[421]	H	GaAs/AlGaAs	100	?	12	3.7	1.5	69	?	?	y?	y?	n	N
[422]	H	GaAs/AlGaAs	65-80	1300	0.6	2.7	4	630-660	?	?	n	n	y	Y
								210-220			n	n	y	Y
[423]	H + AD	GaAs/AlGaAs	80	320	2.5	2.83	0.33	32	?	?	y	n	y	N
			0.3	1.5				130						Y
[389]	H	GaAs/AlGaAs	50-100	900	1.2	2.3	1.3	70-170	?	?	n	n	y	N -Y
[424]	H	GaAs/AlGaAs	?	?	?	?	1.2	25-50	5000-300	?	y	n	n	
[425]	H+grating	GaAs/AlGaAs	37	10000	1.6	7	1.8	1630	60000	l1	y	n	y	Y
[405]	H	GaAs/AlGaAs	50-100-200	?	3	2	0.3-2	30-150	10^3-10^4	l1	y	n	y	N-Y
[426]	vdP	GaAs/AlGaAs QW	5000	5000	25	3.5	1.5	30-150	1-4 $\times 10^4$	l2	y	y	?	Y
[427]	H	GaAs/AlGaAs QW	200	500	1.7-3.2	10	1.5	110-170	?	?	y	y	n	N-Y
[422]	H+top gates	GaAs/AlGaAs QW	65-300	1300	high	2.9	4	100-170	?	?	n	n	y	Y
								200-300						Y
								300-480						Y
								630-660						Y
[428]	H	GaAs/AlGaAs QW	50	?	13	2.7	0.65	100-175	?	?	y	y	y	N-Y
[429]	H+AD	GaAs/AlGaAs QW	39	39	0.15?	3.45	4	1000	FTIR	?	n	n	y	Y
			0.3	0.5			3900							Y
[431]	H	GaAs/AlGaAs QW	100	500	1.8-5.6	1.3 -2.8	1.6	13-80	?	?	n	n	y	N
[432]	H	GaAs/AlGaAs QW	100	?	11	3.3	0.5	95-190	?	?	y	y	n	Y
[433]	H	GaAs/AlGaAs	400	?	8	2.7	1.5	32	?	l	y	n	n	N
[434]								50						Y
[435]	H	GaAs/AlGaAs	?	?	?	?	1.5	45	1000	l,c	y	n	n	
[445]	C	GaAs/AlGaAs QW	500	3000	13	3.6	0.65	57	10-100	?	y	y	n	Y
[437]	H	GaAs/AlGaAs QW	100	200	15	2.8	1.5	80	100000		y	y	n	N
	contactless										n	n	n	
[440]	H	GaAs/AlGaAs QW	50	250	1.1	12.8	4	1.2	4000	?	other	n	n	N
								37-140			y	n	n	N
[438]	H	GaAs/AlGaAs QW	500	?	5	1.9	0.05	60	?	?	y	n	y	Y
[439]	H	GaAs/AlGaAs QW	400	5000	15	2	0.28	2-20	10^5	l	y	y	n	N
[441]	C	GaAs/AlGaAs QW	500	1500	1.9	8	1.6	145	4000	?	y	y	n	Y
[440]	H	GaAs/AlGaAs QW	50	250	0.56	8.5	1.7	140	4000	?	y	y	n	N
[442]	H	GaAs/AlGaAs	200	500	7	3	0.4	10-170	15000	?	y	y	?	N -Y

Ref.	Sample geometry	Material System	$D1$ (µm)	$D2$ (µm)	μ (10^6 cm^2/Vs)	n_s (10^{11} cm^{-2})	T (K)	Source f_S (GHz)	Source P_S (µW)	Source Pol	Effect? MIRO	Effect? ZRS	Effect? MPR	$f_{MW} > f_{MPR}$?
[390]	D	GaAs/AlGaAs	3	4	0.25	5.5	4?	300-3000	?	?	n	n	y	N-Y
[430]	AD	GaAs/AlGaAs QW	0.15	0.35	?	8	2.2	300-6900	FTIR	?	n	n	y	N-Y
[415]	D	GaAs/AlGaAs	1000 600-400	?	4	1 0.96-0.46	4	5 40	?	?	n	m	y	N Y
[418]	H vdP	bilayer 2DEG GaAs/AlGaAs	50 3000	250 3000	1.9	9.1	1.4	35 170	Efield=4.2V/cm	?	y	y	?	N N
[450]	H	SiC graphene	8	20	?	?	1.5	48	4000	?	n	n	n	
[453]	vdP	Ge/SiGe	4000	4000	0.4	2.8	1.5	100	?	?	y	n	n	
[447]	H	p-GaAs/AlGaAs QW	100	?	0.34	3.5	0.5	27	?	?	n?	n	n?	
[451]	H	Si/SiGe	50	100	0.186-0.067	5.8-6.6	1.4	80-120	?	?	n	n	y	
[449]	H	HgTe/CdHgTe	50	100 -250	2-0.5$\times 10^{-4}$	2.5	1.4	35-170	$10^5$0	?	n	n	n	
[448]	H	p-GaAs/AlGaAs QW	100	?	0.7	2.2	4	25-50	?	?	n	n	n	
[454]	H	MgZnO/ZnO	1000	2000	0.075	7.5	1.4	35	1000	?	y	n	n	
	C		400	1000				120						
	vdP		3000	3000										
[452]	H	MgZnO/ZnO	700-6000	700-6000	0.2	0.7-11	0.3	5-65	?	?	n	n	y	

Appendix F

Comparison of the dSRRs with different side lengths

The SRRs used in samples $A1452$ and $B1452$ are almost identical to the ones presented in Fig. 3.2 on page 83 of chapter 3, but not exactly the same. The difference lies in the length of the vertical golden lines: the SRRs used throughout the thesis are 34 µm high while the previous samples have the vertical side that is 36 µm high.

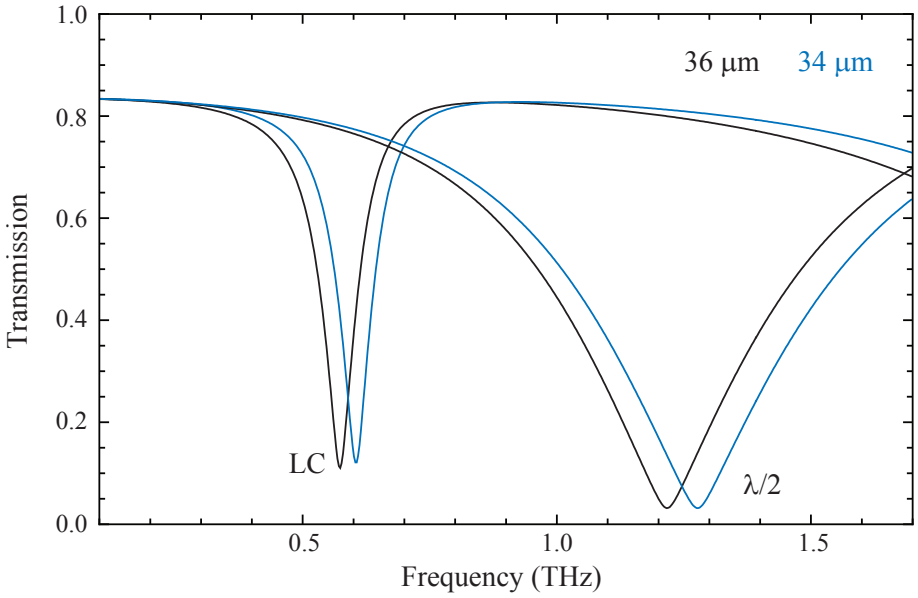

Figure F.1 – Simulated transmission spectra for SRRs with vertical dimension of 34 µm and 36 µm.

For the sake of completeness the simulated transmission spectrum of the two resonators in the parallel polarisation is shown in Fig. F.1 (the simulated substrate is constituted by Si/SiO_x). As expected the difference is small: the shape of the resonances is the same as well as the transmission amplitude while the frequency is slightly shifted, though by

less than 10%. Therefore this difference does not invalidate the whole discussion and all comparisons carried out in the main text.

As a side remark, Fig. F.1 shows the way in which one can tune the frequency of the used SRRs. In fact, a taller SRR, in the RLC-picture, corresponds to a larger L-value. Since the slits were not modified, the capacitance stays the same. Hence, the resonant frequency of the SRR, given by the inverse of the LC-product, shifts to lower values. This is the working principle underlying adaptation of the structure for a specific frequency.

Appendix G

MIRO: further investigation of samples −1452

The first series of samples produced to investigate the MIRO phenomenon discussed in chapter 7 of the main text, encompassed four samples: $A1452$, $B1452$, $C1452$, $D1452$. They were all processed by C. Rössler in the group of Prof. Ensslin at ETHZ and in the clean room facility FIRST, all out of wafer $EV1452$ (growth sheet in appendix A.2 on page 235). The important results on samples $A1452$ and $B1452$ were reported and discussed in chapter 7. This appendix starts with some general complementary data and analysis on all samples, followed by few additional measurements on samples $A1452$ and $B1452$. Finally, a brief discussion of samples $C1452$ and $D1452$ takes place, given the fact their measurements contribute to the width-dependence analysis of section 7.5.1 on page 175 of the main text.

G.1 Samples configuration, composition and characterisation

The structure of samples $A1452$ and $B1452$ was presented in the main text, starting from the realisation of the USC in section 6.4 on page 151, etched in Hall-bars as mentioned in section 7.6.1 on page 180. Samples $C1452$ and $D1452$ are the exact counterpart of the first two, except that the kind of dSRR is different. In turn, to adapt for the different dSRR shape, the channels of the Hall-bars constituting these samples have dimensions of 56×512 µm^2 ($C1452$) and 44×512 µm^2 ($D1452$).

The dSRR used in these samples is identical to the one used in Ref. [47], while a peculiarity of the arrangement is that, contrary to what done in samples $A1452$ and

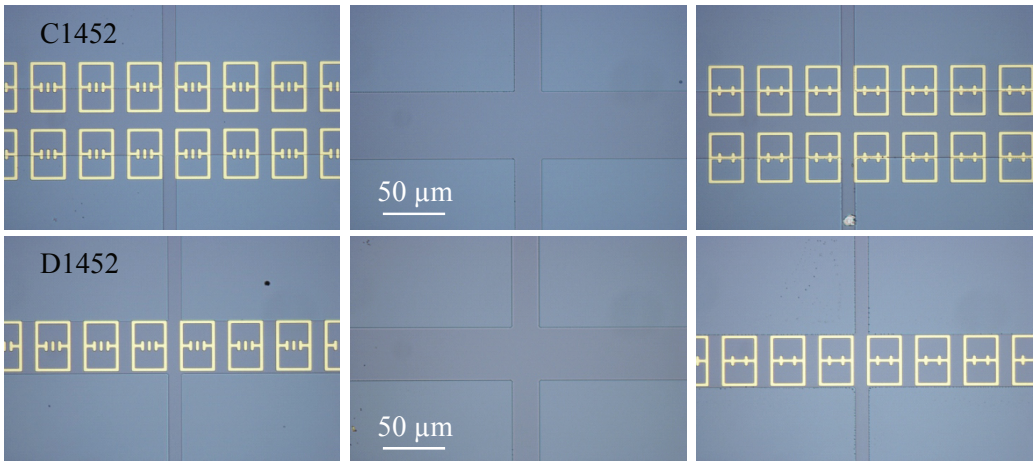

Figure G.1 – Optical micrographs of the different Hall-bars of samples $C1452$ and $D1452$. Samples $A1452$ and $B1452$ are shown in Fig. 7.15 on page 181 of the main text.

$B1452$, samples $C1452$ and $D1452$ have the dSRRs placed such that their LC-mode is excited when the source polarisation is aligned along the channel of the Hall-bars. The samples were also covered by either a single row of SRRs fitting the channel ($D1452$) or by two rows separated by 12 µm, focussing the light on the edges ($C1452$). Photographs of the samples are presented in Fig. G.1.

The SRRs were defined onto the Hall-bars via optical lithography and produced with standard evaporation/lift-off of 5/250 nm of titanium/gold. Again, each sample contains three Hall-bars, one of the lateral covered by SRRs, the central left uncovered, and the third one covered with the same resonators but with shorted gaps, as sketched in Fig. 7.15 on page 181.

The used SRR has its LC-mode at 830 GHz while the dipolar modes are at 2.3 THz and 1.5 THz, in the same and in the orthogonal polarisation, respectively. The simulated spatial mode distributions for the SRRs at resonance for the LC- and the orthogonal dipolar mode are shown in Fig. G.2, for both used SRRs (COMSOL Multiphysics).

The heterostructure and the SRRs are of the same as the ones used in Ref.s [47, 374] where the ultra-strong coupling was demonstrated. This new resonator design used for $C1452$ and $D1452$ displayed a normalised Rabi splitting of 17% for the LC-mode. This allows us to calculate that for the light source frequency of 140 GHz, the lower polariton corresponds to 99.7% matter part and 0.3% photonic part for a magnetic fields of 0.36 T, which has to be related to a cyclotron magnetic field of 0.33 T at the same frequency. Figure G.3 shows the anti-crossings for the two different resonator types as fitted from the measurements.

The uncoupled resonant frequencies of the resonators' main modes for each polarization are reported in Table G.1, along with the magnetic field value resonant with the lower

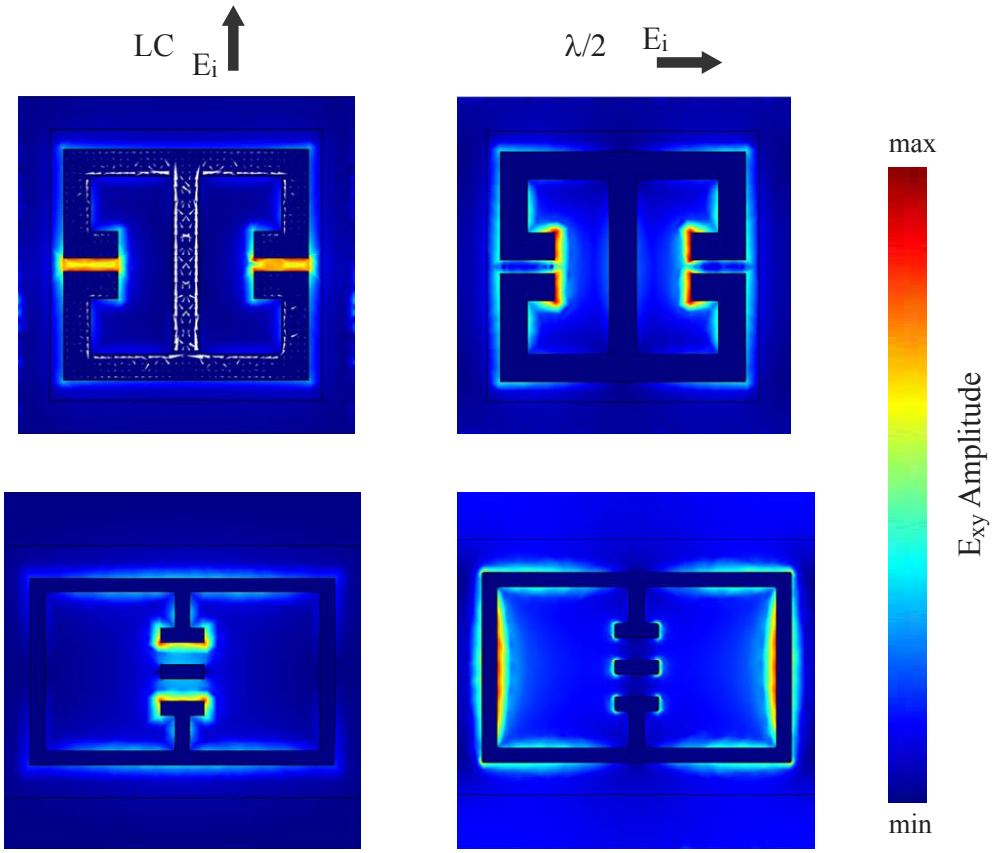

Figure G.2 – Resonators' modes when excited at resonance.

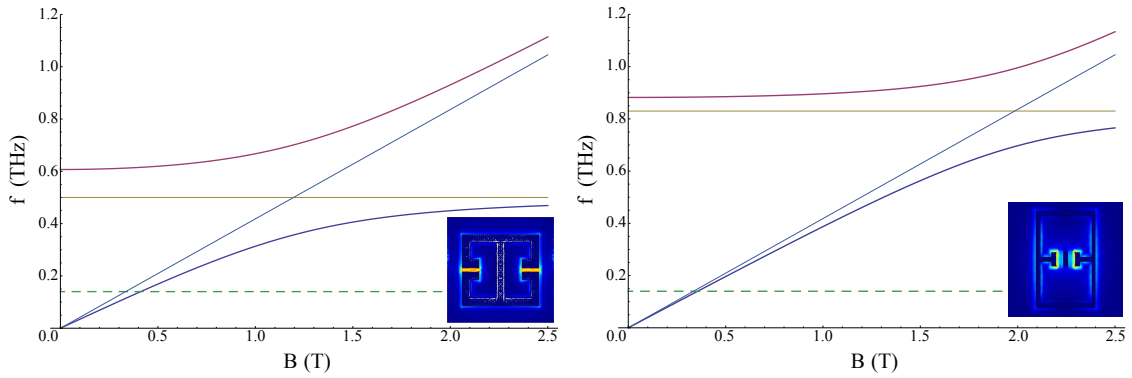

Figure G.3 – USC anticrossing for the two different resonator types as fitted from the measurements. In blue and violet are displayed the lower and upper polaritonic branches for the strong coupling between the *LC*-mode of the two used resonators (yellow thin line) and the cyclotron transition (light blue line). The dashed green line indicates the Gunn diode frequency. As inset, the spatial distribution of the uncoupled modes is presented.

polaritonic branch at 140 GHz ($B_{140}^{LP,USC}$). The magnetic field at which the first MIRO minimum is expected, connected to the lower polariton, is also reported as calculated with $B_{\pm1}^{USC} = \pm\frac{4}{5}B_{140}$.

Table G.1 – Lower polariton resonant field at 140 GHz and expected field for the first MIRO minimum

Sample #	Mode type/polarization	resonant frequency	$B_{140\ \mathrm{GHz}}^{LP,USC}$	$B_{min}^{1,USC}=\frac{4}{5}B_{140\ \mathrm{GHz}}^{LP,USC}$
$A1452$ and $B1452$	LC ($\perp$)	500 GHz	0.41 T	0.33 T
	$\lambda/2$ ($\parallel$)	1.165 THz	0.35 T	0.28 T
$C1452$ and $D1452$	LC ($\parallel$)	830 GHz	0.36 T	0.29 T
	$\lambda/2$ ($\perp$)	1.50 THz	0.34 T	0.27 T
	cyclotron	−−	0.33 T	0.27 T

From the last column is clear why in the main text the attention was concentrated on samples $A1452$ and $B1452$, and only on the LC-mode: this mode is the only one with a seizable shift of the MIROs from the ones of the uncoupled cyclotron.

As references for the presence of the metallic structures onto the Hall-bar channel, the Hall-bars covered by shorted-SRRs were produced. These structures resonate as well, but only with dipolar modes and at frequencies higher than the LC-ones. This is clear form the simulated transmittances (COMSOL Multiphysics) reported in Fig. G.4, along with the mode distribution at 140 GHz. The shorted-SRRs show resonances all above 1 THz, in particular at 1.35 THz and 1.4 THz for the modes with the same polarisation as the LC-ones.

These are, as well in ultra-strong coupling with the cyclotron transition, although with a smaller normalized Rabi frequency than the LC-ones, and, most important, they are far enough from the exciting frequency of 140 GHz to be negligible for the present discussion. This consideration holds for all dipolar modes above 1 THz, both for the ones of the SRRs (cf. Table G.1) and for the ones of the shorted-SRRs.

G.2 Measurements and Discussion

ρ_{xx} and ρ_{xy} were measured on all samples following the same procedure outlined in chapter 7 on page 157 in the main text. The samples were at a temperature $T \simeq 2$ K and were measured with an AC-current of 200 nA at 74.7 Hz.

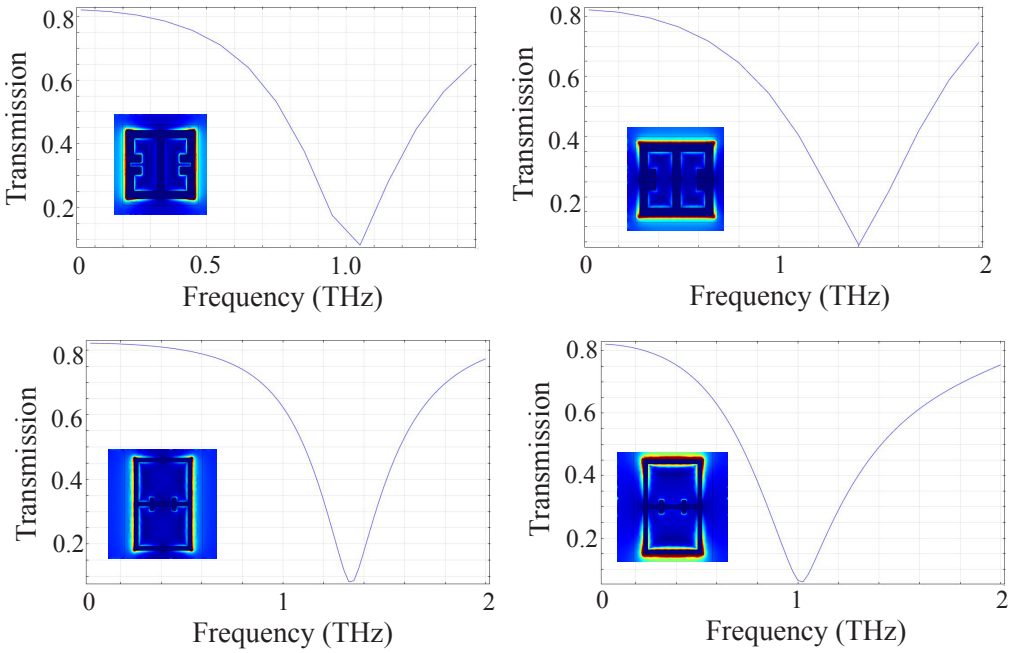

Figure G.4 – Simulated transmission for the shorted resonators in the frequency range 0.05-2 THz with mode distribution at 140 GHz. Top row - SRRs used in samples $A1452$ and $B1452$. Bottom row - SRRs used in samples $C1452$ and $D1452$.

G.2.1 Extraction of sample parameters

From the complete set of traces it is possible to extract the total sheet electron density, the mobility and the sheet density of the electrons participating to the longitudinal transport. The difference between the two electron density values denotes that a part of the total charge is not contributing to the longitudinal transport. The values of Hall density, SdH density and mobility for each of the Hall-bars are collected in Table G.2.

	A			B			C			D		
	free	srtd	SRR	free	srtd	SRR	free	srtd	SRR	free	srtd	SRR
μ (10^5 cm^2/Vs)	855	708	717	814	702	683	835	725	728	1165	1022	1001
	863	689	694	824	703	672	821	702	636	1128	1004	983
	848	700	694	800	691	693	798	695	668	1101	1001	954
n_{xy} (10^{11} cm^{-2})	5.70	5.65	5.63	5.47	5.28	5.30	5.83	5.78	5.76	3.95	3.86	3.88
	5.72	5.64	5.61	5.40	5.24	5.28	5.82	5.77	5.78	3.98	3.87	3.87
	5.71	5.63	5.61	5.47	5.29	5.32	5.82	5.78	5.77	3.96	3.88	3.86
n_{xx} (10^{11} cm^{-2})	3.12	3.13	3.14	2.99	2.90	3.03	3.14	3.16	3.14	3.14	3.07	(2.70)
	3.11	3.11	3.13	2.95	2.78	(2.72)	3.16	3.20	3.17	3.14	3.00	(3.19)
	3.09	3.21	3.20	3.02	-	(2.88)	3.14	3.18	3.17	3.12	3.36	(2.25)

Table G.2 – Mobility, carrier density from SdH oscillations (n_{xx}) and carrier density form QH (n_{xy}), extracted for all measured Hall-bars, uncovered (free), shorted-SRR-covered (srtd) and SRR-covered (SRR). The values in brackets have been derived from few SdH oscillations and therefore subject to a bigger error.

By considering these values altogether, one can conclude that the presence of the SRRs strongly affects the electron mobility, with a decrease of about 14% from uncovered to metal-covered Hall-bars. Concerning their densities, the values derived from the SdH oscillations are all within 3% of the average value in each sample and show no clear pattern related to illumination or presence/absence of resonators. The Hall densities of each Hall-bar are constant within 1% also when varying the illumination condition, but show a clear reduction (though not bigger than 3%) when moving from uncovered sample to covered-one for all illumination conditions.

The parabolic behaviour of ρ_{xx} at small B-fields has in the literature been attributed to the presence of multiple sub-bands[515], fact that would be consistent with the two different electron densities derived from ρ_{xx} and ρ_{xy}. On the other hand, most SdH oscillations show in this range a single periodicity in $1/B$ indicating a single dominant electron band and from other investigations (not shown) the second sub-band exists, but at a much higher energy. The SdH actually show double periodicity only for sample $D1452$.

For sample D, at about ± 0.52T two SdH oscillations collide into each other in the spectra of the resonator-covered Hall-bar, showing no variation in the shorted-ones. The plotting of the maxima as a function of the inverse B-field reveals two slopes as shown in figure G.5. The extraction of the electron density reveals $n_{S,1} = 3.17 \times 10^{11}$ cm^{-2} for the shorted-SRR and the low field region of the non-shorted and $n_{S,2} = 2.57 \times 10^{11}$ cm^{-2} for the high field region of the SRR-covered Hall-bar. The first coincides with the density derivable from the SdH oscillations of the previous samples, whereas the sum of the two, $n_{S,TOT} = 5.74 \times 10^{11}$ cm^{-2}, corresponds to the total carrier density measured from the slope of the transverse resistivity in figure G.5 and it is similar to the values obtained for n_{xy} in all other samples.

G.2.2 Additional measurements on sample $A1452$

Figure G.6 compares the dark traces taken onto sample $A1452$, as done for sample $B1452$ in Fig. 7.16 on page 182.

Also here, although the SdH oscillations are almost in phase and have 0.3 T as a common on-set, the general behaviour of the magneto-resistance is quite different. First, the resistivity at zero magnetic field increases from 12.8 to 15.6 Ω (+22%) from free surface to SRR-covered, denoting a decrease in mobility. Second, the change in resistivity with magnetic field has opposite sign: while for the uncovered Hall-bar the resistivity slowly decreases with magnetic field, for the SRR-covered Hall-bars the resistivity initially strongly increases with a parabolic behaviour and then saturates. This is anyhow much

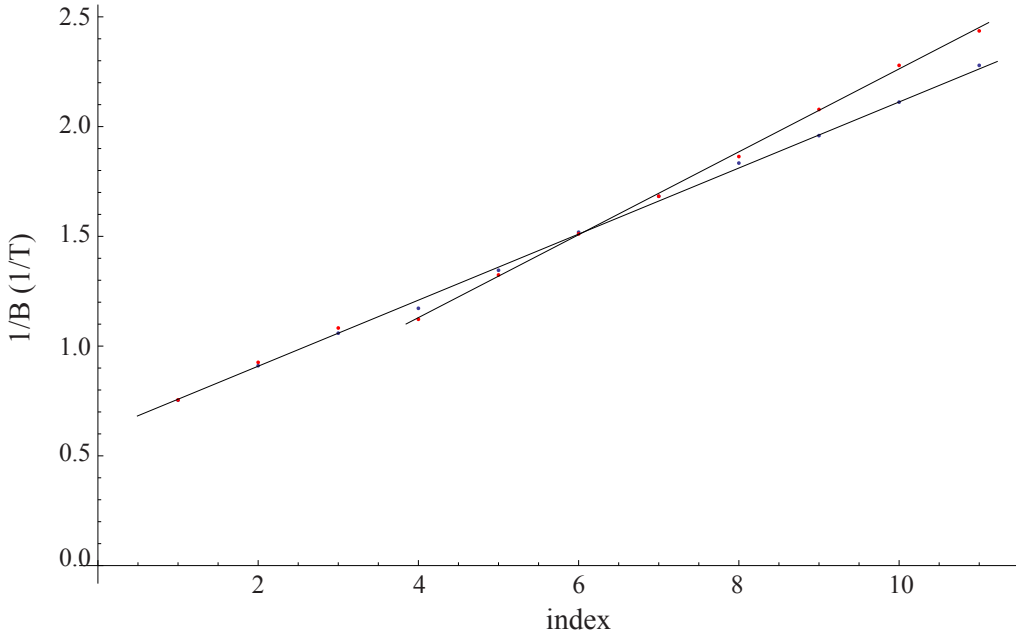

Figure G.5 – Sample D, for the two polarization. Maxima vs inv-B

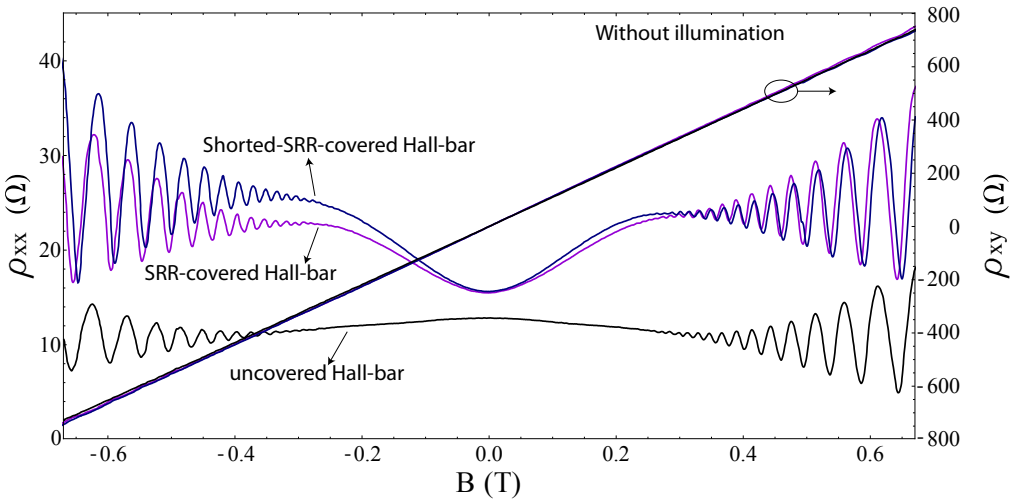

Figure G.6 – ρ_{xx} and ρ_{xy} traces measured on sample $A1452$, without illumination. In black are the traces measured onto the uncovered Hall-bar, in blue the ones on the shorted-SRR-covered Hall-bar and in purple the ones measured on the SRR-covered Hall-bar.

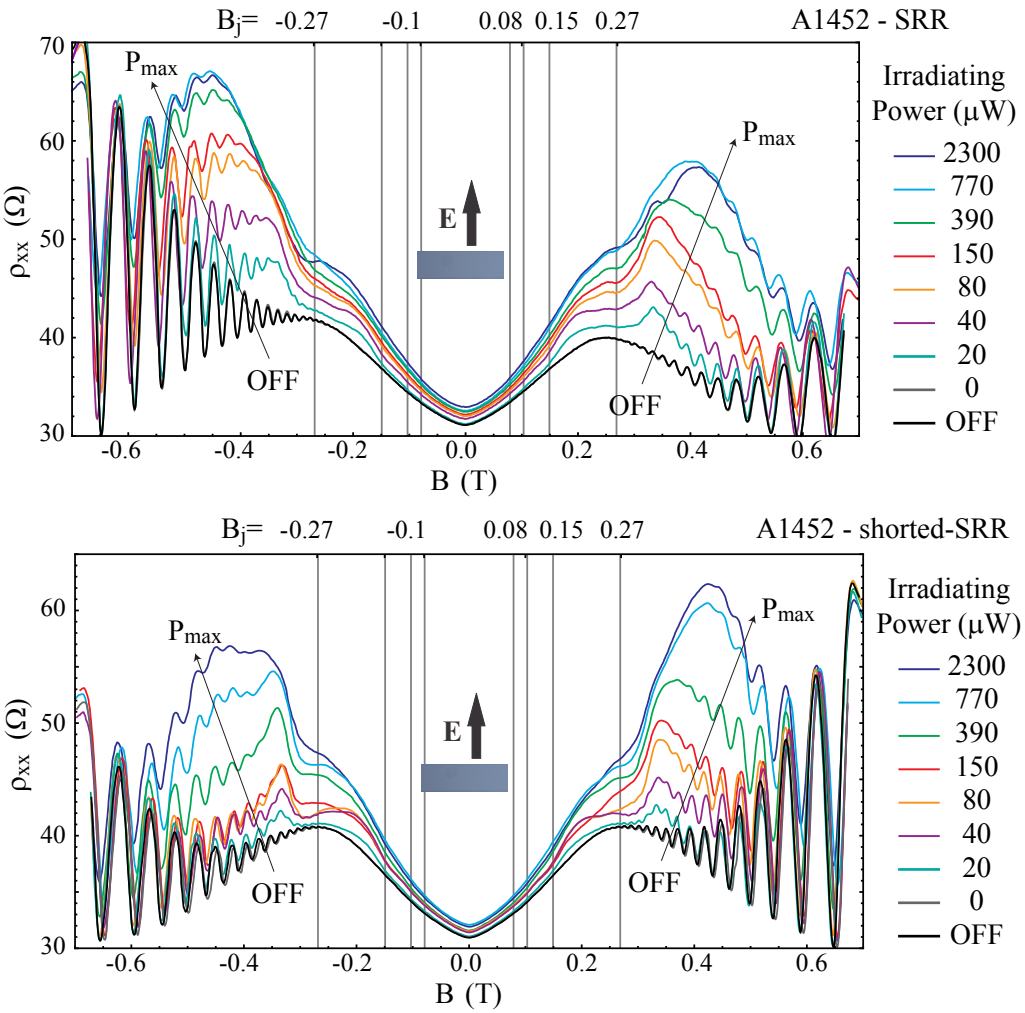

Figure G.7 – Power dependence of the MIRO region for ρ_{xx} of the SRR-covered and shorted-SRR-covered Hall-bar in sample $A1452$ with beam polarization orthogonal to the Hall-bar axis.

less drastic than for sample $B1452$, as compared in Fig. 7.22 on page 189, and it is probably due to size resonances between the cyclotron radii and the SRR-structures. At a certain point, sample $A1452$ allows the electrons to move undisturbed into the central empty channel between resonators, thing not possible in the sample where the SRR-row takes the full width.

Figure G.7 shows the power-depence measurements performed onto the SRR-covered Hall-bars of sample $A1452$: they are similar to the ones presented in section 7.6.1 on page 190 of the main text.

Figure G.8 shows the temperature-depence of the MIRO features, investigated onto the uncovered-Hall-bar of sample $A1452$. It shows that the first MIRO minima are stronger than the SdH and persist till above liquid helium temperature.

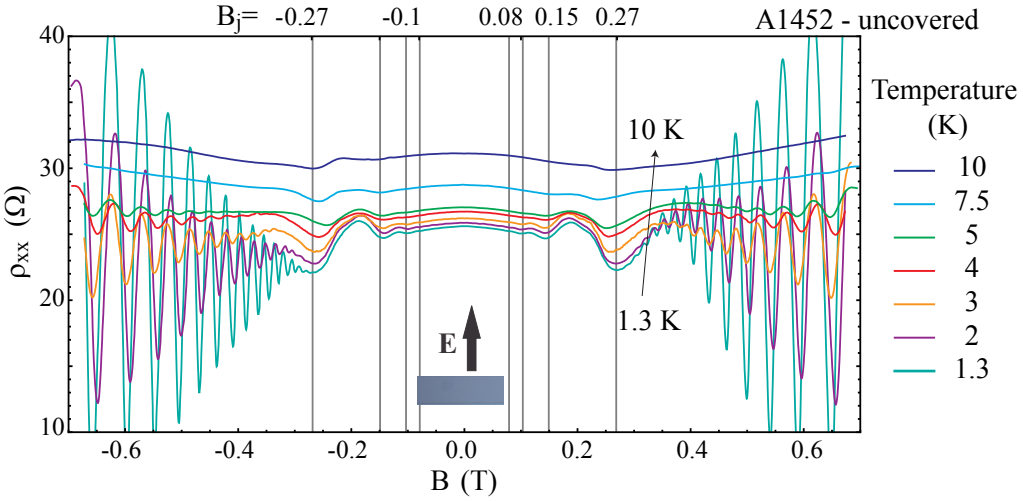

Figure G.8 – Temperature dependence of the MIRO region for ρ_{xx} of the uncovered Hall-bar in sample $A1452$ with beam polarization parallel to the Hall-bar axis.

G.2.3 Measurements on uncovered Hall-bars of samples $C1452$ and $D1452$

The ρ_{xx} and ρ_{xy} traces of the uncovered Hall-bars of samples $C1452$ and $D1452$ are shown in Fig.s G.9 and G.10, respectively. The curves in black show traces measured without irradiation. The Gunn-diode is then switched on with beam polarization orthogonal to the Hall-bar channel and the same measurement performed again: it results in the red curves. The sample is then rotated by 90 ° so that the beam polarization is now parallel to the Hall-bar channel: the measurements are shown in blue.

The irradiation causes the MIRO oscillations to appear in all traces at the expected positions for an infinite GaAs-based 2DEG, while no big change is seen in the Hall traces.

The measurements on the uncovered Hall-bars display the same features already discussed in the main text: the SdH onset is at about ±0.3 T, at least two minima of the MIROs are present at ±0.27 T and ±0.15 T and the MPR peak is either clearly present about ±0.235 T($C1452$) or just a faint shoulder ($D1452$). Again, it is found that the polarization along the Hall-bar channel is the one with higher resistivity.

Considering then the ρ_{xy} traces in this low magnetic field range, all curves superimpose one another. This reveals no change in the total (Hall) carrier density, while varying the mobility and the partial (SdH) carrier density in the different Hall-bars.

Small changes can nonetheless be identified, as shown in the lower panel of Fig. G.9 where a region of the ρ_{xy} traces at high B-field containing two plateaux is shown. From this one can see that there are small variations in the transverse resistivity in general of

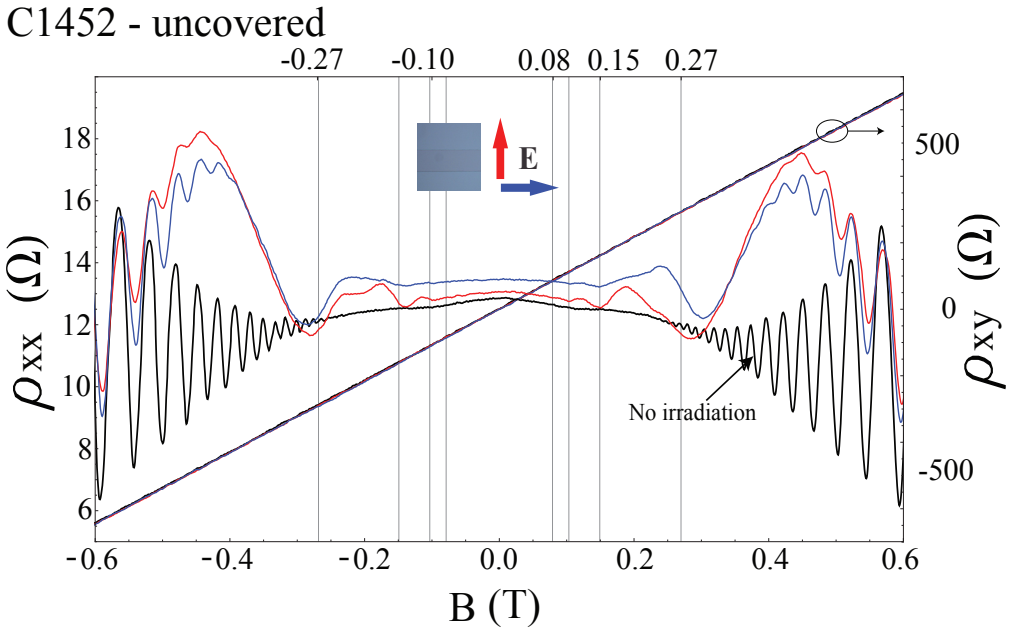

Figure G.9 – ρ_{xx} and ρ_{xy} traces taken on the bare Hall-bar of sample $C1452$.

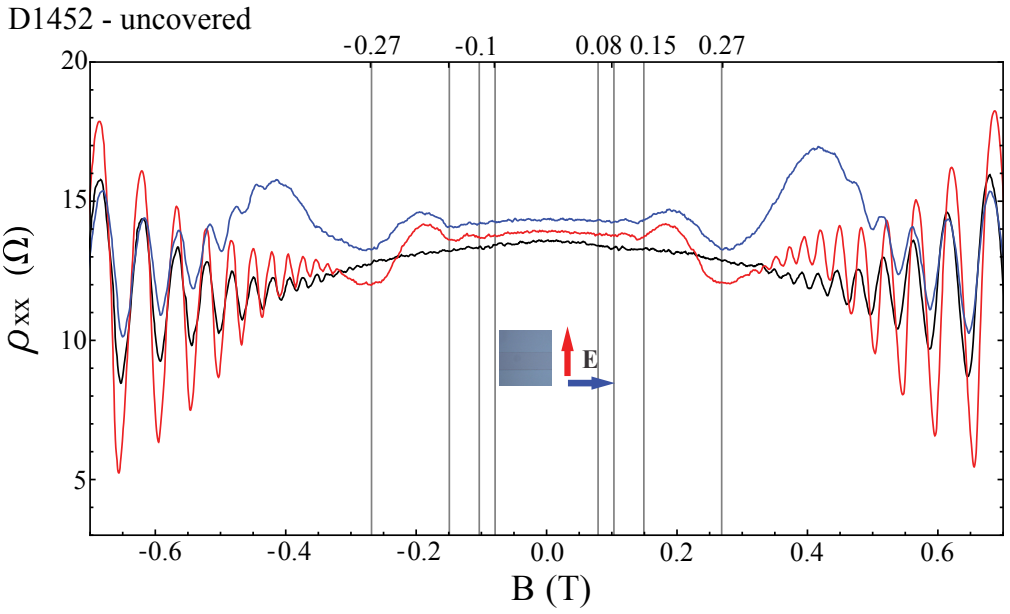

Figure G.10 – ρ_{xx} and ρ_{xy} traces taken on the bare Hall-bar of sample $D1452$.

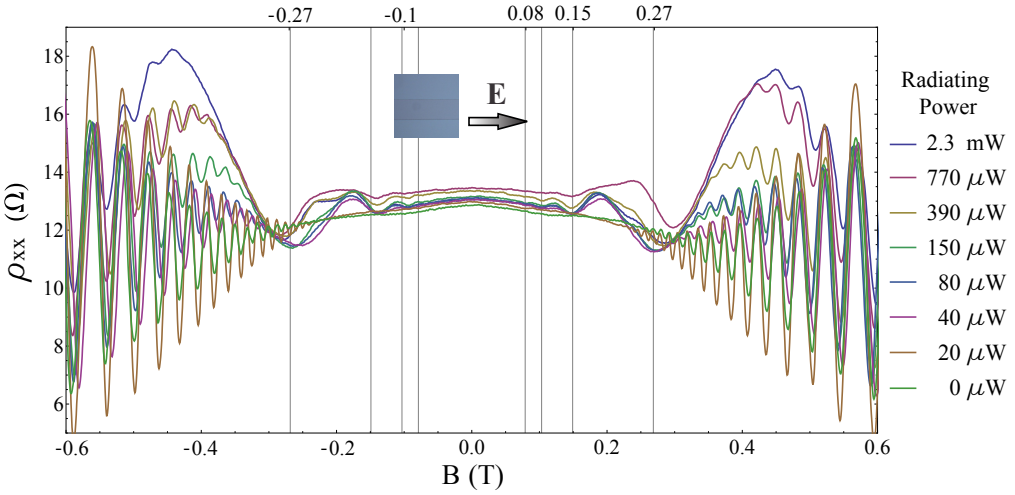

Figure G.11 – Power dependence of the MIRO region for ρ_{xx} of the uncovered Hall-bar in sample $C1452$ with beam polarization parallel to the Hall-bar axis.

the order of a few percent. The plateaux are also slightly reduced in size, but in general negligible modification of the slope is detected indicating that no change in the total electron density can be ascribed to the irradiation.

G.2.4 Power-dependence of the MIRO in $C1452$

In order to get a better insight into the influence of the radiation onto the oscillations appearing under irradiation, the resistivity traces were subsequently recorded at different radiating powers and are plotted in Figure G.11, as done for sample $A1452$ in the main text. The sampling in power was achieved by changing the supplied voltage of the Gunn-diode and resulted in the following power steps: 2.3 mW, 770 µW, 390 µW, 150 µW, 110 µW, 80 µW, 40 µW and 20 µW, with an uncertainty of 20 µW. The dark blue trace presenting the highest shoulder correspond to a power of 2.3 mW (blue trace in Fig. G.9), whereas the green trace with the lowest value of $\rho_{xx}(B = 0\mathrm{T})$ is the one recorded without illumination (black trace in Fig. G.9). In general the oscillations are bigger for stronger irradiation and disappear at 20 µW, almost recovering the non-irradiated trace. The resistance at zero magnetic field is also generally higher than the non-irradiated one.

Let's start considering the biggest peak centred at ±0.45 T. Its amplitude decreases monotonically with irradiation power while it shifts to lower (absolute) magnetic fields in a parabolic fashion. A similar behaviour seems present also for the first MIRO minimum at about ±0.27 T. But this is not the case for all of the traces. The traces taken at the three highest irradiation powers (dark-blue, light-purple and golden) display the first minima at higher magnetic field values between 0.285 T and 0.3 T with also higher resistance values

than almost all of the other traces which display a deeper minimum at about 0.265 T. A second and third minimum are present in almost all of the irradiated traces at +0.15 T, +0.10 T for the positive B-field side and -0.14 T and -0.09 T for the negative side. An additional minimum can be guessed for some traces at ±0.075 T. When now considering the region between the first two minima (±0.27 T–±0.15 T), the power-dependence allows us to better identify the structure of the peaks. Starting from low powers, in such region a single maximum is present at about ±0.185 T. But for high enough powers, a shoulder at ±0.235 T is appearing and growing till becoming a second peak, even the dominant one in the light-purple trace. As already noted, this is the expected magneto-plasmon resonance (MPR) associated with the collective oscillation of the carrier across the channel of the Hall-bar.[389] It is noteworthy that the traces markedly displaying this feature are also the ones having a shifted first minimum, denoting a rather wide MPR. Additionally, the on-set of the SdH oscillations also moves to lower fields with lower irradiation power while the resistance at $B = 0$ T decreases, indicating a decrease in heating and an increase in mobility. Finally, the power dependence immediately makes a separation between those features rapidly decaying in power from the more stable ones, allowing their identification as bulk-related (SdH, MPR, additional peak) or surface-related (MIRO) phenomena.

As a side remark, at high irradiation powers it is also possible to infer a very long thermal relaxation time, considering the relative overlap between the subsequent traces for decreasing powers. This indicates that the system would need several minutes to thermally relax. This also explains why the highest-power trace is not the one displaying the highest resistivity in the low-field region. The dark-blue curve has been measured immediately after the one without irradiation. This instead happened for the light-purple one, the second highest-power trace that in the low-field region dominates over all the others, also displaying the strongest MPR. Nonetheless, this fact does not pose problems within the frame of the present work.

G.2.5 MIRO on SRR-covered Hall-bars of samples $C1452$ and $D1452$

The complete sets of the ρ_{xx} traces (uncovered, SRR-covered, shorted-SRR-covered) for samples $C1452$ and $D1452$ are collected in Figs G.12 and G.13, respectively. As for the figures in the main text, the legends are coded with the following scheme: the measurements without irradiation are plotted in black while the traces recorded under irradiation are in blue and red, these colours indicating the polarisations parallel and orthogonal to the channel, respectively. For clarity the SRR-covered traces were plotted

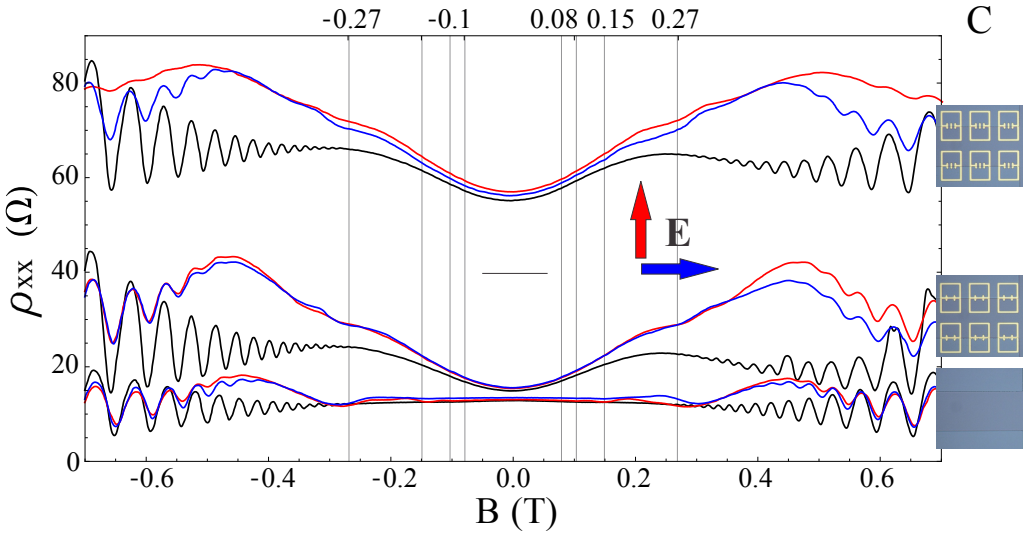

Figure G.12 – ρ_{xx} for sample $C1452$ for all three fields, without irradiation (black) and with longitudinally and orthogonally polarized irradiation (blue and red, respectively). The up-most group has been off-setted for clarity.

offset to the top, the central segment being their referential zero-resistivity.

Considering the figures, it is immediately evident that the discussion done for samples $A1452$ and $B1452$ can be entirely re-mapped onto samples $C1452$ and $D1452$. In general, the SdH oscillations are in phase for the various measurements in the different Hall-bars within each sample. The very different behaviour between the samples with the resonators in the middle of the channel and the one with the two rows of resonators is again present. The non-irradiated traces of sample $C1452$ show a stable oscillation barycentre above ±0.3 T. Once irradiated, the peak at about ±0.45 T arises, with the presence of a clear step at ±0.27 T and no additional features at the expected MIRO minima positions. An additional kink at about ±0.33 T is here present. A peculiar difference is that the red trace corresponding to the irradiation of the SRR-covered Hall-bar illuminated with polarization orthogonal to the Hall-bar axis shows significant general increase of ρ_{xx}. Furthermore, in this same trace the outer peaks are much broader than in the other traces and almost no SdH oscillation is detectable. This behaviour seems to point out that the dipolar mode excited by orthogonal polarization is very effective in heating the 2DEG while the LC-mode, excited in the longitudinal polarization, concentrates the field away from the centre of the Hall-bar resulting in no heating increase. Finally, the SRR-covered traces display under irradiation a higher $\rho_{xx}(B = 0\ \mathrm{T})$ than all others denoting a lower mobility.

The behaviour of sample $D1452$, shown in Fig. G.13, reflects instead sample B, with the resistivity of the SRR-covered Hall-bars parabolically increasing with B-field. The

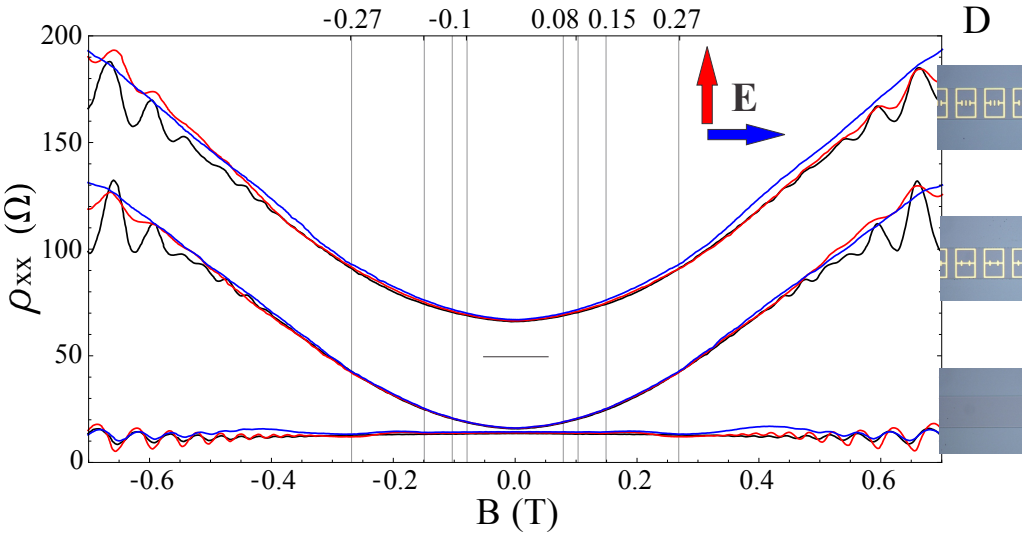

Figure G.13 – ρ_{xx} for sample $D1452$ for all three fields, without irradiation (black) and with longitudinally and orthogonally polarized irradiation (blue and red, respectively). The up-most group has been off-setted for clarity.

SdH oscillations are weak already in the non-irradiated traces and become weaker under irradiation. Also on this sample the longitudinal polarization produces a much stronger heating than the orthogonal one, washing away completely the SdH oscillations. On all traces no feature is self-evident in the low B-field range where the MIRO are expected, apart from small kinks at about ± 0.33 T in the traces where the LC-mode is excited. Moreover, a dephasing of the SdH oscillations, highlighting the presence of two subbands contributing to the longitudinal transport, is present at ± 0.52 T and was discussed in section G.2.1.

In general, more insight into the measurements could be obtained when subtracting the non-irradiated traces from the corresponding irradiated ones but, given the fact that for irradiation at 140 GHz no shift can be resolved, we skip such discussion.

In conclusion, the discussed behaviour might be attributed to the fact that in the samples presenting a partially free surface, there is effectively a thin channel for the Hall-bar where the samples behave conventionally. The presence of the resonators then introduces the additional features. For the samples containing a single row of resonators, instead, the electrons travelling in the Hall-bar constantly encounter the gold structures across its path. It is finally clear that the position of the structures is an effective way of locally heat the 2DEG, as shown by the delayed SdH on-sets.

One can then directly relate the weaker/absent SdH oscillations in samples $B1452$ and $D1452$ when irradiating with polarization along the Hall-bar channel to the SRR position. The resonators' sides concentrate the e.-m. field, creating a periodic heating of

the 2DEG across the entire channel that washes out the oscillations. These are recovered to a good degree when switching the polarization. In the orthogonal polarization instead, the light gets mainly concentrated at the upper and lower edge of the channel, interacting less with the electronic flow.

Appendix H

Processing recipes

H.1 THz-SRRs metasurfaces production

1. Substrate preparation:
   - cleaving the substrate/heterostructure (GaAs- or Si/SiO_2- based);
   - cleaning procedure: acetone → isopropanol → H_2O: each step is performed at about 40° and, when possible, with in a ultrasonic bath. The sample is then dry blown with gaseous nitrogen. If a more thorough cleaning is needed, the sample can be placed in ozone oven for 5 minutes.
2. Definition of the resist mask:
   - for SiO_2 surfaces, the adhesion promoter HMDS is needed. It was spun with revolutions-per-min/acceleration-time (in s)/duration (in s) parameters 4000/4/40;
   - spinning of the reversible resist AZ1542E at 4000/4/40 and baking at 100° for 60 s;
   - edge removal: flood exposure of the edges of the sample where the resist is thicker for 60 s; development in MIF726 for 60 s or longer according to the edge resist thickness;
   - photolithographic definition of resonators: exposure with 48 m J in soft-contact mode; reverse baking at 120°/45 s; flood exposure of the whole sample for 20 s; development in MIF726 for 40 s or longer;
   - (optional, if the photolithographic features are not sharp) O_2-plasma at 250 W for 3 min.
3. Production of the metallic metasurface:
   - metallization in electron-beam evaporator with deposition of Ti/Au with thickness 5 nm/200 nm

- lift-off: hot acetone in ultrasonic bath (when possible) → warm isopropanol → H_2O

The procedure described above allows the realisation of direct SRRs. For complementary SRRs, one must develop directly after the first exposure, avoiding reverse baking and flood exposure.

For the closed-SRRs, one must take care, during lift-off, of letting the resist dissolve and the upper metallisation layer fall back into the holes.

For the spaced-SRRs, one avoids the lift-off: the sample is ready after metallisation. In order to vary the thickness of the resist, different spinning parameters and positive resists were used:

- thinnest resist: AZ1452E at 6000/6/40
- middle resist thickness: AZ1518 at 4000/4/40
- thickest resist: AZ1505 at 3000/4/40.

Note that the gold thickness is chosen such that it is a few times lerger than the absorption length of THz in gold ($\delta \simeq 50$ nm at $f = 0.5$ THz).

H.2 Graphene processing

CVD-growth of graphene

The CVD-graphene used in this thesis was grown with Chemical Vapour Deposition (CVD) technique with two different recipes:

- mixture of H_2/CH_4 with fluxes of 10/25 sccm, respectively, at 1000° for 10 minutes on standard 25µm copper foil. The copper foil was previously cleaned in diluted HCl (2% in weight, 1 min) to remove eventual oxide and dirt;
- alternatively, mixture of $Ar:H_2:C_2H_4$ with fluxes of 1500:20:10 sccm at a pressure of 4 mbar at 900°.

After deposition the pieces of Cu-foil, approx. 5×5 cm^2 large, are well covered on the top-facing side but some graphene is present also on the back.

Transfer of CVD-graphene to an arbitrary substrate

The transfer procedure partially follows Ref. [516].

Cleaning of the back side of the copper foil: spin coating of PMMA 950k on the top face of the Cu-foil with graphene at 500/1/2 followed by a step at 4500/4/45. Then bake on the hot plate at 180° for 80 s. Finally clean the back side of the Cu-foil either with aceton on clean-room paper or with a reactive-ion etching recipe based on Ar:O_2=80:5 sccm at a pressure of 40 mTorr and a power of 35W. A graphene monolayer is etched in approx. 13 s, 30 s are enough for the cleaning;

definition of dimensions: cut form the large Cu-foil smaller pieces as large as the graphene you would like to transfer onto the substrates. Note that the pieces should be smaller than the substrate area to avoid graphene shortened to the back gate vie the sample sides;

Cu-etching: prepare a solution of ammonium persulfate and water $(HN_4)_2S_2O_8$:H_2O=2:100 in weight (etchant from Sigma-Aldrich) and place the Cu-pieces floating on its surface, with the graphene-side upward After few hours the Cu-foil is dissolved and the graphene/PMMA bilayer floats in the becker. An alternative, less clean but faster, etching solution is given by iron chloride and water Fe_2Cl_3:H_2O=1:1 in weight. Note that if the graphene stays exposed for too long to the etchant, it also deteriorates;

Graphene rinsing: using a spoon, the floating bilayer are scooped and moved to a becker containing fresh DI-water to rinse them from the etching solution. Leave them there for about 5 min and repeat the procedure to a becker containing fresh water at least two more times;

Graphene fishing: using a clean substrate, holding it from the sides or from one corner, the graphene/PMMA bilayer is fished from the water-side taking care that it lays flat and without wrinkles onto the substrate, as well as without trapping water or air bubbles below itself. This procedure requires particular patience for hydrophobic surfaces. The bilayer is then shortly and gently blown with gaseous nitrogen to remove most water and left to complete the drying;

PMMA removal: the sample is then heated up to 120° for at least 10 min to soften the PMMA and let the possibly remaining water evaporate. As soon as the sample is removed from the hot plate, it is immersed in warm acetone and left there to dissolve the PMMA for 5 min. The sample is then extracted from the liquid while gently flushing it with a pipette containing acetone, first, and isopropanol afterwards, while immersing it in warm isopropanol. Finally, after 5 min in the warm isopropanol, it is extracted and directly dry-blown with gaseous nitrogen.

Additional processing of graphene-based samples

1. Production of electrical contacts and other metallic structures onto the graphene layer:
    - the photolithography steps are the same as explained in the THz-SRR section above with the resist AZ1452E. Other positive resists of the same family can also be used (e.g. AZ1518 or AZ1505), while the developer MAD533S of the negative resist MAN1440 was found to etch away the exposed graphene layer. Strictly avoid also any other etching like O_2 plasma or Ar-gun before evaporation;
    - metal evaporation: electron-beam evaporation of either Ti/Au or Cr/Au with thicknesses of 5/150 nm. The minimum Au thickness used for purely electrical contacts (no THz-optical requirement) was 45 nm;
    - lift-off: warm acetone, if needed helped with gentle pipetting and in extreme cases with the minimum power of ultrasounds. Then warm acetone and nitrogen blow.
2. Realisation of graphene structures:
    - the photolithography can be carried out following the steps explained in the THz-SRR section;
    - the exposed graphene is then etched with the reactive-ion recipe described for the transferring procedure;
    - the resist left is then cleaned with acetone and isopropanol as described above.

Appendix I

Implanted substrate for low-temperature THz-transmission

In order to perform magneto-transmission onto graphene-based samples, a suitable substrate was needed. It must be transparent to THz-radiation while being conductive at 4 K and being covered by 285 nm of silicon oxide for the identification and gating of the graphene. The issue with the previous substrates was that they are about 500 µm of homogeneously doped material, hence most of the time either they are too doped to leave enough radiation through, or they have good transmission because of few dopants that freeze at low temperatures inhibiting the gating.

The solution was then to implant a low-doped substrate with a thin dense layer of dopants, such that the density of the latter is enough to allow low-temperature gating while its thickness, below the THz-skin depth, would allow high transmissions. Such a solution had not been investigated yet, and also companies offering wafer implantation had no standard for it.

After initial discussion with *IBS*— we received from the company two test implanted wafers to study and characterise. The substrates were 4-inches Si-wafers with high resistivity, implanted with phosphorous with a surface density of 10^{15} cm^{-2} (corresponding to a volume doping of about 10^{20-21} cm^{-3}). Non annealing was performed or oxide was grown.

The annealing is needed to activate the implant, i.e. give the lattice energy to readjust letting the implanted atoms form a conductive layer. It was performed in house, at one of the ETH clean rooms, annealing at approx. 850°C for 30min with a ramp of 10°C/min in forming gas atmosphere. No previous HF-cleaning was performed.

At this point the conduction/transmission tests could be performed to determine the best substrate characteristics. To this purpose, first van-der-Pauw/Hall measurements

were performed at room temperature to determine mobility, resistivity and carrier concentration of the conductive layer[1]. Subsequently, the sample was mounted in the sample holder of the *Oxford Sepctromag* (cf. section 3.5 on page 95) to measure low-temperature IV-curves of the layer and transmission through the sample.

The measurements on the as-implanted wafer gave a surface charge density of 1.33×10^{15} cm^{-2} that resulted too high to have any THz-transmission signal through. A reactive-ion etching recipes was then developed, starting from standard data, based on 25 SCCM of CF_4 at 100 mTorr and 100 W and the calibration gave a not-constant etching rate of about 32 nm/min for the first four minutes, decreasing till 14 nm/min for subsequent additional four minutes, after a cooling pause where the chamber was flushed with nitrogen.

The aim of it is to increasingly etch away part of the implanted layer to determine the optimal dopants density. For each etching step, the previous measurements were performed and the results are summarised in Fig. I.1 on the next page: sheet charge density (black), integrated volume charge density at 50 nm (red), mobility (green), square resistance (blue) and THz-transmission (cyan) are plotted against etching time. Given the fix etching rate, the x-axis can be converted into the distance into the substrate from its surface: this shows the exponential profile of the implanted layer (cf. black and red data sets). Given the measured values, the targeted implant surface charge density was 10^{14} cm^{-2}, high enough to allow gating but at the same time transparent enough to THz-radiation.

One part of the initial wafer was then etched for 5.5 min and annealed in presence of gaseous molecular oxygen for the needed time to grow the wanted 285 nm thermal oxide on the as-etched surface. The THz-transmission decreased to about 10% after the oxide was grown (vs approx. 45%), indicating a redistribution of the charges. To confirm this suspicion the oxide was removed via HF and then the sample was measured again electrically. The data related to this last step are reported with bigger rhombi in Fig.I.1 and reveal an increase of both the surface charge density and of the mobility.

The thermal oxide is usually of a very good quality, therefore preferred to ones grown with deposition techniques. Unfortunately for the present substrates this has two main disadvantages. First, thermally grown oxides being formed per oxidisation of the material surface, consume the superficial layers of the substrates, expectedly in a ratio of 2:1 of Silicon to oxide thickness. This means that to achieve 285 nm of thermal oxide, almost 600 nm of substrate will be converted, redistributing part of the implanted doping, that is expected to be kept in the substrate. Second, the high temperature required for such process, despite having the beneficial effect of thermally activating the implanted layer,

[1] I am indebted to Selamnesh Nida for her kind help in performing those measurements.

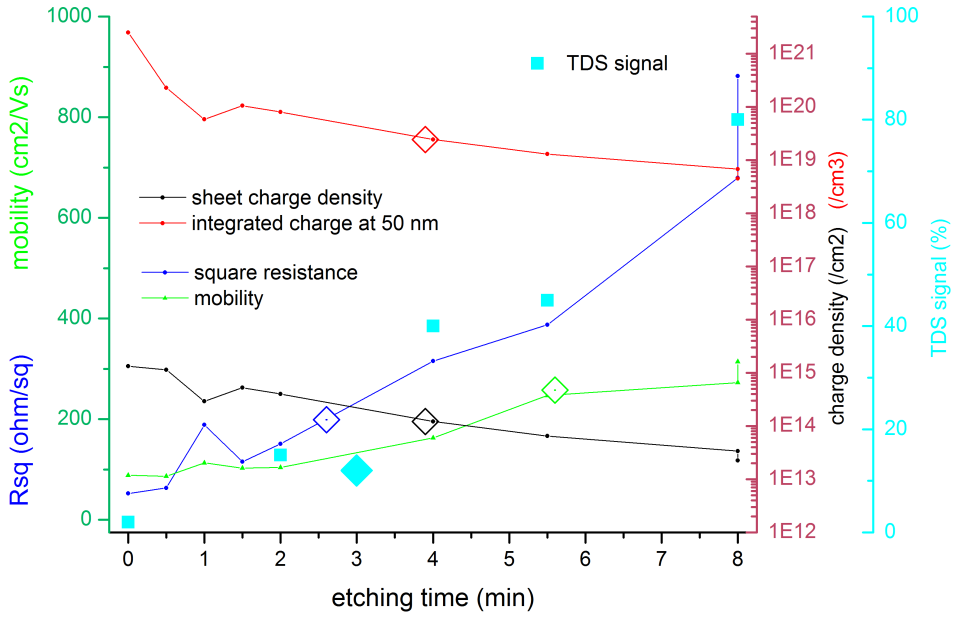

Figure I.1 – The dots are the results of the measurements explained in the text, for different etching times. Rhombi indicate what obtained after growth and removal of the oxide.

when kept for too long time, allows dopants diffusion resulting in a thicker but less volume-doped layer. For these reasons, for the wafers produced afterwards, the first 20 nm of oxide of the final substrates were thermally grown while the remaining 265 nm were deposited by Plasma-Enhanced Chemical Vapour Deposition. Such technique can deposit silicon oxides from gaseous sources at a temperature of 400°C.

Bibliography

"Una volta un tale che doveva fare una ricerca andava in biblioteca, trovava dieci titoli sull'argomento e li leggeva; oggi schiaccia un bottone del suo computer, riceve una bibliografia di diecimila titoli, e rinuncia."

—Umberto Eco, *La bustina di minerva*, L'espresso (2000)

[1] J. M. Chamberlain. *Where optics meets electronics: recent progress in decreasing the terahertz gap*. Philosophical transactions. Series A, Mathematical, physical, and engineering sciences, **362**, 199 (2004). 1

[2] M. C. Nuss, J. Orenstein. *Millimiter and submillimiter wave spectroscopy of solids*. Springer (1998). 1, 4, 95

[3] G. P. Williams. *Filling the THz gap - high power sources and applications*. Reports on Progress in Physics, **69**, 301 (2006). 1

[4] Inductiveload, NASA. *EM Spectrum Properties edit*. Wikimedia Commons. 2

[5] *The terahertz frequency band*. cms.uni-konstanz.de/en/physik/leitenstorfer/research/multi-terahertz-physics-and-technology. 2

[6] D. N. Basov, M. M. Fogler, A. Lanzara, F. Wang, Y. Zhang. *Colloquium : Graphene spectroscopy*. Reviews of Modern Physics, **86**, 959 (2014). 3

[7] D. N. Basov, R. D. Averitt, D. van der Marel, M. Dressel, K. Haule. *Electrodynamics of correlated electron materials*. Reviews of Modern Physics, **83**, 471 (2011). 3

[8] B. S. Williams. *Terahertz quantum-cascade lasers*. Nature Photonics, **1**, 517 (2007). 4, 24, 40, 42

[9] W. Withayachumnankul, D. Abbott. *Survey of terahertz metamaterial devices*. Proc. SPIE 7268, Smart Structures, Devices, and Systems IV, pp. 72681Z–72681Z–10 (2008). 4

[10] M. Choi, S. H. Lee, Y. Kim, S. B. Kang, J. Shin, M. H. Kwak, K.-Y. Kang, Y.-H. Lee, N. Park, B. Min. *A terahertz metamaterial with unnaturally high refractive index*. Nature, **470**, 369 (2011). 4

[11] H.-T. Chen, W. J. Padilla, J. M. O. Zide, A. C. Gossard, A. J. Taylor, R. D. Averitt. *Active terahertz metamaterial devices.* Nature, **444**, 597 (2006). 4, 223

[12] R. A. Herman. *A Treatise on Geometrical Optics.* University Press (1900). 4

[13] J. D. Joannopoulos, S. G. Johnson, J. N. Winn, R. D. Meade. *Photonic Crystals: Molding the Flow of Light.* Princeton University Press (2008). 4, 5

[14] C. M. Soukoulis, M. Wegener. *Past achievements and future challenges in the development of three-dimensional photonic metamaterials.* Nature Photonics, **5**, 523 (2011). 4, 6

[15] D. R. Smith, S. Schultz, P. Markos, C. M. Soukoulis. *Determination of effective permittivity and permeability of metamaterials from reflection and transmission coefficients.* Physical Review B, **65**, 195104 (2002). 5

[16] V. G. Veselago. *The Electrodynamics of Substances with Simultaneously Negative Values of ϵ and μ.* Soviet Physics Uspekhi, **10**, 509 (1968). 5

[17] R. A. Shelby, D. R. Smith, S. Schultz. *Experimental Verification of a Negative Index of Refraction.* Science, **292**, 77 (2001). 5

[18] J. B. Pendry, D. Schurig, D. R. Smith. *Controlling Electromagnetic Fields.* Science, **312**, 1780 (2006). 5

[19] D. Schurig, J. J. Mock, B. J. Justice, S. A. Cummer, J. B. Pendry, A. F. Starr, D. R. Smith. *Metamaterial Electromagnetic Cloak at Microwave Frequencies.* Science, **314**, 977 (2006). 5

[20] J. B. Pendry. *Negative Refraction Makes a Perfect Lens.* Physical Review Letters, **85**, 3966 (2000). 5

[21] N. Fang, H. Lee, C. Sun, X. Zhang. *SubDiffraction-Limited Optical Imaging with a Silver Superlens.* Science, **308**, 534 (2005). 5

[22] D. R. Smith, W. J. Padilla, D. C. Vier, S. C. Nemat-Nasser, S. Schultz. *Composite medium with simultaneously negative permeability and permittivity.* Physical Review Letters, **84**, 4184 (2000). 5

[23] J. B. Pendry, A. J. Holden, D. J. Robbins, W. J. Stewart. *Magnetism from conductors and enhanced nonlinear phenomena.* IEEE Transactions on Microwave Theory and Techniques, **47**, 2075 (1999). 5, 7

[24] P. Muehlschlegel, H.-J. Eisler, O. J. F. Martin, B. Hecht, D. W. Pohl. *Resonant Optical Antennas.* Science, **308**, 1607 (2005). 5

[25] W. N. Hardy, L. A. Whitehead. *Split-ring resonator for use in magnetic resonance from 200-2000 MHz.* Review of Scientific Instruments, **52**, 213 (1981). 6

[26] D. Schurig, J. J. Mock, D. R. Smith. *Electric-field-coupled resonators for negative permittivity metamaterials.* Applied Physics Letters, **88**, 041109 (2006). 7, 82

[27] J. F. O'Hara, E. Smirnova, A. K. Azad, H.-T. Chen, A. J. Taylor. *Effects of Microstructure Variations on Macroscopic Terahertz Metafilm Properties.* Active and Passive Electronic Components, **2007**, 1 (2007). 7, 8, 82, 88, 90, 218

[28] G. Scalari, C. Maissen, S. Cibella, R. Leoni, P. Carelli, F. Valmorra, M. Beck, J. Faist. *Superconducting complementary metasurfaces for THz ultrastrong light-matter coupling.* New Journal of Physics, **16**, 033005 (2014). 8, 16, 146, 155

[29] M. H. Devoret, J. M. Martinis. *Experimental Aspects of Quantum Computing*, pp. 163–203. Springer US, Boston, MA (2005). ISBN 978-0-387-27732-5. 8

[30] C. Kittel. *Introduction to Solid State Physics.* John Wiley & Sons, 8th edition (2005). 9, 12

[31] A. Messiah. *Quantum Mechanics.* Dover Publications Inc. (1999). 9, 16, 46, 47

[32] J. Faist. *Quantum Cascade Lasers.* Oxford University Press (2013). 9, 10, 29, 30, 31, 33, 36, 40, 44, 50, 237

[33] L. Pfeiffer, K. W. West. *The role of MBE in recent quantum Hall effect physics discoveries.* Physica E: Low-Dimensional Systems and Nanostructures, **20**, 57 (2003). 10, 14

[34] V. Umansky, M. Heiblum, Y. Levinson, J. Smet, J. Nübler, M. Dolev. *MBE growth of ultra-low disorder 2DEG with mobility exceeding* $35 \times 10^6 cm^2/Vs$. Journal of Crystal Growth, **311**, 1658 (2009). 10

[35] D. G. Schlom, L. N. Pfeiffer. *Oxide electronics: Upward mobility rocks!* Nature Materials, **9**, 881 (2010). 10, 121

[36] E. H. Hwang, S. Das Sarma. *Limit to two-dimensional mobility in modulation-doped GaAs quantum structures: How to achieve a mobility of 100 million.* Physical Review B, **77**, 235437 (2008). 10

[37] R. Dingle, H. L. Stormer, A. C. Gossard, W. Wiegmann. *Electron mobilities in modulation-doped semiconductor heterojunction superlattices.* Applied Physics Letters, **33**, 665 (1978). 11

[38] N. W. Ashcroft, N. D. Mermin. *Solid State Physics.* Thomas Learning (1976). 12, 220

[39] T. Ihn. *Semiconductor Nanostructures.* Oxford University Press (2010). 12, 15

[40] K. von Klitzing, G. Dorda, M. Pepper. *New Method for High-Accuracy Determination of the Fine-Structure Constant Based on Quantized Hall Resistance.* Physical Review Letters, **45**, 494 (1980). 14

[41] H. L. Stormer, D. C. Tsui, A. C. Gossard. *The fractional quantum Hall effect.* Reviews of Modern Physics, **71**, 298 (1999). 14

[42] R. Willett, J. P. Eisenstein, H. L. Störmer, D. C. Tsui, A. C. Gossard, J. H. English. *Observation of an even-denominator quantum number in the fractional quantum Hall effect.* Physical Review Letters, **59**, 1776 (1987). 14

[43] L. D. Landau, E. M. Lifsits. *Meccanica Quantistica: Teoria non relativistica.* Editori Riuniti, 5th edition (1976). 14, 53

[44] T. Heinzel. *Mesoscopic Electronics in Solid State Nanostructures.* WILEY-VCH Verlag, Weinheim (2003). 15, 177

[45] T. Ando, A. B. Fowler, F. Stern. *Electronic properties of two-dimensional systems.* Reviews of Modern Physics, **54**, 437 (1982). 15, 121

[46] C. Cohen-Tannoudji, J. Dupont-Roc, G. Grynberg. *Photons and Atoms: Introduction to Quantum Electrodynamics* (2004). 16, 144

[47] G. Scalari, C. Maissen, D. Turcinková, D. Hagenmüller, S. De Liberato, C. Ciuti, C. Reichl, D. Schuh, W. Wegscheider, M. Beck, J. Faist. *Ultrastrong coupling of the cyclotron transition of a 2D electron gas to a THz metamaterial.* Science, **335**, 1323 (2012). 18, 151, 171, 183, 199, 203, 253, 254

[48] C. Ciuti, G. Bastard, I. Carusotto. *Quantum vacuum properties of the intersubband cavity polariton field.* Physical Review B, **72**, 115303 (2005). 19, 20, 143, 144, 146, 148, 199

[49] D. Hagenmüller, S. De Liberato, C. Ciuti. *Ultrastrong coupling between a cavity resonator and the cyclotron transition of a two-dimensional electron gas in the case of an integer filling factor.* Physical Review B, **81**, 235303 (2010). 19, 144, 146, 148, 199

[50] E. T. Jaynes, F. W. Cummings. *Comparison of quantum and semiclassical radiation theories with application to the beam maser.* Proceedings of the IEEE, **51**, 89 (1963). 19, 145

[51] M. G. Raizen, R. J. Thompson, R. J. Brecha, H. J. Kimble, H. J. Carmichael. *Normal-Mode Splitting and Linewidth Averaging for 2-State Atoms in an Optical Cavity.* Physical Review Letters, **63**, 240 (1989). 20

[52] Y. F. Zhu, D. J. Gauthier, S. E. Morin, Q. L. Wu, H. J. Carmichael, T. W. Mossberg. *Vacuum Rabi Splitting As a Feature of Linear-Dispersion Theory - Analysis and Experimental-Observations.* Physical Review Letters, **64**, 2499 (1990). 20

[53] J. M. Raimond, M. Brune, S. Haroche. *Colloquium: Manipulating quantum entanglement with atoms and photons in a cavity.* Reviews of Modern Physics, **73**, 565 (2001). 20

[54] C. Weisbuch, M. Nishioka, A. Ishikawa, Y. Arakawa. *Observation of the coupled exciton-photon mode splitting in a semiconductor quantum microcavity.* Physical Review Letters, **69**, 3314 (1992). 20

[55] E. Dupont, H. C. Liu, A. J. SpringThorpe, W. Lai, M. Extavour. *Vacuum-field Rabi splitting in quantum-well infrared photodetectors.* Physical Review B, **68**, 245320 (2003). 20, 156, 203

[56] L. Sapienza, A. Vasanelli, C. Ciuti, C. Manquest, C. Sirtori, R. Colombelli, U. Gennser. *Photovoltaic probe of cavity polaritons in a quantum cascade structure.* Applied Physics Letters, **90**, 201101 (2007). 20, 156, 203

[57] Y. Todorov, P. Jouy, A. Vasanelli, L. Sapienza, R. Colombelli, U. Gennser, C. Sirtori. *Stark-tunable electroluminescence from cavity polariton states.* Applied Physics Letters, **93**, 171105 (2008). 20, 156, 203

[58] L. Sapienza, A. Vasanelli, R. Colombelli, C. Ciuti, Y. Chassagneux, C. Manquest, U. Gennser, C. Sirtori. *Electrically Injected Cavity Polaritons.* Physical Review Letters, **100**, 136806 (2008). 20, 156, 203

[59] P. Nataf, C. Ciuti. *No-go theorem for superradiant quantum phase transitions in cavity QED and counter-example in circuit QED.* Nature Communications, **1**, 1069 (2010). 21, 149

[60] D. Hagenmüller, C. Ciuti. *Cavity QED of the Graphene Cyclotron Transition.* Physical Review Letters, **109**, 267403 (2012). 21, 144, 150, 151

[61] L. Chirolli, M. Polini, V. Giovannetti, A. H. MacDonald. *Drude Weight, Cyclotron Resonance, and the Dicke Model of Graphene Cavity QED.* Physical Review Letters, **109**, 267404 (2012). 21, 150

[62] F. M. D. Pellegrino, L. Chirolli, R. Fazio, V. Giovannetti, M. Polini. *Theory of integer quantum Hall polaritons in graphene.* Physical Review B, **89**, 165406 (2014). 21, 150

[63] J. Faist, F. Capasso, D. L. Sivco, C. Sirtori, A. L. Hutchinson, A. Y. Cho. *Quantum Cascade Laser.* Science, **264**, 553 (1994). 22, 29, 36, 38, 45, 54

[64] G. Taubes. *A new laser promises to put an end to band gap slavery.* Science, **264**, 508 (1994). 22

[65] A. Yariv. *Optical Electronics.* Oxford University Press (1990). 22

[66] I. Vurgaftman, W. W. Bewley, C. L. Canedy, C. S. Kim, M. Kim, C. D. Merritt, J. Abell, J. R. Meyer. *Interband Cascade Lasers With Low Threshold Powers and High Output Powers.* IEEE Journal of Selected Topics in Quantum Electronics, **19**, 1200210 (2013). 23

[67] J. R. Meyer, C. L. Canedy, C. S. Kim, M. Kim, W. W. Bewley, C. D. Merritt, I. Vurgaftman. *High-Brightness Interband Cascade Lasers.* In *CLEO 2015*, pp. 10–11 (2015). 23

[68] J. E. Davey. *Epitaxial GaAs Films Deposited by Vacuum Evaporation.* Journal of Applied Physics, **39**, 1941 (1968). 23

[69] J. R. Arthur. *Interaction of Ga and As2 Molecular Beams with GaAs Surfaces.* Journal of Applied Physics, **39**, 4032 (1968). 23

[70] A. Y. Cho. *Film Deposition by Molecular-Beam Techniques.* Journal of Vacuum Science and Technology, **8**, S31 (1971). 23

[71] B. A. Joyce. *Molecular beam epitaxy.* Reports on Progress in Physics, **48**, 1637 (1985). 23

[72] M. Razeghi. *The MOCVD Challenge.* CRC Press (2010). 23

[73] H. C. Liu, F. Capasso. *Intersubband Transitions in Quantum Wells.* Academic Press (1999). 23

[74] L. Esaki, R. Tsu. *Superlattice and Negative Differential Conductivity in Semiconductors.* IBM Journal of Research and Development, **14**, 61 (1970). 23

[75] R. F. Kazarinov, R. A. Suris. *Electric and Electromagnetic Properties of Semiconductors with a Superlattice.* Soviet Physics of Semiconductors, **6**, 120 (1972). 23

[76] M. Helm, P. England, E. Colas, F. DeRosa, S. J. Allen Jr. *Intersubband Emission from Semiconductor Superlattices Excited by Sequential Resonant Tunneling.* Physical Review Letters, **63**, 74 (1989). 23, 54

[77] R. Köhler, A. Tredicucci, F. Beltram, H. E. Beere, E. H. Linfield, A. G. Davies, D. A. Ritchie, R. C. Iotti, F. Rossi. *Terahertz semiconductor-heterostructure laser.* Nature, **417**, 156 (2002). 24, 36, 37, 38

[78] G. Scalari, C. Walther, M. Fischer, R. Terazzi, H. Beere, D. A. Ritchie, J. Faist. *THz and sub-THz quantum cascade lasers.* Laser and Photonics Reviews, **3**, 45 (2009). 24, 32, 57, 65

[79] S. Fathololoumi, E. Dupont, C. W. I. Chan, Z. R. Wasilewski, D. Ban. *Terahertz quantum cascade lasers operating up to 200 K with optimized oscillator strength and improved injection tunneling.* Optics Express, **20**, 3866 (2012). 24, 38, 41, 48, 76

[80] S. Jung, A. Jiang, Y. Jiang, K. Vijayraghavan, X. Wang, M. Troccoli, M. A. Belkin. *Broadly tunable monolithic room-temperature terahertz quantum cascade laser sources.* Nature Communications, **5**, 4267 (2014). 24

[81] Q. Y. Lu, N. Bandyopadhyay, S. Slivken, Y. Bai, M. Razeghi. *Continuous operation of a monolithic semiconductor terahertz source at room temperature.* Applied Physics Letters, **104**, 221105 (2014). 24

[82] M. Rahm, J.-S. Li, W. J. Padilla. *THz Wave Modulators: A Brief Review on Different Modulation Techniques.* Journal of Infrared, Millimeter, and Terahertz Waves, **34**, 1 (2013). 24

[83] B. Sensale-Rodriguez, T. Fang, R. Yan, M. M. Kelly, D. Jena, L. Liu, H. G. Xing. *Unique prospects for graphene-based terahertz modulators.* Applied Physics Letters, **99**, 113104 (2011). 24, 129, 207

[84] C. Sirtori, F. Capasso, J. Faist, A. L. Hutchinson, D. Sivco, A. Y. Cho. *Resonant tunneling in quantum cascade lasers.* IEEE Journal of Quantum Electronics, **34**, 1722 (1998). 32

[85] A. Wittmann. *High-performance quantum cascade laser sources for spectroscopic applications.* Ph.D. thesis, ETH Zurich (2009). 32

[86] A. Bismuto, S. Riedi, B. Hinkov, M. Beck, J. Faist. *Sb-free quantum cascade lasers in the 3-4 μm spectral range.* Semiconductor Science and Technology, **27**, 045013 (2012). 32, 34, 45

[87] S. Y. Zhang, D. G. Revin, J. W. Cockburn, K. Kennedy, A. B. Krysa, M. Hopkinson. *$\lambda \simeq 3.1$ μm room temperature InGaAs/AlAsSb/InP quantum cascade lasers.* Applied Physics Letters, **94**, 031106 (2009). 32

[88] H. Callebaut, S. Kumar, B. S. Williams, Q. Hu, J. L. Reno. *Importance of electron-impurity scattering for electron transport in terahertz quantum-cascade lasers.* Applied Physics Letters, **84**, 645 (2004). 32

[89] A. Hugi. *Single-mode and Comb Operation of Broadband Quantum Cascade Lasers.* Ph.D. thesis, ETH Zurich (2013). 33

[90] T. Aellen, M. Beck, N. Hoyler, M. Giovannini, J. Faist, E. Gini. *Doping in quantum cascade lasers. I. In AlAs-InGaAs/InP midinfrared devices.* JETP Letters, **100**, 043101 (2006). 34, 35

[91] H. Raether. *Surface Plasmons on Smooth and Rough Surfaces and on Gratings.* Springer (1988). 34

[92] C. Sirtori, C. Gmachl, F. Capasso, D. L. Sivco, A. L. Hutchinson, A. Y. Cho. *Long-wavelength ($\lambda \simeq 811.5 \mu m$) semiconductor lasers with waveguides based on surface plasmons.* Optics Letters, **23**, 1366 (1998). 34, 35, 36, 38

[93] M. Bahriz, G. Lollia, A. N. Baranov, R. Teissier. *High temperature operation of far infrared ($\lambda \simeq 20 \mu m$) InAs/AlSb quantum cascade lasers with dielectric waveguide.* Optics Express, **23**, 1523 (2015). 34

[94] B. S. Williams, S. Kumar, H. Callebaut, Q. Hu, J. L. Reno. *Terahertz quantum-cascade laser at 100 μm using metal waveguide for mode confinement.* Applied Physics Letters, **83**, 2124 (2003). 36, 38

[95] K. Unterrainer, R. Colombelli, C. Gmachl, F. Capasso, H. Y. Hwang, A. M. Sergent, D. L. Sivco, A. Y. Cho. *Quantum cascade lasers with double metal-semiconductor waveguide resonators.* Applied Physics Letters, **80**, 3060 (2002). 36, 37, 38

[96] J. Faist, M. Beck, T. Aellen, E. Gini. *Quantum-cascade lasers based on a bound-to-continuum transition.* Applied Physics Letters, **78**, 147 (2001). 37

[97] D. Hofstetter, M. Beck, T. Aellen, J. Faist. *High-temperature operation of distributed feedback quantum-cascade lasers at 5.3 μm.* Applied Physics Letters, **78**, 396 (2001). 37, 237

[98] J. Faist, D. Hofstetter, M. Beck, T. Aellen, M. Rochat, S. Blaser. *Bound-to-continuum and two-phonon resonance quantum-cascade lasers for high duty cycle, high-temperature operation.* IEEE Journal of Quantum Electronics, **38**, 533 (2002). 37

[99] M. Beck, D. Hofstetter, T. Aellen, J. Faist, U. Oesterle, M. Ilegems, E. Gini, H. Melchior. *Continuous Wave Operation of a Mid-Infrared Semiconductor Laser at Room Temperature.* Science, **295**, 301 (2002). 37

[100] A. Wittmann, T. Gresch, E. Gini, L. Hvozdara, N. Hoyler, M. Giovannini, J. Faist. *High-Performance Bound-to-Continuum Quantum-Cascade Lasers for Broad-Gain Applications.* IEEE Journal of Quantum Electronics, **44**, 36 (2008). 37

[101] C. A. Wang, A. K. Goyal, S. Menzel, D. R. Calawa, M. Spencer, M. K. Connors, D. McNulty, A. Sanchez, G. W. Turner, F. Capasso. *High power (>5W) λ≃9.6μm tapered quantum cascade lasers grown by OMVPE.* Journal of Crystal Growth, **370**, 212 (2013). 37

[102] A. Hugi, G. Villares, S. Blaser, H. C. Liu, J. Faist. *Mid-infrared frequency comb based on a quantum cascade laser.* Nature, **492**, 229 (2012). 37

[103] M. A. Belkin, F. Capasso, A. Belyanin, D. L. Sivco, A. Y. Cho, D. C. Oakley, C. J. Vineis, G. W. Turner. *Terahertz quantum-cascade-laser source based on intracavity difference-frequency generation.* Nature Photonics, **1**, 288 (2007). 37

[104] B. Hinkov, A. Bismuto, Y. Bonetti, M. Beck, S. Blaser, J. Faist. *Singlemode quantum cascade lasers with power dissipation below 1 W.* Electronics Letters, **48**, 3 (2012). 37

[105] W. Schrenk, N. Finger, S. Gianordoli, L. Hvozdara, G. Strasser, E. Gornik. *Surface-emitting distributed feedback quantum-cascade lasers.* Applied Physics Letters, **77**, 2086 (2000). 37

[106] J. P. Commin, K. Kennedy, D. G. Revin, S. Y. Zhang, a. B. Krysa, J. W. Cockburn. *$\lambda = 3.36\mu m$ room temperature InGaAs/AlAs(Sb) quantum cascade lasers with third order distributed feedback grating.* Applied Physics Letters, **97**, 96 (2010). 37

[107] R. Colombelli, K. Srinivasan, M. Troccoli, O. Painter, C. F. Gmachl, D. M. Tennant, A. M. Sergent, D. L. Sivco, A. Y. Cho, F. Capasso. *Quantum Cascade Surface-Emitting Photonic Crystal Laser.* Science, **302**, 1374 (2003). 37

[108] E. Mujagić, S. Schartner, L. K. Hoffmann, W. Schrenk, M. P. Semtsiv, M. Wienold, W. T. Masselink, G. Strasser. *Grating-coupled surface emitting quantum cascade ring lasers.* Applied Physics Letters, **93**, 29 (2008). 37

[109] M. Troccoli, C. Gmachl, F. Capasso, D. L. Sivco, A. Y. Cho. *Mid-infrared ($\lambda \simeq 7.4\mu m$) quantum cascade laser amplifier for high power single-mode emission and improved beam quality.* Applied Physics Letters, **80**, 4103 (2002). 37

[110] A. Hugi, R. Terazzi, Y. Bonetti, A. Wittmann, M. Fischer, M. Beck, J. Faist, E. Gini. *External cavity quantum cascade laser tunable from 7.6 to 11.4 μm.* Applied Physics Letters, **95**, 2007 (2009). 37

[111] P. Fuchs, J. Friedl, S. Höfling, J. Koeth, A. Forchel, L. Worschech, M. Kamp. *Single mode quantum cascade lasers with shallow-etched distributed Bragg reflector.* Optics Express, **20**, 3890 (2012). 37

[112] M. J. Sueess, P. M. Hundt, B. Tuzson, S. Riedi, J. M. Wolf, R. Peretti, M. Beck, H. Looser, L. Emmenegger, J. Faist. *Dual-Section DFB-QCLs for Multi-Species Trace Gas Analysis.* Photonics, **3**, 24 (2016). 37

[113] O. Cathabard, R. Teissier, J. Devenson, J. C. Moreno, A. N. Baranov. *Quantum cascade lasers emitting near 2.6 μm.* Applied Physics Letters, **96**, 141110 (2010). 37

[114] K. Ohtani, M. Beck, M. J. Sueess, J. Faist, A. M. Andrews, T. Zederbauer, H. Detz, W. Schrenk, G. Strasser. *Far-infrared quantum cascade lasers operating in AlAs phonon Reststrahlen band.* submitted (2016). 37

[115] Y. Bai, N. Bandyopadhyay, S. Tsao, S. Slivken, M. Razeghi. *Room temperature quantum cascade lasers with 27% wall plug efficiency.* Applied Physics Letters, **98**, 181102 (2011). 37

[116] M. Rochat, J. Faist, M. Beck, U. Oesterle, M. Ilegems. *Far-infrared (λ=88μm) electroluminescence in a quantum cascade structure.* Applied Physics Letters, **73**, 3724 (1998). 37

[117] B. S. Williams, B. Xu, Q. Hu, M. R. Melloch. *Narrow-linewidth terahertz intersubband emission from three-level systems.* Applied Physics Letters, **75**, 2927 (1999). 37

[118] J. Ulrich, R. Zobl, K. Unterrainer, G. Strasser, E. Gornik. *Magnetic-field-enhanced quantum-cascade emission.* Applied Physics Letters, **76**, 19 (2000). 37, 57, 71

[119] A. Tredicucci, R. udeger Koehler, L. Mahler, H. E. Beere, E. H. Linfield, D. A. Ritchie. *Terahertz quantum cascade lasers - first demonstration and novel concepts.* Semiconductor Science and Technology, **20**, S222 (2005). 37

[120] B. Williams, S. Kumar, Q. Hu, J. Reno. *Operation of terahertz quantum-cascade lasers at 164 K in pulsed mode and at 117 K in continuous-wave mode.* Optics Express, **13**, 3331 (2005). 38, 39, 237

[121] M. A. Belkin, J. A. Fan, S. Hormoz, F. Capasso, S. P. Khanna, M. Lachab, A. G. Davies, E. H. Linfield. *Terahertz quantum cascade lasers with copper metal-metal waveguides operating up to 178 K.* Optics Express, **16**, 3242 (2008). 38, 68, 76

[122] S. Kohen, B. S. Williams, Q. Hu. *Electromagnetic modeling of terahertz quantum cascade laser waveguides and resonators.* Journal of Applied Physics, **97**, 053106 (2005). 39

[123] A. W. M. Lee, Q. Qin, S. Kumar, B. S. Williams, Q. Hu, J. L. Reno. *High-power and high-temperature THz quantum-cascade lasers based on lens-coupled metal-metal waveguides.* Optics Letters, **32**, 2840 (2007). 39

[124] W. Maineult, P. Gellie, A. Andronico, P. Filloux, G. Leo, C. Sirtori, S. Barbieri, E. Peytavit, T. Akalin, J.-F. Lampin, H. E. Beere, D. A. Ritchie. *Metal-metal terahertz quantum cascade laser with micro-transverse-electromagnetic-horn antenna.* Applied Physics Letters, **93**, 183508 (2008). 39

[125] C. Bonzon, I. C. Benea Chelmus, K. Ohtani, M. Geiser, M. Beck, J. Faist. *Integrated patch and slot array antenna for terahertz quantum cascade lasers at 4.7 THz.* Applied Physics Letters, **104**, 161102 (2014). 39

[126] N. Yu, F. Capasso. *Wavefront engineering for mid-infrared and terahertz quantum cascade lasers.* Journal of the Optical Society of America B, **27**, B18 (2010). 39

[127] L. Mahler, R. Köhler, A. Tredicucci, F. Beltram, H. E. Beere, E. H. Linfield, D. A. Ritchie, A. G. Davies. *Single-mode operation of terahertz quantum cascade lasers with distributed feedback resonators.* Applied Physics Letters, **84**, 5446 (2004). 39

[128] S. Kumar, B. S. Williams, Q. Qin, A. W. Lee, Q. Hu, J. L. Reno. *Surface-emitting distributed feedback terahertz quantum-cascade lasers in metal-metal waveguides.* Optics Express, **15**, 113 (2007). 39

[129] M. I. Amanti, M. Fischer, G. Scalari, M. Beck, J. Faist. *Low-divergence single-mode terahertz quantum cascade laser.* Nature Photonics, **3**, 586 (2009). 39

[130] Y. Chassagneux, R. Colombelli, W. Maineult, S. Barbieri, H. E. Beere, D. A. Ritchie, S. P. Khanna, E. H. Linfield, A. G. Davies. *Electrically pumped photonic-crystal terahertz lasers controlled by boundary conditions.* Nature, **457**, 174 (2009). 39

[131] Z. Diao, C. Bonzon, G. Scalari, M. Beck, J. Faist, R. Houdré. *Continuous-wave vertically emitting photonic crystal terahertz laser.* Laser and Photonics Reviews, **7**, 45 (2013). 39

[132] L. Mahler, A. Tredicucci, R. P. Green, F. Beltram, C. Walther, J. Faist, H. E. Beere, D. A. Ritchie. *Vertically emitting microdisk lasers.* Nature Photonics, **3**, 46 (2008). 39

[133] T.-Y. Kao, Q. Hu, J. L. Reno. *Phase-locked arrays of surface-emitting terahertz quantum-cascade lasers.* Applied Physics Letters, **96**, 101106 (2010). 39

[134] C. Sirtori, S. Barbieri, R. Colombelli. *Wave engineering with THz quantum cascade lasers.* Nature Photonics, **7**, 691 (2013). 39, 43

[135] T. Unuma, M. Yoshita, T. Noda, H. Sakaki, H. Akiyama. *Intersubband absorption linewidth in GaAs quantum wells due to scattering by interface roughness, phonons, alloy disorder, and impurities.* Journal of Applied Physics, **93**, 1586 (2003). 39

[136] Y. Chiu, Y. Dikmelik, P. Q. Liu, N. L. Aung, J. B. Khurgin, C. F. Gmachl. *Importance of interface roughness induced intersubband scattering in mid-infrared quantum cascade lasers.* Applied Physics Letters, **101**, 171117 (2012). 39

[137] M. I. Amanti, G. Scalari, R. Terazzi, M. Fischer, M. Beck, J. Faist, A. Rudra, P. Gallo, E. Kapon. *Bound-to-continuum terahertz quantum cascade laser with a single-quantum-well phonon extraction/injection stage.* New Journal of Physics, **11**, 125022 (2009). 40, 41, 73

[138] A. Tredicucci, C. Gmachl, F. Capasso, D. L. Sivco, A. L. Hutchinson, A. Y. Cho. *Long wavelength superlattice quantum cascade lasers at $\lambda \simeq 17\ \mu m$.* Applied Physics Letters, **74**, 638 (1999). 39

[139] B. S. Williams, H. Callebaut, S. Kumar, Q. Hu, J. L. Reno. *3.4-THz quantum cascade laser based on longitudinal-optical-phonon scattering for depopulation.* Applied Physics Letters, **82**, 1015 (2003). 40, 41

[140] G. Scalari, L. Ajili, J. Faist, H. Beere, E. Linfield, D. A. Ritchie, A. G. Davies. *Far-infrared ($\lambda \simeq 87\mu m$) bound-to-continuum quantum-cascade lasers operating up to 90 K.* Applied Physics Letters, **82**, 3165 (2003). 40

[141] G. Scalari, N. Hoyler, M. Giovannini, J. Faist. *Terahertz bound-to-continuum quantum-cascade lasers based on optical-phonon scattering extraction.* Applied Physics Letters, **86**, 181101 (2005). 40, 41

[142] T. Ando, Y. Uemura. *Theory of Quantum Transport in a Two-Dimensional Electron System under Magnetic Fields. I. Characteristics of Level Broadening and Transport under Strong Fields.* Journal of the Physics Society Japan, **36**, 959 (1974). 40, 56

[143] J. Alton, S. Barbieri, J. Fowler, H. Beere, J. Muscat, E. Linfield, D. A. Ritchie, A. G. Davies, R. Köhler, A. Tredicucci. *Magnetic field in-plane quantization and tuning of population inversion in a THz superlattice quantum cascade laser*. Physical Review B, **68**, 081303 (2003). 40, 56

[144] M. Fischer, G. Scalari, K. Celebi, M. I. Amanti, C. Walther, M. Beck, J. Faist. *Scattering processes in terahertz InGaAs/InAlAs quantum cascade lasers*. Applied Physics Letters, **97**, 221114 (2010). 40, 47, 48, 57, 76

[145] S. Kumar, Q. Hu, J. L. Reno. *186 K operation of terahertz quantum-cascade lasers based on a diagonal design*. Applied Physics Letters, **94**, 131105 (2009). 41

[146] C. Deutsch, M. Krall, M. Brandstetter, H. Detz, A. M. Andrews, P. Klang, W. Schrenk, G. Strasser, K. Unterrainer. *High performance InGaAs/GaAsSb terahertz quantum cascade lasers operating up to 142K*. Applied Physics Letters, **101**, 211117 (2012). 41, 45, 48, 76

[147] S. Kumar, C. W. I. Chan, Q. Hu, J. L. Reno. *Two-well terahertz quantum-cascade laser with direct intrawell-phonon depopulation*. Applied Physics Letters, **95**, 141110 (2009). 41

[148] M. A. Belkin, F. Capasso. *New frontiers in quantum cascade lasers : high performance room temperature terahertz sources*. Physica Scripta, **90**, 118002 (2015). 41, 43

[149] L. Li, L. Chen, J. Zhu, J. Freeman, P. Dean, A. Valavanis, A. G. Davies, E. H. Linfield. *Terahertz quantum cascade lasers with >1 W output powers*. Electronics Letters, **50**, 309 (2014). 41

[150] Y.-Y. Li, J.-Q. Liu, T. Wang, F.-Q. Liu, S.-Q. Zhai, J.-C. Zhang, N. Zhuo, L.-J. Wang, S.-M. Liu, Z.-G. Wang. *High-Power and High-Efficiency Operation of Terahertz Quantum Cascade Lasers at 3.3 THz*. Chinese Physics Letters, **32**, 104203 (2015). 41

[151] S. Kumar, C. W. I. Chan, Q. Hu, J. L. Reno. *A 1.8-THz quantum cascade laser operating significantly above the temperature of $\hbar\omega/k_B$*. Nature Physics, **7**, 166 (2011). 42, 77

[152] R. A. Suris. *Prospects for quantum dot structures applications in electronics and optoelectronics*. Future Trends in Microelectronics, pp. 197–208 (1996). 44

[153] N. S. Wingreen, C. A. Stafford. *Quantum-dot cascade laser: Proposal for an ultralow-threshold semiconductor laser*. IEEE Journal of Quantum Electronics, **33**, 1170 (1997). 44

[154] J. Urayama, T. B. Norris, J. Singh, P. Bhattacharya. *Observation of phonon bottleneck in quantum dot electronic relaxation*. Physical Review Letters, **86**, 4930 (2001). 44

[155] E. A. Zibik, T. Grange, B. A. Carpenter, N. E. Porter, R. Ferreira, G. Bastard, D. Stehr, S. Winnerl, M. Helm, H. Y. Liu, M. S. Skolnick, L. R. Wilson. *Long lifetimes of quantum-dot intersublevel transitions in the terahertz range.* Nature Materials, **8**, 803 (2009). 44

[156] C. F. Hsu, J. S. O, P. Zory, D. Botez. *Intersubband quantum-box semiconductor lasers.* IEEE Journal on Selected Topics in Quantum Electronics, **6**, 491 (2000). 44

[157] N. Vukmirovic, D. Indjin, Z. Ikonic, P. Harrison. *Electron Transport and Terahertz Gain in Quantum-Dot Cascades.* IEEE Photonics Technology Letters, **20**, 129 (2008). 44

[158] V. M. Apalkov, T. Chakraborty. *Luminescence spectra of a quantum-dot cascade laser.* Applied Physics Letters, **78**, 1820 (2001). 44

[159] D. Wasserman, S. A. Lyon. *Midinfrared luminescence from InAs quantum dots in unipolar devices.* Applied Physics Letters, **81**, 2848 (2002). 44

[160] S. Anders, L. Rebohle, F. F. Schrey, W. Schrenk, K. Unterrainer, G. Strasser. *Electroluminescence of a quantum dot cascade structure.* Applied Physics Letters, **82**, 3862 (2003). 44

[161] N. Ulbrich, J. Bauer, G. Scarpa, R. Boy, D. Schuh, G. Abstreiter, S. Schmult, W. Wegscheider. *Midinfrared intraband electroluminescence from AlInAs quantum dots.* Applied Physics Letters, **83**, 1530 (2003). 44

[162] V. Liverini, L. Nevou, F. Castellano, A. Bismuto, M. Beck, F. Gramm, J. Faist. *Room-temperature transverse-electric polarized intersubband electroluminescence from InAs/AlInAs quantum dashes.* Applied Physics Letters, **101**, 261113 (2012). 44

[163] G. L. Paravicini-Bagliani, V. Liverini, F. Valmorra, G. Scalari, F. Gramm, J. Faist. *Enhanced current injection from a quantum well to a quantum dash in magnetic field.* New Journal of Physics, **16**, 083029 (2014). 44

[164] N. Zhuo, F. Liu, J. Zhang, L. Wang, J. Liu, S. Zhai, Z. Wang. *Quantum dot cascade laser.* Nanoscale Research Letters, **9**, 144 (2014). 45

[165] A. Tredicucci. *Quantum dots: Long life in zero dimensions.* Nature Materials, **8**, 775 (2009). 45

[166] M. I. Amanti, A. Bismuto, M. Beck, L. Isa, K. Kumar, E. Reimhult, J. Faist. *Electrically driven nanopillars for THz quantum cascade lasers.* Optics Express, **21**, 10917 (2013). 45

[167] T. Grange. *Nanowire terahertz quantum cascade lasers.* Applied Physics Letters, **105**, 141105 (2014). 45

[168] A. Blank, S. Feng. *Suppression of intersubband nonradiative transitions by a magnetic field in quantum well laser devices.* Journal of Applied Physics, **74**, 4795 (1993). 45, 54

[169] C. Ndebeka-Bandou, M. Rösch, K. Ohtani, M. Beck, J. Faist. *Negative free carrier absorption in terahertz quantum cascade lasers.* Applied Physics Letters, **108**, 091102 (2016). 45

[170] C. Sirtori, P. Kruck, S. Barbieri, P. Collot, J. Nagle, M. Beck, J. Faist, U. Oesterle. *$GaAs/Al_xGa_{1-x}As$ quantum cascade lasers.* Applied Physics Letters, **73**, 3486 (1998). 45

[171] E. Benveniste, A. Vasanelli, A. Delteil, J. Devenson, R. Teissier, A. Baranov, A. M. Andrews, G. Strasser, I. Sagnes, C. Sirtori. *Influence of the material parameters on quantum cascade devices.* Applied Physics Letters, **93**, 131108 (2008). 45

[172] L. Ajili, G. Scalari, M. Giovannini, N. Hoyler, J. Faist. *Doping in quantum cascade lasers. II. $GaAs/Al_{0.15}Ga_{0.85}As$ terahertz devices.* Journal of Applied Physics, **100**, 043102 (2006). 45, 47

[173] K. Ohtani, M. Beck, G. Scalari, J. Faist. *Terahertz quantum cascade lasers based on quaternary AlInGaAs barriers.* Applied Physics Letters, **103**, 041103 (2013). 45, 48, 49, 50, 55, 62, 65, 68, 76

[174] M. Brandstetter, M. A. Kainz, T. Zederbauer, M. Krall, S. Schönhuber, H. Detz, W. Schrenk, A. M. Andrews, G. Strasser, K. Unterrainer. *InAs based terahertz quantum cascade lasers.* Applied Physics Letters, **108**, 011109 (2016). 45, 48

[175] H. Cotal, C. Fetzer, J. Boisvert, G. Kinsey, R. King, P. Hebert, H. Yoon, N. Karam. *III-V multijunction solar cells for concentrating photovoltaics.* Energy Environ. Sci., **2**, 174 (2009). 46

[176] M. Nobile, P. Klang, E. Mujagic, H. Detz, a.M. Andrews, W. Schrenk, G. Strasser. *Quantum cascade laser utilising aluminium-free material system: InGaAs/GaAsSb lattice-matched to InP.* Electronics Letters, **45**, 1031 (2009). 47

[177] C. Deutsch, H. Detz, T. Zederbauer, A. M. Andrews, P. Klang, T. Kubis, G. Klimeck, M. E. Schuster, W. Schrenk, G. Strasser, K. Unterrainer. *Probing scattering mechanisms with symmetric quantum cascade lasers.* Optics Express, **21**, 7209 (2013). 48

[178] D. Olego, T. Y. Chang, E. Silberg, E. Caridi, A. Pinczuk. *Compositional dependence of band-gap energy and conduction-band effective mass of $In_{1-x-y}Ga_xAl_yAs$ lattice matched to InP.* Applied Physics Letters, **41**, 476 (1982). 48

[179] K. Alavi, H. Temkin, W. R. Wagner, A. Y. Cho. *Optically pumped 1.55-μm double heterostructure $Ga_xAl_yIn_{1-x-y}As/Al_uIn_{1-u}As$ lasers grown by molecular beam epitaxy.* Applied Physics Letters, **42**, 254 (1983). 48

[180] F. Castellano, K. Ohtani, L. Nevou, J. Faist. *Characterization of thin AlSb/AlAs barriers on InAs by mid-infrared intersubband absorption measurements.* Applied Physics Letters, **102**, 032103 (2013). 48

[181] V. D. Jovanovic, D. Indjin, Z. Ikonic, P. Harrison. *Simulation and design of GaN/AlGaN far-infrared ($\lambda \simeq 34$ μm) quantum-cascade laser.* Applied Physics Letters, **84**, 2995 (2004). 49

[182] G. Sun, R. A. Soref, J. B. Khurgin. *Active region design of a terahertz $GaN/Al_{0.15}Ga_{0.85}N$ quantum cascade laser.* Superlattices and Microstructures, **37**, 107 (2005). 49

[183] E. Bellotti, K. Driscoll, T. D. Moustakas, R. Paiella. *Monte Carlo study of GaN versus GaAs terahertz quantum cascade structures.* Applied Physics Letters, **92**, 101112 (2008). 49

[184] C. Edmunds, J. Shao, M. Shirazi-HD, M. J. Manfra, O. Malis. *Terahertz intersubband absorption in non-polar m-plane AlGaN/GaN quantum wells.* Applied Physics Letters, **105**, 021109 (2014). 49

[185] M. Beeler, C. Bougerol, E. Bellet-Amalric, E. Monroy. *Pseudo-square AlGaN/GaN quantum wells for terahertz absorption.* Applied Physics Letters, **105**, 131106 (2014). 49

[186] C. B. Lim, A. Ajay, C. Bougerol, B. Haas, J. Schörmann, M. Beeler, J. Lähnemann, M. Eickhoff, E. Monroy. *Nonpolar m-plane GaN/AlGaN heterostructures with intersubband transitions in the 5-10 THz band.* Nanotechnology, **26**, 435201 (2015). 49

[187] Y. Arakawa. *Multidimensional quantum well laser and temperature dependence of its threshold current.* Applied Physics Letters, **40**, 939 (1982). 54

[188] U. Bockelmann, G. Bastard. *Phonon scattering and energy relaxation in two-, one-, and zero-dimensional electron gases.* Physical Review B, **42**, 8947 (1990). 54

[189] B. N. Murdin, A. R. Hollingworth, M. Kamal-Saadi, R. T. Kotitschke, C. M. Ciesla, C. R. Pidgeon, P. C. Findlay, H. P. M. Pellemans, C. J. G. M. Langerak, A. C. Rowe, R. A. Stradling, E. Gornik. *Suppression of LO phonon scattering in Landau quantized quantum dots.* Physical Review B, **59**, 7817 (1999). 54

[190] W.-P. Hong, G. I. Ng, P. K. Bhattacharya, D. Pavlidis, S. Willing, B. Das. *Low- and high-field transport properties of pseudomorphic $In_xGa_{1-x}As/In_{0.52}Al_{0.48}As_{(0.53 \leq x \leq 0.65)}$ modulation-doped heterostructures.* Journal of Applied Physics, **64**, 1945 (1988). 54

[191] U. Ekenberg. *Nonparabolicity effects in a quantum well: Sublevel shift, parallel mass, and Landau levels.* Physical Review B, **40**, 7714 (1989). 55

[192] C. Sirtori, F. Capasso, J. Faist, S. Scandolo. *Nonparabolicity and a sum rule associated with bound-to-bound and bound-to-continuum intersubband transitions in quantum wells.* Physical Review B, **50**, 8663 (1994). 55

[193] H. Kosaka, A. A. Kiselev, F. A. Baron, K. W. Kim, E. Yablonovitch. *Electron g-factor Engineering in III-V Semiconductors for Quantum Communications.* **37**, 464 (2001). 55

[194] B. Kowalski, P. Omling, B. K. Meyer, D. M. Hofmann, V. Harle, F. Scholz, P. Sobkowicz. *Optically detected spin resonance of conduction band electrons in InGaAs/InP quantum wells.* Semiconductor Science and Technology, **11**, 1416 (1996). 55

[195] N. Regnault, R. Ferreira, G. Bastard. *Broadening effects due to alloy scattering in a quantum cascade laser.* Physical Review B, **76**, 165121 (2007). 56

[196] A. Wade, G. Fedorov, D. Smirnov, S. Kumar, B. Williams, Q. Hu, J. L. Reno. *Magnetic-field-assisted terahertz quantum cascade laser operating up to 225 K.* Nature Photonics, **3**, 41 (2009). 56, 58, 76, 77

[197] S. Blaser, M. Rochat, M. Beck, D. Hofstetter, J. Faist. *Terahertz intersubband emission in strong magnetic fields.* Applied Physics Letters, **81**, 67 (2002). 56, 57

[198] C. Becker, C. Sirtori, O. Drachenko, V. Rylkov, D. Smirnov, J. Leotin. *GaAs quantum box cascade lasers.* Applied Physics Letters, **81**, 2941 (2002). 56

[199] D. Smirnov, O. Drachenko, J. Leotin, H. Page, C. Becker, C. Sirtori, V. Apalkov, T. Chakraborty. *Intersubband magnetophonon resonances in quantum cascade structures.* Physical Review B, **66**, 125317 (2002). 56

[200] A. Leuliet, A. Vasanelli, A. Wade, G. Fedorov, D. Smirnov, G. Bastard, C. Sirtori. *Electron scattering spectroscopy by a high magnetic field in quantum cascade lasers.* Physical Review B, **73**, 085311 (2006). 56

[201] N. Pere-Laperne, L. A. de Vaulchier, Y. Guldner, G. Bastard, G. Scalari, M. Giovannini, J. Faist, A. Vasanelli, S. Dhillon, C. Sirtori. *Inter-Landau level scattering and LO-phonon emission in terahertz quantum cascade laser.* Applied Physics Letters, **91**, 062102 (2007). 56, 65

[202] M. Raikh, T. Shahbazyan. *Magnetointersubband oscillations of conductivity in a two-dimensional electronic system.* Physical Review B, **49**, 5531 (1994). 57

[203] S. Maero, L.-A. de Vaulchier, Y. Guldner, C. Deutsch, M. Krall, T. Zederbauer, G. Strasser, K. Unterrainer. *Magnetic-field assisted performance of InGaAs/GaAsSb terahertz quantum cascade lasers.* Applied Physics Letters, **103**, 051116 (2013). 57, 58, 65, 76

[204] K. Kempa, Y. Zhou, J. Engelbrecht, P. Bakshi, H. Ha, J. Moser, M. Naughton, J. Ulrich, G. Strasser, E. Gornik, K. Unterrainer. *Intersubband Transport in Quantum Wells in Strong Magnetic Fields Mediated by Single- and Two-Electron Scattering.* Physical Review Letters, **88**, 226803 (2002). 57, 71

[205] G. Scalari, S. Blaser, J. Faist, H. Beere, E. Linfield, D. A. Ritchie, A. G. Davies. *Terahertz Emission from Quantum Cascade Lasers in the Quantum Hall Regime: Evidence for Many Body Resonances and Localization Effects.* Physical Review Letters, **93**, 237403 (2004). 57, 58

[206] M. Helm. *The basic physics of intersubband transitions.* In F. Capasso, H. C. Liu, editors, *Intersubband Transitions in Quantum Wells: Physics and Device Applications I*, pp. 1–99. Academic Press, in edition (2000). 57, 71, 73

[207] G. Scalari, C. Walther, L. Sirigu, M. Sadowski, H. Beere, D. A. Ritchie, N. Hoyler, M. Giovannini, J. Faist. *Strong confinement in terahertz intersubband lasers by intense magnetic fields.* Physical Review B, **76**, 115305 (2007). 58, 73, 77

[208] G. Scalari, D. Turcinkova, J. Lloyd-Hughes, M. I. Amanti, M. Fischer, M. Beck, J. Faist. *Magnetically assisted quantum cascade laser emitting from 740 GHz to 1.4 THz.* Applied Physics Letters, **97**, 081110 (2010). 58, 70

[209] C. Sirtori. *Breaking energy bands.* Nature Photonics, **3**, 13 (2009). 58

[210] A. Benz, G. Fasching, A. M. Andrews, M. Martl, K. Unterrainer, T. Roch, W. Schrenk, S. Golka, G. Strasser. *Influence of doping on the performance of terahertz quantum-cascade lasers.* Applied Physics Letters, **90**, 101107 (2007). 68

[211] Y. Chassagneux, Q. J. Wang, S. P. Khanna, E. Strupiechonski, J. R. Coudevylle, E. H. Linfield, A. G. Davies, F. Capasso, M. A. Belkin, R. Colombelli. *Limiting factors to the temperature performance of THz quantum cascade lasers based on the resonant-phonon depopulation scheme.* IEEE Transactions on Terahertz Science and Technology, **2**, 83 (2012). 68, 77

[212] G. Scalari. *Magneto-spectroscopy and development of terahertz quantum cascade lasers.* Ph.D. thesis, University of Neuchatel (2005). 71

[213] M. V. Kisin, M. A. Stroscio, G. Belenky, S. Luryi. *Electron-plasmon relaxation in quantum wells with inverted subband occupation.* Applied Physics Letters, **73**, 2075 (1998). 71

[214] F. Valmorra, G. Scalari, K. Ohtani, M. Beck, J. Faist. *InGaAs/AlInGaAs THz quantum cascade lasers operating up to 195 K in strong magnetic field.* New Journal of Physics, **17**, 023050 (2015). 76

[215] E. Strupiechonski, G. Xu, M. Brekenfeld, Y. Todorov, N. Isac, A. M. Andrews, P. Klang, C. Sirtori, G. Strasser, A. Degiron, R. Colombelli. *Sub-diffraction-limit semiconductor resonators operating on the fundamental magnetic resonance.* Applied Physics Letters, **100**, 131113 (2012). 82

[216] S. Bagiante, F. Enderli, J. Fabiańska, H. Sigg, T. Feurer. *Giant Electric Field Enhancement in Split Ring Resonators Featuring Nanometer-Sized Gaps*. Scientific Reports, **5**, 8051 (2015). 82

[217] M. A. Seo, H. R. Park, S. M. Koo, D. J. Park, J. H. Kang, O. K. Suwal, S. S. Choi, P. C. M. Planken, G. S. Park, N. K. Park, Q. H. Park, D. S. Kim. *Terahertz field enhancement by a metallic nano slit operating beyond the skin-depth limit*. Nature Photonics, **3**, 152 (2009). 82

[218] H. Merbold, A. Bitzer, T. Feurer. *Second harmonic generation based on strong field enhancement in nanostructured THz materials*. Optics Express, **19**, 7262 (2011). 82

[219] Q.-H. Park. *Optical antennas and plasmonics*. Contemporary Physics, **50**, 407 (2009). 82

[220] W. J. Padilla, M. T. Aronsson, C. Highstrete, M. Lee, A. J. Taylor, R. D. Averitt. *Electrically resonant terahertz metamaterials: Theoretical and experimental investigations*. Physical Review B, **75**, 041102 (2007). 82

[221] W. Withayachumnankul, D. Abbott. *Metamaterials in the terahertz regime*. IEEE Photonics Journal, **1**, 99 (2009). 83

[222] W. J. Padilla, A. J. Taylor, R. D. Averitt. *Dynamical Electric and Magnetic Metamaterial Response at Terahertz Frequencies*. Physical Review Letters, **96**, 107401 (2006). 83

[223] C. Walther, G. Scalari, M. I. Amanti, M. Beck, J. Faist. *Microcavity Laser Oscillating in a Circuit-Based Resonator*. Science, **327**, 1495 (2010). 85

[224] J. D. Jackson. *Classical Electrodynamics*. Academic Press (1998). 86, 114, 241

[225] H.-T. Chen, J. F. O'Hara, A. J. Taylor, R. D. Averitt, C. Highstrete, M. Lee, W. J. Padilla. *Complementary planar terahertz metamaterials*. Optics Express, **15**, 1084 (2007). 87

[226] H.-T. Chen, J. F. O. Hara, A. K. Azad, A. J. Taylor. *Manipulation of terahertz radiation using metamaterials*. Laser and Photonics Reviews, **5**, 513 (2011). 87

[227] J. D. Baena, J. Bonache, F. Martín, R. M. Sillero, F. Falcone, T. Lopetegi, M. A. G. Laso, J. G. García, I. Gil, M. F. Portillo, M. Sorolla, S. Member. *Equivalent-Circuit Models for Split-Ring Resonators and Complementary Split-Ring Resonators Coupled to Planar Transmission Lines*. IEEE Transactions on Microwave Theory and Techniques, **53**, 1451 (2005). 91

[228] K. Fu, R. Zannoni, C. Chan, S. Adams, J. Nicholson, E. Polizzi, S. Yngvesson. *Terahertz detection in single wall carbon nanotubes*. Applied Physics Letters, **92**, 33105 (2008). 91

[229] J. Lloyd-Hughes. *Terahertz time-domain spectroscopy of carrier trapping in semiconductors*. Ph.D. thesis, University of Oxford (2006). 92

[230] G. Jnawali, Y. Rao, H. Yan, T. Heinz. *Observation of a Transient Decrease in Terahertz Conductivity of Single-Layer Graphene Induced by Ultrafast Optical Excitation*. Nano Letters, **13**, 524 (2013). 92, 126

[231] J. Lloyd-Hughes, T.-I. Jeon. *A review of the terahertz conductivity of bulk and nanomaterials*. Journal of Infrared, Millimeter, and Terahertz Waves, **33**, 871 (2012). 92

[232] P. C. M. Planken, H.-K. Nienhuys, H. J. Bakker, T. Wenckebach. *Measurement and calculation of the orientation dependence of terahertz pulse detection in ZnTe*. Journal of the Optical Society of America B, **18**, 313 (2001). 96

[233] T. W. Ebbesen, H. J. Lezec, H. F. Ghaemi, T. Thio. *Extraordinary optical transmission through sub-wavelength hole arrays*. Nature, **391**, 667 (1998). 99

[234] H. A. Bethe. *Theory of Diffraction by Small Holes*. Physical Review, **66**, 163 (1944). 99, 115

[235] C. Genet, T. W. Ebbesen. *Light in tiny holes*. Nature, **445**, 39 (2007). 99

[236] L. Martin-Moreno, F. J. Garcia-Vidal, H. J. Lezec, K. M. Pellerin, T. Thio, J. B. Pendry, T. W. Ebbesen. *Theory of Extraordinary Optical Transmission through Subwavelength Hole Arrays*. Physical Review Letters, **86**, 1114 (2001). 99

[237] F. J. Garcia-Vidal, L. Martin-Moreno, T. W. Ebbesen, L. Kuipers. *Light passing through subwavelength apertures*. Reviews of Modern Physics, **82**, 729 (2010). 99, 100

[238] F. van Beijnum, C. Retif, C. B. Smiet, H. Liu, P. Lalanne, M. P. van Exter. *Quasi-cylindrical wave contribution in experiments on extraordinary optical transmission*. Nature, **492**, 411 (2012). 99

[239] H. T. Hui. *A New Definition of Mutual Impedance for Application in Dipole Receiving Antenna Arrays*. IEEE Antennas and Wireless Propagation Letters, **3**, 364 (2004). 101

[240] H. E. King. *Mutual impedance of Unequal Length antennas in echelon*. IRE Transactions on Antennas and Propagation, p. 306 (1957). 101

[241] A. G. Derneryd. *A Theoretical Investigation of the Rectangular Microstrip Antenna Element*. IEEE Transactions on Antennas and Propagation, **AP-26**, 532 (1978). 101

[242] C. A. Balanis. *Antenna Theory: Analysis and Design*. John Wiley & Sons, 3rd edition (2005). 101, 112

[243] Y. Mushiake. *Self-Complementary Antennas*. Springer London, London (1996). ISBN 978-1-4471-1255-6. 113, 114

[244] V. H. Rumsey. *Frequency Independent Antennas*. Academic Press (1966). 113

[245] G. A. Deschamps. *Impedance Properties of Complementary Multiterminal Planar Structures.* IRE Transactions on Antennas and Propagation, p. S371 (1959). 113

[246] H. G. Booker. *Slot aerials and their relation to complementary wire aerials (Babinet's principle).* J. Inst. Electr. Eng., **93**, 620 (1946). 113

[247] D. Zwanziger. *Quantum Field Theory of Particles with Both Electric and Magnetic Charges.* Physical Review, **176**, 1489 (1968). 114, 241

[248] H. J. Visser. *Antenna Theory and Applications* (2012). 115

[249] A. Chlavin. *A New Antenna Feed Having Equal E- and H-Plane Patterns.* IRE Transactions on Antennas and Propagation, p. 113 (1954). 115

[250] R. P. King, G. H. Owyang. *The Slot Antenna with Coupled Dipoles.* IRE Transactions on Antennas and Propagation, p. 136 (1960). 115

[251] K. Schroeder, K. Soo Hoo. *Electrically small complementary pair (ESCP) with interelement coupling.* IEEE Transactions on Antennas and Propagation, **24**, 411 (1976). 115

[252] B. Halpern, P. Mayes. *The monopole slot as a two-port diversity antenna for UHF land-mobile radio systems.* IEEE Transactions on Vehicular Technology, **33**, 76 (1984). 115

[253] K.-M. Luk, H. Wong. *A New Wideband Unidirectional Antenna Element.* International journal of microwave and optical technology, **1**, 35 (2006). 115, 116

[254] S.-W. Qu, J.-L. Li, Q. Xue, C. H. Chan. *Novel unidirectional slot antenna with a vertical wall.* Progress In Electromagnetics Research, **PIER 84**, 239 (2008). 115

[255] H. Wong, K.-M. Mak, K.-M. Luk. *Wideband Shorted Bowtie Patch Antenna With Electric Dipole.* IEEE Transactions on Antennas and Propagation, **56**, 2098 (2008). 115, 116

[256] A. W. Love. *Some highlights in reflector antenna development.* Radio Science, **11**, 671 (1976). 117

[257] P. Jin, R. W. Ziolkowski. *Metamaterial-Inspired, Electrically Small Huygens Sources.* IEEE Antennas and Wireless Propagation Letters, **9**, 501 (2010). 117

[258] A. Epstein, G. V. Eleftheriades. *Huygens' metasurfaces via the equivalence principle: design and applications.* Journal of the Optical Society of America B, **33**, A31 (2016). 117

[259] M. Parzefall, P. Bharadwaj, A. Jain, T. Taniguchi, K. Watanabe, L. Novotny. *Antenna-coupled photon emission from hexagonal boron nitride tunnel junctions.* Nature Nanotechnology, **10**, 1058 (2015). 117

[260] T. Coenen, A. Polman. *Optical Properties of Single Plasmonic Holes Probed with Local Electron Beam Excitation.* ACS Nano, **8**, 7350 (2014). 117

[261] H. W. Kihm, J. Kim, S. Koo, J. Ahn, K. Ahn, K. Lee, N. Park, D.-S. Kim. *Optical magnetic field mapping using a subwavelength aperture.* Optics Express, **21**, 5625 (2013). 117

[262] H. W. Kihm, S. M. Koo, Q. H. Kim, J. E. Kihm, W. S. Bak, S. H. Eah, C. Lienau, H. Kim, P. Nordlander, N. J. Halas, N. K. Park, D. Kim. *Bethe-hole polarization analyser for the magnetic vector of light.* Nature Communications, **2**, 451 (2011). 117

[263] D. Lee, D.-S. Kim. *Light scattering of rectangular slot antennas : parallel magnetic vector vs perpendicular electric vector.* Scientific Reports, **6**, 18935 (2016). 117

[264] F. Falcone, T. Lopetegi, M. A. G. Laso, J. D. Baena, J. Bonache, M. Beruete, R. Marques, F. Martin, M. Sorolla. *Babinet Principle Applied to the Design of Metasurfaces and Metamaterials.* Physical Review Letters, **93**, 197401 (2004). 117

[265] M. Decker, I. Staude, M. Falkner, J. Dominguez, D. N. Neshev, I. Brener, T. Pertsch, Y. S. Kivshar. *High-Efficiency Dielectric Huygens' Surfaces.* Advanced Optical Materials, **3**, 813 (2015). 117

[266] R. Alaee, M. Albooyeh, A. Rahimzadegan, M. S. Mirmoosa, Y. S. Kivshar, C. Rockstuhl. *All-dielectric reciprocal bianisotropic nanoparticles.* Physical Review B, **92**, 245130 (2015). 117

[267] N. Linh. *The two-dimensional electron gas and its technical applications.* Festkorperprobleme, **XXIII**, 2127 (1983). 121

[268] R. W. van der Heijden, H. M. Gijsman, F. M. Peeters. *The high-field Hall effect and magnetoresistance of electrons on helium.* Journal of Physics C: Solid State Physics, **21**, L1165 (1988). 121

[269] K. S. Novoselov, A. K. Geim, S. V. Morozov, D. Jiang, Y. Zhang, S. V. Dubonos, I. V. Grigorieva, A. A. Firsov. *Electric field effect in atomically thin carbon films.* Science, **306**, 666 (2004). 121

[270] Q. H. Wang, K. Kalantar-Zadeh, A. Kis, J. N. Coleman, M. S. Strano. *Electronics and optoelectronics of two-dimensional transition metal dichalcogenides.* Nature Nanotechnology, **7**, 699 (2012). 121

[271] A. N. Grigorenko, M. Polini, K. S. Novoselov. *Graphene plasmonics.* Nature Photonics, **6**, 749 (2012). 121, 129

[272] F. Bonaccorso, Z. Sun, T. Hasan, A. C. Ferrari. *Graphene photonics and optoelectronics.* Nature Photonics, **4**, 611 (2010). 121, 129

[273] K. Bolotin, K. Sikes, Z. Jiang, M. Klima, G. Fudenberg, J. Hone, P. Kim, H. Stormer. *Ultrahigh electron mobility in suspended graphene.* Solid State Communications, **146**, 351 (2008). 121

[274] P. Neugebauer, M. Orlita, C. Faugeras, A.-L. Barra, M. Potemski. *How Perfect Can Graphene Be?* Physical Review Letters, **103**, 136403 (2009). 121, 127, 140, 221, 227

[275] Y. Zhang, Y.-W. Tan, H. L. Stormer, P. Kim. *Experimental observation of the quantum Hall effect and Berry's phase in graphene.* Nature, **438**, 201 (2005). 122, 221

[276] K. S. Novoselov, A. K. Geim, S. V. Morozov, D. Jiang, M. I. Katsnelson, I. V. Grigorieva, S. V. Dubonos, A. A. Firsov. *Two-dimensional gas of massless Dirac fermions in graphene.* Nature, **438**, 197 (2005). 122, 221

[277] G. Ruess, F. Vogt. *Hoechstlamellarer Kohlenstoff aus Graphitoxyhydroxyd.* Monatshefte fuer Chemie und verwandte Teile anderer Wissenschaften, **78**, 222 (1948). 122

[278] H. P. Boehm, A. Clauss, G. O. Fischer, U. Hofmann. *Das Adsorptionsverhalten sehr duenner Kohlenstoff-Folien.* Zeitschrift für anorganische und allgemeine Chemie, **316**, 119 (1962). 122

[279] P. Wallace. *The band theory of graphite.* Physical Review, **71**, 622 (1947). 122

[280] A. Rycerz, J. Tworzydło, C. W. J. Beenakker. *Valley filter and valley valve in graphene.* Nature Physics, **3**, 172 (2007). 122

[281] A. F. Young, C. R. Dean, L. Wang, H. Ren, P. Cadden-Zimansky, K. Watanabe, T. Taniguchi, J. Hone, K. L. Shepard, P. Kim. *Spin and valley quantum Hall ferromagnetism in graphene.* Nature Physics, **8**, 550 (2012). 122

[282] D. P. di Vincenzo, E. J. Mele. *Self-consistent effective-mass theory for interlayer screening in graphite intercalation compounds.* Physical Review B, **29**, 1685 (1984). 122

[283] A. H. Castro Neto, N. M. R. Peres, K. S. Novoselov, A. K. Geim. *The electronic properties of graphene.* Reviews of Modern Physics, **81**, 109 (2009). 123, 126

[284] S. Das Sarma, S. Adam, E. H. Hwang, E. Rossi. *Electronic transport in two-dimensional graphene.* Reviews of Modern Physics, **83**, 407 (2011). 123

[285] K. S. Novoselov, A. K. Geim, S. V. Morozov, D. Jiang, M. I. Katsnelson, I. V. Grigorieva, S. V. Dubonos, A. A. Firsov. *Two-dimensional gas of massless Dirac fermions in graphene.* Nature, **438**, 197 (2005). 123, 127

[286] Y.-W. Son, M. L. Cohen, S. G. Louie. *Energy Gaps in Graphene Nanoribbons.* Physical Review Letters, **97**, 216803 (2006). 124

[287] M. Y. Han, B. Özyilmaz, Y. Zhang, P. Kim. *Energy band-gap engineering of graphene nanoribbons.* Physical Review Letters, **98**, 206805 (2007). 124

[288] M.-W. Lin, C. Ling, L. A. Agapito, N. Kioussis, Y. Zhang, M. M.-C. Cheng, W. L. Wang, E. Kaxiras, Z. Zhou. *Approaching the intrinsic band gap in suspended high-mobility graphene nanoribbons.* Physical Review B, **84**, 125411 (2011). 124

[289] E. Castro, K. Novoselov, S. Morozov, N. Peres, J. dos Santos, J. Nilsson, F. Guinea, A. K. Geim, a. Neto. *Biased Bilayer Graphene: Semiconductor with a Gap Tunable by the Electric Field Effect.* Physical Review Letters, **99**, 8 (2007). 124

[290] Y. Zhang, T.-T. Tang, C. Girit, Z. Hao, M. C. Martin, A. Zettl, M. F. Crommie, Y. R. Shen, F. Wang. *Direct observation of a widely tunable bandgap in bilayer graphene.* Nature, **459**, 820 (2009). 124

[291] B. Hunt, T. Taniguchi, P. Moon, M. Koshino, R. C. Ashoori. *Massive Dirac Fermions and Hofstadter Butterfly in a van der Waals Heterostructure.* Science, **340**, 1427 (2013). 124

[292] C. Stampfer, J. Güttinger, S. Hellmüller, F. Molitor, K. Ensslin, T. Ihn. *Energy Gaps in Etched Graphene Nanoribbons.* Physical Review Letters, **102**, 056403 (2009). 124

[293] V. P. Gusynin, S. G. Sharapov, J. P. Carbotte. *Magneto-optical conductivity in graphene.* Journal of Physics: Condensed Matter, **19**, 026222 (2007). 124, 125

[294] G. W. Hanson. *Dyadic Green's functions and guided surface waves for a surface conductivity model of graphene.* Journal of Applied Physics, **103**, 064302 (2008). 124, 125

[295] R. R. Nair, A. N. Grigorenko, P. Blake, K. S. Novoselov, T. J. Booth, N. M. R. Peres, T. Stauber, A. K. Geim. *Fine structure constant defines visual transparency of graphene.* Science, **320**, 1308 (2008). 125

[296] L. Ren, Q. Zhang, J. Yao, Z. Sun, R. Kaneko, Z. Yan, S. Nanot, Z. Jin, I. Kawayama, M. Tonouchi, J. M. Tour, J. Kono. *Terahertz and Infrared Spectroscopy of Gated Large-Area Graphene.* Nano Letters, **12**, 3711 (2012). 125

[297] H. Fang, H. A. Bechtel, E. Plis, M. C. Martin, S. Krishna, E. Yablonovitch, A. Javey. *Quantum of optical absorption in two-dimensional semiconductors.* Proceedings of the National Academy of Sciences, **110**, 11688 (2013). 125

[298] A. Witowski, M. Orlita, R. Stpniewski, A. Wysmolek, J. Baranowski, W. Strupiński, C. Faugeras, G. Martinez, M. Potemski, A. Wysmołek, J. Baranowski, W. Strupiński, C. Faugeras, G. Martinez, M. Potemski. *Quasiclassical cyclotron resonance of Dirac fermions in highly doped graphene.* Physical Review B, **82**, 165305 (2010). 126

[299] I. Crassee, M. Orlita, M. Potemski, A. L. Walter, M. Ostler, T. Seyller, I. Gaponenko, J. Chen, A. B. Kuzmenko. *Intrinsic terahertz plasmons and magnetoplasmons in large scale monolayer graphene.* Nano Letters, **12**, 2470 (2012). 126, 134, 229

[300] J. Horng, C.-F. Chen, B. Geng, C. Girit, Y. Zhang, Z. Hao, H. A. Bechtel, M. Martin, A. Zettl, M. Crommie, Y. Shen, F. Wang. *Drude conductivity of Dirac fermions in graphene.* Physical Review B, **83**, 165113 (2011). 126

[301] Y. Zheng, T. Ando. *Hall conductivity of a two-dimensional graphite system.* Physical Review B, **65**, 245420 (2002). 126

[302] Y. Yao, M. Kats, P. Genevet, N. Yu, Y. Song, J. Kong, F. Capasso. *Broad electrical tuning of graphene-loaded plasmonic antennas.* Nano Letters, **13**, 1257 (2013). 126, 128

[303] M. Orlita, M. Potemski. *Dirac electronic states in graphene systems: optical spectroscopy studies.* Semiconductor Science and Technology, **25**, 063001 (2010). 126

[304] J. G. Analytis, R. D. McDonald, S. C. Riggs, J. H. Chu, G. S. Boebinger, I. R. Fisher. *Two-dimensional surface state in the quantum limit of a topological insulator.* Nature Physics, **6**, 960 (2010). 126

[305] A. A. Schafgans, K. W. Post, A. A. Taskin, Y. Ando, X.-L. Qi, B. C. Chapler, D. N. Basov. *Landau level spectroscopy of surface states in the topological insulator* $Bi_{0.91}Sb_{0.09}$ *via magneto-optics.* Physical Review B, **85**, 195440 (2012). 126

[306] X. Yao, A. Belyanin. *Giant Optical Nonlinearity of Graphene in a Strong Magnetic Field.* Physical Review Letters, **108**, 255503 (2012). 128, 129

[307] M. L. Sadowski, G. Martinez, M. Potemski. *Landau Level Spectroscopy of Ultrathin Graphite Layers.* Physical Review Letters, **97**, 1 (2006). 128

[308] M. Schultz, U. Merkt, A. Sonntag, U. Rössler, R. Winkler, T. Colin, P. Helgesen, T. Skauli, S. Løvold. *Crossing of conduction- and valence-subband Landau levels in an inverted HgTe/CdTe quantum well.* Physical Review B, **57**, 14772 (1998). 128

[309] Z. Jiang, E. A. Henriksen, L. C. Tung, Y. J. Wang, M. E. Schwartz, M. Y. Han, P. Kim, H. L. Stormer. *Infrared spectroscopy of landau levels of graphene.* Physical Review Letters, **98**, 197403 (2007). 128

[310] L. G. Booshehri, C. H. Mielke, D. G. Rickel, S. A. Crooker, Q. Zhang, L. Ren, E. H. Hároz, A. Rustagi, C. J. Stanton, Z. Jin, Z. Sun, Z. Yan, J. M. Tour, J. Kono. *Circular polarization dependent cyclotron resonance in large-area graphene in ultrahigh magnetic fields.* Physical Review B, **85**, 205407 (2012). 128

[311] K. Takehana, Y. Imanaka, T. Takamasu, Y. Kim, K.-S. An. *Substrate dependence of cyclotron resonance on large-area CVD graphene.* Current Applied Physics, **14**, S119 (2014). 128

[312] L. Falkovsky, S. Pershoguba. *Optical far-infrared properties of a graphene monolayer and multilayer.* Physical Review B, **76**, 153410 (2007). 129

[313] Q. Bao, K. P. Loh. *Graphene photonics, plasmonics, and broadband optoelectronic devices.* ACS Nano, **6**, 3677 (2012). 129, 207

[314] L. Vicarelli, M. S. Vitiello, D. Coquillat, A. Lombardo, A. C. Ferrari, W. Knap, M. Polini, V. Pellegrini, A. Tredicucci. *Graphene field-effect transistors as room-temperature terahertz detectors.* Nature Materials, **11**, 865 (2012). 129, 207

[315] T. Morimoto, Y. Hatsugai, H. Aoki. *Cyclotron radiation and emission in graphene.* Physical Review B, **78**, 073406 (2008). 129, 150, 208

[316] M. Tokman, X. Yao, A. Belyanin. *Generation of entangled photons in graphene in a strong magnetic field.* Physical Review Letters, **110**, 077404 (2013). 129

[317] F. Bonaccorso, A. Lombardo, T. Hasan, Z. Sun, L. Colombo, A. C. Ferrari. *Production, Processing and Placement of Graphene and Two Dimensional Crystals.* Materials Today, **15**, 564 (2012). 129

[318] J. Wintterlin, M. L. Bocquet. *Graphene on metal surfaces.* Surface Science, **603**, 1841 (2009). 131

[319] X. Li, W. Cai, J. An, S. Kim, J. Nah, D. Yang, R. Piner, A. Velamakanni, I. Jung, E. Tutuc, S. K. Banerjee, L. Colombo, R. S. Ruoff. *Large-area synthesis of high-quality and uniform graphene films on copper foils.* Science, **324**, 1312 (2009). 131, 140

[320] A. Reina, X. Jia, J. Ho, D. Nezich, H. Son, V. Bulovic, M. Dresselhaus, J. Kong. *Large area, few-layer graphene films on arbitrary substrates by chemical vapor deposition.* Nano Letters, **9**, 30 (2009). 131

[321] K. S. Kim, Y. Zhao, H. Jang, S. Y. Lee, J. M. Kim, K. S. Kim, J.-H. Ahn, P. Kim, J.-Y. Choi, B. H. Hong. *Large-scale pattern growth of graphene films for stretchable transparent electrodes.* Nature, **457**, 706 (2009). 131

[322] X. Li, Y. Zhu, W. Cai, M. Borysiak, B. Han, D. Chen, R. D. Piner, L. Colombo, R. S. Ruoff. *Transfer of large-area graphene films for high-performance transparent conductive electrodes.* Nano Letters, **9**, 4359 (2009). 133

[323] J. Li, X.-Y. Wang, X.-R. Liu, Z. Jin, D. Wang, L.-J. Wan. *Facile growth of centimeter-sized single-crystal graphene on copper foil at atmospheric pressure.* J. Mater. Chem. C, **3**, 3530 (2015). 133

[324] P. Y. Huang, C. S. Ruiz-Vargas, A. M. van der Zande, W. S. Whitney, M. P. Levendorf, J. W. Kevek, S. Garg, J. S. Alden, C. J. Hustedt, Y. Zhu, J. Park, P. L. McEuen, D. A. Muller. *Grains and grain boundaries in single-layer graphene atomic patchwork quilts.* Nature, **469**, 389 (2011). 133

[325] Q. Yu, L. A. Jauregui, W. Wu, R. Colby, J. Tian, Z. Su, H. Cao, Z. Liu, D. Pandey, D. Wei, T. F. Chung, P. Peng, N. P. Guisinger, E. A. Stach, J. Bao, S.-S. Pei, Y. P. Chen. *Control and characterization of individual grains and grain boundaries in graphene grown by chemical vapour deposition.* Nature Materials, **10**, 443 (2011). 133

[326] H. S. Song, S. L. Li, H. Miyazaki, S. Sato, K. Hayashi, A. Yamada, N. Yokoyama, K. Tsukagoshi. *Origin of the relatively low transport mobility of graphene grown through chemical vapor deposition.* Scientific Reports, **2**, 337 (2012). 133

[327] L. Banszerus, M. Schmitz, S. Engels, J. Dauber, M. Oellers, F. Haupt, K. Watanabe, T. Taniguchi, B. Beschoten, C. Stampfer. *Ultrahigh-mobility graphene devices from chemical vapor deposition on reusable copper.* Science Advances, **1**, e1500222 (2015). 133, 227

[328] D. V. Badami. *X-Ray studies of graphite formed by decomposing silicon carbide.* Carbon, **3**, 53 (1965). 133

[329] A. J. van Bommel, J. E. Crombeen, A. van Tooren. *LEED and Auger electron observations of the SiC(0001) surface.* Surface Science, **48**, 463 (1975). 133

[330] C. Berger, Z. Song, T. Li, X. Li, A. Y. Ogbazghi, R. Feng, Z. Dai, A. N. Marchenkov, E. H. Conrad, P. N. First, W. A. de Heer. *Ultrathin Epitaxial Graphite: 2D Electron Gas Properties and a Route toward Graphene-based Nanoelectronics.* The Journal of Physical Chemistry B, **108**, 19912 (2004). 133

[331] W. A. de Heer, C. Berger, X. Wu, M. Sprinkle, Y. Hu, M. Ruan, J. A. Stroscio, P. N. First, R. Haddon, B. Piot, C. Faugeras, M. Potemski, J.-S. Moon. *Epitaxial graphene electronic structure and transport.* Journal of Physics D: Applied Physics, **43**, 374007 (2010). 133

[332] W. Norimatsu, M. Kusunoki. *Epitaxial graphene on SiC0001: advances and perspectives.* Physical Chemistry Chemical Physics, **16**, 3501 (2014). 133

[333] K. S. Novoselov, V. I. Fal'ko, L. Colombo, P. R. Gellert, M. G. Schwab, K. Kim. *A roadmap for graphene.* Nature, **490**, 192 (2012). 134

[334] Y. Hernandez, V. Nicolosi, M. Lotya, F. M. Blighe, Z. Sun, S. De, I. T. McGovern, B. Holland, M. Byrne, Y. K. Gun'Ko, J. J. Boland, P. Niraj, G. Duesberg, S. Krishnamurthy, R. Goodhue, J. Hutchison, V. Scardaci, A. C. Ferrari, J. N. Coleman. *High-yield production of graphene by liquid-phase exfoliation of graphite.* Nature Nanotechnology, **3**, 563 (2008). 134

[335] P. Blake, P. D. Brimicombe, R. R. Nair, T. J. Booth, D. Jiang, F. Schedin, L. A. Ponomarenko, S. V. Morozov, H. F. Gleeson, E. W. Hill, A. K. Geim, K. S. Novoselov. *Graphene-based liquid crystal device.* Nano Letters, **8**, 1704 (2008). 134

[336] M. Hirata, T. Gotou, S. Horiuchi, M. Fujiwara, M. Ohba. *Thin-film particles of graphite oxide 1: High-yield synthesis and flexibility of the particles.* Carbon, **42**, 2929 (2004). 134

[337] S. Stankovich, D. A. Dikin, G. H. B. Dommett, K. M. Kohlhaas, E. J. Zimney, E. A. Stach, R. D. Piner, S. T. Nguyen, R. S. Ruoff. *Graphene-based composite materials.* Nature, **442**, 282 (2006). 134

[338] J. Cai, P. Ruffieux, R. Jaafar, M. Bieri, T. Braun, S. Blankenburg, M. Muoth, A. P. Seitsonen, M. Saleh, X. Feng, K. Müllen, R. Fasel. *Atomically precise bottom-up fabrication of graphene nanoribbons.* Nature, **466**, 470 (2010). 135

[339] S. Fratini, F. Guinea. *Substrate-limited electron dynamics in graphene.* Physical Review B, **77**, 195415 (2008). 135

[340] X. Du, I. Skachko, A. Barker, E. Y. Andrei. *Approaching ballistic transport in suspended graphene.* Nature Nanotechnology, **3**, 491 (2008). 135

[341] D.-K. Ki, A. F. Morpurgo. *High-Quality Multiterminal Suspended Graphene Devices.* Nano Lett, **13**, 5165 (2013). 135

[342] X. Wang, M. Zhao, D. D. Nolte. *Optical contrast and clarity of graphene on an arbitrary substrate.* Applied Physics Letters, **95**, 081102 (2009). 135

[343] G. Giovannetti, P. Khomyakov, G. Brocks, P. Kelly, J. van den Brink. *Substrate-induced band gap in graphene on hexagonal boron nitride: Ab initio density functional calculations.* Physical Review B, **76**, 073103 (2007). 136

[344] C. R. Dean, A. F. Young, I. Meric, C. Lee, L. Wang, S. Sorgenfrei, K. Watanabe, T. Taniguchi, P. Kim, K. L. Shepard, J. Hone. *Boron nitride substrates for high-quality graphene electronics.* Nature Nanotechnology, **5**, 722 (2010). 136

[345] W. Wang, J. M. Kinaret. *Plasmons in graphene nanoribbons: Interband transitions and nonlocal effects.* Physical Review B, **87**, 195424 (2013). 136

[346] H. Park, P. R. Brown, V. Bulović, J. Kong. *Graphene As Transparent Conducting Electrodes in Organic Photovoltaics: Studies in Graphene Morphology, Hole Transporting Layers, and Counter Electrodes.* Nano Letters, **12**, 133 (2012). 136

[347] X. Huang, T. Leng, M. Zhu, X. Zhang, J. Chen, K. Chang, M. Aqeeli, A. K. Geim, K. S. Novoselov, Z. Hu. *Highly Flexible and Conductive Printed Graphene for Wireless Wearable Communications Applications.* Scientific Reports, **5**, 18298 (2015). 136

[348] M. Woszczyna, M. Friedemann, K. Pierz, T. Weimann, F. J. Ahlers. *Magneto-transport properties of exfoliated graphene on GaAs.* Journal of Applied Physics, **110**, 043712 (2011). 136

[349] P. Simonet, C. Rössler, T. Krähenmann, A. Varlet, T. Ihn, K. Ensslin, C. Reichl, W. Wegscheider. *Capacitive coupling in hybrid graphene/GaAs nanostructures.* Applied Physics Letters, **107**, 023105 (2015). 136

[350] S. Droscher, P. Roulleau, F. Molitor, P. Studerus, C. Stampfer, K. Ensslin, T. Ihn. *Quantum capacitance and density of states of graphene.* Applied Physics Letters, **96**, 152104 (2010). 137

[351] A. Varlet, M.-H. Liu, V. Krueckl, D. Bischoff, P. Simonet, K. Watanabe, T. Taniguchi, K. Richter, K. Ensslin, T. Ihn. *Fabry-Pérot Interference in Gapped Bilayer Graphene with Broken Anti-Klein Tunneling.* Physical Review Letters, **113**, 116601 (2014). 137

[352] J. Kröll, J. Darmo, K. Unterrainer. *Metallic wave-impedance matching layers for broadband terahertz optical systems.* Optics Express, **15**, 6552 (2007). 137

[353] T. P. Lodge. *A unique platform for materials design.* Science, **321**, 50 (2008). 137

[354] A. Das, S. Pisana, B. Chakraborty, S. Piscanec, S. K. Saha, U. V. Waghmare, K. S. Novoselov, H. R. Krishnamurthy, A. K. Geim, A. C. Ferrari, A. K. Sood. *Monitoring dopants by Raman scattering in an electrochemically top-gated graphene transistor.* Nature Nanotechnology, **3**, 210 (2008). 137, 141, 224

[355] D. Efetov, P. Kim. *Controlling Electron-Phonon Interactions in Graphene at Ultra-high Carrier Densities.* Physical Review Letters, **105**, 256805 (2010). 137

[356] J. H. Cho, J. Lee, Y. Xia, B. Kim, Y. He, M. J. Renn, T. P. Lodge, C. D. Frisbie. *Printable ion-gel gate dielectrics for low-voltage polymer thin-film transistors on plastic.* Nature Materials, **7**, 900 (2008). 137

[357] A. C. Ferrari, J. C. Meyer, V. Scardaci, C. Casiraghi, M. Lazzeri, F. Mauri, S. Piscanec, D. Jiang, K. S. Novoselov, S. Roth, A. K. Geim. *Raman Spectrum of Graphene and Graphene Layers.* Physical Review Letters, **97**, 187401 (2006). 137, 138

[358] Z. Ni, Y. Wang, T. Yu, Z. Shen. *Raman spectroscopy and imaging of graphene.* Nano Research, **1**, 273 (2008). 137, 138

[359] L. M. Malard, M. A. Pimenta, G. Dresselhaus, M. S. Dresselhaus. *Raman spectroscopy in graphene.* Physics Reports, **473**, 51 (2009). 138

[360] I. Calizo, W. Bao, F. Miao, C. N. Lau, A. A. Balandin. *The effect of substrates on the Raman spectrum of graphene: Graphene- on-sapphire and graphene-on-glass.* Applied Physics Letters, **91**, 201904 (2007). 138

[361] Y.-W. Tan, Y. Zhang, K. Bolotin, Y. Zhao, S. Adam, E. H. Hwang, S. Das Sarma, H. L. Stormer, P. Kim. *Measurement of Scattering Rate and Minimum Conductivity in Graphene.* Physical Review Letters, **99**, 10 (2007). 139, 140

[362] A. S. Mayorov, D. C. Elias, I. S. Mukhin, S. V. Morozov, L. A. Ponomarenko, K. S. Novoselov, A. K. Geim, R. V. Gorbachev. *How Close Can One Approach the Dirac Point in Graphene Experimentally?* Nano Letters, **12**, 4629 (2012). 139, 140

[363] J. A. Robinson, M. LaBella, M. Zhu, M. Hollander, R. Kasarda, Z. Hughes, K. Trumbull, R. Cavalero, D. Snyder. *Contacting graphene.* Applied Physics Letters, **98**, 053103 (2011). 139

[364] J. Martin, N. Akerman, G. Ulbricht, T. Lohmann, J. H. Smet, K. von Klitzing, A. Yacoby. *Observation of electronhole puddles in graphene using a scanning single-electron transistor.* Nature Physics, **4**, 144 (2008). 140

[365] Y. Todorov, C. Sirtori. *Intersubband polaritons in the electrical dipole gauge.* Physical Review B, **85** (2012). 143, 144, 146

[366] Y. Todorov, C. Sirtori. *Few-Electron Ultrastrong Light-Matter Coupling in a Quantum LC-Circuit.* Physical Review X, **4**, 041031 (2014). 143

[367] Y. Todorov, L. Tosetto, J. Teissier, A. M. Andrews, P. Klang, R. Colombelli, I. Sagnes, G. Strasser, C. Sirtori. *Optical properties of metal-dielectric-metal microcavities in the THz frequency range.* Optics Express, **18**, 13886 (2010). 144, 146, 203

[368] C. Maissen, G. Scalari, F. Valmorra, M. Beck, J. Faist, S. Cibella, R. Leoni, C. Reichl, C. Charpentier, W. Wegscheider. *Ultrastrong coupling in the near field of complementary split-ring resonators.* Physical Review B, **90**, 205309 (2014). 146, 148, 151, 152, 155, 171, 183, 199

[369] R. Stassi, A. Ridolfo, O. Di Stefano, M. J. Hartmann, S. Savasta. *Spontaneous conversion from virtual to real photons in the ultrastrong-coupling regime.* Physical Review Letters, **110**, 243601 (2013). 148

[370] A. Ridolfo, S. Savasta, M. J. Hartmann. *Nonclassical radiation from thermal cavities in the ultrastrong coupling regime.* Physical Review Letters, **110**, 16301 (2013). 148, 156

[371] A Ridolfo, M Leib, S Savasta, and M J Hartmann. Photon Blockade in the Ultrastrong Coupling Regime. *Physical Review Letters*, 109:193602, 2012. 148

[372] G. Günter, A. A. Anappara, J. Hees, A. Sell, G. Biasiol, L. Sorba, S. De Liberato, C. Ciuti, A. Tredicucci, A. Leitenstorfer, R. Huber. *Sub-cycle switch-on of ultrastrong lightmatter interaction.* Nature, **458**, 178 (2009). 148, 156

[373] C. M. Wilson, G. Johansson, A. Pourkabirian, M. Simoen, J. R. Johansson, T. Duty, F. Nori, P. Delsing. *Observation of the dynamical Casimir effect in a superconducting circuit.* Nature, **479**, 376 (2011). 148, 156

[374] G. Scalari, C. Maissen, D. Hagenmüller, S. De Liberato, C. Ciuti, C. Reichl, W. Wegscheider, D. Schuh, M. Beck, J. Faist. *Ultrastrong light-matter coupling at terahertz frequencies with split ring resonators and inter-Landau level transitions.* Journal of Applied Physics, **113**, 136510 (2013). 151, 171, 183, 254

[375] C. Maissen, G. Scalari, C. Reichl, W. Wegscheider, J. Faist. *Record high light-matter-coupling strength surpassing unity.* In *SPIE Photonics West - OPTO* (2016). 156

[376] P. Jouy, A. Vasanelli, Y. Todorov, A. Delteil, G. Biasiol, L. Sorba, C. Sirtori. *Transition from strong to ultrastrong coupling regime in mid-infrared metal-dielectric-metal cavities.* Applied Physics Letters, **98**, 231114 (2011). 156

[377] M. Geiser, F. Castellano, G. Scalari, M. Beck, L. Nevou, J. Faist. *Ultrastrong coupling regime and plasmon polaritons in parabolic semiconductor quantum wells.* Physical Review Letters, **108**, 106402 (2012). 156

[378] B. Askenazi, A. Vasanelli, a. Delteil, Y. Todorov, L. C. Andreani, G. Beaudoin, I. Sagnes, C. Sirtori. *Ultra-strong lightmatter coupling for designer Reststrahlen band.* New Journal of Physics, **16**, 043029 (2014). 156

[379] T. Niemczyk, F. Deppe, H. Huebl, E. P. Menzel, F. Hocke, M. J. Schwarz, J. J. Garcia-Ripoll, D. Zueco, T. Hümmer, E. Solano, A. Marx, R. Gross. *Circuit quantum electrodynamics in the ultrastrong-coupling regime.* Nature Physics, **6**, 772 (2010). 156, 203

[380] V. M. Muravev, I. V. Andreev, I. V. Kukushkin, S. Schmult, W. Dietsche. *Observation of hybrid plasmon-photon modes in microwave transmission of coplanar microresonators.* Physical Review B, **83**, 75309 (2011). 156

[381] T. Schwartz, J. A. Hutchison, C. Genet, T. W. Ebbesen. *Reversible Switching of Ultrastrong Light-Molecule Coupling.* Physical Review Letters, **106**, 196405 (2011). 156, 203

[382] F. Yoshihara, T. Fuse, S. Ashhab, K. Kakuyanagi, S. Saito, K. Semba. *Superconducting qubit-oscillator circuit beyond the ultrastrong-coupling regime.* arXiv:1602.00415, pp. 1–25 (2016). 156

[383] O. V. Kibis. *How to suppress the backscattering of conduction electrons?* Europhysics Letters, **107**, 57003 (2014). 156, 203

[384] S. Morina, O. V. Kibis, A. A. Pervishko, I. A. Shelykh. *Transport properties of a two-dimensional electron gas dressed by light.* Physical Review B, **91**, 155312 (2015). 156, 203

[385] J. Schachenmayer, C. Genes, E. Tignone, G. Pupillo, E. Orgiu, J. George, J. A. Hutchison, E. Devaux, J. F. Dayen, B. Doudin, F. Stellacci, C. Genet, J. Schachenmayer, C. Genes, G. Pupillo, P. Samorì, T. W. Ebbesen, E. Tignone, G. Pupillo.

Cavity-Enhanced Transport of Excitons. Physical Review Letters, **114**, 196403 (2015). 156, 203

[386] J. Feist, F. J. Garcia-Vidal. *Extraordinary Exciton Conductance Induced by Strong Coupling.* Physical Review Letters, **114**, 196402 (2015). 156, 203

[387] E. Orgiu, J. George, J. A. Hutchison, E. Devaux, J. F. Dayen, B. Doudin, F. Stellacci, C. Genet, J. Schachenmayer, C. Genes, G. Pupillo, P. Samorì, T. W. Ebbesen. *Conductivity in organic semiconductors hybridized with the vacuum field.* Nature Materials, **14**, 1123 (2015). 156, 203

[388] D. Heitmann. *Two-dimensional plasmons in homogeneous and laterally microstructured space charge layers.* Surface Science, **170**, 332 (1986). 157, 158

[389] E. Vasiliadou, G. Muller, D. Heitmann, D. Weiss, K. Klitzing, K. von Klitzing. *Collective response in the microwave photoconductivity of hall bar structures.* Physical Review B, **48**, 17145 (1993). 157, 158, 160, 162, 198, 248, 265

[390] S. J. Allen Jr., H. L. Stoermer, J. C. M. Hwang. *Dimensional resonance of the two-dimensional electron gas in selectively doped GaAs/AlGaAs heterostructures.* Physical Review B, **28**, 4875 (1983). 157, 162, 249

[391] E. Vasiliadou, R. Fleischmann, D. Weiss, D. Heitmann, K. V. Klitzing, T. Geisel, R. Bergmann, H. Schweizer, C. T. Foxon. *Cyclotron-resonance anomalies in an antidot array measured by microwave photoconductivity.* Physical Review B, **52**, R8658 (1995). 157, 162, 163, 248

[392] J. P. Kotthaus, G. Abstreiter, J. F. Koch. *Subharomic Structure of Cyclotron Resonance in an Inverison Layer on Si.* Solid State Communications, **15**, 517 (1974). 158

[393] T. N. Theis. *Plasmons in inversion layers.* Surface Science Letters, **98**, 515 (1980). 158

[394] A. Otto. *Excitation of Nonradiative Surface Plasma Waves in Silver by the Method of Frustrated Total Reflection.* Zeitschrift fuer Physik, **216**, 398 (1968). 158

[395] E. Kretschmann. *The angular dependence and the polarisatino of light emitted by surface plasmons on metals due to roughness.* Optics Communications, **5**, 331 (1972). 158

[396] T. Demel, D. Heitmann, P. Grambow, K. Ploog. *Far-infrared response of one-dimensional electronic systems in single- and two-layered quantum wires.* Physical Review B, **38**, 12732 (1988). 158

[397] E. Diessel, G. Mueller, D. Weiss, K. Von Klitzing, K. Ploog, H. Nickel, W. Schlapp, R. Loesch. *Novel far-infrared-photoconductor based on photon-induced interedge channel scattering.* Applied Physics Letters, **58**, 2231 (1991). 158

[398] R. Merz, F. Keilmann, R. J. Haug, K. Ploog. *Nonequilibrium edge-state transport resolved by far-infrared microscopy.* Physical Review Letters, **70**, 651 (1993). 158

[399] F. Neppl, J. P. Kotthaus, J. F. Koch. *Mechanism of intersubband resonant photoresponse.* Physical Review B, **19**, 5240 (1979). 158

[400] D. Stein, K. Klitzing, G. Weimann. *Electron Spin Resonance on GaAs-$Al_xGa_{1-x}As$ Heterostructures.* Physical Review Letters, **51**, 130 (1983). 158

[401] M. Dobers, K. von Klitzing, G. Weimann. *Electron-spin resonance in the two-dimensional electron gas of GaAs-$Al_xGa_{1-x}As$ heterostructures.* Physical Review B, **38**, 5453 (1988). 158

[402] F. Stern. *Polarizability of a two-dimensional electron gas.* Physical Review Letters, **18**, 546 (1967). 158

[403] S. A. Mikhailov, N. Savostianova. *Microwave response of a two-dimensional electron stripe.* Physical Review B, **71**, 035320 (2005). 159, 198, 201

[404] I. V. Kukushkin, J. H. Smet, S. A. Mikhailov, D. V. Kulakovskii, K. von Klitzing, W. Wegscheider. *Observation of retardation effects in the spectrum of two-dimensional plasmons.* Physical Review Letters, **90**, 156801 (2003). 159

[405] M. A. Zudov, R. R. Du. *Shubnikovde Haas-like oscillations in millimeterwave photoconductivity in a high-mobility two-dimensional electron gas.* Physical Review B, **64**, 201311 (2001). 160, 161, 162, 163, 248

[406] R. G. Mani, J. H. Smet, K. von Klitzing, V. Narayanamurti, W. B. Johnson, V. Umansky. *Zero-resistance states induced by electromagnetic-wave excitation in GaAs/AlGaAs heterostructures.* Nature, **420**, 646 (2002). 160, 161, 162, 163, 248

[407] S. A. Mikhailov. *Microwave-induced magnetotransport phenomena in two-dimensional electron systems: Importance of electrodynamic effects [59].* Physical Review B, **70**, 165311 (2004). 160, 166

[408] M. A. Zudov. *Period and phase of microwave-induced resistance oscillations and zero-resistance states in two-dimensional electron systems.* Physical Review B, **69**, 041304 (2004). 160

[409] R. G. Mani, J. H. Smet, K. V. Klitzing, V. Narayanamurti, W. B. Johnson, V. Umansky. *Demonstration of a 1/4 -Cycle Phase Shift in the Radiation-Induced Oscillatory Magnetoresistance in GaAs/AlGaAs Devices.* Physical Review Letters, **92**, 146801 (2004). 160, 162

[410] I. A. Dmitriev, A. D. Mirlin, D. G. Polyakov, M. A. Zudov. *Nonequilibrium phenomena in high Landau levels.* Reviews of Modern Physics, **84**, 1709 (2012). 160, 164

[411] S. A. Mikhailov. *Microwave-induced zero-resistance states and second-harmonic generation in an ultraclean two-dimensional electron gas.* Physical Review B, **89**, 045410 (2014). 160, 166, 177

[412] A. T. Hatke, M. A. Zudov, J. D. Watson, M. J. Manfra. *Magnetoplasmon resonance in a two-dimensional electron system driven into a zero-resistance state.* Physical Review B, **85**, 121306R (2012). 160, 162, 163, 166, 248

[413] I. V. Andreev, V. M. Muravev, I. V. Kukushkin, S. Schmult, W. Dietsche. *High-frequency response of a two-dimensional electron system under microwave irradiation.* Physical Review B, **83**, 121308 (2011). 162, 163, 248

[414] I. Kukushkin, V. Muravev, J. Smet, M. Hauser, W. Dietsche, K. von Klitzing. *Collective excitations in two-dimensional electron stripes: Transport and optical detection of resonant microwave absorption.* Physical Review B, **73**, 113310 (2006). 162, 248

[415] S. I. Gubarev, A. A. Dremin, V. E. Kozlov, V. M. Murav'ev, I. V. Kukushkin. *Plasma waves in a two-dimensional electron system laterally screened by a metallic gate.* JETP Letters, **90**, 539 (2009). 162, 249

[416] S. A. Studenikin, M. Potemski, A. S. Sachrajda, M. Hilke, L. N. Pfeiffer, K. W. West. *Microwave absorption/reflection and magneto-transport experiments on high-mobility electron gas.* IEEE Transactions on Nanotechnology, **4**, 124 (2005). 162, 248

[417] Z. D. Kvon, D. A. Kozlov, S. N. Danilov, C. Zoth, P. Vierling, S. Stachel, V. V. Bel'kov, A. K. Bakarov, D. V. Dmitriev, A. I. Toropov, S. D. Ganichev. *Terahertz radiation-induced magnetoresistance oscillations of a high-density and high-mobility two-dimensional electron gas.* JETP Letters, **97**, 41 (2013). 162, 248

[418] S. Wiedmann, G. M. Gusev, O. E. Raichev, A. K. Bakarov, J. C. Portal. *Zero-resistance states in bilayer electron systems induced by microwave irradiation.* Journal of Physics: Conference Series, **334**, 012014 (2011). 162, 249

[419] R. G. Mani, A. N. Ramanayaka, W. Wegscheider. *Observation of linear-polarization-sensitivity in the microwave-radiation-induced magnetoresistance oscillations.* Physical Review B, **84**, 085308 (2011). 162, 248

[420] R. G. Mani, J. Smet, K. Klitzing, V. Narayanamurti, W. Johnson, V. Umansky. *Radiation-induced oscillatory magnetoresistance as a sensitive probe of the zero-field spin-splitting in high-mobility $GaAs/Al_xGa_{1-x}As$ devices.* Physical Review B, **69**, 193304 (2004). 162, 248

[421] W. Zhang, M. A. Zudov, L. Pfeiffer, K. West. *Effect of dc excitation on microwave-induced resistance oscillations and zero-resistance states in a two-dimensional electron system.* Physica E: Low-dimensional Systems and Nanostructures, **40**, 982 (2008). 162, 248

[422] M. Bialek, M. Czapkiewicz, J. Wróbel, V. Umansky, J. Łusakowski, V. Umansky, J. Łusakowski. *Plasmon dispersions in high electron mobility terahertz detectors.* Applied Physics Letters, **104**, 263514 (2014). 162, 248

[423] Z. Q. Yuan, C. L. Yang, R. R. Du, L. N. Pfeiffer, K. W. West. *Microwave photoresistance of a high-mobility two-dimensional electron gas in a triangular antidot lattice.* Physical Review B, **74**, 075313 (2006). 162, 163, 248

[424] A. N. Ramanayaka, R. G. Mani, W. Wegscheider. *Microwave-induced electron heating in the regime of radiation-induced magnetoresistance oscillations.* Physical Review B, **83**, 165303 (2011). 162, 248

[425] A. Wirthmann, B. D. McCombe, D. Heitmann, S. Holland, K.-J. Friedland, C.-M. Hu. *Far-infrared-induced magnetoresistance oscillations in $GaAs/Al_xGa_{1-x}As$-based two-dimensional electron systems.* Physical Review B, **76**, 195315 (2007). 162, 248

[426] M. A. Zudov, R. R. Du, L. N. Pfeiffer, K. W. West. *Evidence for a new dissipationless effect in 2D electronic transport.* Physical review letters, **90**, 046807 (2003). 162, 163, 248

[427] A. D. Levin, Z. S. Momtaz, G. M. Gusev, A. K. Bakarov. *Microwave-induced nonlocal transport in a two-dimensional electron system.* Physical Review B, **89**, 161304R (2014). 162, 163, 248

[428] A. T. Hatke, M. A. Zudov, J. D. Watson, M. J. Manfra, L. N. Pfeiffer, K. W. West. *Effective mass from microwave photoresistance measurements in GaAs/AlGaAs quantum wells.* Journal of Physics: Conference Series, **456**, 012040 (2013). 162, 248

[429] B. G. L. Jager, S. Wimmer, A. Lorke, J. P. Kotthaus, W. Wegscheider, M. Bichler. *Edge and bulk effects in Terahertz photoconductivity of an antidot superlattice.* Physical Review B, **63**, 045315 (2001). 162, 163, 248

[430] K. Kern, D. Heitmann, P. Grambow, Y. H. Zhang, K. Ploog. *Collective excitations in antidots.* Physical Review Letters, **66**, 1618 (1991). 162, 163, 249

[431] V. M. Muravev, C. Jiang, I. V. Kukushkin, J. H. Smet, V. Umansky, K. von Klitzing. *Spectra of magnetoplasma excitations in back-gate Hall bar structures.* Physical Review B, **75**, 193307 (2007). 162, 248

[432] A. T. Hatke, M. A. Zudov, L. N. Pfeiffer, K. W. West. *Giant microwave photoresistivity in high-mobility quantum Hall systems.* Physical Review B, **83**, 121301R (2011). 162, 248

[433] P. Q. Liu, F. Valmorra, C. Maissen, J. Keller, G. Scalari, J. Faist. *Large-area gate-tunable terahertz plasmonic metasurfaces employing graphene based structures.* SPIE Photonics West - OPTO, **9357**, 935707 (2015). 162, 248

[434] A. N. Ramanayaka, R. G. Mani, J. Iñarrea, W. Wegscheider. *Effect of rotation of the polarization of linearly polarized microwaves on the radiation-induced magnetoresistance oscillations.* Physical Review B, **85**, 205315 (2012). 162, 248

[435] T. Ye, H.-C. Liu, Z. Wang, W. Wegscheider, R. G. Mani. *Comparative study of microwave radiation-induced magnetoresistive oscillations induced by circularly- and linearly- polarized photo-excitation.* Scientific Reports, **5**, 14880 (2015). 162, 248

[436] X. C. Yang, H. M. Wang, T. R. Wu, F. Q. Huang, J. Chen, X. X. Kang, Z. Jin, X. M. Xie, M. H. Jiang. *Magnetotransport of polycrystalline graphene: Shubnikov-de Haas oscillation and weak localization study.* Applied Physics Letters, **102**, 233503 (2013). 162

[437] I. V. Andreev, V. M. Murav'ev, I. V. Kukushkin, J. H. Smet, K. Klitzing, V. Umanskii. *Contactless measurement of the conductivity of two-dimensional electrons in the regime of microwave-induced giant magnetoresistance oscillations.* JETP Letters, **88**, 616 (2009). 162, 248

[438] S. A. Studenikin, O. N. Fedorych, D. K. Maude, M. Potemski, A. S. Sachrajda, Z. R. Wasilewski, J. A. Gupta, L. I. Magarill. *A quasi-classical mechanism for microwave induced resistance oscillations in high mobility GaAs/AlGaAs 2DEG samples.* Physica E: Low-Dimensional Systems and Nanostructures, **40**, 1424 (2008). 162, 163, 248

[439] R. L. Willett, L. N. Pfeiffer, K. W. West. *Evidence for current-flow anomalies in the irradiated 2D electron system at small magnetic fields.* Physical Review Letters, **93**, 026804 (2004). 162, 248

[440] A. A. Bykov, A. K. Bakarov, D. R. Islamov, A. I. Toropov. *Giant magnetoresistance oscillations induced by microwave radiation and a zero-resistance state in a 2D electron system with a moderate mobility.* JETP Letters, **84**, 391 (2006). 162, 248

[441] A. A. Bykov, I. V. Marchishin, A. V. Goran, D. V. Dmitriev. *Microwave induced zero-conductance state in a Corbino geometry two-dimensional electron gas with capacitive contacts.* Applied Physics Letters, **97**, 082107 (2010). 162, 163, 248

[442] S. I. Dorozhkin. *Giant magnetoresistance oscillations caused by cyclotron resonance harmonics.* Journal of Experimental and Theoretical Physics Letters, **77**, 577 (2003). 162, 164, 248

[443] T. Ye, H.-C. Liu, Z. Wang, W. Wegscheider, R. G. Mani. *Comparative study of microwave radiation-induced magnetoresistive oscillations induced by circularly- and linearly- polarized photo-excitation.* Scientific Reports, **5**, 14880 (2015). 162

[444] J. H. Smet, B. Gorshunov, C. Jiang, L. Pfeiffer, K. West, V. Umanksy, M. Dressel, R. Meisels, F. Kuchar, K. Von Klitzing. *Circular-polarization-dependent study of the microwave photoconductivity in a two-dimensional electron system.* Physical Review Letters, **95**, 116804 (2005). 162

[445] C. L. Yang, M. A. Zudov, T. A. Knuuttila, R. R. Du, L. N. Pfeiffer, K. W. West. *Observation of microwave-induced zero-conductance state in Corbino rings of a two-dimensional electron system.* Physical review letters, **91**, 096803 (2003). 163, 248

[446] A. A. Bykov. *Microwave Photoresistance of a Two-Dimensional Electron Gas in a Ballistic Microbar.* JETP Letters, **89**, 575 (2009). 163, 179, 188

[447] R. R. Du, M. A. Zudov, C. L. Yang, Z. Q. Yuan, L. N. Pfeiffer, K. W. West. *Oscillatory and Vanishing Resistance States in Microwave Irradiated 2D Electron Systems.* International Journal of Modern Physics B, **18**, 3465 (2004). 163, 249

[448] Z. Q. Yuan, R. R. Du, M. J. Manfra, L. N. Pfeiffer, K. W. West. *Landau level spectrum in a two-dimensional hole gas in C-doped (100) GaAs/ $Al_{0.4}Ga_{0.6}As$ square quantum well.* Applied Physics Letters, **94**, 052103 (2009). 163, 249

[449] V. E. Kozlov, S. I. Gubarev, I. V. Kukushkin. *Magnetoplasma resonance in a GaAs/AlGaAs quantum well in a strong parallel magnetic field.* JETP Letters, **94**, 397 (2011). 163, 249

[450] R. G. Mani, J. Hankinson, C. Berger, W. a. de Heer. *Observation of resistively detected hole spin resonance and zero-field pseudo-spin splitting in epitaxial graphene.* Nature Communications, **3**, 996 (2012). 163, 249

[451] S. Sassine, Y. Krupko, E. B. Olshanetsky, Z. D. Kvon, J. C. Portal, J. M. Hartmann, J. Zhang. *Microwave radiation induced collective response in Si/SiGe heterostructures with a 2D electron gas.* Solid State Communications, **142**, 631 (2007). 163, 249

[452] V. E. Kozlov, A. B. Van'Kov, S. I. Gubarev, I. V. Kukushkin, V. V. Solovyev, J. Falson, D. Maryenko, Y. Kozuka, A. Tsukazaki, M. Kawasaki, J. H. Smet. *Microwave magnetoplasma resonances of two-dimensional electrons in MgZnO/ZnO heterojunctions.* Physical Review B, **91**, 085304 (2015). 163, 249

[453] M. A. Zudov, O. A. Mironov, Q. A. Ebner, P. D. Martin, Q. Shi, D. R. Leadley. *Observation of microwave-induced resistance oscillations in a high-mobility two-dimensional hole gas in a strained Ge/SiGe quantum well.* Physical Review B, **89**, 125401 (2014). 163, 249

[454] D. Kärcher, A. V. Shchepetilnikov, Y. A. Nefyodov, J. Falson, I. A. Dmitriev, Y. Kozuka, D. Maryenko, A. Tsukazaki, S. I. Dorozhkin, I. V. Kukushkin, M. Kawasaki, J. H. Smet. *Observation of microwave induced resistance and photovoltage oscillations in MgZnO / ZnO heterostructures.* Physical Review B, **93**, 041410R (2016). 163, 249

[455] D. Konstantinov, K. Kono. *Novel radiation-Induced magnetoresistance oscillations in a nondegenerate two-dimensional electron system on liquid helium.* Physical Review Letters, **103**, 266808 (2009). 163

[456] D. Konstantinov, K. Kono. *Photon-induced vanishing of magnetoconductance in 2D electrons on liquid helium.* Physical Review Letters, **105**, 226801 (2010). 163

[457] C. L. Yang, J. Zhang, R. R. Du, J. A. Simmons, J. L. Reno. *Zener Tunneling Between Landau Orbits in a High-Mobility Two-Dimensional Electron Gas.* Physical Review Letters, **89**, 076801 (2002). 163

[458] M. a. Zudov, I. V. Ponomarev, A. L. Efros, R. R. Du, J. A. Simmons, J. L. Reno. *New class of magnetoresistance oscillations: Interaction of a two-dimensional electron gas with leaky interface phonons.* Physical Review Letters, **86**, 3614 (2001). 163

[459] A. C. Durst, S. Sachdev, N. Read, S. M. Girvin. *Radiation-Induced Magnetoresistance Oscillations in a 2D Electron Gas.* Physical Review Letters, **91**, 086803 (2003). 164, 165

[460] V. Ryzhii, V. Vyurkov. *Absolute negative conductivity in two-dimensional electron systems associated with acoustic scattering stimulated by microwave radiation.* Physical Review B, **68**, 165406 (2003). 164

[461] A. V. Andreev, I. L. Aleiner, A. J. Millis. *Dynamical Symmetry Breaking as the Origin of the Zero-dc-Resistance State in an ac-Driven System.* Physical Review Letters, **91**, 56803 (2003). 164

[462] X. L. Lei, S. Y. Liu. *Radiation-Induced Magnetoresistance Oscillation in a Two-Dimensional Electron Gas in Faraday Geometry.* Physical Review Letters, **91**, 226805 (2003). 164

[463] I. A. Dmitriev, A. D. Mirlin, D. G. Polyakov. *Cyclotron-Resonance Harmonics in the ac Response of a 2D Electron Gas with Smooth Disorder.* Physical Review Letters, **91**, 226802 (2003). 164, 165

[464] J. Iñarrea, G. Platero. *Theoretical Approach to Microwave-Radiation-Induced Zero-Resistance States in 2D Electron Systems.* Physical Review Letters, **94**, 016806 (2005). 164, 166

[465] S. A. Mikhailov. *Theory of microwave-induced zero-resistance states in two-dimensional electron systems.* Physical Review B, **83**, 155303 (2011). 166, 167, 201

[466] M. A. Zudov. *Comment on "Theory of microwave-induced zero-resistance states in two-dimensional electron system" and on "Microwave-induced zero-resistance states and second-harmonic generation in an ultraclean two-dimensional electron ga".* Physical Review B, **92**, 047301 (2015). 166

[467] S. A. Mikhailov. *Reply to Comment on Theory of microwave-induced zero-resistance states in two-dimensional electron systems' and on Microwave-induced zero-resistance states and second-harmonic generation in an ultraclean two-dimensional electron gas'* . Physical Review B, **92**, 047302 (2015). 166

[468] A. D. Chepelianskii, D. L. Shepelyansky. *Microwave stabilization of edge transport and zero-resistance states.* Physical Review B, **80**, 241308 (2009). 166, 167, 179, 187

[469] O. V. Zhirov, a. D. Chepelianskii, D. L. Shepelyansky. *Towards a synchronization theory of microwave-induced zero-resistance states.* Physical Review B, **88**, 1 (2013). 166, 167

[470] G. L. Paravicini-Bagliani, G. Scalari, F. Valmorra, J. Keller, C. Maissen, M. Beck, J. Faist. *Tunable ultra-strong coupling between magneto-plasmon and split-ring cavity.* In *EOS THz topical meeting* (2016). 169, 201

[471] G. Balasubramanian, P. Neumann, D. Twitchen, M. Markham, R. Kolesov, N. Mizuochi, J. Isoya, J. Achard, J. Beck, J. Tissler, V. Jacques, P. R. Hemmer, F. Jelezko, J. Wrachtrup. *Ultralong spin coherence time in isotopically engineered diamond.* Nature Materials, **8**, 383 (2009). 203

[472] J. J. Viennot, M. C. Dartiailh, A. Cottet, T. Kontos. *Coherent coupling of a single spin to microwave cavity photons.* Science, **349**, 408 (2015). 203

[473] M. R. Delbecq, L. E. Bruhat, J. J. Viennot, S. Datta, A. Cottet, T. Kontos. *Photon-mediated interaction between distant quantum dot circuits.* Nature Communications, **4**, 1400 (2013). 203

[474] I. Carusotto, C. Ciuti. *Quantum fluids of light.* Reviews of Modern Physics, **85**, 299 (2013). 203

[475] a. Imamoglu, R. Ram, S. Pau, Y. Yamamoto. *Nonequilibrium condensates and lasers without inversion: Exciton-polariton lasers.* Physical Review A, **53**, 4250 (1996). 203

[476] G. Günter, a. a. Anappara, J. Hees, A. Sell, G. Biasiol, L. Sorba, S. De Liberato, C. Ciuti, A. Tredicucci, A. Leitenstorfer, R. Huber. *Sub-cycle switch-on of ultrastrong light-matter interaction.* Nature, **458**, 178 (2009). 203

[477] S. Komiyama, O. Asta, V. Antonov, T. Kutsuwa, H. Hirai. *A single-photon detector in the far-infrared range.* Nature, **403**, 405 (2000). 203

[478] A. Leitenstorfer, R. Huber, A. Sell, A. A. Anappara, G. Günter, S. Leinss, K. von Volkmann, T. Kampfrath, M. Wolf, S. de Liberato, C. Ciuti, G. Biasiol, L. Sorba, A. Tredicucci. *Terahertz Quantum Optics with Solid-state Systems.* In *35th International Conference on Infrared, Millimeter, and Terahertz Waves*, p. 1. IEEE (2010). 203

[479] C. Riek, D. V. Seletskiy, A. S. Moskalenko, J. F. Schmidt, P. Krauspe, S. Eckart, S. Eggert, G. Burkard, A. Leitenstorfer. *Direct sampling of electric-field vacuum fluctuations.* Science, **350**, 420 (2015). 203

[480] I.-C. Benea-Chelmus, C. Bonzon, C. Maissen, G. Scalari, M. Beck, J. Faist. *Subcycle measurement of intensity correlations in the terahertz frequency range.* Physical Review A, **93**, 043812 (2016). 203

[481] S. H. Lee, M. Choi, T.-T. Kim, S. Lee, M. Liu, X. Yin, H. K. Choi, S. S. Lee, C.-G. Choi, S.-Y. Choi, X. Zhang, B. Min. *Switching terahertz waves with gate-controlled active graphene metamaterials.* Nature Materials, **11**, 936 (2012). 207, 213, 221, 222, 223, 224

[482] V. Ryzhii, A. A. Dubinov, T. Otsuji, V. Mitin, M. S. Shur. *Terahertz lasers based on optically pumped multiple graphene structures with slot-line and dielectric waveguides.* Journal of Applied Physics, **107**, 054505 (2010). 208

[483] F. Rana. *Graphene Terahertz Plasmon Oscillators.* IEEE Transactions on Nanotechnology, **7**, 91 (2008). 208

[484] B. Huard, N. Stander, J. A. Sulpizio, D. Goldhaber-Gordon. *Evidence of the role of contacts on the observed electron-hole asymmetry in graphene.* Physical Review B, **78**, 121402 (2008). 209

[485] T. Mueller, F. Xia, M. Freitag, J. Tsang, P. Avouris. *Role of contacts in graphene transistors: A scanning photocurrent study.* Physical Review B, **79**, 245430 (2009). 209

[486] Y. Zou, P. Tassin, T. Koschny, C. M. Soukoulis. *Interaction between graphene and metamaterials: split rings vs. wire pairs.* Optics Express, **20**, 12198 (2012). 210, 213, 218, 222

[487] L. Ren, Q. Zhang, J. Yao, Z. Sun, R. Kaneko, Z. Yan, S. Nanot, Z. Jin, I. Kawayama, M. Tonouchi, J. M. Tour, J. Kono. *Terahertz and infrared spectroscopy of gated large-area graphene.* Nano Letters, **12**, 3711 (2012). 211

[488] N. Papasimakis, Z. Luo, Z. X. Shen, F. De Angelis, E. Di Fabrizio, A. E. Nikolaenko, N. I. Zheludev. *Graphene in a photonic metamaterial.* Optics Express, **18**, 8353 (2010). 213, 222

[489] J. Kim, H. Son, D. J. Cho, B. Geng, W. Regan, S. Shi, K. Kim, A. Zettl, Y.-R. Shen, F. Wang. *Electrical Control of Optical Plasmon Resonance with Graphene.* Nano Letters, **12**, 5598 (2012). 213, 222

[490] N. K. Emani, T.-F. Chung, X. Ni, A. V. Kildishev, Y. P. Chen, A. Boltasseva. *Electrically tunable damping of plasmonic resonances with graphene.* Nano Letters, **12**, 5202 (2012). 213, 222

[491] B. Sensale-Rodriguez, R. Yan, M. M. Kelly, T. Fang, K. Tahy, W. S. Hwang, D. Jena, L. Liu, H. G. Xing. *Broadband graphene terahertz modulators enabled by intraband transitions.* Nature Communications, **3**, 780 (2012). 213, 222

[492] N. Liu, F. Wen, Y. Zhao, Y. Wang, P. Nordlander, N. J. Halas, A. Alù. *Individual nanoantennas loaded with three-dimensional optical nanocircuits.* Nano Letters, **13**, 142 (2013). 218, 219

[493] J. S. Gomez-Diaz, J. Perruisseau-Carrier, P. Sharma, A. Ionescu. *Non-contact characterization of graphene surface impedance at micro and millimeter waves.* Journal of Applied Physics, **111**, 114908 (2012). 221

[494] I. Maeng, S. C. Lim, S. J. Chae, Y. H. Lee, H. Choi, J.-H. Son. *Gate-controlled nonlinear conductivity of Dirac fermion in graphene field-effect transistors measured by terahertz time-domain spectroscopy.* Nano Letters, **12**, 551 (2012). 221

[495] B. Sensale-Rodriguez, R. Yan, S. Rafique, M. Zhu, W. Li, X. Liang, D. Gundlach, V. Protasenko, M. M. Kelly, D. Jena, L. Liu, H. G. Xing. *Extraordinary control of terahertz beam reflectance in graphene electro-absorption modulators.* Nano Letters, **12**, 4518 (2012). 223

[496] R. Degl'Innocenti, D. S. Jessop, Y. D. Shah, J. Sibik, J. A. Zeitler, P. R. Kidambi, S. Hofmann, H. E. Beere, D. A. Ritchie. *Low-Bias Terahertz Amplitude Modulator Based on Split-Ring Resonators and Graphene.* ACS Nano, **8**, 2548 (2014). 223

[497] Y. Wu, C. La-o vorakiat, X. Qiu, J. Liu, P. Deorani, K. Banerjee, J. Son, Y. Chen, E. E. M. Chia, H. Yang. *Graphene Terahertz Modulators by Ionic Liquid Gating.* Advanced Materials, **27**, 1874 (2015). 223

[498] M. Tamagnone, A. Fallahi, J. R. Mosig, J. Perruisseau-Carrier. *Fundamental limits and near-optimal design of graphene modulators and non-reciprocal devices.* Nature Photonics, **8**, 556 (2014). 224

[499] P. Liu, I. Luxmoore, S. Mikhailov, N. Savostianova, F. Valmorra, J. Faist, G. Nash. *Highly tunable hybrid metamaterials employing split-ring resonators strongly coupled to graphene surface plasmons.* Nature Communications, **6**, 8969 (2015). 224

[500] I. J. Luxmoore, C. H. Gan, P. Q. Liu, F. Valmorra, P. Li, J. Faist, G. R. Nash. *Strong Coupling in the Far-Infrared between Graphene Plasmons and the Surface Optical Phonons of Silicon Dioxide.* ACS Photonics, **1**, 1151 (2014). 224

[501] P. Q. Liu, F. Valmorra, C. Maissen, J. Faist. *Electrically tunable graphene anti-dot array terahertz plasmonic crystals exhibiting multi-band resonances.* Optica, **2**, 135 (2015). 224

[502] S. Zanotto, C. Lange, T. Maag, A. Pitanti, V. Miseikis, C. Coletti, R. Degl'Innocenti, L. Baldacci, R. Huber, A. Tredicucci. *Magneto-optic transmittance modulation observed in a hybrid graphenesplit ring resonator terahertz metasurface.* Applied Physics Letters, **107**, 121104 (2015). 225

[503] F. P. Laussy, E. del Valle, C. Tejedor. *Strong Coupling of Quantum Dots in Microcavities.* Physical Review Letters, **101**, 083601 (2008). 225

[504] M. S. Vitiello, G. Scamarcio, V. Spagnolo, J. Alton, S. Barbieri, C. Worrall, H. E. Beere, D. a. Ritchie, C. Sirtori. *Thermal properties of THz quantum cascade lasers based on different optical waveguide configurations.* Applied Physics Letters, **89**, 021111 (2006). 237

[505] M. S. Vitiello, G. Scamarcio, V. Spagnolo, B. S. Williams, S. Kumar, Q. Hu, J. L. Reno. *Measurement of subband electronic temperatures and population inversion in THz quantum-cascade lasers.* Applied Physics Letters, **86**, 111115 (2005). 237

[506] M. S. Vitiello, G. Scamarcio, J. Faist, G. Scalari, C. Walther, H. E. Beere, D. A. Ritchie. *Probing quantum efficiency by laser-induced hot-electron cooling.* Applied Physics Letters, **94**, 021115 (2009). 237

[507] I. Fernandez-Corbaton, S. Nanz, R. Alaee. *Exact dipolar moments of a localized electric current distribution.* Optics Express, **23**, 33044 (2015). 239

[508] R. Marques, F. Medina, R. Rafii-el idrissi. *Role of bianisotropy in negative permeability and left-handed metamaterials.* Physical Review B, **65**, 144440 (2002). 239

[509] C. R. Simovski, B. Sauviac. *Toward creating isotropic microwave composites with negative refraction.* Radio Science, **39**, RS2014 (2004). 239

[510] M. G. Calkin. *An Invariance Property of the Free Electromagnetic Field.* American Journal of Physics, **33**, 958 (1965). 241

[511] I. Fernandez-Corbaton, X. Zambrana-Puyalto, N. Tischler, X. Vidal, M. L. Juan, G. Molina-Terriza. *Electromagnetic Duality Symmetry and Helicity Conservation for the Macroscopic Maxwell's Equations.* Physical Review Letters, **111**, 060401 (2013). 241, 242

[512] I. Bialynicki-Birula, Z. Bialynicki-Birula. *Beams of electromagnetic radiation carrying angular momentum : The Riemann Silberstein vector and the classical quantum correspondence.* Optics Communications, **264**, 342 (2006). 241

[513] I. Fernandez-Corbaton, G. Molina-Terriza. *Role of duality symmetry in transformation optics.* Physical Review B, **88**, 085111 (2013). 241

[514] I. Fernandez-Corbaton, M. Fruhnert, C. Rockstuhl. *Objects of Maximum Electromagnetic Chirality.* Physical Review X, **6**, 031013 (2016). 242

[515] H. van Houten, J. G. Williamson, M. E. I. Broekaart, C. T. Foxon, J. J. Harris. *Magnetoresistance in a GaAs-$Al_xGa_{1-x}As$ heterostructure with double subband occupancy.* Physical Review B, **37**, 2756 (1988). 259

[516] X. Li, W. Cai, J. An, S. Kim, J. Nah, D. Yang, R. Piner, A. Velamakanni, I. Jung, E. Tutuc, S. K. Banerjee, L. Colombo, R. S. Ruoff. *Large-area synthesis of high-quality and uniform graphene films on copper foils.* Science, **324**, 1312 (2009). 270